SCUOLA DI DOTTORATO

UNIVERSITÀ DEGLI STUDI DI MILANO-BICOCCA

Dipartimento di / Department of
Fisica "Giuseppe Occhialini"

Dottorato di Ricerca in / PhD program **FISICA e ASTRONOMIA** Ciclo / Cycle **XXXVI**

Curriculum in (se presente / if it is) **FISICA SUBNUCLEARE**

TITOLO TESI / THESIS TITLE

SM and EFT interpretation of Vector Boson Scattering measurements at CMS and development of the DAQ system for the Barrel Timing Layer for HL-LHC

Cognome / Surname **Boldrini** Nome / Name **Giacomo**

Matricola / Registration number **800692**

Tutore / Tutor: **Prof. Marco Paganoni**

Supervisor: **Prof. Pietro Govoni**
(se presente / if there is one)

Cotutore / Co-tutor: **Dott. Andrea Massironi**
(se presente / if there is one)

Coordinatore / Coordinator: **Prof. Stefano Ragazzi**

ANNO ACCADEMICO / ACADEMIC YEAR 2022/2023

Contents

Abstract

This comprehensive work presents the culmination of a three-year research activity spanning three key domains.

The foremost focus of this research has been the search for new physics effects in VBS processes with the Effective Field Theory (EFT) approach. To fulfill this purpose a novel statistical model has been crafted to facilitate the interpretation and combination of EFT analyses. To date, this model has been employed in over 10 analyses conducted by the Compact Muon Solenoid (CMS) collaboration. Characterized by a global perspective, this model readily accommodates statistical combinations and lays a robust groundwork for future global EFT fitting within the CMS experiment. In this context, the VBS sensitivity to EFT dimension-six operators has been evaluated through a parton-level exercise involving the combination of Vector Boson Scattering (VBS) channels and a diboson channel, simultaneously constraining 14 Wilson coefficients. These results were compared to an additional combination study involving triboson processes. The knowledge of dimension-six effects in VBS has also been deepened by studying a real-world problem, encompassing background effects and uncertainties, through the analysis of the VBS WV process with a semileptonic final state. Challenges arising from the intricate VBS signature, featuring 6 final-state fermions, were surmounted by devising more efficient methods for matrix-element reweighting. The expected sensitivity to 8 Wilson coefficients was computed utilizing the CMS Run 2 dataset, which amounts to an integrated luminosity of 137 inverse femtobarns. Notably, for a Standard Model (SM) process, limit determinations were performed both for individual operators (with the others set to zero) and globally, allowing all coefficients to vary freely in a maximum likelihood fit.

In anticipation of an upcoming global EFT combination for VBS channels, the logical starting point involves a unified interpretation based on the SM. The combination of eight VBS analyses was executed to quantify the parameters governing vector boson production within the VBS topology. In particular, the interplay between three processes can be instrumental in the observation of two Z bosons scattering through VBS for which CMS only obtained strong evidence.

On the instrumental side, particular emphasis was placed on the development of the Data Acquisition (DAQ) system for the MIP Timing Detector (MTD), which will be installed at CMS during the high luminosity phase of the Large Hadron Collider. The finalization of the back-end component necessitated a comprehensive revision of firmware and software. The software architecture was designed with modularity in mind, establishing a one-to-one relationship between hardware components and software abstractions. Successful testing of this software included communication with the chips comprising the Barrel Timing Layer (BTL) front-end electronics. In order to streamline and optimize the forthcoming detector construction phase, a web-based Graphical User Interface was developed to facilitate interaction with less experienced users, ensuring a prompt, robust, and efficient system for characterizing assembled modules.

Chapter 1

Mathematical foundations of the Standard Model and Effective Field Theory

The standard model (SM) of particle physics, which is a quantum field theory based on local gauge symmetries, has successfully described the fundamental interactions of particles at the highest energies probed in particle physics experiments.

The SM's formulation is the outcome of a combination of theoretical and experimental discoveries dating back to the first half of the 20th century. Mathematically, it can be described as a relativistic Quantum Field Theory (QFT) with quantum fields defined at every point in spacetime as its fundamental entities.

Two essential concepts that have played a crucial role in advancing our understanding of high-energy phenomena are the principle of gauge invariance and Noether's theorem. The principle of gauge invariance asserts that the physical description of a system should not rely on arbitrary coordinate systems but should remain invariant under local gauge transformations. This simple requirement forms the basis for understanding how particles interact with each other. On the other hand, Noether's theorem states that for every conserved local symmetry, there must be a corresponding conserved quantity. This theorem enables us to uniquely identify particles based on the quantum numbers associated with their respective quantum fields.

Consequently, these powerful concepts not only enable us to categorize different fields according to their quantum numbers but also help determine their allowed interactions based on overarching symmetries. The primary objective of the SM is to reduce the laws governing the behaviour and interactions of all known forms of matter and energy into a concise set of fundamental principles.

This chapter focuses on describing the SM, beginning with the concept of symmetry, which is closely related to group theory. It explains the relationship between local symmetries and gauge fields while delving into Quantum Electrodynamics. The discussion then extends to all sectors of the SM, namely the Colour, Electroweak, and Scalar sectors.

1.1 Group Theory

The natural playground to deal with symmetries is group theory. Physicists are particularly interested in a special branch of group theory that studies continuous symmetries called Lie theory. Lie groups are differentiable manifolds that provide the mathematical foundation for the concepts of spatial translations, Lorentz boosts or rotations in an arbitrary space. The interest of physics in continuously generated groups is based on the fact that the general element can be reached by the repeated action of infinitesimal elements. The process may be thought of as an infinitesimal symmetry motion. Any group element g, infinitesimally close to the

identity $\mathbb{1}$ can be written as $g(\alpha) = \mathbb{1} + i\alpha^a T^a$ where α^a is the infinitesimal group parameter and T^a are Hermitian operators called generators of the symmetry group. We can write a general transformation for a finite parameter θ as the repeated action of an infinitesimal transformation $h(\theta) = (\mathbb{1} + i\alpha^a T^a) \cdot (\mathbb{1} + i\alpha^a T^a) \cdot ... = (\mathbb{1} + i\alpha^a T^a)^k$. Expressing the infinitesimal transformation as a function of a large number N we get $h(\theta) = \lim_{N\to\infty}(\mathbb{1} + \theta^a T^a/N)^N = e^{\theta^a T^a}$. The object T^a generates the finite transformation h, which is why it's called the generator [1]. We learn from the Baker-Campbell-Hausdorff-Formula [2] that the natural product of the Lie algebra is the Lie bracket $[,]$. As the set of generators T^a must span the space of infinitesimal group transformations, the commutator of the generators must be a linear combination of them $[T^a, T^b] = T^a T^b - T^b T^a = if^{abc}T^c$ where the numbers f^{abc} are called structure constants and summarize the entire group multiplication law. The Jacobi identity $[T^a, [T^b, T^c]] + [T^b, [T^c, T^a]] + [T^c, [T^a, T^b]] = 0$, which is satisfied by the Lie algebra generators, implies that the structure constants obey $f^{ade}f^{bcd} + f^{bde}f^{cad} + f^{cde}f^{abd} = 0$.

If one of the generators T^a commutes with all the others, it generates an independent continuous Abelian group, that is a group in which the law of composition is commutative. Such group, which has the structure of the group of phase rotations $\psi \to e^{i\alpha}\psi$ we call $U(1)$ [3]. On the contrary, we refer to non-Abelian groups those groups whose elements are not commutative under the group multiplication law.

Lie groups have been extensively classified by Killing and Cartan in the 19th century (for a historical review see [4]). Almost all compact and simple Lie groups can be identified as members of one of three families, known as classical groups namely unitary transformations of N-dimensional vectors ($SU(N)$), orthogonal transformations of N-dimensional vectors ($SO(N)$) and symplectic transformations of N-dimensional vectors ($S_p(N)$).

1.2 Poincaré group

The historical turning point for the development of modern QFTs is Einstein's theory of special relativity [5]. By postulating that phenomena are perceived the same in all inertial frames of reference and that the velocity of light c is invariant under a change of inertial frame of reference, humanity discovered that space and time are deeply connected. The concept of symmetry is manifest when we look for invariants under a transformation of the frame of reference. As there is no preferred frame of reference, physics laws should be written equally for all observers. The group of transformations permitted by the special relativity constraints is called the Poincaré group [6] which is the semidirect product between the Lorentz group and the group of translations in spacetime, as the velocity of light should be invariant under translations.

If we want to preserve the postulates of special relativity the quadratic form $ds^2 = dx_\mu dx_\nu \eta^{\mu\nu} = (cdt)^2 - (dx)^2 - (dy)^2 - (dz)^2$ (where η is the metric of the Minkowski space [7] $\eta_{00} = 1$, $\eta_{11} = \eta_{22} = \eta_{33} = -1$ and $\eta_{ij} = 0$ for $i \neq j$) should be the same in all inertial frames of reference [8]:

$$ds'^2 = dx'_\mu dx'_\nu \eta^{\mu\nu} = ds^2 = dx_\mu dx_\nu \eta^{\mu\nu} \tag{1.1}$$

Therefore the transformed coordinates dx'_μ should be written as a function of an arbitrary constant a_μ and of a constant matrix Λ, such that the scalar product of the Minkowski spacetime is invariant [1]

$$x_\mu \to x'_\mu = \Lambda^\sigma_\mu dx_\sigma + a_\mu \quad ; \quad \eta_{\mu\nu} = \Lambda^\gamma_\mu \Lambda^\delta_\nu \eta_{\gamma\delta} \tag{1.2}$$

These transformations, forming the so-called inhomogeneous Lorentz group or Poincaré group, have the special property that the speed of light is the same in all inertial frames. If in one frame we measure $|d\bar{x}/dt| = c$ then $\eta_{\mu\nu}dx^\mu dx^\nu = dt^2 - d\bar{x}^2 = 0$ from which it follows that also in another inertial frame $\eta_{\mu\nu}dx'^\mu dx'^\nu = 0$ therefore $|d\bar{x}'/dt| = c$. From the right hand side of Equation 1.1 we can see that $\det(\Lambda) = \pm 1$ and if we look at the $\mu = \nu = 0$ component $\Lambda_0^\sigma \eta_{\sigma\rho}\Lambda_0^\rho = (\Lambda_0^0)^2 - \sum_{i>0}(\Lambda_0^i)^2 = \eta_{00} = 1$ from which two solutions arise $\Lambda_0^0 \geq 1$ and $\Lambda_0^0 \leq 1$. The four possible combinations of $\det(\Lambda)$ and value of Λ_0^0 form four disjoint groups not smoothly connected. The proper orthochronous Lorentz group, characterized by $\det(\Lambda) = +1$ and Λ_0^0, is of special interest as it is a Lie group, containing the identity and therefore all of its transformations can be built from infinitesimal transformations. Any Lorentz transformation other than the proper orthochronous ones can be built up as the product of a transformation from the latter group and one or both of two special discrete transformations known as time-reversal and space-inversion. For the inhomogeneous Lorentz group the identity is the transformation $\Lambda_\nu^\mu = \delta_\nu^\mu$, $a_\mu = 0$. If we want to study infinitesimal transformations around the identity we can write $\Lambda_\nu^\mu = \delta_\nu^\mu + \omega_\nu^\mu$, $a_\mu = \epsilon_\mu$ where ω_ν^μ is an antisymmetric second-rank tensor. An infinitesimal Lorentz transformation $U(\mathbb{1} + \omega, \epsilon)$ must then be equal to $\mathbb{1}$ plus terms linear in ω and ϵ [9]:

$$U(\mathbb{1} + \omega, \epsilon) = \mathbb{1} + \frac{1}{2} i\omega_{\mu\nu} J^{\mu\nu} - i\epsilon_\mu P^\mu + ... \tag{1.3}$$

Where P^μ and $J^{\mu\nu}$ are the generators of the inhomogeneous Lorentz group and must be Hermitian in order for $U(\mathbb{1} + \omega, \epsilon)$ to be unitary. In more familiar terms P^μ is the four-momentum operator while $J^{\mu\nu}$ is the relativistic angular momentum tensor. In particular we see that P^1, P^2 and P^3 are the components of the three-momentum operator, P^0 is the energy operator and J^{23}, J^{31} and J^{12} are components of the angular momentum three-vector. The remaining generators J^{10}, J^{31} and J^{30} form a set of transformations that change the current reference frame into a coordinate system that moves with a different constant velocity, commonly referred to as a boost.

The operators, constructed from the generators, that commute with all other operators are Called Casimir operators [10]. It can be proved that for any simple Lie algebra the quadratic operator $T^2 = T^a T^a$ always commutes with the generators. The importance of these operators in QFT stems from the fact that they can serve as a label for any irreducible unitary representations of the Poincaré group. The latter has two Casimir operators:

$$\begin{aligned} &P_\mu P^\mu = m^2 \\ &W_\mu W^\mu = -m^2 s(s+1), \quad m > 0 \end{aligned} \tag{1.4}$$

Where P^μ is the four-momentum vector and $W_\mu = \frac{1}{2}\epsilon_{\mu\nu\rho\sigma} J^{\nu\rho} P^\sigma$ is called the Pauli-Lubanski four-vector which spacial components, in the rest frame, become the generators of the $SU(2)$ algebra [11]. The scalar quantity m is commonly referred to as the invariant mass of particles while s is referred to as spin.

The labels for the irreducible representations of the Poincaré group (m, s) is how elementary particles are classified and the origin of such quantities emerges in QFT in pure group-theoretical terms [12]. For example, particles with spin 0, 1/2 and 1 are described respectively by the (0,0), $(\frac{1}{2}, 0) \oplus (0, \frac{1}{2})$ and the $(\frac{1}{2}, \frac{1}{2})$ representations of the Poincaré group.

Additional labels, called charges, arise spontaneously in the SM from internal symmetries and will be explained in the next chapters.

1.3 The Standard Model Formalism

QFT's historical development has been intrinsically tied to the canonical formalism [13–16]. By utilizing the Lagrangian formalism, achieving Lorentz invariance becomes more straightforward. A Lagrangian density that maintains Lorentz invariance facilitates the creation of operators that fulfill the commutation relations of the Poincarè algebra. The advantage of adopting the Lagrangian approach becomes evident when dealing with non-Abelian theories. In such cases, attempting to construct a suitable Hamiltonian without first starting with a Lorentz-invariant Lagrangian density would be futile [9].

By denoting x the spacetime coordinates, by $\phi(x)$ a generic field and by $\partial_\mu\phi$ its derivatives, we can define a Lagrangian density $\mathcal{L}(\phi, \partial_\mu)$. The Lagrangian density is deeply connected to the action S, which is a scalar quantity describing how a physical system has changed over time

$$S = \int L dt = \int \mathcal{L}(\phi, \partial_\mu\phi) d^4x \tag{1.5}$$

It is always possible to recover the Hamiltonian formalism recalling $H = \sum p\dot{q} - L$

$$H = \int d^3x \left[\frac{\partial \mathcal{L}}{\partial \dot{\phi}(\bar{x})} \dot{\phi}(\bar{x}) - \mathcal{L} \right] \tag{1.6}$$

1.4 Euler-Lagrange Equation

The equations of motion for a system characterized by a Lagrangian density $\mathcal{L}$ are derived from the principle of least action. A system evolving from two configurations in a time Δt will do so along the paths in configuration space that are stationary points of the action functional S namely $\delta S = 0$. The solution to the previous equation is known as the Euler-Lagrange equation of motion for a field

$$\partial_\mu \left(\frac{\partial \mathcal{L}}{\partial(\partial_\mu\phi)} \right) - \frac{\partial \mathcal{L}}{\partial \phi} = 0 \tag{1.7}$$

1.5 Noether's theorem

The concepts frequently employed by physicists to describe nature, such as conserved quantities, are directly associated with symmetries. The theorem summarizing this concept is known as Noether's theorem [17] and states that every continuous symmetry of the action of a physical system (S) with conservative forces has a corresponding conservation law. In classical field theory we can distinguish between spacetime symmetries acting only on spacetime coordinates such as translations $x_\mu \to x_\mu + a_\mu$ and internal symmetries that act on the fields themselves $\phi(x) \to \phi(x) + \alpha\Delta\phi(x)$. In the first case, one can see a translation as a transformation of the field configuration $\phi(x) \to \phi(x) + a_\mu\partial^\mu\phi(x)$. As the Lagrangian density is covariant it must transform in the same way $\mathcal{L} \to \mathcal{L} + a_\mu\partial^\mu\mathcal{L}$. Note that we are allowed to change the Lagrangian density by adding a surface term as it will vanish under the derivatives of the Euler-Lagrange Equation 1.7 yielding the same dynamics for the field system. If we compare the expectation for $\Delta\mathcal{L}$ to the results obtained by varying fields

$$a_\mu\partial^\mu\mathcal{L} = a_\nu\partial^\mu \left(\frac{\partial \mathcal{L}}{\partial(\partial_\mu\phi)} \partial_\nu\phi \right) + a_\nu \left[\frac{\partial \mathcal{L}}{\partial \phi} - \partial_\mu \left(\frac{\partial \mathcal{L}}{\partial(\partial_\mu\phi)} \right) \right] \partial_\nu\phi = 0 \tag{1.8}$$

The term in square brackets vanishes by the Euler-Lagrange equation 1.7 and we are left with

$$a_\nu \partial^\mu (\delta^\nu_\mu \mathcal{L}) - a_\nu \partial^\mu \left(\frac{\partial \mathcal{L}}{\partial(\partial_\mu \phi)} \partial_\nu \phi \right) = 0; \quad \partial^\mu T^\nu_\mu = 0 \tag{1.9}$$

We see from Equation 1.9 that we have four conserved currents (one for each ν). For time translations ($\nu = 0$) the conserved charge is the Hamiltonian or total energy of the system $\partial^0 T^0_0 = -\partial^i T^0_i$. For spacial translations ($\nu = i$, $i = 1, 2, 3$) the total momentum of the field configuration P_i is conserved. T^ν_μ is called the energy-momentum tensor of the field ϕ. Also interestingly, the conserved charges associated with a particular symmetry (such as spatial translations, rotations as well as all internal symmetries) act as generators of the symmetry itself [9].

More generally, the conservation law for a quantity Q_a called charge, can be expressed with the help of the divergence theorem yielding

$$Q_a = \int d^{n-1} x j^0_a \tag{1.10}$$

where j^μ_a is a tensor (whose rank depends on the transformation) called the conserved current and n is the dimension of the manifold.

1.6 Gauge transformations

From Maxwell's equations for electrodynamics, we know that fields are defined in terms of derivatives of the potentials so there is an infinite family of possible potentials that will lead to the same physical phenomena. For example, the electrostatic potential is defined up to an arbitrary additive constant. When dealing with QFT, the fundamental fields cannot be observed directly but we can observe some of their properties. In field theories, various arrangements of unobservable fields can lead to identical observable outcomes. The process of changing from one such field configuration to another is termed a gauge transformation. As the properties of the system are not changed by such transformation we usually refer to this as a gauge symmetry of the system and, therefore, we should also find conserved quantities.

Suppose to have a theory that is invariant under the global symmetry $U(1)$ of phase rotations $\psi \to e^{i\alpha}\psi$. In QFT it is natural to consider local transformations i.e. a point in spacetime is influenced only by its neighboring points in order to avoid action at a distance. The local requirement for such transformations is translated into the space-time dependence of the α parameter: $\alpha \to \alpha(x)$ that implies $\psi(x) \to e^{i\alpha(x)}\psi(x) = C(x)\psi(x)$. Therefore, the action of the ordinary derivative ∂_μ on the transformed field $n^\mu \partial_\mu \psi(x) = \lim_{\epsilon \to 0} \epsilon^{-1} [\psi(x^\mu + n^\mu \epsilon) - \psi(x)]$ does not factorize as in the global case but will be, in general, space-time dependent thus breaking the invariance of the theory. That is because the two subtracted fields have different behaviour under the local transformation $\psi(x) \to C(x)\psi(x)$, $\psi(x + n\epsilon) \to C(x + n\epsilon)\psi(x + n\epsilon)$. In order to subtract the values at neighboring points in a meaningful way we introduce the object $U(y, x)$ called Wilson line [18] that transforms under $U(1)$ as a pure phase $U(y, x) \to e^{i\alpha(y)} U(y, x) e^{-i\alpha(x)}$ and $U(x, x) = \mathbb{1}$. We can therefore define a covariant derivative that transforms the same as the fields D_μ such that $D_\mu \psi(x) \to U(x) D_\mu \psi(x)$ as

$$\eta^\mu D_\mu \psi(x) = \lim_{\epsilon \to 0} \frac{1}{\epsilon} \big[\psi(x + \epsilon\eta) - U(x + \epsilon\eta, x)\psi(x) \big] \tag{1.11}$$

If $U(y,x)$ is a continuous function of the two spacetime points y, x then we can Taylor expand for small ϵ as the $U(1)$ group is a Lie group and we can find infinitesimal transformations close to the identity $U(x+\epsilon n, x) = \mathbb{1} - ie\epsilon n^\mu A_\mu(x) + \mathcal{O}(\epsilon^2)$. The constant e is arbitrary while the coefficient of the displacement ϵn^μ is a new vector field $A_\mu(x)$. Such a field is called an Ehresmann connection [19]. In the infinitesimal limit, the covariant derivative can be written as

$$D_\mu \psi(x) = \partial_\mu \psi(x) + ieA_\mu \psi(x) \tag{1.12}$$

Where now the newly introduced vector field A_μ transforms under the local transformation as

$$A_\mu(x) \to A_\mu(x) - \frac{1}{e}\partial_\mu \alpha(x) \tag{1.13}$$

We are now able to construct all possible Lagrangians that are invariant under a local symmetry. The combination of ψ and its covariant derivatives will also be locally invariant. To complete the construction we need a kinetic term for the vector fields A_μ which is a locally invariant term that depends on A_μ and its derivatives but not on ψ. We find this term to be the electromagnetic field tensor

$$[D_\mu, D_\nu] = ie(\partial_\mu A_\nu - \partial_\nu A_\mu) = ieF_{\mu\nu} \tag{1.14}$$

From this simple example, which poses the basis for quantum electrodynamics by interpreting ψ as electron field, A_μ as the electromagnetic vector potential and the scale factor e as the electric charge, we understand the geometrical origins of the gauge fields as an Ehresmann connection [19], arising naturally when postulating a local symmetry of the fields.

1.7 The Standard Model of Particle Physics

This section is dedicated to the Standard Model of particle physics (SM) that describes elementary particles and their interactions. When we require local gauge invariance of the SM as a quantum field theory, we require that the SM Lagrangian does not change (is invariant) under local transformations from certain Lie groups. The local constraint imposes that the transformation must depend on space-time.
The SM is invariant under local gauge transformations of the symmetry group

$$SU(3)_C \otimes SU(2)_L \otimes U(1)_{Y_L} \tag{1.15}$$

where $SU(3)_C$ is the gauge group of Quantum Chromodynamics (with an associated degree of freedom called colour, C), and $SU(2)_L \otimes U(1)_{Y_L}$ is the gauge group of the Electroweak interactions where L highlights that only left-handed fields can interact through the weak force while Y_L is the $U(1)$ generator called weak hypercharge.

This symmetry group describes three of the four known fundamental interactions in nature, namely the strong, weak and electromagnetic interactions. Including the fourth interaction, the gravitational force, under the same SM theoretical framework is not possible. While gravity dominates the dynamics of galactic bodies, its effect on subatomic particles is negligible (about 10^3 times less powerful than the weak interaction). Moreover, the successful Einstein's theory of relativity describes gravity as a fundamental property of spacetime and not as a force as required by SM formalism. The search for the mechanism that can explain the origin of gravity as well as the SM forces while starting from the same basic principles, usually referred to as the theory of everything, is one of the most tantalizing goals of modern physics.

1.7.1 Quantum Electrodynamics

The first step toward the modern SM has been the development of Quantum Electro-Dynamics (QED). The Lagrangian density of the free electron field (Dirac's Lagrangian [20, 21]) ψ transforming under the $(1/2,0)\oplus(0,1/2)$ representation of the Lorentz group is $\mathcal{L} = \bar{\psi}(i\gamma^\mu\partial_\mu - m)\psi$ where $\bar{\psi} = \psi^\dagger\gamma^0$ and m is the Dirac mass. The dimension of the γ^μ matrices in Minkowsky space is at least 4×4 and they obey the so-called Dirac algebra $\{\gamma^\mu,\gamma^\nu\} = 2\eta^{\mu\nu}\times\mathbb{1}_{n\times n}$. We can write a representation of the Lorentz algebra using γ matrices as $\mathcal{S}^{\mu\nu} = i/4\,[\gamma^\mu,\gamma^\nu]$. In particular $\mathcal{S}^{0i}$ are the generators of the three-dimensional rotations while $\mathcal{S}^{ij}$ are the generators of Lorentz boost. A four-component field ψ that transforms under boosts and rotations as $\mathcal{S}$ is called a Dirac spinor.

From diagonal properties of the γ matrices in the chiral basis, one can show that the Dirac representation of the Lorentz group is reducible and we can form two 2-dimensional representations by considering diagonal blocks separately $\psi = (\psi_L,\psi_R)$ where ψ_L and ψ_R are eigenstates of the chirality operatory $\gamma_5 = i\gamma^0\gamma^1\gamma^2\gamma^3$

$$\psi_L = \frac{1-\gamma_5}{2}\psi;\quad \psi_R = \frac{1+\gamma_5}{2}\psi \tag{1.16}$$

It can be seen that $\mathcal{L}$ is manifestly invariant under a global $U(1)$ symmetry. It was already shown in chapter 1.6 that if one promotes the symmetry by requiring locality, Lorentz invariance is guaranteed by replacing normal derivatives ∂_μ to covariant ones D_μ transforming the same way as the fields ψ namely $\mathcal{L} = i\bar{\psi}(x)(\gamma^\mu\partial_\mu - m)\psi(x) - e\bar{\psi}(x)\gamma^\mu A_\mu\psi(x)$ where we notice a new term summarising the interaction between the fermion field and gauge field. The requirement of the free Lagrangian to be invariant under the local gauge transformation has led to a new term describing the dynamics of the fields. The only Lorentz invariant term, summarising the kinetic behaviour of the new gauge field A_μ, is the tensor $F^{\mu\nu}$ described in chapter 1.6. In order to recover classical electrodynamics, we can write a physical spin 1 Proca Lagrangian [22, 23] for the gauge field with the relative coupling to the fermionic field via covariant derivative. The mass term vanishes by requiring local invariance of the Lagrangian as one would expect for a field describing a photon and one recovers the QED Lagrangian

$$\mathcal{L}_{QED} = \bar{\psi(x)}(i\gamma^\mu D_\mu - m)\psi(x) - \frac{1}{4}F_{\mu\nu}F^{\mu\nu} \tag{1.17}$$

The coupling constant e is usually identified with the electric charge and its conservation follows from Noether theorem 1.5. When the Euler-Lagrange procedure is applied, we recover the Dirac equation in the electromagnetic field $i\gamma^\mu\partial_\mu - m\psi = e\gamma^\mu A_\mu\psi$

1.7.2 Quantum Chromodynamics

The other sectors of the SM are built on the same principles of the earlier QED but with more complex symmetry structures. Yang-Mills theories [24] generalize QED deeply by expanding local invariance to non-Abelian symmetry groups while retaining renomalizability [25, 26].

Quantum Chromodynamics (QCD) is the SM sector devoted to the strong force. Its symmetry group is the non-Abelian $SU(3)_C$ with 8 independent generators i.e. 8 massless spin 1 fields as force carriers. The introduction of a nonvanishing commutator between the generators of such a group implies that the gauge charges, which are conserved thanks to Noether's theorem, are gauge-dependent (i.e. they are not invariant under gauge transformations) and the gauge fields themselves carry gauge charges. The fundamental charge associated with the symmetry is called colour and comes in N = 3 types.

The only matter field interacting via strong force is the quark $q_f(x)$ which is a spin $1/2$ fermion with fractional electric charge and colour charge thus obeying Dirac's equation. Quarks come in different flavours f. The coviariant derivative associated with a local $SU(3)$ symmetry reads as $D_\mu = \partial_\mu - ig_S G^a_\mu \lambda^a/2$ where g_S is the coupling constant of the strong interaction, G^a_μ are the eight gluon gauge fields and λ^a are Gell-Mann matrices [27]. The kinetic term of such gauge fields presents the peculiar self-interaction term $G^a_{\mu\nu} = \partial_\mu G^a_\nu - \partial_\nu G^a_\mu + g_S f^{abc} G^b_\mu G^c_\nu$ coming from the Lie algebra of $SU(3)$. As for QED, the gauge-invariant kinetic term for the gauge fields reads as $-G^a_{\mu\nu} G^{a\mu\nu}/4$. The Lagrangian density for QCD [3] is built analogously to what was done in QED namely a kinetic term for the gauge fields and the Dirac's term for spin $1/2$ fermions

$$\mathcal{L}_{QCD} = \sum_f \bar{q}_f(x)(i\gamma^\mu D_\mu - m_f)q_f(x) - \frac{1}{4} G^a_{\mu\nu} G^{a\mu\nu} \tag{1.18}$$

Colour-charged particles cannot be isolated. For sufficiently strong couplings, QCD exhibits colour confinment [18], meaning that the only finite-energy asymptotic states are singlets of colour $SU(3)_C$ [28].

The QCD Lagrangian density has additional $U(1)$ and $SU(N_f)$ global symmetries. The former rotates by the same angle R and L components and the associated conserved quantity is the baryon number B i.e. the net number of quarks (right-handed plus left-handed) is conserved in QCD interactions. The $SU(N_f)$ is decomposed in the so-called isospin symmetry (with charges I, I_3), which is a rotation in flavour space of the N_f quark fields as QCD interactions are flavour-blind, and a chiral symmetry where L and R quark field components are separately invariant as QCD interactions preserve parity. However, the $SU(N_f)$ symmetry is spontaneously broken [29] meaning that the QCD vacuum state is not invariant under the same symmetries as $\mathcal{L}$. QCD has a nonvanishing vacuum expectation value for a quark pair condensate $\langle 0|\bar{Q}Q|0\rangle = \langle 0|\bar{Q}_L Q_R + \bar{Q}_R Q_L|0\rangle \neq 0$ and this explains why only 1% of the mass of the proton comes from its constituents. $SU(N_f)$ is almost a symmetry for $N_f = 2$ that rotates up and down type quarks because $m_u \simeq m_d$. $N_f = 3$ implies that rotating u, d and s quark fields leads to invariance under $SU(3)$ but this is only approximate as the strange quark is more than an order of magnitude heavier than the up and down quarks.

1.7.3 Weak Interactions and Electroweak unification

The observations of a new force began in the early 1900s while studying the radioactive properties of elements. The experimental evidence puzzled physics for half a century. The first proposed interpretation of the neutron β-decay came from Fermi, describing it as a four-point interaction [30]. Following the experiments of C. S. Wu et al. [31] it was understood that left and right eigenstates of the chirality defined in Equation 1.16 behave differently under the weak force thus violating spatial parity $P : x \to -x$. Christenson et. al. [32] also proved that weak interactions violate the product of charge conjugation and parity by examining the decay of the long-lived neutral kaon K^0_L. The conserved Noether's current (mediated by electrically charged carriers due to conservation of the electromagnetic charge) for a theory describing weak interactions should maximally violate parity, thus presenting a vector and an axial component $V - A$. For leptons l such a current reads as $J_{\mu,l} = \bar{\psi}_{\nu_l}\gamma_\mu(1-\gamma_5)\psi_l = J^V_\mu - J^A_\mu = 2\bar{\psi}^L_{\nu_l}\gamma_\mu\psi^L_l$ where it is explicit that right-handed fermions do not interact.

A theory of charged currents with SM formalism would require a gauge symmetry group with two generators. Such a group does not exist, the closest would be SU(2) with three generators. Such a theory would generate two charged gauge fields $W^\pm$ behaving correctly under the weak force hypothesis of left-handedness and a neutral weak gauge boson Z which would couple

to both left and right-handed states. However, the weak force acts feebly at a short distance thus it should be mediated by massive spin-1 vector bosons (to recover Fermi theory at low energy). On the contrary, QED is mediated by the massless photon and acts at an infinite range. Moreover, the construction of fermion mass terms like $-m_l(\bar{l}_L l_R + \bar{l}_R l_L)$ is forbidden by gauge invariance as l_L and l_R belong to different $SU(2)$ representations thus will have different $U(1)$ charges.

The solution to all these problems came with the electroweak unification from Glashow [33], Salam [34] and Weinberg [35] exploiting the mechanism of spontaneous symmetry breaking, precisely the Higgs [36], Englert, Brout [37] (BEH) mechanism [38]. The EW theory is a chiral theory, meaning that ψ_L and ψ_R behave differently under the gauge group: ψ_L transforms as a doubled under $SU(2)_L$ while ψ_R as a singlet. We can define left-handed quark and lepton $SU(2)_L$ doublets and will denote as ψ_L a general left-handed fermion field in this representation

$$q_L = \begin{pmatrix} u_L \\ d_L \end{pmatrix}, \begin{pmatrix} c_L \\ s_L \end{pmatrix}, \begin{pmatrix} t_L \\ b_L \end{pmatrix} \quad l_L = \begin{pmatrix} v_{eL} \\ e_L \end{pmatrix}, \begin{pmatrix} v_{\mu L} \\ \mu_L \end{pmatrix}, \begin{pmatrix} v_{\tau L} \\ \tau_L \end{pmatrix} \tag{1.19}$$

We assume for the electroweak Yang-Mills theory a gauge group $SU(2)_L \times U(1)_{Y_L}$ which generators are called respectively weak isospin T^a and weak hypercharge Y_L. The gauge fields associated with such generators are called W^a_μ for $SU(2)_L$ and B_μ for $U(1)_{Y_L}$. Before electroweak symmetry breaking (EWSB) the Lagrangian density is composed of four pieces $\mathcal{L}_{EW} = \mathcal{L}_g + \mathcal{L}_f + \mathcal{L}_h + \mathcal{L}_y$ denoting respectively the gauge bosons kinetic term, kinetic term of SM fermions, the Higgs field Lagrangian and lastly Yukawa fermion interactions. Focusing on the first two terms, the Lagrangian density reads as

$$\mathcal{L}_{g+f} = -\frac{1}{4} W^{\mu\nu}_a W^a_{\mu\nu} - \frac{1}{4} B^{\mu\nu} B_{\mu\nu} + \bar{\psi}_L i\gamma^\mu D_\mu \psi_L + \bar{\psi}_R i\gamma^\mu D_\mu \psi_R \tag{1.20}$$

where $B_{\mu\nu}$ and $W^a_{\mu\nu}$ are the field stress tensors related to $U(1)$ and $SU(2)$ as described in chapters 1.7.1 and 1.7.2. The covariant derivative for a fermion field belonging to a general $SU(2)$ representation now reads as

$$D_\mu = \partial_\mu - ig' Y_L B_\mu - igT^a W^a_\mu \tag{1.21}$$

where g' and g are the coupling constants of $U(1)$ and $SU(2)$ respectovely. The electric charge generator Q is $Q = T^3 + Y_L$.

We can derive mass eigenstates for this theory. For the charged mediators we only have a mixing of $SU(2)$ gauge fields $W^\pm = \left(W^1 \pm iW^2\right)/\sqrt{2}$. The third component of $SU(2)_L$ gauge field W^3_μ mixes with the $U(1)_{Y_L}$ gauge field B_μ to create the mass eigenstates called Z_μ and A_μ through a $SO(2)$ representation of rotations as a function of the Weinber angle [39] θ_ω: $(Z_\mu, A_\mu) = R(\theta_\omega)(A^3_\mu, B_\mu)$.

The covariant derivative in terms of the mass eigenstates takes the form

$$\begin{aligned} D_\mu = \partial_\mu - i\frac{g}{\sqrt{2}}\left(W^+_\mu T^+ + W^-_\mu T^-\right) - \frac{ig}{\cos\theta_\omega} Z_\mu \left(T^3 - \sin\theta_\omega{}^2 Q\right) \\ - ieA_\mu Q \end{aligned} \tag{1.22}$$

Where we defined the charged generators $T^\pm = T^1 \pm iT^2$. The angle θ_ω is determined by the fact that QED couples equivalently right and left-handed fermions with strength e so it must be that $g\sin\theta_\omega = g'\sin\theta_\omega = e$ or $\tan\theta_\omega = g'/g$. Charged current couplings are then defined as [40]

$$\mathcal{L}_{CC} = \frac{g}{\sqrt{2}}\left[\bar{\psi}_L T^+ W^+_\mu \psi_L + \bar{\psi}_L T^- W^-_\mu \psi_L\right] \tag{1.23}$$

While with A_μ one recovers the traditional QED neutral currents, we have an additional neutral vector current mediated by a gauge field Z_μ

$$\mathcal{L}_{NC} = \frac{g}{2cos\theta_\omega}\left[\bar{\psi}_L T^3 Z\mu - 2\bar{\psi}Qsin^2\theta_\omega \psi Z^\mu\right] \tag{1.24}$$

We can note some things about weak interactions. Charged weak interactions are currently the sole recognized interactions capable of altering particle flavour. Weak neutral currents can couple both left and right-handed fermion fields however the flavour change is suppressed.

1.7.4 Spontaneous symmetry breaking and Higgs mechanism

The solution to the problem of mass generation of electroweak vector bosons and fermions while retaining gauge invariance is known as the BEH mechanism and is described in $\mathcal{L}_h$. Consider a system of complex scalar fields $\phi \equiv (\phi_u, \phi_d)$ transforming as a doublet under $SU(2)$. If one applies an $SU(2)$ infinitesimal transformation on this system, the difference between the transformed and the original fields depends on the commutator of the $SU(2)$ generators $\sigma_k/2$, $k = 1,2,3$ (σ_k referred to as Pauli matrices[1]) as $\delta S(k) \equiv \phi' - \phi \simeq i\epsilon_k(x)[\sigma_k/2, \phi]$ where $\epsilon_k(x)$ is the infinitesimal parameter. This equation is valid even when we take the expectation value of the fields on the vacuum (v.e.v) $\langle 0|\phi|0\rangle = \langle\phi\rangle_0$. If one postulates a non-vanishing v.e.v. for at least one component of ϕ, then none of the generators can annihilate the vacuum $\sigma_k|0\rangle \neq 0$ and all the commutators $[\sigma_k/2, S]$ are not zero. Thus if we want to impose $SU(2)$ symmetry on this system we find that it is possible to write an invariant Lagrangian but the vacuum will not be invariant. This behaviour is called spontaneous symmetry breaking and a $SU(2)$ invariant Lagrangian with such a property can be written by allowing S to obey a Coleman-Weinberg potential $V(\phi)$ [41]

$$\mathcal{L}_h = (D_\mu\phi)^\dagger(D^\mu\phi) + \underbrace{\mu^2\phi^\dagger\phi - \lambda(\phi^\dagger\phi)^2}_{-V(\phi^\dagger\phi)} \tag{1.25}$$

Where $\lambda > 0$ to ensure a minimum and $\mu^2 > 0$ to make the minimum different from zero as shown in Figure 1.1. The minimum of the potential are infinite at $e^{i\rho}\sqrt{\mu^2/2\lambda}$.

Assuming arbitrarily that $\langle\phi_d\rangle_0 = \sqrt{\mu^2/2\lambda} = v/\sqrt{2}$ and $\langle\phi_u\rangle_0 = 0$ we can shift the field ϕ around the new minimum as

$$\phi(x) = \frac{e^{i\theta_k\frac{\sigma_k}{2}}}{\sqrt{2}}\begin{pmatrix}0\\ v+h(x)\end{pmatrix} \approx \frac{1}{\sqrt{2}}\begin{pmatrix}\eta_1(x)+i\eta_2(x)\\ v+h(x)+i\eta_3(x)\end{pmatrix} \xrightarrow{SU(2)} \frac{1}{\sqrt{2}}\begin{pmatrix}0\\ v+h(x)\end{pmatrix} \tag{1.26}$$

where $\eta_i(x)$ are massless spin-0 Nambu-Goldstone bosons [29, 42], one for each spontaneosuly broken $SU(2)$ generator. No such boson has been observed in nature so they should mathematically disappear. This is true only because the symmetry $SU(2)$ was promoted to a local symmetry thus we can gauge away the Nambu-Goldstone bosons with a suitable gauge choice getting rid of nonphysical degrees of freedom. This is not true if the symmetry is global. For this task it is convenient to work in the unitary gauge which comprises a polar parametrization of the doublet field and a rotation in the $SU(2)$ space to get rid of the exponential factor and is

[1] Pauli matrices are 2×2 complex, hermitian and unitary matrices defined as $\sigma_1 = \begin{pmatrix}0 & 1\\ 1 & 0\end{pmatrix}$, $\sigma_2 = \begin{pmatrix}0 & -i\\ i & 0\end{pmatrix}$ and $\sigma_3 = \begin{pmatrix}1 & 0\\ 0 & -1\end{pmatrix}$ and such that $\sigma_1^2 = \sigma_2^2 = \sigma_3^2 = \mathbb{1}_{2\times 2}$. Pauli matrices obey the following commutation and anticommutation relationships: $[\sigma_i, \sigma_j] = 2i\epsilon_{ijk}\sigma_k$ and $\{\sigma_i, \sigma_j\} = 2\delta_{ij}\mathbb{1}_{2\times 2}$

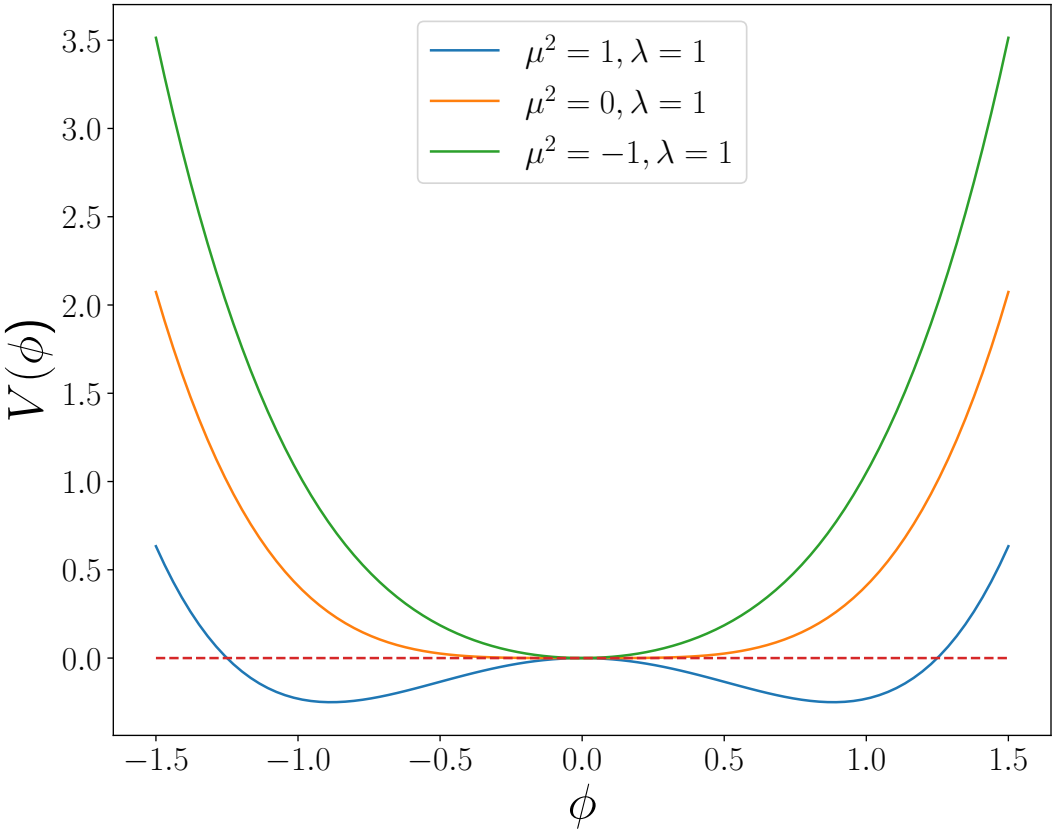

Figure 1.1: Projection of the Coleman-Weinberg potential for a complex scalar field ϕ on the real axis. While the λ parameter is fixed to 1, the potential is drawn for $\mu^2 = -1, 0, 1$ respectively in blue, orange and green showing how only $\mu^2 > 0$ induces a degeneracy of the minima.

highlighted by $\xrightarrow{SU(2)}$ in equation 1.26. The only physical field h is referred to as the Higgs field and in unitary gauge the potential $V(\phi^\dagger\phi)$ takes the form $V(\phi^\dagger\phi) = -\mu^2 h^2 - \lambda v h^3 - \lambda h^4/4$ showing that the quantum of the Higgs field is a scalar boson with mass $m_h = \sqrt{2}\mu = \sqrt{2\lambda}v$.

The origin of the electroweak gauge boson masses comes from the kinetic term of ϕ under the $SU(2)_L \otimes U(1)_{Y_L}$ symmetry group: $(D_\mu\phi)(D^\mu\phi)$. If we take equation 1.21 for the covariant derivative and evaluate it on the v.e.v. retaining only interesting terms

$$\begin{aligned}\left\langle (D_\mu\phi)(D^\mu\phi) \right\rangle_0 &= \frac{1}{2}\begin{pmatrix}0 & v\end{pmatrix}\left(gW_\mu^a T^a + g' Y_L B_\mu\right)^2 \begin{pmatrix}0\\ v\end{pmatrix} \\ &= \frac{1}{2}\frac{v^2}{4}\left[g^2(A_\mu^1)^2 + g^2(A_\mu^2)^2 + (-gA_\mu^3 + g'B_\mu)^2\right]\end{aligned} \tag{1.27}$$

Where we can see that there are three massive gauge bosons with mass proportional to the v.e.v. and a massless one.

$$
\begin{aligned}
W_\mu^\pm &= \frac{1}{\sqrt{2}}(A_\mu^1 \mp iA_\mu^2); \quad m_W = g\frac{v}{2} \\
Z_\mu &= \frac{1}{\sqrt{g^2+g'^2}}(gA_\mu^3 - g'B_\mu); \quad m_Z = \sqrt{g^2+g'^2}\frac{v}{2} \\
A_\mu &= \frac{1}{\sqrt{g^2+g'^2}}(g'A_\mu^3 + gB_\mu); \quad m_A = 0
\end{aligned}
\tag{1.28}
$$

If one allows the Higgs field to couple with fermion fields through a Yukawa term then it can provide the fermion with mass as well. The scalar field allows for gauge invariant terms which couple the left-handed doublet and right-handed singlet states of the form $\bar{\psi}_L \Gamma \psi_R \phi$ where Γ include the coupling constants and make the Yukawa couplings invariant under the Lorentz and gauge groups. After the symmetry is broken, the Yukawa Lagrangian can be written as

$$
\mathcal{L}_y = -\frac{v+h}{\sqrt{2}} \sum_f^{fermions} y_f \bar{\psi}_L^f \psi_R^f \tag{1.29}
$$

Where y_f are the Yukawa couplings or proportionality constant between the mass of a fermion and the Higgs v.e.v. The fermion mass can be written as $m_f = v y_f / \sqrt{2}$.

1.7.5 Gauge and matter fields of the Standard Model

The content of the Standard Model is commonly categorized into matter and gauge fields. The former encompasses all spin 1/2 fermionic matter fields obeying Fermi-Dirac statistics, comprising leptons and quarks. Fermions are organized in exactly three generations, each containing two leptons and two quarks. Between generations, all quantum numbers are identical except for the flavour one and the particle's mass. The first generation contains the lightest fermions that compose stable matter such as the electron and the up and down quarks. Fermions from the second and third generations are more massive and tend to decay into fermions from the first generation. It is unclear why nature prefers exactly three generations but the existence of additional generations is currently ruled out by experiments [43]. The second SM category encompasses the spin 1 gauge fields following Bose-Einstein statistics and is responsible for mediating forces. An extra scalar field, unrelated to any fundamental force, is present – the Higgs field. Table 1.1 summarises spin 1/2 fields while Table 1.2 gauge bosons of the $SU(3)_C \times SU(2)_L \times U(1)_{Y_L}$ gauge symmetry.

1.8 Effective field theory

In the absence of the observation of a new particle, indirect searches for new physics can be fundamental in the discovery of a new theoretical framework. Often indirect searches are ambiguous as they can be an indication of several possible models. This is due to the decoupling theorem [45] which essentially states that if the energy scale of new physics Λ is far greater than the probed energy E, the heavy fields effectively decouple in processes with no outgoing heavy particles. Processes occurring at energies significantly lower than Λ can be effectively characterized by local interactions among SM fields that remain invariant under the SM gauge symmetry. In other words, the low energy behaviour of the complete theory is obtained by integrating out the heavy fields when they appear as internal legs (or propagators) in Feynman diagrams, leading to effective interactions of the light fields only as shown shematically in the right-hand side of Figure 1.2. However, this also means that we can study the low-energy approximation of many different UV-complete and decoupled theories in a model-independent

	ψ	Mass	Q	Colour	T_3	Y_L
1^{st}	ν_e	< 225 eV	0	0	L:+$\frac{1}{2}$; R:0	L:-1; R:0
	e	511 keV	-1	0	L:-$\frac{1}{2}$; R:0	L:-1; R:-2
	u	$2.16^{+0.49}_{--0.26}$ MeV	1/3	r,g,b	L:+$\frac{1}{2}$; R:0	L:+$\frac{1}{3}$; R:+$\frac{4}{3}$
	d	$4.67^{+0.48}_{--0.17}$ MeV	-2/3	r,g,b	L:-$\frac{1}{2}$; R:0	L:+$\frac{1}{3}$; R:-$\frac{2}{3}$
2^{nd}	ν_μ	< 0.19 MeV	0	0	L:+$\frac{1}{2}$; R:0	L:-1; R:0
	μ	105.7 MeV	-1	0	L:-$\frac{1}{2}$; R:0	L:-1; R:-2
	c	1.27 ± 0.02 MeV	1/3	r,g,b	L:+$\frac{1}{2}$; R:0	L:+$\frac{1}{3}$; R:+$\frac{4}{3}$
	s	$93.4^{+8.6}_{--3.4}$ MeV	-2/3	r,g,b	L:-$\frac{1}{2}$; R:0	L:+$\frac{1}{3}$; R:-$\frac{2}{3}$
3^{rd}	ν_τ	< 18.2 MeV	0	0	L:+$\frac{1}{2}$; R:0	L:-1; R:0
	τ	1.777 GeV	-1	0	L:-$\frac{1}{2}$; R:0	L:-1; R:-2
	t	172.69 ± 0.30 GeV	1/3	r,g,b	L:+$\frac{1}{2}$; R:0	L:+$\frac{1}{3}$; R:+$\frac{4}{3}$
	b	$4.18^{+0.03}_{--0.02}$ GeV	-2/3	r,g,b	L:-$\frac{1}{2}$;R:0	L:+$\frac{1}{3}$; R:-$\frac{2}{3}$

Table 1.1: Leptons (e, ν_e, μ, ν_μ, τ, ν_τ) and quarks (u, d, c, s, t, b) masses [44] and charges as spin 1/2 fermions. Fermion fields within the Standard Model are divided into three nearly identical generations (1^{st}, 2^{nd}, 3^{rd}), possessing identical quantum numbers (except for the flavour one) but distinct masses.

	Spin	Mass	Q	Colour	T_3	Y_L
Photon (γ)	1	$< 10^{--18}$ eV	0	0	1,0	0
Gluon (g)	1	~ 0	0	r,g,b	0	0
$\mathbf{Z^0}$	1	91.1876 ± 0.0021 GeV	0	0	1,0	0
$\mathbf{W^\pm}$	1	80.377 ± 0.012 GeV	± 1	0	1	0
h	0	125.25 ± 0.17 GeV	0	0	0	0

Table 1.2: Gauge bosons spin, masses [44] and charges

fashion. This is the concept underlying effective field theories (EFT) which, simply stated, are just general quantum field theories based on the principles of relativity and quantum mechanics but without the restriction of renormalizability and valid up to a certain energy scale Λ. In many cases, EFTs are the low-energy limit of a more complete theory, just as the Fermi 4-point interaction is the low-energy approximation of the electroweak theory. The left-hand side of Figure 1.2 shows how one can produce different types of EFTs, corresponding to different probed energies E, starting from the same UV-complete theory. Technically, the phenomenological analysis of a new theory with energy scale Λ_{NP} is done by computing the EFT parameters at such energy scale, performing the running of such parameters to lower energies (e.g. the electroweak scale v.e.v.) through renormalization group evolution and perform the matching procedure on the EFT parameters, ensuring that the effective low energy and UV predictions agree for small enough external momenta [46].

Effective Field Theories enable the calculation of an experimentally measurable quantity with a finite error. Formally, this is done by expanding the existing theory with new higher-dimensional terms as a function of a small expansion parameter called power counting. Such EFT expansion is systematic in the sense that there is a well-defined procedure to compute higher-order

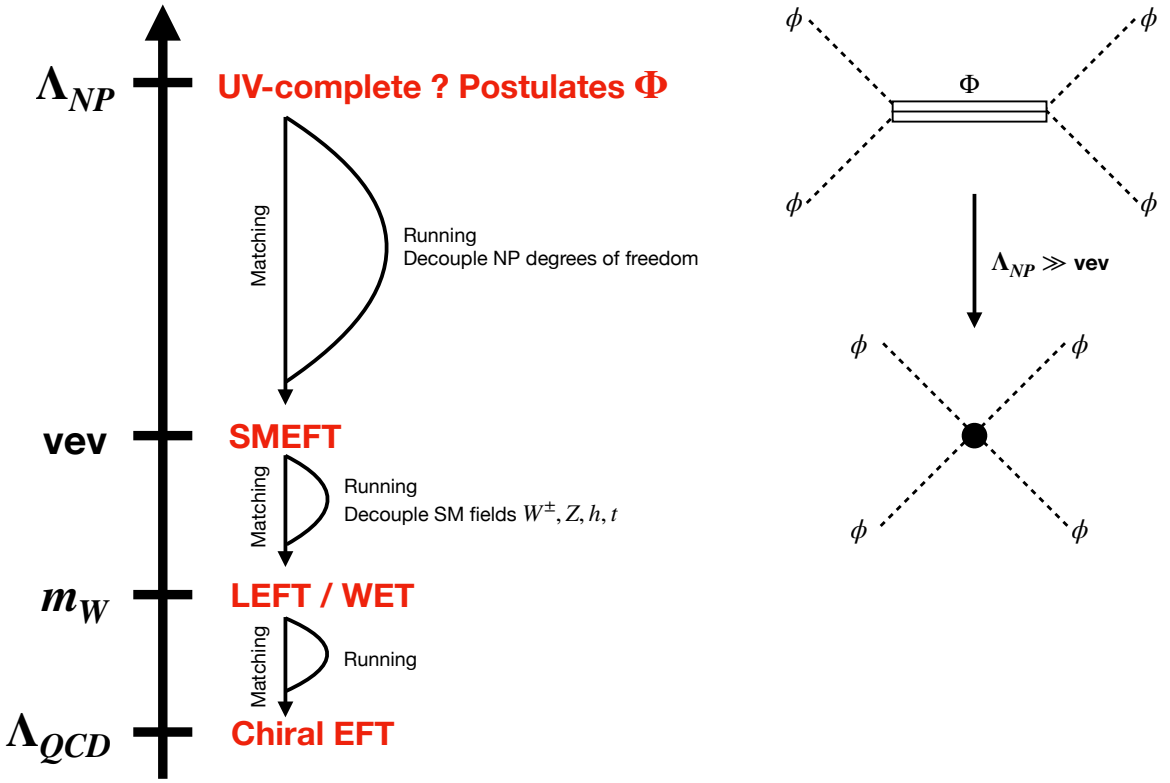

Figure 1.2: Effective field theories as a function of the energy scale. When approximating a higher-energy theory to a low-energy representation, one needs a matching and a running procedure. The former fixes the EFT parameters to ensure the IR and UV predictions agree for small enough external momenta. The latter applies the renormalization group evolution to the EFT parameters, running from an higher energy scale to a lower one. Heavy states (e.g. Φ with mass $m_\Phi \sim \Lambda_{NP}$) can be integrated under the conditions that Φ is always an internal line so it cannot be produced on-shell, effects of Φ are local, going as $1/m_\Phi^2$, and never have non-analyticities at $s = m_\Phi^2$ schematically shown in the right side of the figure.

corrections in the power counting, thus reducing the theoretical error of the predictions.

1.8.1 Counting dimensions and EFT renormalization

The mass dimension of the SM Lagrangian is 4 $[\mathcal{L}] = 4$ and $[D_\mu] = 1$ therefore all terms in the SM Lagrangian have dimension 4 for example

$$\begin{aligned} [D_\mu \phi^\dagger D^\mu \phi] = 4 \rightarrow [\phi] = 1 \\ [X_{\mu\nu} X^{\mu\nu}] = 4 \rightarrow [X_\mu] = 1 \\ [\bar{\psi} D_\mu \psi] = 4 \rightarrow [\psi] = \frac{3}{2} \\ [\bar{\psi} y_L \phi \psi] = 4 \rightarrow [y_L] = 0 \end{aligned} \tag{1.30}$$

Going into higher dimensions we introduce effective operators $\mathcal{L} + = c\mathcal{O}^d$ capturing the new physics effects where the coupling constant c is called the Wilson coefficient and gauges the action of the operator $\mathcal{O}$ while d is the mass dimension of the operator. However, it is known that the SM Lagrangian at $d = 4$ is renormalizable while $d > 4$ theories are not. It can be shown that EFTs are renormalizable order by order i.e. cutting the expansion at a mass dimension d.

Any EFT prediction at a certain order in the power counting is, within its uncertainty, a valid description of nature.

Let's assume a Feynman diagram that contains the loop integral $\int F(p,...)d^4p$. We define the superficial degree of divergence [3] D by the UV behaviour of the integral such that it is given by $\int dp\, p^{D-1}$. This implies that if $D < 0$ the integral is convergent, $D = 0$ the integral is log-divergent and if $D > 0$ it is divergent. We can derive D from the topology of the diagram considering the number of external lines E_f where f is the particle species, the spin of the propagator s_f, the number of involved vertices N_k and the dimension of the operator involved in the interaction d_k as

$$D = 4 - \sum_f E_f(1 + s_f) + \sum_k N_k d_k \tag{1.31}$$

If one assumes to approximate the loop with an EFT vertex, in the limit of infinite mass for the propagator in the loop, we see that the insertion of one ($N_k = 1$) or two ($N_k = 2$) operators of dimension $d_k = 6$ make the integral divergent with $D = 6$ and $D = 8$. If we want the theory to be renormalizable we need counter terms of this dimension to balance the divergencies. The term $-\sum_k N_k(d_k - 4)$ is exactly the power of the mass dimension that regularises the theory. For example using the canonical mass dimension Λ as the power counting parameter we obtain $c\mathcal{O}^d \to c\mathcal{O}^d/\Lambda^{d-4}$.

1.8.2 The Standard Model Effective Field Theory

The Standard Model Effective Field Theory (SMEFT) [47] is a consistent EFT generalization of the SM constructed out of a series of $SU(3)_C \times SU(2)_L \times U(1)_{Y_L}$ invariant higher dimensional operators built from SM fields and including an h field embedded in an $SU(2)$ doublet (see [48] for a recent review). The SMEFT Lagrangian is a systematic expansion of the SM Lagrangian with higher-order terms sorted by canonical dimension

$$\mathcal{L}_{SMEFT} = \mathcal{L}_{SM} + \mathcal{L}^{(5)} + \mathcal{L}^{(6)} + \mathcal{L}^{(7)} + ...; \quad \mathcal{L}^{(d)} = \sum_i^{n_d} \frac{c_i^{(d)}}{\Lambda^{d-4}} \mathcal{O}_i^{(d)} \tag{1.32}$$

Here, Λ represents the scale of new physics, and it is assumed to be significantly greater than the masses of Standard Model particles and the kinematic scales of the processes under investigation. This is indicated by $(E/\Lambda) << 1$, suggesting a state of near decoupling between the new physics sector and the observed processes.

At dimension five, $\mathcal{L}^{(5)}$ contains a single lepton-number-violating $\Delta L = 2$ operator and its Hermitian conjugate $\Delta L = -2$ operator. This operator, called Weinberg operator [49] $\mathcal{L}_5 = c_{ll'}/\Lambda \left[\phi \cdot \bar{l}_L^c\right] \left[l_L' \cdot \phi\right]$ + h.c., give rise to dimension-three Majorana mass terms $m_{ll'} = c_{ll'} \cdot v^2/\Lambda$ for the left-handed neutrinos l_L in the spontaneously broken theory [50].

At dimension six, for three generations of fermions, there are 2499 independent dimension-six operators [51] that do not violate baryon number and lepton number $\Delta B = \Delta L = 0$. These operators give the leading SMEFT contributions under the assumption that the new physics energy scale is well below the lepton-number violation scale $\Lambda \ll \Lambda_{\not{L}}$. Additional 273 dimension-six terms can be constructed with $\Delta B = \Delta L = 1$ allowing for proton decays in SMEFT. Higher order SMEFT operators with $d = 7, 8, ...$ tamed by larger inverse powers of Λ have been extensively studied [52–56] and the number of operators at each mass dimension has been determined and summarised in Figure 1.3.

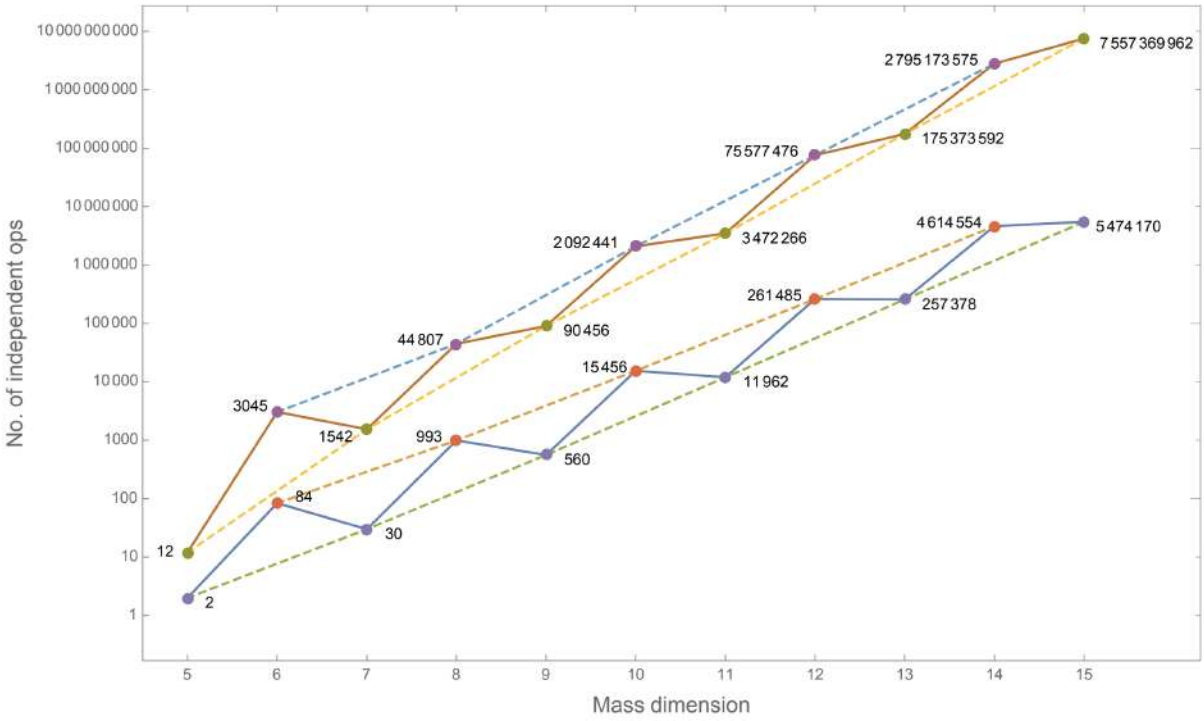

Figure 1.3: Growth of the number of independent operators in the SMEFT from [56]. At each mass dimension, lower points indicate the number of operators assuming one fermion generation while upper ones assume three generations. Dashed lines connect odd and even dimension mass terms.

1.8.3 SMEFT at dimension-six

The leading baryon and lepton number-conserving SMEFT contributions come from dimension-six operators. To identify the minimal set of independent operators, all possible structures built from SM fields and invariant under the SM gauge group $SU(3)_C \times SU(2)_L \times U(1)_{Y_L}$ should be written and redundancies removed by means of integration by parts, conservation of momentum, equation of motion and Fierz identity [57]. An incomplete set of operators is often used in literature as a basis such as the so-called HISZ basis [58], SILH basis [59] or the Buchmüller and Wyler result [47]. However the first non-redundant operator basis for $\mathcal{L}^{(6)}$ has come to be known as the "Warsaw basis" [51], comprising 59 independent operators. Further developments led to a complete SILH basis in recent years [60].

	Fermions					**Scalars**
Field	$l^j_{L,p}$	$e_{R,p}$	$q^{\alpha,j}_{L,p}$	$u^\alpha_{R,p}$	$d^\alpha_{R,p}$	ϕ^j
$\boldsymbol{Y_L}$	$-\frac{1}{2}$	-1	$\frac{1}{6}$	$\frac{2}{3}$	$-\frac{1}{3}$	$\frac{1}{2}$

Table 1.3: SM matter content in $SU(2)$ representation where $j = 1, 2$ denotes the weak isospin, $\alpha = r, g, b$ colour and $p = 1, 2, 3$ is the fermion generation index .

The Warsaw basis is defined in terms of SM fields under in the $SU(2)$ representation and summarised in table 1.3, where $j = 1, 2$ denotes the weak isospin, $\alpha = r, g, b$ colour, $p = 1, 2, 3$ is the fermion generation index and ϕ is the Higgs $SU(2)$ doublet. The conjugate of the Higgs field ($\phi^\dagger$ or $\tilde{\phi}$) is defined though the two-index Levi-Civita tensor ϵ as $\phi^{\dagger,j} = \epsilon_{jk}(\phi^k)^*$. The Hermitian derivative acting on ϕ is defined as $\phi^\dagger i \overleftrightarrow{D}_\mu \phi = \phi^\dagger i D_\mu \phi - i D_\mu \phi^\dagger \phi$ and $\phi^\dagger i \overleftrightarrow{D}^i_\mu \phi =$

$\phi^\dagger i\sigma^i D_\mu \phi - iD_\mu \phi^\dagger \sigma^i \phi$ where σ^i are Pauli matrices. Gauge field strength tensors (generically referred to as $X_{\mu\nu}$) are defined as in the SM for $SU(3)$, namely $G_{\mu\nu}$, $W^a_{\mu\nu}$ for $SU(2)$ and $B_{\mu\nu}$ for $U(1)$, as described in section 1.7.3.

According to the dimension counting described in section 1.8.1, we have various ways to construct dimension-six operators starting from SM terms and we can categorize them according to their field content. The bosonic classes are labelled X^3, ϕ^6, $\phi^4 D^2$, $X^2\phi^2$, $\psi^2 X\phi$, $\psi^2\phi^2 D$. The so-called four-fermion operators modeling point interactions are divided by fermions chirality as $(\bar{L}L)(\bar{L}L)$, $(\bar{R}R)(\bar{R}R)$, $(\bar{L}L)(\bar{R}R)$ and the mixed $(\bar{L}R)(\bar{R}L) + (\bar{L}R)(\bar{L}R)$. The full list of dimension-six operators in the Warsaw basis is given in Table 1.4.

1.8.4 Electroweak input parameters

The Standard Model can make meaningful predictions only if some parameters of the theory, as measured by experiments, are provided as inputs. If one assumes massless neutrinos we need to provide the SM with 19 measured constants. If we allow neutrinos to be massive, 7 more parameters appear leading to a total of 26 as summarised in the following table, where θ_{ij} are the elements of the unitary Cabibbo-Kobayashi-Maskawa (CKM) matrix [61, 62] for flavour mixing, δ the CP-violating phase of the CKM matrix, and U_{ij} the elements of the Pontecorvo-Maki-Nakagawa-Sakata (PMNS) matrix [63, 64] with associated CP-violating phase δ' that accounts for neutrino flavour mixing. The list of the SM fundamental constants under the two hypotheses is reported in Table 1.5.

The Lagrangian parameters $g = \{g_1, ...g_N\}$ are fixed imposing a set of defining conditions that relate them to (pseudo-)observables $\mathcal{O} = \{\mathcal{O}_1, ...\mathcal{O}_M\}$ for $M \geq N$ as $\mathcal{O}_n = F_n^{(0)}(g)$ for $n = 1, ..., M$ where $F_n^{(0)}$ is a function of the parameters g at a chosen perturbative order [65]. If $M = N$ the system is invertible and we can recover the measured values of g from functions K of the observables $\mathcal{O}$ as $g_i = K_i^{(0)}(\mathcal{O})$ for $i = 1, ..., N$.

Going from SM to SMEFT several additional parameters are introduced, namely the cutoff scale Λ and the Wilson coefficients $c_i^{(d)}$. The problem is that the observables $\mathcal{O}$ used to fix the value of the SM parameters g will receive contributions from the SMEFT parameters

$$\begin{aligned} \mathcal{O}_n &= F_n^{(0)}(g) + \frac{1}{\Lambda^2} F_n^{(2)}(g, c^{(6)}) + \frac{1}{\Lambda^4} F_n^{(4)}(g, c^{(8)}) + ... \\ g_i &= K_i^{(0)}(\mathcal{O}) + \frac{1}{\Lambda^2} K_i^{(2)}(\mathcal{O}, c^{(6)}) + \frac{1}{\Lambda^4} K_i^{(4)}(\mathcal{O}, c^{(8)}) + ... \end{aligned} \tag{1.33}$$

A generic predicted observable $\mathcal{P} = P^{(0)}(g) + \sum_{d=2,4,8,...} P^{(d)}(g, c^{4+d})/\Lambda^d$ will receive direct SMEFT contributions from $P^{d\geq 2}$ and indirect SMEFT contributions from g, namely $F_n^{d\geq 2}$. The net effect is that all the EFT corrections to input measurements are recast into corrections to predicted quantities. It can be shown that if $\mathcal{P}$ is an input observable $\mathcal{O}_p$ used to measure g then all EFT corrections cancel order by order. If $\mathcal{P}$ is not an input observable then its prediction will depend on the chosen set of observables $\mathcal{O}$ used to fix the SM values g. The difference in the predicted quantity $\mathcal{P}$ due to a different set of input observables is

$$\mathcal{P}(\mathcal{O}) - \mathcal{P}(\mathcal{O}') = \frac{1}{\Lambda^2}\left[-\frac{\partial P^{(0)}}{\partial F_n^{(0)}} F_n^{(2)} + \frac{\partial P^{(0)}}{\partial F'^{(0)}_n} F'^{(2)}_n \right] + \frac{1}{\Lambda^4} ... \tag{1.34}$$

It is essential to choose carefully the input observables set $\mathcal{O}$ as results for $\mathcal{P}$ depend upon the input parameter set chosen [66].

X^3		ϕ^6 and $\phi^4 D^2$		$\psi^2\phi^3$	
Q_G	$f^{abc}G^{a\nu}_{\mu}G^{b\rho}_{\nu}G^{c\mu}_{\rho}$	Q_ϕ	$(\phi^\dagger\phi)^3$	$Q_{e\phi}$	$(\phi^\dagger\phi)(\bar{l}_p e_r \phi)$
$Q_{\tilde{G}}$	$f^{abc}\tilde{G}^{a\nu}_{\mu}G^{b\rho}_{\nu}G^{c\mu}_{\rho}$	$Q_{\phi\Box}$	$(\phi^\dagger\phi)\Box(\phi^\dagger\phi)$	$Q_{u\phi}$	$(\phi^\dagger\phi)(\bar{q}_p u_r \tilde{\phi})$
Q_W	$\epsilon^{ijk}W^{i\nu}_{\mu}W^{j\rho}_{\nu}W^{k\mu}_{\rho}$	$Q_{\phi D}$	$(D^\mu\phi^\dagger\phi)(\phi^\dagger D_\mu\phi)$	$Q_{d\phi}$	$(\phi^\dagger\phi)(\bar{q}_p d_r \phi)$
$Q_{\tilde{W}}$	$\epsilon^{ijk}\tilde{W}^{i\nu}_{\mu}W^{j\rho}_{\nu}W^{k\mu}_{\rho}$				
$X^2\phi^2$		$\psi^2 X\phi$		$\psi^2\phi^2 D$	
$Q_{\phi G}$	$\phi^\dagger\phi G^a_{\mu\nu}G^{a\mu\nu}$	Q_{eW}	$(\bar{l}_p\sigma^{\mu\nu}e_r)\sigma^i\phi W^i_{\mu\nu}$	$Q^{(1)}_{\phi l}$	$(\phi^\dagger i\overleftrightarrow{D}_\mu\phi)(\bar{l}_p\gamma^\mu l_r)$
$Q_{\phi\tilde{G}}$	$\phi^\dagger\phi\tilde{G}^a_{\mu\nu}G^{a\mu\nu}$	Q_{eB}	$(\bar{l}_p\sigma^{\mu\nu}e_r)\phi B_{\mu\nu}$	$Q^{(3)}_{\phi l}$	$(\phi^\dagger i\overleftrightarrow{D}^i_\mu\phi)(\bar{l}_p\sigma^i\gamma^\mu l_r)$
$Q_{\phi W}$	$\phi^\dagger\phi W^a_{\mu\nu}W^{a\mu\nu}$	Q_{uG}	$(\bar{q}_p\sigma^{\mu\nu}T^a u_r)\tilde{\phi}G^a_{\mu\nu}$	$Q_{\phi e}$	$(\phi^\dagger i\overleftrightarrow{D}_\mu\phi)(\bar{e}_p\gamma^\mu e_r)$
$Q_{\phi\tilde{W}}$	$\phi^\dagger\phi\tilde{W}^a_{\mu\nu}W^{a\mu\nu}$	Q_{uW}	$(\bar{q}_p\sigma^{\mu\nu}u_r)\sigma^i\tilde{\phi}W^i_{\mu\nu}$	$Q^{(1)}_{\phi q}$	$(\phi^\dagger i\overleftrightarrow{D}_\mu\phi)(\bar{q}_p\gamma^\mu q_r)$
$Q_{\phi B}$	$\phi^\dagger\phi B_{\mu\nu}B^{\mu\nu}$	Q_{uB}	$(\bar{q}_p\sigma^{\mu\nu}u_r)\tilde{\phi}B_{\mu\nu}$	$Q^{(3)}_{\phi q}$	$(\phi^\dagger i\overleftrightarrow{D}^i_\mu\phi)(\bar{q}_p\sigma^i\gamma^\mu q_r)$
$Q_{\phi\tilde{B}}$	$\phi^\dagger\phi\tilde{B}_{\mu\nu}B^{\mu\nu}$	Q_{dG}	$(\bar{q}_p\sigma^{\mu\nu}T^a d_r)\phi G^a_{\mu\nu}$	$Q_{\phi u}$	$(\phi^\dagger i\overleftrightarrow{D}_\mu\phi)(\bar{u}_p\gamma^\mu u_r)$
$Q_{\phi WB}$	$\phi^\dagger\sigma^i\phi W^i_{\mu\nu}B^{\mu\nu}$	Q_{dW}	$(\bar{q}_p\sigma^{\mu\nu}d_r)\sigma^i\phi W^i_{\mu\nu}$	$Q_{\phi d}$	$(\phi^\dagger i\overleftrightarrow{D}_\mu\phi)(\bar{d}_p\gamma^\mu d_r)$
$Q_{\phi\tilde{W}B}$	$\phi^\dagger\sigma^i\phi\tilde{W}^i_{\mu\nu}B^{\mu\nu}$	Q_{dB}	$(\bar{q}_p\sigma^{\mu\nu}d_r)\phi B_{\mu\nu}$	$Q_{\phi ud}$	$i(\tilde{\phi}^\dagger D_\mu\phi)(\bar{u}_p\gamma^\mu d_r)$
$(\bar{L}L)(\bar{L}L)$		$(\bar{R}R)(\bar{R}R)$		$(\bar{L}R)(\bar{L}R)+(\bar{L}R)(\bar{R}L)$	
Q_{ll}	$(\bar{l}_p\gamma_\mu l_r)(\bar{l}_s\gamma^\mu l_t)$	Q_{ee}	$(\bar{e}_p\gamma_\mu e_r)(\bar{e}_s\gamma^\mu e_t)$	Q_{le}	$(\bar{l}_p\gamma_\mu r)(\bar{e}_s\gamma^\mu e_t)$
$Q^{(1)}_{qq}$	$(\bar{q}_p\gamma_\mu q_r)(\bar{q}_s\gamma_\mu q_t)$	Q_{uu}	$(\bar{u}_p\gamma_\mu u_r)(\bar{u}_s\gamma_\mu u_t)$	Q_{lu}	$(\bar{l}_p\gamma_\mu l_r)(\bar{u}_s\gamma_\mu u_t)$
$Q^{(3)}_{qq}$	$(\bar{q}_p\gamma_\mu\sigma^i q_r)(\bar{q}_s\gamma_\mu\sigma^i q_t)$	Q_{dd}	$(\bar{d}_p\gamma_\mu d_r)(\bar{d}_s\gamma_\mu d_t)$	Q_{ld}	$(\bar{l}_p\gamma_\mu l_r)(\bar{d}_s\gamma_\mu d_t)$
$Q^{(1)}_{lq}$	$(\bar{l}_p\gamma_\mu l_r)(\bar{q}_s\gamma^\mu q_t)$	Q_{eu}	$(\bar{e}_p\gamma_\mu e_r)(\bar{u}_s\gamma_\mu u_t)$	Q_{qe}	$(\bar{q}_p\gamma_\mu q_r)(\bar{e}_s\gamma_\mu e_t)$
$Q^{(3)}_{lq}$	$(\bar{l}_p\gamma_\mu\sigma^i l_r)(\bar{q}_s\gamma^\mu\sigma^i q_t)$	Q_{ed}	$(\bar{e}_p\gamma_\mu e_r)(\bar{d}_s\gamma_\mu d_t)$	$Q^{(1)}_{qu}$	$(\bar{q}_p\gamma_\mu q_r)(\bar{u}_s\gamma^\mu u_t)$
		$Q^{(1)}_{ud}$	$(\bar{u}_p\gamma_\mu u_r)(\bar{d}_s\gamma^\mu d_t)$	$Q^{(8)}_{qu}$	$(\bar{q}_p\gamma_\mu T^a q_r)(\bar{u}_s\gamma^\mu T^a u_t)$
		$Q^{(8)}_{ud}$	$(\bar{u}_p\gamma_\mu T^a u_r)(\bar{d}_s\gamma^\mu T^a d_t)$	$Q^{(1)}_{qd}$	$(\bar{q}_p\gamma_\mu q_r)(\bar{d}_s\gamma^\mu d_t)$
				$Q^{(8)}_{qd}$	$(\bar{q}_p\gamma_\mu T^a q_r)(\bar{d}_s\gamma^\mu T^a d_t)$
$(\bar{L}R)(\bar{L}R)+(\bar{L}R)(\bar{R}R)$		Barion number violating			
Q_{leqd}	$(\bar{l}^j_p e_r)(\bar{d}_s q^j_t)$	Q_{duq}	$\epsilon^{\alpha\beta\gamma}\epsilon_{jk}\left[(d^\alpha_p)^T C u^\beta_r\right]\left[(q^{\gamma j}_s)^T C l^k_t\right]$		
$Q^{(1)}_{quqd}$	$(\bar{q}^j_p u_r)\epsilon_{jk}(\bar{q}^k_s d_t)$	Q_{qqu}	$\epsilon^{\alpha\beta\gamma}\epsilon_{jk}\left[(q^{\alpha j}_p)^T C q^{\beta k}_r\right]\left[(u^\gamma_s)^T C e_t\right]$		
$Q^{(8)}_{quqd}$	$(\bar{q}^j_p T^a u_r)\epsilon_{jk}(\bar{q}^k_s T^a d_t)$	$Q^{(1)}_{qqq}$	$\epsilon^{\alpha\beta\gamma}\epsilon_{jk}\epsilon_{mn}\left[(q^{\alpha j}_p)^T C q^{\beta k}_r\right]\left[(q^{\gamma m}_s)^T C l^n_t\right]$		
$Q^{(1)}_{lequ}$	$(\bar{l}^j_p e_r)\epsilon_{jk}(\bar{q}^k_s u_t)$	$Q^{(3)}_{qqq}$	$\epsilon^{\alpha\beta\gamma}(\sigma^i\epsilon)_{jk}(\sigma^i\epsilon)_{mn}\left[(q^{\alpha j}_p)^T C q^{\beta k}_r\right]\left[(q^{\gamma m}_s)^T C l^n_t\right]$		
$Q^{(3)}_{lequ}$	$\bar{l}^j_p\sigma_{\mu\nu}e_r)\epsilon_{jk}(\bar{q}^k_s\sigma^{\mu\nu}u_t)$	Q_{duu}	$\epsilon^{\alpha\beta\gamma}\left[(d^\alpha_p)^T C u^\beta_r\right]\left[(u^\gamma_s)^T C e_t\right]$		

Table 1.4: Dimension-six operators as defined in the Warsaw basis [51].

For the Higgs and electroweak sector the SM contains 4 independent quantities $g = \{g, g', v, \lambda\}$ that can be fixed by measuring observables in the set $\mathcal{O} = \{\alpha_{em}, G_F, m_W, m_Z, m_h\}$. The Higgs boson mass m_h is always needed to fix λ, but the choice of the remaining three is arbitrary. Three alternative schemes for electroweak input observables are available. The $\{\alpha_{em}, G_F, m_Z\}$

$m_\nu = 0$	$m_\nu \neq 0$		
✓	✓	α_S, θ_{QCD}	QCD
✓	✓	$y_e, y_\mu, y_\tau, y_u, y_d, y_c, y_s, y_t, y_b$	Yukawas
✓	✓	g, g', v, λ	EW+Higgs
✓	✓	$\theta_{12}, \theta_{13}, \theta_{23}, \delta$	CKM
-	✓	$y_{\nu_e}, y_{\nu_\mu}, y_{\nu_\tau}$	Yukawas
-	✓	$U_{12}, U_{13}, U_{23}, \delta'$	PMNS

Table 1.5: SM fundamental parameters assuming massless or massive neutrinos, respectively denoted as $m_\nu = 0$ and $m_\nu \neq 0$. In the first case, the SM needs 19 measured constants. When assuming massive neutrinos, in addition to the previous 19 constants 7 new parameters appear related to the neutrino mixing and Yukawa interactions, leading to a total of 26 constants to be measured by experiments.

set was historically used by LEP and features the most precisely known parameters from the set. The downside is that m_W now receives SMEFT corrections that will enter many other observables and in the propagator definition of the W boson, leading to a highly non-linear dependence of predictions upon Wilson coefficients. The second set solves the previous problem by incorporating m_W in the input set, thus freezing its value to the measured one $\{G_F, m_Z, m_W\}$. As a downside, SMEFT corrections to the Fermi constant G_F must always be considered even for sets of observables that have no direct connection to leptonic physics. The last set presents α_{em} $\{\alpha_{em}, m_Z, m_W\}$ and has the advantage of avoiding shifts in electroweak couplings that arise from processes depending on G_F, such as the muon decay. However, it can lead to slightly worse electroweak convergences both in the SM and in SMEFT [67]. At the time of writing, the developers of SMEFT tools tend to favor the $\{G_F, m_Z, m_W\}$ set [68].

1.8.5 Flavour assumptions at dimension-six

While the number of independent electroweak structures amounts to only 59 independent dimension-six operators [51], a proliferation of Wilson coefficients occurs when accounting for all the possible flavour structures. If no flavour symmetry is imposed, the SMEFT Lagrangian of equation 1.32 will depend on 1350 CP-even plus 1149 CP-odd independent coefficients for the dimension-six operators [69]. At the time being, it is hopeless to attempt to constrain such a large parameter space, therefore a dimensionality reduction strategy is needed. This is practically done by imposing a flavour symmetry (and symmetry-breaking sector) at the expense of introducing some model dependence. These symmetries are not necessarily fundamental symmetries of the underlying ultraviolet (UV) theory but could be accidental if e.g. the theory discriminates between fermion generations [70]. In the following non-exhaustive list, the most popular flavour symmetries will be explained.

1.8.5.1 Maximal $U(3)^5$ symmetry

The largest group of flavour-symmetry transformations compatible with the gauge symmetries of the SM Lagrangian is $U(3)^5$

$$U(3)^5 = U(3)_l \times U(3)_q \times U(3)_e \times U(3)_u \times U(3)_d = SU(3)^5 \times U(1)^5 \tag{1.35}$$

$U(3)^5$ essentially states that fermions with the same electroweak quantum numbers are not distinguished by gauge interactions [71]. The most restrictive assumption that can be made is

that $U(3)^5$ is an exact symmetry of the beyond-the-SM sector. This is only valid if one neglects Yukawa couplings.

1.8.5.2 Linear Minimal Flavour Violation

In the SM Yukawa couplings $Y_{e,u,d}$ and the CKM phase δ explicitly break the $U(3)^5$ flavour symmetry. Flavour violation is realized by elevating Yukawa couplings to spurions of the flavour symmetry [72]. This involves enforcing a $U(3)^5$ symmetry on the fermion fields, which permits unrestricted $U(3)^5$-invariant insertions of these spurious parameters in the currents. These insertions are responsible for generating flavour-violating effects [65]. Spurion insertions are organized in a power expansion of the Yukawa couplings, e.g. for a single insertion $\mathcal{O}(Y_{u,d,e})$ or double insertions $\mathcal{O}(Y_u^2)$, $\mathcal{O}(Y_u Y_d)$, $\mathcal{O}(Y_u^2 Y_d)$ and so on [70].

1.8.5.3 $U(2)^3$ symmetry in the quark sector

The CKM description of flavour mixing and CP-violation in the quark sector is incredibly precise. However, the underlying mechanism generating quark masses and mixing is still unknown. The Minimal Flavour Violation anastz [73] with a broken $U(3)^3$ does not provide any clue about the origin of the hierarchal nature of the Yukawa couplings. In order to recover the level of flavour violation suppression observed in experiments, a minimally broken $U(2)^3$ flavour symmetry acting on the first two generations of quarks can arguably be more interesting [74, 75]. In this way, the quarks of the first two generations transform differently under this symmetry. Denoting by (q_p, u_p, d_p) left and right-handed fields for the first and second generations (with generation index $p = 1, 2$), by (Q, t, b) left and right-handed fields for the third generation and with Ω a generic $U(2)$ transformation, the symmetry under which only light quarks transform can be written as

$$\begin{aligned} &U(2)^3 = U(2)_q \times U(2)_u \times U(2)_d \\ &q \to \Omega_q q, \quad u \to \Omega_u, \quad d \to \Omega d, \quad Q \to Q, \quad t \to t, \quad b \to b \end{aligned} \tag{1.36}$$

The lepton sector decouples from the quark sector and there is freedom to relax or tighten the lepton flavour restrictions. Several options are in use. The most restrictive case is the $U(3)^2 = U(3)_l \times U(3)_e$ symmetry, as done in the maximal assumption and Minimal Flavour Violation scenarios. One can increasingly relax this requirement imposing for example $U(2)^2 = U(2)_l \times U(2)_e$ (when combining with quark sector leads to $U(2)^5$ [74]) or even assume flavour diagonality $U(1)^3_{l+e} = U(1)_e \times U(1)_\mu \times U(1)_\tau$ [65, 76].

The number of parameters for each flavour assumption is given in Table 1.6.

	General		$U(3)^5$		**MFV**		$U(2)^3 \times U(1)^3$		$U(2)^3 \times U(3)^2$	
	All	CP	All	CP	All	CP	All	CP	All	CP
X^3	4	2	4	2	2	-	4	2	4	2
ϕ^6 and $\phi^4 D^2$	3	-	3	-	3	-	3	-	3	-
$\psi^2 X \phi$	8	4	8	4	4	-	8	4	8	4
$\psi^2 \phi^3$	54	27	6	3	7	-	14	7	10	5
$\psi^2 X \phi$	144	72	16	8	20	-	36	18	28	14
$\psi^2 \phi^2 D$	81	30	9	1	14	-	21	2	15	2
$(\bar{L}L)(\bar{L}L)$	297	126	8	-	10	-	31	-	16	-
$(\bar{R}R)(\bar{R}R)$	450	195	9	-	19	-	40	2	27	2
$(\bar{L}L)(\bar{R}R)$	648	288	8	-	28	-	54	4	31	4
$(\bar{L}R)(\bar{L}R) + (\bar{L}R)(\bar{R}L)$	810	405	14	7	13	-	64	32	40	20
total	2499	1149	85	25	120	-	275	71	182	53

Table 1.6: Number of independent parameters for each class of dimension-six operators as defined in the Warsaw basis under different flavour assumptions. Table from [65]

Chapter 2

SMEFT interpretation of Vector Boson Scattering

2.1 Vector Boson Scattering

Since the discovery of a new scalar boson by the CMS and ATLAS collaborations in 2012 [77, 78], its properties, such as its couplings with other SM particles, have been studied in depth showing that the observations are compatible with an excitation of the Higgs field [79, 80]. The study of the high-energy behaviour of the electroweak W and Z bosons can shed light on the EWSB mechanism in an independent way. Vector Boson Scattering (VBS) happens when two electroweak vector bosons scatter off one another. In proton-proton collisions at the LHC, these electroweak vector bosons are radiated by the initial state partons producing a striking signature inside the detector, characterized by two highly energetic jets in the forward and backward direction, close to the beamline, along with two electroweak bosons.

The SM Higgs boson plays a crucial role in VBS. The VBS signature can produced through triple and quartic gauge couplings among electroweak bosons. In this scenario, the scattering amplitude of longitudinally polarized vector bosons $V_L V_L \rightarrow V_L V_L$ would violate unitarity at center-of-mass energies of order 1 TeV [81, 82] (see the left side of Figure 2.1). The VBS diagrams involving a Higgs boson exchange cancel exactly the energy growth of bosonic-induced diagrams thus preserving unitarity at high energies, as predicted in the SM [83, 84]. At the time of writing the measurements of the Higgs boson properties agree with the SM within experimental uncertainties however any deviation in the coupling of the Higgs boson to the gauge bosons would break the VBS delicate diagram cancellation, thus allowing a test of the EW symmetry breaking mechanism (EWSB) of the SM (see right side of Figure 2.1).

The data collected by LHC experiments during Run I and Run II allow for precise measurements of the VBS process in different final states, thus probing the high-energy behaviour of the SM scalar sector.

2.2 The need for SMEFT interpretation of VBS

One key aspect of SMEFT interpretations is that they can provide a meaningful and model-independent description of nature at any order in the truncated SMEFT expansion only if all the relevant parameters are included. However, as highlighted in table 1.6, even under the most restrictive scenarios the number of parameters becomes unfeasibly large. This implies that when performing a global SMEFT fit, one must navigate a vast parameter space, which may contain numerous degenerate directions or combinations of parameters that produce similar observable outcomes. It is hopeless to attempt to constrain all the SMEFT parameters with a single process. State-of-the-art global SMEFT analyses are based on Higgs, diboson, LEP and

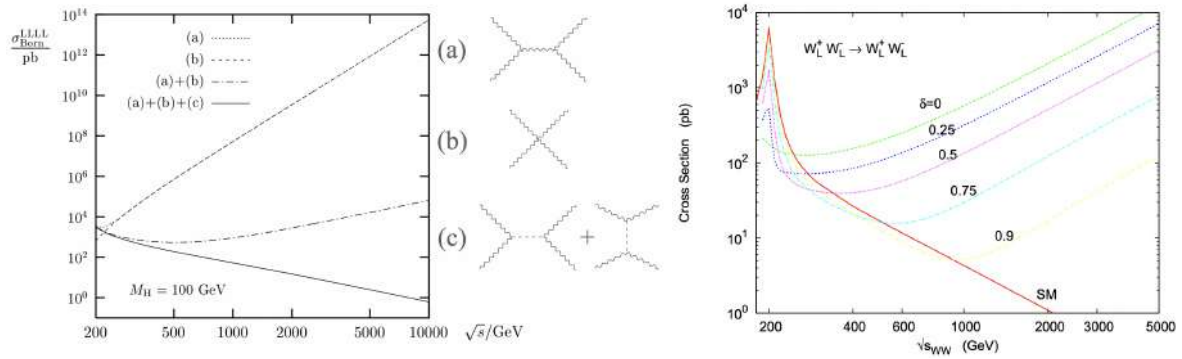

Figure 2.1: Left figure from [83] shows how the cross section for $V_LV_L \to V_LV_L$ diverges in the absence of Higgs-mediated diagrams (a)+(b) while is it unitarized by s and t-channel Higgs diagrams (a)+(b)+(c). In the right figure the authors of [84] assume that the hW^+W^- coupling is a fraction $\sqrt{\delta}$ of its SM value thus the cancellation of the energy growth of amplitudes is only partial and distorts the spectrum of the diboson invariant mass $\sqrt{s_{WW}}$ in the process $W_L^+W_L^- \to W_L^+W_L^-$

top quark measurements in order to constrain approximately 30 SMEFT Wilson coefficients simultaneously [85–92], with the possibility to relax CP and flavour assumptions [93] as well as in incorporating information from B-meson observables [94–96].

Thanks to the unprecedented amount of data collected by the CERN Large Hadron Collider (LHC), VBS measurements are quickly populating the experimental landscape. The analysis of Run-II data by the ATLAS and CMS collaborations has recently led to the observation of VBS in the same-sign and opposite-sign WW [97–100], WZ [101, 102] and ZZ [103, 104] final states, and to strong evidence in the semileptonic WV final state [105]. VBS processes with a photon, a heavy vector boson and two jets were recently observed as well [106–109].

VBS processes are among the most interesting signatures in order to enlarge the set of analyses used for global SMEFT constraints [110] as they allow the extraction of new constraints on the EW sector that are complementary to those from Higgs and diboson measurements. Specifically, VBS processes provide tree-level sensitivity to effective operators inducing modifications of triple (TGC) and quartic gauge couplings (QGC), as well as Higgs-gauge couplings away from the Higgs mass-shell, and even contact interactions among four light quarks. The rich SMEFT phenomenology present in VBS processes is summarised in Figure 2.2 and compared to diboson, multi-jet, Higgs and top-related processes. Historically, previous investigations of EFT effects in VBS have been driven by the leading QGC sensitivity and were often restricted to dimension-8 operators that generate genuine QGC corrections while leaving TGCs unaffected [111]. The impact of dimension-6 operators was explored systematically only recently, driven by the interest in incorporating these measurements into global SMEFT analyses [112–114], showing that even if VBS measurements typically yield weaker constraints, compared to EW precision observables, Higgs or inclusive diboson measurements, they can play a significant role in global analyses by constraining new directions in the parameter space and providing a link between the EW, Higgs and four-quarks sectors. In this direction, new phenomenological papers compare the limits on several Wilson coefficients considering just inclusive diboson or triboson production versus the inclusion of VBS [115–117] showing a 15 to 50% weaker constraints when VBS is not included.

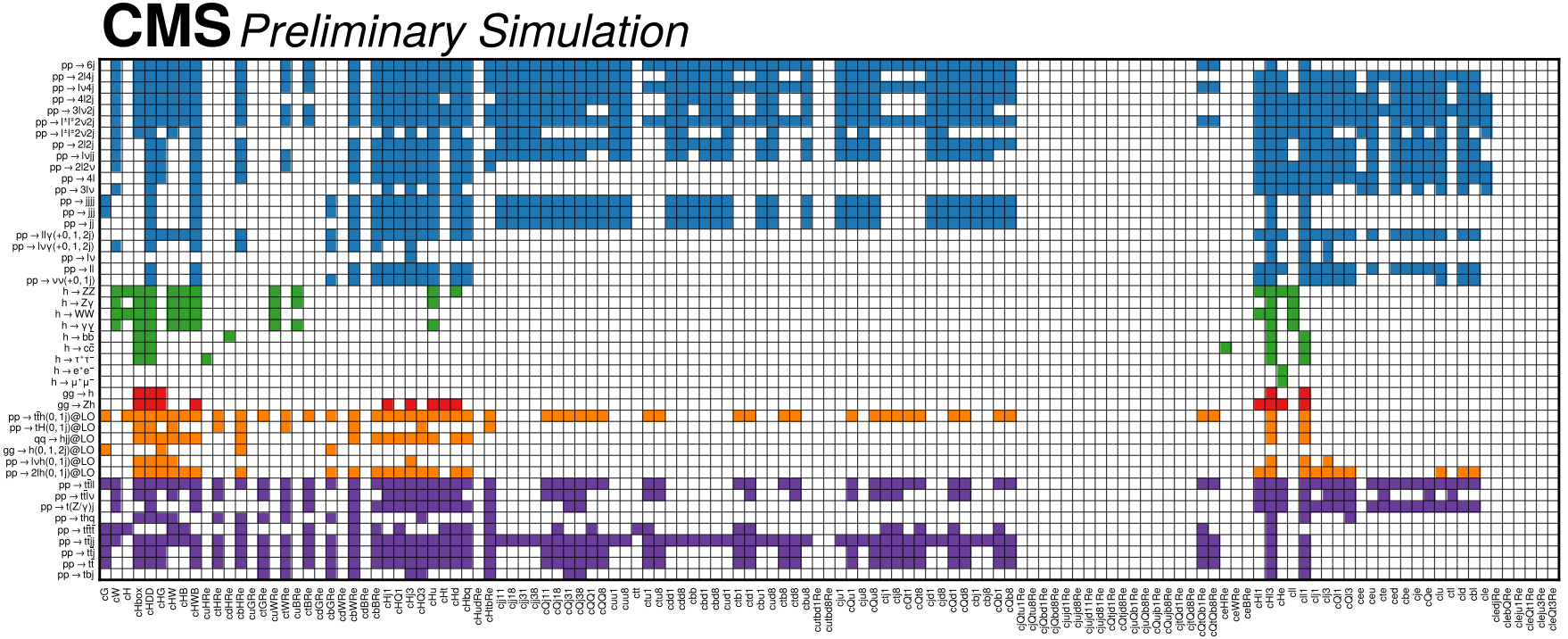

Figure 2.2: Summary table for SMEFT effects in typical LHC processes. The y-axis reports the process definition while the x-axis enumerates the Wilson coefficients associated with SMEFT operators under the $U(2)^3 \times U(3)_l \times U(3)_e$ flavour symmetry. A cell is coloured if there exists an SMEFT diagram for the given topology and the given operator. Blue rows correspond to VBS, triboson, diboson, single boson and multi-jet processes [48, 65]. Green and red rows list the NLO Higgs decay [118–120] and production [121] modes respectively. Orange rows correspond to LO Higgs production modes while purple rows to top-related processes [48, 65]. The operators for which no process is sensitive are proportional to Yukawa couplings which are set to zero in the generation as typically done for LHC simulations.

$Q_{Hl}^{(1)} = (H^\dagger i\overleftrightarrow{D_\mu} H)(\bar{l}_p \gamma^\mu l_p)$	$Q_{Hl}^{(3)} = (H^\dagger i\overleftrightarrow{D_\mu^i} H)(\bar{l}_p \sigma^i \gamma^\mu l_p)$
$Q_{Hq}^{(1)} = (H^\dagger i\overleftrightarrow{D_\mu} H)(\bar{q}_p \gamma^\mu q_p)$	$Q_{Hq}^{(3)} = (H^\dagger i\overleftrightarrow{D_\mu^i} H)(\bar{q}_p \sigma^i \gamma^\mu q_p)$
$Q_{qq}^{(1)} = (\bar{q}_p \gamma_\mu q_p)(\bar{q}_r \gamma^\mu q_r)$	$Q_{qq}^{(1,1)} = (\bar{q}_p \gamma_\mu q_r)(\bar{q}_r \gamma^\mu q_p)$
$Q_{qq}^{(3)} = (\bar{q}_p \gamma_\mu \sigma^i q_p)(\bar{q}_r \gamma^\mu \sigma^i q_r)$	$Q_{qq}^{(3,1)} = (\bar{q}_p \gamma_\mu \sigma^i q_r)(\bar{q}_r \gamma^\mu \sigma^i q_p)$
$Q_{HD} = (H^\dagger D_\mu H)(H^\dagger D^\mu H)$	$Q_{H\Box} = (H^\dagger H)\Box(H^\dagger H)$
$Q_{HWB} = (H^\dagger \sigma^i H) W^i_{\mu\nu} B^{\mu\nu}$	$Q_{HW} = (H^\dagger H) W^i_{\mu\nu} W^{i\mu\nu}$
$Q_W = \varepsilon^{ijk} W^{i\nu}_\mu W^{j\rho}_\nu W^{k\mu}_\rho$	$Q_{ll}^{(1)} = (\bar{l}_p \gamma_\mu l_r)(\bar{l}_r \gamma^\mu l_p)$

Table 2.1: The subset of Warsaw basis CP-even operators considered in the VBS dimension-six sensitivity study. Repeated indices are understood to be summed over. p, r are flavour indices, and a $U(3)^5$-invariant flavour structure is assumed.

2.3 A sensitivity study of VBS and diboson WW to dimension-6 SMEFT operators

In order to understand the impact of VBS in global EFT fits, the expected individual and combined sensitivity of five different VBS channels to a set of 14 dimension-6 operators in the Warsaw basis is studied at parton-level [116]. The performance of the VBS channels is evaluated in comparison to a diboson process, which has conventionally been the primary domain for dimension-6 EFT analyses. This preference arises from their substantial production cross-sections and favorable signal-to-background ratios. VBS processes are treated as $2 \to 6$ scatterings at leading-order (LO) in QCD namely α^6, retaining EFT contributions to non-resonant diagrams. Where appropriate, EFT contributions from the irreducible QCD-induced VBS production at order $\alpha_S^s \alpha^4$ are included. Similarly, the diboson process is treated as a $2 \to 4$ process.

The SMEFT Lagrangian truncated at dimension-six is defined as in the SMEFTSIM package implementation [65, 122]

$$\mathcal{L}_{SMEFT} = \mathcal{L}_{SM} + \frac{1}{\Lambda^2} \sum_\alpha c_\alpha Q_\alpha + \mathcal{O}(\Lambda^{-4}) \tag{2.1}$$

The index α runs over the labels of the Warsaw basis. Fermionic operators are required to be invariant (up to insertions of the Yukawa couplings) under a $U(3)^5$ flavour symmetry. CP conservation is assumed and the $\{m_W, m_Z, G_F\}$ set is assumed as input to the electroweak sector. The subset of operators from the Warsaw basis considered for this study is summarised in Table 2.1. These operators enter via modification of electroweak input quantities ($Q_{Hl}^{(3)}, Q_{ll}^{(1)}, Q_{HD}, Q_{HWB}$), triple gauge couplings (Q_W), modification to vector bosons couplings to fermions Vff ($Q_{Hl}^{(1)}$, $Q_{Hl}^{(3)}$, $Q_{Hq}^{(1)}$, $Q_{Hq}^{(3)}$), modification to the couplings of the Higgs boson to vector bosons HVV (Q_{HD}, Q_{HW}, Q_{HWB}, $Q_{H\Box}$) or via four-quarks contact terms ($Q_{qq}^{(1)}$, $Q_{qq}^{(3)}$, $Q_{qq}^{(1,1)}$, $Q_{qq}^{(3,1)}$).

At the order Λ^{-2}, a generic SMEFT scattering amplitude has the form

$$\mathcal{A} = \mathcal{A}_{\text{SM}} + \sum_\alpha \frac{c_\alpha}{\Lambda^2} \cdot \mathcal{A}_{Q_\alpha} \tag{2.2}$$

Where $\mathcal{A}_{Q_\alpha}$ is the total amplitude obtained with only one insertion of the operator Q_α and scales linearly with the Wilson coefficient c_α. By squaring the absolute value of the amplitude,

the expected number of events in a given phase space is expected to scale with the Wilson coefficient as follows, for the generic case where two Wilson Coefficients are left free to float

$$N \propto |\mathcal{A}|^2 = |\mathcal{A}_{\mathrm{SM}}|^2 + \sum_{\alpha} \frac{c_\alpha}{\Lambda^2} \cdot 2\Re(\mathcal{A}_{\mathrm{SM}}\mathcal{A}^\dagger_{Q_\alpha}) + \sum_{\alpha,\beta} \frac{c_\alpha c_\beta}{\Lambda^4} \cdot (\mathcal{A}_{Q_\alpha}\mathcal{A}^\dagger_{Q_\beta}) \tag{2.3}$$

$$N = N_{SM} + \sum_{\alpha} \left[\frac{c_\alpha}{\Lambda^2} N^{\mathrm{int}}_\alpha + \frac{c^2_\alpha}{\Lambda^4} N^{\mathrm{quad}}_\alpha \right] + \sum_{\alpha \neq \beta} \frac{c_\alpha c_\beta}{\Lambda^4} N^{\mathrm{mix}}_{\alpha,\beta} \tag{2.4}$$

where for $\alpha = \beta$ the last term of Eq. 2.4 reduces to $(c^2_\alpha/\Lambda^4)|\mathcal{A}_{Q_\alpha}|^2 = (c^2_\alpha/\Lambda^4)N^{\mathrm{quad}}_\alpha$. The terms $N^{\mathrm{SM}} \propto |\mathcal{A}_{\mathrm{SM}}|^2$, $N^{\mathrm{int}}_\alpha \propto 2\Re(\mathcal{A}_{\mathrm{SM}}\mathcal{A}^\dagger_{Q_\alpha})$, $N^{\mathrm{quad}}_\alpha \propto |\mathcal{A}_{Q_\alpha}|^2$, $N^{\mathrm{mix}}_{\alpha,\beta} \propto 2\Re(\mathcal{A}_{Q_\alpha}\mathcal{A}^\dagger_{Q_\beta})$ can be computed numerically and equation 2.4 holds for inclusive and differential observables.

2.3.1 Analysis procedure and event generation

Five different VBS channels without photons and a diboson W^+W^- one are considered. All channels present a leptonic decay of the scattered vector bosons except for the VBS-ZV, where the Z boson decays into a lepton pair while the other V boson ($W^\pm$ or Z) decays in a pair of quarks. In the fully leptonic channels, the final states include electrons and muons and, for simplicity, the two vector bosons are required to decay into a charged lepton (or lepton-neutrino) pairs of a different flavour. At the analysis level, the requirement of leptons of different flavours drastically reduces the background contamination and therefore presents a more favorable signal-over-background ratio. The list of generated processes both for the purely electroweak induced processes (EW) at α^6 and for the QCD irreducible backgrounds (QCD) at order $\alpha^2_S\alpha^4$ is summarised in Table 2.2. Events are simulated at parton-level at the LO in QCD with MADGRAPH5_AMC@NLO (v. 2.6.5) [123] interfaced to the SMEFTSIM package (v. 3) [65, 122]. The syntax used to generate the SM component along with specifications for the SMEFT terms is summarised in Table 2.2.

The simulations are produced for pp collisions at a center-of-mass energy of 13 TeV, using the NNLO parton distribution functions provided by the NNPDF collaboration [124], $\alpha_S = 0.118$ and in the four-flavour scheme (LHAPDF identification code 325500). Renormalization and factorization scales are determined dynamically by the generator as the transverse mass of the $2 \to 2$ scattering after k_T clustering. The EFT parametrization in equation 2.4 for n operators depends on n linear and quadric components ($N^{\mathrm{int}}, N^{\mathrm{quad}}$) and $n(n-1)/2$ mixed contributions (N^{mix}) and can be determined by computing N at a total of $n(n+3)/2$ (119 for n = 14) independent points in the parameter space. N_{SM} as well as $N^{\mathrm{int}}, N^{\mathrm{quad}}, N^{\mathrm{mix}}$ for individual and pairs of operators can be generated directly via independent simulations for each contribution exploiting the interaction-order syntax in MADGRAPH5_AMC@NLO and SMEFTSIM. While this method precisely samples the EFT phase space, especially in the tail of the SM distribution, it is computationally expensive requiring $n(n+3)/2$ different generations and can lead to non-physical negative yields in bins of differential observables. The latter behaviour is due to the independence of the phase spaces for each of the components. To overcome the issue the MADGRAPH5_AMC@NLO reweighting method [125] is also employed. In this case, the events are generated only once, for a particular choice of Wilson coefficients, and are subsequently reweighted to match a different set of values. As this procedure relies on the calculation of the matrix elements at a fixed phase-space point, the dependence of the weights on the Wilson coefficients is computed exactly. Both techniques are used and the predictions are cross-checked

WW	`generate p p > e+ ve mu- vm~ SMHLOOP=0`
SSWW+2j EW	`generate p p > e+ ve mu+ vm j j QCD=0 SMHLOOP=0`
OSWW+2j EW	`generate p p > e+ ve mu- vm~ j j QCD=0 SMHLOOP=0`
WZ+2j EW	`generate p p > e+ e- mu+ vm j j QCD=0 SMHLOOP=0`
ZZ+2j EW	`generate p p > e+ e- mu+ mu- j j QCD=0 SMHLOOP=0`
ZV+2j EW	`generate p p > z w+(w-,z) j j QCD=0 SMHLOOP=0, z > l+ l-, w+(w-,z) > j j`
OSWW+2j QCD	`generate p p > e+ ve mu- vm~ j j QCD==2 SMHLOOP=0`
WZ+2j QCD	`generate p p > e+ e- mu+ vm j j QCD==2 SMHLOOP=0`
ZZ+2j QCD	`generate p p > e+ e- mu+ mu- j j QCD==2 SMHLOOP=0`
ZV+2j QCD	`generate p p > z w+(w-,z) j j QCD==2 SMHLOOP=0, z > l+ l-, w+(w-,z) > j j`
$\mathbf{N^{int}_{ff,vert}}$	`+ NPprop=0 NP=1 NP^2==1`
$\mathbf{N^{quad}_{ff}}$, $\mathbf{N^{mix}_{fffi}}$	`+ NPprop=0 NP=1 NP^2==2`

Table 2.2: Upper block: MADGRAPH5_AMC@NLO strings used to generate the SM components of the processes of interest. Where relevant, the charged conjugate processes were included in the generation. The charged lepton shortcut `l-` stands for electron or muon. Lower block: strings added to the SM ones in order to generate the three main classes of SMEFT corrections, following the SMEFTSIM conventions.

to agree within the statistical precision. Table 2.3 summarises the sensitivity of all the processes considered to the chosen set of dimension-six operators.

2.3.1.1 Event selection and analysis strategy

Simulated events are filtered applying selections that reflect typical detector acceptance for leptons and jets reconstruction in LHC experiments and isolating a phase space region where the VBS signal is particularly enhanced with respect to the backgrounds. A template-based analysis is performed using differential distributions for the SM, linear and quadratic components as a function of leptonic and partonic observables. As the VBS and diboson processes exhibit a great kinematic complexity, a comparative study of several kinematic variables for each channel is performed, to determine which observables are most sensitive to each dimension-6 operator. The full list of observables considered and the selections applied for each channel are summarised in Table 2.4, where p_{T,l^i} is the transverse momentum of the i-th charged lepton (sorted from largest to smallest) with respect to the beam axis and η_{l^i} its pseudo-rapidity, m_{ll} the invariant mass of two leading-p_T charged leptons, MET the missing transverse energy, p_{T,j^i} the transverse momentum of the i-th outgoing parton (sorted in p_T), η_{j^i} and ϕ_{j^i} its pseudo-rapidity and azimuthal angle. The m_{jj} refers to the invariant mass of the dijet system built with the two leading-p_T outgoing partons, $\Delta\eta_{jj}$ their pseudo-rapidity separation and $\Delta\phi_{jj}$ their angular separation in the azimuthal plane. $\Delta R(l,j)$ refers to the lepton-parton separation defined as the Euclidean distance in the η-ϕ plane namely $\Delta R = \sqrt{\Delta\eta + \Delta\phi}$.

2.3.1.2 Inclusive W^+W^-

The inclusive production of two opposite sign W bosons decaying into a lepton-neutrino pair is experimentally well studied (see e.g. [126, 127] for most recent experimental results). In the phase space defined in Table 2.4 the background contribution is dominated by $t\bar{t}$ events and its yield is less than half compared to that of the signal, therefore it is neglected. The large cross-section of this process and its favorable signal-over-background ratio make it an ideal

	WW	SSWW+2j EW	OSWW+2j EW	WZ+2j EW	ZZ+2j EW	ZV+2j EW	OSWW+2j QCD	WZ+2j QCD	ZZ+2j QCD	ZV+2j QCD
Q_{HD}	✓	✓	✓	✓	✓	✓	✓	✓	✓	✓
$Q_{H\Box}$	✓	✓	✓	✓	✓	✓				
Q_{HW}		✓	✓	✓	✓	✓				
Q_{HWB}	✓	✓	✓	✓	✓	✓	✓	✓	✓	✓
Q_{W}	✓	✓	✓	✓	✓	✓	✓	✓		✓
$Q_{Hq}^{(1)}$	✓	✓	✓	✓	✓	✓	✓	✓	✓	✓
$Q_{Hq}^{(3)}$	✓	✓	✓	✓	✓	✓	✓	✓	✓	✓
$Q_{Hl}^{(1)}$	(✓)	(✓)	✓	✓	✓	✓	✓	✓	✓	✓
$Q_{Hl}^{(3)}$	✓	✓	✓	✓	✓	✓	✓	✓	✓	✓
$Q_{ll}^{(1)}$	✓	✓	✓	✓	✓	✓	✓	✓	✓	✓
$Q_{qq}^{(3)}$		✓	✓	✓	✓	✓				
$Q_{qq}^{(3,1)}$		✓	✓	✓	✓	✓				
$Q_{qq}^{(1,1)}$		✓	✓	✓	✓	✓				
$Q_{qq}^{(1)}$		✓	✓	✓	✓	✓				

Table 2.3: Summary table for the dependence of the processes under investigation on the 14 benchmark EFT operators. Empty cells indicate that there are no diagrams for that operator for a given process. The brackets indicate that the operator only enters non-resonant diagrams.

Process	Variables of interest	Selections	Expected events
WW $(pp \to 2l2\nu)$	MET, m_{ll}, p_{T,l^i}, $p_{T,ll}$, η_{l^i}	MET > 30 GeV $m_{ll} > 60$ GeV $p_{T,l^1} > 25$ GeV $p_{T,l^2} > 20$ GeV $\lvert\eta_{l^i}\rvert < 2.5$	(EW) 30600
SSWW+2j $(pp \to 2l2\nu jj)$	MET, m_{jj}, m_{ll}, ϕ_{j^i}, p_{T,j^i} p_{T,l^i}, $p_{T,ll}$, $\Delta\eta_{jj}$, $\Delta\phi_{jj}$, η_{j^i}, η_{l^i}	MET > 30 GeV $m_{jj} > 500$ GeV $m_{ll} > 20$ GeV $p_{T,l^1} > 25$ GeV $p_{T,l^2} > 20$ GeV $p_{T,j^i} > 30$ GeV $\Delta\eta_{jj} > 2.5$ $\lvert\eta_{j^i}\rvert < 5$ $\lvert\eta_{l^i}\rvert < 2.5$	(EW) 197
OSWW+2j $(pp \to 2l2\nu jj)$			(EW) 493 (QCD) 1967
WZ+2j $(pp \to 2e\mu\nu jj)$	MET, m_{jj}, m_{ll}, ϕ_{j^i}, p_{T,j^i}, p_{T,l^i} $p_{T,ll}$, $\Delta\eta_{jj}$, $\Delta\phi_{jj}$, η_{j^i}, η_{l^i}, m_{3l} $p_{T,3l}$, m_{WZ}, $\delta\eta_{WZ}$, $\delta\phi_{WZ}$, Φ_{planes} θ_{lW}, θ_{lZ}, θ^*		(EW) 35 (QCD) 90
ZZ+2j $(pp \to 2e2\mu 2j)$	m_{jj}, $m_{l^1l^2}$, m_{ll}, m_{4l}, ϕ_{j^i}, p_{T,j^i}, p_{T,l^i}, p_{T,l^1l^2}, $p_{T,l^\pm l^\pm}$, $p_{T,l^\pm l^\mp}$, $p_{T,Z}$, $\Delta\phi_{jj}$, $\Delta\eta_{jj}$, η_{j^i}, η_{l^i}	$m_{jj} > 400$ GeV $60 < m_{ll} < 120$ GeV $m_{4l} > 180$ GeV $p_{T,l^1} > 20$ GeV $p_{T,l^2} > 10$ GeV $p_{T,l^i} > 5$ GeV $p_{T,j^{1,2}} > 30$ GeV $\Delta\eta_{jj} > 2.4$ $\lvert\eta_{j^i}\rvert < 4.7$ $\lvert\eta_{l^i}\rvert < 2.5$ $\Delta R(l^i, j^k) > 0.4$	(EW) 11 (QCD) 176
ZV+2j $(pp \to 2ljjjj)$	m_{jj}^{max}, m_{jj}^{nomax}, m_{ll}, ϕ_{j^i}, p_{T,j^i}, p_{T,l^i} $p_{T,ll}$, $\Delta\eta_{jj}$, $\Delta\eta_{jj}^{nomax}$, $\Delta\phi_{jj}^{max}$ $\Delta\phi_{jj}^{nomax}$, $\eta_{j^i}\eta_{l^i}$	$m_{jj} > 1500$ GeV $60 < m_{jj}^V < 110$ GeV $85 < m_{ll} < 95$ GeV $p_{T,l^1} > 25$ GeV $p_{T,l^2} > 20$ GeV $p_{T,j^i} > 100$ GeV $\Delta\eta_{jj} > 3.5$ $\lvert\eta_{j^i}\rvert < 5$ $\lvert\eta_{l^i}\rvert < 2.5$	(EW) 142 (QCD) 50

Table 2.4: Summary table for processes, variables and selections considered in this work. The second column lists the observables examined, while the third one summarises the parton level phase space definition used in this analysis. The last column reports the expected SM event yields of the EW and QCD-induced processes after the analysis selections, for an integrated luminosity of 100 fb^{-1}. The charged lepton shortcut l stands for electron or muon.

probe for the electroweak sector and the study of new phenomena at high energies. Differential measurements of diboson WW are included in most global analyses of dimension-six EFT operators [85, 86, 89–92]. At the LHC, the creation of a WW pair at LO in QCD occurs via the annihilation of a $q\bar{q}$ pair or through a t-channel exchange of a parton. Within this approximation, Higgs ($Q_{H\Box}$, Q_{HW}) and four-fermion operators ($Q_{qq}^{(1)}$, $Q_{qq}^{(3)}$, $Q_{qq}^{(1,1)}$, $Q_{qq}^{(3,1)}$) only enter at one-loop in QCD and are therefore neglected in this study. The main EFT contributions to the diboson WW process happen via modification of triple gauge couplings (Q_W) and of couplings of the weak bosons to fermions ($Q_{Hq}^{(1)}$, $Q_{Hq}^{(3)}$, $Q_{Hl}^{(3)}$) as well as corrections to the electroweak inputs (Q_{HD}, $Q_{ll}^{(1)}$, Q_{HWB}). For most of these operators, the diboson WW process is expected to give more stringent constraints than VBS mainly due to the enhanced cross sections, larger by approximately two orders of magnitude. However, it is expected to give sub-leading constraints for operators particularly sensitive to processes involving s-channel exchange of a Z boson or to Z/γ couplings to fermions such as $Q_{Hl}^{(1)}$ and Q_{HD}. Example differential distributions for the diboson WW process after the analysis selections for some operators of interest are shown in Figure 2.3.

2.3.1.3 VBS Same-Sign $W^{\pm}W^{\pm} + 2j$

Among the VBS processes, the production of two same-sign W bosons (SSWW) decaying leptonically plus two jets presents the cleanest signature in the detector. This process has been observed by the LHC Collaborations with a significance far greater than 5σ [128, 129]. The final state is characterized by two leptons of the same charge, moderate MET, and two jets with a large rapidity separation and a large dijet mass. The absence of gluon-initiated diagrams, attributed to the same-sign nature of the W bosons, distinguishes this process as it shows the highest ratio of EW to QCD-induced production when compared to other VBS processes. Additionally, the QCD-induced irreducible background with exactly two QCD vertices can be kinematically separated from the signal and, for these reasons, it has been neglected in this study. Among the reducible backgrounds, the main source comes from jet-induced fake leptons, mostly stemming from b quarks in $t\bar{t}$ events, however, their impact is highly suppressed in the high-energy tails where most of the EFT sensitivity is expected to arise. Therefore all sources of backgrounds are neglected for the SSWW channel as their contribution is expected to affect only marginally the EFT sensitivity. As shown in Figure 2.4 this process is particularly sensitive to four-quark operators inducing distortions in differential distributions both in energy and angular observables. The SSWW is expected to yield weaker bounds on Q_{HD} and Q_{HWB} with respect to other VBS processes. The latter operator dominantly enters via corrections to the weak mixing angle, to which SSWW has limited sensitivity, while the former favors processes involving Z/γ bosons coupling to fermions. Example differential distributions for the SSWW process after the analysis selections for some operators of interest are shown in Figure 2.4.

2.3.1.4 VBS Opposite-Sign $W^{+}W^{-} + 2j$

The scattering of two W bosons of opposite charge (OSWW) benefits of the largest cross sections among VBS processes. However, it has been observed experimentally only very recently by the LHC Collaborations [99, 100]. The major challenge for this final state is to suppress the large QCD-induced background. When both W bosons decay leptonically, the background composition is closely related to the flavour composition of the final state. When the two charged leptons have the same flavour and opposite charge, the phase space is overwhelmed by Drell-Yan events. In the different-flavour scenario, the dominant background source to OSWW is the irreducible $t\bar{t}$ production. The latter phase-space drives the sensitivity and has a more favorable

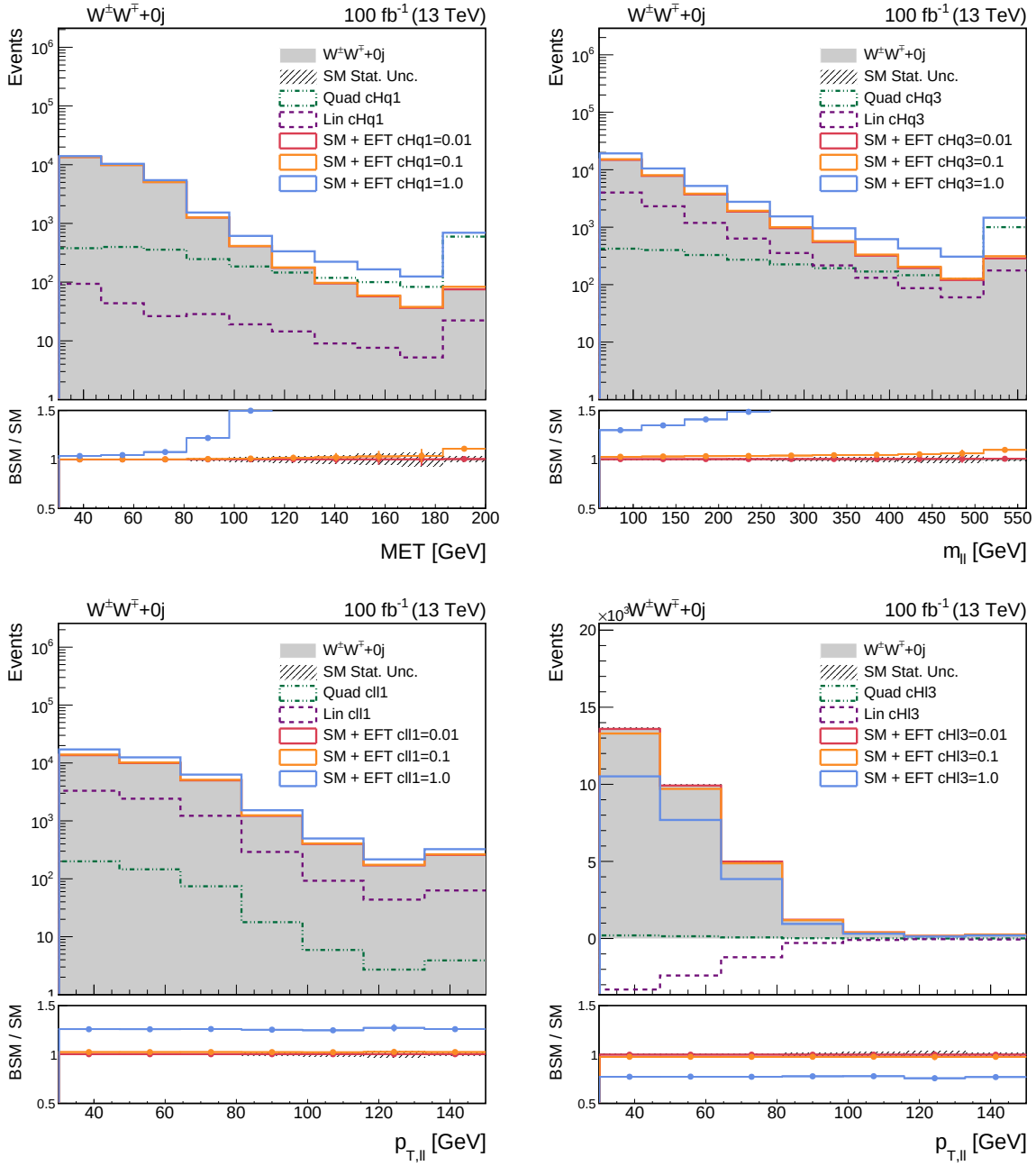

Figure 2.3: SM (grey filled histograms) and BSM (coloured lines) differential distributions for the inclusive diboson W^+W^- process, normalized to an integrated luminosity of 100 fb$^-$. The full BSM prediction considering one Wilson coefficient at a time is shown for different values of the coupling $c_\alpha/\Lambda^2 = 0.01$ (red), 0.1 (orange) or 1 TeV^{-2} (blue). Pure linear and quadratic EFT components are shown overlaid as purple and green dashed lines respectively and assuming $c_\alpha/\Lambda^2 = 1$ TeV^{-2}.

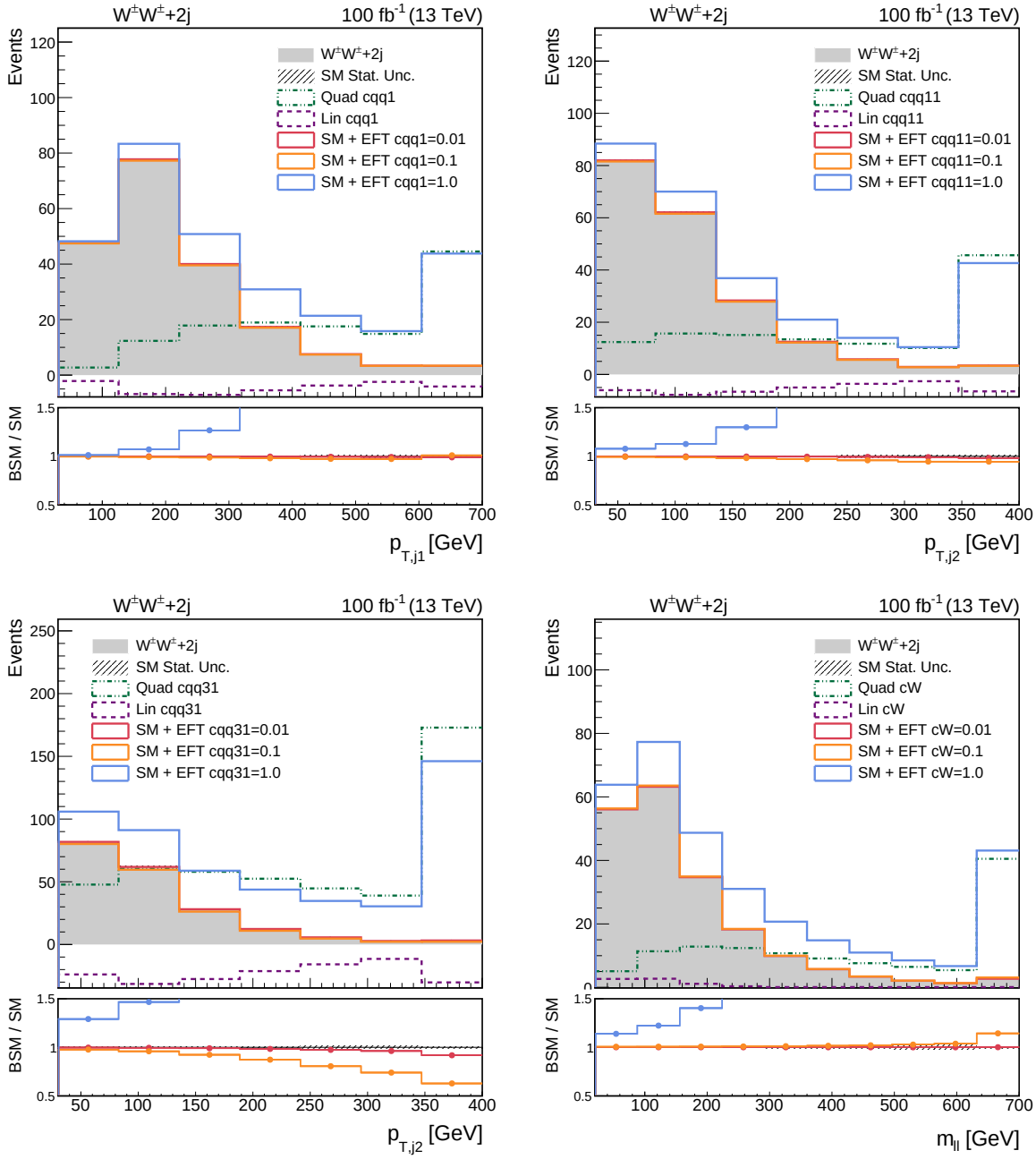

Figure 2.4: SM (grey filled histograms) and BSM (coloured lines) differential distributions for the SSWW process, normalized to an integrated luminosity of 100 fb^{-}. The full BSM prediction considering one Wilson coefficient at a time is shown for different values of the coupling $c_\alpha/\Lambda^2 = 0.01$ (red), 0.1 (orange) or 1 TeV^{-2} (blue). Pure linear and quadratic EFT components are shown overlaid as purple and green dashed lines respectively and assuming $c_\alpha/\Lambda^2 = 1$ TeV^{-2}.

signal-over-background ratio as the $t\bar{t}$ process has a lower cross-section than Drell-Yan and it can be suppressed even more by identifying b-jets in the event. This study focuses on the latter scenario, namely a final state with $e^{\pm}\mu^{\mp}\nu\nu + 2j$. The QCD induced production of W^+W^-+2j (order $\alpha_{EW}^4\alpha_{QCD}^2$) is sizeable and taken into account. Residual contributions from the Vector Boson Fusion Higgs production are present even after the selections reported in Table 2.4. Thanks to the presence of s-channel diagrams and the relatively large cross-section, OSWW is the most sensitive channel to anomalous Higgs couplings ($c_{H\Box}, c_{HW}$). Example differential distributions for the OSWW process after the analysis selections for some operators of interest are shown in Figure 2.5.

2.3.1.5 VBS $W^{\pm}Z + 2j$

The VBS production of a W and Z boson where the Z boson decays into electrons and the W boson into a muon-neutrino pair benefits from the purity of the multi-leptonic final state. The choice of different flavour decays for the Z and the W bosons provides an efficient discrimination between the two bosons. The VBS WZ process has a small cross-section and provides significant contamination to the SSWW final state in case a Z decay lepton is lost. This process was observed with the LHC Run II dataset by both ATLAS and CMS collaborations [101, 102]. CMS also studied this process in the final state where one of the three leptons is a hadronically decaying τ with an observed significance of 2.7σ above the background [130]. The irreducible QCD-induced background has a significant yield in the analysis region therefore its contribution is also generated at the LO $\alpha_S^2\alpha^4$. The presence of a single neutrino as a product of the W boson decay allows to kinematically reconstruct the longitudinal momentum of the neutrino along the beam-axis by imposing a m_W constraint on the decay products, see e.g. [131] for a description. Knowing the four-momenta of all the outgoing particles, the WZ system can be fully reconstructed and one can extract the invariant mass of the WZ system m_{WZ}, the angular separations between the vector bosons $\delta\eta_{WZ}$, $\delta\phi_{WZ}$ and the separation between their decay planes Φ_{planes}. Knowing the collision center-of-mass boost allows for the construction of more sophisticated observables, such as the emission polar angles of the leptons with respect to the direction of the decaying bosons in the rest frame of the latter, θ_{lW} and θ_{lZ}, and the vector bosons emission angle in the center-of-mass reference frame, θ^*. The WZ channel compensates its lower cross-section, compared to other VBS processes, by leveraging its Z boson s-channel contributions making it particularly sensitive, and competitive to the VBS-ZZ process, to the operators Q_{HD} and $Q_{Hl}^{(1)}$. Example differential distributions for the WZ process after the analysis selections for some operator of interest are shown in Figure 2.6.

2.3.1.6 VBS $ZZ + 2j$

The VBS ZZ in the four-lepton final state is the rarest VBS process considered and is among the least frequently observed processes within the Standard Model up to this point in time. ATLAS observed this process with the full LHC Run II dataset [103] and recently reported evidence for the longitudinally polarized scattering [132] while CMS recently reported strong evidence [104, 133]. Despite the very clean signature characterized by four charged leptons, the irreducible QCD-induced background constitutes a significant source of background. In order to isolate the two components multivariate techniques are often used by both ATLAS and CMS collaboration. For the sake of simplicity, the sensitivity study for EFT contribution in the VBS ZZ process is done using less sophisticated observables after the selection reported in Table 2.4 and considering only the case where a Z boson decays into a pair of electrons and the other into a pair of muons to ease the identification. Excluding typical variables common to all VBS processes, additional observables related to the Z bosons are analyzed such as the invariant

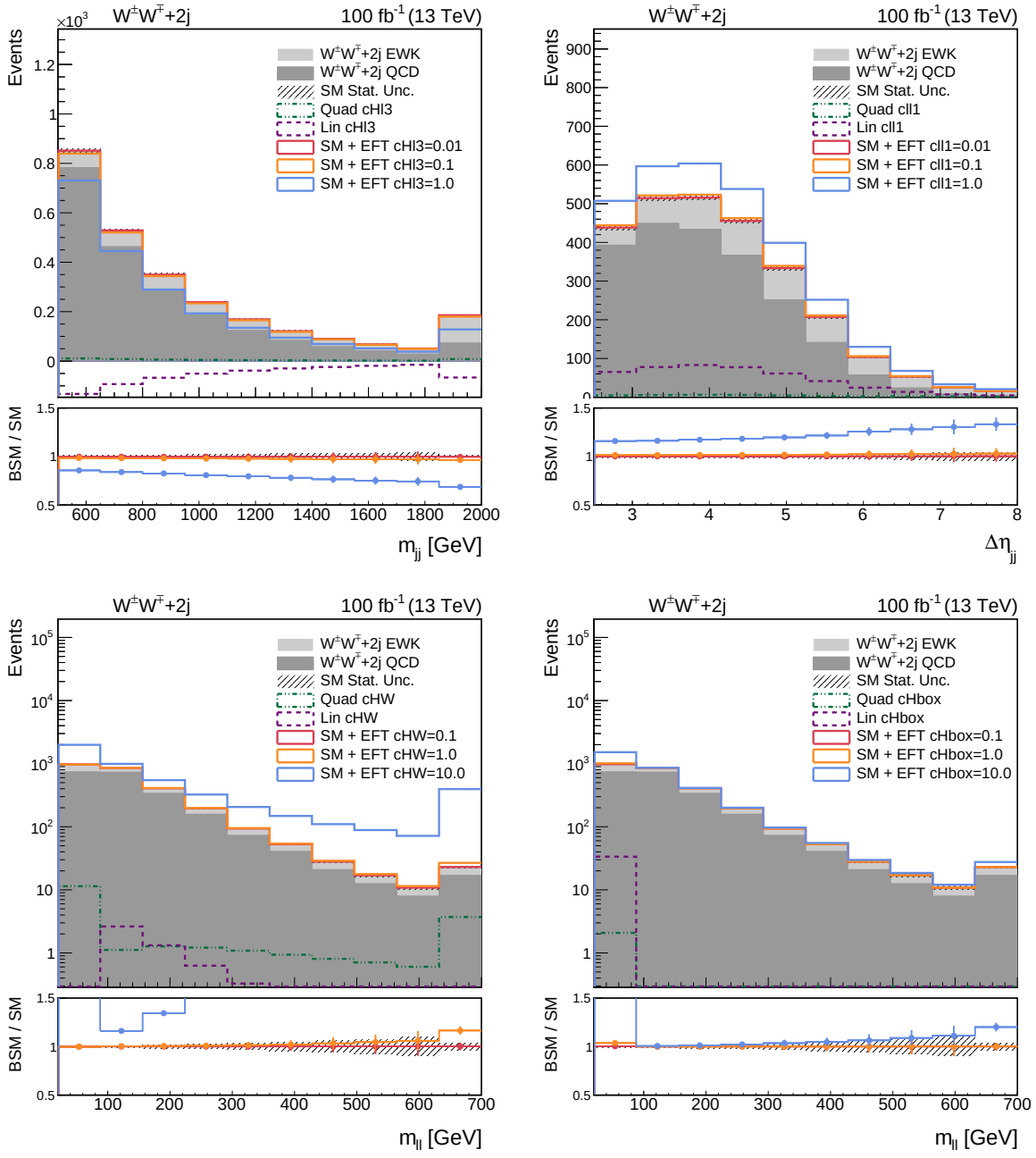

Figure 2.5: SM (grey filled histograms) and BSM (coloured lines) differential distributions for the OSWW process, normalized to an integrated luminosity of 100 fb^{-}. The full BSM prediction considering one Wilson coefficient at a time is shown for different values of the coupling $c_\alpha/\Lambda^2 = 0.01$ (red), 0.1 (orange) or 1 TeV^{-2} (blue). Pure linear and quadratic EFT components are shown overlaid as purple and green dashed lines respectively and assuming $c_\alpha/\Lambda^2 = 1$ TeV^{-2}.

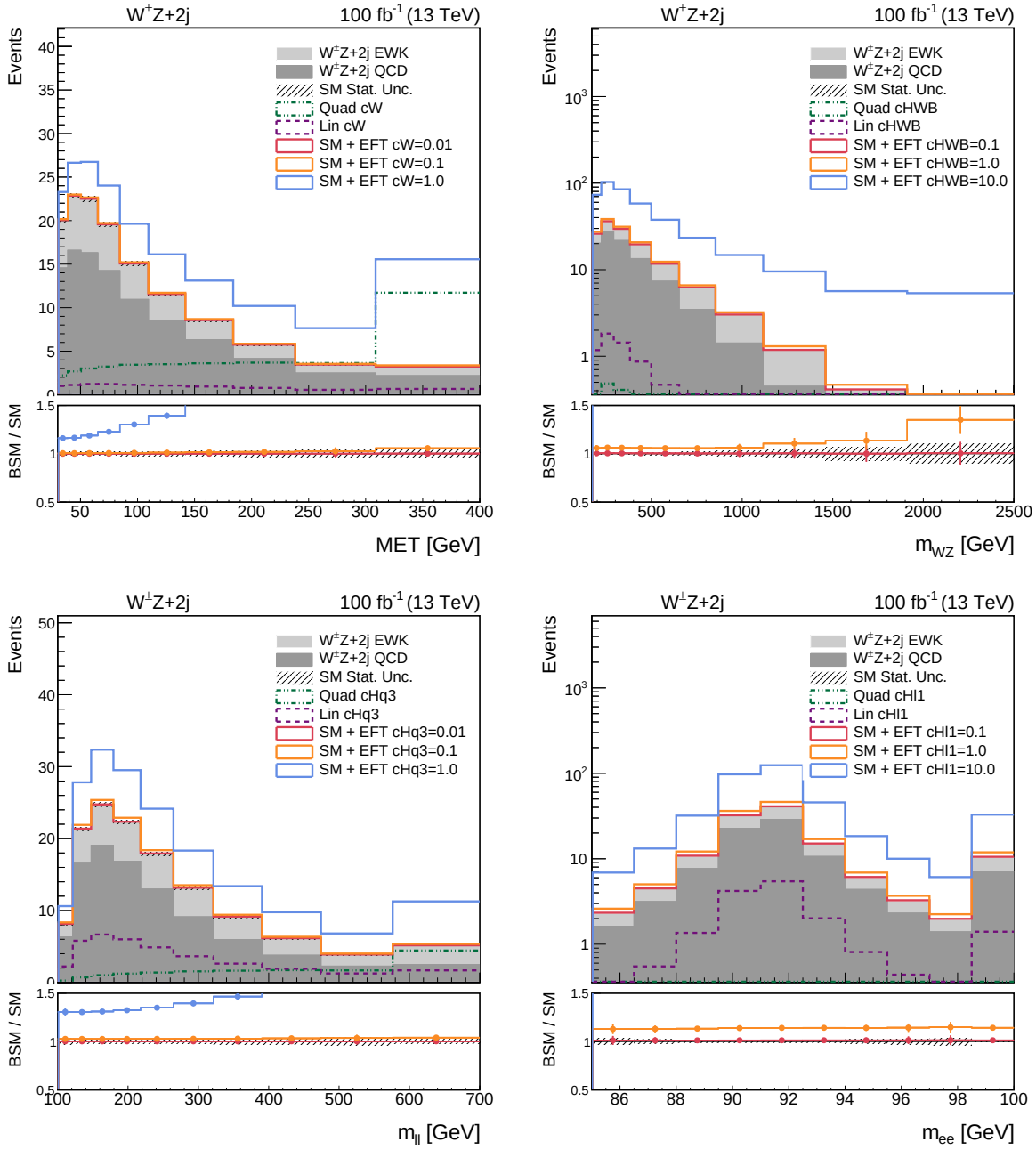

Figure 2.6: SM (grey filled histograms) and BSM (coloured lines) differential distributions for the WZ process, normalized to an integrated luminosity of 100 fb^{-}. The full BSM prediction considering one Wilson coefficient at a time is shown for different values of the coupling $c_\alpha/\Lambda^2 = 0.01$ (red), 0.1 (orange) or 1 TeV^{-2} (blue). Pure linear and quadratic EFT components are shown overlaid as purple and green dashed lines respectively and assuming $c_\alpha/\Lambda^2 = 1$ TeV^{-2}.

mass and total transverse momentum of the lepton pair with the largest transverse momentum $m_{l^1l^2}$, p_{T,l^1l^2}, the invariant mass of the four-lepton system m_{4l}, the total transverse momentum of the same-sign lepton pair $p_{T,e^\pm\mu^\pm}$ and the transverse momentum of the dilepton system e^+e^- or $\mu^+\mu^-$ with invariant mass closest to m_Z , taken as a proxy for $p_{T,Z}$. The sensitivity of this channel is mainly limited by its low cross-section and signal-over-background ratio however it is competitive in constraining operators that specifically target Z-boson physics such as Q_{HD}, $Q_{Hl}^{(1)}$ and also Q_{HWB} [113]. Example differential distributions for the ZZ process after the analysis selections for some operators of interest are shown in Figure 2.7.

2.3.1.7 VBS semileptonic $ZV + 2j$

VBS processes with a fully leptonic final state present clean signatures in the detector. However, the branching ratio for a hadronically decaying vector boson (about 67% for W bosons and 70% for Z bosons) is twice as large as its leptonic counterpart [44]. The higher jet multiplicity poses some serious challenges concerning background suppression and non-trivial jet tagging [134], however, the VBS of a leptonically decaying W or Z boson and a hadronically decaying V boson (either W or Z) were shown to be among the most sensitive channels to dimension-8 EFT effects [135, 136]. This sensitivity study aims to explore dimension-six SMEFT contributions to the VBS ZV process with a semileptonic final state characterized by four jets and a pair of electrons or muons. To make the study realistic, the generator-level information about the origin of the outgoing partons is ignored and algorithms are designed as would be done in a real LHC analysis. The algorithm used to identify the two tagging jets coming from the partons that scattered and the ones from the hadronic decay products of the vector boson selects first the jet pair, within acceptance, with the highest invariant mass as the one produced by the scattering partons while the remaining are considered as a candidate for the boson decay. This method correctly matches final state partons to the corresponding vector boson or scattering parton for at least 75% of the events under investigation. The production of three vector bosons, two of which decay hadronically, produces the same final state topology but is vetoed in order to focus on the electroweak VBS contribution. The irreducible QCD-induced $l^+l^- + 4j$ sample (order $\alpha_S^2\alpha^4$) is included in the study, however, the major source of background contamination for the VBS ZV comes from Z+jets events and is neglected due to the computational complexity of its simulation. To prevent this choice from introducing a bias in the global analysis, the ZV+2j results will be analyzed separately from the other channels. Example differential distributions for the ZV process after the analysis selections for some operator of interest are shown in Figure 2.8.

2.3.1.8 Likelihood construction

The likelihood function $\mathcal{L}$ is built upon Eq. 2.4 to determine $N_k(\boldsymbol{c})$, that stands for the expected number of events in the k-th bin of a differential distribution as a function of the Wilson coefficient vector $\boldsymbol{c}$ surviving the analysis selections, and follows the Poisson statistics.

$$\mathcal{L}(\mathbf{c}) = \prod_k \frac{(N_k(\mathbf{c}))^{n_k}}{n_k!} e^{-N_k(\mathbf{c})} \times \prod_{j \in syst} \mathcal{G}(\theta_j^0 | \theta_j, \Delta\theta), \tag{2.5}$$

As no real data is present in this analysis, we study the difference in the expected number of events when including SMEFT contributions versus the expected number of events according to the SM, defined as $n_k \equiv N_k(\mathbf{0})$. When the QCD-induced processes are relevant, their SMEFT contribution is accounted for in the definition of $N_k(\boldsymbol{c})$ and summed to the electroweak counterpart. An integrated luminosity of 100 fb^{-1} is always assumed if not otherwise stated. No

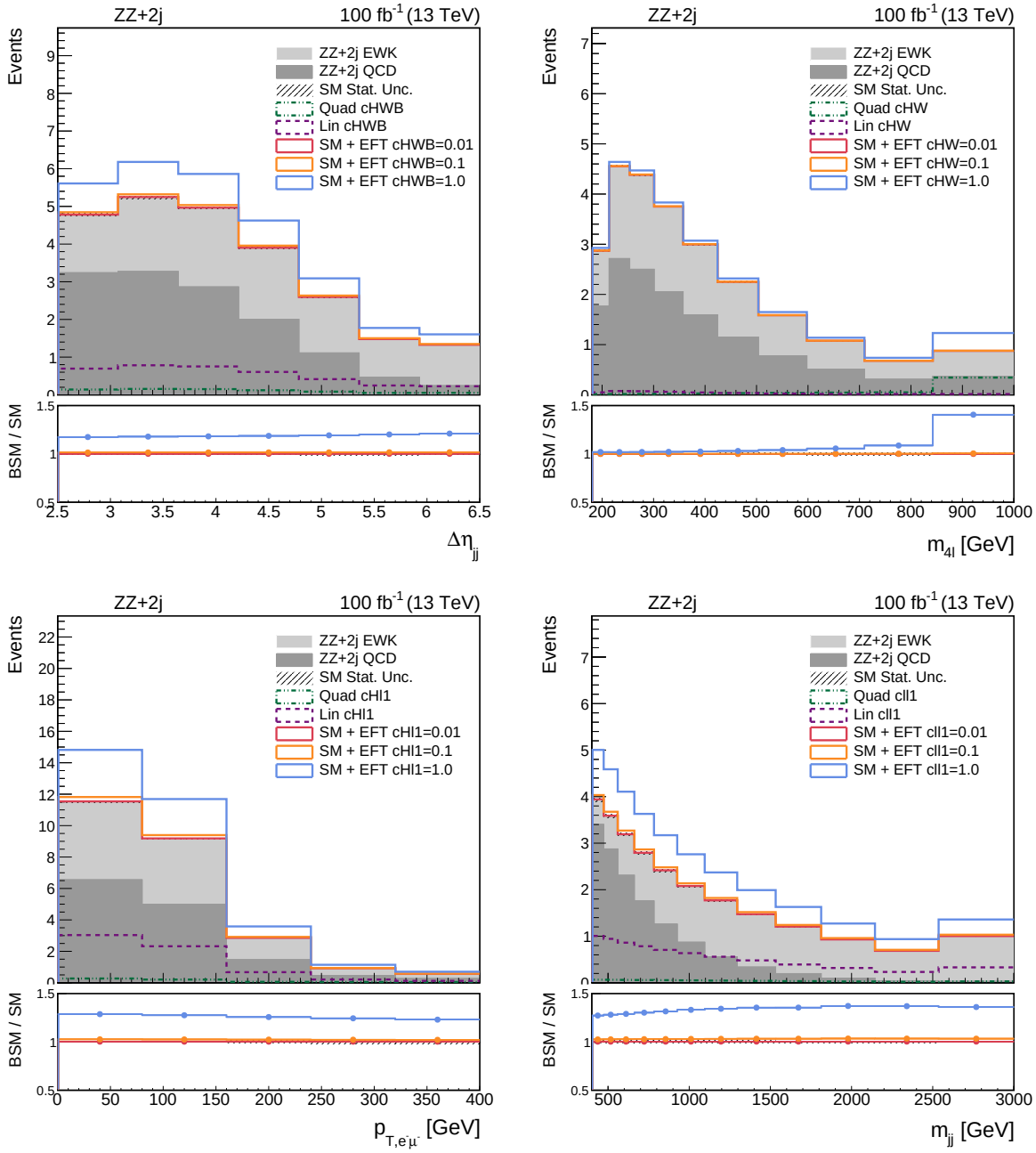

Figure 2.7: SM (grey filled histograms) and BSM (coloured lines) differential distributions for the ZZ process, normalized to an integrated luminosity of 100 fb^{-}. The full BSM prediction considering one Wilson coefficient at a time is shown for different values of the coupling $c_\alpha/\Lambda^2 = 0.01$ (red), 0.1 (orange) or 1 TeV^{-2} (blue). Pure linear and quadratic EFT components are shown overlaid as purple and green dashed lines respectively and assuming $c_\alpha/\Lambda^2 = 1$ TeV^{-2}.

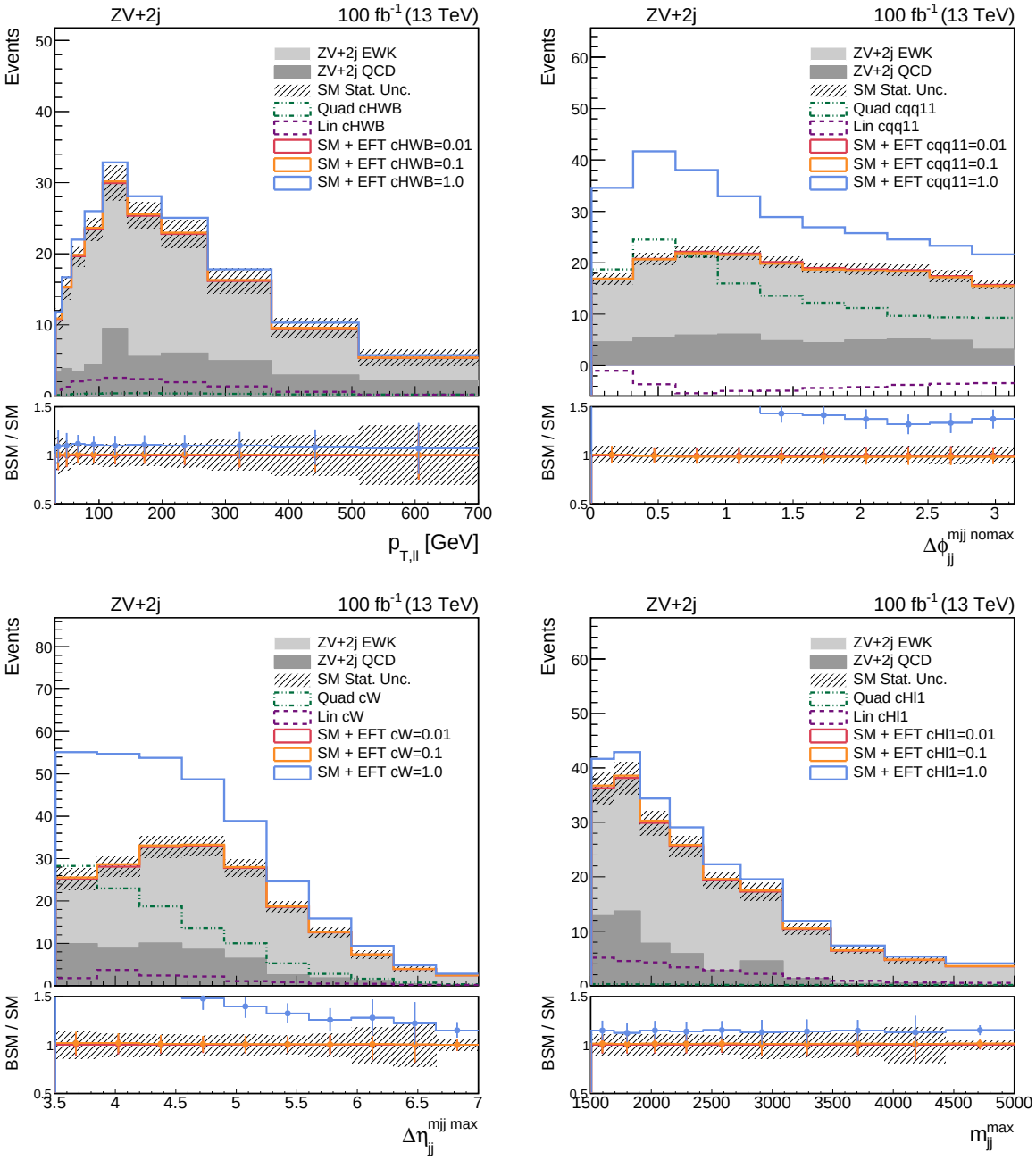

Figure 2.8: SM (grey filled histograms) and BSM (coloured lines) differential distributions for the ZV semileptonic process, normalized to an integrated luminosity of 100 fb^{-}. The full BSM prediction considering one Wilson coefficient at a time is shown for different values of the coupling $c_\alpha/\Lambda^2 = 0.01$ (red), 0.1 (orange) or 1 TeV^{-2} (blue). Pure linear and quadratic EFT components are shown overlaid as purple and green dashed lines respectively and assuming $c_\alpha/\Lambda^2 = 1$ TeV^{-2}.

source of uncertainty is considered in this study except for a correlated $\Delta\theta = 2\%$ variation across all yields, samples and bins that emulates the typical luminosity uncertainty in LHC experiments. The luminosity uncertainty is labeled with θ in Eq. 2.5 and it is constrained to follow the distribution $\mathcal{G}$ that, in this study, is a log-normal distribution.

For each of the considered processes, only one observable is used to construct the likelihood. For individual fits to Wilson coefficients, setting all the other ones to their SM value, such observable is selected as the one yielding the most stringent constraints at 68% confidence level (C.L.). This ranking procedure is operator-dependent, therefore constraints on different Wilson coefficients are generally derived with different, optimized likelihoods. This ranking procedure is applied to individual fits truncating the amplitude of Eq. 2.4 at the order Λ^{-2} or at Λ^{-4} and for two-dimensional fits, retaining the observable yielding the smallest area inside the 68% C.L. contour in the bi-dimensional plane. When allowing all Wilson coefficients to freely float in the likelihood minimization, the profiled constraint on each Wilson coefficient is derived from a likelihood that implements, for each process, the same observable as in the corresponding 1D case. The sensitivity to the single Wilson coefficients at 68% and 95% C.L is extracted from the likelihood profile by requiring $-2\Delta\log\mathcal{L} < 1$ and $-2\Delta\log\mathcal{L} < 3.84$ respectively. For bi-dimensional scans the intervals are instead $-2\Delta\log\mathcal{L} < 2.30$, $-2\Delta\log\mathcal{L} < 5.99$ [44].

2.3.2 One-dimensional and bi-dimensional fits

The most optimistic scenario is to assume that only few operators from the set in Table 2.1 are allowed by the new physics phenomena at energies Λ. One-dimensional constraints are extracted by fitting only one Wilson coefficient at a time, freezing all the other ones to their SM expectation of 0. Expanding the allowed dimensions in the parameter space one can also study the correlation for pairs of operators by letting two Wilson coefficients freely floating in the likelihood minimization. Figure 2.9 shows the one-dimensional likelihood profiles for the 14 operators of interest, for all the channels involved and for their combination (excluding the semileptonic ZV+2j channel as explained in Sec. 2.3.1.7).

The 68% and 95% C.L. intervals obtained are reported in Figure 2.10 for the leptonic channels, and in Figure 2.11 separately for the semileptonic ZV+2j final state.

In the figures summarising the C.L. intervals, boxes highlight the expected limits including the quadratic EFT dependence in the likelihood defined at Eq. 2.4 while solid lines are the limits obtained by neglecting them. The likelihoods for the linear-only and quadratic fits are built using independent optimal observables to obtain unbiased comparisons. For the 1D fits, the list of most sensitive observables is reported in Table 2.5. As a general comment, four-quark operators tend to favor jet-related variables as their effect mostly affect the kinematics of the VBS jets. For bosonic operators Q_{HW}, Q_W and $Q_{H\Box}$ the variables that play the most important role are related to the kinematic properties of the leptonic final state or related to the diboson scattering system. In the semileptonic ZV+2j channel, the most sensitive variables are related to the transverse momentum of the hadronic decay products of one of the scattered vector bosons.

The diboson WW dominates the sensitivity for most of the operators. However, VBS is found to generally be competitive. For four-quark and Higgs ($Q_{H\Box}$, Q_{HW}) operators, diboson WW is by construction insensitive so the only constraint power comes from VBS processes. As explained in Sec. 2.3.1.7, VBS OSWW+2j, WZ+2j and ZZ+2j are particularly sensitive to Q_{HD}, Q_{HWB}, $Q_{Hl}^{(1)}$ an provide competitive constraints. Among VBS processes, SSWW+2j and OSWW+2j dominate the sensitivity mainly due to their higher cross-section compared to WZ+2j and ZZ+2j, penalized by the lower $Z \to ll$ branching ratio. The constraints coming from the semileptonic ZV+2j channel are also competitive to those of the diboson WW, which justifies further studies

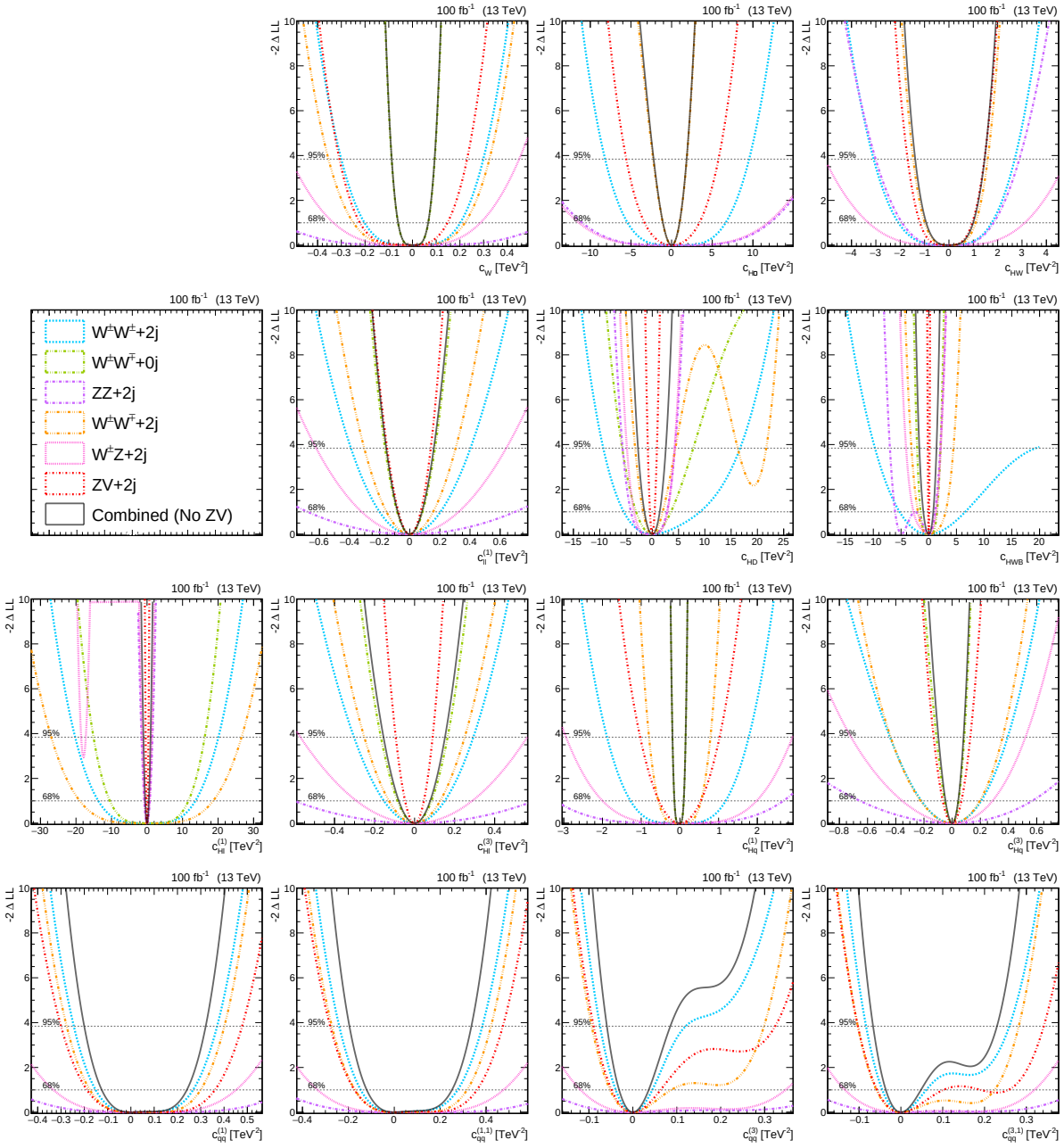

Figure 2.9: Profiles of $-2\Delta \log \mathcal{L}$ reported for the individual channels (coloured lines) and their combination (solid black line, excluding ZV+2j) as a function of the Wilson coefficients. Horizontal dashed lines mark the 68% and 95% confidence levels respectively, taken at $-2\Delta \log \mathcal{L} = 1$ and $-2\Delta \log \mathcal{L} = 3.84$. For each coefficient, the likelihood was built by taking, for each channel, the distribution in the most constraining variable at 68% c.l. (see Table 2.5). Only the shown Wilson coefficient is varied at each time, and the others are set to 0. The sensitivity estimate for the OSWW+2j, WZ+2j, ZZ+2j and ZV+2j channels includes contributions from the respective QCD-induced processes.

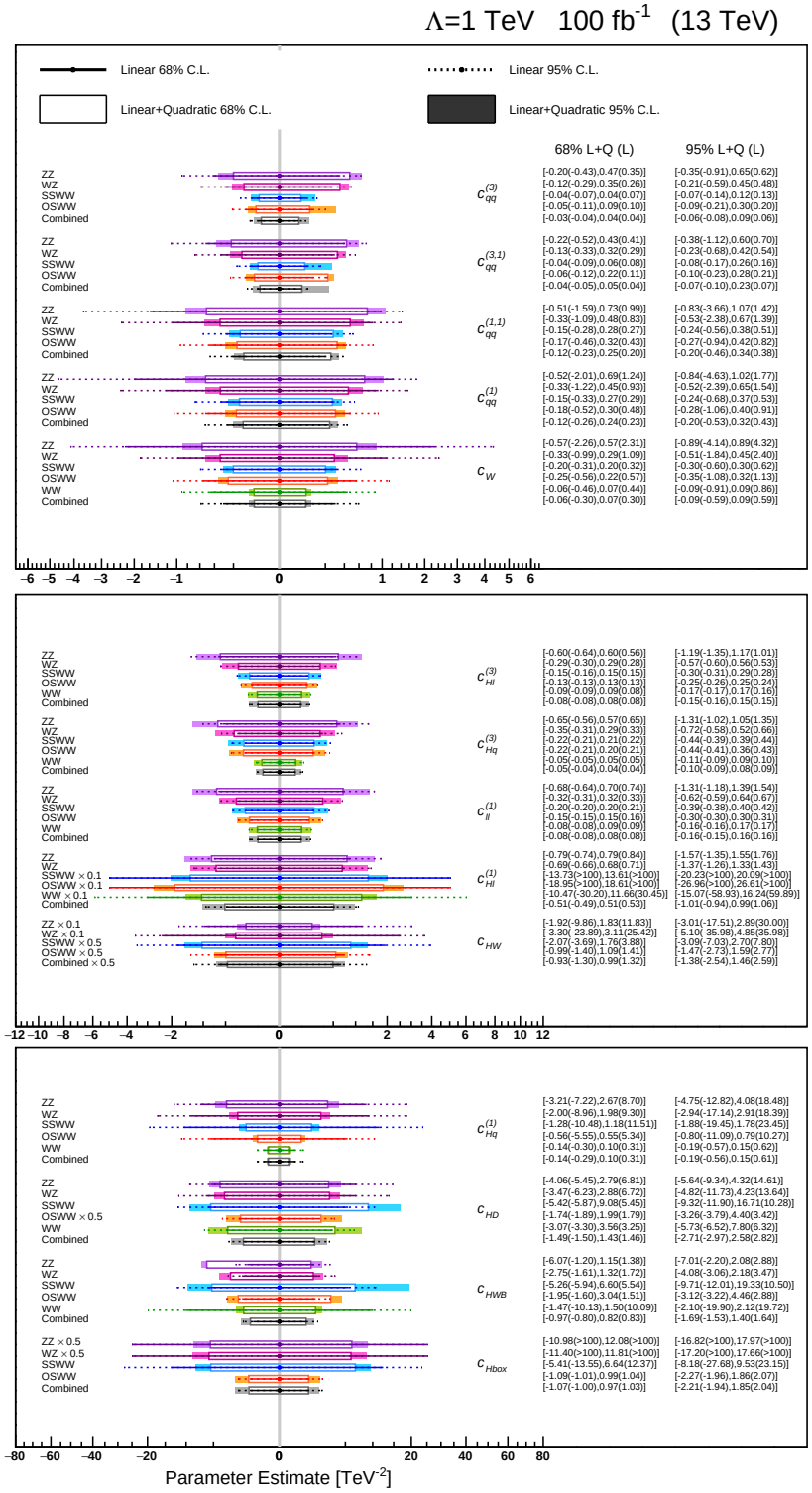

Figure 2.10: Individual expected constraints on Wilson coefficients from the leptonic VBS channels ZZ+2j, WZ+2j, SSWW+2j, OSWW+2j and diboson WW. The solid points represent the SM expectation. Solid (dashed) lines indicate the 68% (95%) confidence intervals obtained including only terms linear in the Wilson coefficients in the signal predictions. Open (filled) boxes indicate 68% (95%) confidence intervals obtained including both linear and quadratic EFT components.

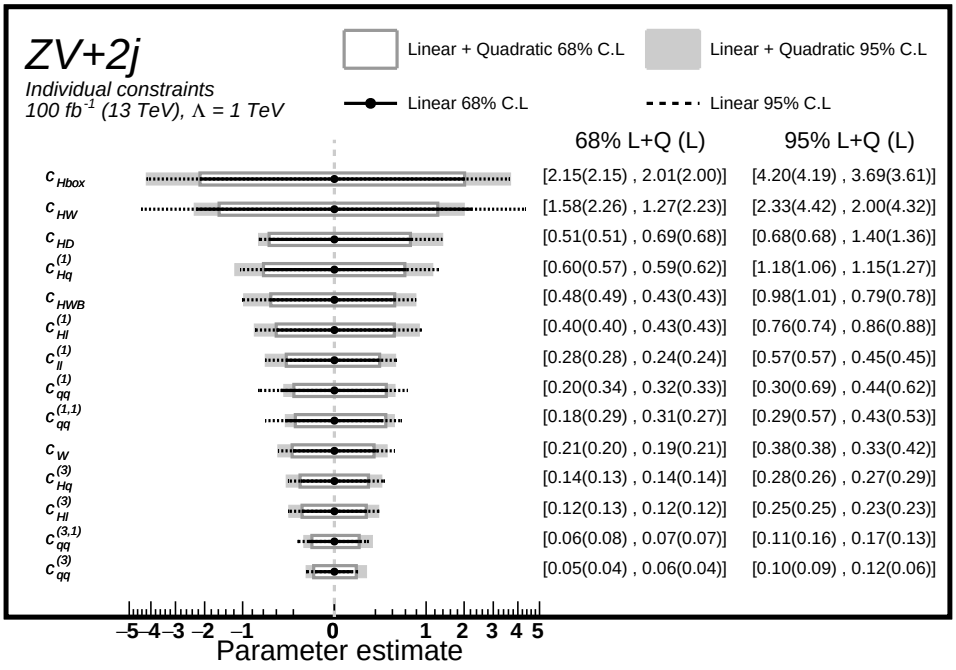

Figure 2.11: Individual expected constraints on Wilson coefficients from the VBS ZV+2j channel in the semileptonic final state. The solid points represent the SM expectation. Solid (dashed) lines indicate the 68% (95%) confidence intervals obtained including only terms linear in the Wilson coefficients in the signal predictions. Open (filled) boxes indicate 68% (95%) confidence intervals obtained including both linear and quadratic EFT components. The QCD-induced EFT dependence was included when relevant. Note that the constraints shown in this figure neglect effects due to the main background for this final state, i.e. Z+jets Drell-Yan production.

for this final state with an appropriate treatment of the background sources.

In order of sensitivity, the most constrained operators from the combination of diboson WW and VBS processes are the four-quark operators $Q_{qq}^{(3)}$, $Q_{qq}^{(3,1)}$, $c_{qq}^{(1)}$, $c_{qq}^{(1,1)}$, the Q_W operator modifying TGCs and QGCs and the operators $Q_{Hq}^{(1)}$, $Q_{Hq}^{(3)}$, $Q_{Hl}^{(3)}$, $Q_{ll}^{(1)}$. The remaining operators present bounds greater than 0.15 at 68% C.L. for $\Lambda = 1$ TeV. These results agree with the finding of Ref. [113] for the ZZ+2j case. Among the four-quark operators, the coefficients $c_{qq}^{(3))}$ and $c_{qq}^{(3,1)}$ enter in the charged current iteractions such as $(\bar{u}d)(\bar{s}c)$ and are favoured by SSWW+2j and OSWW+2j in spite of their neutral counterparts $c_{qq}^{(1))}$ and $c_{qq}^{(1,1)}$. The coefficients c_W, $c_{Hq}^{(1)}$, $c_{Hq}^{(3)}$, $c_{Hl}^{(3)}$ are mostly constrained by diboson WW but induce visible effects also in VBS processes. In particular $c_{Hq}^{(1),(3)}$ give particularly momentum-enhanced signals in the longitudinally-polarized component of the WW scattering and c_W in the transverse one [137].

The coefficients $c_{ll}^{(1)}$, c_{HWB} and c_{HD} only enter as modification of the electroweak inputs. Their net effect for all channels is just a rescaling of the overall normalization thus they tend to be better constrained by processes with large cross sections such as diboson WW and VBS OSWW+2j. Of the two, Q_{HD} is found to be the less constrained.

Higgs operators $Q_{H\Box}$ and Q_{HW} only enter via modification of Higgs to electroweak boson cou-

plings and they are mostly constrained by OSWW+2j, which presents contributions from diagrams with an s-channel Higgs boson. However, these limits are expected to be subdominant with respect to dedicated analyses targeting Higgs boson production and decays.

Finally, the coefficient $c_{Hl}^{(1)}$ is significantly constrained in the ZZ+2j and WZ+2j VBS, which only give mild bounds.

The validity of the EFT expansion is strictly tailored to the energy regime probed. This study considers distributions that extend to the high-energy regime and may violate the EFT assumptions. Techniques to mitigate this problem such as the so-called clipping or the unitarisation of the scattering amplitude are ignored in this study, but a qualitative assessment of the EFT validity is performed by comparing the bounds obtained retaining terms at order Λ^{-2} versus Λ^{-4}. A dominance of terms that scale quadratically with the Wilson coefficients may indicate a potential sensitivity to neglected higher-dimensional operators and a possible breakdown of the EFT validity. In Figs. 2.10, 2.11 one observes that quadratic terms are significant for less than half of the operators. For example, $c_{Hq}^{(3)}$, $c_{Hl}^{(3)}$ and $c_{ll}^{(1)}$ are dominantly constrained through their linear contributions in all the VBS processes as well as in the inclusive WW. In the case of $c_{Hl}^{(1)}$, c_{HD}, $c_{H\Box}$, the sensitivity to quadratic terms varies among processes and the processes leading the sensitivity (WZ+2j for $c_{Hl}^{(1)}$ and OSWW+2j for c_{HD} and $c_{H\Box}$) tend to favor the linear component instead of the quadratic one. The case of c_{HWB} is slightly different, as at the quadratic level diboson WW dominates the sensitivity while its role is reversed in the linear-only scenario. The loss in sensitivity is however compensated by a combination of other VBS channels leaving the final result nearly unchanged. Among four-quarks operators, $c_{qq}^{(3)}$ and $c_{qq}^{(3,1)}$ show little sensitivity to quadratic components while the opposite is true for $c_{qq}^{(1)}$ and $c_{qq}^{(1,1)}$. The most sensitive channel to these operators is SSWW+2j and, as shown in Fig. 2.4, these operators show a negative linear component close in size to the quadratic component already at $c_\alpha/\Lambda^2 = 1$ TeV. It can be seen that limits at 68% and 95% for $c_{qq}^{(3)}$ and $c_{qq}^{(3,1)}$ lie in the parameter region where the linear component still dominates while this is not true for $c_{qq}^{(1)}$ and $c_{qq}^{(1,1)}$ where the magnitude of the linear component compared to the quadratic one is slightly smaller. This in turn allows for partial cancellations of the linear and quadratic component which spoils the sensitivity and it is most visible for $c_{qq}^{(1,1)}$.

The bi-dimensional analysis follows the same principles as the one-dimensional one but allows two operators to vary at the same time, fixing the other ones to zero. As above, EFT contributions to QCD-induced components of the VBS processes are accounted for in the fit. The observable ranking is repeated for the linear and quadratic case separately and for each pair of operators and the best ones, used to build the likelihoods for each channel, are summarised in Tables A.1–A.5 in Appendix A. Fig. 2.12 reports a subset of the likelihood scans obtained.

Examining two-dimensional likelihoods can offer valuable insights into the resolution of potential degeneracies between operators during the fitting process. These instances commonly occur in two scenarios: among four-quark operators in Vector Boson Scattering (VBS), and between the coefficients $c_{Hl}^{(3)}$ and $c_{ll}^{(1)}$ across all processes as highlighted in Fig. 2.12. All four-quark operators present an unconstrained direction in the linear case which is lifted by the introduction of quadratic terms as can be seen in the $c_{qq}^{(3)}, c_{qq}^{(3,1)}$ panel in Fig. 2.12. For all four-quark pairs, the combined contour is dominated by the SSWW+2j contribution. The degeneracy introduced by singlet versus tripled $SU(2)$ contractions in the four-quark case (i.e. $c_{qq}^{(3),(3,1)}$ versus $c_{qq}^{(1),(1,1)}$), are generally better resolved than the degeneracy between different flavour contrac-

Op.	SSWW+2j		OSWW+2j		WZ+2j		ZZ+2j		ZV+2j		WW	
	L	L+Q	L	L+Q	L	L+Q	L	L+Q	L	L+Q	L	L+Q
$c_{Hl}^{(1)}$	-	m_{ll}	-	MET	$m_{ee}{}^{\dagger}$	m_{WZ}	$p_{T,e^-\mu^-}{}^{\dagger}$	$p_{T,e^-\mu^-}{}^{\dagger}$	p_{T,j_1}^{V}	p_{T,j_1}^{V}	p_{T,l^1}	MET
$c_{Hl}^{(3)}$	$\Delta\eta_{jj}{}^{\dagger}$	$\Delta\eta_{jj}{}^{\dagger}$	$m_{jj}{}^{\dagger}$	$m_{jj}{}^{\dagger}$	$m_{jj}{}^{\dagger}$	m_{jj}	$m_{jj}{}^{\dagger}$	$m_{jj}{}^{\dagger}$	$\Delta\eta_{jj}^{V}$	$\Delta\eta_{jj}^{V}$	$m_{ll}{}^{\dagger}$	$m_{ll}{}^{\dagger}$
$c_{Hq}^{(1)}$	p_{T,j^1}	p_{T,j^1}	m_{jj}	m_{ll}	m_{jj}	p_{T,j^1}	m_{jj}	p_{T,j^1}	m_{jj}^{VBS}	m_{jj}^{VBS}	MET	MET
$c_{Hq}^{(3)}$	$\Delta\phi_{jj}$	$\Delta\phi_{jj}$	m_{ll}	m_{ll}	$\Delta\phi_{jj}{}^{\dagger}$	p_{T,l^1}	$\Delta\phi_{jj}{}^{\dagger}$	p_{T,l^4}	p_{T,j_2}^{VBS}	p_{T,j_2}^{VBS}	p_{T,l^1}	p_{T,l^1}
$c_{qq}^{(3)}$	$m_{ll}{}^{\dagger}$	p_{T,j^2}	m_{jj}	p_{T,j^2}	m_{jj}	p_{T,j^2}	m_{jj}	p_{T,j^1}	$p_{T,l^1}{}^{\dagger}$	$\Delta\phi_{jj}^{VBS}$	-	-
$c_{qq}^{(3,1)}$	$\Delta\phi_{jj}$	p_{T,j^2}	m_{jj}	p_{T,j^2}	m_{jj}	p_{T,j^2}	m_{jj}	p_{T,j^1}	$\Delta\eta_{jj}^{V\dagger}$	$\Delta\phi_{jj}^{VBS}$	-	-
$c_{qq}^{(1,1)}$	$\Delta\phi_{jj}$	p_{T,j^1}	p_{T,j^2}	p_{T,j^2}	p_{T,j^2}	p_{T,j^1}	p_{T,j^2}	p_{T,j^2}	$\Delta\phi_{jj}^{VBS}$	p_{T,j_1}^{VBS}	-	-
$c_{qq}^{(1)}$	p_{T,j^1}	p_{T,j^1}	p_{T,j^2}	p_{T,j^2}	p_{T,j^2}	p_{T,j^2}	p_{T,j^2}	p_{T,j^2}	$\Delta\phi_{jj}^{VBS}$	p_{T,j_1}^{VBS}	-	-
c_{HD}	p_{T,j^1}	m_{ll}	$\Delta\eta_{jj}$	$\Delta\eta_{jj}$	m_{ee}	$\Delta\eta_{jj}{}^{\dagger}$	$p_{T,e^+\mu^+}$	$p_{T,e^+\mu^+}{}^{\dagger}$	p_{T,l^2}	p_{T,l^2}	p_{T,l^1}	p_{T,l^1}
$c_{H\Box}$	p_{T,j^1}	m_{ll}	m_{ll}	m_{ll}	-	m_{WZ}	-	$\Delta\eta_{jj}$	p_{T,j_2}^{V}	p_{T,j_2}^{V}	-	-
c_{HW}	$\Delta\phi_{jj}$	m_{ll}	$\Delta\phi_{jj}$	m_{ll}	$\eta_{l^3}{}^{\dagger}$	m_{WZ}	m_{jj}	m_{4l}	p_{T,j_1}^{VBS}	p_{T,j_2}^{V}	-	-
c_{HWB}	p_{T,j^1}	p_{T,j^1}	$\Delta\eta_{jj}$	m_{ll}	m_{ee}	m_{WZ}	$m_{\mu\mu}{}^{\dagger}$	$\Delta\eta_{jj}$	$\Delta\eta_{jj}^{V}$	$\Delta\eta_{jj}^{V}$	p_{T,l^1}	MET
c_{W}	$\Delta\phi_{jj}$	$p_{T,ll}$	$\Delta\phi_{jj}$	m_{ll}	p_{T,l^1}	m_{WZ}	$\Delta\phi_{jj}$	p_{T,l^4}	$\Delta\phi_{jj}^{VBS\dagger}$	$\Delta\phi_{jj}^{VBS\dagger}$	MET	MET
$c_{ll}^{(1)}$	$m_{jj}{}^{\dagger}$	$m_{jj}{}^{\dagger}$	$m_{jj}{}^{\dagger}$	$m_{jj}{}^{\dagger}$	$m_{jj}{}^{\dagger}$	m_{jj}	$m_{jj}{}^{\dagger}$	$m_{jj}{}^{\dagger}$	$\Delta\eta_{jj}^{V\dagger}$	$\Delta\eta_{jj}^{V\dagger}$	$p_{T,ll}{}^{\dagger}$	p_{T,l^2}

Table 2.5: Most sensitive observable for each VBS process and SMEFT Wilson coefficient, inferred from individual fits and employed in the final statistical combination. The columns marked with L and L+Q indicate the results for fits including respectively linear and linear+quadratic terms in the Wilson coefficients. A $-$ indicates no sensitivity to an operator in a given process. A † indicates that the preference for the variable indicated is very mild, as most observables give similar sensitivity.
EFT corrections to QCD backgrounds were retained for OSWW+2j, WZ+2j, ZZ+2j and ZV+2j.

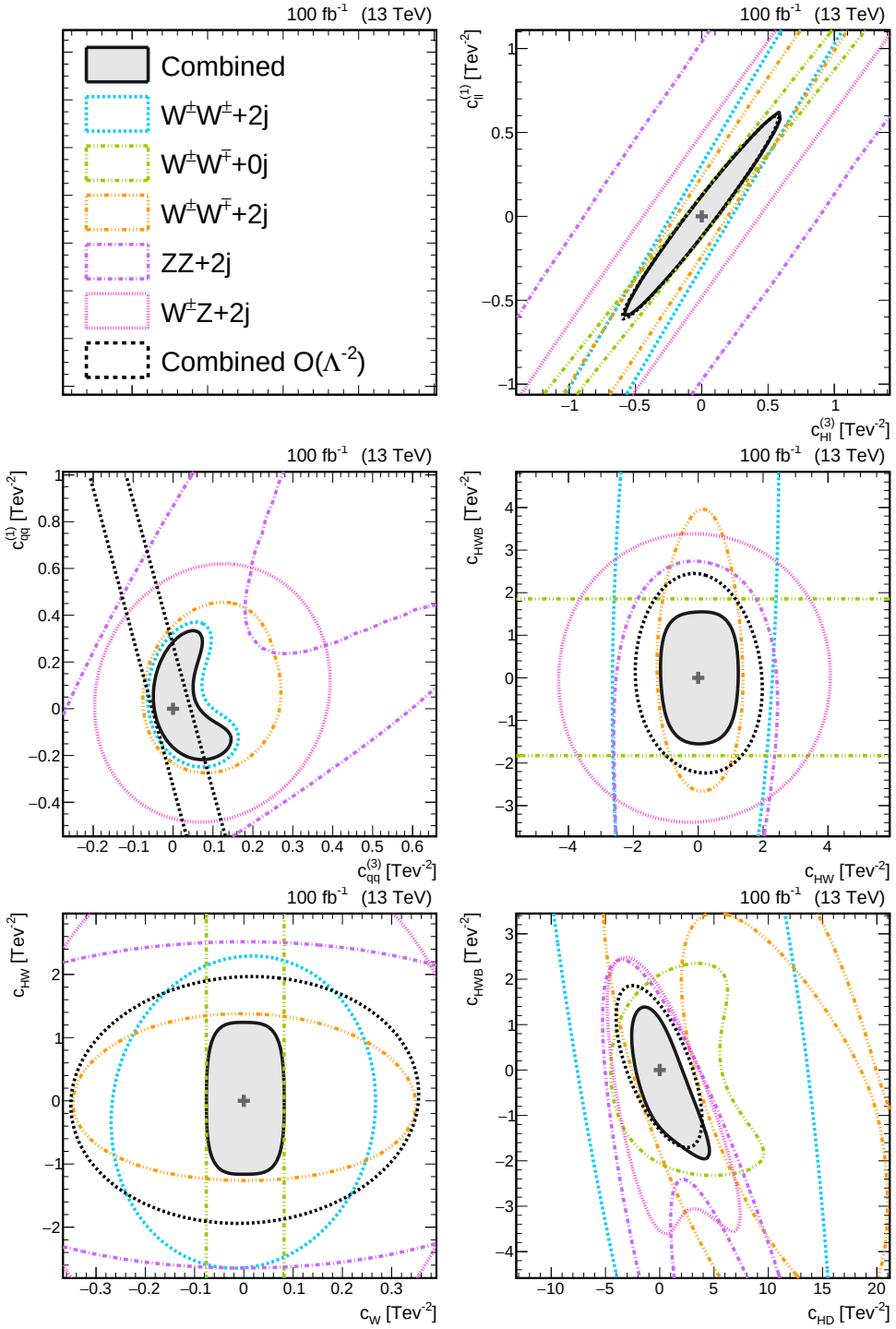

Figure 2.12: Bi-dimensional likelihood contours for $-2\Delta \log \mathcal{L} = 2.3$ (68%c.l.), for individual channels (in colour) and for their combination (black). The VBS $W^+W^- + 2j$, $W^\pm Z + 2j$, $ZZ + 2j$ channels include the respective QCD-induced processes. Only two Wilson coefficients are varied at a time, while the others are fixed to zero. Quadratic EFT contributions are included in all baseline cases. For comparison, the black dashed line shows the contour for the combined likelihood obtained truncating the EFT parametrization at the linear level.

tions and is consistent with the one-dimensional findings. All leptonic processes exhibit a degeneracy in the $c_{ll}^{(1)}$, $c_{Hl}^{(3)}$ plane which is not resolved by the introduction of quadratic terms, but rather thanks to the interplay between the various processes presenting slightly different slopes of the unconstrained directions. The combined constraint is dominated by the interplay of the inclusive WW and SSWW+2j, whose scattering amplitudes scale with $(c_{Hl}^{(3)} - c_{ll}^{(1)})$ and $(4c_{Hl}^{(3)} - 3c_{ll}^{(1)})$ respectively. This correlation arises due to the interaction between corrections affecting the vertices involved in WW production processes. These corrections scale according to $\Delta G_F = 2c_{Hl}^{(3)} - c_{ll}^{(1)}$. Additionally, corrections impacting $Wl\nu$ vertices are dependent solely on the coefficient $c_{ll}^{(1)}$. The impact of including quadratic terms in bi-dimensional EFT scans is in general sizable for each channel but qualitatively consistent with the one-dimensional findings. In particular, four-quark operators are particularly sensitive to the inclusion of quadratic terms due to the unconstrained direction in the bi-dimensional plane for the linear case. When paired with other coefficients different from four-point interactions, only $c_{qq}^{(3)}, c_{qq}^{(3,1)}$ show significant differences between the linear and quadratic fits. Among bosonic operators, the Wilson coefficients whose constraints vary the most depending on whether or not the quadratics are retained are c_W and $c_{Hq}^{(1)}$. The coefficients $c_{Hl}^{(1)}, c_{Hl}^{(3)}, c_{Hq}^{(3)}, c_{ll}^{(1)}$ are the least sensitive to the introduction of quadratics, as their projected bounds remain essentially unchanged in all 2D planes. The constraints on the remaining parameters $(c_{HW}, c_{HD}, c_{HWB}, c_{H\Box})$ typically exhibit disparities between results obtained with and without quadratic terms. However, the extent of this variation varies based on the specific combination of operators under consideration. At the two-dimensional level, the inclusion of quadratic terms typically results in a distortion of the likelihood contours. Consequently, in numerous scenarios, it becomes possible to identify regions within the parameter space (sufficiently distant from the Standard Model point) that are allowed at a 68% confidence level in the quadratic fit, whereas they are disallowed in the linear fit. Conversely, there are also regions where the opposite holds. This phenomenon is present e.g. for the operators pairs $(c_{qq}^{(3)}, c_{qq}^{(1)})$ and (c_{HD}, c_{HWB}).

2.3.3 Projected one-dimensional constraints for LHC Run III and HL-LHC

The limits reported in Sec. 2.3.2 were obtained assuming an integrated luminosity of 100 fb^{-1} as a proxy for the recorder luminosity of the LHC Run II. The Run III is instead expected to deliver twice as much data, amounting to approximately 200 fb^{-1}. Combined with the Run I and Run II statistics, the data set will then amount to more than 300 fb^{-1}. Following the end of Run III, the LHC will be shut down to allow for several improvements regarding detectors and the beam-pipe apparatus pushing the machine to the so-called high-luminosity phase (HL-LHC). The instantaneous luminosity will be increased up to about $5 - 7.5 \times 10^{34}\,\text{cm}^{-2}\text{s}^{-1}$, allowing the LHC to deliver approximately 3000 fb^{-1} in 10 years of data taking.

The limits obtained for the one-dimensional fits in Sec 2.3.2 can be scaled to these new upcoming scenarios by assuming only an improvement in the overall statistics. The center of mass energy is kept fixed at the Run II value of 13 TeV in both cases. No scaling of the constraint on the 2% luminosity uncertainty is applied. Figure 2.13 shows the individual exclusion ranges at 95% c.l. expected for the VBS-only and the VBS and inclusive WW combinations at $100, 300, 3000\,\text{fb}^{-1}$, including the relevant QCD-induced contributions and quadratic terms in the EFT predictions. At parton level, the projection shows that the VBS combination alone should be able to constrain all the operators between $[-1, 1]$ at 95% C.L. by the end of the HL-LHC while including the inclusive diboson WW process lowers the expected bounds to the $[-0.5, 0.5]$ level, reaching a few percent for the most constrained operators.

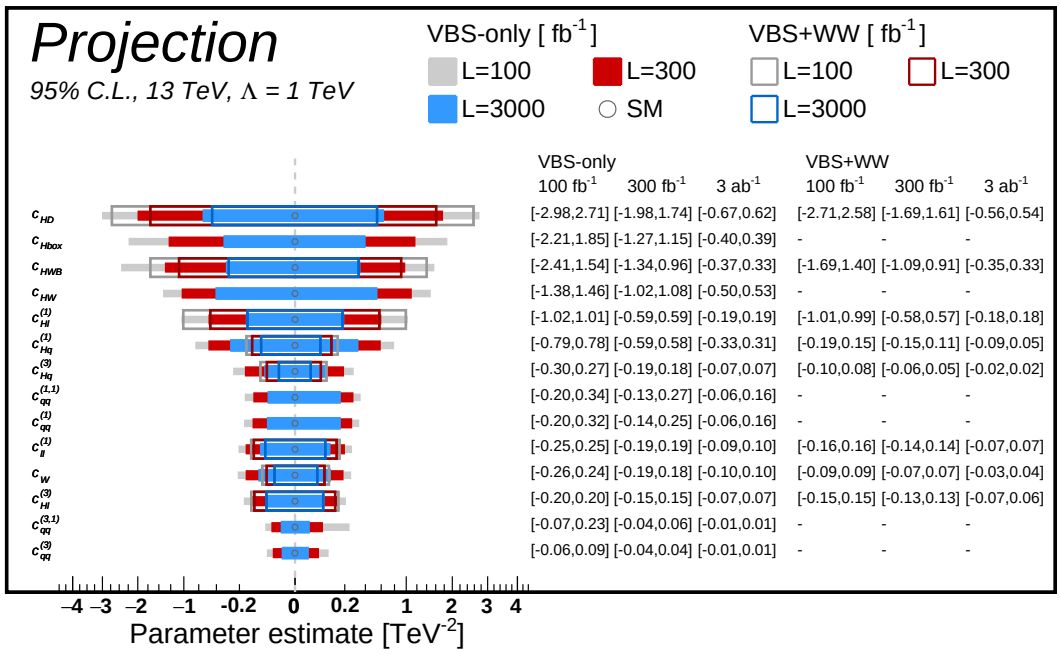

Figure 2.13: Expected 95% c.l. constraints on individual SMEFT operators for an integrated luminosity of 100 fb^{-1} (grey), 300 fb^{-1} (red) and 3 ab^{-1} (blue). Constraints expected from the combination of the VBS channels SSWW+2j, OSWW+2j, WZ+2j, ZZ+2j are depicted as filled coloured boxes while the combination of VBS and WW channels as hollow boxes with a coloured borderline. EFT effects in the QCD-induced processes are included whenever relevant. The result for VBS+WW is not indicated for operators that do not enter WW. In this case, the limits from the VBS+WW combination would coincide with those from VBS only.

2.3.4 Impact of the QCD-induced sample

Typical LHC analyses only focus on SMEFT modification of the electroweak signal, neglecting all sources of SMEFT contributions from the background. By simulating SMEFT contribution to the QCD-induced background this study can address the effect of including or not additional new physics contributions from them as well. The study is only done at the one-dimensional level, where Wilson coefficients are fit individually while fixing the remaining to their SM value. Figure 2.14 shows that for all operators and in all channels, the inclusion of the QCD EFT dependence never weakens the sensitivity: in some cases its impact is negligible, but in many other ones it leads to an improvement of the constraints by up to a factor of 2. As a general principle, constraints in which the electroweak+QCD and electroweak outcomes exhibit minimal discrepancies are primarily influenced by the contributions stemming from the electroweak-induced processes. Constraints that demonstrate substantial enhancements with the inclusion of QCD effects are those related to $c_{Hq}^{(3)}$ and $c_{Hq}^{(1)}$ where the $W^{\pm}W^{\mp} + 2j$ phase space is overwhelmed by the QCD-induced component. For the remaining constraints that display noteworthy improvements, their results arise from a complex interplay between the electroweak and QCD bounds. These findings were cross-validated using fits focused solely on the QCD-induced components.

2.3.5 Profiled Bounds

When matching a UV-complete theory to the SMEFT basis it has been shown that typically more than one non-zero Wilson coefficient is introduced [138, 139]. The precise mapping de-

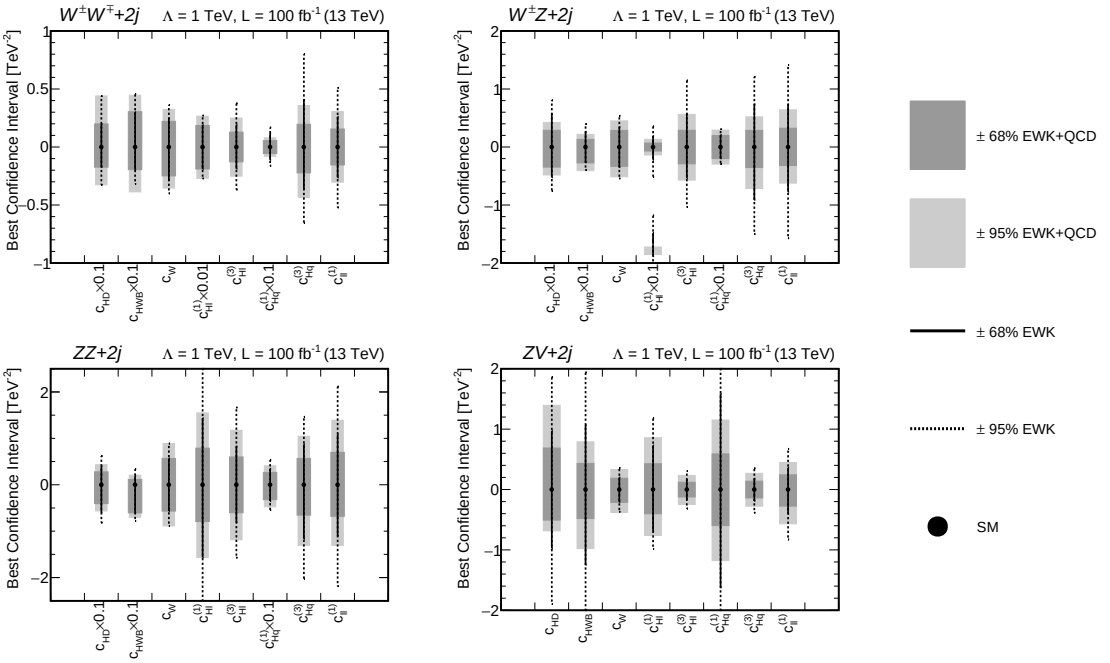

Figure 2.14: Impact of EFT corrections to the QCD backgrounds on the fit sensitivity, for the channels OSWW+2j (upper left), WZ+2j (upper right), ZZ+2j (lower left) and ZV+2j (lower right). The black solid (dashed) lines represent the 68% c.l. (95% c.l.) expected limits obtained neglecting QCD EFT contributions. The dark (light) grey bands represent the 68% c.l. (95% c.l.) limits including the QCD EFT dependence in the fits. The black points correspond to the SM expectation.

pends on the model chosen, corresponding to the unknown underlying new physics phenomena. Upper bounds on the sensitivity to SMEFT operators can be estimated in a worst-case scenario, where all the operators being investigated are concurrently present with non-zero Wilson coefficients. One-dimensional results obtained in Sec. 2.3.2 are compared to the ones obtained by letting all Wilson coefficients freely floating in the likelihood minimization built using the same observables. Limits on each Wilson coefficient of interest are obtained by profiling all the other ones treated as unconstrained nuisances. The comparison is done at the quadratic level only, as including only linear EFT components could result in non-physical negative predictions. The comparison is shown in Figure 2.15. By definition, the profiled constraints are always equal to or worse than the individual ones. The differences between the two approaches are strictly dependent on the Wilson coefficient and its correlations with the other ones in the studied set. The values of c_W, $c_{Hq}^{(1)}$, $c_{qq}^{(3)}$, and $c_{qq}^{(3,1)}$ experience minimal changes due to the inclusion of extra parameters in the likelihood. This observation indicates that these directions are already effectively well-resolved within the specific processes that predominantly dictate the constraints. Specifically, the inclusive WW process is influential for the first two coefficients, while the SSWW+2j process plays a significant role for the latter two. The largest deterioration in the constraints is observed for $c_{ll}^{(1)}$ and $c_{Hl}^{(3)}$, which is in agreement with the two-dimensional study, showing a nearly unconstrained direction in this plane clearly visible in Figs. 2.12 and discussed deeply in Sec. 2.3.2.

2.3.6 SMEFT corrections in propagators

Insertions of SMEFT operators into the scatter amplitudes can happen both in vertices and in propagators of particles via correction to their masses and decay widths. Using the $\{m_W, m_Z, G_F\}$

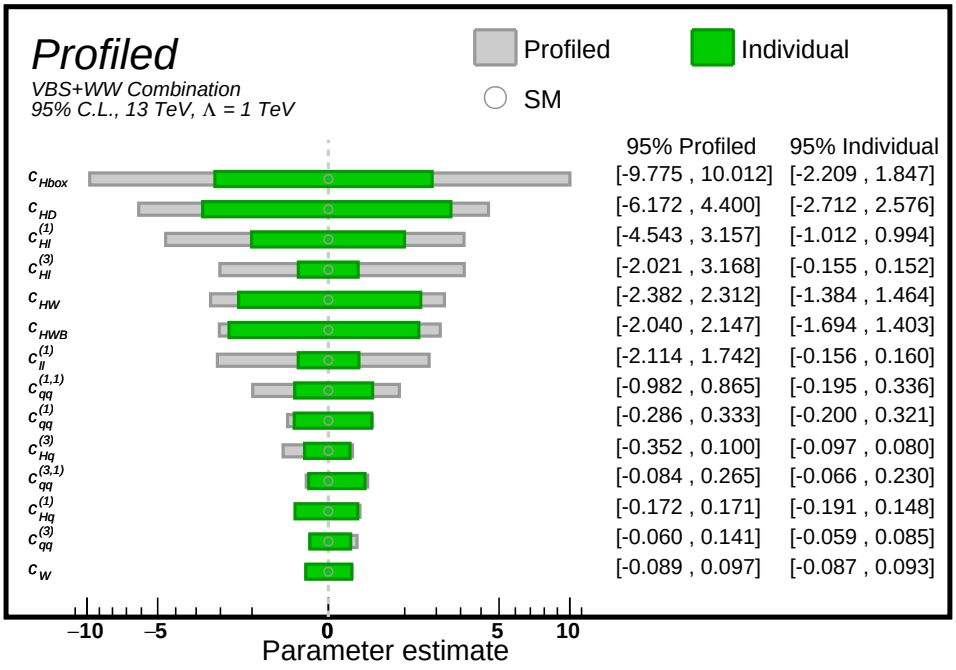

Figure 2.15: Sensitivity of the combined analysis of VBS SSWW+2j, OSWW+2j, WZ+2j, ZZ+2j and diboson WW to the dimension-six operators considered, when the remaining Wilson coefficients are set to zero (green) or profiled away (grey). The QCD-induced EFT dependence was included where relevant.

input scheme, all the masses are fixed to the input provided and the only propagator corrections come from modifications of the W, Z and Higgs bosons decay widths $\delta\Gamma_W$, $\delta\Gamma_Z$ and $\delta\Gamma_h$ that modify the denominator of the vector and scalar propagators. These corrections are polynomial and happen at the denominator of the propagator function, which induces technical problems when evaluating their effect at the quadratic order Λ^{-4}. The quadratic propagator contributions provide only partial predictions at the Λ^{-4} order, neglecting e.g. corrections from the inclusion of two EFT operators in the same amplitude that present the same order in Λ. While the distinction between double insertions and standard quadratics is clearly defined for vertex corrections, it becomes less straightforward for propagator corrections. The comparison therefore focuses on the linear terms where propagator corrections are well defined [140] and available in Monte Carlo tools [65]. The expected number of events for the insertion of an operator α in the linear case considering both vertex and propagator correction becomes

$$N_\alpha^{\text{int}} = N_{\alpha,\text{vert.}}^{\text{int}} + N_{\alpha,\delta\Gamma_W}^{\text{int}} + N_{\alpha,\delta\Gamma_Z}^{\text{int}} + N_{\alpha,\delta\Gamma_h}^{\text{int}} \tag{2.6}$$

The term $N_{\alpha,\text{vert.}}^{\text{int}}$ is the contribution from the insertion of EFT operators in vertices while the terms $N_{\alpha,\delta\Gamma_W}^{\text{int}}$, $N_{\alpha,\delta\Gamma_Z}^{\text{int}}$ and $N_{\alpha,\delta\Gamma_h}^{\text{int}}$ come from EFT insertions in the W, Z and H propagators respectively. Linear propagator corrections are estimated via the interaction-order syntax of MADGRAPH5_AMC@NLO and SMEFTSIM and summed to the previously analysed vertex contributions. Propagator corrections have identical shapes for all contributing operators with different normalizations and signs. For example, for any observable, the following relationship holds for $\alpha = c_{Hq}^{(3)}$

$$N^{int}_{c^{(3)}_{Hq},\delta\Gamma_W} = -N^{int}_{c^{(3)}_{Hl},\delta\Gamma_W} = \frac{4}{3}N^{int}_{c^{(1)}_{ll},\delta\Gamma_W} \tag{2.7}$$

and similar relationships exist for the other $N^{\text{int}}_{\alpha,\delta\Gamma}$ terms. All terms can be estimated with only one simulation per process and heavy boson (W, Z, h). The full contributions to the boson's decay widths with the operator set described in Tab. 2.1 are:

$$\begin{aligned}
\frac{\Lambda^2}{v^2}\frac{\delta\Gamma_W}{\Gamma_W^{SM}} &= \frac{4}{3}c^{(3)}_{Hq} - \frac{4}{3}c^{(3)}_{Hl} - c^{(1)}_{ll}\,, \\
\frac{\Lambda^2}{v^2}\frac{\delta\Gamma_Z}{\Gamma_Z^{SM}} &= 1.61c^{(3)}_{Hq} - 1.37c^{(3)}_{Hl} + c^{(1)}_{ll} + 0.47c^{(1)}_{Hq} - 0.18c^{(1)}_{Hl} - 0.07c_{HD} + 0.46c_{HWB}\,, \\
\frac{\Lambda^2}{v^2}\frac{\delta\Gamma_H}{\Gamma_H^{SM}} &= 0.36c^{(3)}_{Hq} - 2.62c^{(3)}_{Hl} + 1.40c^{(1)}_{ll} + 1.83c_{H\Box} - 0.46c_{HD} - 1.26c_{HW} + 1.23c_{HWB}\,.
\end{aligned} \tag{2.8}$$

that have been normalized to $c^{(1)}_{ll}$ for the W and Z bosons, which is the only contribution that is generated. For the Higgs boson, the only contribution generated is the one induced by $c^{(3)}_{Hq}$. At the technical level, the SMEFTsim syntax to be added to the SM generation strings of Tab. 2.2 in order to recover propagator corrections for an operator is `NP=0 NPprop=2 NPprop^2==2`, along with the activation of the option `linearPropCorrections=1` which is otherwise disabled.

Figure 2.16 presents the comparison between the outcomes derived from individual fits that account for propagator contributions versus those that do not.

To ensure coherence, the latter contributions were included in both the electroweak and QCD-induced processes. The two fits were conducted utilizing the same optimal variables in both scenarios. The inclusion of propagator corrections does not alter significantly the observable ranking.

The impact of width corrections is significant only within the phase space where the intermediate boson is approximately on-shell. As a consequence, the contributions stemming from $\delta\Gamma_h$ are considerably subdued in all channels except for OSWW+2j. Generally, in each channel, the most noteworthy propagator corrections are linked to the reconstructed bosons [116].

The impact of propagator corrections is most pronounced on constraints involving $c^{(3)}_{Hq}, c^{(1)}_{ll}$, and $c^{(3)}_{Hl}$, which contribute significantly to the total widths of W and Z bosons. These coefficients lead to notable changes in multiple VBS channels due to their significant influence on $\delta\Gamma_W$ and $\delta\Gamma_Z$. However, cancellations between vertex and propagator contributions lead to worsened constraints, often by a factor of 2 or more, especially for $c^{(3)}_{Hl}$ in diboson WW. In the OSWW+2j channel, only $c_{H\Box}$ is significantly affected by propagator corrections due to specific cancellations. In ZZ+2j and WZ+2j, constraints on $c^{(1)}_{Hq}$ and c_{HWB} change by a factor of 2 but in opposite directions, while those on c_{HD} and $c^{(1)}_{Hl}$ change less due to smaller contributions to $\delta\Gamma_Z$. Overall, combined results show significant changes in constraints only for $c^{(3)}_{Hl}, c^{(1)}_{ll}$, and $c_{H\Box}$ as all other variations in the individual channels either compensate each other or appear in subdominant processes that do not lead the sensitivity anyway (e.g. the constraint on $c^{(1)}_{Hq}$ remains dominated by diboson WW).

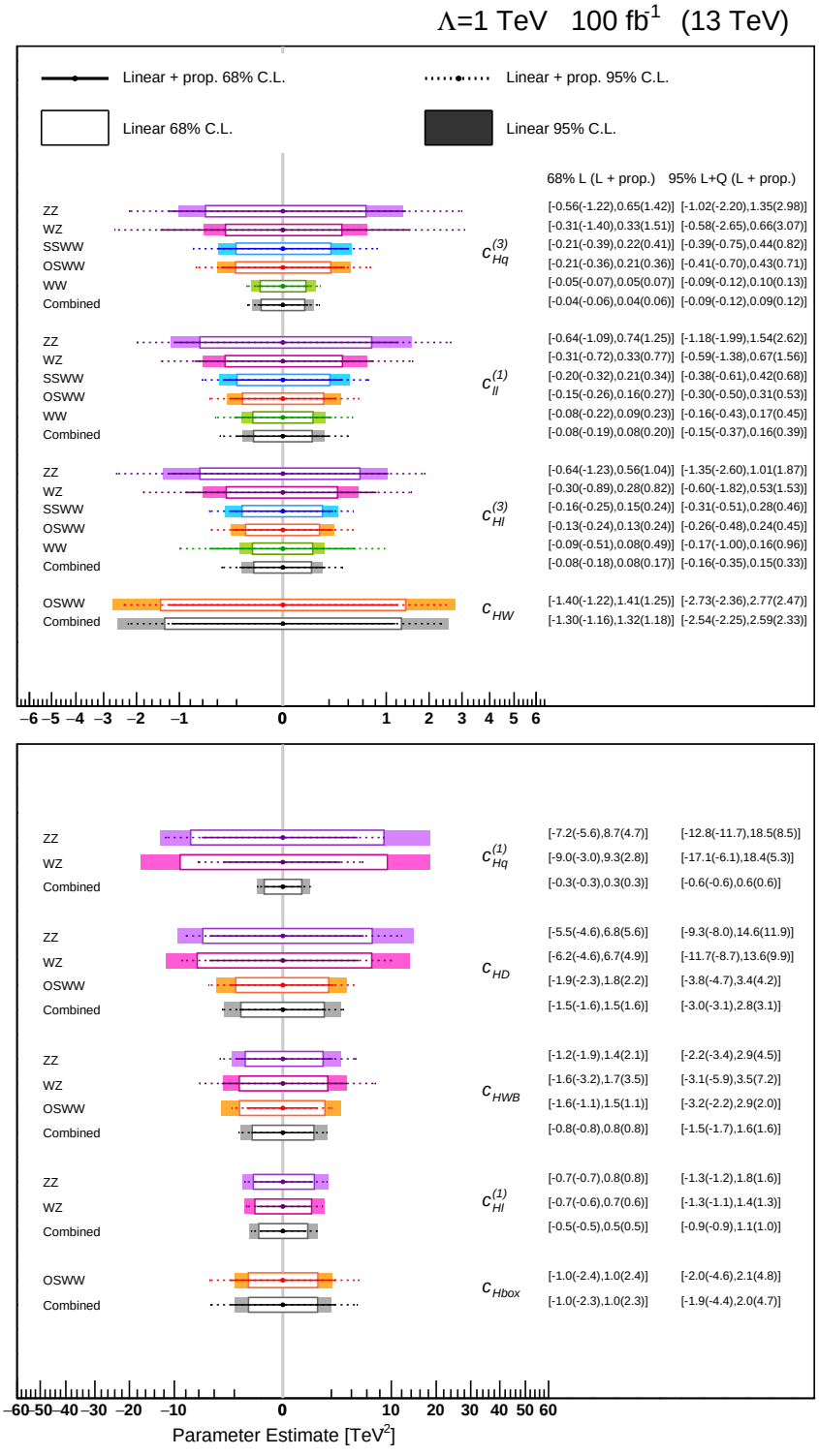

Figure 2.16: Impact of linear EFT contributions entering via corrections to the W, Z and Higgs propagators. Solid (dashed) lines indicate the 68% (95%) confidence level intervals obtained in individual fits, including corrections from both vertex and propagator insertions. Open (filled) boxes indicate 68% (95%) confidence level intervals obtained including only vertex contributions. The figure only shows Wilson coefficients and channels for which the propagator contribution is non-negligible. In all other cases, the results coincide with the linear-only limits shown in Fig. 2.10. The combined constraints are computed with all channels, including those not shown.

2.4 Comparison of SMEFT constraints from VBS and Triboson

A sensitivity study of SMEFT effects in triboson processes carried on with similar procedures as the ones previously described has been recently published [117]. The study targets six operators from the bosonic X^3 class and operators affecting HVV and Hff couplings from $X^2\phi^2$ and $\phi^4 D^2$ classes of the Warsaw basis in Tab. 1.4, namely Q_W, Q_{HW}, Q_{HB}, Q_{HWB}, Q_{HD}, $Q_{H\Box}$. These triboson processes are extremely interesting because they provide unique access to TGCs and QGCs of electroweak vector bosons independently with respect to the VBS topology. Furthermore, they present the same final state signature as VBS but the processes can be almost completely separated thanks to kinematic selections. The study targets four triboson processes, three of which involve a photon. Of these, two channels present a fully leptonic final state $WZ\gamma$ and $ZZ\gamma$. The remaining $VZ\gamma$ is studied in the semileptonic final state along with the process VZZ with the V boson (either a W or Z boson) decaying hadronically. All processes are modeled as $2 \to 6$ or $2 \to 4 + \gamma$ with the inclusion of non-resonant and VBS diagrams, which however are strongly suppressed by the request of central jet pairs ($|\eta_j| < 2.5$) with an invariant mass close to the nominal W or Z boson peak. The QCD-induced EFT and SM contributions have been simulated for the semileptonic $ZV\gamma$ and VZZ processes, as this background is dominant with respect to the electroweak-induced counterpart. Several observables are ranked for each process. The number of such observables ranges between 18 and 28 depending on the process and includes also complex observables such as the Fox-Wolfram moments [141, 142]. All specific details about the processes, selections, and generation are omitted in this discussion but are explicitly stated in Ref. [117]. The focus of the discussion is summarised in Table 2.6 from [117], where one-dimensional limits on the operators of interest for triboson and VBS for an integrated luminosity of 300 fb^{-1} are compared.

The combination of triboson channels shows a higher or compatible sensitivity with respect to VBS to the anomalies induced by the operators Q_{HW}, Q_{HWB}, Q_{HD} and Q_W. The most sensitive triboson channel is found to be the fully leptonic WZγ for Q_W, Q_{HB} and Q_{HW}, while the semileptonic $VZ\gamma$ dominates the sensitivity for the remaining Q_{HWB}, Q_{HD}. For Q_{HW}, which only affects hVV vertices, the higher sensitivity of triboson with respect to VBS is not expected. This is attributed to the tree-level HZγ coupling induced by the Q_{HB} and Q_{HW} operators, which results in a dominant quadratic term and a negligible linear interference. Channels not presenting both a Z and a photon exhibit less sensitivity than all VBS channels of Ref. [116] and the semi-leptonic VZZ.

For a fair comparison, a common binning choice should also be adopted, which is not the case e.g. $p_T(Z)^\gamma$, built with 20 bins in triboson WZγ while all VBS differential distributions present only 10 bins. Nonetheless, the triboson sensitivity study shows the importance of multiboson processes to constrain dimension-six EFT operators.

↶ Processes	Operators →	Q_W	Q_{HB}	Q_{HW}	Q_{HWB}	Q_{HD}
WZγ	Best var.	p_T^{l1}	$p_{T(Z)}^{\gamma}$	$p_{T(Z)}^{\gamma}$	$p_{T(Z)}^{\gamma}$	$p_{T(WZ)}^{l1}$
	68% C.L.	[-0.20,0.21]	[-0.41,0.41]	[-0.44,0.44]	[-0.50,0.73]	[-1.36,1.79]
	95% C.L.	[-0.31,0.32]	[-0.60,0.60]	[-0.65,0.65]	[-0.79,1.04]	[-2.50,11.2]
ZZγ	Best var.		$p_{T(Z_1)}^{\gamma}$	$m_{\mu\mu}$	$m_{\mu\mu}$	$p_T^{e^+\mu^+}$
	68% C.L.	No diagrams	[-0.62,0.61]	[-0.68,0.68]	[-0.81,1.06]	[-1.91,4.55]
	95% C.L.		[-0.90,0.90]	[-0.98,0.99]	[-1.23,1.49]	[-3.27,6.53]
VZγ	Best var.	p_T^{l1}	m_{jj}	m_{jj}	$p_{T(\gamma)}^{l1}$	$p_{T(\gamma)}^{l2}$
	68% C.L.	[-0.26,0.26]	[-0.55,0.54]	[-0.60,0.60]	[-0.11,0.11]	[-0.17,0.17]
	95% C.L.	[-0.37,0.37]	[-0.77,0.76]	[-0.84,0.84]	[-0.22,0.23]	[-0.33,0.34]
VZZ	Best var.	p_T^{l1}		p_T^V	$m_{\mu\mu}$	$p_T^{e^+\mu^+}$
	68% C.L.	[-0.63,0.63]	Negligible	[-4.78,4.08]	[-0.80,0.65]	[-2.73,1.82]
	95% C.L.	[-0.97,0.97]		[-6.91,6.17]	[-2.22,1.20]	[-3.78,2.82]
Combination	68% C.L.	[-0.18,0.19]	[-0.37,0.37]	[-0.40,0.40]	[-0.11,0.11]	[-0.17,0.17]
	95% C.L.	[-0.27,0.28]	[-0.53,0.53]	[-0.57,0.57]	[-0.21,0.21]	[-0.33,0.33]
VBS	95% C.L.	[-0.19,0.18]	-	[-1.02,1.08]	[-1.34,0.96]	[-1.98,1.74]

Table 2.6: Confidence intervals on the estimates of the Wilson coefficients, relative to the subset of operators considered, extracted from the respective likelihood scan for the most sensitive variable, for each channel studied. This table reports the confidence intervals obtained by combining all the triboson channels involving diagrams induced by operators individually included in the SM Lagrangian. The last line reports the results obtained in the study of Ref. [116] combining many VBS channels. All the reported results are obtained considering an integrated luminosity of 300 fb^{-1}. Table from [117]

Chapter 3

The Large Hadron Collider and the Compact Muon Solenoid

3.1 The Large Hadron Collider

The Large Hadron Collider (LHC) is a double-ring superconducting hadron accelerator and collider, sitting at CERN in the 27 km long tunnel that housed the Large Electron-Positron machine (LEP) [143]. The driving force behind the construction and design of the LHC is the investigation of the scalar sector of the SM to unravel the origin of the electroweak symmetry breaking, for which the Higgs mechanism is presumed to be responsible. The physics program of the LHC is not only limited to the search for the Higgs boson but allows to test the SM validity at the TeV scale. Furthermore, precision studies of QCD, electroweak and flavour physics are possible as well as searches for exotic particles and forces predicted by UV-complete models.

The unprecedented peak performances of the LHC, characterized by a center-of-mass energy of 13 TeV and an instantaneous luminosity of the order $\mathcal{O}(10^{34})$ cm^{-2}s^{-1}, represent a remarkable technological challenge. The required beam intensity and collimation exclude the possibility of a particle-antiparticle collider which is an appealing option exploiting a common vacuum and and magnetic system for both beams. Therefore the LHC is designed as a proton-proton collider with separate magnetic fields and vacuum chambers in the main arcs implemented as a twin-bore magnet architecture due to restrictions imposed by the limited internal diameter of the tunnel of only 3.7 meters. Out of the eight possible interaction regions, only four have been equipped with detectors in order to suppress beam crossings and prevent unnecessary disruption of the beams. The peak energy of 7 TeV per beam inside the LEP tunnel implies a peak dipole field of 8.33 T achievable only using superconducting magnets. For this reason, the LHC is equipped with 1232 superconducting dipole magnets and 858 superconducting quadrupole magnets made of a Niobium-Titanium compound and cooled with superfluid Helium to an operating temperature of 1.9 K.

Protons within the LHC are accelerated using 16 superconducting Radio Frequency (RF) cavities, with eight allocated per beam. These cavities function at a frequency of 400 MHz. Their role involves both decelerating swift protons and accelerating slower ones, ensuring that proton bunches remain densely compacted both in physical and momentum space. This effect is achieved through the principle of phase stability. To maintain the operational efficiency of the RF cavities, they are contained within cylindrical refrigeration units and are sustained at a temperature of 4.5 K. The operational configuration of the LHC involves accelerating a proton bunch every ten cycles of the RF frequency. In terms of the 27 km circumference ring, there is adequate room for approximately 3600 bunches. Yet, when accounting for the extra spacing necessary to insert and remove the particle beams from the machine, the capacity narrows

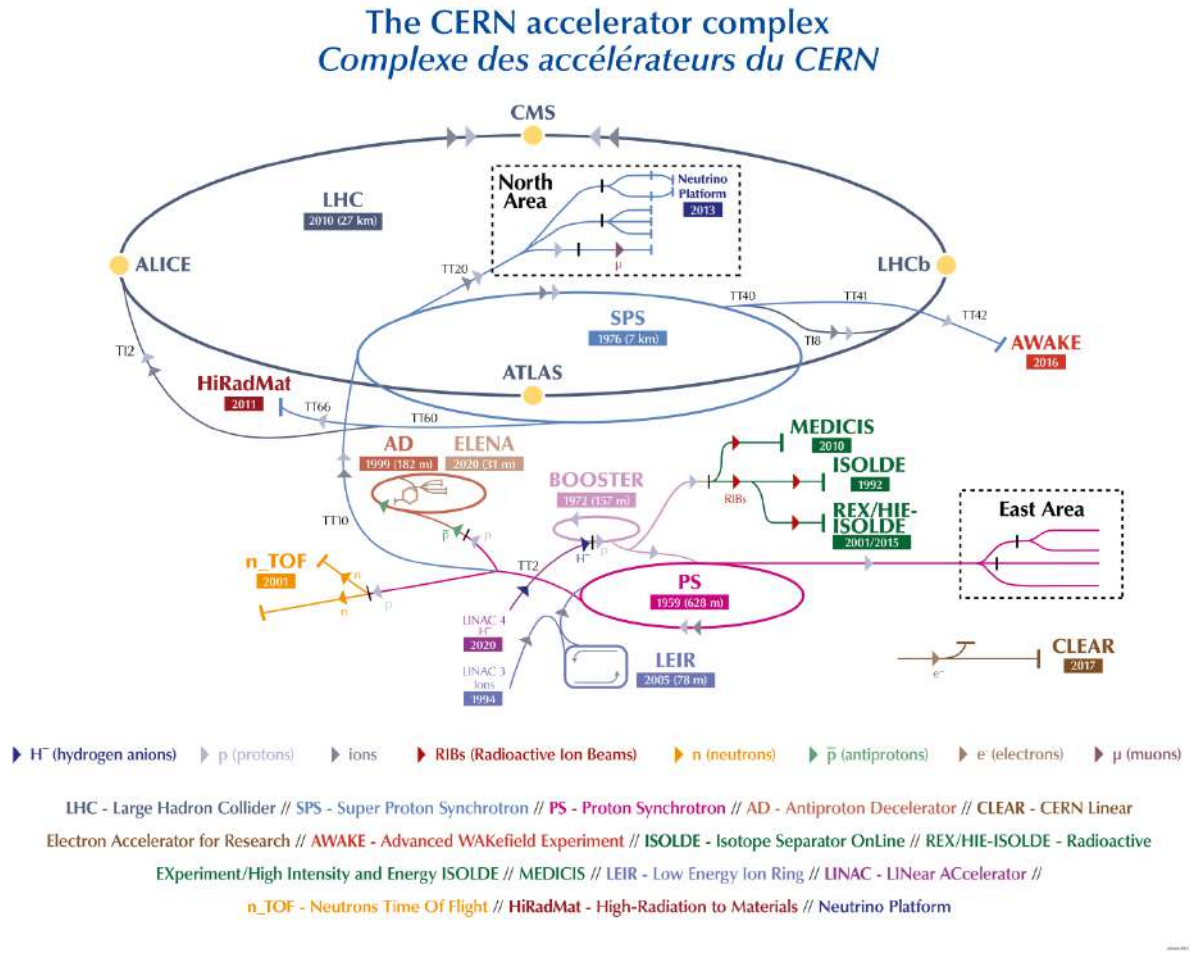

Figure 3.1: CERN accelerator complex, experiments and injection chain

down to accommodating 2808 bunches per beam. This configuration corresponds to an average time interval of 25 nanoseconds between bunches, and therefore a collision rate of roughly 40 MHz.

In order to progressively accelerate protons to the design energy, the LHC accelerator is served by a complete injection chain. Protons are first accelerated by the Linac-2 (lead ions are instead accelerated by the Linac-3) up to 50 MeV, transit through the Proton Synchrotron Booster (PSB) before being injected into the Proton Synchrotron (PS) that boosts the energy up to 26 GeV. Protons from the PS are collected by the Super Proton Synchrotron (SPS) which further boosts their energy up to 450 GeV before the final injection into the LHC.

Four large experiments sit at the four crossing points of the LHC beams. Among these, two are general-purpose detectors positioned at the high-luminosity cross locations with a peak luminosity of 10^{34} cm^{-2}s^{-1}. Specifically, there is A Toroidal LHC ApparatuS (ATLAS) detector situated at Point 1, and the Compact Muon Solenoid (CMS) detector positioned at Point 5. Conversely, the remaining two detectors, the Large Ion Collider Experiment (ALICE) and the Large Hadron Collider beauty (LHCb) detectors, have more specialized purposes. These detectors are stationed at cross points with lower luminosity levels of 10^{27} cm^{-2}s^{-1} and 2×10^{29} cm^{-2}s^{-1} respectively. The layout of the LHC is illustrated in Fig. 3.1.

The probabilistic character of the physical processes being investigated at the LHC makes

searches for BSM processes and accurate measurements of previously understood physics processes only possible when a statistically significant number of these events can take place at the LHC. The production cross-section of a process, σ, the machine luminosity L, the detector efficiency ϵ and the detector geometrical acceptance A are used to calculate the expected number of events N

$$N = L\sigma \cdot \epsilon \cdot A \tag{3.1}$$

The machine luminosity depends on the beam parameters and, for a Gaussian beam distribution, can be written as

$$L = \frac{N_b^2 n_b f_{rev} \gamma_r}{4\pi\epsilon_n \beta^*} F \tag{3.2}$$

Where N_b and n_b are respectively the number of particles per bunch and the number of bunches in the beam, f_{rev} the revolution frequency, γ_r a relativistic factor, ϵ_n the normalized emittance of the beams and β^* is the machine betatron function related to the size of the beam at the interaction point. F is the so-called geometric luminosity reduction factor and is related to the beam crossing angle, transverse RMS beam size and RMS bunch length at the interaction point. The integrated machine luminosity $\int_0^t Ldt$ measures the amount of data delivered to the experiments.

Symbol	Description	2016	2017	2018
$\sqrt{s}$	centre-of-mass energy (TeV)	13	13	13
Δt	Bunch spacing (ns)	25	25	25
L	Instantaneous luminosity peak (10^{34} cm^{-2}s^{-1})	1.4	2.1	2.1
μ	Average pileup	25	38	37
n_b	Bunches per beam	2220	2556/1868	2556
N_b	Protons per bunch (stable beam) (10^{11})	1.0-1.25	1.0-1.25	1.0-1.25
ϵ_n	Transverse emittance (μm)	2.2	2.2	1.9
f_{rev}	Revolution frequency (Hz)	11245	11245	11245
β^*	Beta function (cm)	40	40-30	30-25

The LHC began its operational period in 2009 with the first delivered proton-proton collision at a center-of-mass energy of 0.9 TeV. During 2010 the center-of-mass energy was increased to 7 TeV, collecting 45 pb^{-1}. In 2011 the peak luminosity was recorder at 4×10^{33} cm^{-2}s^{-1}, collecting 6 fb^{-1} of data. The first stable run (Run-I) came in 2012 with a center-of-mass energy of 8 TeV and a luminosity of 6×10^{33} cm^{-2}s^{-1}, stable for almost the entire year. After approximately two years of shutdown in order to consolidate the high current splices between the superconducting magnets, the machine entered a long-term phase of operations at 13 TeV known as the Run-II. In this period from 2015 to 2018, the instantaneous luminosity exceeded the design specifications with peaks of 2.1×10^{34} cm^{-2}s^{-1} with consequently higher number of simultaneous interactions, or pileup (PU), with a mean of 40 and peaks of 70 in 2018. The LHC Run-II delivered an integrated luminosity of approximately 140 fb^{-1} to each experiment.

A second shutdown from 2019 to 2021 prepared the machine for its last upgrade called the High Luminosity phase (HL-LHC), which is expected to start in 2026. In 2022 the Run-III of the machine started with a center-of-mass energy of 13.6 TeV, close to the design value, and is expected to deliver an additional 200 fb^{-1} of data. The maximum center-of-mass energy is expected to be reached in the HL-LHC phase with an instantaneous luminosity of seven times the nominal value 7×10^{34} $cm^{-2}s^{-1}$.

3.2 The Compact Muon Solenoid

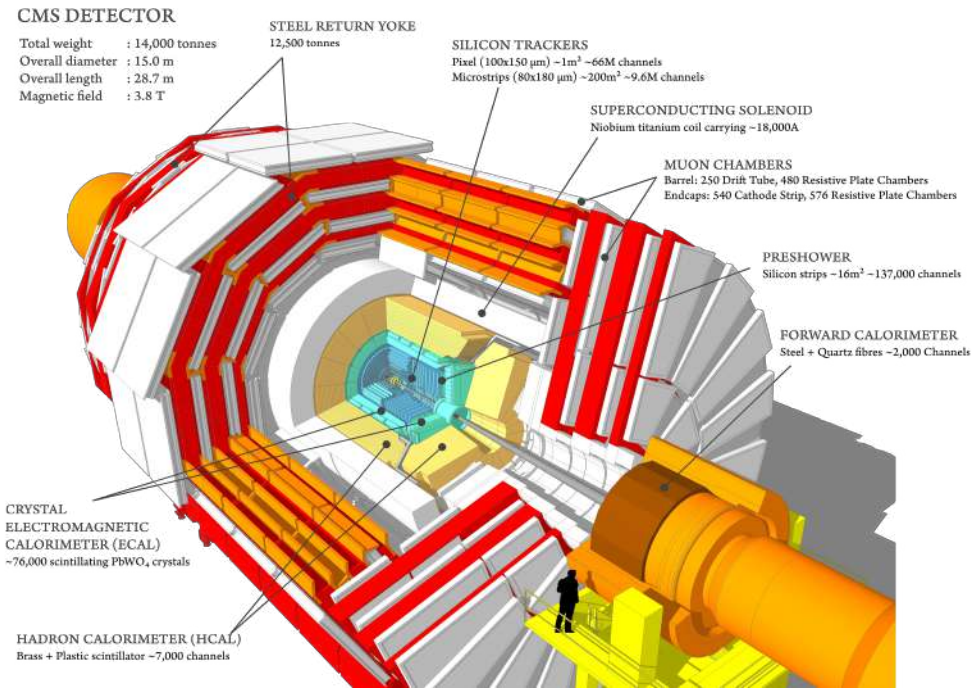

Figure 3.2: CMS detector layout

The CMS detector, one of the two general-purpose ones at the LHC, was specifically designed to investigate high-momentum interactions and exhibits excellent performances in the detection of electrons, photons, and muons. CMS incorporates a niobium-titanium superconducting solenoid magnet at its core capable of generating a 3.8 T magnetic field spanning its entire 6-meter diameter, making it one of the largest ever constructed, weighing approximately 2000 tons. Its unique geometry allows the detector to maintain a compact size, fitting within the experimental cavern about 100 meters underground LHC Point 5. The extensive range of physics inquiries necessitated careful consideration during the detector design and development. This focus led to the outstanding performance of the electromagnetic calorimeter (ECAL), muon detectors, and the inner tracker, all designed to precisely identify particles and to measure their momenta. Given that many Beyond the Standard Model (BSM) particles exhibit minimal interaction with detector materials, potential signals of new physics could manifest as missing energy in the final state compared to the energy of the colliding beams. To address this, both the ECAL and the hadron calorimeter (HCAL) were engineered as hermetic detectors, offering extensive geometric coverage that nearly encompasses the entire solid angle surrounding the interaction region, ensuring the efficient detection of collision products within the CMS volume. The trackers represent the innermost detectors within CMS, positioned as close as three centimeters to the particle beams. Alongside the ECAL and HCAL, these trackers are located within the solenoid, utilizing its magnetic field to measure the curvature and momentum

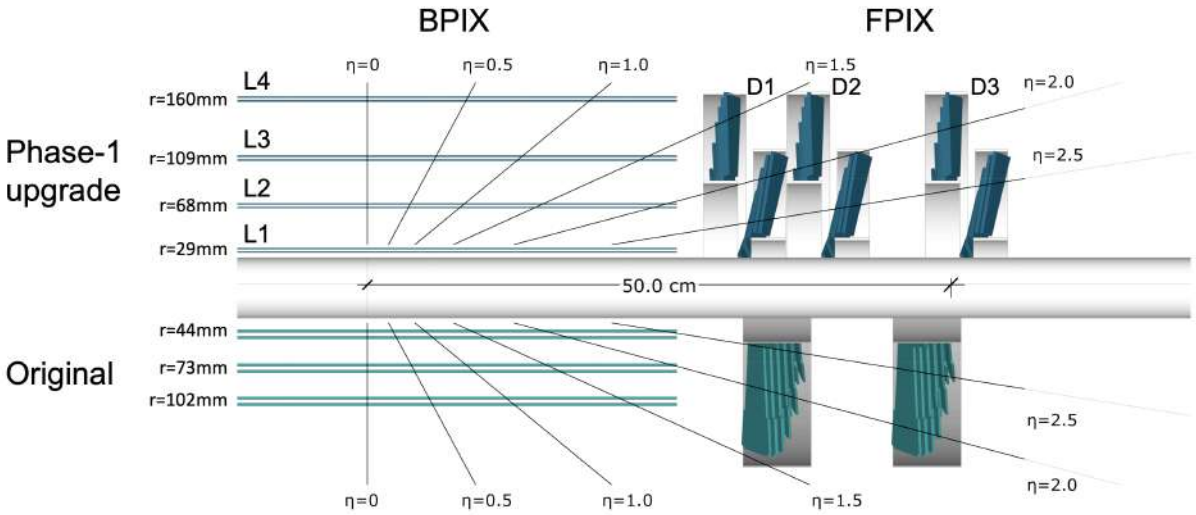

Figure 3.3: Schematic view of the CMS tracking system in the $r-z$ plane after the upgrades introduced during the 2016/2017 year-end technical stop [145]

of charged particles. Beyond the solenoid, in the return yoke, the magnetic field strength is roughly 2 T and there lie three types of detectors collectively referred to as the muon chambers, comprising the outermost layer of CMS [144]. Due to the different amounts of particle flux, CMS subdetectors are often divided into a central section or barrel and two forward regions called endcaps typically presenting different detector design choices. A schematic representation of CMS is shown in Figure 3.2

A right-handed Cartesian coordinate system is used to describe the CMS detector and its collision products. Its origin coincides with the nominal interaction point, the x-axis points toward the center of the detector, the y-axis points up (perpendicular to the LHC plane) and the z-axis along the anticlockwise beam direction. A polar coordinate system is also used where θ indicates the polar angle with respect to the z-axis, ϕ represents the azimuthal angle in the $x-y$ plane and r the radial distance. The pseudorapidity $\eta = -\log\tan(\theta/2)$ is often used instead of θ to describe the angle of emission for a particle with respect to the beam axis because differences in rapidity prove to be Lorentz-invariant and the production of particles at hadron colliders is approximately constant as a function of η. Spatial separation is often defined in terms of the angular Euclidean distance in the $\eta-\phi$ plane as $(\Delta R)^2 = (\Delta\eta)^2 + (\Delta\phi)^2$. Transverse quantities with respect to the beam axis are often used as they are invariant under Lorentz boosts resulting from the initial momentum of the interacting partons, e.g. the projected momentum of a particle onto the transverse plane is defined as $(p_T)^2 = (p_x)^2 + (p_y)^2$

3.2.1 Tracking system

The tracking system is the closest CMS detector to the interaction point [146]. It extends to a length of 5.6 meters and up to 2.4 meters in the radial direction. Its total active area is close to 200 m^2 with approximately 80 million channels. The harsh radiation environment of this region led to a two-tiered design optimized to use a minimum amount of material. A full silicon detector technology is deployed, providing a large surface of thin, finely segmented, active detectors. Thanks to the uniform magnetic field within the tracker volume, the measurements of the position of charged particles, or hits, can be combined to form tracks allowing for a measurement of the particle's momentum and electric charge. The combined measurement of multiple particle tracks allows the identification of hard scatter interaction point (primary ver-

tex) and its discrimination against other simultaneous $p-p$ collisions that can happen during the same bunch crossing known as pileup. Additionally, the tracking system allows for the reconstruction of in-flight decays, such as those involving hadrons constituted by bottom or charm quarks, C-hadrons or τ leptons, referred to as secondary vertices. Due to the decreasing particle flux with increasing radial distance (r), the innermost section of the tracker, where r is less than 20 cm, consists of high-granularity silicon detectors referred to as pixels. In the region where r falls between 20 and 250 cm, CMS utilizes silicon strips with a pitch that is directly proportional to the radial distance, effectively adapting to the changing particle density. The pixel detector is disposed of in three cylindrical layers in the barrel and two disks in the endcaps with a pseudorapidity coverage up to 2.5. Following a significant upgrade in 2017 for data collection during the 2017/2018 period, an additional layer has been added to the pixel detector both in the endcap and in the barrel region, positioned in the latter at radii of 2.9, 6.8, 10.2, and 16.0 cm from the beam-line. Each pixel measures about $100 \times 150\,\mu\text{m}^2$ resulting in 66 million silicon pixels (almost 90% of the full tracker detector channels) and an active area of $1\,\text{m}^2$. Each pixel achieves a spatial resolution of $10\,\mu$m in the (r, ϕ) plane and of $20\,\mu$m along the z direction. For the outermost part of the tracker detector, larger silicon modules have been preferred with a pitch correlated with the radial distance ranging from 80 to 180 μm. The coarser geometry is acceptable due to the lower particle fluxes in this region and for the economic unfeasibility of covering an area of $200\,\text{m}^2$ with finely spaced silicon detectors. The strip detector in the barrel is divided into an inner region (TIB) spanning up to $|z| < 65$ cm and an outer region (TOB) up to $|z| < 110$ cm comprising respectively 4 and 6 active layers. Along the z-direction, the 45 cm gap between the TIB and the TOB is filled with four Tracker Inner Disks (TID). To expand the coverage in terms of rapidity up to $|\eta| < 2.5$, two Tracker End Caps (TEC) are deployed. These TECs are constructed with a total of 9 disks, covering the range of $120 < |z| < 280$ cm. The resolution for a single point varies depending on r, with values ranging from 20 to 50 μm in the radial direction and from 200 to 500 μm in the longitudinal direction. In order to minimize radiation damage and to absorb the heat produced by the on-board electronics for the readout, the strip and the pixel detectors are cooled at an operating temperature of about -15 °C and -20 °C respectively. A schematic representation of the CMS tracker system is illustrated in Figure 3.3.

3.2.2 Electromagnetic Calorimeter

The Electromagnetic Calorimeter (ECAL) [147] is a homogeneous calorimeter, made of 75848 lead tungstate ($PbWO_4$) scintillating crystals, specifically designed to measure energy deposits of mainly photons and electrons. An explanatory sketch of ECAL geometry and layout is shown in Figure 3.4 The ECAL crystals act both as the dense interacting material and the active scintillating medium, granting excellent resolution. The choice of $PbWO_4$ with a density of $8.28\,\text{g/cm}^3$, radiation length of 0.89 cm and Molière radius of 2.19 cm has been mainly motivated by its excellent capabilities in the containment of the electromagnetic showers within the crystal. Furthermore, lead tungstate is a radiation-tolerant material and grants fast responses as 80% of its scintillation light is emitted within 25 ns making it suitable for the high bunch crossing rates of 40 MHz at the LHC. The main disadvantage of $PbWO_4$ is its low light yield of approximately 30 photons per MeV of deposited energy (depending on the operating temperature) that requires the use of photodetectors with internal amplification inside the 3.8 T axial magnetic field of CMS. In the barrel region of the ECAL, avalanche photodiodes are used to detect the scintillation photons while vacuum photo triodes are used in the endcap region as being more radiation-tolerant. The front-end electronics amplify the signals captured by these photodetectors, which are then sampled using a 12-bit analog-to-digital converter at a rate of 40 MHz. The barrel region of ECAL comprises 61200 crystals organized in 36 supermodules, 18 in

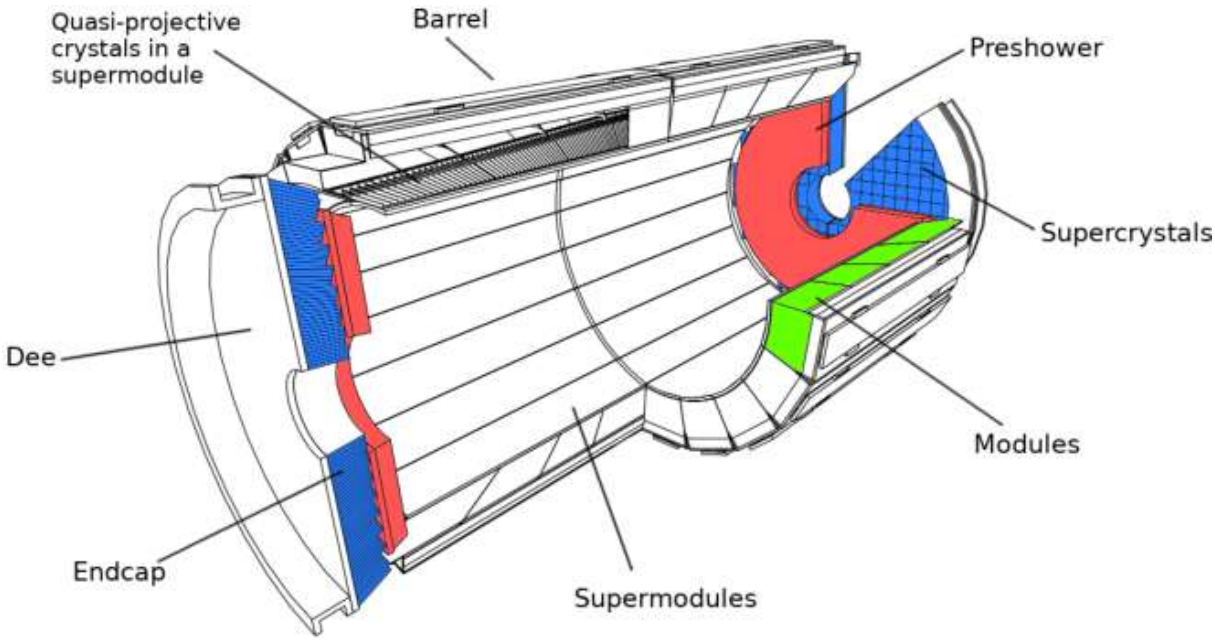

Figure 3.4: ECAL layout and geometry

each half barrel, each covering 20° in ϕ. Crystals have a transverse section of 22×22 mm^2 and a length of 23 cm, covering the region of pseudorapidity $|\eta| < 1.479$. The barrel crystals have a truncated pyramid shape. The barrel is extended up to $|\eta| = 3$ by two endcap disks, each made of 7324 equally shaped crystals with a frontal transverse section of 2.86×2.86 cm^2 and located at approximately 314.4 cm from the interaction point. Endcap crystals are organised in the so-called super-crystal (SC) modules which is an array of 5×5 crystals. Each endcap is divided into 2 halves, called Dees, each composed of 3662 crystals making up 138 standard SCs and 18 special partial super-crystals. In the forward region, ECAL is equipped with a SiPb sampling detector called preshowe which helps to distinguish prompt photons from photon pairs produced in the decay of neutral pions.

In both the barrel and the endcaps, $PbWO_4$ crystals are mounted in quasi-projective geometry so that their axes make a small angle (3°) with respect to the nominal interaction vertex, both in the ϕ and η projections [147]. This ensures no energy loss as a function of η from the crystal interstices between the crystals.

The $PbWO_4$ and photodetectors' light yield heavily depends on the operating temperature (respectively -2%/°C and -2.3%/°C): ECAL is equipped with a state-of-the-art cooling system designed to efficiently remove the heat generated by the readout electronics while keeping the crystal temperature stable with fluctuations of ± 0.05°C in the barrel and ± 0.1°C in the endcaps. The working temperature of ECAL of 18°C is chosen to naturally recover its wavelength-dependent loss of light transmission experienced through its operation due to high doses of ionizing radiation to which the crystals are exposed. In order to ensure optimal resolution, the optical transparency is monitored and corrected with the injection of a 440 nm laser light in each crystal to derive time-dependent correction factors.

The resolution of a calorimeter can be parametrized in terms of three factors. The first one is a stochastic term that models the fluctuations of the number of scintillating photons n produced in the interaction as $\sqrt{n}$, which is directly related to the energy of the incident particle E. A second term accounts for the noise in the detector and does not depend on E. The last term, which dominates the energy resolution for high-energy electrons and photons, accounts for

detector inhomogeneities, constant as a function of E, and issues like non-uniformity in the longitudinal light collection, energy leakage from the rear of the calorimeter, as well as variations in single-channel response uniformity and thermal stability. The overall parametrization of the calorimetric resolution as a function of the energy can be written as

$$\left(\frac{\sigma}{E}\right) = \frac{S}{\sqrt{E}} \oplus \frac{N}{E} \oplus C \tag{3.3}$$

where S, N and C denote respectively the stochastic, noise and constant terms. The ECAL resolution has undergone comprehensive testing using both electron beams and cosmic rays data. With an electron beam, Ref. [148] reports the following values for the resolution of a 3×3 ECAL barrel crystal matrix in a setup with no magnetic field or inert material in front of the calorimeter: $S = 2.8\%$, $N = 12\%$, $C = 0.3\%$. The ECAL response undergoes calibration to establish both the absolute energy scale and the inter-calibration between channels. This calibration is particularly essential to address inherent variations in crystal light yield (approximately 15%) and the dispersion in endcap phototriodes (around 25%). The initial calibration obtained via dedicated laboratory experiments or with cosmic rays exposure of the crystals is now enhanced by in-situ measurements using collision events. This refinement has led to an energy resolution of approximately 2% for 45 GeV electrons within the barrel region and 2–5% in other areas. Furthermore, this resolution improves to around 1.5% for electrons located in the central portion of the detector, where minimal energy is emitted due to bremsstrahlung radiation. For a comprehensive review of ECAL energy calibration and resolution in pp collisions at $\sqrt{s} = 7$ TeV see Ref. [149].

3.2.3 Hadron Calorimeter

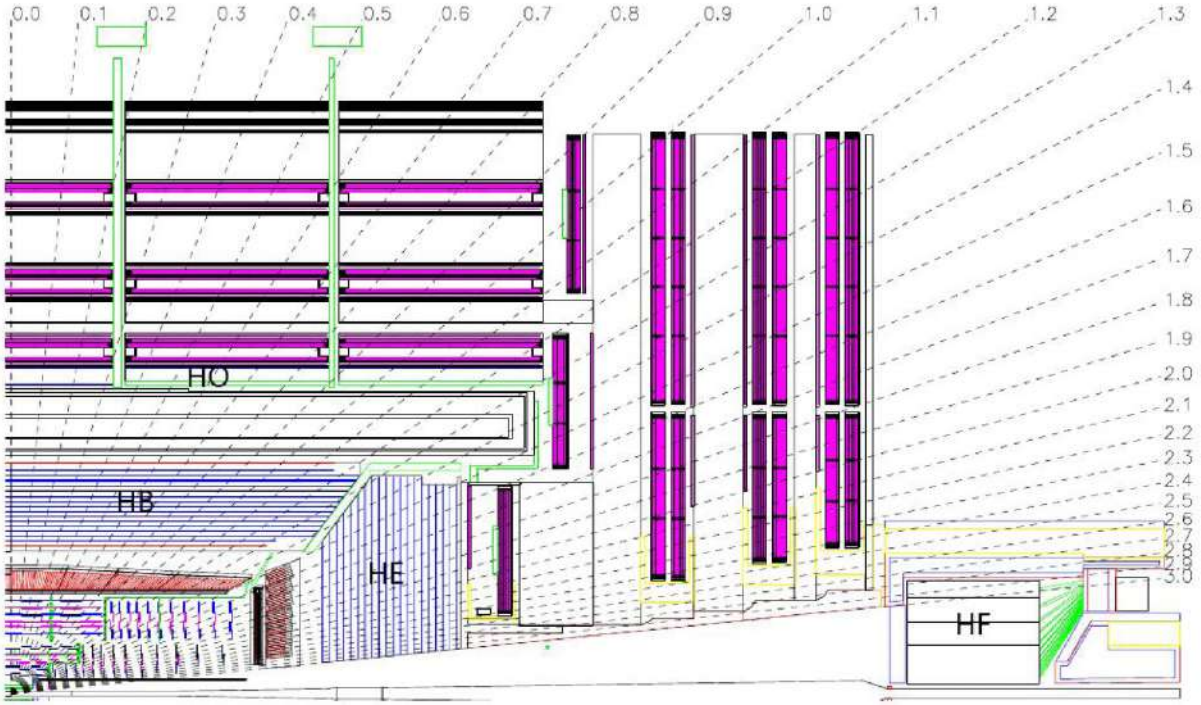

Figure 3.5: HCAL layout and geometry. The longitudinal view shows the barrel (HB) in between ECAL and the solenoid, the endcaps (HE), the outer barrel (HO) outside the solenoid, and the forward calorimeter (HF)

The CMS brass and scintillator hadron calorimeter (HCAL) is designed to measure the energy of hadrons that typically traverse ECAL without being stopped. Hadron energies are intrinsically more difficult to measure from hadron showers in HCAL with respect to their electromagnetic counterpart in ECAL. Nuclear and hadronic interactions lead to non-Poissonian effects in the development of particle showers, causing the production of numerous undetectable particles as well. Furthermore, hadronic showers typically present an electromagnetic component due to π^0 decaying into pairs of photons, and the electromagnetic shower inside HCAL is characterized by a different detector response with respect to the hadronic one. All these effects limit the intrinsic resolution of hadron energies that can only be recovered with more advanced offline techniques such as particle flow. Despite these constraints, the HCAL remains a crucial component in reconstructing final states that include hadron jets or non-interacting particles like neutrinos (thanks to its hermiticity, neutrinos can be detected from the difference between the initial and final transverse momentum). The design of the HCAL is significantly influenced by the choice of magnet parameters. It plays a crucial role in extending the detector hermeticity to cover up to $|\eta| < 5$, which is essential for accurately measuring the imbalance in missing transverse energy. Due to the limited space between the ECAL and the magnet, a sampling configuration was selected. The HCAL uses alternating layers of brass absorber and plastic scintillator materials. Brass was chosen as the absorber because it is non-magnetic and has a short nuclear interaction length (16.24 cm). As incoming hadrons traverse the absorber material, they interact vigorously with the brass nuclei, initiating the hadronic shower. These shower of particles eventually enter the plastic layers, where their energy is measured based on the light emitted by the scintillators. The HCAL comprises approximately 70,000 scintillating tiles and is divided into several subsystems in different regions: in the central area, between ECAL and the solenoid, there's the HCAL barrel (HB) covering up to $|\eta| < 1.3$. The limited volume of HB does not allow for a full containment of the secondary interaction shower therefore HCAL is equipped with the HCAL outer detector (HO) located between the solenoid and the muon system in the region $|\eta| < 1.26$ that is designed to collect the energy that escapes the HB, extending the total interaction depth to about 11 λ_0, consequently increasing the energy resolution of the HCAL. In the endcap region, there's the HCAL endcap (HE) covering $1.3 < |\eta| < 3.0$ and HCAL forward (HF) located 11.2 m away from the interaction point and extending the coverage up to $|\eta| = 5.2$. A sketch of the HCAL geometry is reported in Figure 3.5. Differently from HB, HO and HE which present a brass absorber and an active plastic scintillating material, the elevated radiation levels in the forward region forced the design of the HF that uses 1.65 m thick steel absorbers and 0.6 mm radiation-hard quartz fibers as the active medium that generate light through the Cherenkov effect. The scintillation light from HB and HE plastic scintillator is gathered through wavelength shifter fibers integrated within the tiles and detected by hybrid photodiodes (HPDs). Each reading cell is constructed by stacking a "tower" of scintillating tiles within a specific spatially localized area. These cells have a transverse dimension of approximately 0.087 in both η and ϕ in the HB and about 0.17 in both η and ϕ in the HE. The Cherenkov light in the HF is detected by photomultiplier tubes (PMTs). To assess both the electromagnetic and hadronic aspects of the shower, fibers of two distinct lengths are installed. The overall energy resolution of the HCAL is primarily influenced by the imperfect confinement of the hadronic shower. This leads to a raw resolution stochastic term of approximately $S = 110\%$ and a constant term of $C = 9\%$, as determined through measurements in pion test beams (energy between 4 and 300 GeV) [150].

3.2.4 Muon chambers

Located outside the solenoid, the outermost part of CMS accommodates the muon-dedicated detector, which covers a vast area of 25,000 m^2 [151]. Muons, being more massive than elec-

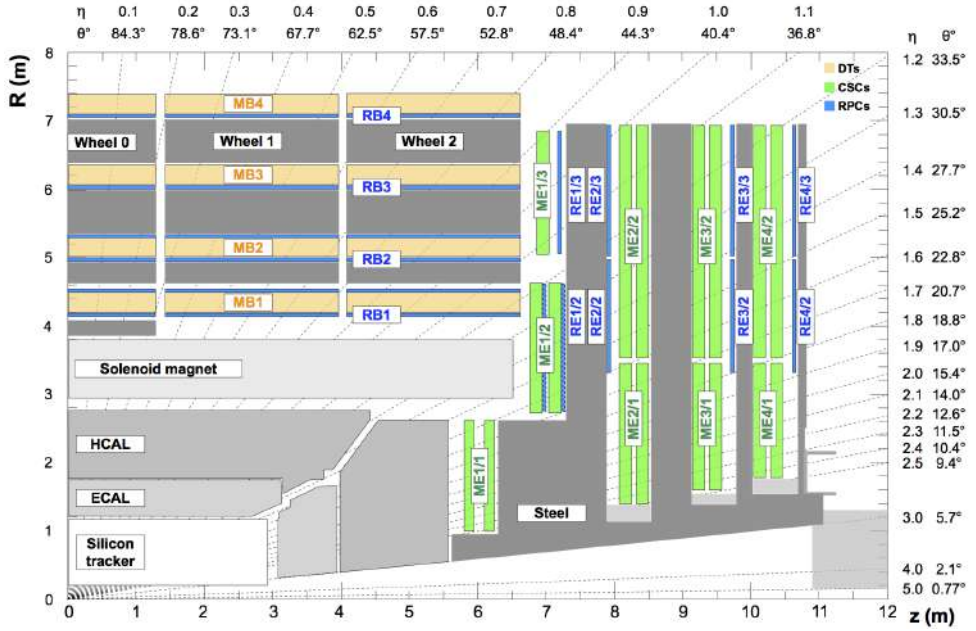

Figure 3.6: $r - z$ cross-section of a quarter of CMS in its longitudinal direction. Orange, green, and blue regions denote respectively the DTs, CSCs, and RPCs subsystems while the dark grey areas represent the steel support disks.

trons, undergo fewer radiative losses, interacting weakly or electromagnetically within the tracker material, and can penetrate through the ECAL and HCAL calorimeters and the solenoid. Therefore, the muon chambers play a dual role: they identify these particles and also offer an extra measurement of their momentum. The latter is measured using the 2 T return field of the solenoid inside the iron structure in which the muon detectors are embedded. Isolated muons are clear signatures of interesting events, and thus they are measured twice within CMS: once within the tracker and subsequently in the final muon chambers. The muon system in CMS comprises a cylindrical detector featuring a barrel section and two endcap sections. It employs three types of gaseous detectors according to the expected background rates and uniformity of the magnetic field namely drift tubes (DTs), cathode strip chambers (CSCs), and resistive plate chambers (RPCs). This technological choice was driven by the ability of gaseous detectors to efficiently cover expansive surfaces in a cost-effective manner and related to the different radiation environments. For an illustrative representation of the muon system see Figure 3.6. In the barrel region up to $|\eta| < 1.2$, where the muon and neutron background rates are low and the magnetic field is mostly uniform with strength below 0.4 T, CMS employs 250 DTs uniformly distributed in five barrel sections along the z direction, the so-called "wheels" (where wheel 0 centered at $z = 0$ and wheels W+1 and W+2 in the $+z$ direction and W-1 and W-2 in the $-z$ direction). Each of the 5 wheels of the Barrel Detector is divided into 12 sectors, with each covering a 30° in ϕ. Along the radial direction, DT chambers are grouped in four stations at radii of approximately 4.0, 4.9, 5.9 and 7.0 m from the beam axis [152] interspersed between plates of the steel support disks in the magnet flux return yoke. The basic element of the DT system is the drift cell with a transverse size of 42×13 mm^2 and a 50 μm diameter anode wire at the center [153] and filled with a gas mixture (85%/15%) of Ar/CO_2 providing good quenching properties, saturated drift velocity of about 55 μm/ns and a maximum drift time of 400 ns. The effective drift field is shaped by four electrodes two of which are cathode strips on the side of the cell while the remaining are placed above and below the wires on the ground planes between the layers. DT chambers are composed of three superlayers (SL) which are in turn composed of four staggered layers of parallel DT cells. In the DT chamber, two

SLs are dedicated to the measurement of $r - \phi$ coordinates with wires parallel to the beamline, while an orthogonal SL measures the $r - z$ coordinate. Each DT cell offers a spatial resolution of approximately 200 μm. Consequently, when combined for a global chamber measurement, this results in an overall resolution ranging from 80 μm to 120 μm in position and 1 mrad in angle. DTs also offer a fast trigger signal with a resolution of 5 ns based on the muon transverse momentum.

In the endcap regions at $0.9 < |\eta| < 2.4$, the rates of muon interactions and background events are elevated, and the magnetic field is both strong and non-uniform. In this region, the CMS muon system is equipped with CSCs since they can withstand the non-uniformity of the magnetic field, can be finely segmented and have a fast response. A CSC is constructed as a multi-wire gas proportional chamber with a cathode strip readout that precisely measures the position at which a muon crosses the gas volume [154]. It has a trapezoidal shape and it is composed of six layers of anode wires interposed between seven cathode strips disposed in the orthogonal direction. CSCs are organized in four stations in each endcap with the chambers running perpendicular to the beam line and the cathode strips running radially outward in order to provide a measurement in the z direction and in bending $r - \phi$ plane respectively. All CSCs use a gas mixture of 50% CO_2, 40% Ar, and 10% CF_4 which is ionized upon the passage of a muon. A CSC hit is reconstructed at the intersection points of hit strips and wire groups and has also an associated time, which is calibrated such that hits from muons produced promptly in the triggering bunch crossing have a time distribution centered around zero. The signal hit has a resolution of 100 μm and 10 mrad in the r and ϕ directions respectively. The DT and CSC muon detector elements together cover the full CMS pseudorapidity interval $|\eta| < 2.4$ with no acceptance gaps, ensuring good muon identification in this region.

The muon system is also equipped with a dedicated system for complementary triggering with excellent timing properties, used to enhance the precision in the measurement of the beam crossing time, especially at the highest LHC luminosities. The technology chosen for this purpose is based on RPCs that are installed in both the barrel and endcaps to cover the region $|\eta| < 1.6$. RPCs are constructed of two parallel high-voltage resistive plates made of a 2 mm thick bakelite layer and separated by a narrow gap which volume is filled with a gas mixture that consists of 95.2% Freon ($C_2H_2F_4$), 4.5% isobutane (i-C_4H_10), and 0.3% sulfur hexafluoride (SF_6) [153]. Water vapor is added to reach 40%–50% levels of humidity. The RPCs are operated in avalanche mode and the passage of a charged particle inside their active volume will create an avalanche due to the high electric field inside the gas volume. The avalanche-induced image charge is picked up by the readout strips. The strips are aligned along the η direction with a pitch of up to 2 cm, providing a modest spatial resolution ranging from 0.8 to 1.2 cm. Because the ionization charge from a muon can be distributed across multiple strips, neighboring strips are grouped to reconstruct a single hit as the centroid of the strip cluster. RPCs offer exceptional temporal resolution, approximately 1 ns, enabling unambiguous identification of bunch crossings.

3.2.5 Trigger system

At the LHC design luminosity of 10^{34} cm^{-2}s^{-1}, the proton-proton collision rate exceeds 1 GHz. The majority of these collisions are inelastic, producing low-energy multi-jet events with a cross-section $\sigma_{\text{inel}} \sim 70$ mb several orders of magnitude greater than the cross-section of interesting processes for the CMS physics program ($\sigma < 10^5$ pb). These collisions happen every 25 ns and, combined with the highly granular information recorded by the detector, generate approximately 70 Tb/s of data. At the time being, it is unfeasible to read out, store and analyze such large volumes of data. The trigger system of CMS is designed to discriminate collisions

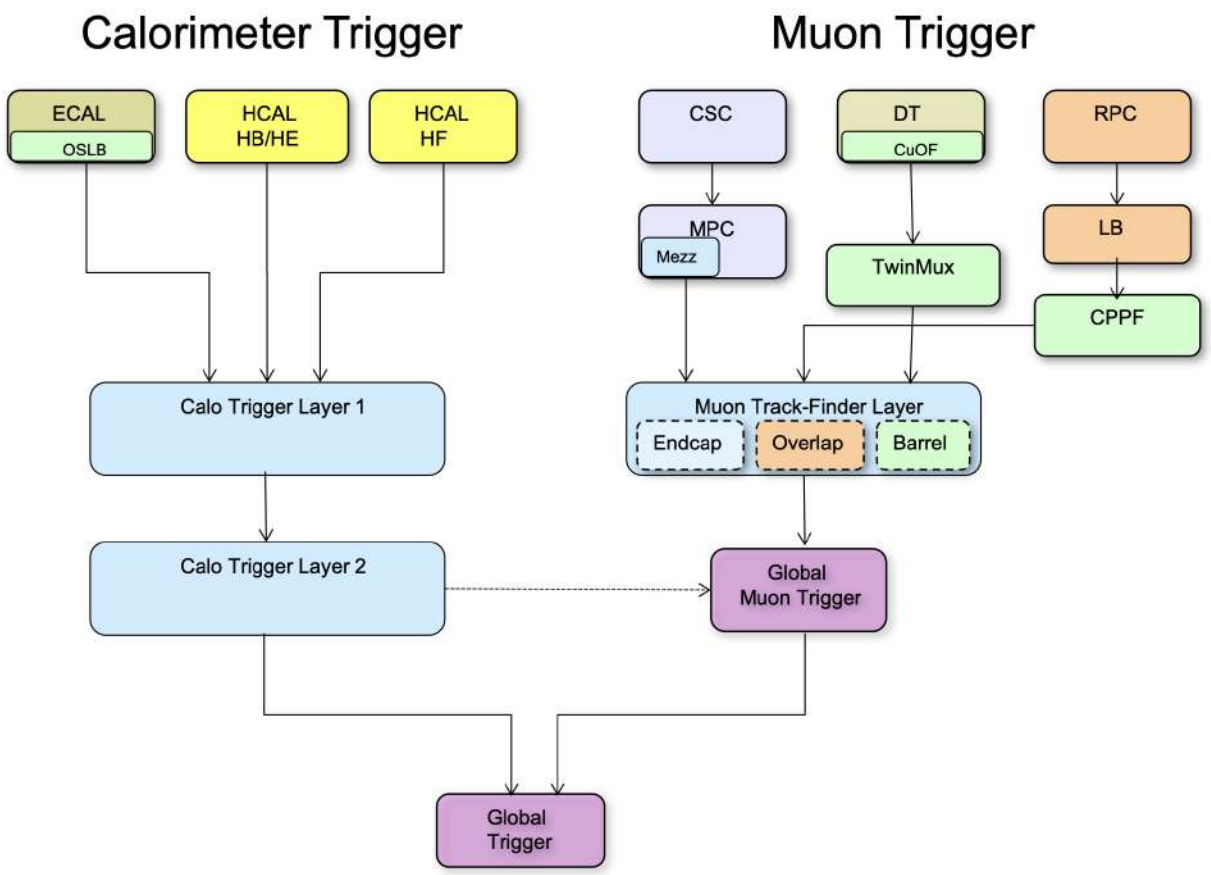

Figure 3.7: Schematic representation of the CMS L1 trigger system from [155]

of interest from the sea of proton-proton inelastic collisions, as to reduce the rate of events to a sustainable amount of about 10^5 events/s for detector readout, and about 10^3 events/s for offline storage. To achieve this goal CMS employs a two-tiered solution, whose components are referred to as Level-1 Trigger (L1) and High Level Trigger (HLT).

3.2.5.1 Level-1 Trigger

The L1 trigger is implemented in custom hardware and can access calorimetric and muon information only with reduced granularity with respect to the detector capabilities. It operates with a constant latency, meaning there is a fixed time window for data processing, which lasts for 3.8 μs. During this period, the critical decision to accept a collision is made, and the event rate is decreased to approximately 100 kHz. The tracker information is not available at L1 as the trigger system cannot sustain its readout at 40 MHz. Specialized boards are currently in the design phase, to enable the outer tracker to be read out at a rate of 40 MHz. These boards will be installed at CMS for the LHC High Luminosity phase [156]. The absence of tracking information at the L1 level makes it unable to distinguish between objects generated by different collisions within the same bunch crossing. Furthermore, electrons and photons are indistinguishable and result in a similar experimental signature at this stage. The L1 selection process is carried out through a series of algorithms referred to as seeds. These seeds typically involve criteria applied to one or more candidate objects such as ionization deposits reconstructed as muons, or energy clusters associated with electrons, photons, jets, τ leptons and missing transverse energy E_T^{miss}. The L1 objects are built from low-level inputs called trigger primitives coming from each of the CMS subdetectors. Most seeds require the events to have N candidate objects with minimum thresholds on their E_T and pseudorapidity. The majority of the algorithms are

composed of single and double object seeds, which collectively account for roughly 75% of the available bandwidth. As of 2018, the L1 trigger system supports the implementation of up to 512 algorithms.

A summary schema of the L1 trigger architecture is represented in Figure 3.7 from Ref. [155]. Two parallel paths process calorimetric information from ECAL, HCAL (HB/HE/HF) and from the muon subsystems namely DT, RPC and CSC. The output from these subsystems is gathered by the micro global trigger (μGT), which combines this information to decide whether to accept or reject the event.

Experience from Run I led to an upgrade to the calorimeter system [157] allowing for a full-granularity readout instead of the 4×4 trigger tower granularity of the regional calorimeter trigger. The L1 granularity in $\Delta\eta \times \Delta\phi$ is of 0.087×0.087 radians in most of the calorimeter acceptance (high η has a slightly coarser granularity). This approach requires the transmission of the full trigger tower granularity to a single electronic board for each bunch crossing and is therefore computationally expensive. To address the issue, the calorimeter trigger follows a time-multiplexed trigger built into a two-layered system. The benefits of time-multiplexing include the removal of regional boundaries for object reconstruction and full granularity when computing energy sums. Calorimeter trigger primitives are treated in parallel by the 18 boards of the Layer-1 dedicated to pre-processing operations such as the calibration of the total trigger tower energy from ECAL and HCAL deposits and timing organization of data. These boards are advanced mezzanine cards equipped with a Xilinx Virtex-7 FPGA called CTP7 [158] specialized for data sharing with the other boards in the same crate. The output is fed to the second layer (Layer-2) composed of nine nodes where the identification and reconstruction algorithms are performed. Shape vetoes and dedicated algorithms aim for the identification of hadronic jets, hadronically decaying τ leptons, photons and electrons. The Layer-2 nodes are master processor cards (MP7) embedding, as the Layer-1, a Xilinx Virtex-7 FPGA [155] with a design that targets flexibility in the development and implementation of algorithms. A demultiplexer (DeMux) board then reorders, re-serializes, and formats the events for the μGT processing.

The muon L1 trigger combines the redundancy from the muon sub-detectors to reconstruct muon tracks. A barrel (BMTF), overlap (OMTF) and endcap (EMTF) track finder systems are implemented in three distinct pseudorapidity regions for LHC Run II. The inputs to the BMTF are primitives from DT and RPC chambers in the barrel ($|\eta| < 0.83$), that are combined in the so-called super-primitives in the TwinMUX system. The redundancy of the measurements from these subsystems improves the accuracy in determining the position of the muon hits. Additionally, the bending angle information obtained from the DT is utilized in a track-finding algorithm that relies on road-search extrapolation techniques. All three muon subsystems contribute to the OMTF ($0.83 < |\eta| < 1.24$) tracks in the overlapping region between the barrel and endcap of the detector while for the forward region ($|\eta| > 1.24$), the EMTF uses information from CSC and RPC to reconstruct endcap muons. The latency of this system is only 750 ns therefore advanced pattern-recognition algorithms are implemented to convert hit-patterns to muon p_T assignments and muon quality criteria. Each track finder can transmit as many as 36 muon candidates to the global muon trigger. The latter then handles the resolution of duplicates originating from different boards and forwards a maximum of eight muons, ranked by p_T and quality criteria, to the μGT.

The three L1 muon trigger systems implement different hardware choices related to the complexity of the algorithms involved in the respective pseudorapidity region. The BMTF requires large computing power MP7 cards are used while the OMTF and EMTF primarily need large memories in order to use pattern-recognition algorithms and therefore implement modular

track finder cards [159].

The final trigger decision is made by the μGT based on information from the calorimeter and muon triggers. The μGT is specialized in computing multi-object correlation and global event quantities, as the invariant mass of pairs of reconstructed candidates, their spatial separation, and their spatial momentum sum. The μGT runs in parallel with each of the L1 seed algorithms on MP7 boards granting large computational power. During the Run 2 data collection period, the CMS μGT selection consisted of approximately 350-400 algorithms.

3.2.5.2 High Level Trigger

Events accepted by the L1 trigger are further processed by the HLT stage. While the L1 stage's main objective is to reduce the rate for a sustainable detector readout, the HLT one is to identify events of interest for sustainable offline storage. The major limitations to the HLT come from timing requirements and from the request to be able to measure the trigger efficiency from data. The HLT latency is not fixed as it is for the L1 but on average the HLT has approximately 260 ms to make a decision. The computational time is directly correlated with event complexity and can take up to $\mathcal{O}(1\text{s})$. This difference with respect to the L1 level is due to the fact that the latter is a hardware-based system while the HLT hardware consists of a single processor farm composed of commercial CPUs, the event filter farm (EVF), which runs Scientific Linux. The EVF is a two-part system consisting of builder and filter units. The builder units, upon request from the filter units, are capable of retrieving event fragments from the detector that originate from a specific L1 algorithm. These fragments are then assembled to form complete events. On the other hand, the filter units unpack the raw data, perform reconstructions, and execute trigger filtering processes. The builder-filter units are implemented within a single multi-core machine. In total, the EVF hosts approximately 36,000 CPU cores, enabling it to process the input data of 100 kHz from the L1 down to a final output rate of less than 1 kHz, limited by the size of the events and the ability of the downstream systems to process them. Accepted data by the HLT are handled by the storage manager, stored locally on disk and eventually transferred to the CMS Tier-0 which handles the offline-processing requests and the permanent storage of CMS data [160]. About half of these events are promptly reconstructed using offline algorithms (within 48 hours), while the other lower-priority half is parked for later reconstruction.

The HLT is designed around the concept of the so-called paths, which are sequences of algorithmic steps run in a predefined order that reconstruct physics objects and successively make selections on them. Each HLT path is seeded by a specific L1 selection. The path steps present increasing complexity with respect to reconstruction refinement and physics sophistication. In the early stages of the path, initial criteria based on calorimetric information and data from muon detectors are employed to lower the event rate before the computationally intensive tracking reconstruction is executed. A typical coarse representation of jets, τ leptons, electrons photons and muons retrieved with calorimetric and muon information has a time budget at the HLT of approximately 50 ms. The additional tracking information is more time-consuming but makes it possible to distinguish between photons and electrons, identify heavy-flavoured jets and hadronically decaying τ leptons, evaluate the lepton isolation, and measure precisely the lepton momentum. The latter is run only on a subset of events and only in a limited pseudorapidity region (regional tracking). Finally, the particle-flow (PF) [161] sequence provides the most accurate description of the objects achievable at the HLT. The HLT PF sequence is the most time-consuming algorithm available and is a simplified version of the offline reconstruction process, making use of a streamlined version of the tracking algorithm.

Chapter 4

SMEFT dimension-six interpretation of semileptonic VBS WV

4.1 Standard Model measurement

The target of the analysis is the extraction of the VBS WV process measuring its cross-section, signal strength and significance in the semileptonic final state where the V boson (either a W or Z) decays into a pair of quarks as shown in Figure 4.1 for the purely EW induced Feynman diagrams.

The semileptonic VBS final state benefits from a larger cross-section with respect to the fully leptonic ones however it is plagued by the presence of multi-jet processes as backgrounds, diminishing the signal over background ratio in all phase spaces and posing serious issues in simulations due to the high jet multiplicity. This final state, featuring one charged lepton, moderate MET and four jets, is known today only at the leading order in perturbation theory. Studies on semileptonic VBS processes have been reported by both ATLAS and CMS with a partial dataset of 36 fb^{-1} at a center-of-mass energy of 13 TeV. While the ATLAS search [162]

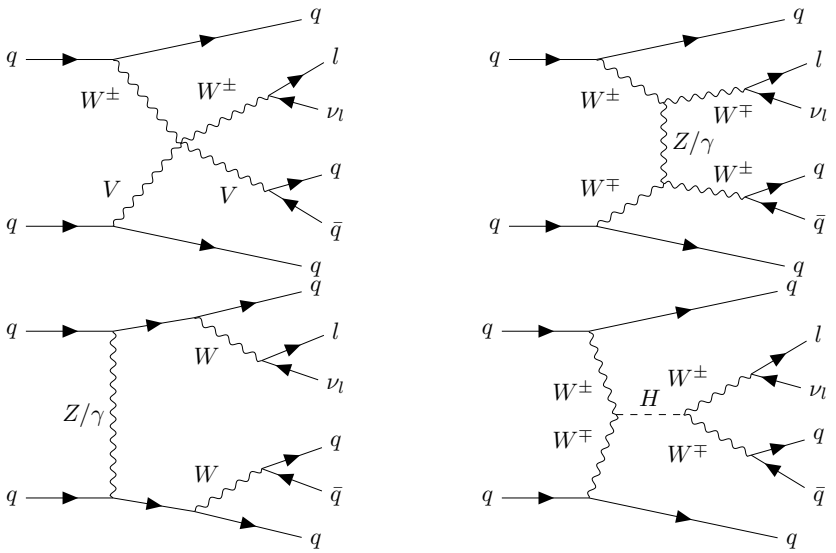

Figure 4.1: Feynman diagrams for purely EW processes (α^6) contributing to the VBS final state comprising one charged lepton and the associate neutrino plus four jets. The VBS WV process shows a rich phenomenology, presenting tree-level sensitivity to EW vector boson quartic gauge coupling (top left), triple gauge couplings (top right), Higgs-induced diboson production (bottom right) and other peripheral processes (bottom left).

targeted the SM measurement combining both WV and ZV processes reaching an observed significance of 2.7σ, the CMS analysis [136] was devoted to the BSM interpretation and to constrain dimension-eight Wilson coefficients, proving that these processes are sensitive probes to new physics. With the full Run II dataset with an integrated luminosity of 137 fb^{-1}, CMS reported for the first time strong evidence for a semileptonic VBS process [105]. The VBS process at the LO in perturbation theory is characterized by diagrams involving two partons in the initial state, producing a six-fermion final state involving only electroweak (EW) vertices $\mathcal{O}(\alpha^6)$. Different topologies contribute to this type of process namely the vector boson scattering diagrams involving the emission of two vector bosons by the initial state partons that interact via QGCs, double TGCs in t- or s-channel and t- or s- channel exchange of an Higgs boson. The six-fermion final state can also be generated via triboson production, where either a vector boson is produced in s-channel by the colliding partons followed by a QGC with three vector bosons, or by a t-channel exchange of a parton that couples to three different and independent vector boson legs. An easy way to practically decouple these processes, isolating the one of interest, is to employ the production times decay approximation with its limitations [110]. Even if it is impossible to completely isolate the VBS diagrams, it is possible to select a phase space almost pure in this kind of process exploiting kinematic properties of VBS such as the high invariant mass and pseudorapidity separation of the pair of jets coming from the initial state partons.

4.1.1 Data sets and MC simulations

Data events are selected using isolated single electron and muon triggers. Due to the increasing luminosity throughout Run II, the p_T thresholds of the trigger selections were accordingly increased to keep the path rate at a constant value. Table 4.1 summarises the list of HLT trigger paths used in the analysis and the charged lepton p_T threshold. Only events certified with good data quality by sub-detector experts are considered for further analysis. The data amounts to a total integrated luminosity of 36.3 fb^{-1} for 2016, 41.5 fb^{-1} for 2017 and 59.7 fb^{-1} for 2018.

Year	Dataset	HLT path	p_T threshold
2016	SingleMuon	HLT_Iso(Tk)Mu24	24 GeV
2017	SingleMuon	HLT_IsoMu27	27 GeV
2018	SingleMuon	HLT_IsoMu24	24 GeV
2016	SingleElectron	HLT_Ele27_WPTight_Gsf HLT_Ele25_eta2p1_WPTight_Gsf	27 GeV
2017	SingleElectron	HLT_Ele35_WPTight_Gsf	35 GeV
2018	SingleElectron	HLT_Ele32_WPTight_Gsf	32 GeV

Table 4.1: HLT single electron and muon trigger paths used for the VBS WV semileptonic Run II analysis.

The analysis targets a template-based fit to extract the VBS-WV significance and cross-section and it relies on MC simulations for the signal and all major backgrounds except for contributions from fake objects that are derived based on real data.

The signal sample is generated using MADGRAPH5_AMC@NLO version 2.6.5 as a $2 \to 4$ process for the VBS production, with two vector bosons and two quarks in the final state. The intermediate vector bosons are decayed with MadSpin [163] under the narrow width approximation to partially account for finite-width effects and spin correlations. One vector boson is decayed leptonically to e, μ, τ and the corresponding neutrinos while the second one into a pair of light quarks (u, d, s, c, b plus charged conjugates). The dipole recoil method is employed within the parton shower simulation of PYTHIA [164] for generating the Monte Carlo

sample of the VBS signal. This approach aims to achieve the most accurate representation of the extra jet emissions within the VBS topology [165]. A precise description of simulation parameters for the MC signal is given in Sec. 4.3.2. The QCD-induced VBS production at the order $\alpha_S^2\alpha^4$, along with its interference with the EW VBS signal with order $\alpha_S\alpha^5$, are generated via MADGRAPH5_AMC@NLOversion 2.6.5 similarly to the production of the purely EW sample. Parton level selections require charged leptons and jets with $p_T > 15$ GeV an invariant mass greater than 200 GeV for the dijet system defined in the hard scatter. While the interference for $W^{\pm}W^{\pm}$ and $W^{\pm}Z$ is positive in this fiducial region (with cross sections of 8.2 fb and 4.5 fb respectively), the interference for W^+W^- is larger and negative and amounts to -44.1 fb. In the analysis regions, the interference amounts to 2.6%-3.8% of the signal depending on the selections, therefore the VBS EW-QCD interference with perturbative order $\alpha_S\alpha^5$ is neglected in the analysis.

Regarding the backgrounds, the major contribution comes from the production of a single W boson with a leptonic decay accompanied by jets (referred to as W+jets), semileptonic $t\bar{t}$ plus jets and the non-resonant QCD induced diboson production. Minor contributions to the background noise come from single top quark production (in s- and t-channel or associated with a W), Drell-Yan (DY), W and Z boson production in association with a photon ($W\gamma$ and $Z\gamma$), triboson production and single vector boson production in VBF topology (VBF-V). Most of the backgrounds are simulated at the next-to-leading order (NLO) in the strong coupling α_S using MADGRAPH5_AMC@NLO, POWHEG [166–168] or MCFM [169, 170]. The W+jets major background along with the QCD-induced diboson production, VBF-V and $W\gamma$ are produced at LO with MADGRAPH5_AMC@NLO. An NLO W+jets sample is available, however it includes only two jets at NLO in the matrix element calculation. The negative weights due to the NLO generation reduce the statistical power of the sample leading to a not sufficient number of weighted simulated events in the tails of most distributions where the EW VBS process is expected to be seen. For this reason, the LO sample is preferred and is corrected via a differential data-driven estimation as discussed in Section 4.1.4.

For all processes, GEANT4 package [171] is used to model the detector response based on a detailed description of the CMS detector.

All MC simulations are corrected with event-by-event weights that account for discrepancies between simulations and data. Among those, HLT inefficiencies are corrected with weights dependent on the lepton p_T and pseudorapidity. The trigger efficiency is estimated via a tag-and-probe method directly on data. Anomalous events containing missing transverse energy due to detector inefficiencies are properly weighted out. Further event weights account for the difference in the number of pileup vertices in simulation and data, scale factors for lepton reconstruction and identification efficiencies as a function of the charged lepton p_T and η, scale factors for the heavy-flavour tagging efficiency to correct the behaviour of the b-tagging discriminator as a function of the p_T, η and flavour of the jets. The last scale factors account for the pileup jet ID computed at the loose working point and the τ_{21} boosted W scale factor that corrects the tagging algorithm that identifies large radius boosted jets as originating from a vector boson based on the τ_{21} subjettiness [172]. Additional event-weights are computed only for 2016 and 2017 years including the so-called L1 prefiring correction and the DY p_T reweighting [173]. Similarly, the modeling of the p_T of the top quark in $t\bar{t}$ samples is improved via a p_T reweighting [174, 175]. The Pileup Per Particle Identification, referred to as PUPPI[1] [176, 177], soft drop

[1]The PUPPI algorithm discriminates particles coming from the hard scatter from particles originating from pileup interactions through a local shape α [176]. For each particle i, the shape is defined as $\alpha_i = \log \sum_{j \neq i} \frac{p_{T,j}}{\Delta R_{ij}} \times \Theta(R_{\min} \leq \Delta R_{ij} \leq R_0)$ where Θ is the Heavyside function, ΔR_{ij} is the euclidean distance in the $\eta - \phi$ plane between

mass of large radius jets used in the analysis is rescaled (both in data and MC) and smeared (only in MC) to calibrate it and make the MC resolution equal to the data one. An additional correction is applied to calibrate the quark-gluon likelihood discriminator, used as an input to a neural network in order to better separate the W+jets background, where jets typically arise from gluon emission, from the EW signal where jets originate from purely EW vertices.

4.1.2 Analysis strategy

In this section, the analysis strategy for the SM measurement is summarized. The strategy remains unchanged for the EFT interpretation. In particular in Section 4.1.2.1 the physics objects of interest will be described and Section 4.1.2.2 summarizes analysis regions and selections.

4.1.2.1 Object definition

Offline leptons are required to have a transverse momentum p_T of at least 35 and 30 GeV for electrons and muons respectively and a pseudorapidity within CMS acceptance of $|\eta| < 2.5$ and 2.4 for electrons and muons respectively. The p_T requirement of leptons is as close as possible to the online trigger selection however it is made more restrictive to ensure that data and simulation respond similarly to the application of the trigger (in other terms, the trigger turn-on region is avoided). Jets are clustered with an anti-k_T algorithm with $R = 0.4$ or 0.8 depending on their properties and labeled AK4 and AK8 respectively in the following paragraphs. Charged particles coming from pileup vertices are discarded and corrections are applied for the residuals contribution. All AK4 jets in the analysis are required to have $p_T > 30$ GeV to mitigate pile-up contributions and $|\eta| < 4.7$. AK8 jets are more energetic, arising typically from the hadronic decay of boosted objects, and are required to have $p_T > 200$ GeV and $|\eta| < 2.4$. Jets overlapping within $\Delta R < 0.3$ with a loosely identified electron and jets failing the loose working point of the pileup jet discriminator are discarded from the event. Due to additional detector noise, in 2017 tighter selections were applied to jets in the rapidity range of $2.65 < |\eta| < 3.139$ and $p_T < 50$ GeV, requiring a tighter threshold on the pileup jet discriminator. The PUPPI algorithm is employed when reconstructing AK8 jets in order to remove pileup tracks. A grooming algorithm is also employed in order to remove soft contributions from the underlying event and pileup in AK8 jets, enhancing their mass resolution known as soft-drop (SD) [178–180]. The ratio between the 2- and 1-subjettiness ($\tau_{21} < 0.45$) is used to identify AK8 jets, with a groomed mass between 40 and 250 GeV, as originating from boosted W and Z boson.

4.1.2.2 Analysis categories

Two regimes are studied in order to enhance the sensitivity to the SM VBS signal. The first one presents at least four AK4 jets compatible with the VBS topology resolved in the ΔR plane by having non-intersecting cones at $\Delta R > 0.4$. As the hadronically decaying V boson can be boosted, its products can be reconstructed as a single AK8, large area jet in association with two small radius jets coming from the initial scattering partons. For both of these regimes, two dedicated control regions are identified in order to correct the W+jets background modeling and to measure the normalization of the top-related backgrounds directly from data. A schema of the analysis strategy is pictured in Figure 4.2.

All events are required to present a tightly identified charged lepton (e, μ) and missing transverse momentum p_T^{miss} of at least 30 GeV accounting for the leptonic decay of the W boson.

particle i and j and R_0 defines a cone around particle i so that only particles with $\Delta R_{ij} < R_0$ enter the computation of α_i. Particles with $\Delta R_{ij} < R_{\text{min}}$ are also neglected in the computation. The value of α tends to be large for particles originating from the hard scatter and small for pileup particles.

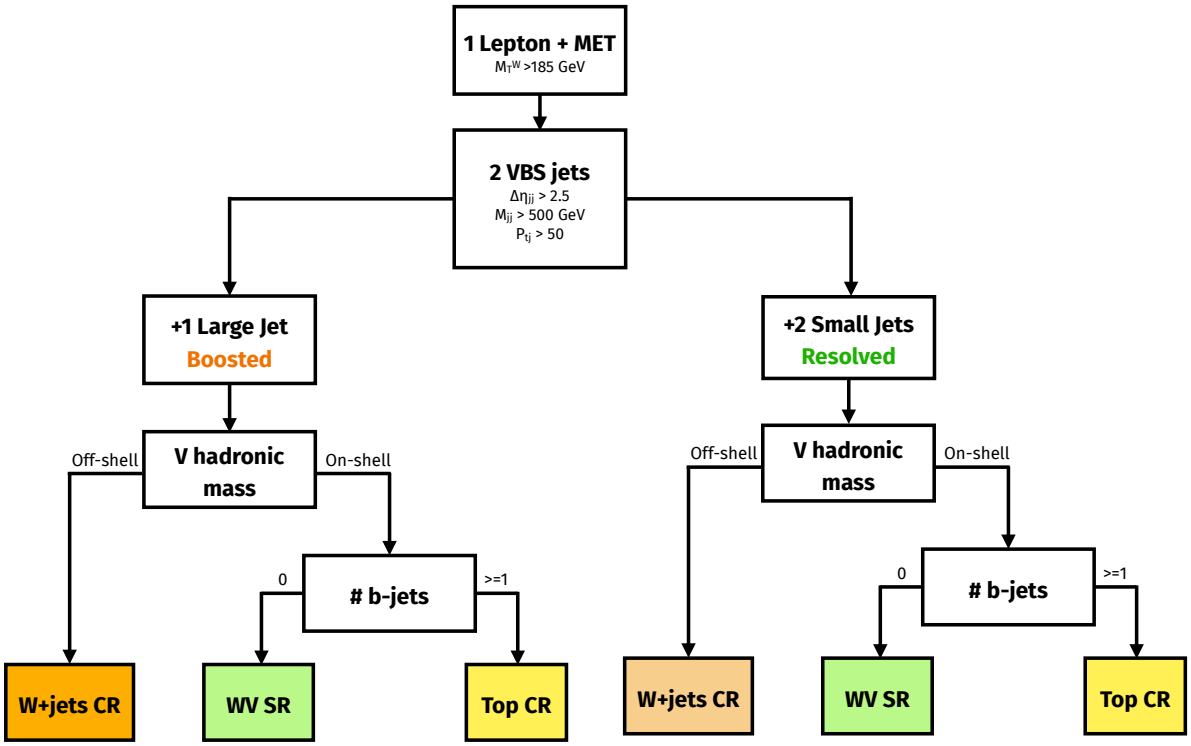

Figure 4.2: Sketch of the analysis workflow. The two branches of the tree represent the two analysis regimes: boosted on the left and resolved on the right. Orange and yellow boxes represent control regions (CR) while green boxes refer to signal regions (SR)

A veto on a second loosely identified charged lepton with $p_T > 10$ GeV is applied. In both resolved and boosted categories, the AK4 jet pair with larger invariant mass is identified as the VBS jets. In the resolved category, from the remaining AK4 jets, the jet pair with invariant mass closest to 85 GeV (average between W and Z mass peaks) is selected as decay products of the hadronically decaying V boson. In the boosted regime, the AK8 jet is assumed to come from a boosted W or Z boson. This algorithm has a limited efficiency of approximately 72% (77.8% matching efficiency for VBS jets and 78.3% efficiency for V-jets) in the resolved region and was studied along with other types of tagging criteria.

The signal-over-background ratio is enhanced by exploiting the EW VBS kinematic features by requiring $m_{jj}^{\text{VBS}} > 500$ GeV and a large value for the pseudorapidity separation $\Delta\eta_{jj}^{\text{VBS}}$. The leading VBS jet is required to have a transverse momentum of at least 50 GeV and the transverse mass of the leptonically decaying W, computed assuming leptons to be massless, is required to be $M_W^T < 185$ GeV. The signal region is then defined requiring the hadronically decaying V boson to be on the mass shell, thus m_V to be between 65 and 105 GeV in the resolved region and 70-115 in the boosted region and that no b-jets are present in the event according to the DeepCSV multivariate tagger [181] (that presents a b-tagging efficiency of 85% and a mistag probability of 20%). Events failing the m_V requirement and still showing $m_V > 40$ GeV and presenting no b-jets fall in the W+jets contro region. Events satisfying the m_V on-shell requirement but presenting at least one b-jet from the top control region. Signal and control regions for both resolved and boosted regimes are analyzed separately according to their lepton flavour.

4.1.3 Signal extraction

None of the standard VBS kinematic variables, such as m_{jj}^{VBS}, $\Delta\eta_{jj}^{\text{VBS}}$ or the Zeppenfeld variable [182] defined as $Z_{\text{lep}} = |\eta_{\text{lep}} - (\eta_{\text{j1}}^{\text{VBS}} + \eta_{\text{j2}}^{\text{VBS}})|/\Delta\eta_{jj}^{\text{VBS}}$ can effectively separate background processes from the purely EW VBS one. A more powerful approach is needed in order to extract the signal. A feed-forward neural network was trained to separate the signal from the background. The network acts as an encoder, being fed with n input quantities x_i from an event and returning a scalar number in the range $[0, 1]$, referred to as the DNN output, representing the posterior probability for that event to be a signal event $P(\text{c=signal}|\{x_1, ..., x_n\})$. The training of the network is done by creating two labeled samples from MC simulations, one with only the VBS EW signal (with class label 1) and the other with a mixture of background processes (class label 0) so that the network effectively capture the kinematic of the varied background composition. The datasets are in turn split into a training sample (80% of the events) and a validation dataset (20%) used to monitor the performances of the network throughout the training process and to avoid overtraining. Two separate fully connected networks have been trained respectively in the boosted and resolved regions to optimize the performances. A common model is shared for the muon and electron categories and all the years. The Boosted network comprises one input layer with 13 nodes, four hidden layers with 64, 32, 32, and 32, nodes respectively and an output node. The resolved network has a similar structure but is fed with 15 input variables and all four hidden layers present 64 nodes each. All hidden layers are ReLU-activated while the output activation is the sigmoid function, typically used for binary classification problems. Appropriate L2 and batch normalization procedures are applied to the hidden layers in order to reduce overtraining while granting optimal performances. The addition of dropout was tested but found to not increase the performance or generalization capabilities of the networks. Both networks are trained to minimize the binary cross-entropy loss function via a stochastic gradient descent algorithm and use the Adam optimizer [183]. In order to prevent overtraining, the training of the network proceeds as long as the loss on the validation dataset does diminish by at least 10^{-4}.

The input variables used for training the final discriminators have been selected using the SHAP algorithm [184]. The latter exploits a game theoretical approach to assign each input feature an importance value (or SHAP value) for a particular prediction. Features with a high SHAP value are considered to play an important role in the model prediction. Variables with low SHAP values have been discarded as it was shown that models with a high number of input features are more susceptible to overtraining. However, by providing more input features we allow the network to better learn the underlying p.d.f. of the two samples. This trade-off led to the choice of 15 observables for the resolved discriminator and 13 observables for the boosted one. The full list of inputs is summarised in Table 4.2 [105].

Prefit plots for the resolved and boosted DNN spectra in control and signal regions are shown in Figure 4.3 for the muon channel only for brevity. Similar trends are observed for the electron channel.

4.1.4 Background treatment

Three background sources need special treatment either to estimate their contribution in the analysis regions or to measure their cross sections directly from data. Firstly the simulation of the irreducible $t\bar{t}$ process is controlled in the b-tag control regions both in resolved and boosted regimes and split by lepton flavour. The data to MC agreement does not show any trends within the nominal value of the nuisance parameters as defined before the fit and before the application of any data-driven correction. Due to the overall good description of the $t\bar{t}$ process

Observable	Symbol	Resolved	Boosted
Lepton pseudorapidity	η^{l}	✓	✓
Lepton p_T	p_T^{l}	✓	✓
Zeppenfeld variable [182] for the lepton	Z_{lep}	✓	✓
Number of AK8 jets $p_T > 30$ GeV	N_{jets}	-	✓
Number of AK4 jets $p_T > 30$ GeV	N_{jets}	✓	-
Leading VBS jet p_T	$p_T^{\text{VBS,1}}$	-	✓
Trailing VBS jet p_T	$p_T^{\text{VBS,2}}$	✓	✓
VBS jets pseudorapidity gap	$\Delta\eta_{jj}^{\text{VBS}}$	✓	✓
Quark/gluon discriminator of leading VBS jet	$\text{QGL}^{\text{VBS,1}}$	✓	✓
Quark/gluon discriminator of leading V-jet	$\text{QGL}^{\text{V,1}}$	✓	-
Quark/gluon discriminator of trailing V-jet	$\text{QGL}^{\text{V,2}}$	✓	-
Azimuthal angle between VBS jets	$\Delta\phi_{jj}^{\text{VBS}}$	✓	-
Invariant mass of the VBS dijet pair	m_{jj}^{VBS}	✓	✓
p_T of the leading V-jet	$p_T^{\text{V,1}}$	✓	-
p_T of the trailing V-jet	$p_T^{\text{V,2}}$	✓	-
V jets pseudorapidity gap	$\Delta\eta_{jj}^{\text{V}}$	✓	-
p_T of AK8 jet	p_T^{V}	-	✓
Invariant mass of the AK8 jet	m_{V}	✓	✓
Zeppenfeld variable for V	Z_{V}	-	✓
Centrality	C	-	✓

Table 4.2: Input variables for the boosted and resolved discriminators from Ref. [105].

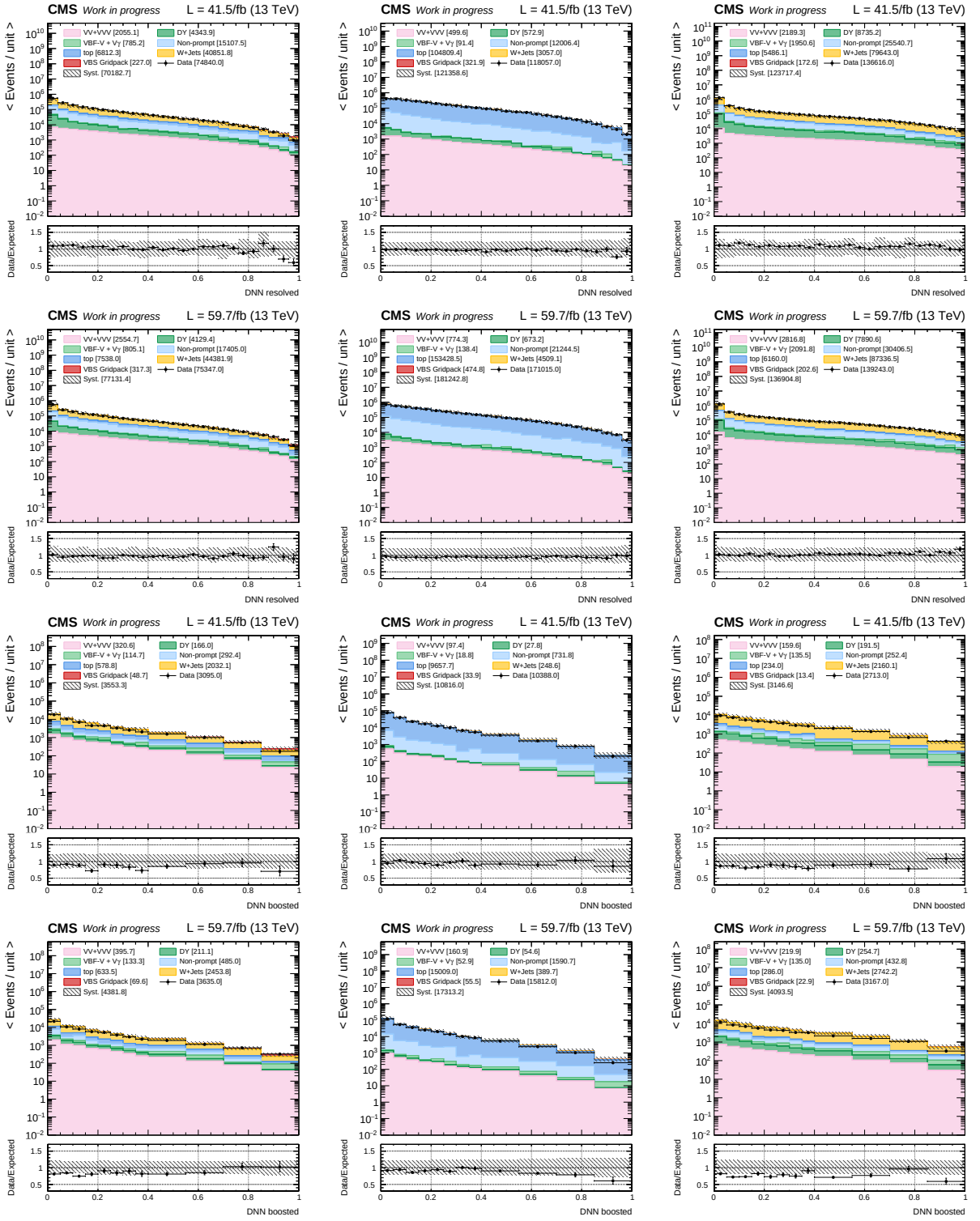

Figure 4.3: Prefit DNN distributions in all analysis regions. The top two rows show the DNN output score in the resolved region for 2017 and 2018. The bottom two rows show the DNN output in the boosted region for 2017 and 2018. From left to right the figure shows the signal region, the top control region and the W+jets control region.

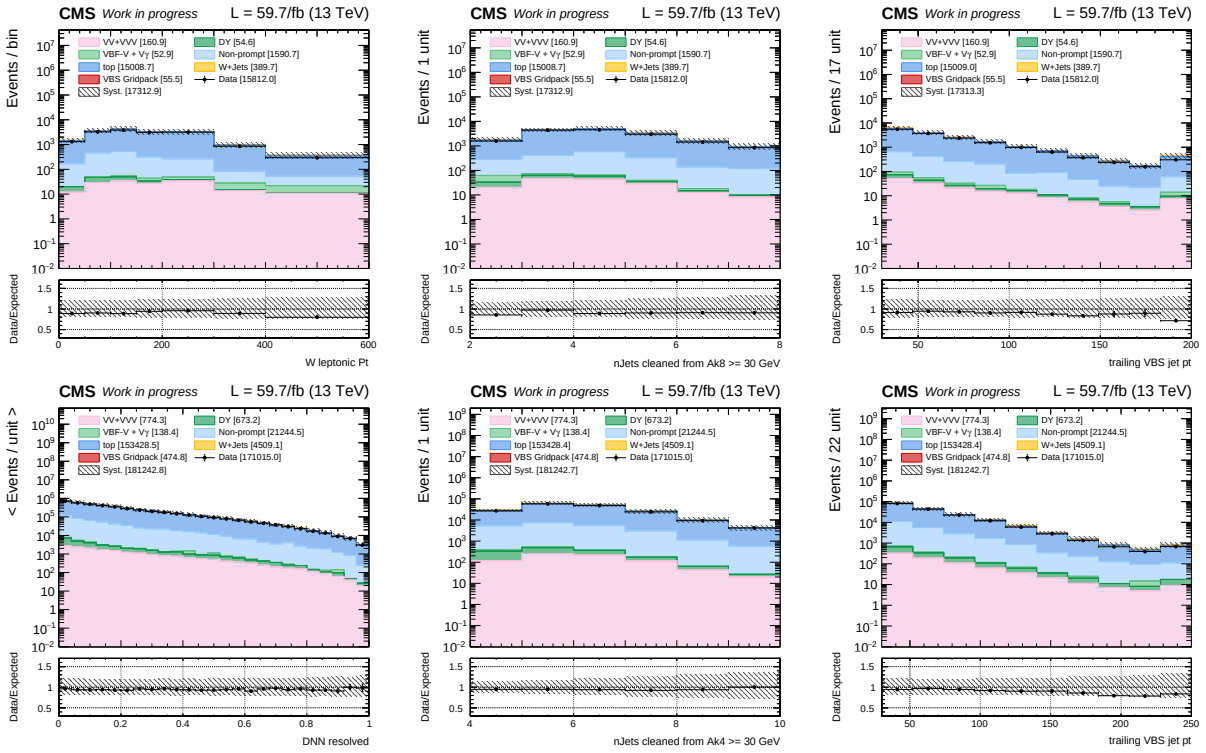

Figure 4.4: Data and MC distribution in the muon top CR for the 2018 year. The top row shows the distribution of the p_T of the leptonically decaying W boson, the number of large area jets and the p_T of the trailing VBS jet in the boosted region. The bottom row shows the DNN spectra, the number of jets and the p_T of the trailing VBS jet in the resolved region. Similar trends are observed for the electron category and the remaining years.

from simulations, only the overall normalization of this background is left free to float, so that its cross-section can be measured directly from data thus reducing the overall uncertainty in the fit procedure. Plots for some important kinematic observables, such as the transverse momentum of the leptonically decaying W boson, the number of jets, the transverse momentum of the trailing VBS jet and the DNN spectra in the b-tag control region before the fit are shown in Figure 4.4. Only the 2018 muon category is reported as trends are similar for the electron counterpart and for the other years.

The second background needing special attention is the W+jets, which is the dominant one in the signal regions. The control region for this background is defined by vetoing b-jets and restricting the hadronically decaying V boson to be off-the-mass shell, namely $40 \leq m_V \leq 65$ or $m_V \geq 105$ in the resolved region and $40 \leq m_V \leq 70$ or $m_V \geq 115$ in the boosted region. The W+jets MC simulation is computed at LO in bins of H_T. The W+jets CR shows large disagreements with respect to the observation, especially in the jets kinematic in the resolved region. As observed by other CMS analyses, the p_T of the leptonically decaying W boson is not well modeled by the W+jets LO simulation. These trends are shared across regions and years and are therefore attributed to the limited precision of the matrix element calculation, showering and hadronization. In order to correct the observed trends, a data-driven approach to estimate the W+jets background directly from data is employed. As the transverse momentum of VBS jets and of the leptonically decaying W boson show correlated and large trends, the W+jets MC sample is split into subcategories using bins of $p_T^{W,l}$ and trailing VBS jet p_T in the resolved region, and only in bins of $p_T^{W,l}$ in the boosted region and the normalization of each of these bins

is measured directly from data in a simultaneous fit with all regions. Thanks to this procedure, the correction to the W+jets sample obtained in the W+jets CRs can be effectively propagated to the signal region while properly accounting for its uncertainty. Table 4.3 summarises the W+jets subcategories while Figure 4.5 shows the prefit templates used as input in the fit for the W+jets CR in both the boosted and resolved muon categories for 2018. Similar trends can be seen for the 2017 dataset while the disagreement is reduced in 2016 due to a different choice of the tune parameters, used to model non-perturbative phenomena in PYTHIA.

	Bin	$p_T^{W,l}$	$p_T^{VBS,2}$
Resolved	1	$p_T^{W,l} < 100$GeV	$p_T^{VBS,2} < 55$ GeV
	2		$55 \leq p_T^{VBS,2} < 75$ GeV
	3		$75 \leq p_T^{VBS,2} < 100$ GeV
	4		$100 \leq p_T^{VBS,2} < 135$ GeV
	5		$135 \leq p_T^{VBS,2} < 170$ GeV
	6		$p_T^{VBS,2} \geq 170$ GeV
	7	$100 \leq p_T^{W,l} < 200$GeV	$p_T^{VBS,2} < 55$ GeV
	8		$55 \leq p_T^{VBS,2} < 75$ GeV
	9		$75 \leq p_T^{VBS,2} < 100$ GeV
	10		$100 \leq p_T^{VBS,2} < 135$ GeV
	11		$135 \leq p_T^{VBS,2} < 170$ GeV
	12		$p_T^{VBS,2} \geq 170$ GeV
	13	$200 \leq p_T^{W,l} < 300$GeV	$p_T^{VBS,2} < 90$ GeV
	14		$90 \leq p_T^{VBS,2} < 125$ GeV
	15		$125 \leq p_T^{VBS,2} < 160$ GeV
	16		$p_T^{VBS,2} \geq 160$ GeV
	17	$300 \leq p_T^{W,l} < 400$GeV	$p_T^{VBS,2} < 90$ GeV
	18		$p_T^{VBS,2} \geq 90$ GeV
	19	$400 \leq p_T^{W,l} < 500$GeV	$p_T^{VBS,2} < 85$ GeV
	20		$p_T^{VBS,2} \geq 85$ GeV
	21	$p_T^{W,l} \geq 500$	-
Boosted	1	$p_T^{W,l} < 50$GeV	-
	2	$50 \leq p_T^{W,l} < 100$GeV	-
	3	$100 \leq p_T^{W,l} < 150$GeV	-
	4	$150 \leq p_T^{W,l} < 200$GeV	-
	5	$200 \leq p_T^{W,l} < 300$GeV	-
	6	$300 \leq p_T^{W,l} < 400$GeV	-
	7	$p_T^{W,l} \geq 400$GeV	-

Table 4.3: W+jets boosted and resolved subcategories for the data-driven correction to the LO MC sample. While the resolved category is split in bins of $p_T^{W,l}$ and $p_T^{VBS,2}$, the boosted region presents a stratification in $p_T^{W,l}$ only.

4.1.5 Systematic uncertainties

Different types of systematic uncertainties have been included in the measurement of the semileptonic VBS WV process. Uncertainties are modeled as nuisance parameters in the likelihood and

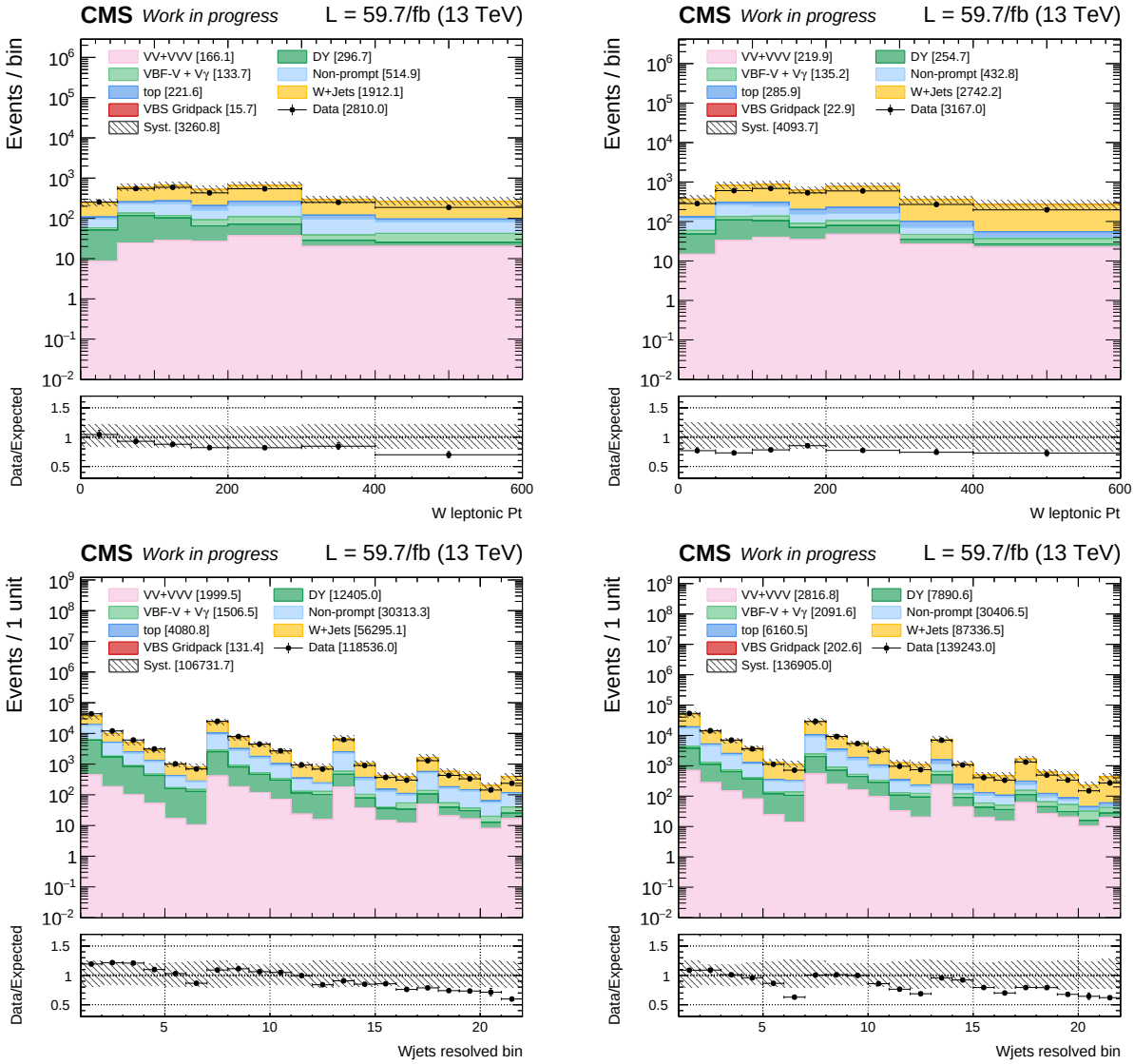

Figure 4.5: W+jets CR input templates to the fit. The normalization of each of the shown W+jets MC bins is left free to float in the fit. The top row shows the input distributions for the boosted electron (left) and muon (right) regions. The bottom row shows the input distributions in the resolved region for electron (left) and muon (right) regions.

can either affect the shape of a differential distribution for a specific process or simply scale its overall normalization. In the former case, the varied templates are provided by recomputing the relevant quantities by shifting up and down the uncertainty on some parameter by its value. A continuous estimate in each bin as a function of the nuisance parameter is obtained by means of vertical morphing [185]. All sources of uncertainty are either fully correlated (positively or negatively) or uncorrelated, as partially correlated uncertainties can be broken down to a composition of fully correlated and independent components [186]. This procedure allows the inclusion of all systematic uncertainties in the likelihood in a factorized form. Table 4.4 summarises all sources of systematic uncertainties considered in the SM measurement.

4.1.6 Results

The SM measurement [105] reports three results obtained with maximum likelihood fits for different scenarios, namely the measurement of the pure EW VBS signal strength $\mu_{\text{EW}} = \sigma^{\text{obs}}_{\text{EW}}/\sigma^{\text{SM}}_{\text{EW}}$, the combined EW+QCD signal strength measurement $\mu_{\text{EW+QCD}} = \sigma^{\text{obs}}_{\text{EW+QCD}}/\sigma^{\text{SM}}_{\text{EW+QCD}}$ and the bi-dimensional fit to both μ_{EW} and μ_{QCD} simultaneously. All the signal strengths agree with the SM expectation within one standard deviation. Regarding the pure EW measurements the observed signal strength is

$$\mu_{\text{EW}} = 0.85 \pm 12(\text{stat})^{+0.19}_{-0.17}(\text{syst}) = 0.85^{+0.23}_{-0.21} \tag{4.1}$$

with an expectation of $\mu^{\text{exp}}_{\text{EW}} = 1^{+0.24}_{-0.22}$, corresponding to a measured cross section of $1.90^{+0.53}_{-0.46}$ pb. The observed significance for the VBS EW production of a WV pair with a semileptonic final state is 4.4 standard deviations above the background (5.1 expected). The combined EW+QCD measurement is still in agreement with the SM expectation with a measured signal strength of $\mu_{\text{EW+QCD}} = 0.97 \pm 0.06(\text{stat})^{+0.19}_{-0.21}(\text{syst})$

4.2 Statistical framework for EFT measurements

The agreement of MC predictions to data is quantified through statistical methods. Similarly to new physics searches, in EFT one needs to assess the consistency of the observation sample with the SM-only hypothesis H_b or with the hypothesis of additional new physics induced by the effect of higher dimensional operators H_s. This problem is referred to as a statistical hypothesis test, where observations are used to decide which hypothesis is favored or rejected by nature. The hypothesis test is defined in terms of a test statistic, a number encoding the properties of the observations with respect to the hypothesis.

4.2.1 Likelihood ratio

At the LHC the test-statistic definition follows from the Neyman-Pearson lemma stating that when comparing two hypotheses the ratio of the likelihood functions represents the most powerful test to reject one or the other hypothesis in favor of its counterpart. In the following H_s represents the presence of both the SM background and the SMEFT signal where the expected number of events in each phase space is given by Eq. 2.4 and we can summarise as $N = SM + f(\boldsymbol{c})$ where $\boldsymbol{c}$ is a vector of Wilson coefficients. H_b represents the presence of the SM alone $N = SM$. By labelling $\vec{x}_i$ the i-th observation, and $\vec{\theta}$ the nuisance parameters, the likelihood ratio is defined as

$$\lambda(\boldsymbol{c}, \vec{\theta}) = \frac{\mathcal{L}_s(\vec{x}_1, ..., \vec{x}_n | \boldsymbol{c}, \vec{\theta})}{\mathcal{L}_b(\vec{x}_1, ..., \vec{x}_n | \vec{\theta})} \tag{4.2}$$

Legend: When the uncertainty is not affecting a specific year the symbol X is used. In case of no correlation the symbol − is used. In case of partial correlation e.g. if the uncertainty is composed of multiple sources some correlated and others not, the symbol ∼ is used. If the uncertainty is correlated the symbol ✓is used.

	Syst. Uncertainty	Process	Type	2016	2017	2018
Experimental / Background modelling	Luminosity	All MC except W+jets, top	lnN	∼	∼	∼
	Fake rate stat.	non-prompt	shape	-	-	-
	Fake rate syst.	non-prompt	lnN	-	-	-
	b-tag scale factor	all MC	shape	∼	∼	∼
	Trigger efficiency	all MC	shape	-	-	-
	Prefiring	all MC	shape	-	-	X
	Lepton ID efficiency	all MC	shape	-	-	-
	Lepton p_T scale	all MC	shape	-	-	-
	Jet energy scale	all MC	lnN	∼	∼	∼
	Jet energy resolution	all MC	lnN	-	-	-
	FatJet energy scale	all MC	lnN	∼	∼	∼
	FatJet energy resolution	all MC	lnN	-	-	-
	FatJet mass scale	all MC	lnN	-	-	-
	FatJet mass resolution	all MC	lnN	-	-	-
	τ_{21} scale factor	all MC	shape	-	-	-
	τ_{21} p_T extrapolation	all MC	shape	-	-	-
	Jet pileup ID scale factor	all MC	shape	-	-	-
	Unclustered MET	all MC	lnN	-	-	-
	Pileup	all MC	lnN	-	-	-
	Top sample composition	top	shape	✓	✓	✓
	Top p_T reweighting	top	shape	✓	✓	✓
	QGL morphing	all MC	shape	-	✓	✓
Theory	PS FSR and ISR	all MC (split)	shape	✓	✓	✓
	μ_F and μ_R scales	all MC (split)	shape	✓	✓	✓
	PDF	all MC except W+jets, top	shape	-	✓	✓
	Underlying Event	all MC except W+jets, top	shape	-	✓	✓
Data-driven SF	Top normalization boost e	top	SF	-	-	-
	Top normalization resolved e	top	SF	-	-	-
	Top normalization boost μ	top	SF	-	-	-
	Top normalization resolved μ	top	SF	-	-	-
	W+jets normalization boost e	W+jets bins	SF	-	-	-
	W+jets normalization resolved e	W+jets bins	SF	-	-	-
	W+jets normalization boost μ	W+jets bins	SF	-	-	-
	W+jets normalization resolved μ	W+jets bins	SF	-	-	-

Table 4.4: Systematic uncertainties and their modeling in the template fit for SM measurement of the VBS WV with semileptonic final state from [105]. Uncertainties are classified as experimental or due to the background modeling, theory uncertainties and scale factors (SF) introduced for a data-driven estimate of the top and W+jets backgrounds. Luminosity, jet or fatjet energy scales and b-tag scale factors uncertainties are split into sub-components and correlated according to the CMS guidelines.

The maximum of the likelihood ratio indicates the best-fit value for the parameter of interest $\boldsymbol{c}$ given the observations $\vec{x}_i$. For technical reasons, it is more convenient to search for the values of $\boldsymbol{c}$ that minimize $-2\log\lambda(\boldsymbol{c}, \vec{\theta})$. If the best-fit $\boldsymbol{c}$ is different from zero it indicates the possible presence of a signal.

4.2.2 Signal significance

If an excess is observed ($\boldsymbol{c} \neq \mathbf{0}$), the compatibility of the observations with the H_b hypothesis is expressed in terms of a p-value, which encodes the probability for the background to randomly fluctuate to produce an excess of events as significant as or greater than the one observed. Conversely, a limit can be put on the allowed dynamic for the signal, excluding H_s in favor of H_b for some parameter moderating the H_s predictions, e.g. Wilson coefficients in SMEFT searches. In this case, the p-value is defined as

$$p = \int_{t_{\text{obs}}}^{\infty} f(t|H_b)dt \tag{4.3}$$

where $f(t|H_b)$ denotes the probability distribution of the test statistic t under the background-only hypothesis H_b. In particle physics, p-values are usually converted into an equivalent significance Z defined such that in the limit of a large number of observations a variable is found to be Z standard deviations above its mean and has an upper-tail probability of p [187]

$$Z = \Phi^{-1}(1-p) \tag{4.4}$$

where Φ^{-1} is the inverse cumulative distribution of the normal distribution $\mathcal{G}(0,1)$.

4.2.3 Profile likelihood

The computation of the statistical significance usually proceeds by generating a large number of toy experiments to estimate the probability distribution for the test statistic under the SM-only hypothesis ($\boldsymbol{c} = \mathbf{0}$). This method, although very precise if the number of toys is large, is computationally expensive and is often replaced by an asymptotic approximation. Wilk's theorem [188] proves the asymptotic behaviour of the log-likelihood ratio test statistics. This is useful as hypothesis tests generally require the knowledge of the probability distribution of the test statistic which is often intractable. Given two hypotheses H_s and H_b defined in terms of a set of parameters $\boldsymbol{c} = (c_1, ..., c_m)$, the condition that H_s is true implies that $\boldsymbol{c} \in \Theta$ where Θ is the full parameter space. On the other hand, the condition that H_b is true can be written as $\boldsymbol{c} \in \Theta_b$ where Θ_b is the subset of the full parameter space associated with H_b. Given n observed measurements $(\vec{x}_1, ..., \vec{x}_n)$ the quantity

$$\chi^2 = -2\log\frac{\sup_{\boldsymbol{c}\in\Theta_b}\prod_{i=1}^{n}\mathcal{L}(\vec{x}_i|\boldsymbol{c})}{\sup_{\boldsymbol{c}\in\Theta}\prod_{i=1}^{n}\mathcal{L}(\vec{x}_i|\boldsymbol{c})} \tag{4.5}$$

is distributed as a χ^2 distribution under the null hypothesis H_b in the limit of $n \to \infty$. The number of degrees of freedom of the χ^2 is equal to the difference of dimensionality of the two sets Θ_b and Θ. For SMEFT fits, the signal hypothesis can be written as $\boldsymbol{c} = (\boldsymbol{c}, \vec{\theta})$ where $\boldsymbol{c}$ is the Wilson coefficients vector and $\vec{\theta}$ is the vector of nuisance parameters while the null hypothesis H_b implies $\boldsymbol{c} = (\mathbf{0}, \vec{\theta})$, giving

$$\chi^2 = -2\log\frac{\sup_{\vec{\theta}}\prod_{i=1}^{n}\mathcal{L}(\vec{x}_i|\mathbf{0},\vec{\theta})}{\sup_{\boldsymbol{c},\vec{\theta}}\prod_{i=1}^{n}\mathcal{L}(\vec{x}_i|\boldsymbol{c},\vec{\theta})} \tag{4.6}$$

In the numerator, the supremum (sup) of the likelihood is only determined by the nuisance parameters $\hat{\vec{\theta}}$. At the denominator, the likelihood function is evaluated at parameters $\boldsymbol{c} = \hat{\boldsymbol{c}}$ and $\vec{\theta} = \hat{\vec{\theta}}$ that maximize it. The final test statistic is the so-called profile-likelihood [187]

$$\chi^2(\mathbf{0}) = -2\log\frac{\mathcal{L}(\vec{x}|\mathbf{0},\hat{\vec{\theta}})}{\mathcal{L}(\vec{x}|\hat{\boldsymbol{c}},\hat{\vec{\theta}})} \tag{4.7}$$

where the numerator maximizes $\mathcal{L}$ for a given and fixed value of $\boldsymbol{c} = \mathbf{0}$ while the denominator maximizes $\mathcal{L}$ for both $\boldsymbol{c}$, $\vec{\theta}$. According to Wilk's theorem, the significance can be extracted as $\chi^2(\mathbf{0})$ in the asymptotic scenario, from a χ^2 distribution with degrees of freedom equal to the number of nuisance parameters. The significance in this regime is then computed as $Z \simeq \sqrt{2\log\lambda(\hat{\boldsymbol{c}})}$.

4.2.4 EFT statistical model

The EFT statistical model is implemented in the COMBINE tool, developed for the discovery of the Higgs boson and now widely spread in CMS [185–187]. A major downside when using standard tools for EFT searches is that linear terms, being interference ones, can be negative. COMBINE is a high-level API running RooFit [189] and RooStat [190] in the background. These statistical frameworks are specifically designed to model event data distributions where each event is a discrete occurrence in time. As a consequence, experiments like these yield datasets that adhere to Poisson (or binomial) statistical distributions. The natural statistical framework for such kind of dataset is probability distribution functions that however are positively defined. It is not possible to work with a negative linear interference out of the box using these frameworks, therefore the baseline model defined in Eq. 2.4 has to be re-written such that only non-negative defined inputs are provided. This trick is done by exploiting the fact that the modulus square of amplitudes are positive-defined quantities for all observables and phase spaces. For example, the SM component is the result of $|\mathcal{A}_{\text{SM}}|^2$ while the quantity $\text{Quad}_i = |\mathcal{A}_{Q_i}|^2$ and finally the quantity $\text{SM} + \text{Lin}_i + \text{Quad}_i$ is the modulus square of the amplitude defined in 2.4 including only one operator and setting its Wilson coefficient to $k = 1$. The formula in Eq. B.2 then becomes:

$$N = (1-k)\cdot\text{SM} + k\cdot(\text{SM} + \text{Lin}_i + \text{Quad}_i) + (k^2 - k)\cdot\text{Quad}_i \tag{4.8}$$

while the more complex one defined in Eq. B.3 becomes:

$$
\begin{aligned}
N = \mathrm{SM} \cdot (1 - \sum_i k_i + \sum_{i,i<j} \sum_j k_i \cdot k_j) \\
+ \left[\sum_i k_i - \sum_{i \neq j} k_i \cdot k_j \right] \cdot (\mathrm{S} + \mathrm{Lin}_i + \mathrm{Quad}_i) \\
+ \sum_i \left(k_i^2 - k_i\right) \cdot \mathrm{Quad}_i \\
+ \sum_{i,i<j} \sum_j k_i \cdot k_j \cdot \left[\mathrm{SM} + \mathrm{Lin}_i + \mathrm{Lin}_j + \mathrm{Quad}_i + \mathrm{Quad}_j + 2 \cdot \mathrm{Mix}_{ij} \right]
\end{aligned}
\tag{4.9}
$$

exploiting the fact the last term is still a squared amplitude including two operators and setting $k_i = k_j = 1$ namely $|\mathcal{A}_{\mathrm{SM}} + \mathcal{A}_{Q_i} + \mathcal{A}_{Q_j}|^2$. The alternative formulation is also valid:

$$
\begin{aligned}
N = \mathrm{SM} \cdot (1 - \sum_i k_i) \\
+ \sum_i k_i \cdot (\mathrm{SM} + \mathrm{Lin}_i + \mathrm{Quad}_i) \\
+ \sum_i \left(k_i^2 - k_i - \sum_{i \neq j} k_i \cdot k_j \right) \cdot \mathrm{Quad}_i \\
+ \sum_{i,i<j} \sum_j k_i \cdot k_j \cdot \left[2 \cdot \mathrm{Mix}_{ij} + \mathrm{Quad}_i + \mathrm{Quad}_j \right]
\end{aligned}
\tag{4.10}
$$

The derivation for the coefficients in front of each non-negative component, expressed in terms of Wilson coefficients is given in Appendix B

4.2.5 EFT model validation

We provided the EFT model with templates for the respective positively-defined components depending on the algebra. These templates will be used to build the overall p.d.f. using ROOFIT and ROOSTAT . The three models defined in Sec. 4.2.4 have been labeled as "EFTPos" referring to results obtained with the model defined at Eq. 2.4 (model with possible negative terms), "EFTNeg" to the model defined at Eq. 4.9 and "EFTNeg-alt" to the alternative model built with non-negative-definite yields at Eq. 4.10. Starting from two operators, the models will implement different syntaxes regarding the mixed terms between operators. Table 4.5 shows an example for template definitions (process syntax to be specified in COMBINE datacards) and coefficient expression for the relative template for the two non-negative models. The coefficients c_G and $c_{\tilde{G}}$ are arbitrary. The datacard process syntax (Process name) is also specified to ease the user in building them. For the one-operator case, both the new models analytically coincide.

Tests have been done to check the behaviour of the models in simple scenarios. In particular, for the one operator case, in the scenario where interferences are positive, it is checked that the same likelihood profile is obtained for the simple equation 2.4 and the one with only non-negatively defined components Eq. 4.8. The collapse of a multidimensional model to a simple one-operator model has been checked to yield the same likelihood profile. Lastly, the model behaviour has been studied in the presence of more than three operators.

Process name	Model	Expression (expr::)
sm	EFTNeg	func_sm("@0*(1-(@1+@2-@1*@2))",r,k_cG, k_cGtil)
quad_cG	EFTNeg	func_quadratic_cG("@0*(@1*@1-@1)",r,k_cG)
sm_lin_quad_cG	EFTNeg	func_sm_linear_quadratic_cG("@0*(@1 * (1-(@2)))",r,k_cG, k_cGtil)
quad_cGtil	EFTNeg	func_quadratic_cGtil("@0*(@1*@1-@1)",r,k_cGtil)
sm_lin_quad_cGtil	EFTNeg	func_sm_linear_quadratic_cGtil("@0*(@1 * (1-(@2)))",r,k_cGtil, k_cG)
sm_lin_quad_mixed_cG_cGtil	EFTNeg	func_sm_linear_quadratic_mixed_cG_cGtil("@0*@1*@2",r,k_cG,k_cGtil)
sm	EFTNeg-alt	func_sm("@0*(1-(@1+@2))",r,k_cG, k_cGtil)
quad_cG	EFTNeg-alt	func_quadratic_cG("@0*(@1*@1-@1-@1*(@2))",r,k_cG, k_cGtil)
sm_lin_quad_cG	EFTNeg-alt	func_sm_linear_quadratic_cG("@0*(@1)",r,k_cG)
quad_cGtil	EFTNeg-alt	func_quadratic_cGtil("@0*(@1*@1-@1-@1*(@2))",r,k_cGtil, k_cG)
sm_lin_quad_cGtil	EFTNeg-alt	func_sm_linear_quadratic_cGtil("@0*(@1)",r,k_cGtil)
quad_mixed_cG_cGtil	EFTNeg-alt	func_quadratic_mixed_cG_cGtil("@0*@1*@2",r,k_cG,k_cGtil)

Table 4.5: Table summarising an example datacard with processes names for each model and the expression for the EFT model algebra in terms of the coefficients in the two operators case.

Two counting experiments have been generated with different statistics for test purposes. The yields for each component are summarized in Table 4.6 for each operator i. Terms that involve the interference between operators, Mix_{ij}, are defined when implementing at least two operators. An additional background contribution named "other" has been added with a magnitude equal to the SM yield.
If not specified, only one nuisance is defined for the SM component of 0.2% (namely lnN 1.002). The nuisance is propagated to other terms that depend on the S yield as:

$$\sigma_\tau = (\sigma_{\text{SM}} - 1) \times \frac{\text{SM}}{\tau} + 1 \tag{4.11}$$

where σ_{SM} represents the nuisance value of the SM component and τ represents any component dependent on the SM value (e.g. S+L_i+Q_i).

Test	S	L_i	Q_i	2·M_{ij}	S+L_i+Q_i	S+L_i+Q_i+L_j+Q_j+2·M_{ij}	Q_i+Q_j+2 · M_{ij}	other
High Statistics	154	5	20	13	179	217	53	154
Low Statistics	30	1	2	1	33	37	17	30

Table 4.6: Summary of the yields in the two counting experiments named High Statistics and Low Statistics. The various models will be tested on an appropriate combination of these yields which are self-consistent by construction.

Results for the one operator case are represented in Figure 4.6 for the low and high-statistic datasets, where the new model algebra EFTNeg and EFTNeg-alt collapse to the same Eq. 4.8. All models are found to agree as the likelihood profiles are perfectly overlapping.

In the second stage, more operators have been implemented. The models automatically combine all the contributions. The multi-dimensional fit is collapsed to only one parameter of interest. All other operators are frozen and their nominal value is set to zero. Figure 4.7 represents the likelihood profiles while implementing 2,4 and 8 operators in the high and low statistics datasets. All the tests show a perfect agreement between the models as the likelihood profiles are perfectly overlapping.

The same tests have been conducted in two dimensions, collapsing the multi-dimensional fit to two arbitrary parameters of interest. Figure 4.8 represents the two-dimensional likelihood

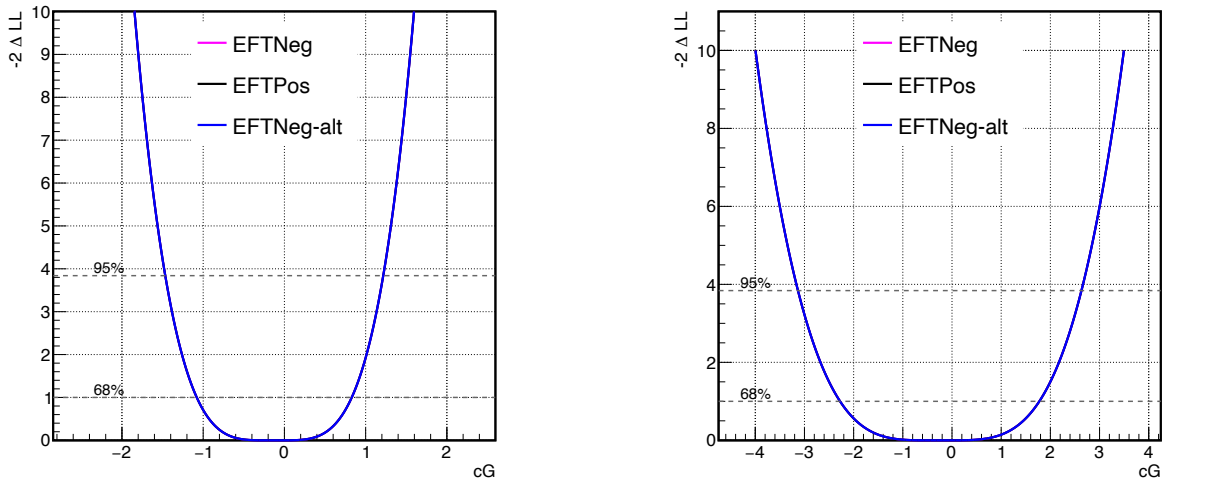

Figure 4.6: Likelihood profiles for the parameter c_G which represent an arbitrary operator. The left figure represents the results obtained using the high statistics test. The right figure represents the results obtained using the low statistics test. In both tests, all the models are found to agree as the likelihood profiles are indistinguishable.

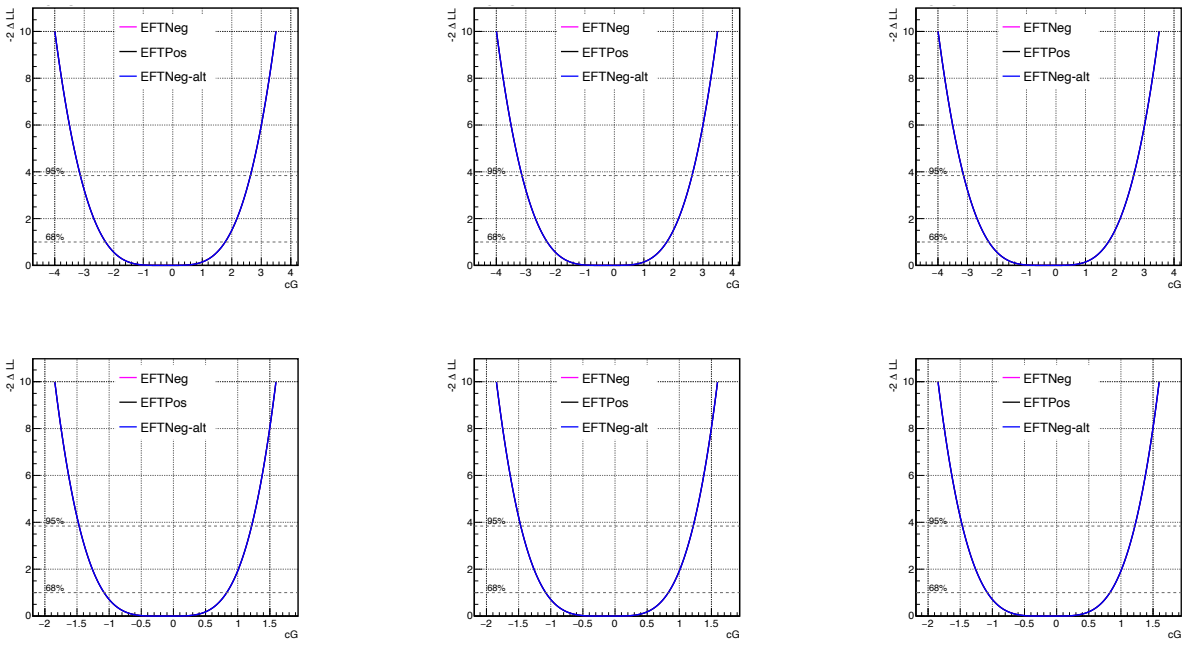

Figure 4.7: Likelihood profiles for the parameter c_G using the low statistic dataset in the upper row and the high statistics test in the bottom row. From left to right, the models implement 2, 4 and 8 operators and collapse the multidimensional likelihood to only one freely-floating operator. The likelihood profiles are perfectly overlapping.

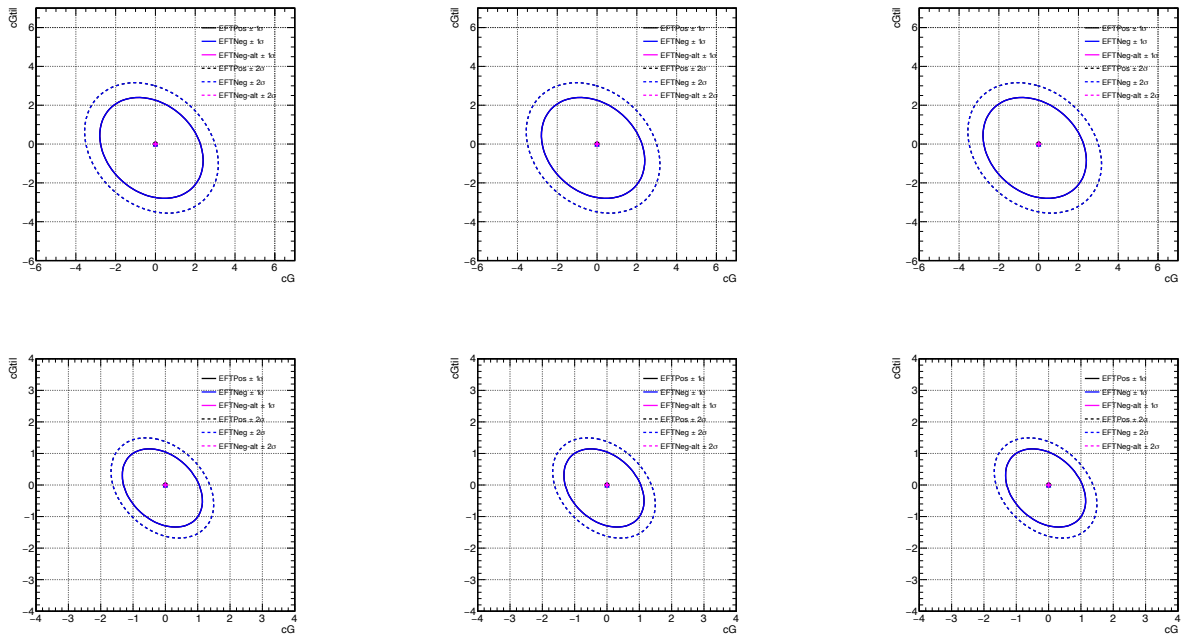

Figure 4.8: Two-dimensional likelihood profiles for the parameters c_G, c_{Gtil} using the low statistic dataset in the upper row and the high statistics test in the bottom row. From left to right, the models implement 2, 4 and 8 operators and collapse the multidimensional likelihood to two freely-floating operators. The likelihood profiles are perfectly overlapping.

profiles while implementing 2,4 and 8 operators in both the low and high statistics tests. All the tests show a perfect agreement between the models.

Additional nuisance parameters do not spoil the agreement between the different models, in case all contributions are non-negative defined, as expected. Additional validations have been made against a well-known EFT model previously used for aTGC searches at CMS but not maintained anymore called ATGCROOSTATS. The validation showed perfect agreement between the two with minor differences due to the differences in nuisance handling between both implementations.

The statistical EFT models to be used under the COMBINE framework can be found at the repository [2].

4.3 Signal production

4.3.1 EFT Monte Carlo generation for the VBS WV

Effective field theory MC predictions for the purely EW VBS WV with a semileptonic final state are generated at the LO with SMEFTSIM [65, 122] assuming a $U(2)^3$ symmetry in the quark sector (the so-called topU3l flavour assumption, previously described in Sec 1.8.5.3) and MADGRAPH5_AMC@NLO [123] version 2.6.5 (MG5), with up to one dimension-six EFT operator per diagram. Diagrams with the insertion of two operators, giving corrections to two vertices, have been neglected as they provide dimension-eight effects. All leptons and light-flavour quarks (including the b-quark) are assumed to be massless. The 5-flavour scheme is

[2] https://github.com/amassiro/AnalyticAnomalousCoupling

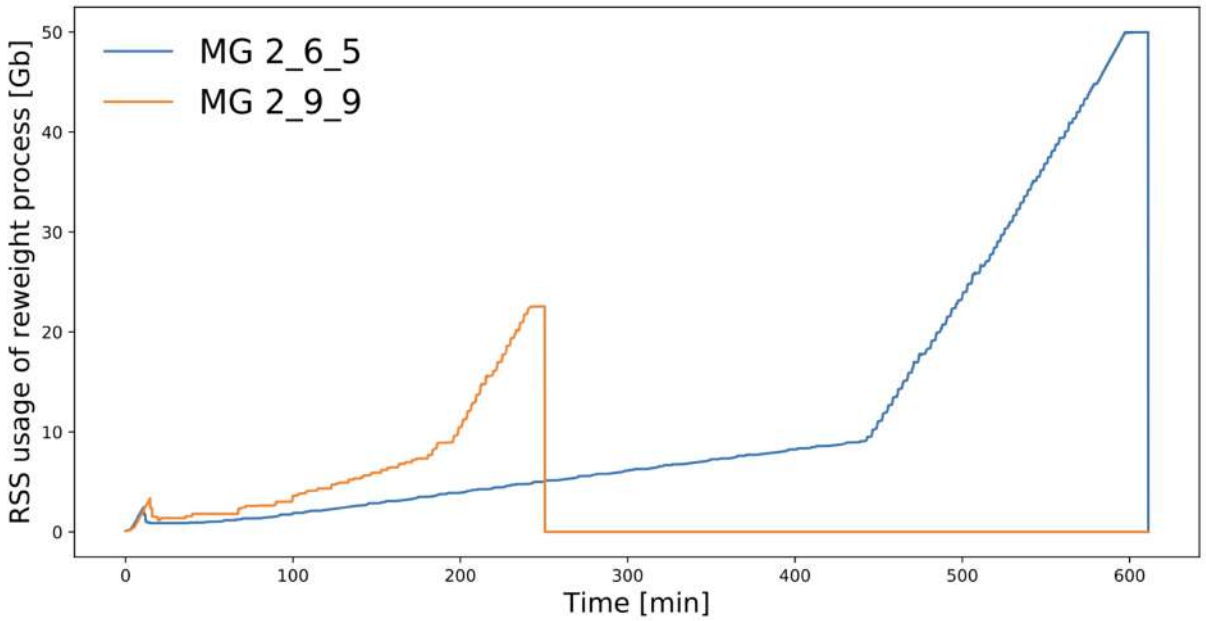

Figure 4.9: RAM usage versus time for the MG5 reweighting step. Two MG5 versions are tested, v2.9.9 in orange and v2.6.5 in blue. The sudden stop at $t \sim 250$ and $t \sim 600$ minutes correspond to the time at which the operating system stops the reweighting routine due to lack of resources.

employed with the NNLO parton distribution functions provided by the NNPDF collaboration with $\alpha_S = 0.118$ (LHAPDF identification code 325300) [124]. The showering, hadronization and underlying event simulation are handled by PYTHIA [164] with the CP5 tune [191]. The EW VBS WV signal is treated as a $2 \to 6$ process with six fermions in the final state, four of which are quarks. The MG5 reweight functionality [125] is used to compute the event weights for the EFT hypothesis, allowing a single event generation and avoiding non-physical negative yields that would appear in independent generations due to the differences in the phase spaces as described in Section 2.3.1.

4.3.1.1 Madgraph reweighting memory pressure

The complex topology of this final state involves approximately $\mathcal{O}(200\text{k})$ diagrams for the SM, for each lepton flavour and charge. This number drastically increases, along with the computational time, when introducing dimension-six EFT operators. An appealing solution is to integrate a limited phase space (e.g. only SM or SM plus a few dimension-six operators) and only compute new event weights corresponding to a point in the EFT parameter space through MG5 reweighting functionality. Each event is assigned a new weight computed as $\omega_{\text{new}} = \omega_{\text{orig}} \cdot |M_{\text{new}}|^2/|M_{\text{orig}}|^2$ [125] where $\omega_{\text{orig}} = f_1(x_1, \mu_F) \cdot f_2(x_2, \mu_F) \cdot |M_{\text{orig}}|^2 \cdot \Omega_{\text{PS}}$ with f denoting parton distribution functions and Ω_{PS} is the phase space measure associated to the event. However, the computation of $|M_{\text{new}}|^2$ is done retrieving all possible EFT diagrams for the $2 \to 6$ process even if their Wilson coefficients are set to zero. This leads to a saturation of the resources, hitting at most 50 GB of RAM pressure before being stopped by the operating system. This behaviour is independent of the MG5 version and is shown in Figure 4.9 while generating $pp \to e^+\nu_e jjjj$ and including 15 dimension-six operators at reweighting.

This problem was overcome by introducing the parallelization of the reweighting step. In order to extract the templates needed for the EFT parametrization, we need to compute the EFT weights at $1 + n(n+3)/2$ fixed points where n is the number of operators considered. These

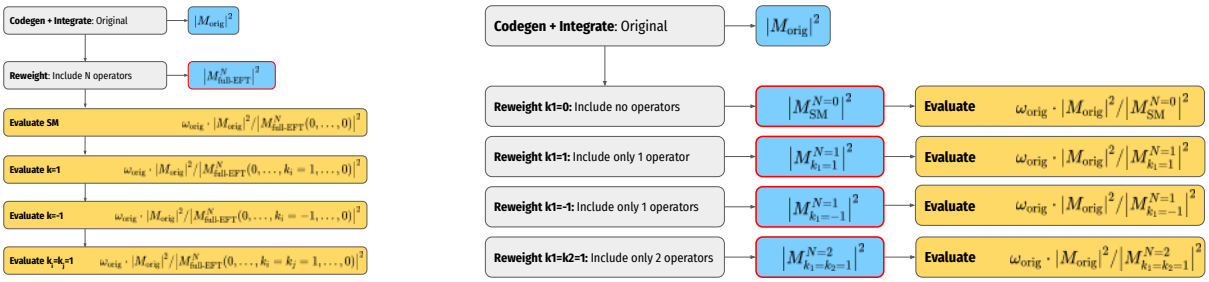

Figure 4.10: Sketch of the traditional MG5 reweight approach (left) and the parallelized version for EFT predictions (right). The original hypothesis, used to gather Feynman diagrams and integrate the phase space, is arbitrary and user-defined. The computation of $|M^N_{\text{full-EFT}}|^2$ for N operators is both time and memory-consuming and is substituted with $1 + n(n+3)/2$ matrix element computation with at most $N = 2$ operators, with which one can obtain the full EFT parametrization. The two methods mathematically coincide.

points can be computed while including at most two operators simultaneously, independently of n. By denoting k a general Wilson coefficient, the event weight ω will depend on the Wilson coefficients as

$$\begin{aligned} \omega(k) &= \omega(\text{SM} + k\text{Lin} + k^2\text{Quad}) \\ \omega(k_m, k_n) &= \omega(\text{SM} + \sum_{i\in[m,n]} k_i\text{Lin}_i + k_i^2\text{Quad}_i + 2\text{Mix}_{ij}) \end{aligned} \tag{4.12}$$

The weights corresponding to the components of the EFT parametrization can be retrieved via simple algebra obtaining (for arbitrary $k = 1$ for simplicity):

$$\begin{aligned} \omega_{\text{SM}} &= \omega(k=0) \\ \omega_{\text{Lin}} &= \frac{1}{2}[\omega(k=1) - \omega(k=-1)] \\ \omega_{\text{Quad}} &= \frac{1}{2}[\omega(k=1) + \omega(k=-1) - 2\omega(k=0)] \\ \omega_{\text{Mix}_{ij}} &= \omega(k_i = k_j = 1) + \omega(k_i = k_j = 0) - \omega(k_i = 1, k_j = 0) - \omega(k_i = 0, k_j = 0) \end{aligned} \tag{4.13}$$

As $|M_{\text{orig}}|^2$ is fixed by the initial point, used to integrate the phase space, one needs to evaluate $|M_{\text{new}}|^2$ with the insertion of one operator at $k = -1, 0, +1$ and for the insertion of two operators at $k_i = k_j = 1$ and the operation can be done in parallel saving memory and computational time without loss in precision. The procedure is schematically summarised in Figure 4.10.

4.3.1.2 Initial point for phase space integration

While it was proven in the previous chapter that the reweight step is feasible with an arbitrary number of dimension-six operators, the only problem remaining is how to choose the baseline hypothesis used to integrate the phase space and to compute $|M_{\text{orig}}|^2$. A critical caveat of the MG5 reweighting procedure is that the phase space related to the original hypothesis should cover sufficiently the phase space associated with the new hypothesis. In general, the phase space of the new hypothesis, introduced at reweighting, should be a subset of the original one and ω_{orig} should always be non-vanishing when ω_{new} is non-vanishing. If this overlapping condition is not satisfied, the weights associated with the new theory for events

falling in a phase space region where the original hypothesis lacks coverage will be large, thus implying a large statistical uncertainty of the reweighted sample and the resulting predictions unreliable [125]. This is the case for EFT, as dimension-six operators typically induce large differences in the tails of energy-related distributions with respect to the SM. Assuming $|M_{\text{orig}}|^2 = |M_{\text{SM}}|^2$ and then reweighting to a new point in the EFT parameter space will typically lead to unphysical predictions for most parameters. Taking the SM as the baseline hypothesis by setting each Wilson coefficient to zero is an extreme scenario. Also attempting to integrate $|M_{\text{orig}}|^2$ starting from Wilson coefficients different from zero can induce some problems with the reweighted samples. The chosen values of the Wilson coefficient will weigh the contribution of the linear and quadratic term from the EFT parametrization: if the chosen value is too large, the phase space will be dominated by the quadratic component and vice-versa. This fact can lead to large statistical uncertainties when computing the weights from the algebra described in Equation 4.13. As an example, setting $k = 1$ for a dimension-six operator will imply that $\text{SM} + k\text{Lin} + k^2\text{Quad} \sim \text{SM} + k^2\text{Quad}$ within numerical precision and therefore $\omega(k = 1) = \omega(k = -1)$, and the weight associated to the linear component $\omega_{\text{Lin}} \sim \omega(k = 1) - \omega(k = -1)$ will vanish. Ideally, the preferred value for the Wilson coefficients lies in the 2σ interval from the likelihood profile for the single operator while assuming the SM, where contributions from the linear and quadratic terms are compatible in size. However, this value is not apriori known and can be hard to retrieve, as it needs a dedicated analysis. As the computation of the SM for VBS WV is rather simple, the MG5 reweighting starting from the SM was tested on 59 operators affecting both EW and QCD VBS production up to the order $\alpha_S^2\alpha^4$ (38 operators when considering EW production only at order α^6). The reweighted templates built from one million parton-level events and with no selections have been compared to the ones generated directly via independent simulations of 100.000 parton-level events for each contribution exploiting the interaction-order syntax in MG5 and SMEFTSIM that grants a precise sampling of the EFT phase space. It can be seen from Figure 4.11 that for some operators the agreement between the two templates lies within the statistical uncertainty, suggesting that the new phase space induced by the dimension-six dynamics is similar to the SM one. On the other hand for other operators, the templates can be non-smooth, dominated by statistical uncertainties or non-physical as shown in Figure 4.12.

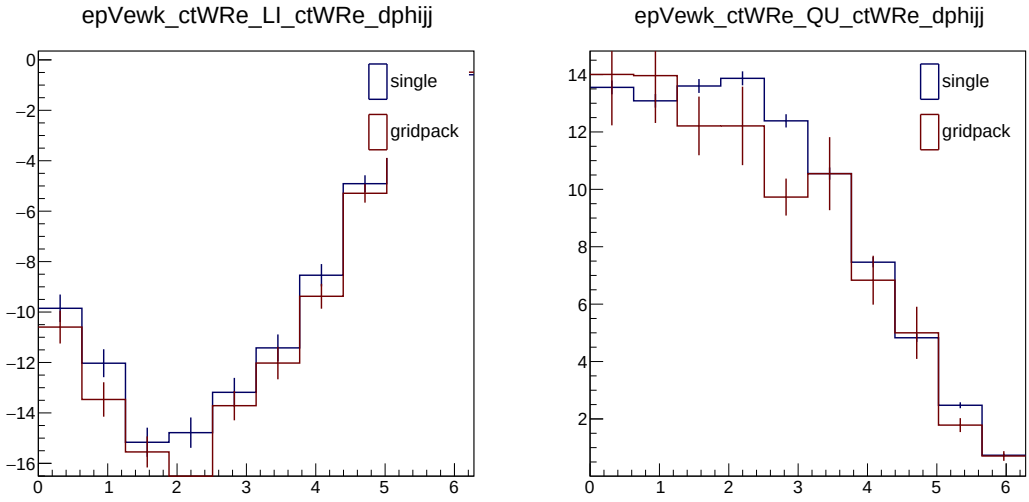

Figure 4.11: $\Delta\phi_{jj}^{\text{VBS}}$ in $pp \to e^+\nu_e jjjj$ for linear (left) and quadratic (right) templates of Q_{tW}

The choice of SM as a starting point for the generation is not reliable for a complex process such as a $2 \to 6$ one and therefore this option is discarded.

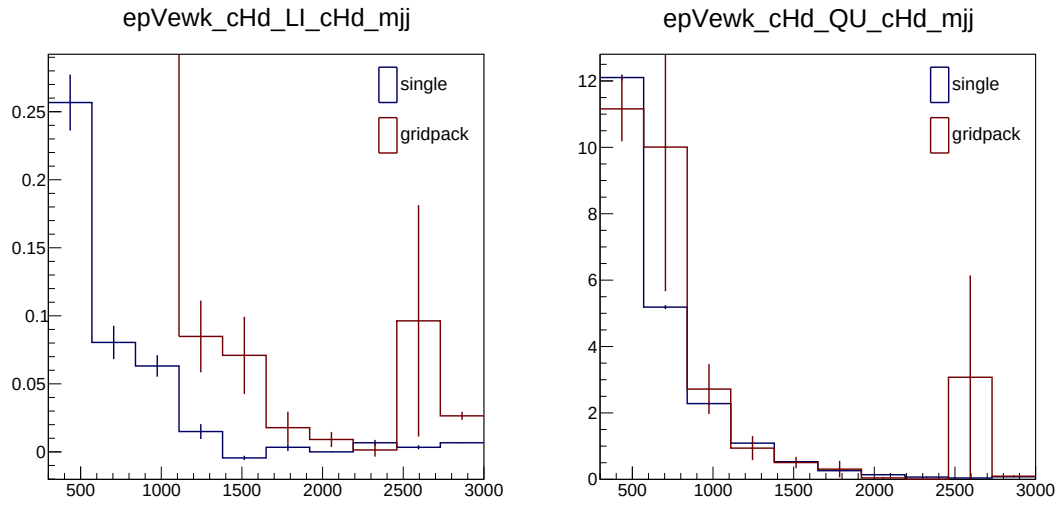

Figure 4.12: m_{jj}^{VBS} in $pp \to e^+\nu_e jjjj$ for linear (left) and quadratic (right) templates of Q_{Hd}

In order to obtain reliable predictions, EFT operators have been added to the baseline hypothesis incrementally for the $pp \to e^+\nu_e jjjj$. While this method is proven to give reliable reweighting predictions, it won't work with an arbitrary number of operators. Operators have been added incrementally up to the point where the number of Feynman diagrams saturates MG5 or the machine's capabilities. Table 4.7 summarises all the incremental steps along with the number of diagrams involved and the computational time spent to retrieve Feynman diagrams.

Legend: Group1: $\{Q_W, Q_{HWB}, Q_{Hbox}\ Q_{HW}\ Q_{HB}\}$, Group2: $\{Q_{Hj}^{(1)}, Q_{HQ}^{(1)}, Q_{Hl}^{(1)}\}$, Group3: $\{\tilde{Q}_W, \tilde{Q}_{HW}, \tilde{Q}_{HWB}, \tilde{Q}_{HB}\}$

Operators	**N.**	**Diagrams**	**Time (s)**	**Status**
Q_W	1	192582	445	✓
Group1 + $Q_{Hl}^{(1)}$	6	724100	1164	✓
Group1 + Q_{tW} + $Q_{Hl}^{(1)}$	7	733428	1469	X
Group1 + Group2	8	930084	2366	✓
Group1 + Group2 + Q_{tW}	9	939412	1354	X
Group1 + Group2 + $Q_{Hl}^{(3)}$	9	1650780	4268	X
Group1 + Group2 + $Q_{Hl}^{(3)}$ + Q_{tW}	10	1660108	3320	X
Group1 + Group2 + $Q_{Hl}^{(3)}$ + $Q_{Hj}^{(3)}$	10	2069530	4797	X
Group1 + Group3 + $Q_{Hl}^{(3)}$ + $Q_{Hl}^{(1)}$	11	1596096	6082	X

Table 4.7: Tests for the choice of the operators set to be included in the baseline hypothesis while computing $|M_{\text{orig}}|^2$ to get more precise predictions while reweighting to EFT components. If the row has a status ✓ the production runs successfully. Otherwise, in the presence of status X the compilation failed. The row highlighted in grey is chosen for production, corresponding to the maximal set of operators among the ones tested.

All Wilson coefficients are set to one for the integration of the phase space. The maximal set of operators, for which the MG5 computation of $|M_{\text{orig}}|^2$ is successful, is taken as the baseline hypothesis for the integration of the phase space and the production of the events and is reported in the following Table 4.8. For simplicity and to ensure that the reweighting step provides reliable predictions, these eight operators will be the only ones studied. Additional operators can be added at the reweighting step but the closure of the reweighted templates should be

checked with the interaction order syntax. The latter is not a trivial task by itself and won't be investigated in the context of this study.

$Q_{Hl}^{(1)} = (H^\dagger i\overleftrightarrow{D_\mu} H)(\bar{l}_p \gamma^\mu l_p)$	$Q_{HB} = (H^\dagger i\overleftrightarrow{D_\mu^i} H)(\bar{l}_p \sigma^i \gamma^\mu l_p)$
$Q_{Hj}^{(1)} = (H^\dagger i\overleftrightarrow{D_\mu} H)(\bar{q}_p \gamma^\mu q_p)$	$Q_{HQ}^{(1)} = (H^\dagger i\overleftrightarrow{D_\mu^i} H)(\bar{q}_p \sigma^i \gamma^\mu q_p)$
$Q_W = \varepsilon^{ijk} W_\mu^{iv} W_\nu^{j\rho} W_\rho^{k\mu}$	$Q_{H\Box} = (H^\dagger H)\Box(H^\dagger H)$
$Q_{HWB} = (H^\dagger \sigma^i H) W_{\mu\nu}^i B^{\mu\nu}$	$Q_{HW} = (H^\dagger H) W_{\mu\nu}^i W^{i\mu\nu}$

Table 4.8: Definitions of the dimension-six EFT operators investigated in the VBS WV analysis.

The phase space is integrated setting all Wilson coefficients to 1. A comparison between the reweighted templates obtained from one million parton-level events and the ones generated directly by independent simulations of 100.000 parton-level events is given in Figure 4.13. All the templates are found to be in reasonable agreement within statistical uncertainties. It can be seen how the generated phase space from the reweighted sample is dominated by quadratic components specifically from the Q_W operator, whose cross-section for $c_W = 1$ is approximately three orders of magnitude larger than all the other linear components. This phase space dominance leads to a very good description of quadratic components (except for $Q_{Hl}^{(1)}$) while yielding a statistically dominated description of the linear ones. This behaviour is taken into account in the full analysis by generating a large number of events.

4.3.2 Closure with pre-existing signal sample

In order for the algebra defined in Section 4.2.4 to work it is needed for the EFT and SM templates to share a common phase space. If the phase spaces differ for the two, for example in the case of independent generations, there will be a set of values of c_i for which the overall SM+EFT differential distribution presents non-physical negative bin yields. Even if this negative behaviour might be covered by statistical uncertainties, it is impossible to build a probability distribution function from negative templates. Due to this fact, the existing sample used for the VBS WV SM analysis [105] has to be replaced with the newly generated sample, reweighted for the SM hypothesis. The two samples differ in the process definition (as shown in Table 4.9), generator level cuts and number of diagrams involved which might lead to sensitive differences between the two samples thus invalidating the results. A comprehensive comparison has been performed in order to address the differences between the two and possibly understand missing systematic uncertainties affecting the reweighted sample.

Other differences regarding generation parameters can also be a source of disagreement. The origin of this difference is due to updates on some parameters, following developments from theory and CMS communities, and for the UFO model to work properly. The latter is the case for the choice of the dynamical scale algorithm as will be discussed next. A summary of these differences is given in Table 4.10.

A key difference between the two generations, apart from the number of processes involved, is the computation of the factorization and renormalization scales μ_R, μ_F when dealing with a 4-particle final state and a 6-particle one. The LHC accelerates protons up to energies where their constituents, called partons, can be regarded as free due to the asymptotic freedom of QCD. These particles are the ones that interact producing the scattering. To calculate the cross section for processes in collisions involving hadrons in the initial state, the partonic cross section $\hat{\sigma}$ is convolved with the corresponding parton distribution functions (PDFs) that describe the

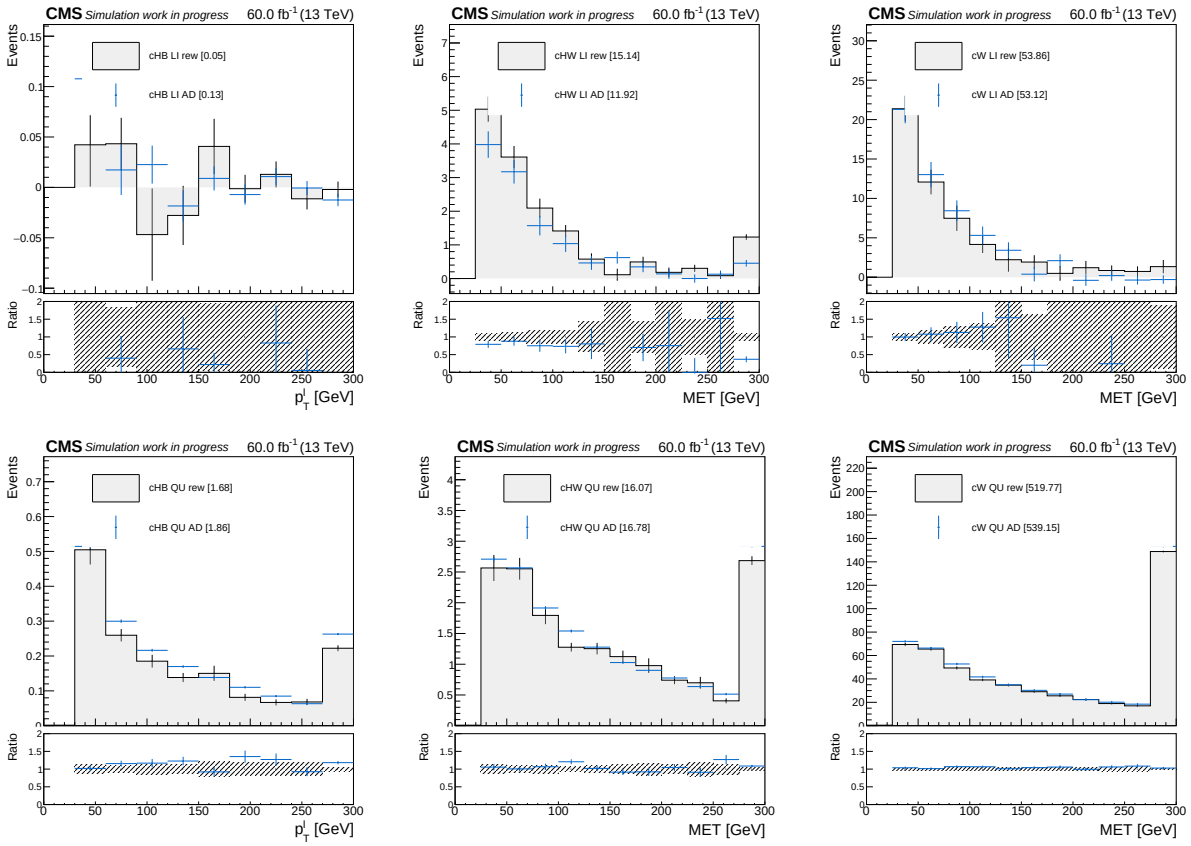

Figure 4.13: Templates comparison at parton-level for linear (upper row) and quadratic (bottom row) components from the reweighted generation and from the direct amplitude decomposition (AD) generation, the latter taken as the ground truth. From left to right the p_T of the charged lepton for Q_{HB}, missing transverse energy for Q_{HW} and Q_W. All the remaining operators follow a similar pattern where the quadratic component presents a lower statistical uncertainty with respect to the linear counterpart (except for $Q_{Hl}^{(1)}$ where the quadratic and linear cross sections are compatible at $c_{Hl}^{(1)} = 1$). This behaviour is corrected by generating more events at the analysis level.

WV Analysis	Process definition

SM	`generate p p > w+ w+ j j QED=4 QCD=0, w+ > l+ vl, w+ > j j`
	`generate p p > w+ w- j j QED=4 QCD=0, w+ > l+ vl, w- > j j`
	`generate p p > w- w+ j j QED=4 QCD=0, w- > l- vl~, w+ > j j`
	`generate p p > w- w- j j QED=4 QCD=0, w- > l- vl~, w- > j j`
	`generate p p > w+ z j j QED=4 QCD=0, w+ > l+ vl, z > j j`
	`generate p p > w- z j j QED=4 QCD=0, w- > l- vl~, z > j j`
	`generate p p > w+ z j j QED=4 QCD=0, w+ > l+ vl, z > j j`

EFT	`generate p p > l+ vl j j j j QCD=0` `generate p p > l- vl~ j j j j QCD=0`

Table 4.9: Table summarising signal MADGRAPH5_AMC@NLO generation syntaxes for the published SM analysis [105] and the EFT interpretation. `l` refers to a charged lepton in e, μ, τ while `vl` to neutrinos in ν_e, ν_μ, ν_τ. The symbol ~ refers to the antiparticle operator. `QED` and `QCD` commands specify the order in α_{EW} and α_S respectively for the diagrams. If not specified the lowest order is assumed. The operator = is interpreted as $<=$.

fraction of the proton momentum carried by each valence or sea parton. The PDFs are not fixed but depend on the energy scale at which they are probed Q^2, and their behaviour as a function of Q is given by the DGLAP equation [192]. Performing QCD calculations beyond the leading order gives singularities that must the reabsorbed. The partonic cross section is Taylor-expanded in orders of α_S and physical quantities are approximated with a truncation to a given order. The α_S value is dependent on an arbitrary scale μ_R called the renormalization scale needed to renormalize the strong coupling. When introducing PDFs in the computation, a need for another scale appears to absorb divergencies. PDFs and the partonic cross section are made dependent on a so-called factorization scale, that can be physically motivated as a factorization of the short-distance physics of the hard scatter from the long-distance physics. In summary, the master formula for a generic $pp \to N$ scattering reads as

$$\sigma(pp \to N) = \sum_{ab} \int dx_1 dx_2 f_a(x_1, \mu_F) f_b(x_2, \mu_F) \times \hat{\sigma}(ab \to N; \mu_F; \mu_R, \alpha_S(\mu_R)) \tag{4.14}$$

where a, b are the partonic species involved in the scattering, x_1, x_2 their fraction of the proton momenta and f_1 and f_2 their PDFs with the dependence on μ_F and μ_R is made explicit. The new scales are in principle non-physical. When computing σ to all orders in α_S, the dependency on μ_F and μ_R disappears. However, at any finite order, the calculated cross section depends on both μ_F and μ_R and [193]. This dependence is usually more significant at lower orders in α_S. The most reliable predictions are obtained when the order of α_S is high enough to reduce significantly the dependence of the cross section on μ_F, μ_R, however, this is not attainable for most of the processes investigated at the LHC such as VBS, where the choice of the factorization and normalization scales is of primary importance. Typically, both the renormalization and factorization scales are chosen to be close to the natural scale of the problem like the four-momentum transfer Q or $\hat{s}$ [194]. Uncertainty on the predictions due to missing higher order terms can be roughly estimated by varying both μ_F and μ_R, typically in the interval from 0.5μ to 2μ.

The MADGRAPH5_AMC@NLO Monte Carlo program allows one to specify a fixed value for the scales for each of the generated events or to dynamically compute a proxy for the natural scale of the process. The functional forms are arbitrary, but commonly one of the following

WV Analysis	Generator parameter						
	lhaid	dyn_scale	cut_decays	ptl	etal	drjj	mmjj
SM	306000	-1	False	0	0	0.4	100
EFT	325300	3	True	10	3.0	0.01	40
	OS		SCRAM		CMSSW		MG
SM	sl6		gcc481		7_1_30		2.4.2
EFT	sl7		gcc700		10_6_19		2.6.5
	lamWS		AWS		rhoWS		etaWS
SM	2.253e-01		8.080e-01		1.320e-01		3.410e-01
EFT	-		-		-		-
	MT	MTA	MZ	MH	MW	GF	aS
SM	1.730e+02	1.777e+00	9.1188e+01	1.250e+02	80.419	1.16639e-05	1.180e-01
EFT	1.727e+02	0.000	9.1187e+01	1.251e+02	80.387	1.16637e-05	1.179e-01
	ymt	ymtau	decay_T	decay_TA	decay_Z	decay_W	decay_H
SM	1.730e+02	1.777e+00	1.491e+00	2.270e-12	2.441e+00	2.049e+00	6.382e-03
EFT	1.727e+02	0.000	1.330e+00	0.000	2.495e+00	2.045e+00	4.070e-03

Table 4.10: Summary table comparing different generator parameters regarding PDF sets (lhaid), dynamical scale functional form (dyn_scale), generator-level selections (ptl, etal, drjj, mmjj), software environment (OS, SCRAM, CMSSW), MADGRAPH5_AMC@NLO version (MG), CKM parameters in Wolfenstein parametrization that are only present for the SM generation as in the EFT the CKM matrix is assumed to be diagonal (lamWS, AWS, rhoWS, etaWS). Differences are present in the two UFO models for masses and decays definitions (M, decay) for top quark, τ lepton and heavy vector bosons W, Z, h as well as Yukawa couplings (ym) for the top quark and τ lepton. Lastly different values for the QCD coupling aS and Fermi constant GF are present.

options is implemented at the LO level (for a complete description see Ref. [195]):

- transverse mass of the $2 \to 2$ system resulting of a k_{T} clustering $\frac{1}{2}\sum_{i=1}^{N}\sqrt{m_i^2 + p_{T,i}^2}$.
- total transverse energy of the event $\sum_{i=1}^{N}\frac{E_i \cdot p_{T,i}}{\sqrt{p_{x,i}^2+p_{y,i}^2+p_{z,i}^2}}$.
- sum of the transverse mass $\sum_{i=1}^{N}\sqrt{m_i^2 + p_{T,i}^2}$.
- half of the sum of the transverse mass $\frac{1}{2}\sum_{i=1}^{N}\sqrt{m_i^2 + p_{T,i}^2}$.
- partonic energy $\sqrt{\hat{s}}$.

It is therefore clear that the particle multiplicity of the hard scattering defined in MADGRAPH5_AMC@NLO plays a fundamental role in the computation of μ_F and μ_R, which in turn affect the computation of inclusive and differential cross-sections.

A comparison of the two samples has been done at the parton level, however when comparing a $2 \to 4$ with a $2 \to 6$ generation one needs to be careful in applying a common phase space selection. In order to do so, events from the $2 \to 6$ generation have been filtered by requiring a dijet pair in the final state, decay products of a V boson (V=$W^{\pm}$, Z). The remaining dijet pair in the event is assumed to be one of scattered VBS partons. The latter are required not to be decay products of a vector boson. Events, where neither of the four jets is produced by a decaying vector boson, are vetoed. As the $2 \to 4$ generation applies a dijet invariant mass greater than 100 GeV, the algorithm was tested on the existing SM sample and summarised in Figure 4.14, where it is shown that one recovers successfully the generator level selections.

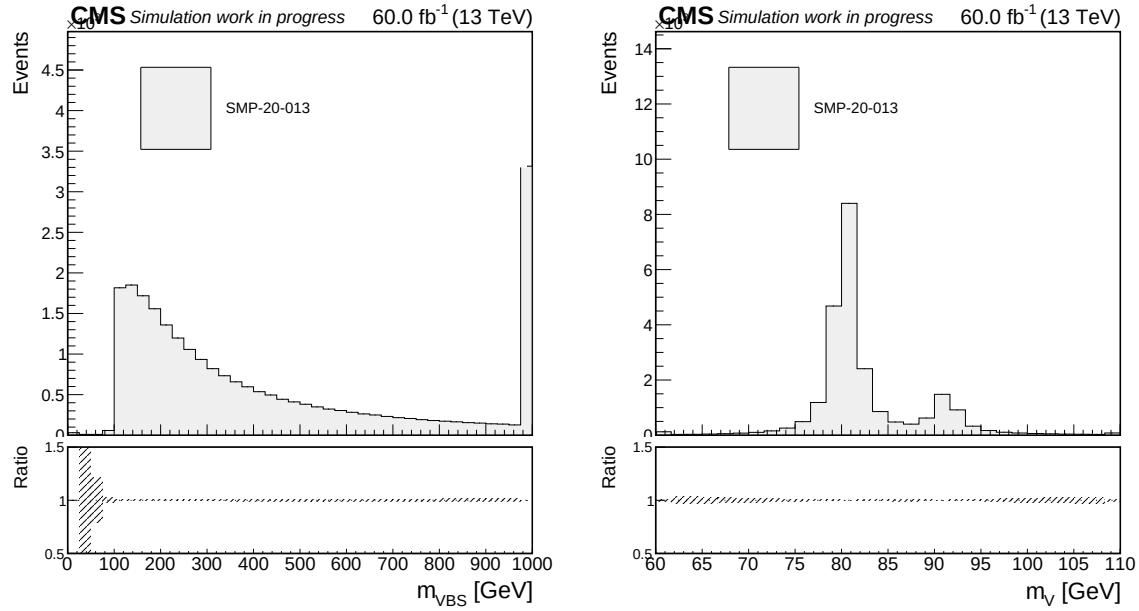

Figure 4.14: Parton level differential distributions for m_{jj}^{VBS} (left) and m_{jj}^{V} (right), the reconstructed invariant mass of the hadronically decaying vector boson with the existing SM VBS WV sample for the EW signal. The sample is generated as a $2 \to 4$ process with a $m_{jj}^{\mathrm{VBS}} > 100$ GeV cut. The knowledge of the two jets at matrix-element is lost after the decay of the V boson ($\mathrm{W}^{\pm}$ or Z) producing two additional jets in the final state. While for the existing $2 \to 4$ sample it is possible to tag exactly the four jets, though particle history, this is not possible for the $2 \to 6$ one. This figure shows that the tagging algorithm employed, agnostic in the decay history, correctly reproduces the $m_{jj}^{\mathrm{VBS}} > 100$ GeV cut used in the existing $2 \to 4$ sample (left) and the invariant mass of the hadronically decaying vector bosons (right). This fact validates the algorithm and allows us to identify a common phase space where the two samples can be compared. It is shown that the jet-tagging algorithm used to identify VBF-jets and V-jets in a 6-particle final state correctly reproduces the gen level selection of $m_{jj}^{\mathrm{VBS}} > 100$ GeV.

Kinematic selections are applied to both $2 \to 4$ and $2 \to 6$ processes to cover for the differences in the generators parameters as highlighted in Table 4.10, namely a minimum invariant mass for all dijet pairs of 40 GeV, the R distance for all pairs of lepton-jet pairs and dijet pairs is required to be greater than 0.4. Additional kinematic selections are applied to restrict the phase space closer to the analysis region, namely a VBS invariant mass greater than 300 GeV, transverse momentum for the two leading p_T jets greater than 50 GeV and greater than 30 GeV for the remaining ones, charged lepton transverse momentum and MET greater than 30 GeV. Both jets and the charged lepton are required to be within the acceptance of CMS namely $|\eta_l| < 3.0$ and $|\eta_j| < 4.7$. Additional stratification is made by requiring regions with 0,1 and 2 b-jets to isolate different process contributions. Results are shown in Figure 4.15 for the $W^+ \to e^+\nu_e$ case only. The existing $2 \to 4$ SM samples ($W^{\pm}Z$, W^+W^- and W^+W^+) have been scaled by a factor 0.327 that is the branching fraction for $\Gamma(W \to e\nu_e)/\Gamma(W \to l\nu_l)$. An arbitrary luminosity of 60 fb^{-1} is assumed as a proxy for the luminosity recorded by CMS in 2018.

A disagreement is observed both in the overall cross-section and in the high-energy dependence of the $2 \to 6$ generations with respect to the $2 \to 4$. The disagreement is more pronounced in the 0 b-jet region that corresponds roughly to the signal region. Regions containing b-jets present a significant contribution from processes involving top quarks. In particular, the

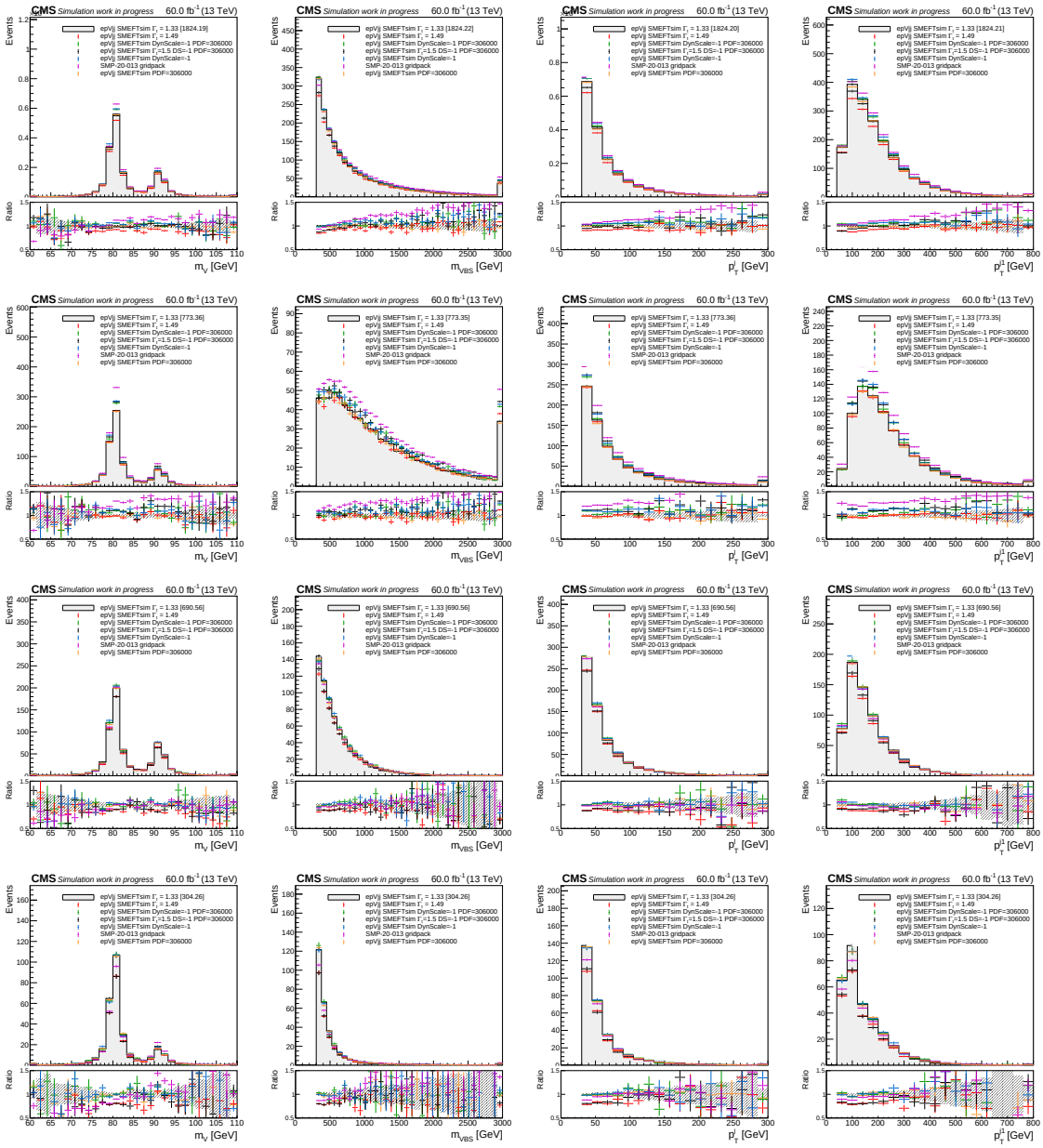

Figure 4.15: Parton level comparison of the existing VBS WV sample used for the SM analysis (SMP-20-013) produced as a $2 \rightarrow 4$ process and the SM reweighted sample used for the EFT interpretation (epVjj) with different values of generator parameters such as top width Γ_t, different choice of the dynamical scale functional form, different set of PDFs. From top to bottom differential distribution in an inclusive region and 0,1,2 b-jet regions are shown. From left to right the figures display the differential distributions of the invariant mass of the dijet system compatible with the hadronic vector boson decay m_{jj}^{V}, the dijet invariant mass of the VBS system m_{jj}^{VBS}, the lepton p_T and the p_T of the leading jet.

2 b-jets region is dominated by $t\bar{t}$. The latter corresponds approximately to the analysis top control region used to check the modelization of top-induced backgrounds. The disagreement is partially recovered when changing the dynamical scale functional form, suggesting that disagreements can be due to the way MADGRAPH5_AMC@NLO computes the natural scale of the process. This is checked by fixing both the factorization and renormalization scale to a constant value. An arbitrary value of $\mu_F = \mu_R = m_Z \sim 91.1880$ GeV was chosen for the test. Results are shown in Figure 4.16, where it can be seen that the shape disagreement for all distributions is negligible.

Only an overall normalization of approximately 15%, not covered by the statistical uncertainty, is observed in the 0 b-jet region, populated mostly by the EW-induced VBS signal. The origin of this disagreement can be traced back to the different number of diagrams involved and to the different parameters employed by the two generations. This assumption is justified by the fact that the normalization disagreement is not observed in the 1 and 2 b-jet regions. Here the set of diagrams involved for the $2 \to 4$ and $2 \to 6$ exactly coincide because the top quark decays for more than 99% of the cases in a Wb pair. The normalization deficit in the signal region for the $2 \to 6$ sample seems to agree with an observed EW-only signal strength for the $2 \to 4$ generation of $0.85^{+0.23}_{-0.21}$[105], further justifying the usage of the $2 \to 6$ SM generation of the EFT interpretation. Additional checks have been carried out at full reco-level including parton shower, detector interaction and reconstruction, to assess the overall data-MC agreement in all analysis regions and retrieve significances and observed signal strength for the alternative $2 \to 6$ production. The results will be described in Section 4.3.3.

4.3.3 Closure with SM WV analysis

The VBS WV$\to$ $lvjj$ analysis has been reproduced with the reweighted SM MC sample. The same strategy described in Section 4.1.2 is adopted. Figures of merit to assess the closure with the official analysis are the observed signal strength μ_{EW} and significance σ_{EW} for the EW signal, keeping the QCD WV production contribution fixed to the SM prediction $\mu_{\text{QCD}} = 1$. Also, visual inspection of the post-fit distributions, using the parameters extracted from the EW-only fit performed on the data, is useful to address possible differences, especially in the signal-enriched regions. The full Run II dataset collected by the CMS experiment has been used. Table 4.11 summarises the significance comparison across the years with the official analysis with the reproduced one, showing a good agreement. The expected significance is computed by fitting to data in all regions, profiling all uncertainties while fixing $\mu_{\text{EW}} = 1$. The difference between the significance comes from the additional uncertainty on the EFT reweighted SM sample. In the official SM analysis, the QCD scale uncertainty is computed as an envelope of eight templates varying $k \cdot \mu_F$ and $k \cdot \mu_R$ for $k \in [0.5, 1.0, 2.0]$ around the nominal scale. For the reweighted SM sample starting from an EFT phase space, the same uncertainty is computed as an envelope of 44 templates computed varying $k \in [0.5, 1.0, 2.0]$ and for all possible scale choices reported in Section 4.3.2 as to cover for the discrepancies between the existing $2 \to 4$ SM simulation and the reweighted $2 \to 6$ one.

Post-fit distributions of the input templates for the SM measurement are shown in Figure 4.17 for both the resolved and boosted regions. The ratio of observed data and MC expectation in the W+jets control regions is very close to one as the normalization of each bin of the W+jets template is free to float in the maximum likelihood fit to correct the trends observed for the W+jets simulation in a data-driven fashion.

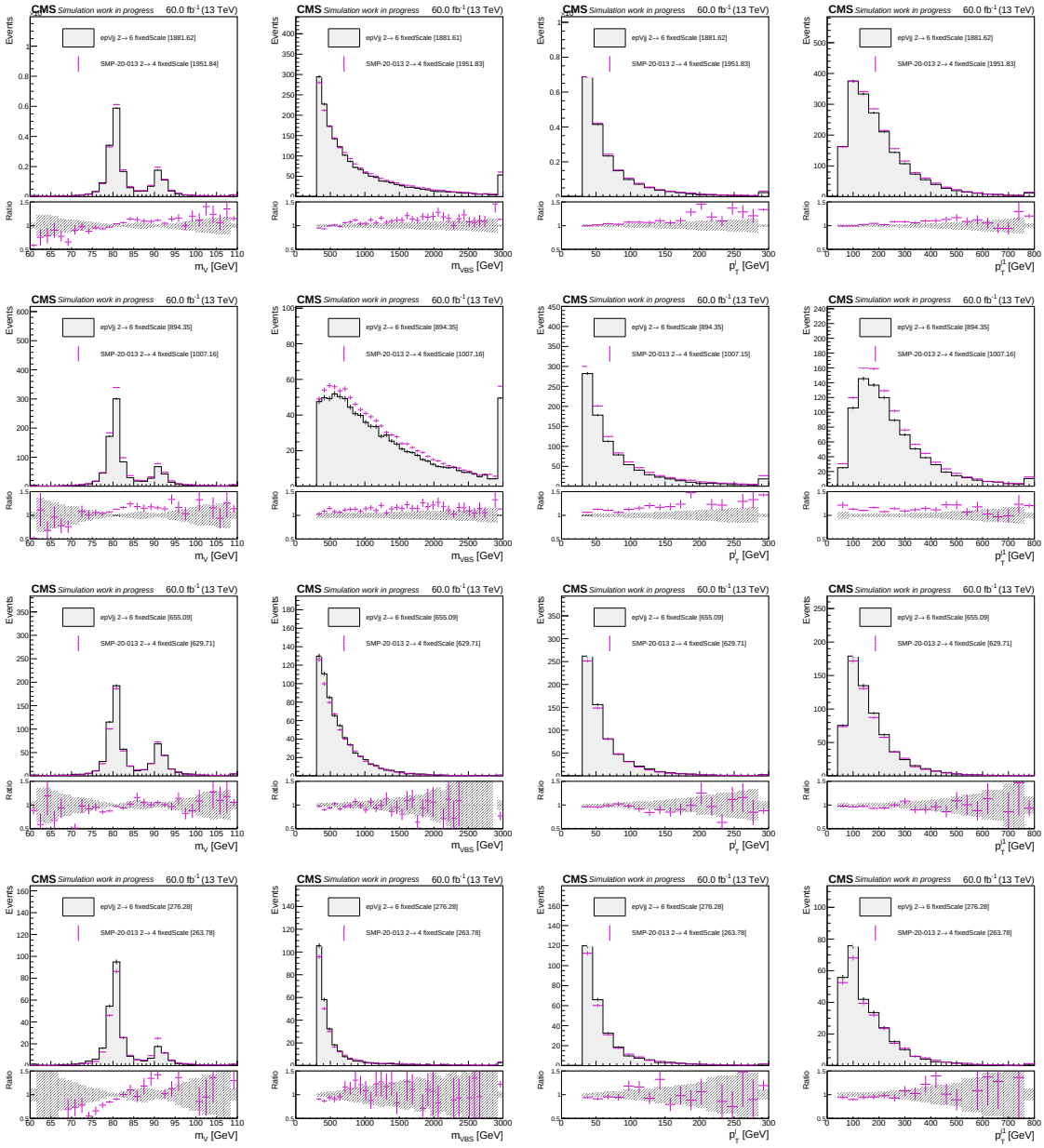

Figure 4.16: Parton level comparison of the existing VBS WV sample used for the SM analysis (SMP-20-013) produced as a $2 \rightarrow 4$ process and the SM reweighted sample used for the EFT interpretation (epVjj) by fixing the normalization and factorization scales μ_F, μ_R of both generations to a fixed value of 91.1880 GeV. From top to bottom differential distribution in an inclusive region and 0,1,2 b-jet regions are shown. From left to right the figures display the differential distributions of the invariant mass of the dijet system compatible with the hadronic vector boson decay m_{jj}^{V}, the dijet invariant mass of the VBS system m_{jj}^{VBS}, the lepton p_T and the p_T of the leading jet.

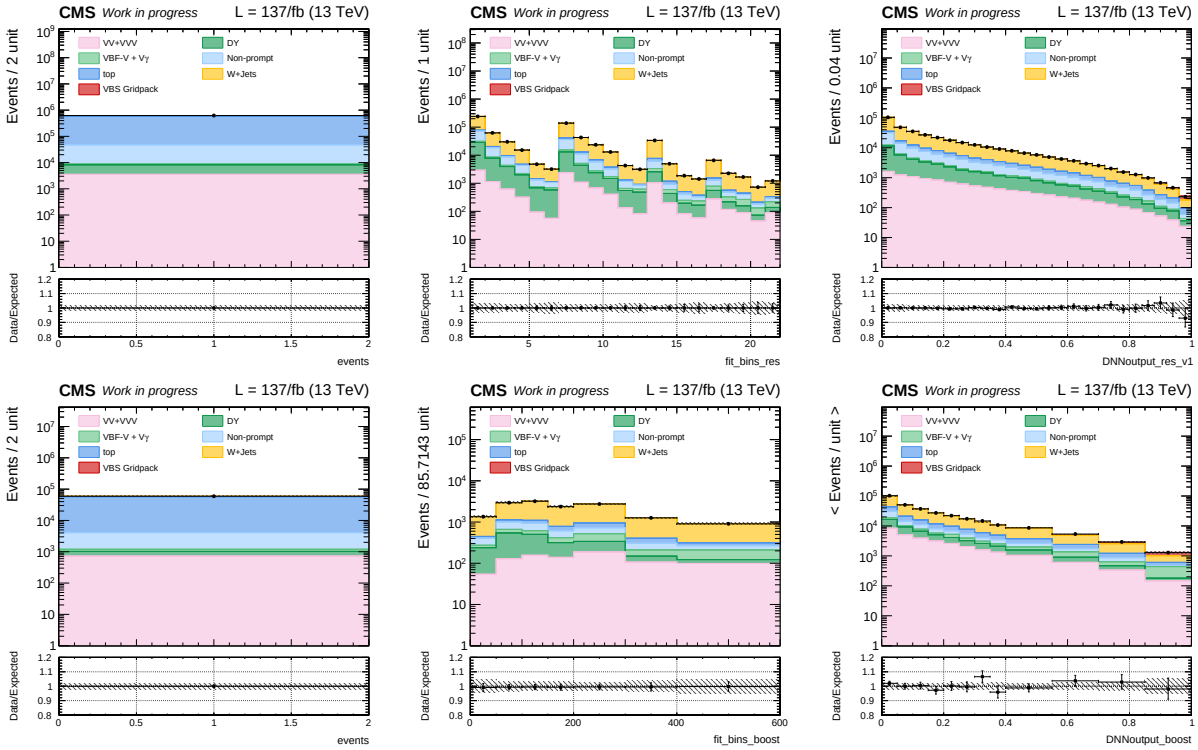

Figure 4.17: Postfit distributions of the input templates to the SM fit. Upper row 2017+2018 resolved regions, bottom row boosted regions. From left to right top CR, W+jets CR and the signal region. The uncertainty band on the background estimate is taken from a signal plus background fit. The signal is plotted stacked on the background with a solid red colour. The W+jets CR presents a perfect agreement as each bin of the W+jets background is free to float in the maximum likelihood fit.

		SM Analysis				EFT Analysis			
σ	Category	2016	2017	2018	Combined	2016	2017	2018	Combined
Expected	Boosted	2.3	2.0	2.7	3.7	2.0	1.7	2.1	3.1
	Resolved	2.4	1.8	3.2	3.6	2.1	1.4	2.9	3.8
	Combined	3.1	2.6	4.1	5.3	2.5	1.9	3.5	4.7
Observed	Boosted	1.4	1.5	3.8	3.8	1.2	1.6	3.8	3.7
	Resolved	2.4	0.0	3.7	3.6	1.7	0.0	3.7	3.6
	Combined	2.2	0.7	4.9	4.4	2.0	0.7	5.0	4.6

Table 4.11: Expected (data-Asimov) and observed significance for the 2016, 2017, and 2018 years and their combination and split for boosted and resolved regimes. Columns for the SM analysis refer to the results obtained with the existing $2 \rightarrow 4$ SM sample as described in Ref. [105] while the EFT analysis columns report the same results using the reweighted SM sample starting from an EFT phase space.

4.4 EFT Analyses regions

New regions are defined for maximal sensitivity to EFT effects. As EFT dimension-six operators are only included in the purely EW VBS production, the output of the DNN is used to identify phase space regions with a high signal-over background ratio. The overall structure of the SM analysis, including the boosted and resolved W+jets and top control regions is retained for the extraction of the limits on the Wilson coefficients. EFT contributions in those regions for some observables and all the years are shown in Figure 4.18 for the top CR and in Figure 4.19 for the W+jets CR. Both the boosted and resolved signal regions are split into a low DNN signal region DNN$\leq$ 0.5, or EFT control region, and a high DNN signal region DNN$>$ 0.5 or EFT signal region. While the latter is expected to give the strongest constraints on the dimension-six operators, the former is still included in the fit for additional statistics. The yield for all the backgrounds and the EFT signal templates according to the model defined in Section 4.2.4 are provided in Table C.1 for 106, Table C.2 for 2017 and Table C.3 for 2018 and all the analysis regions in Appendix C.

4.5 Optimal observable for EFT limit setting

The EFT VBS WV interpretation involves eigth dimension-six operators that induce different types of dynamics with respect to the purely EW SM prediction. Many operators introduce novel coupling configurations and present intricate kinematic features. While analyzing only a single kinematic variable, such as transverse momenta, invariant masses or angular correlations, typically fails to efficiently limit the entire parameter space it can yield sub-optimal physics results that are easily interpretable by both the experimental and theoretical communities. Using a handful of handpicked binned observables to constrain the EFT parameter space can be optimal for a specific operator subset. However, there can be directions with limited or no sensitivity. The choice of the optimal observable to constrain EFT at dimension six is an active area of research and typically involves Machine Learning techniques to engineer high-level discriminants that can fully capture the EFT dynamics over a wide range of features [196, 197]. While these approaches yield optimal constraints, their interpretation is non-trivial and therefore they have been neglected in this work. Instead, physics-driven observables have been studied to understand their behaviour under the influence of the selected set of dimension-six operators. A strategy similar to the one explained in Section 2.3.1.8 is employed with few differences. Instead of building the likelihood with the insertion of only one operator at a time,

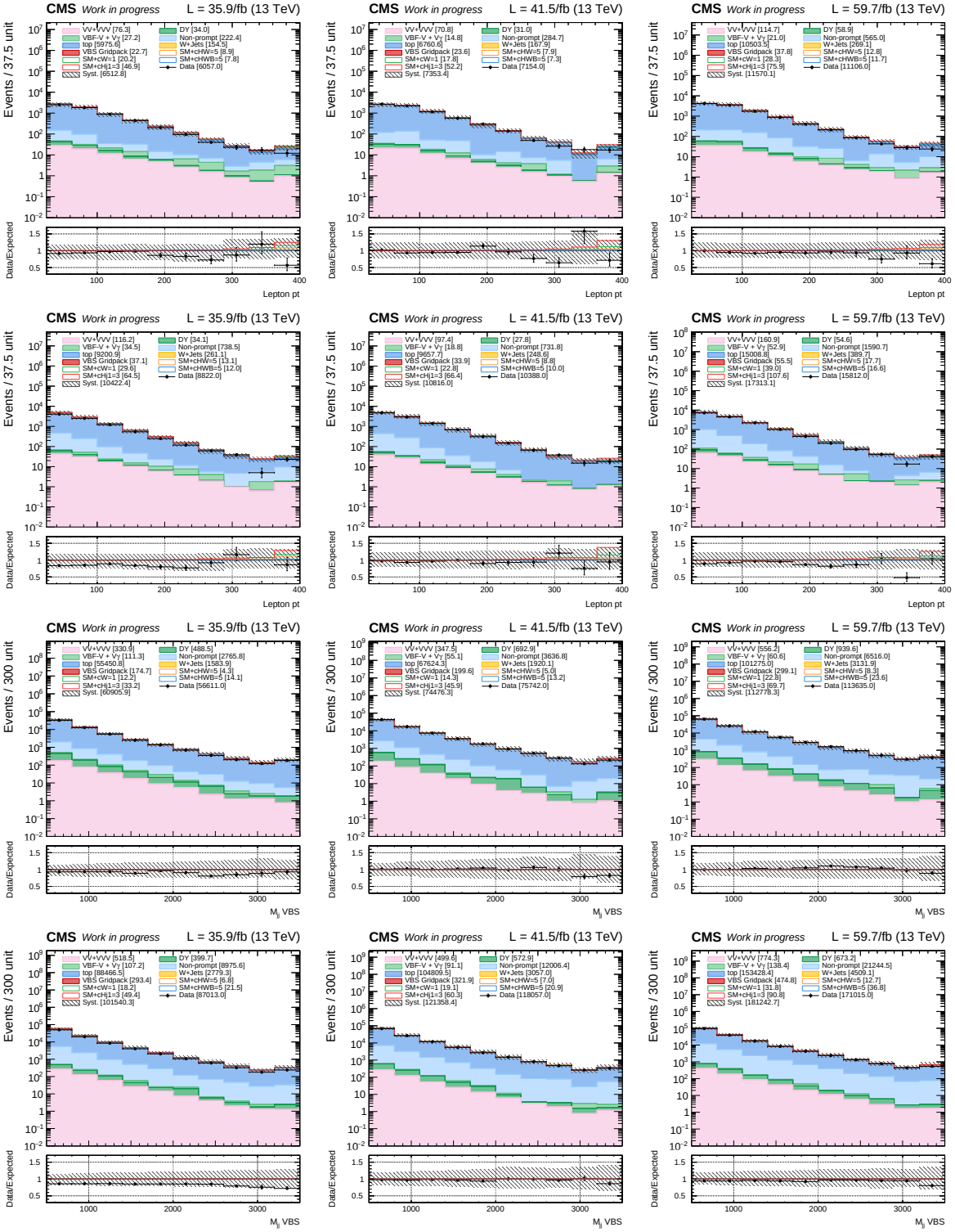

Figure 4.18: Differential distributions in the top CR from the VBS WV analysis. EFT contributions from Q_W, Q_{HWB}, Q_{HW} and $Q_{Hj}^{(1)}$ are included and shown as solid coloured lines stacked on top of the backgrounds and SM VBS signal. From top to bottom, the rows show the charged lepton p_T in the resolved electron and muon categories and the m_{jj}^{VBS} in the boosted electron and muon regions. From left to right the distributions in the 2016, 2017 and 2018 years are shown.

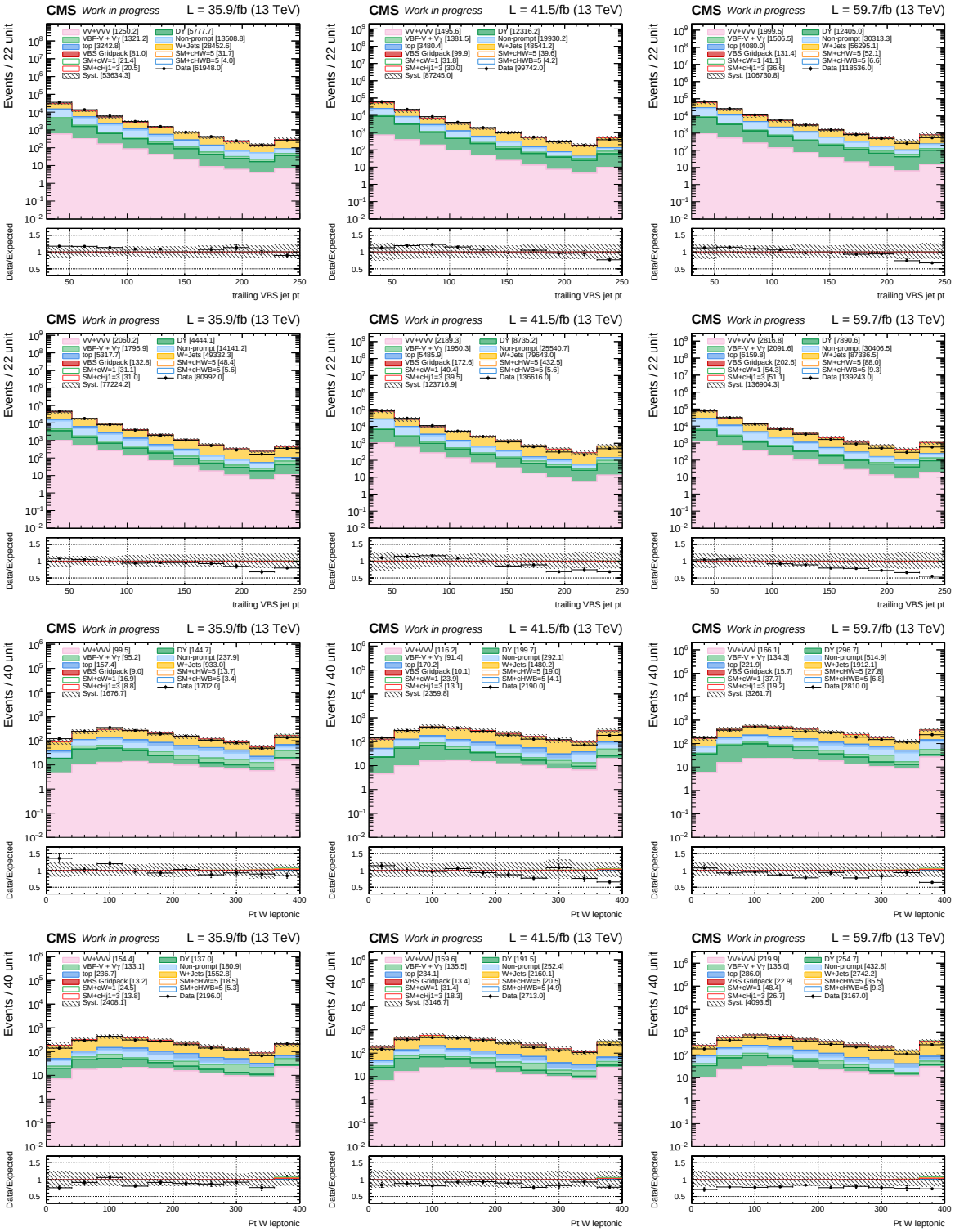

Figure 4.19: Differential distributions in the W+jets CR from the VBS WV analysis. EFT contributions from Q_W, Q_{HWB}, Q_{HW} and $Q_{Hj}^{(1)}$ are included and shown as solid coloured lines stacked on top of the backgrounds and SM VBS signal. From top to bottom, the rows show the p_T of the leading VBS jet in the resolved electron and muon categories and the p_T of the leptonically decaying W boson in the boosted electron and muon regions. From left to right the distributions in the 2016, 2017 and 2018 years are shown.

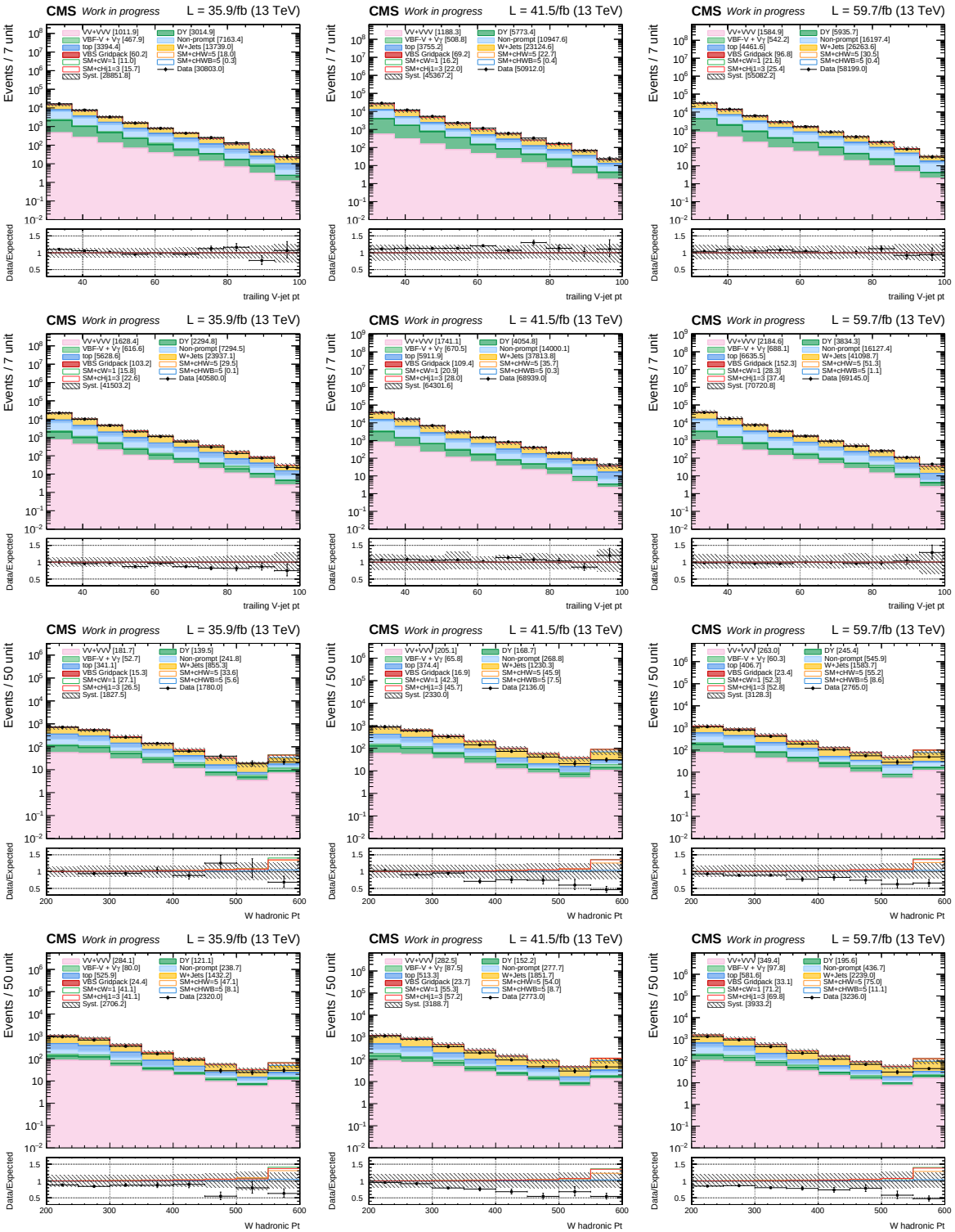

Figure 4.20: Differential distributions in the DNN<0.5 regions from the VBS WV analysis. EFT contributions from Q_W, Q_{HWB}, Q_{HW} and $Q_{Hj}^{(1)}$ are included and shown as solid coloured lines stacked on top of the backgrounds and SM VBS signal. From top to bottom, the rows show the leading p_T of the jet from the hadronically decaying vector boson in the resolved electron and muon categories and the p_T of the hadronically decaying vector boson in the boosted electron and muon regions. From left to right the distributions in the 2016, 2017 and 2018 years are shown.

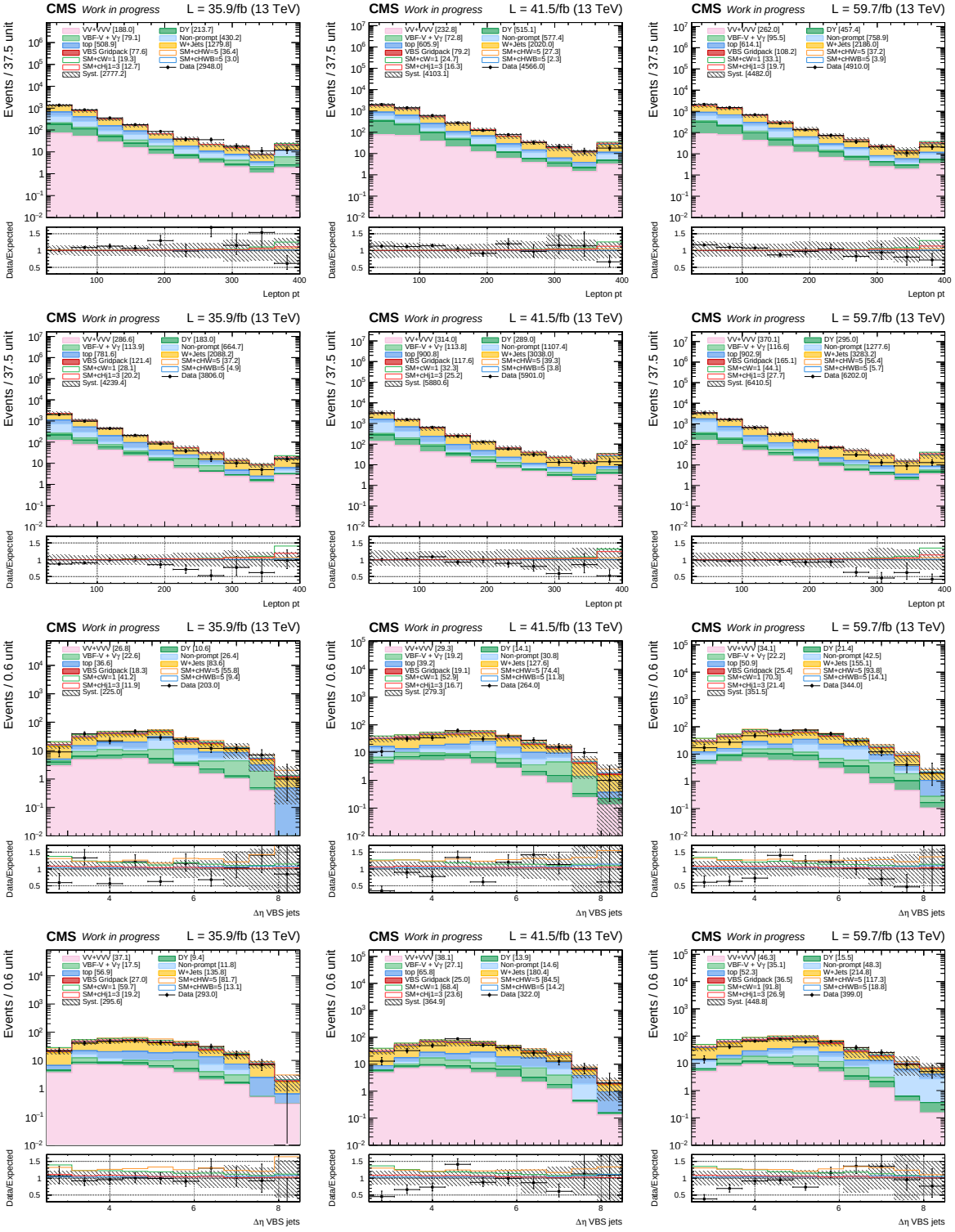

Figure 4.21: Differential distributions in the DNN>0.5 region from the VBS WV analysis. EFT contributions from Q_W, Q_{HWB}, Q_{HW} and $Q_{Hj}^{(1)}$ are included and shown as solid coloured lines stacked on top of the backgrounds and SM VBS signal. From top to bottom, the rows show the charged lepton p_T in the resolved electron and muon categories and the $\Delta\eta_{jj}^{\text{VBS}}$ in the boosted electron and muon regions. From left to right the distributions in the 2016, 2017 and 2018 years are shown.

performing a maximum likelihood fit, and extracting the 1σ interval, the likelihood is built with all the dimension-six operators. Each Wilson coefficient is then fitted to each differential distribution and all the other ones are left free to float in the minimization and profiled out. In this way, the expected sensitivity also accounts for all relevant correlations between the Wilson coefficients which would be otherwise neglected. It is important to highlight that it is not expected for a single observable to dominate the sensitivity for all the operators as the latter typically induce different physical effects. The study has been conducted on the 2018 dataset only, in the boosted EFT signal region with a DNN$>$ 0.5 selection as this is the region that is expected to dominate the analysis sensitivity. While we assume the SM in the signal region, thus fixing all Wilson coefficients to zero at the best-fit point, the W+jets differential correction and the top sample normalization are left free to adapt to the observed data in the control regions in order to obtain a more realistic estimate and to not bias the result with data from the control regions. All differential distributions of the observables are built with a conservative number of bins $N = 10$. The studied observables are related to the dynamics of the leptonically decaying W boson, of the VBS tagged jets and to the product of the hadronically decaying V boson and are listed in the following, where Z is the Zeppenfeld variable [182] and C is the centrality: $p_T^{\mathrm{VBS},1}$, $p_T^{\mathrm{VBS},2}$, $\mathrm{Z_{V,1}}$, p_T^{V}, m_{jj}^{VBS}, p_T^l, $\Delta\eta_{\mathrm{VBS}}$, Z_l, $\mathrm{DNN_{boost}}$, m_{WV}, $\mathrm{N_{jets}}$, $\mathrm{N_{events}}$, $p_T^{\mathrm{W},l}$, $\Delta\phi_{\mathrm{VBS}}$, η^l, $\mathrm{C_{WV}}$. The results of the observable ranking for all the operators are reported in Figure 4.22 where it can be clearly stated that for all the operators, the invariant mass of the WV system is the optimal observable.

The latter is defined as

$$m_{\mathrm{WV}} = \begin{cases} \sqrt{(p^{\mu}_{\mathrm{W},lep} + (p^{\nu}_{\mathrm{V,AK4,1}} + p^{\nu}_{\mathrm{V,AK4,2}}))^2} & \text{resolved} \\ \sqrt{(p^{\mu}_{\mathrm{W},lep} + p^{\mu}_{\mathrm{V,AK8}})^2} & \text{boosted} \end{cases} \tag{4.15}$$

where p^{μ}_{V} is the four momenta of the hadronically decaying V-boson and $p^{\mu}_{\mathrm{W},lep}$ the four momenta of the leptonically decaying W boson. The $p^{\mu}_{\mathrm{W},lep}$ can be reconstructed assuming that all the missing transverse energy is entirely due to the transverse component of the neutrino. Enforcing a constrain on the W mass peak $m_{\mathrm{W}} = \sqrt{(p^{\mu}_l + p^{\mu}_{\nu})^2} = 80.379\,\mathrm{GeV}$ results in two solutions for the longitudinal momentum of the neutrino:

$$p_{z,\nu} = \frac{\alpha \cdot p_{z,l}}{p^2_{T,l}} \pm \sqrt{\frac{\alpha^2 \cdot p^2_{z,l}}{p^4_{T,l}} - \frac{E^2_l \cdot p_T^{\mathrm{miss}^2} - \alpha}{p^2_{T,l}}} \tag{4.16}$$

with $\alpha = m^2_{\mathrm{W}} + \bar{p}_{T,l} \cdot \bar{p}_T^{\mathrm{miss}}$. The $p_{z,l}$ is defined as the smaller absolute value in the case of two real solutions or as the real part in the case of a complex solution.

This variable is the one that will be used for the extraction of the final limits including all regions and nuisances. A dedicated binning choice is needed when considering backgrounds in order to cope with the limited statistics from the Monte Carlo samples, especially in the tails of the distributions of the DNN$>$ 0.5 region where the background statistic is smaller. The final m_{WV} EFT discriminant is optimized for boosted and resolved regions. In the former one, the VBS WV analysis can probe harder regimes up to approximately 3 TeV. The fit observable is then built with eight bins, that optimize the number of background MC events in the tail of the distribution, with variable bin width {200, 400, 600, 800, 1000, 1200, 1500, 2000, 3000} GeV for both the DNN$<$ 0.5 and DNN$>$ 0.5 regions. The resolved regime on the other hand

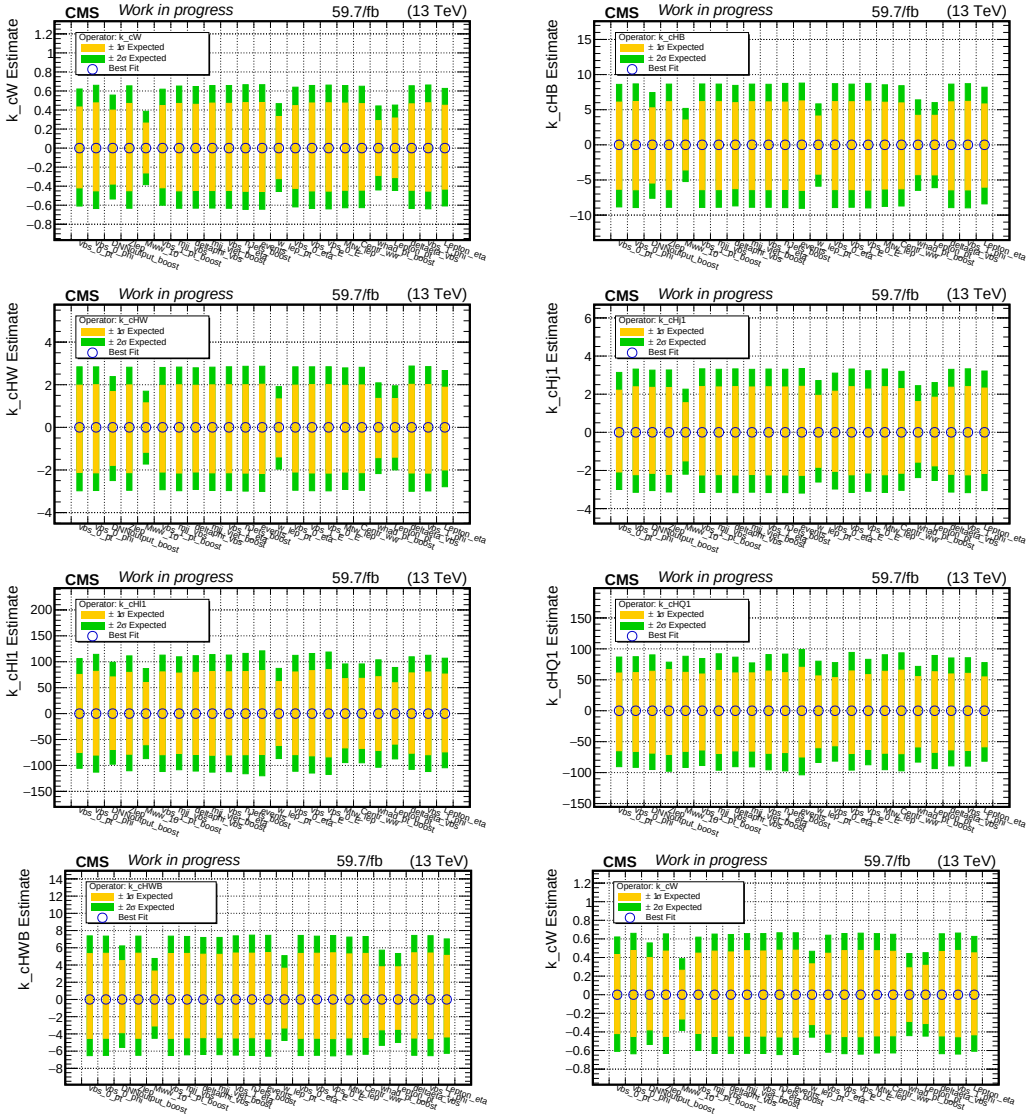

Figure 4.22: Observable ranking in the boosted DNN$>$ 0.5 analysis region with 2018 data. For each operator the likelihood is constructed with a 10 bins template and all the remaining Wilson coefficients are profiled in the minimization, treating them as unconstrained nuisances. All W+jets differential correction and top normalization parameters are left free to float in the fit and measured from data in their respective control regions. Yellow and green bands correspond respectively to 1 and 2 S.D. The SM is assumed in the signal region fixing the best-fit expected value for all Wilson coefficients to zero.

probes softer interactions reaching reliable MC predictions for the backgrounds up to 2 TeV. The fit observable in both resolved DNN$<$ 0.5 and DNN$>$ 0.5 regions is built with six bins with variable bin width {200, 400, 600, 800, 1000, 1200, 2000} GeV. All the observables entering in the fit for the extraction of the EFT sensitivity are shown blind in Figure 4.23

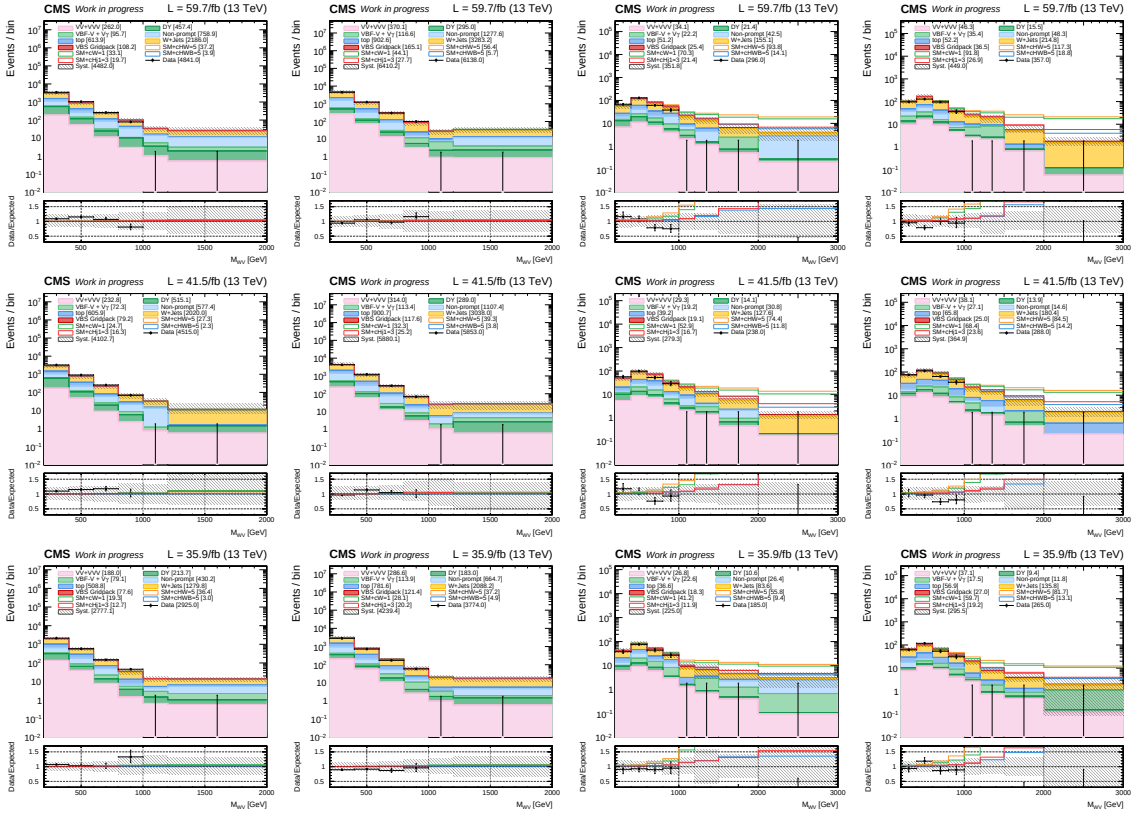

Figure 4.23: m_{WV} observable in the EFT signal region after a DNN$>$ 0.5 selection. Differential distributions are blinded for $m_{\mathrm{WV}} > 1000$ GeV. These templates are the ones used to extract the expected limits on dimension-six EFT coefficients, which effect is represented as solid coloured lines above the SM background for Q_W, Q_{HW}, Q_{HWB} and $Q_{Hj}^{(1)}$. From top to bottom, the rows show the m_{WV} distributions for 2018, 2017 and 2016. From left to right resolved electron, muon and boosted electron and muon.

4.6 Results

The expected limits on the eight dimension-six Wilson coefficients have been extracted under different hypotheses. As discussed in Section 2.3.2, one-dimensional fits are extracted both by fixing all Wilson coefficients to their SM value of zero or by treating them as unconstrained nuisance parameters in the likelihood minimization and profiling them out. For the former scenario, a comparison between limits obtained including terms up to Λ^{-2} versus including also the quadratic terms at order Λ^{-4} is done in order to assess the validity of the EFT expansion in the energy regime probed by this analysis. As VBS is intrinsically sensitive to dimension-eight effects, it is important to understand whether the computed limits suffer from the missing higher order terms, specifically the interference between the SM and dimension-eight operators at order Λ^{-4} that could cancel the positive growth of the quadratic terms at dimension-six. Bi-dimensional scans are also provided, fixing all other Wilson coefficients to 0, in order to better understand the correlation between the parameters. The sensitivity to the

single Wilson coefficients at 68% and 95% C.L is extracted from the likelihood profile by requiring $-2\Delta \log \mathcal{L} < 1$ and $-2\Delta \log \mathcal{L} < 3.84$ respectively. For bi-dimensional scans the intervals are instead $-2\Delta \log \mathcal{L} < 2.30$, $-2\Delta \log \mathcal{L} < 5.99$ [44]. In all the reported results, all Wilson coefficients best-fit values are enforced to be 0 as predicted by the SM in order to blind the analysis. Data are used in the control regions in order to derive the data-driven W+jets differential correction and to measure the top sample cross-section.

The most realistic procedure in order to obtain unbiased limits on the Wilson coefficients is to let all the parameters to freely float in the minimization as described in Section 2.3.5. This can ensure correct matching of the EFT onto complete UV models and limits the model dependence of the computed results. Due to technical limitations, this procedure is only applicable to fits including linear and quadratic terms, as including only interference terms could lead to negative bin yields of the full EFT description for some value of the Wilson coefficients thus leading to non-physical results.

Results of individual fits, letting only one operator floating and freezing the other one to zero (both at linear Λ^{-2} and quadratic Λ^{-4} level) are compared to the profiled limits obtained by letting all operators floating in the maximum likelihood fit as shown in Figure 4.24. Bi-dimensional likelihood profiles for all possible operator permutations are shown in Appendix C. The likelihood profiles used to build Figure 4.24 are reported in Figure C.1 in Appendix C.

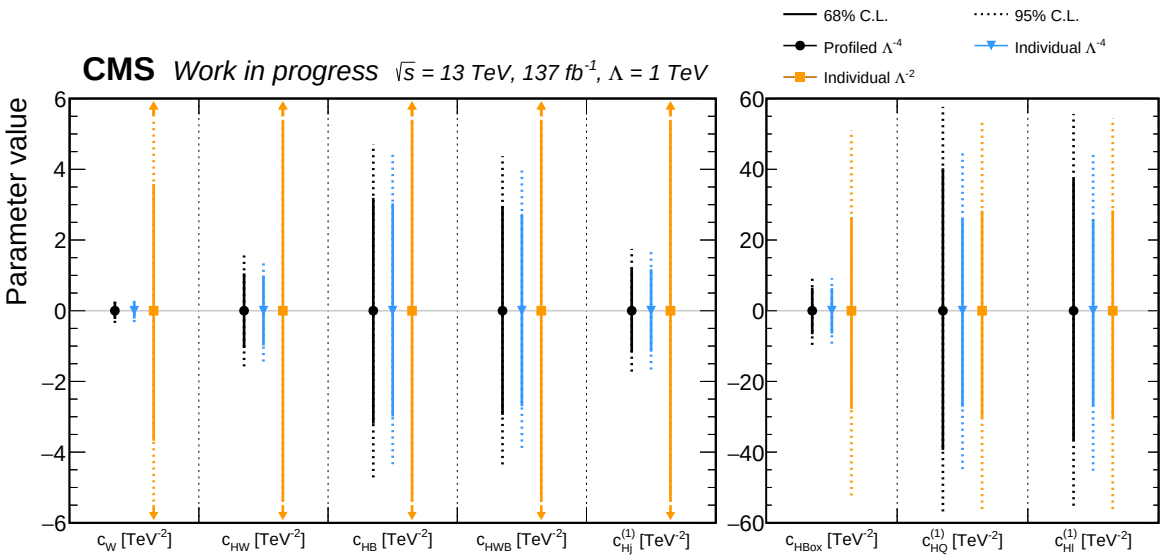

Figure 4.24: Expected sensitivity to the eight dimension-six operators, reported on the x-axis, considered in the VBS WV Run II analysis (137 fb^{-1}). The sensitivity is computed while letting all Wilson coefficients free to float in the maximum likelihood fit, a procedure that includes both linear and quadratic components, represented as black solid lines for the 68% C.L. and with dashed lines for 95% C.L. Additionally, limits are obtained by freezing all other Wilson coefficients except for the one of interest both including quadratic components at order Λ^{-4} (Blue lines) and including linear only components at order Λ^{-2} (Orange lines).

As the likelihood profile shows some degenerate directions in the EFT parameter space especially for $c_{Hl}^{(1)}$ and $c_{HQ}^{(1)}$, the profiled minimization performed including all nuisance parameters can be problematic and the profiled likelihoods for the operators present a highly oscillating and non-smooth behaviour. The origin and solution for this problem, of a technical nature, is

described in the following Section 4.6.1.

4.6.1 Navigating likelihood local minima

The shape of the multidimensional likelihood when considering all the eight dimension-six Wilson coefficients and all the nuisance parameters can be highly non-trivial. Interference between the EFT parameters and the SM may cause multi-dimensional local minima in the $-2\Delta\log\mathcal{L}$ profile, leading to discontinuities in the profiled scans in cases where the fit gets stuck in a local minimum. This is a common problem in Machine Learning (ML) where cost functions used in neural networks are non-convex and present both local and global minima. To avoid the minimization of getting stuck on gradient-zero points (either maxima or local minima), ML typically exploits the Stochastic Gradient Descent algorithm that solves the problem by adding an element of randomness to the search effectively reaching global minima in most cases. When working with profiled EFT fits and the statistical model described in Section 4.2.4 the problem of local minima becomes more apparent. When performing a maximum likelihood fit to one Wilson coefficient c_{POI}, letting all the others $\bar{c}$ to freely float in the maximization, one maximizes the full likelihood as a function of $\bar{c}$ at fixed c_{POI} values. All $\bar{c}$ parameters are treated as unconstrained nuisance parameters in the model and for each of them a flat prior is assigned with a user-defined range. For each value of c_{POI} the fit procedure starts from the user-defined expected values for the remaining Wilson coefficients $\bar{c}$ that correspond to zero in case the SM is assumed and to a random value in case of fit to real data. This lack of randomness in the fit procedure, initializing the profiled parameters always at the same value, may cause the likelihood of getting stuck in local minima and thus yielding discontinuous results. In order to obtain a more robust estimate of the $-2\Delta\log\mathcal{L}$, solving the discontinuities observed, we adopt the method developed by [198] to navigate false minima. This approach makes use of random starting points for the profiled parameters of interest in an arbitrary range of $[1^{-30}, 1^{30}]$. The fit is repeated n times, always drawing different and random initial points for the profiled parameters. The minimum $\min_n(-2\Delta\log\mathcal{L})$ is taken as the $-2\Delta\log\mathcal{L}$ for the given c_{POI} scan point. This procedure avoids inconsistencies in the identification of the global best-fit point. The drawback of this method is that it is computationally expensive and one does not know the apriori value for n in order for the fit to efficiently converge to the global minima. In the previous results, a value of $n = 10$ is used and always proved to be sufficient for a reliable convergence.

4.6.2 On the role of linear templates

The expected limits reported in Figure 4.24 show a significant contribution from quadratic terms with respect to the linear-only fits while considering only one Wilson coefficient and fixing all the other ones to their SM value. This often suggests a breakdown of the EFT expansion, pointing to the possibility of sensitivity to overlooked higher-dimensional effects. However, the origin of such a difference could be traced back to the choice in the generation parameters for the VBS WV signal. A problem in the linear templates was previously mentioned in Section 4.3.1.2 and shown clearly in Figure 4.13. Linear templates suffer from statistical fluctuations because the phase space, including all the eight dimension-six operators with a Wilson coefficient value of one, is dominated by quadratic components from the Q_W operator. This fact is better-justified a-posteriori as it can be seen from Figure 4.24 where the $c_W = 1$ value lies well outside the expected $2\,\sigma$ bounds meaning that the quadratic term of the EFT expansion is expected to dominate. To address this problem, and to properly populate the signal regions at high values of m_{jj}^{VBS} with respect to the generation one ($m_{jj}^{\text{VBS}} > 40$ GeV), 10 millions of event per lepton flavour and charge have been generated. This amounts to approximately 50 million

Monte Carlo signal events per year. This number might not be sufficient to properly model linear templates for some specific operators. The results should then be cross-checked with other strategies for the generation of the signal. The first strategy neglects the EFT contributions from the decay of the EW vector bosons. The VBS process is then treated as a $2 \to 4$ process and EFT contributions are only allowed in production. While this check could be biased by the reduced number of Feynman diagrams involving EFT contributions, it can properly populate the signal region as the presence of only two jets at matrix element allows to apply consistently a m_{jj}^{VBS} selection, thus resulting in a better MC description of the EFT in the high-energy regime. Secondly, the phase space of both $2 \to 4$ and $2 \to 6$ generations can be optimized to the expected sensitivity reported in Figure 4.24. Instead of sampling a phase space with all Wilson coefficients set to one, the $\pm 2\,\sigma$ bound could be used. Inside this Wilson coefficient range the contributions of the linear and quadratic EFT components should be comparable, leading to a balanced phase space for the extraction of more reliable templates. Lastly, the $2 \to 6$ generation can be optimized by a generator level cut requiring at least one dijet pair with invariant mass above a certain value, close to the one of the signal region. This should allow to better populate the analysis regions without inducing any bias in the generation that would be otherwise impossible due to the presence of four jets at the matrix element.

The results reported for the VBS WV semileptonic analysis will be carefully examined with the options previously described in future iterations of the analysis and are outside the scope of this work.

4.7 Comparison with other analyses

The expected sensitivity from the VBS WV semileptonic analysis has been compared to existing limits from the literature. Only six operators have been considered as for $Q_{Hj}^{(1)}$ and $Q_{HQ}^{(1)}$ no results in literature has been found. Furthermore, the eight operators studied in this work and reported in Table 4.8, mostly involve bosonic fields (except $Q_{Hl}^{(1)}$, $Q_{Hj}^{(1)}$ and $Q_{HQ}^{(1)}$), leading to a lack of overlap with the operator sets studied in top-related analyses. Only analyses targeting the Higgs boson signature or the ones that aim to study the EW sector of the SM have been included in the comparison.

It is not possible to always make a fair correspondence between the reported limits due to the different analysis choices. Expected C.L. obtained with a linear plus quadratic EFT parametrization has been used. If the expected results are not mentioned, the observed limits are used instead. The results from the VBS $WV \to l\nu qq$ have been reported in the profiled case while all the remaining analyses only provide individual constraints to single Wilson coefficients while freezing all the other ones to zero. While this choice could bias the comparison, it is to be reminded that the difference between the expected profiled and individual limits (including both linear and quadratic components) in this work is shown in Figure 4.24. Furthermore, profiled limits give a hint of the real achievable sensitivity in a global fit combining different final states. The results reported in this work show that no degenerate direction in the Wilson coefficients parameter space is found for the VBS $WV \to l\nu qq$ process, proving that it can be a suitable candidate for a joint fit with top, Higgs and other EW channels.

Only one publicly available VBS analysis features dimension-six studies for the operators Q_W, Q_{HW}, $Q_{H\Box}$ that is the VBS production of two V bosons ($W^{\pm}$ or Z) decaying hadronically, forming a final state with six jets [199]. The analysis targets the boosted regime for both the V bosons therefore the phase space of interest for EFT searches comprises two large radius jets and two small radius ones, the latter tagged as VBS jets. As shown in this work, EFT perturbations

are more noticeable in the boosted regimes that drive the sensitivity. For this reason, the VBS $VV \rightarrow 4q$ reports tighter expected C.L of about 30% for c_{HW} and $c_{H\Box}$ while it is compatible with this work for c_W.

It is also important to understand the differences in the constraining power of VBS with respect to diboson processes that benefit from the higher cross-section while presenting a similar vertex topology involving EW vector bosons. This interplay was studied at parton level and reported in Chapter 2. At the time of writing, only one CMS diboson analysis provides a limit on the Warsaw basis operator Q_W that is the $W^{\pm}\gamma$ one [200]. The constraints are derived via a parametrization of the fiducial cross-section in p_T^{γ} and $|\phi_f|$ where f is the final state charged lepton from the decay of the W boson. This bi-dimensional observable is proven to enhance the sensitivity to the linear interference between the SM and EFT amplitude and the approach is known as "interference resurrection" [201]. Other results from diboson processes feature a dimension-six interpretation, in the so-called HISZ basis [58], for the operators $\mathcal{O}_{WWW}$, $\mathcal{O}_W$, $\mathcal{O}_B$, $\tilde{\mathcal{O}}_W$, $\tilde{\mathcal{O}}_{WWW}$. The conversion between the HISZ and Warsaw basis is reported in Ref. [202] however a one-to-one mapping of the Wilson coefficients is only possible for a handful of operators: Q_W, $Q_{Hl}^{(1)}$, Q_{HG} and $Q_{Hl}^{(3)}$. For completeness, Table 4.12 reports the conversion rules in order to convert the reported limits for the aforementioned four Wilson coefficients from the HISZ (f) to the Warsaw (c) basis.

$c_{Hl}^{(1)} = \frac{g'^2}{8} f_B$	$c_W = \frac{g^3}{4} f_{WWW}$
$c_{Hl}^{(3)} = -\frac{g^2}{8} f_W$	$c_{HG} = -\frac{\alpha_s}{8\pi} f_{GG}$

Table 4.12: Conversion rules between Warsaw basis (left-hand sides) and HISZ (right-hand sides) Wilson coefficients. Only Wilson coefficients with a one-to-one mapping between the two bases and of interest for the VBS WV semileptonic analysis are reported (the entire conversion rules can be found in Ref. [202]).

As this analysis does not study the effect of $Q_{Hl}^{(3)}$ and Q_{HG}, only results from literature reporting limits on O_W and $\mathcal{O}_{WWW}$ from the HISZ basis can be compared directly to the ones obtained for Q_W and $Q_{Hl}^{(1)}$ from the Warsaw basis. The conversion is made using a value of $vev = 246.22$ GeV for the vacuum expectation value and $m_{\mathrm{W}} = 80.377$ GeV, $m_{\mathrm{Z}} = 91.188$ GeV from Ref. [44] that can be used to extract the value of the $SU(2)$ and $U(1)$ coupling constants as $g = 2m_{\mathrm{W}}/vev = 0.653$ and $g' = 2\sqrt{m_{\mathrm{Z}}^2 - m_{\mathrm{W}^2}/vev} = 0.350$.

Diboson results obtained with this conversion are reported for the CMS $WZ \rightarrow 3l\nu$ [203] reporting limits on c_W and $c_{Hl}^{(1)}$, CMS $WW \rightarrow 2l2\nu$ [126] reporting limits on c_W and $c_{Hl}^{(1)}$ and the CMS semileptonic $WV \rightarrow l\nu qq$ [204] reporting limits on c_W and $c_{Hl}^{(1)}$.

The VBF signature is similar to the VBS one but features only TGC vertices and produces a final state with two forward jets with high invariant mass and a weak vector boson (either W, Z or γ). VBF processes typically present a higher cross-section with respect to VBS, due to their lower order in perturbation theory (α^4 versus α^6), and for this reason, they are typically preferred in EFT global fits with other experimental analyses (see Ref. [205] for a recent example). Results from CMS $Z + 2j$ [206] and CMS $W + 2j$ [207] both using only 2016 data and from ATLAS $Z + 2j$ with the full Run II luminosity of 139 fb^{-1} [208] have been included in the comparison.

As many of the studied operators in the VBS $WV \rightarrow l\nu qq$ analysis involve the presence of the Higgs field (such as Q_{HW}, Q_{HWB}, Q_{HB} and $Q_{H\Box}$ affecting HVV couplings) it is natural to compare the obtained results to analyses dedicated to the study of the Higgs boson. Among the published results, the CMS VBF+VH+$H \rightarrow 4l$ [209] provides EFT limits including quadratic

terms to eight Wilson coefficients from the Warsaw basis. Additionally, the ATLAS Run II $H \to WW$ analysis [210] and ATLAS $pp \to 4l$ one [211] have been included in the comparison.

Figure 4.25 shows the comparison with eleven analyses from CMS or ATLAS that feature an EFT interpretation at dimension six. To provide a numerical contrast, Table 4.13 offers 95% confidence levels for all the relevant analyses.

Analyses / W.C. [TeV^{-2}]	cW	cHW	cHB	cHWB	cHbox	cHl1
CMS VBS $WV \to lvqq$	-0.35,0.34	-1.56,1.57	-4.71,4.72	-4.35,4.35	-9.56,9.67	-55.66,55.16
CMS VBF+VH+$H \to 4l$ [209]	-	-0.28,0.39	-0.08,0.03	-0.31,0.42	-0.93,0.75	-
CMS VBS $VV \to 4q$ [199]	-0.26,0.26	-1.30,1.30	-	-	-5.88,6.20	-
CMS $W^{\pm}\gamma$ [200]	-0.06,0.05	-	-	-	-	-
ATLAS $H \to WW$ [210]	-	-1.40,1.40	-0.59,0.66	-1.20,1.10	-	-
ATLAS Zjj [208]	-0.31,0.29	-	-	-3.11,2.10	-	-
ATLAS $pp \to 4l$ [211]	-	-	-	-0.21,0.20	-	-0.37,0.38
CMS $WZ \to 3l\nu$ [203]	-0.09,0.09	-	-	-	-	-1.32,1.91
CMS $WW \to 2l2\nu$ [126]	-0.19,0.19	-	-	-	-	-0.21,0.20
CMS $WV \to lvqq$ [204]	-0.11,0.11	-	-	-	-	-0.13,0.12
CMS Zjj [206]	-0.26,0.25	-	-	-	-	-
CMS Wjj [207]	-0.17,0.17	-	-	-	-	-0.95,0.93

Table 4.13: Numerical comparison of the expected results of this work (CMS VBS $WV \to lvqq$) with results reported in the literature.

The results show that while VBS $WV \to lvqq$ is competitive in constraining c_W, where limits from the diboson $W^{\pm}\gamma$ dominate, and c_{HW}, where the most sensitive channel is the CMS VBF+VH+$H \to 4l$, it is sub-dominant for all other Wilson coefficients. In particular for c_{HB}, c_{HWB}, $c_{H\Box}$ and $c_{Hl}^{(1)}$, processes involving a neutral EW vector bosons (Z,γ) dominate the sensitivity by more than a factor 10 with respect to the VBS $WV \to lvqq$. For $c_{Hl}^{(1)}$ on the other hand the most sensitive analysis is found to be the semileptonic diboson $WV \to lvqq$, benefiting from the V=Z process. The sub-leading sensitivity of this work is expected as VBS processes present a lower cross-section with respect to the other analyses included in this comparison. Furthermore, analyses that target specifically the dynamics of the Higgs boson will be by construction more sensitive to operators affecting its decay. However, VBS presents a rich phenomenology in terms of EFT sensitivity, benefiting from six vertices in the Feynman diagrams that could be affected by dimension-six EFT operators, and was clearly shown in Figure 2.2. The role of VBS in the EFT landscape is not to provide stringent limits on single dimension-six EFT operators, for which it will be superseded by dedicated analyses targeting Higgs, top or EW dynamics. VBS should be considered as a link between analyses that feature a high sensitivity to a limited subset of operators. This link can be highly effective when simultaneously constraining the large parameter space of the full Warsaw basis by resolving degenerate direction that would otherwise inflate the observed C.L. This fact has been proved in this work while constraining simultaneously a limited subset of eight dimension-six operators. The role of VBS in global EFT combination is an active area of research and is documented by multiple combination exercises (see Refs. [90, 91] for recent examples).

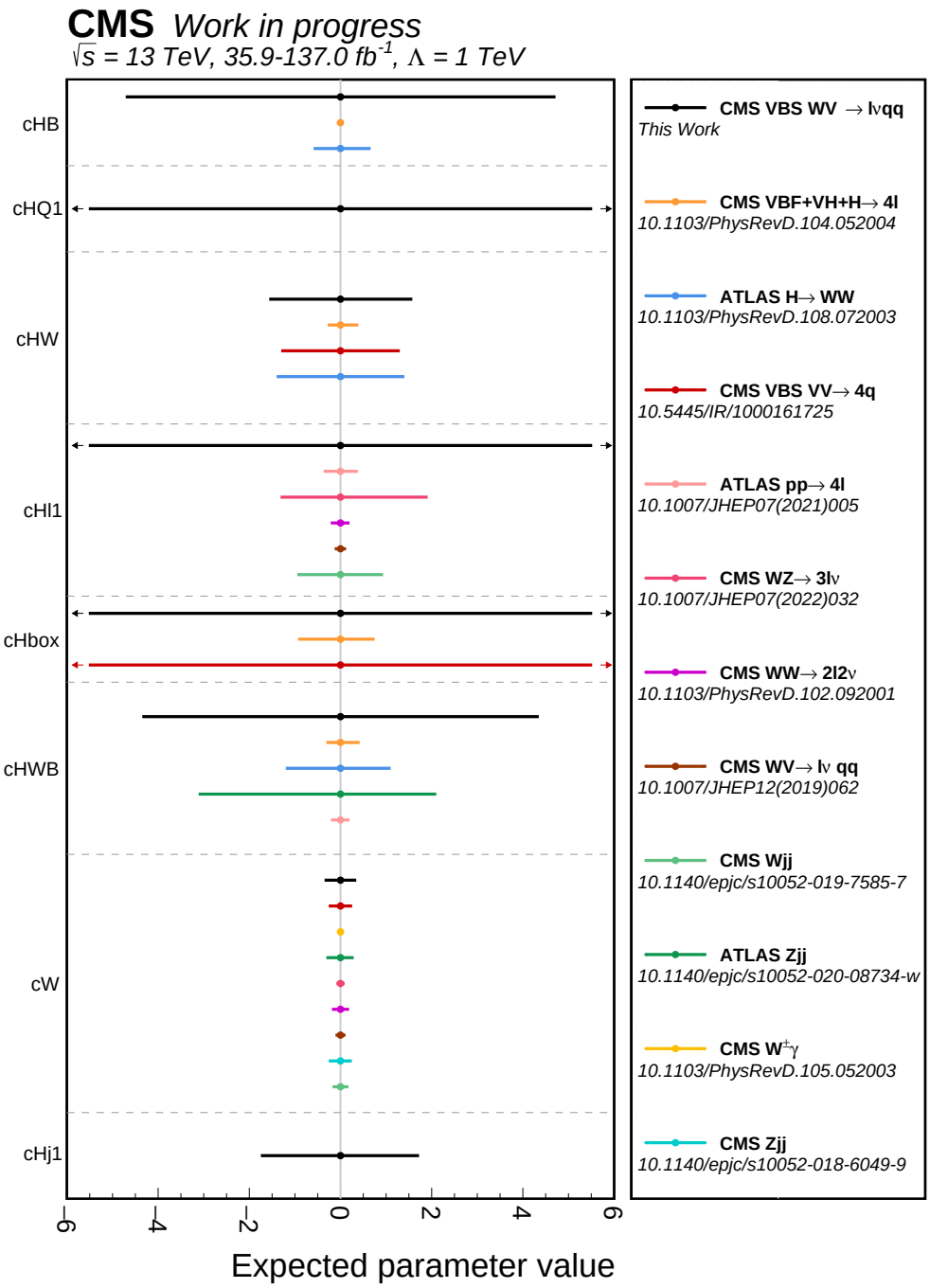

Figure 4.25: Summary plot comparing the 95% C.L. from the profiled bounds of the VBS $WV \rightarrow lvqq$ analysis (black) with eleven public results from ATLAS and CMS (coloured lines). The full list of analyses and respective digital object identifiers are reported on the right side of the figure. Six out of the eight operators have been included as for the remaining $Q_{Hj}^{(1)}$ and $Q_{HQ}^{(1)}$ no results were found in the literature. The results of this work have been compared with the ones obtained with another VBS channel and other classes of processes such as diboson, VBF and Higgs (WW or ZZ decay). For all analyses except the one from this work, limits are reported with an EFT parametrization including components scaling quadratically with the Wilson coefficients and from individual fits by freezing all the Wilson coefficients except for the one of interest to their SM value.

Chapter 5

The Run II combination of VBS measurements

5.1 Vector Boson Scattering at CMS

VBS measurements at CMS and ATLAS started with the dataset collected at $\sqrt{s} = 8$ TeV with an integrated luminosity of approximately 20 fb^{-1} [212, 213]. Target signatures with leptonic decays of the electroweak vector bosons produce a clean signal in the detector, allowing for a good background isolation [212]. Final states including photons and leptons present a clean signature and an enhanced cross-section due to their lower order in perturbation theory compared to VBS processes featuring six final state fermions [214, 215]. During the Run II data taking, started in 2016 up to 2018, the center-of-mass energy was increased to $\sqrt{s} = 13$ TeV. The integrated luminosity increased by a factor of seven compared to the previous LHC Run I, allowing CMS to get evidence and observation for VBS processes with different production modes and in a wider spectrum of fermion composition of the final state. Table 5.1 summarizes all previous and ongoing CMS analyses with VBF/VBS topologies starting from Run I. In particular, semi-leptonic final states started to be analyzed yielding the first evidence for VBS with a hadronically decaying weak boson with an observed significance of $4.4\,\sigma$ [105]. Thanks to the increased luminosity, also leptonic channels plagued by the overwhelming backgrounds began to be visible from a statistical point of view. For example, the scattering of two oppositely charged W bosons presents major contaminations from $t\bar{t}$ in the final state with two charged leptons of different flavours and the Drell-Yan process dominates the same flavour category. CMS observed this process for the first time analyzing the Run II dataset with an integrated luminosity of 137 fb^{-1}, excluding the background-only hypothesis with a significance of 5.6σ [99].

Ongoing analyses target more complicated final states as well as final states with lower branching ratios. Among the current ongoing efforts, the ones of interest for this chapter are the analysis of the semi-leptonic VBS production of a Z boson and a hadronically decaying V boson, the production of two W boson with the same electric charge one decaying into a lepton (e, μ) and relative neutrino while the other decays into a hadronically decaying τ lepton and the associated neutrino, and finally the VBS production of two Z bosons where one decay into a charged lepton pair and the other one into a neutrino pair. The list of analyses involved in the combination is described in section 5.2 where also a brief description of the analysis strategy is presented.

5.2 The analyses and measurement strategy

This statistical combination targets VBS processes without photons in the final state. All analyses target final states with six fermions produced from the hard scatter. Both leptonic and hadronic decays of the weak vector bosons W$^{\pm}$, Z are taken into consideration. The objective

$\sqrt{s}$	$\mathcal{L}_{INT}$	Process	Article	Comments
8 TeV	19.7 fb^{-1}	EW $Zjj(l^+l^-jj)$	Eur.Phys.J.C75(2015)66	2016: $\gg$ **5**σ
	19.7 fb^{-1}	EW $W^{\pm}jj(l^{\pm}\nu jj)$	JHEP11(2016)147	2016: **4**σ , Run II: Ongoing
	19.4 fb^{-1}	EW $W^{\pm}W^{\pm}jj(2l2\nu jj)$	PhysRevLett.114.051801	CMS finds 2σ
	19.7 fb^{-1}	EW $Z\gamma jj(\nu\nu/ll\gamma jj)$	PhysLettB770(2017)380-402	CMS finds 3σ
	19.7 fb^{-1}	EW $W^{\pm}\gamma jj(l\nu\gamma jj)$	JHEP06(2017)106	CMS finds 2.7σ
	19.4 fb^{-1}	EW $W^{\pm}Zjj(3l\nu jj)$	PhysRevLett.114.051801	CMS finds 2σ
13 TeV	35.9 fb^{-1}	EW $Zjj(l^+l^-jj)$	Eur.Phys.J.C78(2018)589	2016: $\gg$ **5**σ , Run II: Ongoing
	35.9 fb^{-1}	EW $W^{\pm}jj(l^{\pm}\nu jj)$	Eur.Phys.J.C80(2020)43	2016: $\gg$ **5**σ , Run II: Ongoing
	137 fb^{-1}	EW $W^{\pm}W^{\pm}jj(2l2\nu jj)$	PhysLettB809(2020)	2016: **5.5**σ , Run II: $\gg$ **5**σ
	137 fb^{-1}	EW $W^{\pm}Zjj(3l\nu jj)$	PhysLettB809(2020)135710	Run II: **6.8**σ
	137 fb^{-1}	EW $ZZjj(4ljj)$	PhysLettB812(2021)135992	2016: 2.7σ , Run II: **4**σ
	137 fb^{-1}	EW $Z\gamma jj(ll\gamma jj)$	PhysRevD.104.072001	2016: **4.7**σ , Run II: $\gg$ **5**σ
	35.9 fb^{-1}	EW $W^{\pm}\gamma jj(l\nu\gamma jj)$	PhysLettB811(2020)135988	2016: **5.3**σ , Run II: Ongoing
	138 fb^{-1}	EW $W^{\pm}Vjj(l\nu jjj)$	PhysLettB834(2022)137438	Run II: **4.4**σ
	138 fb^{-1}	EW $W^{\pm}W^{\mp}jj(2l2\nu jj)$	PhysLettB841(2023)137495	Run II: **5.6**σ
	138 fb^{-1}	EW $W^{\pm}W^{\pm}jj(l\tau_h 2\nu jj)$	CMS-PAS-SMP-22-008	CMS finds 2.7σ
	138 fb^{-1}	EW $VVjj(4j/2j2\nu jj)$	...	Run II: Ongoing
	138 fb^{-1}	EW $VVpp(4jpp)$	...	Run II: Ongoing
	138 fb^{-1}	EW $ZVjj(2ljjjj)$	...	Run II: Ongoing
	138 fb^{-1}	EW $ZZjj(2l2\nu jj)$	...	Run II: Ongoing

Table 5.1: Summary table for Run I and Run II VBS/VBF analyses at CMS. Columns report the collision center-of-mass energy ($\sqrt{s}$), the integrated luminosity $\mathcal{L}_{INT}$, the electroweak target process, reference to the published results and the observed significance or the status of the analysis.

of this analysis is to measure the VBS signal strengths defined by two statistical models with respectively four and six free parameters. The first model aims at simultaneously measuring four signal strengths by merging the charge of the W bosons: the production of two W bosons with the same electrical charge, namely $W^{\pm}W^{\pm}$ (SSWW in the following), the production of two W bosons of opposite electric charge $W^{\pm}W^{\mp}$ (OSWW in the following), the production of a W boson associated with a Z boson $W^{\pm}Z$ (WZ in the following) and the production of two Z bosons (ZZ in the following).

If we distinguish the electric charge of the W bosons, the SSWW and WZ signal strengths can be split into two separate parameters for the production of positively and negatively charged final states. The full set of signal strengths to be constrained by the second statistical model with six free parameters is W^+W^+, W^-W^-, W^+Z, W^-Z, ZZ, $W^{\pm}W^{\mp}$.

The analyses included in the combination to constrain both sets of four and six signal strength are summarised in Table 5.2, where the signal composition for both the statistical models is shown to highlight the interplay of each analysis to measure the target signal strengths. Additionally, Figure 5.1 shows the signal fractions for the six and four-parameter models for each analysis, considering all the regions entering the final fit.

The following sub-sections will briefly describe the analysis strategies, highlighting possible phase space overlaps, background composition and systematic nuisance treatment.

5.2.1 Same-sign $W^{\pm}W^{\pm}$ and $W^{\pm}Z$ fully leptonic ($2l2\nu$, $3l\nu$)

These measurements are performed jointly in the leptonic decay modes $W^{\pm}W^{\pm} \rightarrow l^{\pm}\nu l^{\pm}\nu$ and $W^{\pm}Z \rightarrow l^{\pm}\nu l'^{\pm}l^{\mp}$ where $l, l' = e, \mu$. The necessity of a common analysis strategy for these two VBS processes of interest arises from the fact that the EW WZ contribution is significant

	OSWW	SSWW		WZ		ZZ
Analysis	W^+W^-	W^-W^-	W^+W^+	W^-Z	W^+Z	ZZ
$WVjj \to l\nu jjjj$	✓	✓	✓	✓	✓	-
$ZVjj \to 2ljjjj$	-	-	-	✓	✓	✓
$W^+W^-jj \to 2l2\nu jj$	✓	-	-	-	-	-
$W^\pm W^\pm jj \to 2l2\nu jj$	-	✓	✓	-	-	-
$W^\pm Zjj \to 2l2\nu jj$	-	-	-	✓	✓	-
$ZZjj \to 4ljj$	-	-	-	-	-	✓
$W^\pm W^\pm jj \to l\tau_h 2\nu jj$	-	✓	✓	-	-	-
$ZZjj \to 2l2\nu jj$	-	-	-	-	-	✓
$VVjj \to 6j$	✓	✓	✓	✓	✓	✓

Table 5.2: Summary table for analyses involved in the combination. The table reports the analysis process, the status of the analysis within CMS, the reference cadi line for internal use and a list of 6 signal strengths highlighting the parameters each analysis can measure. The very top row enumerates the 4 parameters obtained by merging for W boson charge and corresponds to the 4 parameters model. The horizontal middle row separates the analyses included in the combination from the analyses we could include but are at an early stage

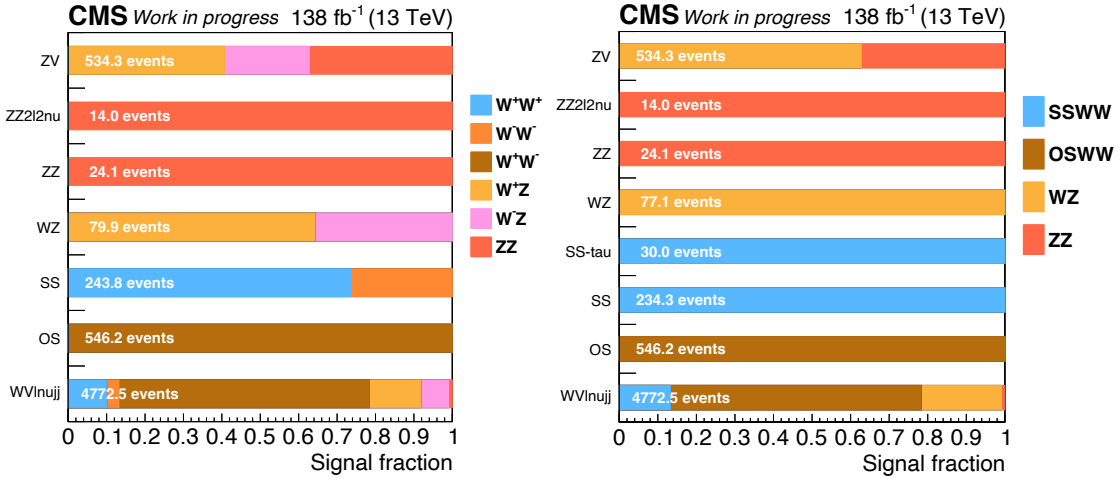

Figure 5.1: Matrices summarising the signal fractions for each analysis. Rows indicate the analysis involved in the combination. The x-axis specifies the signal fraction. Colours, as reported in the legend, highlight each different signal parameter we aim to measure. The matrix on the left shows the signal fractions for the 6 components split by W-boson charge while the right matrix is the counterpart for 4 components.

in a SSWW-enriched region. This cross-talk happens if a charged lepton from the Z decay of a WZ event eludes detection, producing the same experimental signature of the SSWW process. For this reason, it is natural to analyze both processes together. Events selected for the joint measurement of the $W^\pm W^\pm$ and $W^\pm Z$ production cross-sections contain either two leptons of the same electric charge or three leptons with total charge equal to ± 1, moderate missing transverse momentum p_T^{miss} and two jets with large invariant mass and large pseudorapidity separation. The Zeppenfeld variable [216] $z_l* = |\eta_l - \bar{\eta}_j|/|\Delta\eta_{jj}|$ is used to further isolate the EW-VBS signal, exploiting the fact that the EW production, in contrast to other production channels, presents a hadron-depleted region inside the rapidity gap of the two scattered partons.

While the 3-lepton category is plagued by QCD-induced VBS contributions at order $\alpha_S^2\alpha^4$, the

presence of two same-sign leptons in the two-leptons category reduces significantly the contamination from QCD-induced VBS processes which makes SSWW a golden channel for VBS measurements. The analysis defines five regions, all included in a maximum likelihood fit to extract the cross-sections and signal strengths. All regions request two VBS jets characterized by a large pseudorapidity gap $|\Delta\eta_{jj}| > 2.5$ and large dijet invariant mass $m_{jj} > 500$ GeV. Regions are divided by the number of charged leptons (N_{lep} = 2,3,4). The regions targeting the SSWW process request moderate missing transverse momentum $p_T^{\text{miss}} > 30$ GeV, two charged leptons with charge ± 2 with moderate transverse momentum of $p_T^{l,1} > 25$ GeV for the leading-p_T lepton and $p_T^{l,2} > 20$ GeV for the subleading lepton. In the di-electron category, the dilepton invariant mass is required to be 15 GeV away from the Z boson mass peak. This cut helps reduce the mischarge contribution coming from $Z \to e^+e^-$ where the charge of one electron is wrongly assigned. This cut is not applied in the different flavour $e\mu$ category due to the absence of DY processes and neglected in the dimuon category as the charge assignment for muons is more precise when exploiting muon chambers in association with calorimetric and tracking information. A lower bound on the dilepton invariant mass is also applied $m_{ll} > 20$ GeV. The maximum value of the Zeppenfeld variable computed with the two charged leptons is required to be $max(z_l^*) < 0.75$. Events with at least one hadronically decaying τ lepton are identified and rejected in order to suppress electroweak backgrounds. The SSWW signal region (SR) additionally requests the absence of b-jets whereas a control region for the dominant background in the SSWW region requests the presence of at least one b-jet. The latter region is enriched in events where jets or converted photons are misidentified as leptons (fake leptons) as well as the so-called nonprompt leptons produced by leptonic decays of heavy hadrons. The major sources of fake and nonprompt leptons in this region are the W+jets and $t\bar{t}$ processes. The regions targeting the WZ signature present the same selections on jets and missing transverse momentum as the SSWW regions. Three leptons of total charge ± 1 are requested with transverse momentum p_T^l greater than 25, 20 and 10 GeV. Two of the three leptons are required to be compatible with a Z boson decay, namely, they should have the same flavour (ee, $\mu\mu$) and a dilepton invariant mass compatible with the one of the Z boson $|m_{ll} - m_Z| < 15$ GeV. The invariant mass of the three charged leptons is required to be $m_{3l} > 100$ GeV. The maximum value of the Zeppenfeld variable computed with the three charged leptons is required to be $max(z_l^*) < 1$. Events with at least one hadronically decaying τ lepton are identified and rejected. As the SSWW regions, the WZ is further split in a WZ SR, enriched in EW VBS-WZ events, that requires the absence of b-jets and a tVX control region, identifying the top quark decay by requiring the presence of at least one b-jet. An additional ZZ control region for the minor QCD-induced background process $ZZjj$ is identified by requiring four charged leptons with a neutral overall charge. The same jets selection of the SSWW and WZ regions is applied also to the ZZ region. Both pairs of $Z \to ll$ candidates are required to be compatible with the Z boson decay $|m_{ll} - m_Z| < 15$ GeV. The maximum value of the Zeppenfeld variable computed with the four charged leptons is required to be $max(z_l^*) < 0.75$. A schema summarizing the analysis regions and selections is shown in Figure 5.2.

A binned maximum-likelihood fit is performed by combining the SSWW and WZ SRs as well as the nonprompt, tVX, and ZZ CRs. The normalization scale factors for the tVX and ZZ background processes are included as free parameters in the maximum-likelihood fit together with the EW SSWW, EW WZ, and QCD WZ signal strengths.

For the SSWW signal extraction a bidimensional (m_{jj}, m_{ll}) observable is employed. The former observable is motivated by the fact that the VBS process peaks at high values of the dijet invariant mass while the latter is used to better discriminate the signal with respect to the dominant nonprompt background which typically peaks at low m_{ll} values.

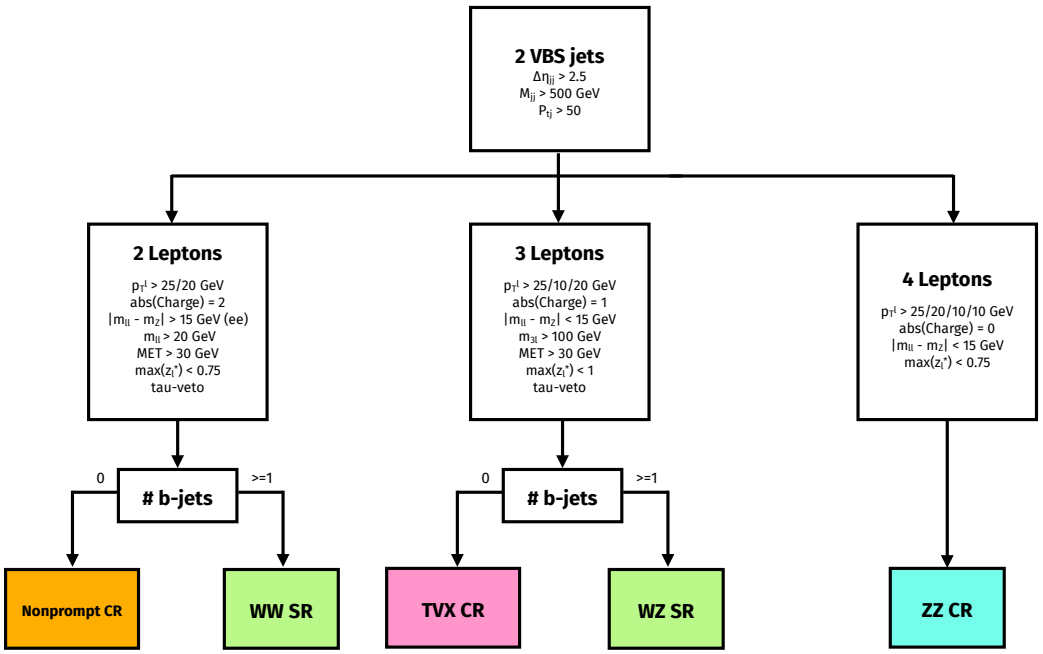

Figure 5.2: Schema summarising the SSWW/WZ analysis regions and selections

In order to extract the VBS WZ signal a more sophisticated approach needs to be used to isolate the pure EW component from the overwhelming QCD-induced background. A Boosted Decision Tree (BDT) is trained using the TMVA package [217].

In all control regions, a 4-bin m_{jj} distribution is employed in order to control background uncertainties and background normalizations.

The full list of selections, regions and observables entering in the fit is reported in Table 5.3.

Variable	SSWW SR	WZ SR	tVX CR	Nonprompt CR	ZZ CR
Leptons	2 leptons $p_T > 25/20$ GeV	3 leptons $p_T > 25/10/20$ GeV	3 leptons $p_T > 25/10/20$ GeV	2 leptons $p_T > 25/20$ GeV	4 leptons $p_T > 25/20/10/10$ GeV
p_T^j	> 50 GeV	> 50 GeV	> 50 GeV	> 50 GeV	> 50 GeV
$\lvert m_{ll} - m_Z \rvert$	> 15 GeV (ee)	< 15 GeV	< 15 GeV	> 15 GeV (ee)	< 15 GeV (both pairs)
m_{3l}	-	> 100 GeV	> 100 GeV	-	-
m_{ll}	> 20 GeV	-	-	> 20 GeV	-
p_T^{miss}	> 30 GeV	> 30 GeV	> 30 GeV	> 30 GeV	-
b-veto	Required	Required	-	-	-
$\max(z_l*)$	< 0.75	< 1	< 1	< 0.75	< 0.75
m_{jj}	> 500 GeV	> 500 GeV	> 500 GeV	> 500 GeV	> 500 GeV
$\Delta\eta_{jj}$	> 2.5	> 2.5	> 2.5	> 2.5	> 2.5
Fit Observable	2D $m_{jj} : m_{ll}$	BDT	m_{jj}	m_{jj}	m_{jj}

Table 5.3: Summary table of the SSWW/WZ analysis regions, selections and observables used in the maximum-likelihood fit

The results of the SSWW and WZ VBS analyses include the statistical significance for the two signal processes and the measured signal strength. This analysis studies in depth the interplay between the QCD and EW VBS WZ production along with the effect of including or not their interference terms at order $\alpha_S\alpha^5$. The significance for the SSWW and WZ signals split for the

three years of the LHC Run II are summarised in Table 5.4 while the measured and expected signal strengths for the pure EW productions and the QCD WZ process are summarised in Table 5.5.

Signal	2016	2017	2018	Combination
EW WW (observed / expected)	4.6/5.2	7.2/7.2	7.9/7.2	11.5/11.3
EW WZ (observed / expected)	2.6/2.7	4.4/2.8	4.6/3.7	6.8/5.3

Table 5.4: Observed and expected significances for the EW SSWW and EW WZ processes split in data taking years and their combination.

μ	Observed	Expected
EW WW	$1.024^{+0.158}_{-0.142}$	$1.000^{+0.157}_{-0.141}$
EW WZ	$1.247^{+0.336}_{-0.290}$	$1.000^{+0.321}_{-0.277}$
QCD WZ	$1.010^{+0.160}_{-0.152}$	$1.000^{+0.157}_{-0.149}$
EW WW	$1.022^{+0.155}_{-0.142}$	$1.000^{+0.157}_{-0.141}$
EW+QCD WZ	$1.080^{+0.108}_{-0.101}$	$1.000^{+0.105}_{-0.098}$

Table 5.5: Observed and expected signal strengths (μ) for the EW SSWW, EW WZ, and QCD WZ processes. Results are reported with two and three individual signal strengths.

5.2.2 Opposite-sign $W^{\pm}W^{\mp}$ with fully leptonic final state ($2l2\nu$)

This measurement is performed in the leptonic decay mode $W^{\pm}W^{\mp} \to l^{\pm}\nu l^{\mp}\nu$ where $l = e, \mu$. Differently from the previously described same-sign analysis in Chapter 5.2.1, the events for the opposite-sign WW analysis are selected by requiring two charged leptons of opposite electric charge, moderate missing transverse momentum and two jets with large invariant mass and large pseudorapidity separation. The background composition for this final state is strictly related to the flavour composition of the latter. In the final state where the two charged leptons have the same flavour ($ee, \mu\mu$) the dominant background comes from Drell-Yan events where the two extra jets, misidentified as VBS-jets, come from initial or final state radiation (ISR or FSR). In the different-flavour category $e\mu$, the dominant background comes from $t\bar{t}$ events and the Drell-Yan is suppressed with a residual contribution coming from DY-$\tau\tau$ process where the τ leptons decay leptonically.

The analysis presents multiple regions, designed to control and reduce the overwhelming backgrounds. Events are preselected requiring two opposite-sign leptons with invariant mass $m_{ll} > 50\,\text{GeV}$ and transverse momentum $p_T^{ll} > 30\,\text{GeV}$, moderate missing transverse energy $E_T^{\text{miss}} > 20\,\text{GeV}$ and at least two $p_T^j > 30\,\text{GeV}$ jets with $\Delta\eta_{jj} > 2.5$ and invariant mass $m_{jj} > 300\,\text{GeV}$. Three overall regions are identified to isolate DY contributions, $t\bar{t}$ contributions and the VBS-enriched region for signal extraction. Each region discriminates between the same-flavour and different-flavour final state.

The signal region in the different flavour category requires no b-jets, to reduce the $t\bar{t}$ contamination, a transverse mass for the candidate diboson system $m_T > 60\,\text{GeV}$ defined as $m_T = \sqrt{2p_T^{ll}p_T^{\text{miss}}[1 - cos\Delta\phi(p_T^{ll}, p_T^{\text{miss}})]}$. The same-flavour category presents tightened cuts to reduce the DY contribution, requiring no b-jets, $E_T^{\text{miss}} > 60\,\text{GeV}$ and $m_{ll} > 120\,\text{GeV}$. For

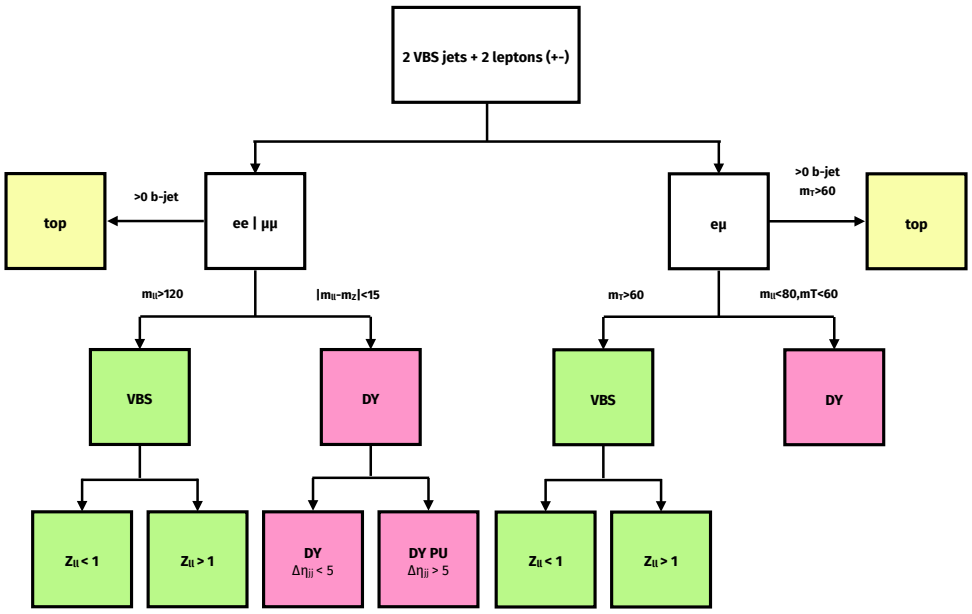

Figure 5.3: Schema summarising the OSWW analysis regions and selections

both the same- and different-flavour final states, the regions are further divided based on the dilepton Zeppenfeld variable [216] $Z_{ll} = 0.5(Z_{l1} + Z_{l2})$ to optimize the signal extraction. The different flavour VBS category with lower values of Z_{ll} dominates the sensitivity to the VBS-OSWW signal.

The top region requires at least one b-jet, $m_{ll} > 50$ GeV in the different-flavour final state and $m_{ll} > 120$ GeV in the same-flavour one. For the latter an additional $E_T^{\text{miss}} > 60$ GeV cut is applied.

The last region is designed to control the DY background. For all flavour compositions of the final state, a b-jet veto is applied. In the different-flavour final state, the DY region is defined by a low transverse mass $m^T < 60$ GeV, a dilepton invariant mass close to the Z-boson peak, accounting for the energy loss of the leptonic τ-decay 50 GeV $< m_{ll} <$ 80 GeV. The same-flavour category requires the two leptons to be compatible with a Z-boson decay $|m_{ll} - m_Z| < 15$ GeV and moderate missing transverse energy $E_T^{\text{miss}} > 60$ GeV. The same-flavour category is further divided based on the pseudorapidity gap between the two jets $\Delta\eta_{jj} \geq 5$ and $\Delta\eta_{jj} < 5$. This further stratification helps in controlling two different sources of DY contribution: one coming directly from the hard scatter and one where at least one of the two leading jets is identified as coming from pile-up (PU). This identification procedure is made with a geometrical-p_T match between the leading reconstructed jets and generator-level jets. If no match is found, the reconstructed jet is assumed to have originated from a PU and vice versa. As one expects to find mainly PU jets outside the tracker acceptance, the $\Delta\eta_{jj} \geq 5$ control region is dominated by DY-PU events while the orthogonal region $\Delta\eta_{jj} < 5$ is dominated by hard DY events. A schema summarising all analysis regions is pictured in Figure 5.3.

The extraction of the VBS OSWW signal is based on a binned maximum likelihood fit done in a flavour-dependent fashion. All nine regions are fitted simultaneously. The DY and $t\bar{t}$ control regions are used to measure the cross-section of the two DY components, treated independently in the fit procedure where two parameters are left to freely float, together with the cross-section of the $t\bar{t}$ background. The VBS signal is measured in the VBS-enriched regions at low and high

Region		Selection		Fit observable
VBS	$e\mu/\mu e$	$Z_{ll} < 1$ $Z_{ll} \geq 1$	$m_T > 60$ GeV $m_{ll} > 50$ GeV b-veto	DNN spectra
	ee	$Z_{ll} < 1$ $Z_{ll} \geq 1$	$m_{ll} > 120$ GeV $E_T^{\text{miss}} > 60$ GeV b-veto	8 bins $300 < m_{jj} < 500$ GeV, $2.5 < \lvert\Delta\eta_{jj}\rvert < 3.5$ $m_{jj} > 500$ GeV, $2.5 < \lvert\Delta\eta_{jj}\rvert < 3.5$ $300 < m_{jj} < 500$ GeV, $\lvert\Delta\eta_{jj}\rvert > 3.5$
	$\mu\mu$	$Z_{ll} < 1$ $Z_{ll} \geq 1$		
top	$e\mu/\mu e$	$m_{ll} > 50$ GeV b-veto		Number of Events
	ee	$m_{ll} > 120$ GeV $E_T^{\text{miss}} > 60$ GeV $E_T^{\text{miss}} > 60$ GeV b-veto		
	$\mu\mu$			
DY	$e\mu/\mu e$	$m_T < 60$ GeV 50 GeV $< m_{ll} < 80$ GeV b-veto		Number of Events
	ee	$\Delta\eta_{jj} < 5$ $\Delta\eta_{jj} \geq 5$	$\lvert m_{ll} - m_Z\rvert < 15$ GeV $E_T^{\text{miss}} > 60$ GeV b-veto	
	$\mu\mu$	$\Delta\eta_{jj} < 5$ $\Delta\eta_{jj} \geq 5$		

Table 5.6: Summary table for OSWW analysis regions, selections and observable entering in the binned maximum likelihood fit

values of the Zeppenfeld variable. In order to increase the significance over the SM background, a deep neural network is trained for the different flavour regions to isolate the signal from the backgrounds. To further optimize the analysis, two independent models are trained for the $Z_{ll} > 1$ and $Z_{ll} < 1$ regions. For the same-flavour category, subleading in sensitivity, different discriminating variables are chosen as a function of m_{jj} and $|\Delta\eta_{jj}|$. Each discriminating variable is the same for each flavour composition (ee, $\mu\mu$) and Z_{ll} category ($Z_{ll} > 1$ and $Z_{ll} < 1$). The observable is built combining five uniform bins of m_{jj} for $m_{jj} > 500$ GeV and $\Delta\eta_{jj} > 3.5$, having largest signal-over-background ratio, and additional three bins defined as:

- $300 < m_{jj} < 500$ GeV and $2.5 < |\Delta\eta_{jj}| < 3.5$
- $m_{jj} > 500$ GeV and $2.5 < |\Delta\eta_{jj}| < 3.5$
- $300 < m_{jj} < 500$ GeV and $|\Delta\eta_{jj}| > 3.5$

An overall summary of the OSWW analysis regions, selections and observables entering in the fit procedure is given in Table 5.6. The expected and observed significance and signal strengths split by data-taking years are summarised in Table 5.7.

5.2.3 ZZ fully leptonic ($4l$)

The search for VBS production of two Z bosons with a fully leptonic final state targets the signature $ZZ \to lll'l'$ where $l, l' = e, \mu$. A first search, done by CMS with an integrated luminosity of 35.9 fb^{-1} and a center of mass energy of $\sqrt{s} = 13$ TeV, resulted in an observed significance of 2.7 σ [133]. With the expansion to the full Run-II dataset (137 fb^{-1}) CMS was able to claim evidence for the VBS production of two Z bosons with fully leptonic final state with an observed

	2016	2017	2018	Combination
σ (exp. / obs.)	2.35	2.70	3.44	4.82 / 5.60
μ (exp. / obs.)	$1^{+0.49}_{-0.44}$	$1^{+0.42}_{-0.39}$	$1^{+0.31}_{-0.30}$	$1^{0.23}_{-0.22}$ / $1.32^{+0.29}_{-0.27}$

Table 5.7: Observed and expected significances (σ) and signal strength (μ) for the OSWW processes split in data-taking years and for their combination.

significance of 4.0 σ [104]. The measurement of the VBS-ZZ signal strength, significance and the total fiducial cross-section is performed in a ZZjj inclusive signal region. An event candidate falling in this region is required to contain two Z boson candidates, each formed from a pair of oppositely charged leptons with same flavour (l, l'). Electrons (muons) are required to have a transverse momentum greater than 7 (5) GeV. The leading lepton in order of p_T is required to have a $p_T > 20$ GeV while the subleading one is required to have a transverse momentum greater than 10 GeV. All leptons are required to be resolved in the $\eta - \phi$ plane by the selection $\Delta R(l_1, l_2) > 0.02$. Furthermore, Z boson decay candidates should be sufficiently separated so as to uniquely identify the Z boson decay with $\Delta R(e, \mu) > 0.05$. Z boson candidates are built considering all possible permutations of lepton pairs compatible with the vector boson decay. Of these dilepton pairs, the one with greater transverse momentum is denoted as Z_1 while the subleading one as Z_2 and both dilepton masses are required to be inside the Z boson mass window $60 < m_{Z_{1,2}} < 120$ GeV. All pairs of leptons, neglecting flavour pairing, are required to have $m_{ll'} > 4$ GeV to suppress the QCD-induced background. The invariant mass of the di-Z system built from the four charged lepton candidates is required to have $m_{Z_1+Z_2} = m_{4l} > 180$ GeV. Ambiguities in the case of multiple ZZ candidates are resolved by selecting the ZZ configuration that maximizes $p_T^{Z_2}$. Additional selections target the VBS jet's peculiar signature. At least two jets are required in the event, each of them well separated from the ZZ candidate by $\Delta R(ZZ, j) > 0.4$. The two leading-p_T jets are tagged as the VBS-jets and their invariant mass is required to be greater than 100 GeV. Two additional signal regions with tighter cuts on the EW-VBS topology are defined. A VBS enriched region, used to extract an additional total and EW fiducial $4ljj$ cross-section, is defined as the ZZjj inclusive region with an additional $\Delta\eta_{jj} \geq 2.4$ and tighter $m_{jj} > 400$ GeV selection. The tight VBS signal region is also used for aQGC search and presents additional $|\Delta\eta_{jj}| > 2.4$ and tighter $m_{jj} > 1$ TeV selections on top of the inclusive ZZjj selection. A background control region is defined with events from the ZZjj inclusive region failing at least one of the VBS-enriched region requirements.

The dominant background in all regions is the QCD production of two Z bosons with the addition of two jets. Its yield and shape are taken directly from the simulation. The background is split for the quark-induced production $q\bar{q} \to ZZjj$ and the gluon-induced one $gg \to ZZjj$. The former is simulated at the NLO with MADGRAPH5_AMC@NLO up to two extra parton emissions and NNLO corrections from MATRIX are applied as k-factors as a function of m_{ZZ}. The loop-induced $gg \to ZZjj$ production is simulated at LO with MADGRAPH5_AMC@NLO up to two extra parton emissions and a NLO/LO k-factor is applied according to Ref. [218] with differences up to 100% in bins of differential distributions. Minor irreducible backgrounds include processes that produce high-p_T isolated leptons namely $pp \to t\bar{t}Z$ + jets and $pp \to$ VVZ+jets and estimated with MC simulations. Lastly, a minor contribution comes from non-prompt leptons and jets misidentified as leptons in Z+X events (predominantly Z+jets but also $t\bar{t}$+jets and WZ+jets). The latter contribution is estimated with a data-driven method, weighting events by a lepton misidentification rate measured in a control region (one Z boson candidate + a third lepton). Table 5.8 summarises the analysis regions included in the final fit for the extraction of the EW VBS signal strength.

Variable	ZZjj inclusive				VBS-enriched loose				VBS-enriched tight			
Leptons	4 leptons $p_T^e > 20/10/7$ GeV $p_T^\mu > 20/10/5$ GeV				4 leptons $p_T^e > 20/10/7$ GeV $p_T^\mu > 20/10/5$ GeV				4 leptons $p_T^e > 20/10/7$ GeV $p_T^\mu > 20/10/5$ GeV			
$\Delta R(l_1, l_2)$	> 0.02				> 0.02				> 0.02			
$\Delta R(ZZ, j)$	> 0.4				> 0.4				> 0.4			
$\Delta R(e, \mu)$	> 0.05				> 0.05				> 0.05			
$\lvert m_{l_1,l_2} - m_Z \rvert$	< 30 GeV				<30 GeV				<30 GeV			
$m_{ll'}$	> 4 GeV				> 4 GeV				> 4 GeV			
m_{4l}	> 180 GeV				> 180 GeV				> 180 GeV			
p_T^j	> 30 GeV				> 30 GeV				> 30 GeV			
m_{jj}	> 100 GeV				> 400 GeV				> 1000 GeV			
$\lvert \Delta\eta_{jj} \rvert$	-				> 2.4				> 2.4			
Sig. & Bkg. fractions	EW-ZZ	QCD-ZZ	Irr.	Z+X	EW-ZZ	QCD-ZZ	Irr.	Z+X	EW-ZZ	QCD-ZZ	Irr.	Z+X
	6.5%	82.3%	8.7%	2.5%	21.0%	71.7%	5.3%	2.1%	48.4%	46.2%	3.7%	1.7%

Table 5.8: Summary table for the VBS-ZZ analysis regions. All three signal regions are used to extract the total fiducial cross-section measurement for the EW signal while the VBS-enriched tight is also used for aQGC search. l_1 and l_2 refer to a pair of oppositely charged leptons with same flavour, candidate as Z-boson decay products, while l and l' refer to two leptons of different flavour. The signal and background compositions are reported in the bottom row for each region where the signal fraction increases with a tighter m_{jj} cut, despite the reduction in statistics.

The EW VBS signal is extracted in all regions with a matrix element discriminant (K_D) that disentangles the signal from the dominant QCD-induced ZZ production. The performances of the K_D discriminant were compared with a boosted decision tree showing no significant differences between the two approaches. A binned maximum likelihood fit is performed on the K_D spectra with 50 bins in the ZZjj inclusive region and 25 bins in the VBS-enriched region. The analysis regions are analyzed separately as the ZZjj inclusive region includes by definition events in the ZZjj enriched regions.

5.2.4 WV semileptonic ($lvjj$)

The SM search for the VBS production of a W boson decaying leptonically and a V boson (either a W or Z boson) decaying hadronically $pp \to W(l\nu)V(jj)$+2 jets was thoroughly described in Section 4.1.2. A summary of the analysis workflow is sketched in Figure 4.2. As a brief overview, the analysis targets the presence of an isolated charged lepton (e, μ) and moderate missing transverse energy, compatible with a W boson decay ($m_T^W > 185$ GeV). Two jets targeting the VBS topology are selected with $p_T^j > 50$ GeV, $m_{jj} > 500$ GeV and $|\Delta\eta_{jj}| > 2.5$. The analysis then defines two regimes based on the decay products of the V boson. A resolved regime searches for two more additional small-radius jets well separated in $\Delta R > 0.4$. If the V boson is boosted its decay products will be collimated and a large-radius jet should be present in the event. If this is the case, the analysis defines a boosted regime. For both regimes, a W+jets control region is defined by requiring the V boson to be off-the-mass-shell, outside a mass window defined for both Z or W bosons. If the V boson is on-shell, a control region to measure the normalization of the top-induced background processes directly from data is defined by requiring at least one b-tagged jet in the events. Events with zero b-jets otherwise fall in the VBS signal region.

Due to the lack of precision in simulating the dominant background in the signal region,

namely the W+jets, a differential data-driven approach has been designed. The W+jets sample is split in 21 (7) bins in the resolved (boosted) regions as a function of $p_T^W - p_T^{\mathrm{VBS},2}$ (p_T^W) and their normalizations are left free to float in the maximum likelihood fit and are mostly constrained in the W+jets control region. The effect is automatically propagated, along with parameter uncertainties, to the signal region.

The signal is extracted with two DNNs trained separately for the resolved and boosted regimes. A binned maximum likelihood fit is performed, combining 12 regions per year of data taking (splitting in e and μ), on the DNN spectra to extract the pure EW signal strength and the joint EW+QCD one.

5.2.5 ZV semileptonic ($2ljj$)

While CMS reported for the first time evidence for the VBS production of a WV pair with a semileptonic final state, the VBS ZV counterpart remains unexplored. Only recently efforts were made to analyze the final state produced by $pp \to l^+l^-jjjj$ in order to extend the previous results, reported by CMS with an integrated luminosity of 35.9 fb^{-1} [136], to the full Run II statistics. The event selection targets events with two oppositely-charged leptons with the same flavour (either e or μ), compatible with the decay of a Z boson, with $p_T > 35$ GeV and within CMS acceptance $|\eta| < 2.5$ (2.4) for electrons (muons). Two VBS jets should be present in the event and should satisfy requirements tailored to the VBS topology such as $p_T^j > 50$ GeV, $m_{jj} > 500$ GeV and $|\Delta\eta_{jj}| > 2.5$. Similarly to the semileptonic WV analysis, two regimes are defined based on the kinematic of the hadronically decaying V boson: a boosted regime, characterized by the presence of a reconstructed large-radius jet, and a resolved regime where two additional small-radius jets are present in the event and well separated in $\Delta R > 0.4$. In the latter regime, the ambiguity in the jet association is resolved using the same algorithm employed by the WV analysis and follows from dedicated studies. Of all the jets in a resolved event, the dijet pair with the invariant mass closest to the W or Z boson mass is selected as a candidate for the hadronically decaying V-boson. Out of the remaining jets in the event, the dijet pair with the highest invariant mass is chosen as the VBS tag jets. For each kinematic regime, three regions are defined. A control region for the major background, the DY+jets, is defined by requiring for the hadronically decaying V-boson to be off-the-mass shell ($m_{\mathrm{V}} \notin (65, 105)$ GeV). If the V boson has an invariant mass compatible with the one of a Z or W boson ($m_{\mathrm{V}} \in (65, 105)$ GeV) then a top control region is defined by requiring that the two leptons in the event have a different flavour. If the event contains two leptons with the same flavour, and is compatible with a Z-boson decay in terms of the invariant mass, then the event will fall in the VBS signal region. Both the DY control region and the VBS signal region present an additional splitting based on the number of b-tagged jets to isolate regions with possibly different background compositions. Figure 5.4 summarises the ZV analysis regions.

As for the semileptonic WV analysis, the simulation of the major background, DY+jets, is limited at the LO accuracy up to four additional jets at the matrix element and shows large disagreement in the DY control region. A differential data-driven correction is derived by splitting the DY sample into phase spaces characterized by similar disagreement and assigning to each a normalization parameter. The latter are left free to float in the joint fit with the signal region and the correction along with its uncertainty is propagated to the signal region for the measurement of the figures of interest. The DY+jets sample is split in twelve bins of $p_T^Z - p_T^{\mathrm{VBS},2}$ (five bins in p_T^Z) for 2017 and 2018 resolved (boosted) regimes. For the 2016 data-taking, where the discrepancies between data and MC simulations are less significant, only five bins in p_T^Z are used to correct the DY+jets sample for both resolved and boosted regimes. The splitting is applied equally for both b-tagged and b-vetoed DY control regions. The top control region shows

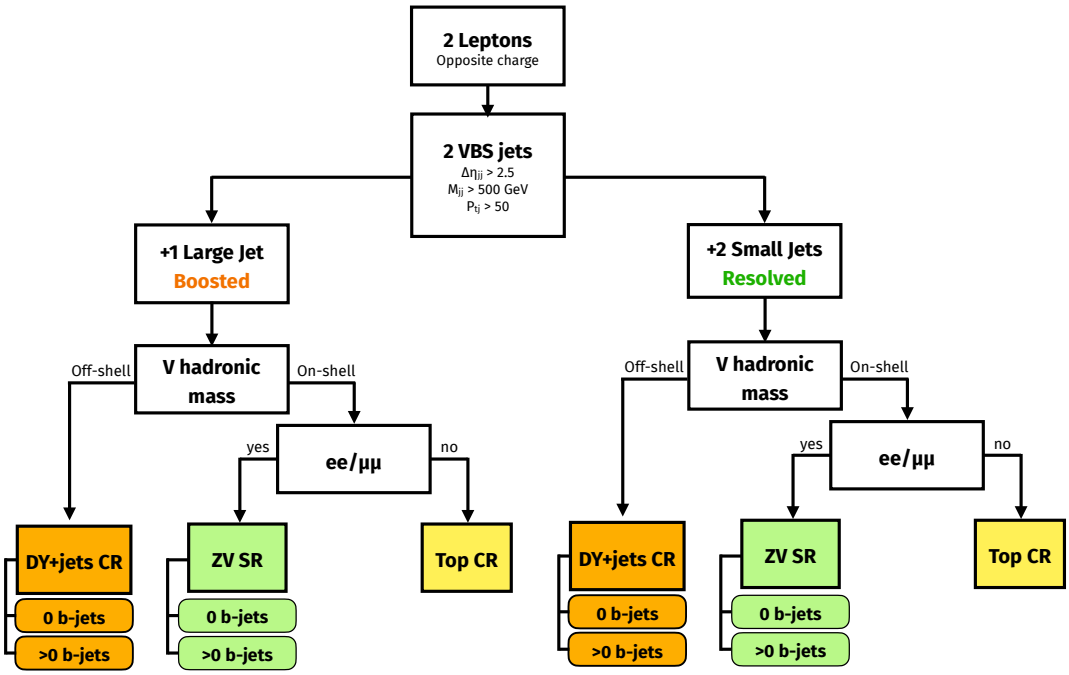

Figure 5.4: Schema summarising the semileptonic VBS ZV analysis regions and selections

a good agreement between data and simulations benefiting from the NNLO (NLO) precision in the $t\bar{t}$ (tW) samples, nevertheless, the normalization of the top background is measured from data to reduce the uncertainty on its estimate. The shape and yield of minor backgrounds such as W+jets, tZq production, diboson and triboson production are taken directly from the MC simulation.

The signal is extracted with eight different DNN models trained to separate the EW signal from the dominant backgrounds. A single model for all years has been trained for each boosted signal region (b-veto and b-tagged). For the resolved counterpart, each year is analyzed separately and a DNN model is trained for each b-tagged region (six models in total). The DNN spectrum in the signal regions is provided as input to a binned maximum likelihood fit jointly with the DY and top control regions.

The analysis is still ongoing so the significance, reported in Table 5.9, is computed assuming the SM to build an Asimov dataset, without using actual data. The Asimov dataset is a synthetic dataset built from the MC or data-driven templates and setting all parameters to their nominal value (assuming the SM, all signal strengths and background parameters to measure their cross-sections will be set to 1 while all nuisance parameters will have a nominal value of 0). Due to the lower cross-section for the VBS production of a ZV pair with respect to a WV pair, the expected significance assuming the SM is approximately half compared to the semileptonic VBS-WV analysis. Despite the low signal over background ratio, the VBS ZV semileptonic process is the only channel that up to now can provide an independent constraint to the ZZ signal strength, along with the fully leptonic ZZ($4l$) channel.

	2016	**2017**	**2018**	**Combination**
σ (exp)	0.72	0.99	1.15	1.8

Table 5.9: Expected significance assuming the SM for the semileptonic VBS-ZV processes split in data taking years and for their combination.

5.3 Nuisance parameters treatment

The treatment of the correlation between the uncertainties of the analyses involved is a crucial aspect of the combination. The VBS Run II combination follows the prescriptions for the ATLAS and CMS Higgs combination in order to properly correlate the uncertainties as described in Ref. [186]. However some remarks are needed as the VBS combination involves analyses that were published, or are still ongoing, that span a timescale of up to four years. Due to this fact, some studies present very different structures in their correlation patterns as almost no harmonization has been done because of a possible combination. In general, such patterns are left untouched and the uncertainties are left uncorrelated. Analysis-specific uncertainties, such as Higgs-related uncertainties in OSWW or QGL uncertainties in WV are also left untouched.

In general, the following approach has been carried wherever possible:

- Luminosity uncertainties have been redefined for all the analyses to the latest recommendations. For each year the luminosity uncertainty is split into a component correlated among all processes and analyses but not across the years, and six components correlate across all years, processes and analyses.
- Theory systematical uncertainties, such as QCD scales (μ_F and μ_R variations), have been correlated among all signal processes. For background processes, the QCD scales have been correlated only for similar processes or groups of processes (e.g. for tVX and tZq respectively in SSWW and ZV).
- PDFs have been loosely correlated. Two of the analyses (WV, ZV) define a common log-normal uncertainty correlated across all processes and between 2017 and 2018 data-taking periods (2016 is uncorrelated from 2017 and 2018). SSWW and WZ analyses define a single parameter correlated across all processes and years. Other analyses define uncorrelated PDF uncertainties for specific processes or groups of processes that never overlap.
- Underlying Event uncertainties have been correlated across years and analyses whenever available.
- PU uncertainties have been correlated across years and analyses whenever available.
- PS uncertainties have been correlated across years and analyses whenever available. The WV analysis is the only one defining an uncorrelated PS (ISR or FSR) uncertainty for each process.
- Trigger uncertainties have been correlated between OSWW, WV and ZV.
- Lepton efficiency and momentum scale/resolution uncertainties have been correlated across all analyses, not correlated across years. the SSWW and WZ only provide a single uncertainty correlated across all processes and years. The latter is left uncorrelated.
- Nuisances regarding the fake lepton background estimate affect all channels, however, the processes leading to a nonprompt lepton or a jet misidentified as lepton are very different. For this reason, only the statistical part of the fake uncertainty has been correlated across all analyses and split by years, accounting both for the limited size of the samples used to measure the fake rates and for the difference in the flavour composition of the jets faking the leptons between the measurement sample and the signal region, while the statistical component (log-normal 30% added to properly cover for the uncertainty due to flavour variation) is left uncorrelated.
- JES and JER uncertainties on small-radius (AK4) jets have been correlated among

OSWW, WV and WZ. These analyses implement the full split set of JES uncertainty sources [219]. Other channels, implementing a different split are correlated on their own.

- All sources of uncertainty on the large-radius jets (AK8) such as JES, JER, jet mass scale and resolution have been correlated between WV and ZV, the only analyses targeting boosted regimes.
- b-tagging uncertainties have been correlated across OSWW, WV and ZV as they provide the full split of the uncertainty sources in four components correlated across all processes and bins but uncorrelated across years, and five components correlated across all processes, bins and years. The b-tag uncertainty of the remaining channels is left uncorrelated.
- Jet pileup identification uncertainties, split across years, have been correlated across OSWW, WV and ZV. Other analyses do not define such an uncertainty.
- Uncertainties related to the limited number of simulated events are taken into account with the Barlow-Beeston-lite approach [185, 220] and the threshold is left untouched to the value defined by each analysis (the threshold, above which the uncertainty will be modeled with the Barlow-Beeston-lite approach, is set to 10 unweighted events in the majority of the bins).

The full list of nuisances and their correlation, split by channel, is reported in Tables 5.10 and 5.11. For analyses that implement the same uncertainty but with a different type, for example, log-normal and shape, by default the log-normal uncertainty will be treated as a shape uncertainty.

Nuisance	type	OS	SS WZ	ZZ	WV	ZV	Nuisance	type	OS	SS WZ	ZZ	WV	ZV
QCDScale_qcdloop_ZZ	lnN	-	-	✓	-	-	QCDscale_AsLnN	lnN	✓	-	-	-	-
QCDscale_DY	shape	✓	-	-	✓	✓	QCDscale_IntfWW_ACCEPT	shape	-	✓	-	-	-
QCDscale_IntfWZ_ACCEPT	shape	-	✓	-	-	-	QCDscale_Other_ACCEPT	shape	-	✓	-	-	-
QCDscale_QCD_OSWW	shape	✓	-	-	✓	-	QCDscale_QCD_SSWW	shape	-	✓	-	✓	-
QCDscale_QCD_WZ	shape	-	-	-	✓	-	QCDscale_QCD_ZZ	shape	-	-	-	✓	-
QCDscale_TVX	shape	-	✓	-	-	✓	QCDscale_VBF-V	shape	-	-	-	✓	✓
QCDscale_VBS_VV_QCD	shape	-	-	-	-	✓	QCDscale_VG_ACCEPT	shape	-	✓	-	-	-
QCDscale_VH	lnN	✓	-	-	-	-	QCDscale_VV	shape	✓	-	-	-	-
QCDscale_VVV	shape	-	-	-	✓	✓	QCDscale_VZ	shape	-	-	-	-	✓
QCDscale_Vg	shape	-	-	-	✓	✓	QCDscale_VgS	shape	-	-	-	✓	✓
QCDscale_WJets	shape	-	-	-	✓	✓	QCDscale_WS_ACCEPT	shape	-	✓	-	-	-
QCDscale_WWewk_AsLnN	lnN	✓	-	-	-	-	QCDscale_WZ_ACCEPT	shape	-	✓	-	-	-
QCDscale_ZZ_ACCEPT	shape	-	✓	-	-	-	QCDscale_ewk_OSWW	shape	✓	-	-	✓	-
QCDscale_ewk_SSWW	shape	-	✓	-	✓	-	QCDscale_ewk_WZ	shape	-	✓	-	✓	-
QCDscale_ewk_ZZ	shape	-	-	✓	✓	-	QCDscale_ggVV	lnN	✓	-	-	-	-
QCDscale_ggZH	lnN	✓	-	-	-	-	QCDscale_gg_ACCEPT	lnN	✓	-	-	-	-
QCDscale_qcd_ZZ	shape	-	-	✓	-	-	QCDscale_qqH	lnN	✓	-	-	-	-
QCDscale_qqbar_ACCEPT	lnN	✓	-	-	-	-	QCDscale_top	shape	✓	-	-	✓	✓
QCDscale_ttH	lnN	✓	-	-	-	-	QCDscale_ttZ_tribos	lnN	-	-	✓	-	-
UE_CP5	lnN	✓	-	-	✓	✓	UE_CUET	lnN	✓	-	-	✓	✓
lumi_13TeV_2016	lnN	✓	✓	✓	✓	✓	lumi_13TeV_2017	lnN	✓	✓	✓	✓	✓
lumi_13TeV_2018	lnN	✓	✓	✓	✓	✓	lumi_13TeV_BBDefl	lnN	✓	✓	✓	✓	✓
lumi_13TeV_CurrCalib	lnN	✓	✓	✓	✓	✓	lumi_13TeV_DynBeta	lnN	-	-	-	✓	✓
lumi_13TeV_Ghosts	lnN	✓	✓	✓	✓	✓	lumi_13TeV_LSCale	lnN	✓	✓	✓	✓	✓
lumi_13TeV_XYFact	lnN	✓	✓	✓	✓	✓	pdf_1718	shape	-	-	-	✓	✓
pdf_Higgs_gg	lnN	✓	-	-	-	-	pdf_Higgs_gg_ACCEPT	lnN	✓	-	-	-	-
pdf_Higgs_qqbar	lnN	✓	-	-	-	-	pdf_Higgs_qqbar_ACCEPT	lnN	✓	-	-	-	-
pdf_Higgs_ttH	lnN	✓	-	-	-	-	pdf_ewk_ZZ_16	lnN	-	-	✓	-	-
pdf_ewk_ZZ_1718	lnN	-	-	✓	-	-	pdf_ewk_ZZ_1718bar	lnN	-	-	✓	-	-
pdf_gg_ACCEPT	lnN	✓	-	-	-	-	pdf_qcd_16	lnN	-	-	✓	-	-
pdf_qcdloop_16	lnN	-	-	✓	-	-	pdf_qcdloop_1718	lnN	-	-	✓	-	-
pdf_qqbar	shape	✓	✓	-	-	-	pdf_qqbar_ACCEPT	lnN	✓	-	-	-	-
CMS_eff_e	shape	-	✓	-	-	-	CMS_eff_e_2016	shape	✓	-	✓	✓	✓
CMS_eff_e_2017	shape	✓	-	✓	✓	✓	CMS_eff_e_2018	shape	✓	-	✓	✓	✓
CMS_eff_m	shape	-	✓	-	-	-	CMS_eff_m_2016	shape	✓	-	✓	✓	✓
CMS_eff_m_2017	shape	✓	-	✓	✓	✓	CMS_eff_m_2018	shape	✓	-	✓	✓	✓
CMS_eff_prefiring_2016	shape	✓	✓	✓	✓	✓	CMS_eff_prefiring_2016_ewk_ZZ	shape	-	-	✓	-	-
CMS_eff_prefiring_2017	shape	✓	✓	✓	✓	✓	CMS_eff_prefiring_2017_ewk_ZZ	shape	-	-	✓	-	-
CMS_eff_prefiring_2018	shape	-	✓	-	-	-	CMS_eff_trigger_2016	shape	✓	-	-	✓	✓
CMS_eff_trigger_2017	shape	✓	-	-	✓	✓	CMS_eff_trigger_2018	shape	✓	-	-	✓	✓
CMS_fakeE3L_2016	shape	-	✓	-	-	-	CMS_fakeE3L_2017	shape	-	✓	-	-	-
CMS_fakeE3L_2018	shape	-	✓	-	-	-	CMS_fakeE_2016	shape	-	✓	-	-	-
CMS_fakeE_2017	shape	-	✓	-	-	-	CMS_fakeE_2018	shape	-	✓	-	-	-
CMS_fakeM3L_2016	shape	-	✓	-	-	-	CMS_fakeM3L_2017	shape	-	✓	-	-	-
CMS_fakeM3L_2018	shape	-	✓	-	-	-	CMS_fakeM_2016	shape	-	✓	-	-	-
CMS_fakeM_2017	shape	-	✓	-	-	-	CMS_fakeM_2018	shape	-	✓	-	-	-
CMS_fake_e_2016	shape	✓	-	-	✓	✓	CMS_fake_e_2017	shape	✓	-	-	✓	✓
CMS_fake_e_2018	shape	✓	-	-	✓	✓	CMS_fake_m_2016	shape	✓	-	-	✓	✓
CMS_fake_m_2017	shape	✓	-	-	✓	✓	CMS_fake_m_2018	shape	✓	-	-	✓	✓
CMS_fake_stat_e_2016	shape	✓	-	-	✓	✓	CMS_fake_stat_e_2017	shape	✓	-	-	✓	✓
CMS_fake_stat_e_2018	shape	✓	-	-	✓	✓	CMS_fake_stat_m_2016	shape	✓	-	-	✓	✓
CMS_fake_stat_m_2017	shape	✓	-	-	✓	✓	CMS_fake_stat_m_2018	shape	✓	-	-	✓	✓
CMS_fake_syst	lnN	-	-	-	-	✓	CMS_fake_syst_e	lnN	✓	-	-	-	-
CMS_fake_syst_e_WV	lnN	-	-	-	✓	-	CMS_fake_syst_em	lnN	-	-	-	-	✓
CMS_fake_syst_m	lnN	✓	-	-	-	-	CMS_fake_syst_m_WV	lnN	-	-	-	✓	-
CMS_res_j_2016	shape	-	✓	✓	-	-	CMS_res_j_2017	shape	✓	✓	✓	✓	✓
CMS_res_j_2018	shape	✓	✓	✓	✓	✓	CMS_scale_JESAbsolute	shape	✓	-	-	✓	✓
CMS_scale_JESAbsolute_2016	shape	✓	-	-	✓	✓	CMS_scale_JESAbsolute_2017	shape	✓	-	-	✓	✓
CMS_scale_JESAbsolute_2018	shape	✓	-	-	✓	✓	CMS_scale_JESBBEC1	shape	✓	-	-	✓	✓
CMS_scale_JESBBEC1_2016	shape	✓	-	-	✓	✓	CMS_scale_JESBBEC1_2017	shape	✓	-	-	✓	✓
CMS_scale_JESBBEC1_2018	shape	✓	-	-	✓	✓	CMS_scale_JESEC2	shape	✓	-	-	✓	✓
CMS_scale_JESEC2_2016	shape	✓	-	-	✓	✓	CMS_scale_JESEC2_2017	shape	✓	-	-	✓	✓
CMS_scale_JESEC2_2018	shape	✓	-	-	✓	✓	CMS_scale_JESFlavorQCD	shape	✓	-	-	✓	✓
CMS_scale_JESHF	shape	✓	-	-	✓	✓	CMS_scale_JESHF_2016	shape	✓	-	-	✓	✓
CMS_scale_JESHF_2017	shape	✓	-	-	✓	✓	CMS_scale_JESHF_2018	shape	✓	-	-	✓	✓
CMS_scale_JESRelativeBal	shape	✓	-	-	✓	✓	CMS_scale_JESRelative_2016	shape	✓	-	-	✓	✓
CMS_scale_JESRelative_2017	shape	✓	-	-	✓	✓	CMS_scale_JESRelative_2018	shape	✓	-	-	✓	✓
CMS_scale_cleanfatJER_2016	shape	-	-	-	-	✓	CMS_scale_cleanfatJER_2017	shape	-	-	-	-	✓
CMS_scale_cleanfatJER_2018	shape	-	-	-	-	✓	CMS_scale_cleanfatJES_2016	shape	-	-	-	-	✓
CMS_scale_cleanfatJES_2017	shape	-	-	-	-	✓	CMS_scale_cleanfatJES_2018	shape	-	-	-	-	✓
CMS_scale_e	lnN	-	✓	-	-	-	CMS_scale_e_2016	shape	✓	-	-	✓	✓
CMS_scale_e_2017	shape	✓	-	-	✓	✓	CMS_scale_e_2018	shape	✓	-	-	✓	✓
CMS_scale_j_2016	shape	-	✓	✓	-	-	CMS_scale_j_2017	shape	-	✓	✓	-	-
CMS_scale_j_2018	shape	-	✓	✓	-	-	CMS_scale_m	lnN	-	✓	-	-	-
CMS_scale_mVjer_2016	shape	-	-	-	-	✓	CMS_scale_mVjer_2017	shape	-	-	-	-	✓
CMS_scale_mVjesTotal_2016	shape	-	-	-	-	✓	CMS_scale_mVjesTotal_2017	shape	-	-	-	-	✓
CMS_scale_mVjesTotal_2018	shape	-	-	-	-	✓	CMS_scale_m_2016	shape	✓	-	-	✓	✓
CMS_scale_m_2017	shape	✓	-	-	✓	✓	CMS_scale_m_2018	shape	✓	-	-	✓	✓
CMS_scale_met_2016	lnN	✓	-	-	✓	-	CMS_scale_met_2017	lnN	✓	-	-	✓	-
CMS_scale_met_2018	lnN	✓	-	-	✓	-	CMS_trigger_2016	shape	-	✓	-	-	-
CMS_trigger_2017	shape	-	✓	-	-	-	CMS_trigger_2018	shape	-	✓	-	-	-
CMS_2e2mu_Zjets_2016	lnN	-	-	✓	-	-	CMS_2e2mu_Zjets_2017	lnN	-	-	✓	-	-
CMS_2e2mu_Zjets_2018	lnN	-	-	✓	-	-	CMS_4e_Zjets_2016	lnN	-	-	✓	-	-
CMS_4e_Zjets_2017	lnN	-	-	✓	-	-	CMS_4e_Zjets_2018	lnN	-	-	✓	-	-
CMS_4mu_Zjets_2016	lnN	-	-	✓	-	-	CMS_4mu_Zjets_2017	lnN	-	-	✓	-	-
CMS_4mu_Zjets_2018	lnN	-	-	✓	-	-	CMS_PS_FSR_DY	shape	-	-	-	✓	-
CMS_PS_FSR_QCD_WV	shape	-	-	-	✓	-	CMS_PS_FSR_QCD_ZV	shape	-	-	-	✓	-
CMS_PS_FSR_VBF-V_dipole	shape	-	-	-	✓	-	CMS_PS_FSR_VBS_WV	shape	-	-	-	✓	-
CMS_PS_FSR_VBS_ZV	shape	-	-	-	✓	-	CMS_PS_FSR_VVV	shape	-	-	-	✓	-
CMS_PS_FSR_Vg	shape	-	-	-	✓	-	CMS_PS_FSR_VgS	shape	-	-	-	✓	-
CMS_PS_FSR_Wjets_boost_1	shape	-	-	-	✓	-	CMS_PS_FSR_Wjets_boost_2	shape	-	-	-	✓	-
CMS_PS_FSR_Wjets_boost_3	shape	-	-	-	✓	-	CMS_PS_FSR_Wjets_boost_4	shape	-	-	-	✓	-
CMS_PS_FSR_Wjets_boost_5	shape	-	-	-	✓	-	CMS_PS_FSR_Wjets_boost_6	shape	-	-	-	✓	-
CMS_PS_FSR_Wjets_boost_7	shape	-	-	-	✓	-	CMS_PS_FSR_Wjets_res_1	shape	-	-	-	✓	-
CMS_PS_FSR_Wjets_res_10	shape	-	-	-	✓	-	CMS_PS_FSR_Wjets_res_11	shape	-	-	-	✓	-
CMS_PS_FSR_Wjets_res_12	shape	-	-	-	✓	-	CMS_PS_FSR_Wjets_res_13	shape	-	-	-	✓	-
CMS_PS_FSR_Wjets_res_14	shape	-	-	-	✓	-	CMS_PS_FSR_Wjets_res_15	shape	-	-	-	✓	-
CMS_PS_FSR_Wjets_res_16	shape	-	-	-	✓	-	CMS_PS_FSR_Wjets_res_17	shape	-	-	-	✓	-
CMS_PS_FSR_Wjets_res_18	shape	-	-	-	✓	-	CMS_PS_FSR_Wjets_res_19	shape	-	-	-	✓	-
CMS_PS_FSR_Wjets_res_2	shape	-	-	-	✓	-	CMS_PS_FSR_Wjets_res_20	shape	-	-	-	✓	-

Table 5.10: Uncertainty correlation for the Run II VBS combination

Nuisance	type	OS	SS WZ	ZZ	WV	ZV	Nuisance	type	OS	SS WZ	ZZ	WV	ZV
CMS_PS_FSR_Wjets_res_21	shape	-	-	-	✓	-	CMS_PS_FSR_Wjets_res_3	shape	-	-	-	✓	-
CMS_PS_FSR_Wjets_res_4	shape	-	-	-	✓	-	CMS_PS_FSR_Wjets_res_5	shape	-	-	-	✓	-
CMS_PS_FSR_Wjets_res_6	shape	-	-	-	✓	-	CMS_PS_FSR_Wjets_res_7	shape	-	-	-	✓	-
CMS_PS_FSR_Wjets_res_8	shape	-	-	-	✓	-	CMS_PS_FSR_Wjets_res_9	shape	-	-	-	✓	-
CMS_PS_FSR_ggWW	shape	-	-	-	✓	-	CMS_PS_FSR_top	shape	-	-	-	✓	-
CMS_PS_ISR_DY	shape	-	-	-	✓	-	CMS_PS_ISR_QCD_WV	shape	-	-	-	✓	-
CMS_PS_ISR_QCD_ZV	shape	-	-	-	✓	-	CMS_PS_ISR_VBF-V_dipole	shape	-	-	-	✓	-
CMS_PS_ISR_VBS_WV	shape	-	-	-	✓	-	CMS_PS_ISR_VBS_ZV	shape	-	-	-	✓	-
CMS_PS_ISR_VVV	shape	-	-	-	✓	-	CMS_PS_ISR_Vg	shape	-	-	-	✓	-
CMS_PS_ISR_VgS	shape	-	-	-	✓	-	CMS_PS_ISR_Wjets_boost_1	shape	-	-	-	✓	-
CMS_PS_ISR_Wjets_boost_2	shape	-	-	-	✓	-	CMS_PS_ISR_Wjets_boost_3	shape	-	-	-	✓	-
CMS_PS_ISR_Wjets_boost_4	shape	-	-	-	✓	-	CMS_PS_ISR_Wjets_boost_5	shape	-	-	-	✓	-
CMS_PS_ISR_Wjets_boost_6	shape	-	-	-	✓	-	CMS_PS_ISR_Wjets_boost_7	shape	-	-	-	✓	-
CMS_PS_ISR_Wjets_res_1	shape	-	-	-	✓	-	CMS_PS_ISR_Wjets_res_10	shape	-	-	-	✓	-
CMS_PS_ISR_Wjets_res_11	shape	-	-	-	✓	-	CMS_PS_ISR_Wjets_res_12	shape	-	-	-	✓	-
CMS_PS_ISR_Wjets_res_13	shape	-	-	-	✓	-	CMS_PS_ISR_Wjets_res_14	shape	-	-	-	✓	-
CMS_PS_ISR_Wjets_res_15	shape	-	-	-	✓	-	CMS_PS_ISR_Wjets_res_16	shape	-	-	-	✓	-
CMS_PS_ISR_Wjets_res_17	shape	-	-	-	✓	-	CMS_PS_ISR_Wjets_res_18	shape	-	-	-	✓	-
CMS_PS_ISR_Wjets_res_19	shape	-	-	-	✓	-	CMS_PS_ISR_Wjets_res_2	shape	-	-	-	✓	-
CMS_PS_ISR_Wjets_res_20	shape	-	-	-	✓	-	CMS_PS_ISR_Wjets_res_21	shape	-	-	-	✓	-
CMS_PS_ISR_Wjets_res_3	shape	-	-	-	✓	-	CMS_PS_ISR_Wjets_res_4	shape	-	-	-	✓	-
CMS_PS_ISR_Wjets_res_5	shape	-	-	-	✓	-	CMS_PS_ISR_Wjets_res_6	shape	-	-	-	✓	-
CMS_PS_ISR_Wjets_res_7	shape	-	-	-	✓	-	CMS_PS_ISR_Wjets_res_8	shape	-	-	-	✓	-
CMS_PS_ISR_Wjets_res_9	shape	-	-	-	✓	-	CMS_PS_ISR_ggWW	shape	-	-	-	✓	-
CMS_PS_ISR_top	shape	-	-	-	✓	-	CMS_PU_2016	shape	✓	-	-	✓	✓
CMS_PU_2017	shape	✓	-	-	✓	✓	CMS_PU_2018	shape	✓	-	-	✓	✓
CMS_btag_cferr1	shape	✓	-	-	✓	✓	CMS_btag_cferr2	shape	✓	-	-	✓	✓
CMS_btag_heavy_2016	shape	-	✓	-	-	-	CMS_btag_heavy_2017	shape	-	✓	-	-	-
CMS_btag_heavy_2018	shape	-	✓	-	-	-	CMS_btag_hf	shape	✓	-	-	✓	✓
CMS_btag_hfstats1_2016	shape	✓	-	-	✓	✓	CMS_btag_hfstats1_2017	shape	✓	-	-	✓	✓
CMS_btag_hfstats1_2018	shape	✓	-	-	✓	✓	CMS_btag_hfstats2_2016	shape	✓	-	-	✓	✓
CMS_btag_hfstats2_2017	shape	✓	-	-	✓	✓	CMS_btag_hfstats2_2018	shape	✓	-	-	✓	✓
CMS_btag_jes	shape	✓	-	-	✓	✓	CMS_btag_lf	shape	✓	-	-	✓	✓
CMS_btag_lfstats1_2016	shape	✓	-	-	✓	✓	CMS_btag_lfstats1_2017	shape	✓	-	-	✓	✓
CMS_btag_lfstats1_2018	shape	✓	-	-	✓	✓	CMS_btag_lfstats2_2016	shape	✓	-	-	✓	✓
CMS_btag_lfstats2_2017	shape	✓	-	-	✓	✓	CMS_btag_lfstats2_2018	shape	✓	-	-	✓	✓
CMS_btag_light_2016	shape	-	✓	-	-	-	CMS_btag_light_2017	shape	-	✓	-	-	-
CMS_btag_light_2018	shape	-	✓	-	-	-	CMS_embed_veto_2016	lnN	✓	-	-	-	-
CMS_embed_veto_2017	lnN	✓	-	-	-	-	CMS_embed_veto_2018	lnN	✓	-	-	-	-
CMS_fatjet_jmr_2016	shape	-	-	-	✓	✓	CMS_fatjet_jmr_2017	shape	-	-	-	✓	✓
CMS_fatjet_jmr_2018	shape	-	-	-	✓	✓	CMS_fatjet_jms_2016	shape	-	-	-	✓	✓
CMS_fatjet_jms_2017	shape	-	-	-	✓	✓	CMS_fatjet_jms_2018	shape	-	-	-	✓	✓
CMS_fatjet_res_2017	lnN	-	-	-	✓	-	CMS_fatjet_res_2018	shape	-	-	-	✓	✓
CMS_fatjet_tau21eff_2016	shape	-	-	-	✓	-	CMS_fatjet_tau21eff_2017	shape	-	-	-	✓	-
CMS_fatjet_tau21eff_2018	shape	-	-	-	✓	-	CMS_fj_scale_JESAbsolute	lnN	-	-	-	✓	-
CMS_fj_scale_JESAbsolute_2016	lnN	-	-	-	✓	-	CMS_fj_scale_JESAbsolute_2017	lnN	-	-	-	✓	-
CMS_fj_scale_JESAbsolute_2018	lnN	-	-	-	✓	-	CMS_fj_scale_JESBBEC1	lnN	-	-	-	✓	-
CMS_fj_scale_JESBBEC1_2016	lnN	-	-	-	✓	-	CMS_fj_scale_JESBBEC1_2017	lnN	-	-	-	✓	-
CMS_fj_scale_JESBBEC1_2018	lnN	-	-	-	✓	-	CMS_fj_scale_JESEC2	lnN	-	-	-	✓	-
CMS_fj_scale_JESEC2_2016	lnN	-	-	-	✓	-	CMS_fj_scale_JESEC2_2017	lnN	-	-	-	✓	-
CMS_fj_scale_JESEC2_2018	lnN	-	-	-	✓	-	CMS_fj_scale_JESFlavorQCD	lnN	-	-	-	✓	-
CMS_fj_scale_JESHF	lnN	-	-	-	✓	-	CMS_fj_scale_JESHF_2016	lnN	-	-	-	✓	-
CMS_fj_scale_JESHF_2017	lnN	-	-	-	✓	-	CMS_fj_scale_JESHF_2018	lnN	-	-	-	✓	-
CMS_fj_scale_JESRelativeBal	lnN	-	-	-	✓	-	CMS_fj_scale_JESRelativeS_2016	lnN	-	-	-	✓	-
CMS_fj_scale_JESRelativeS_2017	lnN	-	-	-	✓	-	CMS_fj_scale_JESRelativeS_2018	lnN	-	-	-	✓	-
CMS_fj_tau21ptextr_2016	shape	-	-	-	✓	-	CMS_fj_tau21ptextr_2017	shape	-	-	-	✓	-
CMS_fj_tau21ptextr_2018	shape	-	-	-	✓	-	CMS_hww_CRSR_accept_DY	lnN	✓	-	-	-	-
CMS_hww_CRSR_accept_top	lnN	✓	-	-	-	-	CMS_hww_VZScale	lnN	✓	-	-	-	-
CMS_hww_VgStarScale	lnN	✓	-	-	-	-	CMS_jetpuid_2016	shape	✓	-	-	✓	✓
CMS_jetpuid_2017	shape	✓	-	-	✓	✓	CMS_jetpuid_2018	shape	✓	-	-	✓	✓
CMS_pu	shape	-	✓	-	-	-	CMS_topPtRew	shape	-	-	-	✓	✓
CMS_wseff	shape	-	✓	-	-	-	EWKCorrVVWZ	shape	-	✓	-	-	-
EWKqqZZCorr	shape	-	✓	-	-	-	PS_FSR	shape	✓	-	-	-	✓
PS_ISR	shape	✓	-	✓	-	✓	QGLmorph_gluon_he_16	shape	-	-	-	✓	-
QGLmorph_gluon_he_1718	shape	-	-	-	✓	-	QGLmorph_gluon_le_16	shape	-	-	-	✓	-
QGLmorph_gluon_le_1718	shape	-	-	-	✓	-	QGLmorph_quark_he_16	shape	-	-	-	✓	-
QGLmorph_quark_he_1718	shape	-	-	-	✓	-	QGLmorph_quark_le_16	shape	-	-	-	✓	-
QGLmorph_quark_le_1718	shape	-	-	-	✓	-	THU_ggH_Mig01	shape	✓	-	-	-	-
THU_ggH_Mig12	shape	✓	-	-	-	-	THU_ggH_Mu	shape	✓	-	-	-	-
THU_ggH_PT120	shape	✓	-	-	-	-	THU_ggH_PT60	shape	✓	-	-	-	-
THU_ggH_Res	shape	✓	-	-	-	-	THU_ggH_VBF2j	shape	✓	-	-	-	-
THU_ggH_VBF3j	shape	✓	-	-	-	-	THU_ggH_qmtop	shape	✓	-	-	-	-
THU_qqH_EWK	shape	✓	-	-	-	-	THU_qqH_JET01	shape	✓	-	-	-	-
THU_qqH_Mjj1000	shape	✓	-	-	-	-	THU_qqH_Mjj120	shape	✓	-	-	-	-
THU_qqH_Mjj1500	shape	✓	-	-	-	-	THU_qqH_Mjj350	shape	✓	-	-	-	-
THU_qqH_Mjj60	shape	✓	-	-	-	-	THU_qqH_Mjj700	shape	✓	-	-	-	-
THU_qqH_PTH200	shape	✓	-	-	-	-	THU_qqH_PTH25	shape	✓	-	-	-	-
THU_qqH_YIELD	shape	✓	-	-	-	-	WZTauH	shape	-	✓	-	-	-
WZTauL	shape	-	✓	-	-	-	ggZZCorr	shape	-	✓	-	-	-

Table 5.11: Uncertainty correlation for the Run II VBS combination

5.4 Expected results

A binned maximum likelihood fit is performed including simultaneously all analysis regions. A total of 161 phase spaces, 108 processes and 359 uncertainties are included in the fit. Additionally, due to the data-driven corrections in the semileptonic WV and ZV channels, along with data-driven estimates of some sample cross-sections, 1123 rate parameters are simultaneously measured. The statistical procedures employed to obtain the reported results have been thoroughly described in Section 4.2.

The four or six parameters of interest are always left free to float in the minimization procedure and profiled out if not of interest. As the semileptonic ZV analysis is still blinded in the signal region, only expected results assuming the SM are reported. An Asimov dataset is built by fitting real data in the control regions and profiling all nuisances and normalization parameters while keeping all the signal strengths (four or six depending on the model) gauging the EW VBS signals fixed to 1. The expected results in terms of significance over the background-only hypothesis and signal strengths are summarised in Table 5.12 for both statistical models.

		OSWW	SSWW		WZ		ZZ
4-POI	μ	$1.000^{+0.181}_{-0.172}$	$1.000^{+0.174}_{-0.155}$		$1.000^{+0.291}_{-0.248}$		$1.000^{+0.403}_{-0.344}$
	σ	6.2	10.8		5.5		3.7
		W^+W^-	W^+W^+	W^-W^-	W^+Z	W^-Z	ZZ
6-POI	μ	$1.000^{+0.184}_{-0.176}$	$1.000^{+0.178}_{-0.156}$	$1.000^{+0.300}_{-0.261}$	$1.000^{+0.328}_{-0.277}$	$1.000^{+0.451}_{-0.374}$	$1.000^{+0.412}_{-0.349}$
	σ	6.2	11.7	4.6	4.9	3.4	3.7

Table 5.12: Expected significance and signal strength from the full VBS Run-II combination. The top row reports the results for the four-parameter model while the bottom row reports the same results but splitting the signal strength for the W electrical charge.

The likelihood profiles for the four-parameter model are reported in Figure 5.5. While the black curve represents the full combination with six channels and all nuisances profiled, the red curve is the statistical-only limit, obtained by freezing all the constrained nuisances to their best-fit value. The green curve is the likelihood scan obtained from the most sensitive analysis that drives the sensitivity for specific signal strength.

5.4.1 Nuisances impacts

The impact of the nuisances on the parameter of interest is determined by re-evaluating the fit procedure and changing the nuisance value. Firstly the best fit-value for the parameter of interest $\hat{\mu}$ is computed by profiling all the nuisances. The nuisances at the best-fit point are characterized by a nominal value $\hat{\theta}$ and a 68% uncertainty $\sigma_{\pm}(\hat{\theta})$. All constrained (unconstrained) nuisances pre-fit value is fixed to 0 (1) as we rely on MC templates, and the nuisance pull is defined as $(\hat{\theta} - \theta_0)/\sigma(\hat{\theta})$. The value of a nuisance is then changed in its confidence interval by setting it to $\hat{\theta} + \sigma_+(\hat{\theta})$ and then to $\hat{\theta} - \sigma_-(\hat{\theta})$. Two maximum likelihood fits are then performed, keeping the nuisance fixed, and a new estimate for the parameter of interest is obtained $\mu_{\pm}$. The impact of such nuisance on the parameter of interest is then computed as the distance of the parameters obtained with $\hat{\theta} \pm \sigma_{\pm}(\hat{\theta})$ from the best-fit parameter $\Delta\mu = \mu_{\pm} - \hat{\mu}$. The impact values for the top-30 nuisances in the VBS SM combination are summarised, for each of the parameters defined in the four signal strengths model, in Figures 5.6, 5.7, 5.8, 5.9. The parameters are sorted by their impact on the parameter of interest. The figure reports only the

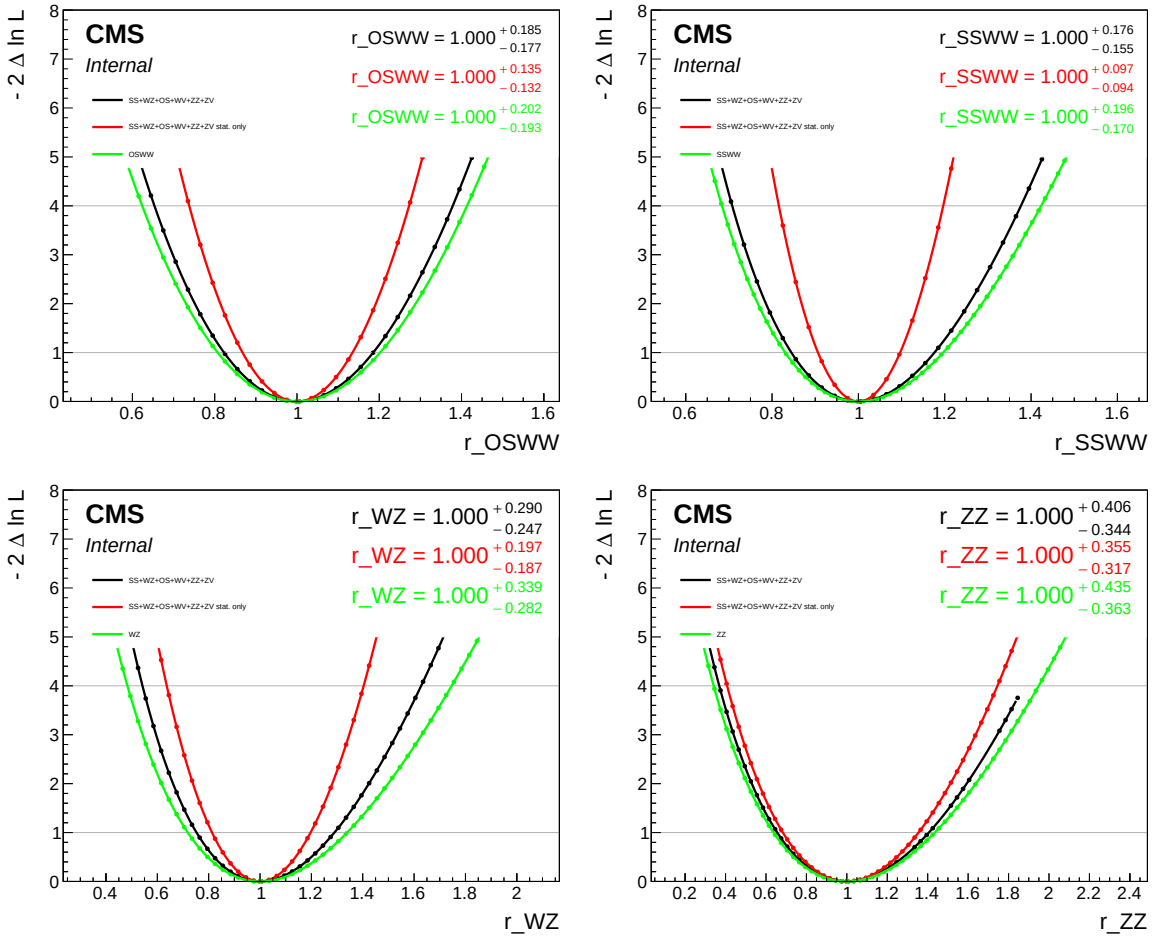

Figure 5.5: Likelihood profiles for the full VBS combination with four free parameters including all nuisances (black) and the statistical-only limit (red). The green curve is the expected profile from only one analysis that is expected to drive the sensitivity for a particular parameter. In the fits, all four signal strengths are left free to float in the minimization and profiled out. From top to bottom, left to right the likelihood profiles are shown for the parameters: OSWW, SSWW, WZ and ZZ.

impact of constrained parameters while neglecting the effect of the normalization ones (such as data-driven corrections to W+jets and DY+jets backgrounds), which are usually among the top-ranked ones depending on the signal strength investigated. The result is that nuisance impacts are found to be under control within each single analysis stability.

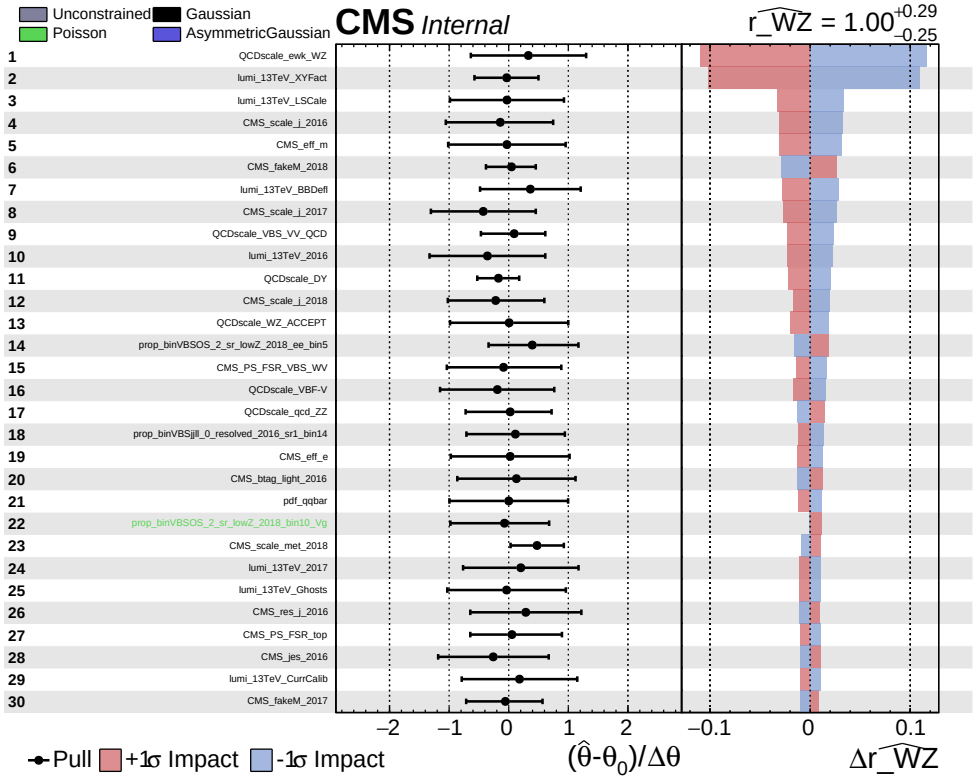

Figure 5.6: Top 30 nuisances from S+B fit (μ_{WZ}=1). An Asimov dataset is used to generate toys where the nuisances are fitted directly to data while fixing the parameter of interest to 1

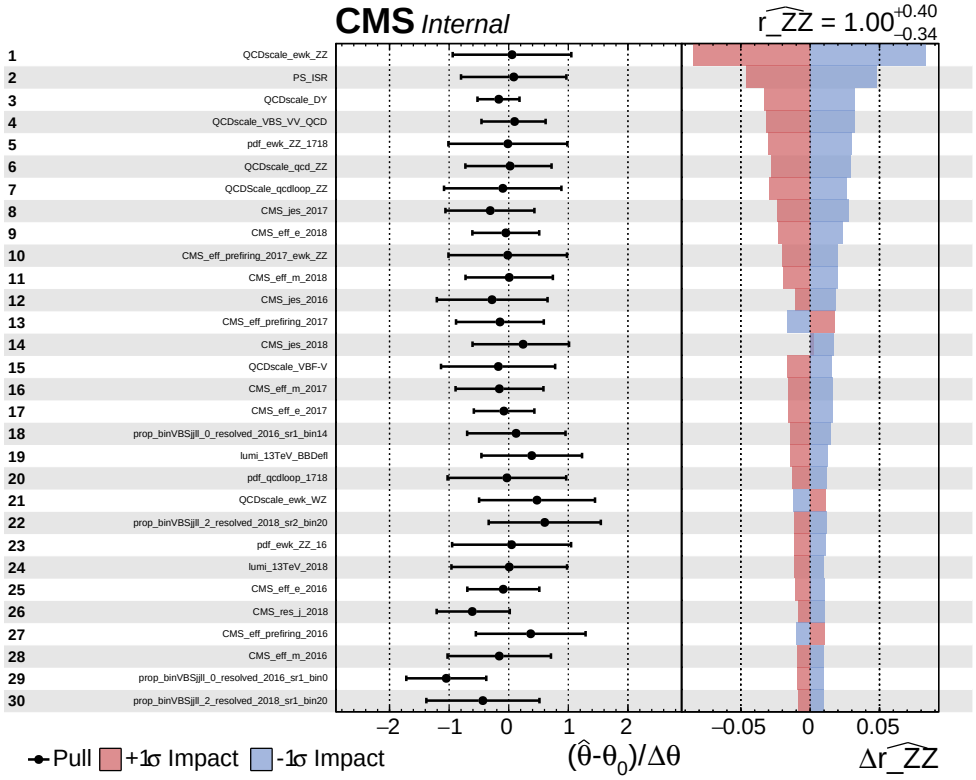

Figure 5.7: Top 30 nuisances from S+B fit (μ_{ZZ}=1). An Asimov dataset is used to generate toys where the nuisances are fitted directly to data while fixing the parameter of interest to 1

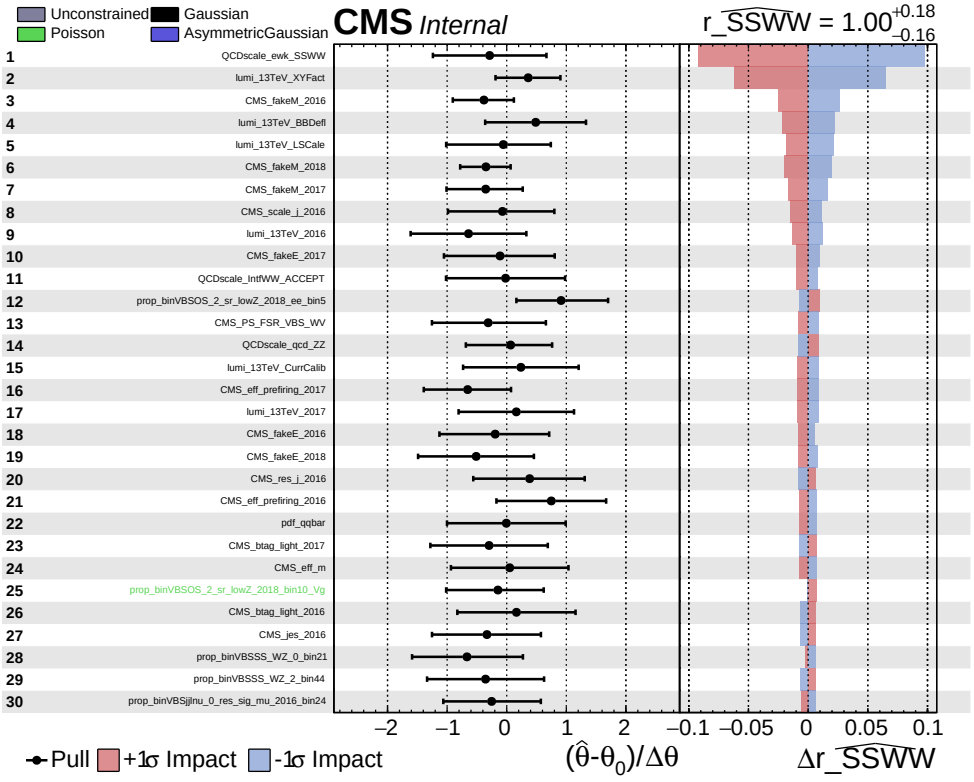

Figure 5.8: Top 30 nuisances from S+B fit (μ_{SSWW}=1). An Asimov dataset is used to generate toys where the nuisances are fitted directly to data while fixing the parameter of interest to 1

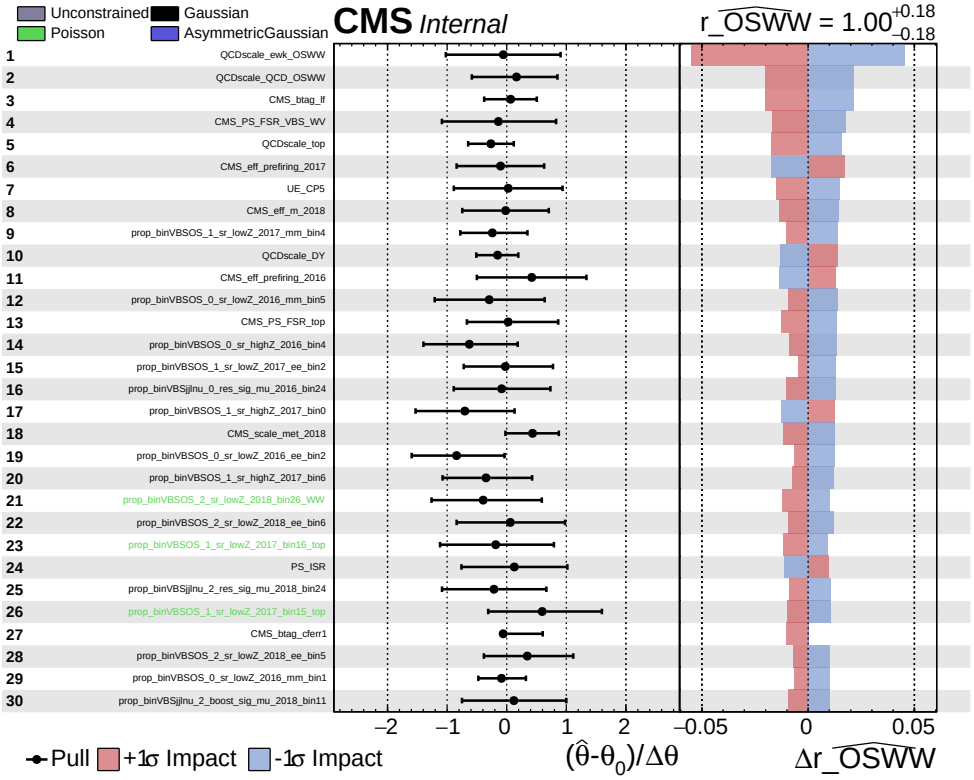

Figure 5.9: Top 30 nuisances from S+B fit (μ_{OSWW}=1). An Asimov dataset is used to generate toys where the nuisances are fitted directly to data while fixing the parameter of interest to 1

5.4.2 Post-fit distributions

Post-fit distributions in the signal regions are shown for each channel and reported in Appendix D. The observable used for the signal extraction is shown as a result of a data-Asimov fit for the normalization parameters to be measured in the CRs and profiling out nuisances while keeping the four or six signal strengths fixed to one. For this reason, the displayed data, corresponding to the Asimov dataset, matches by construction the MC prediction for backgrounds plus the sum of all the signals, scaled by their post-fit scale factor. The uncertainty band on the background prediction is computed by exploiting the full fit parameters by throwing 500 toys from the best post-fit values assuming the SM for the signal strengths. The toys are then fitted and the uncertainty on each distribution bin is taken to be the 68% interval from the distribution of the fit values. While this method proves to be accurate it is computationally expensive and 500 toys are not enough to sample correctly the tails of each bin distribution, making the 95% estimate of the uncertainty unreliable.

To better visualize the result of the VBS combination, in terms of signal excess over the SM background, post-fit distributions of the signal over background bin scores (S/B) are computed for each of the four signal strengths. A distribution of the S/B scores, with nine bins, is filled considering all the observables and phase spaces entering in the final fit and assuming the post-fit background yields. For a specific signal strength μ_i and each bin k of the post-fit templates the value $\log[S(\mu_i = 1)/B]_k$ is computed. The bin of the final distribution containing the value $\log[S(\mu_i = 1)/B]_k$ is then incremented with the number of background, i-signal and data (Asimov) events in the k-th original bin. To estimate the error associated with each bin of the S/B distribution, the uncertainties of each of the k-th bins, falling in a specific S/B bin, are summed. Bin-by-bin correlations are not taken into account in this procedure. The final distributions are shown in Figure 5.10 for all the four signal strengths μ_{ZZ}, μ_{WZ}, μ_{OSWW}, μ_{SSWW}.

5.4.3 Bi-dimensional likelihood profiles

Correlations between the parameters of interest can provide useful insights regarding VBS. Figure 5.11 shows the expected bi-dimensional likelihood profiles for the six signal strengths statistical model. Such fits are performed over a bi-dimensional grid of values for pairs of parameters. All the possible permutations are explored. All other parameters, including nuisances, are profiled in the maximum likelihood fit. No significant correlation is observed among the six or four parameters studied.

5.4.4 Inclusion of $ZZ(2l2\nu)$ and SSWW+τ_h

Two additional VBS analyses can be combined in order to increase the sensitivity to μ_{ZZ} and μ_{SSWW}. The first analysis is the VBS of a pair of Z bosons, one decaying into a pair of charged leptons and the other decaying into neutrinos. The final state of this analysis, namely l^+l^-jj+MET, can overlap with the one from the scattering of two oppositely charged W bosons (OSWW). The selections employed by the $ZZ(2l2\nu)$ analysis are summarised in Table 5.13.

The VBS OSWW analysis combines the opposite flavour category $e\mu$ and two same-flavour categories ee, $\mu\mu$ for the VBS signal region, top and DY control regions. The VBS OSWW $e\mu$ regions are by construction orthogonal to the $ZZ(2l2\nu)$ SR, DY CR and $3l$ CR by the different flavour requirements. They are also orthogonal to the $ZZ(2l2\nu)$ non-resonant CR thanks to a veto on b-jets. The same flavour signal region of OSWW (ee, $\mu\mu$) is instead orthogonal to all $ZZ(2l2\nu)$ regions because of the $m_{ll} > 120$ GeV selection that discards events inside the Z mass window. The same m_{ll} requirement is applied in the OSWW top CR for the same-flavour categories ee, $\mu\mu$.

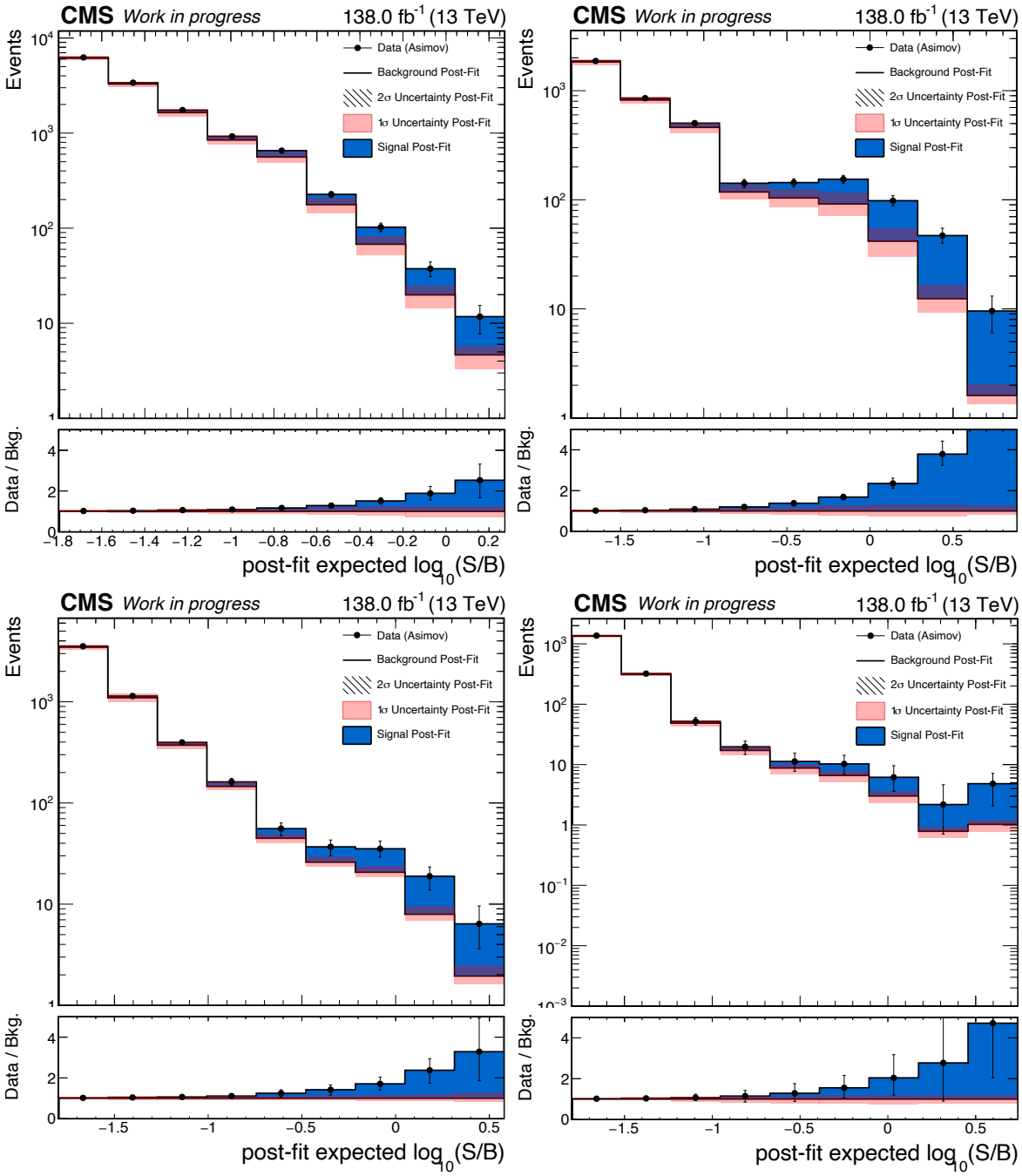

Figure 5.10: Post-fit $\log[S(\mu_i = 1)/B]$ distributions for the VBS SM combination and four parameters model. From left to right, top to bottom, the blue stacked histograms represent the signal yields for μ_{OSWW}, μ_{SSWW}, μ_{ZZ} and μ_{WZ}. Data points are taken from an Asimov dataset built by fitting real data in control regions, profiling nuisances and rate parameters for the backgrounds while fixing the best-fit value for all signal strengths to $\mu_i = 1$ (i =ZZ, WZ, OSWW, SSWW). The post-fit 68% uncertainty band, shown in pink, on the overall background template (filled white) is computed as a sum of the uncertainty of all the input bins. These uncertainties are in turn computed by throwing and fitting 500 toys.

Significant overlaps between the two analyses happen between the $ZZ(2l2\nu)$ signal region and the OSWW DY control region. In the different flavour category, the OSWW analysis applies a b-jet veto making it orthogonal to the $ZZ(2l2\nu)$ non-resonant CR. All other regions are orthogonal

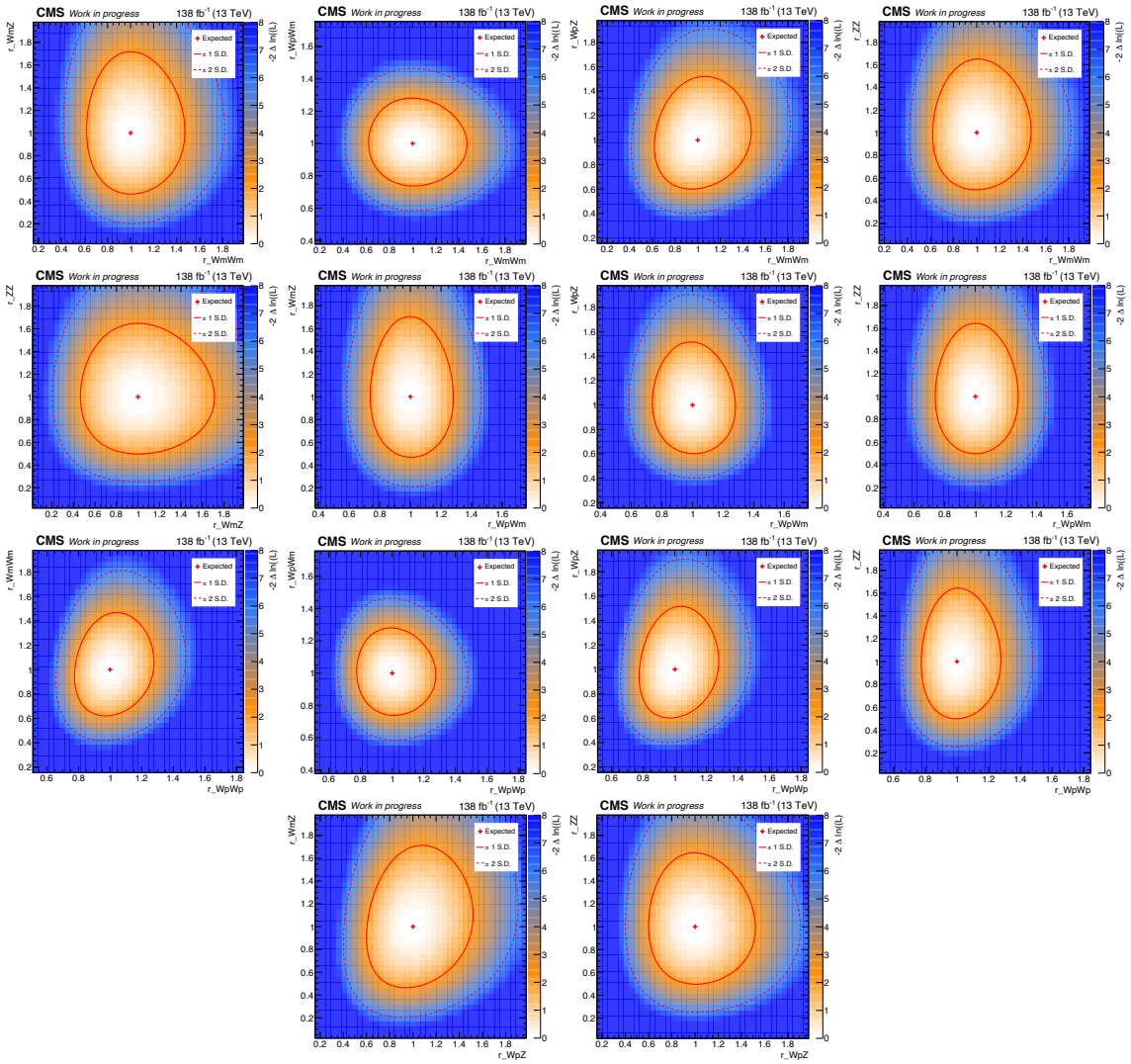

Figure 5.11: Expected bi-dimensional likelihood profiles for the SM VBS combination and 6 parameter model. All parameters are left free to float in the minimization and the ones not of interest are profiled with the nuisance parameters.

by construction thanks to the different flavour requirement. In the same flavour case ee, $\mu\mu$, the OSWW analysis selects events under the Z invariant mass peak $|m_{ll} - m_Z| < 15$ GeV as it is done in the $ZZ(2l2\nu)$ analysis. The OSWW DY CR overlaps with both the $ZZ(2l2\nu)$ signal region and DY CR due to a cut on the missing transverse momentum. OSWW requires $p_T^{\text{miss}} > 60$ GeV while the $ZZ(2l2\nu)$ signal and DY regions require respectively $p_T^{\text{miss}} > 100$ GeV and $50 < p_T^{\text{miss}} < 100$ GeV. While this overlap is significant, the contribution of the EW $ZZ(2l2\nu)$ in the OSWW DY CR is minimal with respect to the overwhelming DY background, making the two analyses effectively decoupled from a statistical point of view. However, this argument will need further investigations by the analysts and strategies should be adopted for the ongoing $ZZ(2l2\nu)$ to mitigate the overlap. Another possibility is to exclude the same-flavour regions of the OSWW analysis as the $e\mu$ categories drive the sensitivity. The latter approach would decrease the sensitivity to OSWW parameters by approximately 20%.

The second analysis that can be combined is the recently public VBS of two leptonically decaying W bosons with a hadronic τ in the final state [221]. The targeted final state is therefore $pp \to l^{\pm}\nu_l\tau_h^{\pm}\nu_\tau jj$ where $l = e, \mu$ and is by construction orthogonal to all other analyses. Its ob-

Variable	SR	DY CR	3l CR	Non-resonant CR
Leptons	2 leptons (+-) ee, $\mu\mu$	2 leptons (+-) ee, $\mu\mu$	2 leptons (+-) +1l ee, $\mu\mu$ +1l	2 leptons (+-) $e\mu$
$p_T(l_1)$	>25 GeV	>25 GeV	>25 GeV	>25 GeV
$p_T(l_2)$	>20 GeV	>20 GeV	>20 GeV	>20 GeV
$p_T(l_3)$	veto	veto	>10 GeV	>10 GeV
$\lvert m_{ll} - m_Z \rvert$	$<$ 15 GeV	$<$ 15 GeV	$<$ 15 GeV	$<$ 15 GeV
p_T^{miss}	$>$ 100 GeV	50-100 GeV	$>$ 100 GeV	$>$ 100 GeV
$p_T(ll)$	$>$ 60 GeV	$>$ 60 GeV	$>$ 60 GeV	$>$ 60 GeV
p_T^j	$>$ 30 GeV	$>$ 30 GeV	$>$ 30 GeV	$>$ 30 GeV
N_{jets}	≥ 2	≥ 2	≥ 2	≥ 2
m_{jj}	$>$ 400 GeV	$>$ 400 GeV	$>$ 400 GeV	$>$ 400 GeV
$\lvert \Delta\eta_{jj} \rvert$	$>$ 2.5	$>$ 2.5	$>$ 2.5	$>$ 2.5
$p_T^{\text{miss}} / p_T(ll)$	0.4-1.8	0.4-1.8	0.4-1.8	0.4-1.8
$\lvert \Delta\phi(p_T^{\text{miss}}, p_T(ll)) \rvert$	$>$ 0.5	$>$ 0.5	$>$ 0.5	$>$ 2.6
b-veto	Required	Required	Required	-
Had. τ	veto	veto	vero	veto

Table 5.13: Summary of the VBS $ZZ(2l2\nu)$ categories and selections

served significance of 2.74 σ suggests that this analysis will bring only a marginal contribution to the combination as the SSWW analysis without τ leptons reaches a sensitivity much larger than $5\,\sigma$.

For the time being, preliminary results will be shown where no attempt is made to resolve the overlaps or properly correlating uncertainties for both the SSWW+τ_h and $ZZ(2l2\nu)$ analyses. The impact of each additional analysis is evaluated by combining them one at a time with the remaining six channels. The expected significance is then extracted, for the four signal strengths model only, and compared to the baseline combination scenario without SSWW+τ_h or $ZZ(2l2\nu)$ analyses, in order to assess their improvement. Table 5.14 summarises the expected significance to the four-parameter model when including or neglecting the two aforementioned analyses in the combination.

POI	σ_{exp}	σ_{exp} (w ZZ($2l2\nu$))	σ_{exp} (w SSWW-τ_h)	σ_{exp} single channel
SSWW	10.8	10.8	10.8	10.4
OSWW	6.2	6.2	6.2	5.5
WZ	5.5	5.5	5.5	4.7
ZZ	3.7	4.2	3.7	3.6

Table 5.14: Expected significance to the 4 parameter model for the combination of six analyses (σ_{exp}) and with the addition of $ZZ(2l2\nu)$ or with the addition of SSWW+τ_h. A 15% improvement in the ZZ parameter expected significance is observed with the addition of $ZZ(2l2\nu)$. Adding SSWW+τ_h brings marginal gains to the combination due to the leading contribution of SSWW without τ leptons, presenting alone a very high signal significance as reported in the last column. The latter column reports the sensitivity for the dominant channel before the combination.

Figure 5.12 shows the likelihood profiles for the baseline combination and for the addition of the SSWW+τ_h and $ZZ(2l2\nu)$ analyses for the parameters of interest μ_{SSWW} and μ_{ZZ} that are expected to be the ones mostly affected by the inclusion of the new channels.

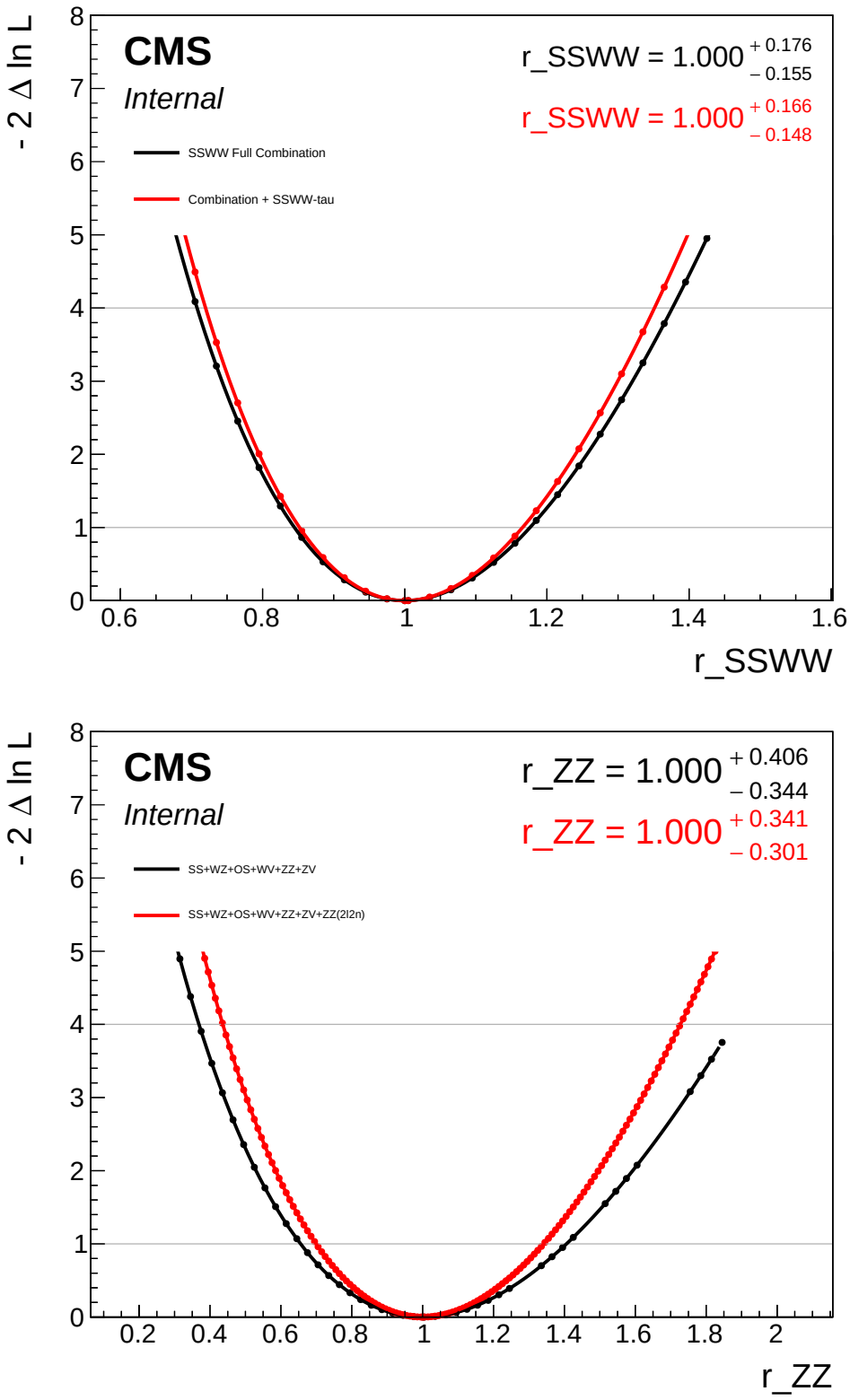

Figure 5.12: Expected likelihood profiles for μ_{SSWW} (left) and μ_{ZZ} (right) from the baseline combination of 6 channels (black) and with the addition of the SSWW+τ_h or $ZZ(2l2\nu)$, displayed as red curves. The uncertainties of the additional channels have been added out of the box. The $ZZ(2l2\nu)$ presents overlaps with OSWW analysis that are not resolved in these scans.

Chapter 6

Data acquisition system for the CMS MIP Timing Detector

6.1 The LHC High Luminosity phase and its challenges

In order to harness the full physics capabilities of the Large Hadron Collider (LHC), CERN established the high-luminosity LHC project in late 2010 with a twofold purpose: reach the machine peak instantaneous luminosity of $5 - 7.5 \times 10^{34}$ cm^{-2}s^{-1} and deliver an integrated luminosity per year of approximately 250 fb^{-1} thus collecting 3000 fb^{-1} for the 12 years of machine operation [222]. In this decade the machine will reach its nominal design beam energy of 7 TeV. The collection of a dataset with such a large integrated luminosity opens a new era for precision physics in all sectors of the SM. A precise determination of the Higgs boson properties and its connection to the symmetry-breaking mechanism are the culprit of the HL-LHC physics programme [223]. The primary Higgs boson couplings, as well as the boson width Γ_h, will be assessed at the High-Luminosity LHC (HL-LHC) with precision reaching the percentage level [224]. When looking at Higgs boson pair production, a direct probe for the Higgs trilinear coupling λ, ATLAS and CMS collaborations project an expected combined sensitivity to the HH signal of approximately 4 s.d. under the SM hypothesis. The nature of the EWSB mechanism will also be studied at energies greater than m_h, with unprecedented precision, by processes involving pairs or triplets of EW gauge bosons [225]. The combined measurement of the individual polarization contributions to the same-sign WW scattering by ATLAS and CMS is expected to yield a significance greater than 3 s.d. for the $W_L W_L$ production thus probing the delicate cancellation between Higgs-mediated processes and processes involving only EW gauge bosons. The production of three massive gauge bosons is expected to be measured with a 20% precision and a significance greater than 3 s.d. for most of the final state. Fundamental parameters of the SM such as $\sin^2\theta_{\text{eff}}$, m_W and m_{top} will be measured with unparallel precision at the per mille level. Other measurements will benefit from the statistical power of the HL-LHC dataset such as direct searches for BSM signatures of dark matter and SUSY candidates [226]. The knowledge of PDFs will be largely improved by the HL-LHC by studying a wide range of processes with jets, top quarks, photons and EW gauge bosons and is expected to reduce the PDF uncertainty by a factor between 2 and 4 [225].

In order to realize the broad HL-LHC physics program, the detectors are expected to efficiently operate under high pile-up conditions, survive the exceedingly high radiation levels for the 12 years of operations and be able to transport a much higher rate of data from the detectors to the storage sites. At the nominal instantaneous luminosity of HL-LHC, the average number of interactions in a single bunch crossing will be approximately 140 with peaks up to 200 for the ultimate scenario of 7.5×10^{34} cm^{-2}s^{-1}. The presence of extra tracks and energy deposits resulting from these simultaneous collisions will impair the ability to identify and reconstruct

the primary interaction, potentially leading to an elevated rate of false triggers.

The LHC experiments will undergo upgrades involving cutting-edge components and state-of-the-art technologies, which are imperative for withstanding radiation damage effects and effectively addressing the challenge presented by the high rate of pileup. Concerning the computing challenges, the expected increase of a factor greater than 10 in the trigger rates and the collected data will be addressed by improvements in software efficiency, scalability and performance, and by making use of advances in heterogeneous computing, storage and network technologies [227].

6.2 CMS upgrades for the HL-LHC

The fundamental objective of the Phase II upgrade is to preserve the outstanding performance of the CMS detector, recorded during the LHC operation, by ensuring efficiency, precision in measurement, and effective rejection of background events for all physics objects used in data analysis [228]. The detector updates are primarily influenced by the impact of radiation damage and pileup, aiming to minimize any deterioration in CMS performance as the integrated luminosity approaches 3 ab^{-1}. The extent of damage caused by radiation varies among the different sub-detectors. For detectors employing silicon active media, radiation produces defects in the silicon lattice and a reduction in the charge collection efficiency. These concurrent effects increase the voltage needed to deplete the full thickness of the detector from charge carriers up to unsustainable values, enforcing operation under partial depletion and consequently lowering the number of recorded signals. Regarding CMS calorimeters, made of scintillating $PbWO_4$ crystals and plastic scintillating materials with embedded wavelength-shifting fibers, the radiation will degrade the transmission properties of the media through which the scintillating light travels with a signal reduction of up to 90%. The effects of the increased number of pileup collisions for each bunch crossing mainly affect the physics performance of CMS and increase the amount of data that has to be read out. With as many as 200 simultaneous interactions, both pileup flavours, namely the in-time pileup and out-of-time pileup (OOT), need to be taken into account in the design of the detector. The presence of additional hits in the tracking detectors may lead to mis-measured or misidentified tracks. These additional tracks may affect the capability to identify isolated leptons, namely leptons with little hadronic activity in their surrounding, that are typically produced in interesting EW processes. An increased pileup will also affect calorimetric measurements by providing additional energy deposits that cannot be easily disentangled from the ones of the hard scatter. In order to correctly identify pileup collisions, tracking detectors for the HL-LHC will be equipped with highly granular sensors thus providing a correct association between charged particles and the originating interaction vertices even with 200 concurrent collisions. While calorimeters cannot associate energy deposits with their interaction vertices, advanced algorithms such as the widely used Particle Flow [229] can link charged tracks in the shower with a particular vertex allowing the subtraction of the pileup contributions from the measurements [176, 230]. The effect of OOT depends mainly on the electronics readout of each sub-detector. Fast shaping times, such as those implemented in the tracking system, with respect to the inter-bunch spacing of 25 ns are preferred in order to suppress OOT. On the contrary, sub-detectors needing longer shaping times, such as CMS calorimeters, are more affected by OOT as pulses from early or late pileup collisions might be integrated with the triggered signal as shown in the right side of Figure 6.1. Timing and pulse shape information can be used to subtract this contribution and will play a significant role in the HL-LHC era.

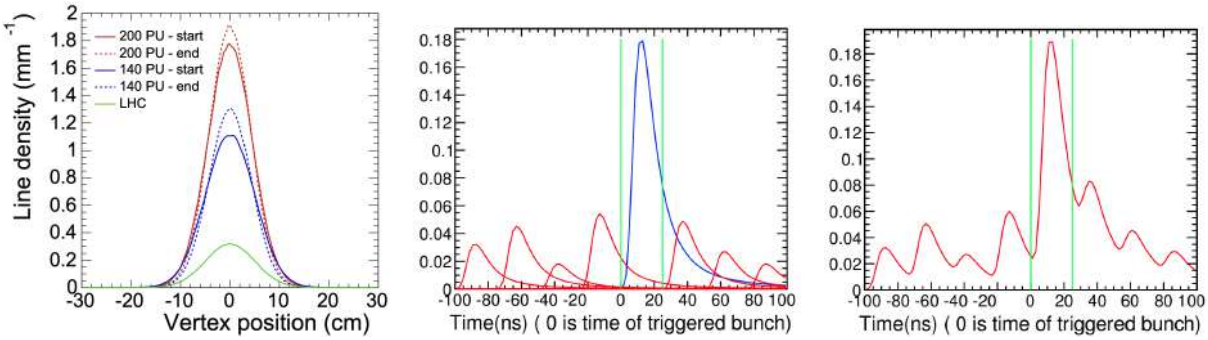

Figure 6.1: The Left plot from [231] shows the distribution of the number of vertices and their z-position along the beam direction at the LHC (green) with $\sim$ 30 pileup collisions and at the HL-LHC with 140 (blue) or 200 (red) pileup. Solid (dashed) lines indicate the expected distributions at the beginning (end) of a fill. The middle and right plots from [228] show the effect of the out-of-time pileup. In the middle, the individual pulses are shown against time. The blue pulse is the triggered signal bounded by the green vertical lines and presents overlaps with the previous and next pileup collisions represented in red. When summing the pulse height in the right plot, the triggered signal will need to be corrected for the additional energy deposited by the overlapping pileup signals.

Tracker

Both the strip and pixel detectors of the tracker subsystem will need to be replaced before the start of the HL-LHC. The radiation damage accumulated by the pixel sensors will eventually lead to deteriorated spatial resolution and reduced hit efficiency [232]. The strip tracker, on the other hand, will experience elevated sensor depletion voltage and increased leakage current. Although cooling the sensors can partially mitigate the latter issue, the former presents a challenge that cannot be effectively resolved. Dedicated studies showed that the current strip detector cannot be operated anymore after the collection of an integrated luminosity of 1000 fb^{-1}. Radiation damage poses serious technical challenges for the design of the HL-LHC tracker as it reaches a maximum of 1 MeV neutron equivalent fluence of 2.3×10^{16} n_{eq}/cm^2 in the innermost regions. In order to ensure efficient tracking performances with a pileup of 140-200, the HL-LHC tracker granularity is increased by a factor of 4 with respect to the LHC design. The tracker's coverage is also extended in the endcaps, reaching up to $|\eta| = 4$, to align more effectively with the coverage of the calorimeters (as shown in Figure 6.2).

The material budget is reduced and track-finding algorithms will be updated to cope with the higher track density. The L1 will also benefit from the tracking information at 40 MHz for tracks with $p_T > 2$ GeV, thus providing efficient background rejection at the earliest stage, limiting significantly the output rate. The updated tracker will be composed of two subsystems: the inner tracker (IT) and the outer tracker (OT). The IT is the detector closest to the beamline and therefore subject to higher doses of radiation. Two types of sensors are being investigated with an active area of 2500 μm^2, which is roughly 1/6 the area of the current Phase I detector. The first type of sensor presents a planar geometry with cell sizes of 25×100 μm^2 or 50×50 μm^2. An alternative option being actively pursued is to employ 3D silicon sensors that possess higher radiation tolerance but also higher manufacturing costs, allowing their usage only in the regions of the highest particle fluence. The readout of the IT sensors is handled by 65 nm ASICs based on CMOS technology (CMS Read Out Chips) bump-bonded to a single pixel sensor and developed under the RD53 project [233]. Utilizing this technology decreases the amount of power cables entering the detector, thereby reducing the material budget of the Inner Tracker. The initial LHC configuration, featuring 4 barrel layers and 3 forward disks,

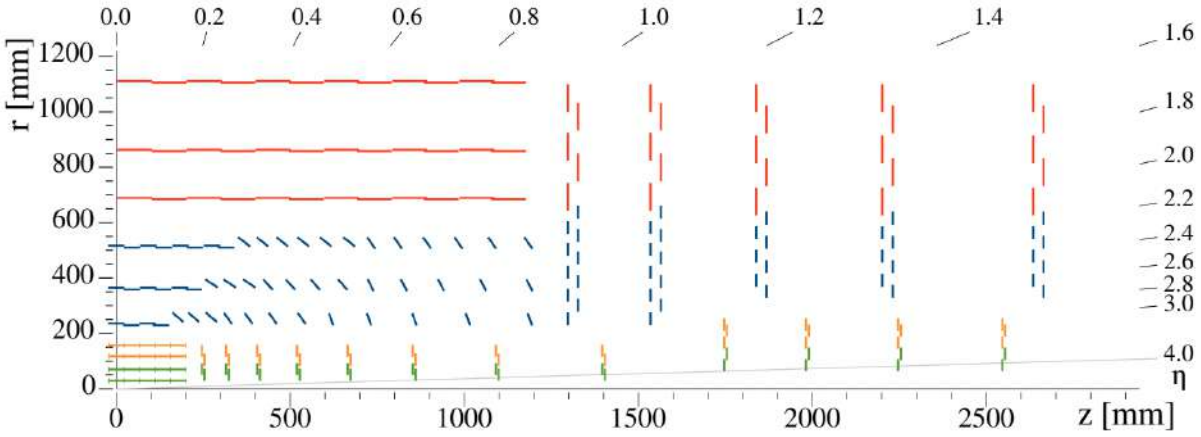

Figure 6.2: Sketch of a quarter of the tracker in the $r - z$ plane. The inner tracker modules in green (orange) are made of pixel modules read by two (four) chips and extend the coverage up to $|\eta| = 4$. Blue (red) lines correspond to the outer tracker PS (2S) modules.

serves as the baseline geometry, with additional layers to reach the full $|\eta| = 4$ pseudorapidity coverage. The OT starts at $r \sim 200$ mm from the interaction point with a reduction of one order of magnitude in the particle flux with respect to the IT reaching up $1.5 \times 10^{15} n_{eq} cm^{-2}$. The OT is designed to cover up to $|\eta| = 2.4$ and will employ two types of sensors [228]. The so-called PS modules, divided into PS-p and PS-s, use respectively pixel (p) and strip (s) sensors and are employed in the three innermost barrel layers and in the endcap region closest to the beam pipe. PS-s sensors present two strips with a length of 5 cm and a 100 μm pitch. The PS-p sensors are elongated macro-pixels with a length of 1.5 mm and a pitch of 100 μm. Both types have a length of 10 cm in the $r\phi$ plane and 5 cm width. The 2S modules, used in the rest of the OT, are composed of two strip sensors of 5 cm length and 90 μm pitch. The area covered by a 2S module amounts to 10×10 cm. OT sensors will be assembled in parallel pairs known as p_T-modules, separated by a gap ranging from 1.6 to 4 mm. This configuration allows to correlate the hits in the two sensors, using dedicated ASICs, reducing the number of interesting tracks to about 2.4% if a cut-off is set to $p_T > 2$ GeV. The two OT module types are read out by two custom ASICs. The 2S modules are read by a 130 nm CMOS ASIC called CMS Binary Chip (CBC) that can process data from 254 strip sensors, identify clusters, perform the hit correlation and provide data for the L1 trigger selection with a rate of 40 MHz. A second 65 nm CMOS ASIC is also employed in 2S modules to aggregate the data from eight CBCs with a bandwidth of 10 bits at 160 Mb/s. The PS modules come in two types and are therefore read by two types of front-end electronics based on 65 nm CMOS technology. The PS-p pixel sensors are read by the Macro-Pixel ASIC (MPA) while PS-s strip sensors are read by the Short-Strip ASIC (SSA). The latter plays a role similar to the aforementioned CBC. It processes the strip signals and sends the unsparsified data to the MPA at 40 MHz. 16 MPAs are bump-bonded to each macro-pixel module resulting in 2000 bumps per MPA. The MPA performs the hit correlation between macro-pixel and strip modules. The OT sensors will be operated at -20°C at the beginning of the HL-LHC, with the capability of reaching -30°C with the full HL-LHC luminosity.

Muon Detectors

The current muon detector system was designed to work under an instantaneous luminosity up to 10^{34} $cm^{-2}s^{-1}$. Major HL-LHC upgrades to the muon detector aim at limiting the radiation damage, coping with the increased L1 trigger rate and latency with new electronic systems and extending the pseudorapidity coverage of the system to $|\eta| > 2.4$. Additionally, the challenging region of $1.6 < |\eta| < 2.4$, where the background rates are highest and the muon bending

is reduced, will be instrumented with novel detectors [228]. To maximize the advantages of the increased luminosity, it is essential to ensure that the efficiency of the L1 muon trigger remains high, while simultaneously keeping the p_T thresholds low enough to investigate a broad spectrum of physics processes. With the proposed upgrades to the CMS muon subsystems, the excellent performances shown during Phase I of the LHC should be maintained at the HL-LHC. Regarding the existing muon detectors, longevity tests show that most of the existing chambers are expected to operate efficiently until the end of Phase II. DT chambers in MB1 and MB4 will be the most affected by aging as the deposits forming on the anode wires are expected to diminish the hit efficiency below 50% if the projected radiation dose is multiplied by a safety factor of three. Benefiting from the high number of recorded hits in the muon system, even a 50% efficiency loss in DT affects only marginally the efficiency of the full detector which will remain above 90% in the barrel and 95% in the barrel-endcap overlap. The upgrades to the existing muon detectors involve the replacement of the front-end electronics for DT and CSC and an upgrade of the RPC link system. Upgrades to the existing DT and CSC read-out electronic boards are necessary to meet the more demanding trigger requirements. For the RPC, all electronic boards, including front-end boards, are expected to cope well with the radiation expected at the HL-LHC. On the other hand, the RPC link system uses obsolete and weak electronic components therefore will be replaced by improved ones, able to fully exploit the intrinsic timing capabilities of the RPCs. The Gas Electron Multiplier (GEM) technology has proved to be radiation tolerant and can efficiently work under the harsh conditions of the HL-LHC. For this reason, two GEM stations will be installed for redundant muon hits in the region $1.6 < |\eta| < 2.4$ (GE1/1 and GE/2) each made of two layers of triple-GEMs. These additional forward detectors will complement the CSC measurements that fail to reject low-p_T muons or punch-through segments within the stations. The high precision measurement granted by the GEM detectors will increase the path length within each station to 28-55 cm, a factor 2-5 greater than the previous design [234]. In the 3rd and 4th muon stations, CSC chambers will be paired with improved RPC chambers (RE3/1 and RE4/1) that will further reduce the neutron-induced background. As the new RPCs show excellent timing properties, with a resolution of 100 ps, they can be useful for pileup mitigation. The pseudorapidity extension of the muon system is justified by the improvements in the pixel tracking, covering up to $|\eta| = 4$, and by the fact that endcap calorimeters will be replaced with more compact detectors, releasing $\sim$ 30 cm in the z direction. The pseudorapidity region from $2.1 < |\eta| < 2.8$ will be instrumented with a six-layered GEM station (ME0), placed in front of the ME1/1 layer, that can easily cope with the approximately 10 - 100 kHz/cm^2 background hit rates expected in this forward region. The novel RPC and GEM detectors increase the trigger efficiency and the excellent GEM spatial resolution provides accurate measurements of the L1 muon transverse momentum, thus allowing for a low p_T trigger threshold of 20 GeV with an affordable trigger rate of $\sim$ 1 kHz. In the region $2.1 < |\eta| < 2.4$, the trigger rate is reduced by an order of magnitude thanks to the redundant GEM information and the efficiency is increased by about 10%.

Electromagnetic and hadronic calorimeters

The CMS electromagnetic calorimeter (ECAL) was designed for the LHC Phase I with optimal performances up to an integrated luminosity of 500 fb^{-1}. The $PbWO_4$ scintillating mechanism is unaffected by the high radiation doses of the HL-LHC that mainly create crystal defects, altering the crystal transparency and reducing the light output. While the damage induced by electromagnetic showers during Phase I could be recovered spontaneously at room temperature, at the HL-LHC radiation damage due to energetic hadrons is not negligible and the necessary annealing temperature for these defects cannot be reached in situ ($\sim$ 350°C). The radiation damage affects the energy resolution of ECAL in the stochastic, noise and constant

terms. This effect is mitigated in the ECAL barrel (EB) by reducing the operating temperature from 18°C down to 9°C. The loss in the light output, compared to the ECAL 2010 conditions is between 50% and 65% depending on $|\eta|$ for an integrated luminosity of 3000 fb^{-1} [235]. The EB photodetectors (APDs), operated with a gain factor of 50, are damaged by γ-rays and by energetic hadrons, increasing the leakage current and therefore electronic noise. This performance degradation is recovered by the cooling system at 9°C, therefore APDs are expected to be able to operate for the entire HL-LHC decade. The upgrades to the EB are mainly driven by the new requirements of L1 trigger latency of 12.5 μs and a rate of 750 kHz. The front-ends will be instrumented with fast electronic components enabling a sampling rate of 160 MHz with 12-bit resolution at the expense of an increase in the data rate. This upgrade allows the EB to perform precision timing measurements for spike rejection, pileup suppression and vertex association, as well as providing single-crystal information to the calorimeter trigger instead of the current 5×5 trigger tower. The Phase II improvements to EB will lead to a 99% spike rejection and electromagnetic signal acceptance at 3000 fb^{-1} and with a mean pileup of 140. The upgrades to the electronics, with a reduced shaping time by a factor of 2, mitigate the radiation-induced noise, restoring the Phase I energy resolution. The hadronic barrel calorimeter (HB) will also experience significant light loss at 3000 fb^{-1} affecting photons and electron identification as well as affecting neutral hadron reconstruction. While new SiPMs, with a photo-detection efficiency 2.5 times greater than the design value, will last for the whole HL-LHC era, some scintillating tiles closest to the beam pipe will be replaced with a doubly-doped plastic scintillator. In the presence of radiation damage, an increased dopant concentration can lead to a more stable but reduced light output. The off-detector electronics will be merged with the EB as the addition of HB data represents only a 10% increase in bandwidth [228].

The expected radiation damage at the highest $|\eta|$ in the EB after 10 years of HL-LHC is equal to the radiation damage in the ECAL endcaps (EE) after 30 fb^{-1}. The loss of physics performance due to radiation damage in the EE is unacceptable. Moreover, the high rate of QCD multijet events at 140 pileup in the forward region makes the identification of electromagnetic objects more challenging (e.g. for VBF or VBS topologies). To face this challenge CMS is going to replace both EE and HE with a single high-granularity sampling calorimeter (HGC) based on silicon and plastic scintillators, able to withstand fluences up to $1.5 \times 10^{16} n_{eq}/cm^2$ [236]. The concept of the newly proposed endcap detector is inherited from ILC/CALICE for 3D measurement of showers also implementing timing capabilities. HGC is composed of a tungsten/copper-silicon sampling electromagnetic calorimeter EE with a depth of 1.5 interaction lengths (λ). The EE is followed by a 3.5λ deep brass-silicon hadron calorimeter, the FH. The last calorimeter, BH, is situated in a low radiation region and therefore employs a brass-scintillator sampling calorimeter, 5λ deep. The high granularity calorimeter will have a pseudorapidity coverage of $1.5 < |\eta| < 3.0$ and will operate at a temperature of -30°C to reduce the leakage current on the silicon sensors induced by radiation. The HGC active elements are 320 μm thick silicon sensors with the ability to detect minimum ionizing particles with an acceptable efficiency. HGC is expected to read a total of 6 million channels. The energy resolution of the new endcap calorimeter was estimated via MC simulations and presented a stochastic term of 20-24 % and a constant term below 1% for electrons in the energy range between 5 and 500 GeV.

6.2.1 Minimum Ionizing Particles Timing Detector

The CMS minimum ionizing particles (MIP) Timing Detector (MTD) is a brand-new detector that will be employed at CMS during the HL-LHC phase. Its purpose is to provide superior timing information for MIP particles in order to disentangle the spatial overlap of tracks and

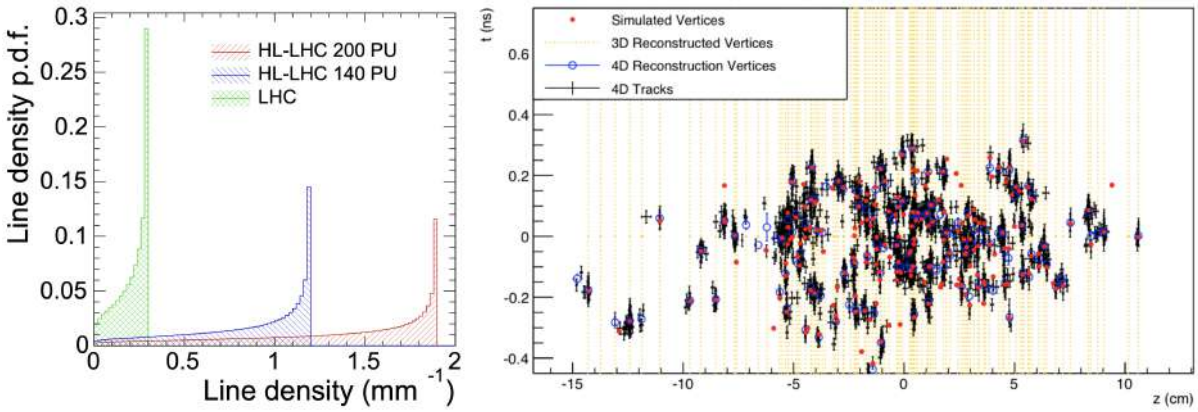

Figure 6.3: Left: probability density functions for the density of interaction vertices along the beam axis for a pileup rate around 30 as a proxy for LHC conditions (green), for the nominal conditions of HL-LHC of 140 (blue) and for the most extreme scenario of 200 (red). Right: reconstructed and simulated vertices (red) at 200 pileup in the case of no timing information as dashed yellow lines with evident spatial overlap if two simulated vertices happen to be on the same vertical line. The addition of timing in the vertex (track) reconstruction, shown as blue dots (black crosses), resolves the spatial degeneracy.

energy deposits from the additional 200 pileup collisions that negatively affect the identification and reconstruction of the hard scattering. The time resolution of MTD is expected to be about 30-40 ps at the beginning of Phase II and 50-60 ps after accumulating 3000 fb^{-1} of data. Such resolution is approximately 5 times smaller than the time spread of the 200 simultaneous collisions happening in each bunch crossing. This time difference, with a rms of about 180-200 ps, is due to the longitudinal extent of the bunches. The additional timing information for tracks can be used to discard overlapping tracks, coming from the same spatial region as the primary vertex, but happening at an earlier or later time. MTD will provide timing information in both barrel and endcap regions up to $|\eta| = 3$. While the upgraded CMS tracker and pixel detectors will be able to identify primary vertices and vertices from pileup collision at a rate of 140 simultaneous collisions per bunch crossing thanks to their enhanced granularity, the peak line density at 200 simultaneous collisions is so high that pileup identification algorithms based on particle flow will fail at a substantial rate. Simulations show that a degradation in the resolutions, efficiencies, and misidentification rates happens for a line density ≥ 1 mm^{-1}. In these extreme conditions, isolated leptons receive significant contributions from pileup tracks. Jets and missing transverse energy will also be affected by pileup, leading to higher background rates. To recover the original performances, the particle flow algorithm will be improved by the additional MTD timing information and will be able to slice the beam spot in consecutive time windows of 30-40 ps. Each time window can be analysed separately therefore reducing the overall 140-200 pileup collisions in time windows containing each 40-60 interactions as shown in Figure 6.3. The MTD time resolution will allow CMS pileup reduction algorithms to work in similar conditions to the ones recorded during Phase I, where they proved superior performances.

The impact of MTD on physics analyses is closely related to the improvements expected with a time-aware object reconstruction. Jets will benefit from the improved pileup rejection capabilities with additional timing information, where the rate of pileup jets is expected to be reduced by 25-40%, depending on the MTD resolution. VBF and VBS topologies will benefit from the improved jet objects. The 15% degradation in the resolution of missing transverse momentum at 200 pileup rate will be partially recovered with the additional timing information, result-

ing in an improvement of 10-15% in the resolution. Searches for new phenomena are largely driven by p_T^{miss} sensitivity, and its 10% improvement due to track-timing reflects a reduction of about 40% in the tails above 130 GeV, recovering the performance degradation of e.g. SUSY searches. Heavy flavour tagging relies on displaced secondary vertices that will suffer from the additional pileup tracks. A time-aware tagging would reduce by 30% the number of spurious reconstructed secondary vertices. Di-Higgs searches, that exploit the large branching ratio of H$\rightarrow b\bar{b}$ in order to gain in statistics, will largely benefit from b-tagging improvements, increasing signal yields of about 20% with respect to a scenario without MTD at a pileup of 200 and constant background. The efficiency in identifying isolated leptons with a pileup of 200 is improved by 3-4% in the barrel and 6-7% in endcaps. A correct identification of isolated leptons is crucial in order to study precisely EW-induced processes such as H$\rightarrow 4l$, H$\rightarrow \tau\tau$.

The MTD design is mainly driven by scientific and engineering requirements such as withstanding the large magnetic fields, maintaining robust mechanical design for the HL-LHC program's duration, and integrating into the existing CMS detector while adhering to the upgrade schedule. Regarding scientific requirements on the delivered timing resolution, simulations show that a resolution of 30–40 ps is effective in significantly mitigating the impact of pileup, achievable at the start of HL-LHC operation. This level of performance remains effective throughout HL-LHC operation, even as radiation damage causes the resolution to degrade to 50–60 ps after the collection of 3000 fb^{-1}. Since many of the subdetector upgrades for HL-LHC and the necessary service channels for cooling, power, and data transmission have already received approval, it is expected that the MTD can seamlessly integrate into the currently planned CMS geometry offering nearly complete coverage.

The MTD will be installed in the gap between the outer tracker (OT) and the EB. In order to provide timing information up to forward directions at $|\eta| = 3$, MTD will be composed of a cylindrical barrel timing layer (BTL) covering $|\eta| < 1.5$ and two endcap timing layer disks (ETL) extending the coverage in the range $1.6 < |\eta| < 3.0$. BTL will be installed on the support tube for the OT, extending up to 40 mm inward towards the beam. All services such as cables, cooling pipes and fibers will be integrated with the OT ones. The ETL will be installed between the HGC node and the tracker. HGC geometry prevents ETL from matching the tracker coverage up to $|\eta| = 4$. The space available for the ETL integration extends up to 45 mm. The geometry of MTD is shown in Figure 6.4.

The BTL and ETL design follows requirements on radiation tolerance in the region close to the interaction point and up to $|\eta| = 3$. The particle fluences for BTL and ETL differ by one order of magnitude and amount respectively to 1.9×10^{14} n_{eq}/cm^2 and 1.6×10^{15} n_{eq}/cm^2 for an integrated luminosity of 3000 fb^{-1}. While ETL will be accessible for maintenance during HL-LHC stops, BTL won't be accessible for repairs and therefore must be robust enough to withstand the aging process throughout the entire HL-LHC period. For these reasons, ETL will be instrumented with silicon-based Low Gain Avalanche Detectors (LGADs), while BTL will employ scintillating crystals of Cerium-doped Lutetium-Yttrium Oxyorthosilicate (LYSO:Ce) readout by SiPMs. Both barrel and endcap sensors will be operated at -35° with a dedicated cooling system, in order to limit the electronic noise and leakage currents. To mitigate the degradation of the BTL timing resolution, expected due to an increase in the Dark Current Rate (DCR) caused by radiation damage, the sensors will undergo annealing thermal cycles, during HL-LHC shutdowns, reaching up to +40°C/+60°C.

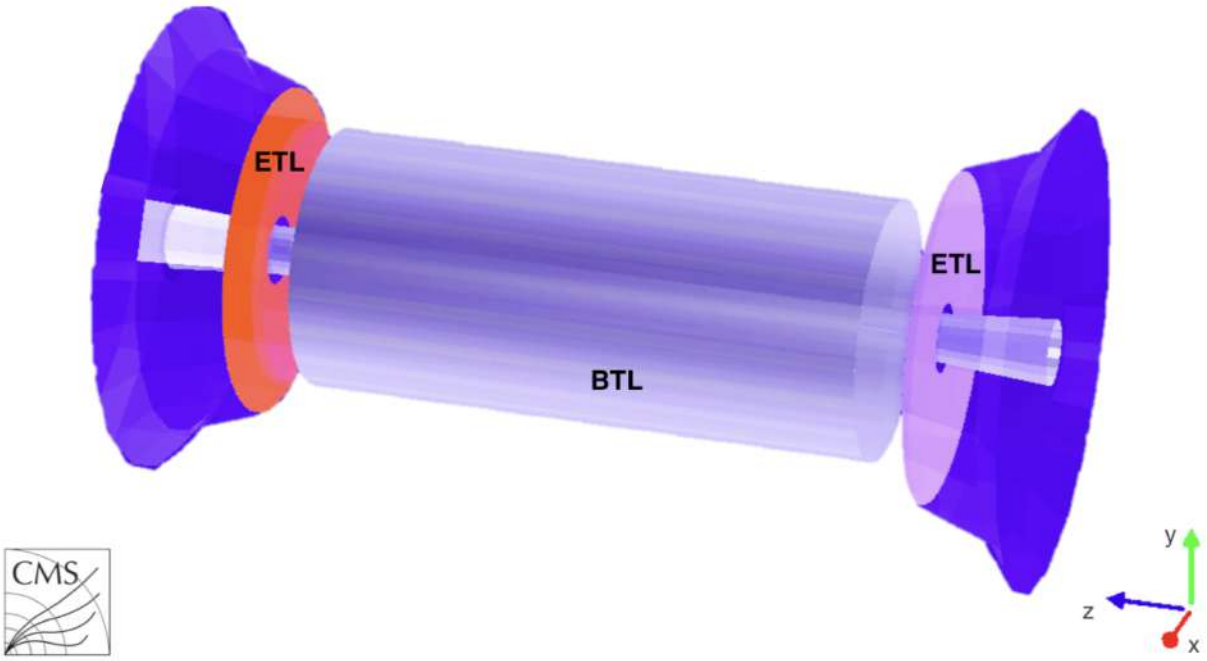

Figure 6.4: Geometry of the CMS MIP timing detector

6.3 The Barrell Timing Layer

6.3.1 BTL overview

The BTL detector is the central hollow cylindrical component of MTD covering a range up to $|\eta| = 1.48$. The cylinder will be installed on the tracker support system and has a thickness of 40 mm ranging from 1144 mm to 1188 mm with respect to the beam axis, between the OT and the EB, and has an extent of 5000 mm parallel to the z direction. The BTL active elements are LYSO:Ce bars of 57 mm length, 3.12 mm width and an average thickness of 3 mm, that emit scintillation light when a MIP passes through their active volume. The crystals' thickness along the detector's z-axis will be constant across η and amounts to 3.75 mm. The scintillation light is converted into electronic signals by 32 SiPMs, each coupled to a bar end, operated in Geiger mode with a gain factor of 10^5. The additional voltage over the breakdown value (OV) induces a dark current rate which is roughly doubled by an increase in temperature of 10°C. For this reason, the modules are connected to an aluminum plate kept at -35°C during HL-LHC operation by a CO_2 evaporative cooling system. To further reduce the DCR noise contribution, thermo-electric coolers (TECs) will be glued on the rear side of the SiPM packages as described in Sec. 6.3.3.2. TECs will allow a decrease in the operating temperatures down to -45°C while simultaneously allowing to reach up to +60°C during shutdown periods to induce thermal annealing in the SiPM lattice in order to soothe the radiation-induced damage. As the OV also determines the photon detection efficiency (PDE), the trade-off between signal size and noise rate is addressed by smoothly reducing the SiPMs operative voltage during the detector lifetime. The SiPM active area will be tailored to the LYSO:Ce scintillating tiles geometry. The SiPM active area is optimized to match the crystal's front face to maximize the number of scintillation photons hitting the SiPM sensors as described in Sec. 6.3.3.1. As for the crystals, the SiPM active area will diminish as a function of $|\eta|$ in order to limit the noise and maintain maximum light extraction. A BTL detector module is composed of two arrays of 16 LYSO:Ce bars, and their respective SiPMs, packed in a copper housing and connected to a custom ASIC called TOFHIR that collects the electric signals for further processing. TOFHIR provides precise timing data for 32 SiPMs. This information is obtained by discriminating the leading edges of

their pulses and subsequently measuring them with a time-to-digital converter (TDC). A BTL readout unit comprises 3×8 detector modules. Six readout units form a tray covering half of the BTL length. The entire surface of the detector is covered by 72 trays. Overall, BTL will provide timing information from 331.776 SiPMs and 165.888 LYSO:Ce bars.

The time resolution for a MIP traversing a BTL detector module will depend on the number of photons generated by LYSO:Ce crystals per MeV of deposited energy (light yield) and by the fraction of these photons detected by the SiPMs and converted to photoelectrons. The signal produced can be discriminated and digitized to obtain a timing measurement for the MIP. For two independent measurements at the two ends of the crystal bar with a common clock jitter, the time resolution is given by

$$\sigma_t^{\mathrm{BTL}} = \sigma_t^{\mathrm{clock}} \oplus \sigma_t^{\mathrm{digi}} \oplus \sigma_t^{\mathrm{ele}} \oplus \sigma_t^{\mathrm{photo}} \oplus \sigma_t^{\mathrm{DCR}} \tag{6.1}$$

where $\sigma_t^{\mathrm{clock}}$ is due to CMS clock distribution, σ_t^{digi} depends on the time jitter of the digitization process, σ_t^{ele} accounts for the electronics, $\sigma_t^{\mathrm{photo}}$ is due to the stochastic fluctuations in the time of arrival of photons, σ_t^{DCR} is a noise term introduced by the SiPM dark count rate. As the photostatistics and noise terms will eventually drive the timing resolution of BTL, a great effort was made for their optimization.

The photostatistics term is proportional to $\sigma_t^{\mathrm{photo}} \sim \sqrt{\tau_r \tau_d / N_{\mathrm{phe}}}$ where τ_r and τ_d are respectively the rise and decay time of the scintillation pulse. LYSO:Ce crystals provide faster scintillation rise times, of about 100 ps, and shorter decay times, of about 40 ps, with respect to other inorganic scintillators. The number of detected photons upon a passage of a MIP N_{phe} is the figure of merit to be maximized and depends linearly upon the energy deposited by the MIP, by the light yield of the material (LY), by the light collection efficiency (LCE), and by the PDE of the SiPMs. In LYSO:Ce, the deposited energy follows a Landau distribution with the most probable value (MPV) of 0.86 MeV/mm [231] and the mean deposited energy is about 4.2 MeV. With an LCE of 15% and PDE of 20%, each MIP will trigger the emission of approximately 5000 scintillation photons by the LYSO:Ce bars. This translates in a time jitter due to photostatistics of about $\sigma_t^{\mathrm{photo}}$ ~25-30 ps.

6.3.2 BTL performances at the beginning of HL-LHC

A thorough analysis of LYSO:Ce crystals started in 2019 with the study of 57 mm long bars from 12 different vendors in order to measure the key features responsible for the timing performance of the crystals and reported in Ref. [237]. The performance of LYSO:Ce crystals has been assessed using crystal samples with no wrapping. This evaluation encompassed an examination of various mechanical, optical and scintillation properties which were studied before and after irradiation to simulate the end-of-life conditions after 3000 fb^{-1}. The crystals were operated at temperatures down to -30°C. The study proved that all LYSO:Ce samples from all the vendors are suitable candidates for timing measurements at the HL-LHC, with a spread in characteristics of about 10%. Only a 9% light output loss was observed after irradiation but was demonstrated to be fully recoverable after 5 days of dark annealing [238]. The role of the crystal thickness, properties of the SiPMs such as PDE, and impact angle of the MIP have been studied using a 120 GeV proton beam, from the Fermilab test-beam facility, hitting on non-irradiated BTL modules [239]. LYSO:Ce crystal bars of length 57 mm and variable thickness between 2,3 and 4 mm were tested and their light output was collected by two SiPM types, respectively manufactured by Hamamatsu (HPK) and Fondazione Bruno Kessler (FBK). Measurements showed the behaviour of the time resolution with the overvoltage and PDE for the

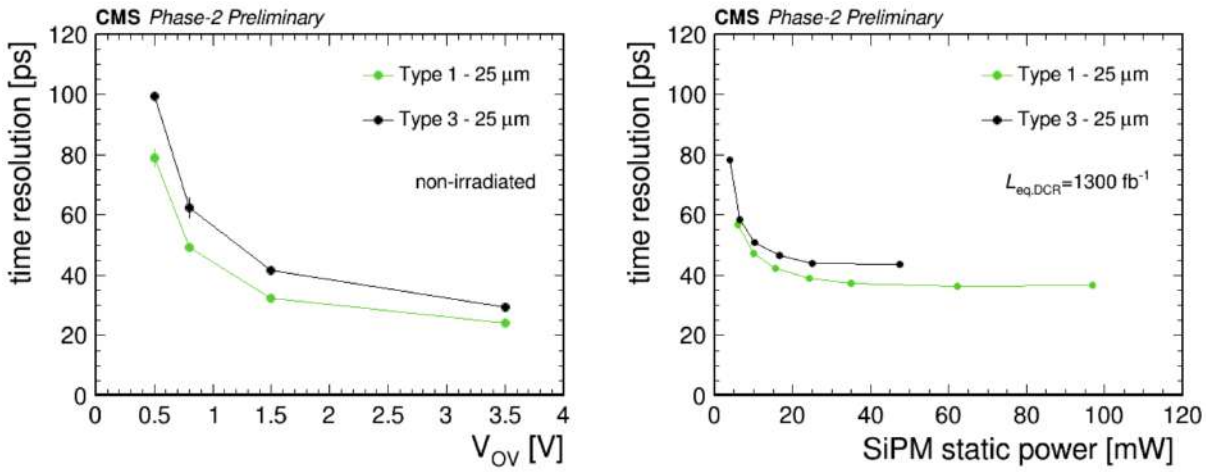

Figure 6.5: Left: time resolution as a function of the overvoltage for LYSO:Ce bars with dimension $3.75 \times 3.00 \times 54.7$ mm^3 (green) and $2.4 \times 3.00 \times 54.7$ mm^3 (black) coupled to non-irradiated SiPMs with an active area matching the crystals face. Right: time resolution against SiPM power for the same bar geometry but with irradiated SiPMs with a DCR similar to the expected one after collecting 1300 fb^{-1} of data at the HL-LHC.

two different SiPMs, showing that the photostatistic term is dominant in FBK while there is a significant contribution from the noise term for HPK sensors. The time resolution was found to scale with the inverse of the square root of the thickness and was measured with an OV of 6 V to be approximately 36 ps for a 2 mm thick crystal and 26 ps for a 4 mm thick one. Overall, the test-beam measurement proved that the BTL sensor design can provide a uniform time response with a resolution below 30 ps at the beginning of the HL-LHC lifetime. These results are in agreement with the original proposal for a MIP timing detector.

6.3.3 Stratregies for performance recovery at the end of life

While BTL meets the required performances regarding time resolution at the start of HL-LHC operations, it was observed to fail after module irradiation as a proxy for the end-of-life conditions. The time resolution achievable with the original design goes beyond 100 ps after an integrated luminosity of 3000 fb^{-1}, against the proposed $\sim$ 60 ps. Several strategies have been developed in order to restore the expected performances at the detector end of life, optimizing the active components' geometries and operational conditions as well as optimizing the front-end electronics. With the precautions explained in the following sub-chapters, BTL can meet the desired specifications.

6.3.3.1 Modules optimisation

The scintillating tiles of LYSO:Ce have been optimized to reach the highest possible light output. Three types of geometries have been investigated, namely, types 1,2,3 corresponding respectively to a crystal thickness of 3.75, 3.00 and 2.40 mm. While granting a higher light output and therefore a higher number of photoelectrons, the usage of thicker crystals imposes the coupling of SiPMs to the larger active area. When irradiated, large-area SiPMs show higher DCR therefore partially canceling the benefit of the increased number of scintillation photons on the time resolution. The optimal tradeoff was assessed in test beams and lab measurements, proving that the usage of type-1 LYSO:Ce tiles will be instrumental in order to recover the expected performances at the end of life as shown in Figure 6.5.

BTL will be populated by type-1 LYSO:Ce bars only with a uniform thickness across η instead

of the original design foreseeing three different thicknesses. This choice has no impact on either MTD design or schedule and has a limited impact on the amount of material in front of ECAL.

A 10% improvement in the light collection efficiency (LCE) was also achieved by optimization of the LYSO:Ce packaging and described in detail in Ref. [240]. The total LCE, at first order, can be parametrized as the product of three efficiency terms LCE $= \epsilon_{\text{coll}}\epsilon_{\text{ext}}\epsilon_{\text{det}}$. The first term is the efficiency for a scintillation photon to reach the end of the crystal and includes the effects of light propagation inside the material and the reflection at the lateral surfaces of the crystal. ϵ_{ext} accounts for the reflection of a photon at the front face of the crystal that is coupled with the SiPM, and depends on the refractive index and thickness of the medium between the crystal and the SiPM (either air, glue or grease). The last term ϵ_{det} is the fraction of photons hitting the SiPM active area and is maximized by matching the latter with the crystal face dimensions.

ϵ_{coll} was maximized by reducing at a minimum the amount of glue between the wrapping and the crystals, allowing most of the lateral surfaces to be separated by a thin air gap that provides better reduction of optical cross-talks between adjacent bars when compared to glue or grease. The photon extraction efficiency ϵ_{ext} is significantly increased (+47%) if optical grease or glue is used as an interface between the crystal bar end faces and the SiPMs, benefiting from a refractive index closer to the LYSO:Ce one. The LCE has also been improved by reducing the thickness of the SiPM protective window. An improvement in LCE of 15% was observed between a 300 μm thick resin material and a 20 μm thin quartz layer deposition.

6.3.3.2 Thermo-electric coolers and thermal annealing

The barrel crystals and SiPMs of MTD will experience accumulated radiation levels of 50 kGy of ionizing dose and a neutron fluence of the order $10^{14}\text{n}_{\text{eq}}/\text{cm}^2$ during the HL-LHC phase. The behaviour of the SiPMs from the two manufacturers, HPK and FBK was studied in detail and summarised in Ref. [241, 242]. The SiPMs show an increase in DCR that grows linearly with the neutron fluence up to $5 \times 10^{13}\text{n}_{\text{eq}}/\text{cm}^2$. Above this threshold, which will be reached during the HL-LHC operation, new effects become sizable. After $2 \times 10^{14}\text{n}_{\text{eq}}/\text{cm}^2$ the breakdown voltage increases for both SiPMs types, and therefore a reduction of the signal amplitude of about 25% is observed for an OV of 1 V. The latter phenomenon suggests that at such a high fluence, the SiPM internal gain might be reduced determining a degradation of the PDE. Another problem that arises with such high fluences is the SiPM power dissipation which could lead to self-heating, affecting the operating OV. BTL was originally designed to reach stable temperatures down to -35°C as the DCR scales by a factor of 1.9 every 10°C irrespective of the quantity of radiation absorbed. By the BTL end of life, the DCR is expected to amount to 10-100 GHz depending on the operating OV, temperature and annealing history and will represent the major source of degradation of BTL performances.

Radiation-induced damage in silicon can be partially mitigated through the process of annealing. Thermal annealing can soothe radiation-induced damage thus reducing the DCR. For instance, during shutdowns or other downtime periods, annealing at room temperature can effectively recover the BTL time resolution by decreasing the DCR time jitter. Several measurements on the two SiPM prototypes have been done to assess their radiation tolerance and performance after undergoing various durations and temperatures of annealing as reported in Ref. [243]. One SiPM array was placed in a +40°C oven for various time intervals while a second one was placed for 40 minutes in a +70°C oven. The results show that annealing silicon sensors at +40°C for approximately 4 days would cut the DCR in half as shown in the left side Figure 6.6. The right side of the figure shows that the DCR would be further halved by a reduction of 10°C below the BTL operative temperature from the original design.

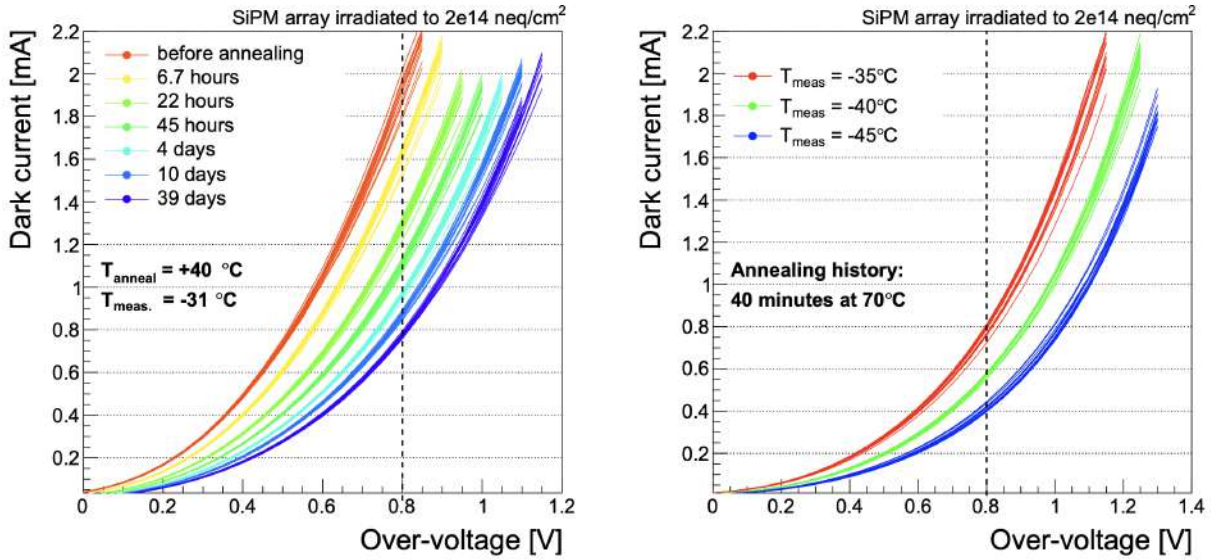

Figure 6.6: Left: dependence of the DCR by the operating overvoltage for various annealing times ranging from 0h to 39 days. Right: behaviour of DCR as a function of overvoltage for different operating temperatures below or equal to the design one of -35°C after 40 minutes of annealing at +70°C

During the HL-LHC technical stops, the cold-plate support for the BTL sensors, housing the CO_2 cooling pipes, can be heated from -35°C up to only +10°C. As said in the previous chapters, the BTL will not be available for maintenance for the full 12-year period of the HL-LHC so it is not possible to act on the detector if not by modifying its initial design. A new proposal was derived to solve the DCR problem in a twofold way. Firstly by decreasing the operating temperature of an additional 10°C, down to -45°C. Secondly to increase the SiPMs temperature, during the HL-LHC stops, from +10°C up to about +60°C. While in the original BTL design, the SiPMs were in direct contact with the copper housing, this new solution proposes to weld small thermo-electric coolers (TECs) to the back of the SiPMs package that effectively acts as a thermal interface between the SiPMs and the copper housing. The expected DCR as the luminosity approaches 3000 fb^{-1} for a SiPM operated at an OV of 1 V is shown in Figure 6.7 considering various operating and annealing temperatures. The proposed solution would decrease the DCR at the end of life by more than a factor of 5, expecting approximately 10 GHz for an operating (annealing) temperature of -45°C (+60°C), restoring and even enhancing the BTL timing performances throughout the full detector lifetime.

6.3.3.3 SiPM larger cell size

Significant efforts were made to understand the time resolution dependence on SiPM parameters. A parametric model of the SiPM response was derived based on Ref. [244] and validated with data. The model has been extended by applying the TOFHIR transfer function, determined empirically via a DFT analysis, to the SiPM pulse shape. The simulated response for the full BTL chain was plugged into an evolution model, predicting the expected time resolution as a function of the integrated luminosity. It was shown that a twice as large SiPM cell size, with respect to the baseline design, would improve by $\sim 30-40\%$ the performances of BTL at the end of life. This improvement can be attributed to a steeper electrical signal going from a cell dimension of 15 μm to 30 μm which would significantly reduce the impact of the electronic noise. Furthermore, a larger cell size implies an increased PDE with improvements for photo statistics and DCR contributions, that are expected to dominate the BTL timing resolu-

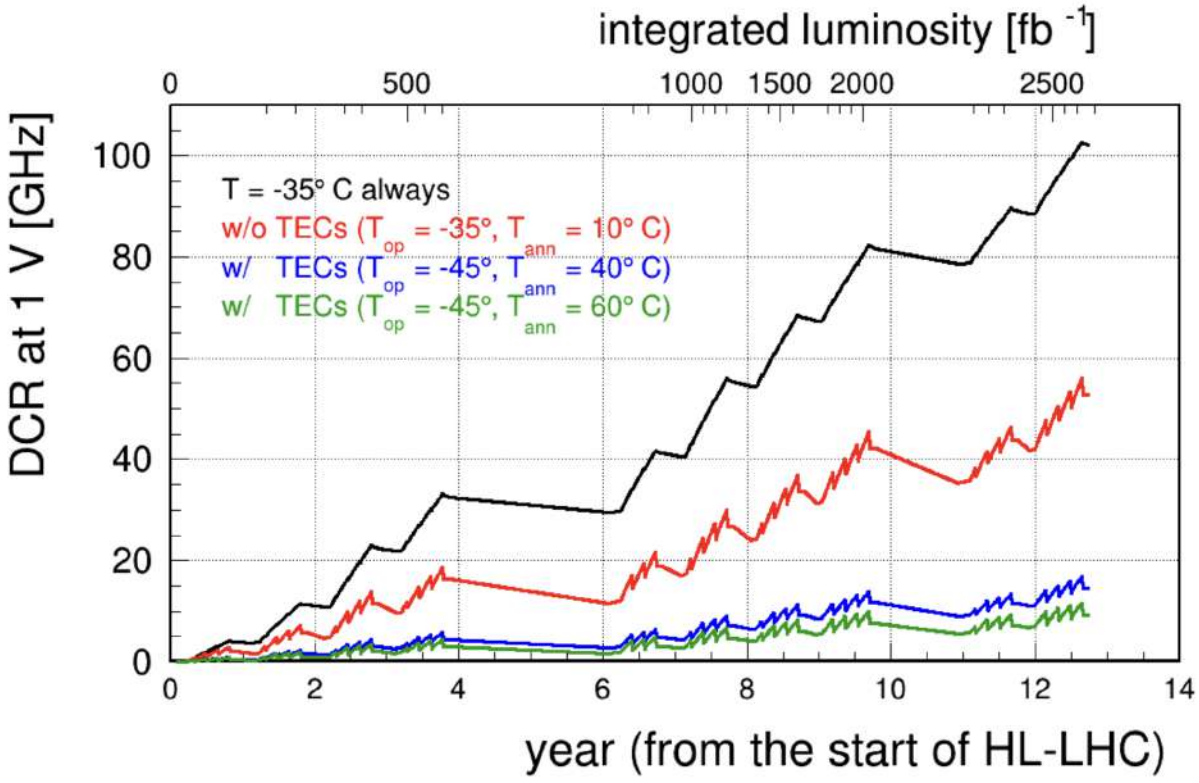

Figure 6.7: Expected SiPMs dark current rate as a function of the recorder integrated luminosity or HL-LHC lifetime under different scenarios. The baseline corresponding to the BTL original design with an operating temperature of -35°C is shown in black. The effect of annealing at +10°C using the existing cooling system is shown in red. The advantage of the additional TEC technology is shown in blue and green curves for an operational temperature of -45°C and an annealing temperature of respectively +40°C and +60°C. The OV is assumed to be fixed at 1 V.

tion after 3000 fb^{-1}. This assumption has been tested in recent test beams with irradiated and non-irradiated SiPMs, proving that BTL would benefit from a larger SiPM cell size.

6.3.4 State of the art BTL performances

The BTL module design is almost complete at the time being and slightly differs from the original proposal in order to meet the required resolution both at the beginning and at the end of its lifetime. BTL will be instrumented with LYSO:Ce tiles of dimension $3.75 \times 3 \times 54.7$ mm^3 with a constant thickness for the full pseudorapidity coverage up to $|\eta| = 1.48$. Adjacent bars will be separated with a reflective layer of enhanced specular reflector (ESR). A detector module will be made of 16 bars and the bottom and top of the entire array will be wrapped with the same reflective layer. The scintillation light will be read, on both ends of the bar, by SiPMs with an active area matching the front face of the crystals. The SiPMs will have a cell size of 25 μm. The SiPM protective window will be made of a 20 μm thin quartz layer and glued to the front face of the crystal. TECs will be used to decrease the operating temperature to -45°C and to increase the temperature to 40-60°C during the LHC shutdowns for thermal annealing. The SiPM signals will be analyzed by a custom ASIC called TOFHIR. The first version of the chip has been updated with a new technology based on CMOS 130 nm with improved behaviour under radiation [245]. The new TOFHIR (v2) will feature a DCR noise cancellation circuit, helping to improve the performance at the end of the lifetime. The TOFHIR gain will be increased approaching 3000 fb^{-1} to cope with the reduction of the SiPMs overvoltage that will negatively

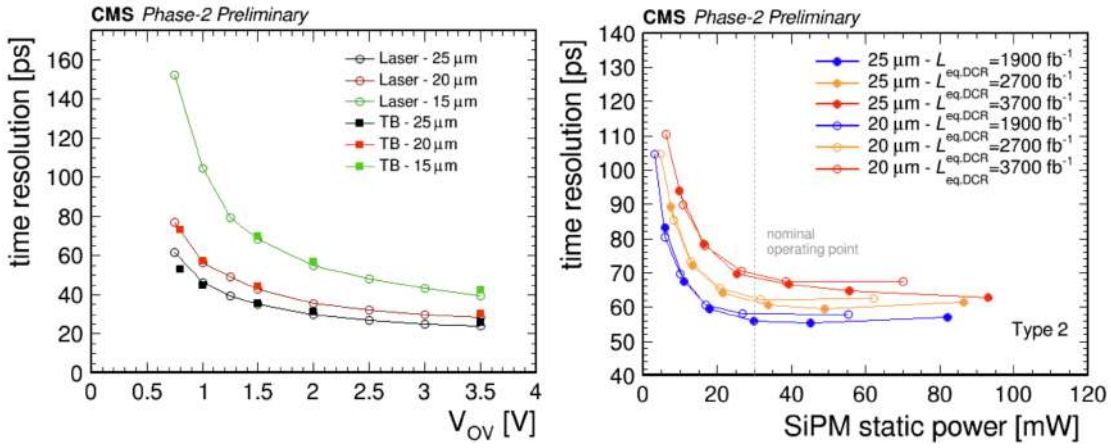

Figure 6.8: Left: time resolution as a function of the overvoltage for different SiPM cell sizes of 15, 20 and 25 μm as measured with UV-induced scintillation light (Laser) and with data from a beam test (TB). Right: Time resolution versus SiPM power for irradiated SiPMs of 20 (open dots) and 25 (filled dots) μm cell sizes. SiPMs have been irradiated to 2×10^{14} 1 MeV n_{eq}/cm^2 and different lifetime conditions of 1900, 2700 and 3700 fb^{-1} have been simulated by changing the operation temperature.

affect the PDE.

The latest test beam studies proved that BTL will meet the design performances with a time resolution of 20 ps at the beginning of HL-LHC operations and of about 60 ps after 3000 fb^{-1}. The results are shown in Figure 6.8 where a comparison with the original design, with a SiPM cell size of 15 μm, shows that the optimization of the detector modules improves the performances up to a factor 3. The expected time resolution after 3700 fb^{-1} is 70 ps for a SiPM cell size of 25 μm, assuming an operation temperature of $-45°C$ and annealing at $+60°C$.

Figure 6.9 shows the projected performances of BTL against integrated luminosity from test beam data for two types of crystal thickness (3.75 mm for type 1 and 3.00 mm for type 2) and SiPM cell sizes of 20 and 25 μm. An operating temperature of $-45°C$ and an annealing temperature of $+60°C$ are assumed. The combination of thicker crystals and larger SiPMs cell size matches the BTL required performances thus justifying the detector configuration choice.

6.4 MTD Data acquisition system

The data acquisition system (DAQ) of the MIP timing detector comprises a combination of radiation-resistant electronic components at the front-end (inside the experimental cavern) and electronic boards employing Field Programmable Gate Arrays (FPGAs) at the back-end of the detector [231] (outside the experimental cavern). The system is linked to the central CMS DAQ system [246] that is shared among all CMS sub-detectors. Upon receiving an L1 trigger signal from other CMS subsystems, the MTD front-end electronics will transmit the corresponding data from the detector via high-speed optical links to the back-end system. Following the current detector layout and the expected data rates, BTL will require 864 links, while the ETL will need 1688 links. The MTD DAQ will be shared among BTL and ETL, providing bi-directional links for fast and slow control signals to on-detector electronics.

The DAQ is also responsible for the distribution of a low-jitter sampling clock, synchronized with the 40 MHz bunch crossing rate, to the front-end electronic. To attain the targeted timing resolution for the MTD, the clock distribution system must ensure that the link-to-link jitter

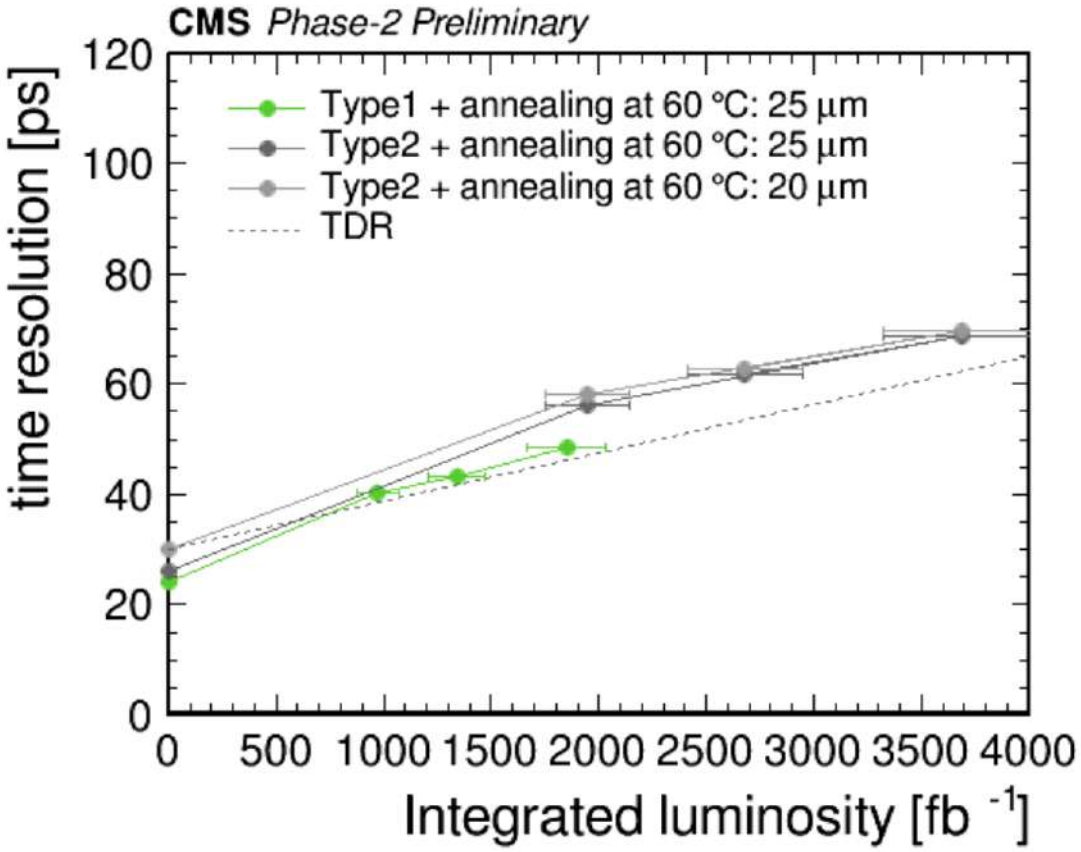

Figure 6.9: BTL time resolution as a function of the integrated luminosity assuming an operating temperature of $-45°C$ and an annealing temperature of $+60°C$. The projections are obtained from test beam data on irradiated and non-irradiated SiPMs. Grey dots correspond to crystals with a thickness of 3.00 mm. Dark (light) grey dots present a SiPM cell size of 25 (20) μm. The BTL's final choice is to use crystals with a thickness of 3.75 mm and a SiPM cell size of 25 μm which is represented with green dots. The BTL design expectations are represented as a grey dashed line, showing almost perfect agreement with the final detector configuration.

remains below 15 ps rms across all links. As an example, a 35 ps timing resolution for MTD sensors and electronics would be degraded by 3 ps for a 15 ps clock time jitter. The current LHC clock distribution, provided directly by the RF system, presents a 9 ps rms jitter. Once received by the CMS central systems, the clock is forwarded to both the off-detector electronics and the on-detector electronics through multi-mode fiber cables. Two clock distribution schemas are available. In the baseline approach, the bidirectional DAQ links will carry an encoded clock signal to the on-detector readout electronics. If this approach falls short of meeting the necessary performance criteria, the sampling clock will be directly distributed without encoding. However, the latter option dictates the use of additional optical fibers and transceivers. A dedicated fanout ASIC has been developed for this purpose, acting as a clock multiplexer, called RAFAEL. The latter strategy is the preferred one for MTD as measurements showed a 3.2 ps RMS jitter which is well within MTD specifications [247].

This section is organized as follows: a brief overview of the hardware elements of the MTD DAQ is given in Sec. 6.4.1. The following Sec. 6.4.2 will describe the ongoing efforts towards a homogeneous MTD software and firmware framework. Particular care is devoted to the description of the software architecture in Sec. 6.4.2 which has been built from scratch and

represents the major contribution of this work. As an additional novel contribution to the MTD DAQ, Sec. 6.4.3 describes the development of a graphic user interface tailored to the upcoming needs of BTL, namely for the assembly of the detector itself and for system tests.

6.4.1 Overview of the DAQ hardware

In this section, both the on-detector and principal off-detector electronic components of the BTL DAQ will be described. While some front-end instrumentation differs between BTL and ETL, due to different design strategies, the off-detector circuits are shared. The BTL DAQ should be able to communicate with the on-detector electronics in a bi-directional fashion in order to transfer the clock, chips configurations, sync/reset signals, L1 trigger signal and power and receive the fast data readout as well as slow monitoring signals such as SiPM temperature and voltage readings.

TOFHIR chip

The TOFHIR2 ASIC acquires and digitizes the signals from the SiPMs. The chip is radiation tolerant and its design is tailored to MTD timing requirements for the digitization of time and energy of the traversing MIP. Additionally, TOFHIR can reject low-energy signals from particles below the MIP threshold. The frontend chip can measure the time of arrival for MIP particles with a time jitter of 14 ps. The timing threshold discriminator has a precision of 6 bits and is customizable in the 0-100 photoelectrons range. Upon the passage of a MIP, two timestamps are digitized by the TOFHIR chip and stored in the ASIC memory, corresponding to the time when the signal exceeds a threshold. The two times correspond to the timing threshold and MIP threshold. The conversion is done with a time-to-digital converter (TDC) circuit at two configurable triggers. The first timing measurement is done on the rising edge, while the second is either on the falling edge or on the rising edge of the signal. The difference between the two measurements, referred to as the time-over-threshold can be used to assess the signal's width. The TDC has a time quantization of 20 ps and consists of a time-to-amplitude converter (TAC) followed by a 40MHz 10-bit SAR analog-to-digital converter (ADC) [248]. A coarse 16-bit digitization is done on the TDC output counting the number of cycles of the external 160.32 MHz reference clock. A fine counter provides the fine resolution within one period of the reference clock [231]. TOFHIR also features a charge-to-digital converter QDC, composed of a charge-to-amplitude converter (QAC) followed by the same ADC used for the timing measurement. The integration has a time window of 25 ns starting from the rising edge trigger.

The TOFHIR will store the information corresponding to a MIP hit with two digitized times, the signal amplitude and the associated clock cycle number. These data words will be shipped to other electronic components for further processing as twelve 8/10-bit encoded symbols. The initial symbol is K28.1, while the subsequent 11 symbols collectively represent 88 bits of data their content is described in Table 6.1.

The data words can be sent upon the reception of an external trigger signal or via a self-triggering mechanism. TOFHIR is instrumented with two output ports dedicated to data transmission through E-links [249] at 320 Mb/s. An additional E-link input port, operated at 80 Mb/s, allows communication with the ASIC from the outside e.g. for configuring the chip. Two additional input ports are dedicated to the handling of fast control commands. The first of these ports handles L0 and L1 signals. The second port can receive RESET and RESYNC commands that reset the timing coarse and fine counters and, in the case of RESET, also the content of all FIFO registers and state machines. The TOFHIR identification number can be configured with four dedicated pins.

Bits	Stored information
0-3	channel ID
4-5	time-to-amplitude converter ID
6-15	charge measurement
16-25	fine counter of the 2nd time measurement
26-35	fine counter of the 1st time measurement
36-45	coarse counter of the previous event crossing the timing threshold
46-55	coarse counter of the end of charge integration
56-65	coarse counter of the 2nd time measurement
66-81	coarse counter of the 1st time measurement
82-85	status of the trigger bits for previous event
86-87	trailing bits ”11”

Table 6.1: The TOFHIR frame from the DAQ perspective, where each bit/s content is described

Figure 6.10: Left: A BTL array of 16 LYSO:Ce bars wrapped with a ESR foil and glued on both ends with SiPMs. SiPMs are connected to flex circuits for the connection to TOFHIR (orange). Right: the BTL front-end board with two TOFHIR2 chips (green), each connected through the 32 flexes (orange) to the SiPMs, two ALDO2 chips each serving one TOFHIR (cyan). Four TECs (red) are installed back-to-back with the SiPM array. One TEC serves 4 SiPMs.

Front-end board

The BTL front-end module is the unit element of the BTL DAQ system. Since the MTD technical design proposal, the design of the front-end boards evolved. The current BTL module design presents two arrays of 16 LYSO:Ce bars glued on each side to 16 SiPMs for readout and four TECs per side to allow reaching a SiPM operational temperature of -45°C. Two TOFHIR2 chips handle the signals from each of the two crystal arrays and are connected to the 32 SiPMs via flex circuits. Two ALDO2 chips [250] are also integrated in the front-end module. Each TOFHIR2 is served by an ALDO2 chip providing it with regulated voltage and current up to 500 mA which is sufficient for the SiPM arrays operation. Images of the crystal packaging and of the front-end boards are shown in Figure 6.10. front-end boards are connected to the concentrator card and the communication in both uplink and downlink is handled by the low-power Giga-Bit transceivers.

Low-power Giga-Bit transceivers (lpGBT)

Optical data links to and from the off-detector DAQ are established using the Low-power Giga-Bit-Versatile link system [251], which operates bidirectionally, connecting the detector to the

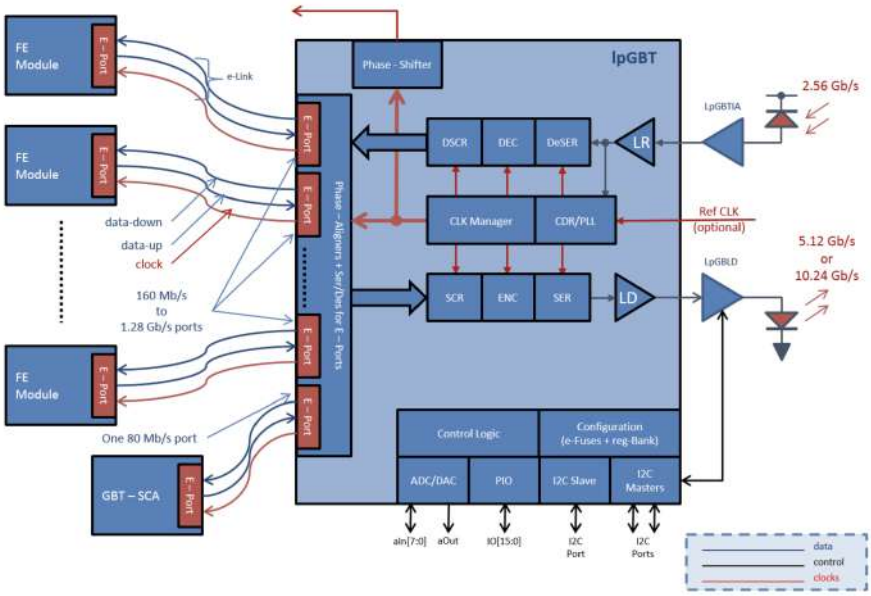

Figure 6.11: The Low-power Giga-Bit transceiver architecture. Figure from [251]

DAQ boards. TOFHIR data are sent through E-link ports, to two lpGBTs with a bandwidth of 320 Mb/s. The front-end chip configurations, as well as fast signals like RESYNC and trigger bits, are sent from an lpGBT E-link operated at 80 Mb/s to the TOFHIR2 and ALDO2 chips. The lpGBT is also responsible for the clock distribution to the TOFHIR ASICs with a frequency of 160 MHz. The lpGBT architecture is shown in Figure 6.11 and its connection to both the back-end and front-end will be described in the following. The lpGBT is a radiation-tolerant ASIC suitable for creating versatile high-speed bidirectional optical links in high-energy physics experiments. This ASIC facilitates 2.56 Gb/s links from the counting room to the detectors (downlink) and offers 5.12 or 10.24 Gb/s links from the detectors to the counting room (uplink), depending on the chosen operational mode. The lpGBT provides very front-end electronics with three data paths for timing, trigger control, DAQ and slow control information. The lpGBT is an extremely versatile device with 11 configuration pins that need to be set through hard-wiring and 494 8-bit registers that can be programmed to tailor its functionality. It has three operational modes namely it can work either as a bidirectional transceiver, as a simple receiver or as a simple transmitter offering a large variety of applications.

The transmission from lpGBT to the detector modules happens via E-links that are driven by a series of ePorts (ePortTx) matched to the front-end devices. ePorts are grouped in eGroups, each composed of four ePorts. Each of the latter is associated with an eClock differential line that transmits the clock to the front-end. Both clocks and data are transmitted and received through the ePorts by ePort Line Drivers (eTx) and Line Receivers (eRx) implementing the standard CLPS protocol. Transmission ePorts serialize the downlink parallel data before sending it to the front-end devices. The reception of data from the front-end modules to the lpGBT is handled via Receiving ePorts (ePortRx) that de-serializes the data so that it can be scrambled and coded with a Forward Error Correction (FEC) before being sent to the off-detector electronics. A laser driver, configured via an "I2C" connection from the lpGBT, handles the uplink communication between the lpGBT and the off-detector electronics. While the lpGBT's main function is that of a transceiver, it is instrumented with control and monitoring functionalities: three I2C masters to control the laser driver, a 16-bit programmable I/O port, a 10-bit ADC, on-chip temperature reading, configurable current sources for external temperature sensors and an 8-bit voltage DAC.

Downlink data is transmitted from the counting room to the lpGBT in a 64-bit frame at 2.56 Gb/s. The frame consists of three fields. The Internal Control field (IC) sends ASICs control information and operates with a bandwidth of 80 Mb/s. The External Control field (EC) has a dedicated ePort with 80 Mb/s bandwidth and was designed to be compatible with the GBT-SCA [252] chip, an ASIC dedicated for control and monitoring applications. The last field (DC) is dedicated to user data to be transmitted to the front-end ASICs with a bandwidth of 1.28 Gb/s. The uplink frame from the lpGBT to the counting room presents the same fields but the data rate can be either 5.12 Gb/s or 10.24 Gb/s with a frame size of 128-bits and 256-bits respectively. Additionally, two FECs can be used to correct up to 5 (FEC5) or 12 (FEC12) consecutive bits. While IC and EC bandwidths are the same as for the downlink, the uplink DC presents a bandwidth of 3.84 Gb/s (4.48 Gb/s) with FEC12 (FEC5) encoding for a data rate of 5.12 Gb/s. When operating at 10.24 Gb/s IC and EC fields are unchanged while the DC bandwidth doubles.

The uplink frame, as seen by a lpGBT user, assuming a 5.12 Gb/s data rate with FEC5 is shown in Figure 6.12.

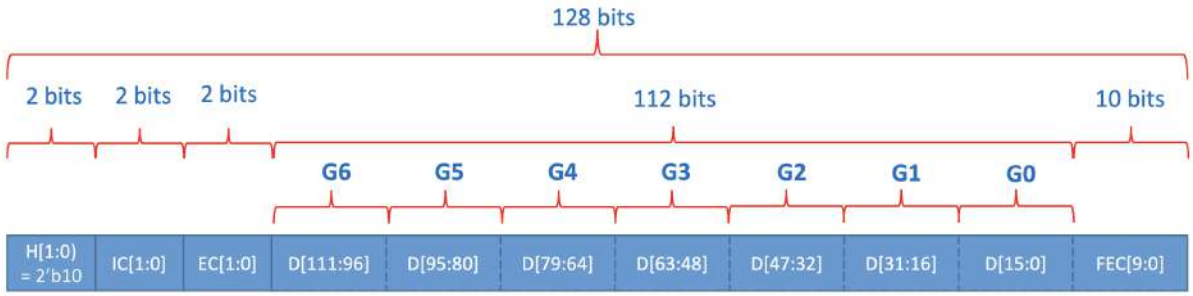

Figure 6.12: lpGBT uplink frame for a data rate of 5.12 Gb/s and FEC5. This frame is the one received by a user after the processing from the lpGBT-FPGA. G0-6 are the bits reserved for the ePort groups. In the case of downlink the number of eGroups is 4 due to the asymmetry in the data rate and the frame is 64-bit long.

The number of eLink connections to the front-end ASICs depends on the uplink data rate, uplink FEC coding, and uplink/downlink connection bandwidth as summarised in Table 6.2.

	Downlink e-links			**Uplink e-links**											
Data rate	2.56 Gb/s			5.12 Gb/s						10.24 Gb/s					
FEC coding	-			FEC5			FEC12			FEC5			FEC12		
eLink Bandwidth (Mb/s)	80	160	320	160	320	640	160	320	640	320	640	1280	320	640	1280
Number	16	8	4	28	14	7	24	12	6	28	14	7	24	12	6

Table 6.2: Number of available uplink and downlink lpGBT electrical eLinks

Due to the asymmetric bandwidth of the up and downlinks, the number of lpGBT input and output eLinks will be different. The number of available eClocks is independent of the programmed clock frequency and is 29. The timing reference for the eClocks in the lpGBT is either provided externally (at the LHC bunch crossing frequency) or by the downlink data stream. In order to work properly, the clock provided to the lpGBT should have a well-defined phase relationship with respect to the LHC bunch crossing clock. If this is the case, eClocks and eLinks data outputs will have a fixed phase with respect to the LHC bunch crossing. Such a phase is hardcoded in the lpGBT and cannot be user-defined. The lpGBT also provides 4 special programmable clock signals but with a phase resolution of 50 ps. In order to guarantee a phase-uniformity of the eLinks data, the lpGBT is equipped with a phase aligning mechanism.

GBT-SCA

Even if the lpGBT provides slow control and monitoring, they are not enough to cover the BTL needs. For this reason, two GBT-SCA chips will be used providing additional functionalities for control and monitoring. The GBT-SCA ASIC inherits the Giga-Bit Transceiver optical link architecture and is therefore radiation tolerant. The SCA (Slow Control Adapter) was specifically designed to distribute control and monitoring signals to the on-detector front-end electronics while also carrying out monitoring tasks for environmental parameters of the detector [251]. The GBT-SCA is designed to communicate through EC with a special ePort of the lpGBT with a bandwidth of 80 Mb/s and a rate of 40 MHz. The ASIC provides several user interface ports to connect to the on-detector electronics: 16 I2C master controllers, 1 JTAG master controller and 32 general-purpose IO pins (GPIO). Additionally, the GBT-SCA chip includes 31 analog inputs multiplexed to a 12-bit ADC featuring offset calibration and gain correction, used to measure temperatures and currents of the SiPM sensors. The transmission through the eLink port on the SCA adheres to the HDLC standard (the e-link transport protocol) with a data packet summarised in Figure 6.13.

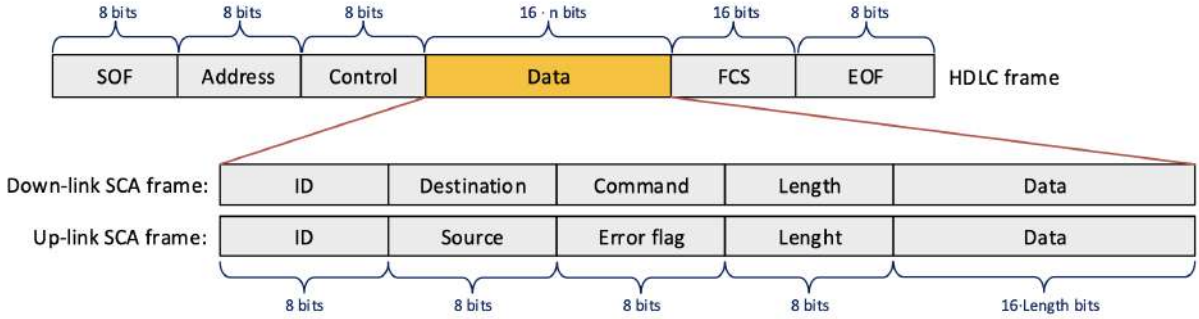

Figure 6.13: Data structure of the GBT-SCA uplink and downlink communication

The latter is comprised of an 8-bit start-of-frame delimiter character (SOF), composed of six consecutive "1s", an 8-bit address field, an 8-bit control field, a payload field of variable size, a 16-bit Frame Check Sequence (FCS) and another frame delimiter, determining the end of the frame (EOF). The variable length payload is built following the SCA channel command protocol to address the on-chip interface channels. It is composed of four 8-bit fields encapsulating the transaction identification number, a Destination/Source address field (depending on the direction of the communication), an 8-bit Command or ErrorFlag field, an 8-bit register for the data length, and a variable length data field. The Control field can be used to instruct the SCA with three special commands: CONNECT will activate the SCA ePort in order to receive data, RESET will clear the ePort, FIFOs and state machines, TEST to activate a loop-back mode of the ePort for testing purposes.

Readout Unit

A BTL readout unit (RU) is composed of a PCB Concentrator Card (CC) housing two lpGBT chips gathering data from 12 front-end boards, two GBT-SCA chips, two RAFAEL chips for clock distribution and two power converter cards (PCC-bPOL12) supplying low voltage power to all ASICs previously described. The RU will support 768 SiPM readings by interfacing lpGBT chips to the 24 TOFHIR ASICs. The two lpGBTs will be operated in the transceiver mode each with an uplink data rate of 5.12 Gb/s for a total of 10.24 Gb/s. This decision is driven by the fact that the expected average data rate for each of the 24 eLinks is approximately 230 Mb/s, based on calculations considering an 8% occupancy, 120 bits per hit, and a 0.75 MHz L1 rate [231]. This amounts to 5.5 Gb/s that can be handled employing two lpGBTs at their

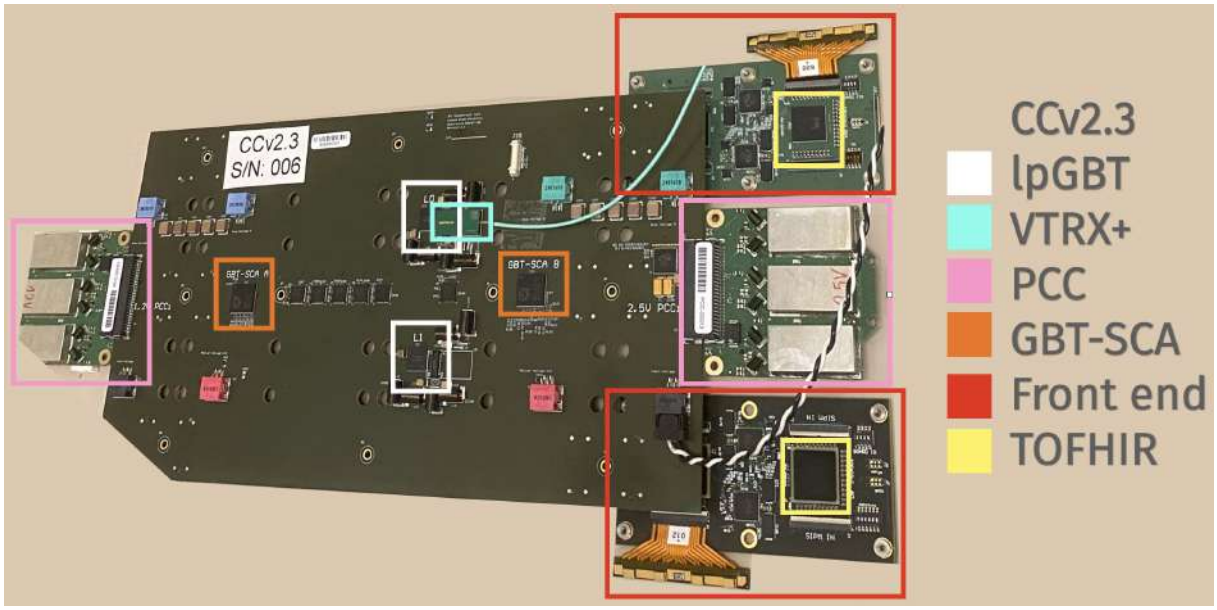

Figure 6.14: Layout of the BTL readout unit with CCv2.3 final design with two front-end boards connected.

lower uplink bandwidth. PCC cards will house three radiation and magnetic field tolerant DC/DC converters based on the FEASTMP_CLP ASIC [253]. The two GBT-SCA on the CC will serve for slow control and monitoring. In particular, they will be used for controlling the 6 DC/DC output voltages and performing temperature monitoring for the SiPM sensors and every single sensor on the front-end boards, PCCs, and CC. Additionally, they should monitor the SiPMs bias currents (one per group of 16 SiPMs, for a total of 48). The design of the CC and its printed circuits will determine the ASIC connections. The hardware design is strongly coupled with the firmware and software development as the precise knowledge of the ASICs ports connection is necessary in order to perform read and write operations on the chips. A picture of the readout unit, with the final CC design presenting all of the principal components, is shown in Figure 6.14

Back-end electronics

The off-detector electronics will be shared among BTL and ETL. The back-end will receive and further process data from 864 (1600) lpGBTs in BTL (ETL). The data from the lpGBTs is sent via radiation-tolerant optical transceivers (VTRx+) to the back-end with 70 m multi-mode optical fibers. Data are received by Firefly transceivers on the MTD DAQ nodes that process and package the information to be sent to the Timing and Control Distribution System (TCDS) through the use of a DAQ and Timing Hub (DTH400) board [254] with additional data bandwidth provided by the DAQ800 board. The DTH400 board will provide 400 Gb/s of DAQ throughput while the DAQ800 board will extend the available bandwidth of 800 Gb/s. The communication between a single MTD DAQ node and the DTH board happens at 25 Gb/s through front-panel optical connections. The data collected from all MTD DAQ boards will be sent to the event builder using the 100 Gb/s data-to-surface (D2S) protocol [231]. The form factor chosen for the CMS Phase II upgrade is based on the Advanced Telecommunications Architecture (ATCA). Electronic boards will be installed in ATCA crates and the board number depends on the required bandwidth for data transmission. The DAQ configuration should be able to handle the expected data rate computed assuming an 8% (6%) channel occupancy, an event size of 120 bits and an L1 rate of 750 kHz which amounts to 5.5 Gb/s (1.5 Gb/s) per readout unit in BTL

(ETL). As BTL (ETL) will employ 432 (1136 full-size service hybrids) readout units to cover the full detector area, an approximate data throughput of 2300 Gb/s (1900 Gb/s) is expected. These requirements can be met by installing in the ATCA crate four (eight) MTD DAQ boards, one DTH400 and two DAQ800 boards for the BTL (ETL) detector. Two ATCA crates will be employed for both BTL and ETL as described in the following table:

Component	BTL	ETL	Component Bandwidth [Gb/s]
lpGBT links	864	1688	5.12 BTL - 5.12 ETL
Serenity boards	8	16	25 BTL - 16 ETL
DTH400	2	2	400
DAQ800	4	4	800
Crates	2	2	-

The core of the MTD-specific DAQ system is the MTD DAQ node board. The Serenity platform [231, 255] was chosen for this task and is shared with other subdetectors such as the tracker, HGC and the L1 trigger system. The Serenity is an ATCA-compliant platform consisting of three essential components: an ATCA Carrier Card providing power, clocking, optical interfaces and electrical connections, an IPMC mezzanine card for the management of AdvancedTCA blades and finally an on-board CPU. The processing of the data, coming from the lpGBTs, is handled by daughter cards implementing FPGAs. In addition to the hardware setup, a versatile framework of generic and flexible firmware and software is also integrated into the system. The FPGAs are connected to 12 SAMTEC Firefly transceivers providing 72 bidirectional optical lines. The board will host two FPGAs therefore providing 144 bidirectional links with the lpGBTs on the front-end boards or with the DTH400 / DAQ800 boards. The Serenity platform and firmware are flexible enough to accommodate different types of FPGA architectures. For the final layout, MTD will use two Xilinx Virtex Ultrascale Plus VU9P FPGA symmetrical boards.

The full DAQ chain, from very front-end electronics up to the DTH400 board, is summarised in Figure 6.15.

6.4.2 Development of the DAQ software framework

The Serenity board comes with a set of firmware and software tools. The flexibility of the board in terms of FPGA architecture poses some challenges for a common firmware development framework. As the Serenity back-end is shared among HGC, tracker, L1-trigger and MTD, the development of a common and homogeneous firmware framework would be beneficial. The Serenity design leverages a universal approach to firmware, utilizing what is known as the EMP framework. The EMP framework serves as the primary firmware development platform, enabling the separation of the primary FPGA infrastructure from algorithmic development and deployment, often referred to as the "payload." It implements top-level designs for different FPGAs and boards supported by the Serenity platform. Each of these designs connects the FPGA input/output ports to the clocking infrastructure, control bus and input or output buffers. The main idea of the EMP framework is to support arbitrary user-created payload firmware for various FPGA architectures. The firmware is based on the Very High-Speed Integrated Circuits Hardware Description Language (VHDL), one of the most common languages for the design of electrical digital systems. The EMP framework supports High-Level

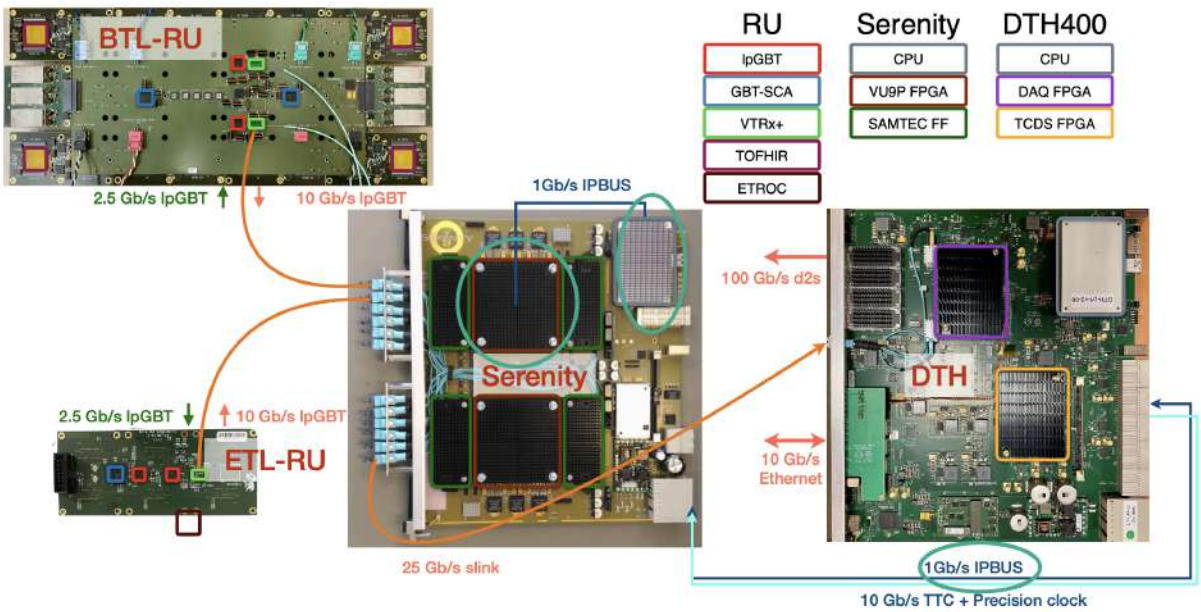

Figure 6.15: The MTD DAQ chain from on-detector electronics (Readout units, RU) to off-detector electronics (Serenity and DTH400). Picture from Ö. Sahin.

Synthesis (HLS) exploiting VivadoHLS to convert algorithms written in a high-level language (C, C++) into firmware (RTL - register transfer level). As firmware projects for modern FPGAs typically involve a large number of files and packages or components from different sources, the IPBB tool was designed to manage firmware projects in order to ease their creation, building and reproduction. Additional tools, SMASH and IPMC are provided for slow control monitoring, controlling and diagnostics. The EMP framework implements a specific hardware control protocol called IPBus for communication between the control room and the Serenity board. The IPBus is a control protocol for reading and modifying memory-mapped resources within FPGA-based IP-aware hardware devices [256]. The IPBus comes in a suite of firmware and software instruments. The IPBus firmware implements the IPBus protocol into the user hardware. The ControlHub is a software application that handles simultaneous hardware access from multiple clients. μHal is a C++ and Python software suite to enable the user programming interface for writes, reads and RMW operations. The EMP framework is continuously updated with common developments from each of the sub-detectors.

Software-wise, the different sub-detectors have relatively high freedom in the architecture design, driven by different working configurations for the various ASICS. The needed software has been developed from scratch and tailored to the needs of BTL but allows for the accommodation of ETL. The chosen software architecture is based on low-level C++ functions and high-level Python handles that allow us to provide an easily readable, manageable yet efficient code. A modular framework seemed like a natural choice from both the production and testing perspectives and is built with a one-to-one relationship between the hardware components, previously described in Sec. 6.4.1, and their high-level Python abstractions. While the real communication will be handled under the hood by optimized C++ functions, the user will interact with simpler Python functions that provide a high level of freedom in the design of the ASICs initialization routines, data readout and slow control monitoring. Most of the features of each ASIC have been tested with the new software, proving that it is scalable, reliable and can accommodate efficiently the full MTD granularity. The procedures used to initialize and communicate with the various BTL chips will be described in the following chapters in detail. For the ASICs initialization a set of configuration files, tailored to each of the chips,

has been designed to be human readable yet providing a high level of flexibility or synthesis. Custom software components have been developed to read the configuration files and convert their content from the human domain to the ASIC software domain in an efficient way by means of keywords. The chosen approach suppresses the proliferation of configuration files while retaining all necessary information for bookkeeping as explained in Sec. 6.4.2.11. While the developed software presents a high level of abstraction it may still be difficult to use for non-experienced users. This will be the case for the upcoming MTD assembly centers where the DAQ software will be instrumental in testing the detector quality at different hierarchical levels of complexity. Due to time constraints, users with varying levels of experience will need to interface with MTD's DAQ software in order to promptly retrieve basic quality information for the assembled detector. A web-based graphic user interface (GUI), tailored to the underlying MTD DAQ software, has been developed for this purpose by further abstracting the DAQ complexity. The GUI provides predefined routines for system initialization and data-taking exploiting a finite-state machine that prevents erroneous steps in the acquisition chain. The GUI also supports bookkeeping functionalities as well as live monitoring of detector sensors (such as temperature and humidity). Lastly, it is designed to run reconstruction steps on multiple servers and to promptly visualize graphics and figures of merit for the acquisition of interest. The design of the GUI and its functionalities is described in detail in Sec. 6.4.3.

While the firmware focuses on the hardware communication protocols and connections, the MTD software should be able to handle the user communication, the chips configuration and sensor monitoring for all the ASICs in the detector. After a first version, designed for the readout of TOFHIRs data with a provisional back-end, the MTD DAQ software and firmware have been re-designed from scratch to be compliant with the Serenity back-end standard. The new software is comprised of a modular and scalable Python high-level interface, connected to a set of C++ functions handling the hardware communication. The new MTD DAQ software framework is flexible enough to accommodate both BTL and ETL needs by matching the software abstraction to the hardware configuration. As the Serenity board will be the final MTD back-end during Phase II of the LHC, the developed DAQ firmware and software suite targets the online operation during the delicate commissioning, integration and data-taking phases of the MTD detector.

The main idea of the software architecture is to identify each MTD ASIC as an independent object. Higher abstractions that aggregate ASICs in groups follow from the hardware design. A simplified schema of the MTD DAQ software architecture is shown in Figure 6.16.

All ASIC classes embed three components with an incremental level of abstraction. The top component provides high-level functions to the user, implementing predefined routines for the chip initialization and settings. A middle layer is thought of as a high-level abstraction for the communication interfaces and just implements write and read functions. The real communication is handled by the low-level class through I2C, IC or EC data paths and interacts with the pybinded C++ functions from the μHal hardware access library. The details of the communication are hidden from the user thanks to the abstraction.

Each ASIC is configured through a complex system of configuration files, storing essential parameters. Configurations are stored as initialization text files, providing a human-readable structure. The files are read by a custom configuration parser. The latter handles a large number of write/read register operations by enabling the user to specify keywords for simultaneously setting multiple registers. This feature allows configuration files to be small enough to be easily readable even by inexperienced users. Each ASIC configuration file has its parser in order to meet each chip's specific needs. Hardware connection files and ASIC links for the firmware are

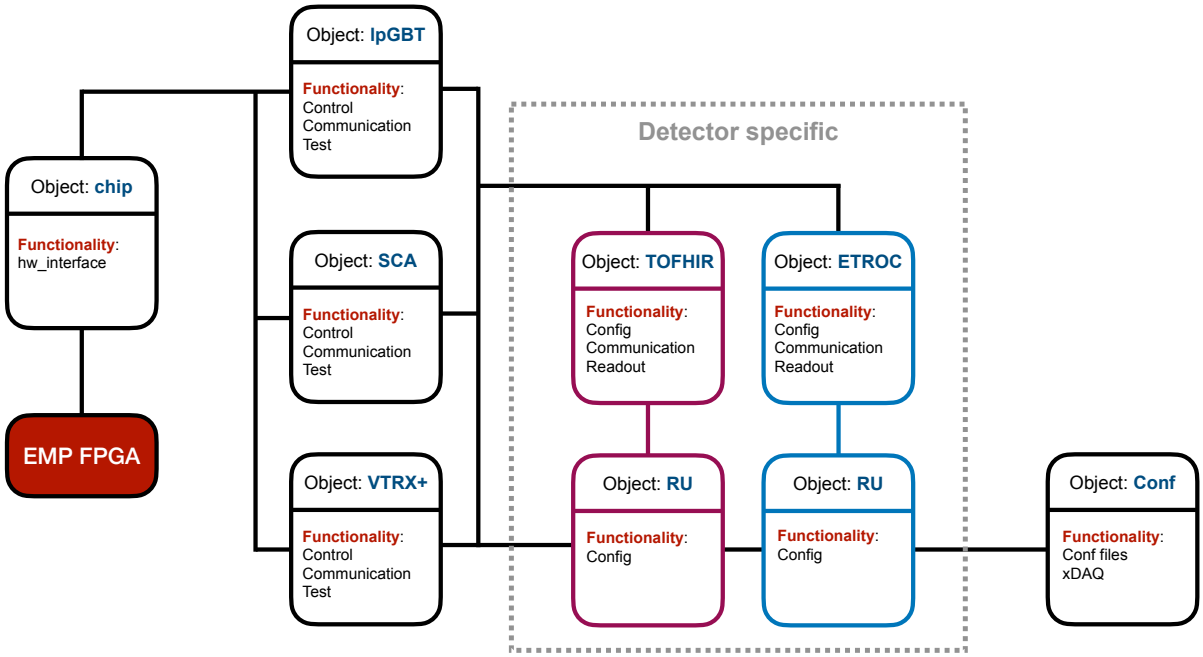

Figure 6.16: Software architecture for the Phase II MTD DAQ

also stored in an appropriate configuration. As most of the detector ASICs will share the same settings during operation, the strategy implemented for the MTD DAQ software design allows to suppress the proliferation of configuration files. Such a high granularity of information also allows for precise bookkeeping of the ASIC's operational conditions during data-taking. The modularity of the ASIC-to-ASIC software structure further allows for a multi-thread/-process initialization of the chips, leveraging at best the computational power of the CPU installed on the Serenity board.

6.4.2.1 Hardware communication

The hardware communication for all ASICs is inherited from the so-called `chip` class. The latter provides a handle to μHal by providing a file specifying the IP address and communication protocol for the IPBus communication end-points namely the Serenity board FPGAs. An additional file is needed containing the address layout of the IPbus endpoints that are used to identify all ASIC connections. Both of the files are written in XML metalanguage. The first file contains the reference to the two FPGAs (x0, x1) with an identical address table:

```
<?xml version="1.0" encoding="UTF-8"?>
<connections>
  <connection
   id="artix"
   uri="ipbuspcie-2.0:///dev/xdma/card0/h2c0,/dev/xdma/card0/c2h0"
   address_table="file://serenity_services.xml"
  />
  <connection
   id="x0"
   uri="ipbuspcie-2.0:///dev/serenity_pcie/x0/h2c,/dev/serenity_pcie/x0/c2h"
   address_table="file://addrtab/top_emp.xml"
  />
  <connection
   id="x1"
   uri="ipbuspcie-2.0:///dev/serenity_pcie/x1/h2c,/dev/serenity_pcie/x1/c2h"
   address_table="file://addrtab/top_emp.xml"
  />
</connections>
```

The `id` field is a unique identifier field. The `uri` field specifies the protocol and location to access a target device. For the MTD DAQ featuring IPBus 2.0 hardware, the protocol `ipbuspcie-2.0`

was chosen. The address_table field specifies the relative path to the address table file. The address file contains the reference to all the accessible registers and is strictly tailored to the firmware architecture. Each memory space at a specific address can be accessed from the high-level software by a unique identifier. As the IPBus protocol is an A32/D32 bus, it supports addresses up to 32 bits wide and data spaces up to 32 bits wide regardless of the specific firmware/ASIC behaviour.

The address table registers are directly coupled to the software through the EMP interface. For example, Slow Control Commands as implemented in the IC and EC fields are defined in the XML as

```
<node description="slow command control registers" fwinfo="endpoint;width=6" class="SCCNode">
   <node id="ic" address="0x10" class="SCCICNode">
        ...
        <node id="reply_data_count" address="0x2"/>
        <node id="gbtx_addr"        address="0x3"/>
        <node id="txdata_fifo"      address="0x4" size="0x200" mode="port"/>
        <node id="rxdata_fifo"      address="0x5" size="0x200" mode="port"/>

    <node id="ec" address="0x20" class="SCCECNode">
        <node id="txram">
                <node id="data"       address="0x0" size="0x400" mode="port"/>
                <node id="input_addr" address="0x1"/>
                <node id="frame_addr" address="0x2"/>
        </node>
        <node id="rxram" address="0x4">
                <node id="data" address="0x0" size="0x400" mode="port"/>
                <node id="output_addr" address="0x1"/>
                <node id="frame_addr"  address="0x2"/>
        </node>
        ...
```

Transmitted and received data can be easily retrieved from the software interface navigating the hierarchical structure of the XML file. For example, to transmit data in the lpGBT EC field e.g. from the Serenity board to the lpGBT through high-speed links and from lpGBT to the SCA, one can simply write into ec.txram.data. The response from the ASIC can then be read with some latency by querying ec.rxram.data.

6.4.2.2 lpGBT - Communication and initialization

The lpGBT suite comprises three objects following increasing levels of abstraction. Two classes handle the lpGBT communication which is hidden to the user. The main class, implementing typical initialization routines, inherits from the central lpgbt_control_lib in order to leverage support from original lpGBT developers.

The low-level class lpgbt_com has direct access to the μHal interface inheriting from the chip class. It implements IC read and write actions. A specialised function allows the user to optimise write operations through IC by scattering multiple data frames gaining a factor 2 in speed of communication. In normal read/write mode, upon a query data will be sent or retrieved from the ASICs. In the multi-write mode, data and addresses will be stored in a temporary vector. Upon a read request, data and addresses will be sent in block to the ASICs thus minimizing the I/O rate bottleneck. Additionally, the lpgbt_com interface can handle I2C communication through the GBT-SCA. A wrapper to the lpgbt_com is provided in a class lpgbt_cont that implements only a read and a write function. It will manipulate the input or output data according to the datapath and protocol chosen by the user.

The lpgbt_chip class is the high-level class designed for typical users' needs. Upon creation, the object will handle the initialization of the FPGA-lpGBT communication.

The lpGBT implements three major configuration flows, using serial controls, I2C, and e-fuses. In the current status, the serial control channel is used to initialize the lpGBT. The flow provides

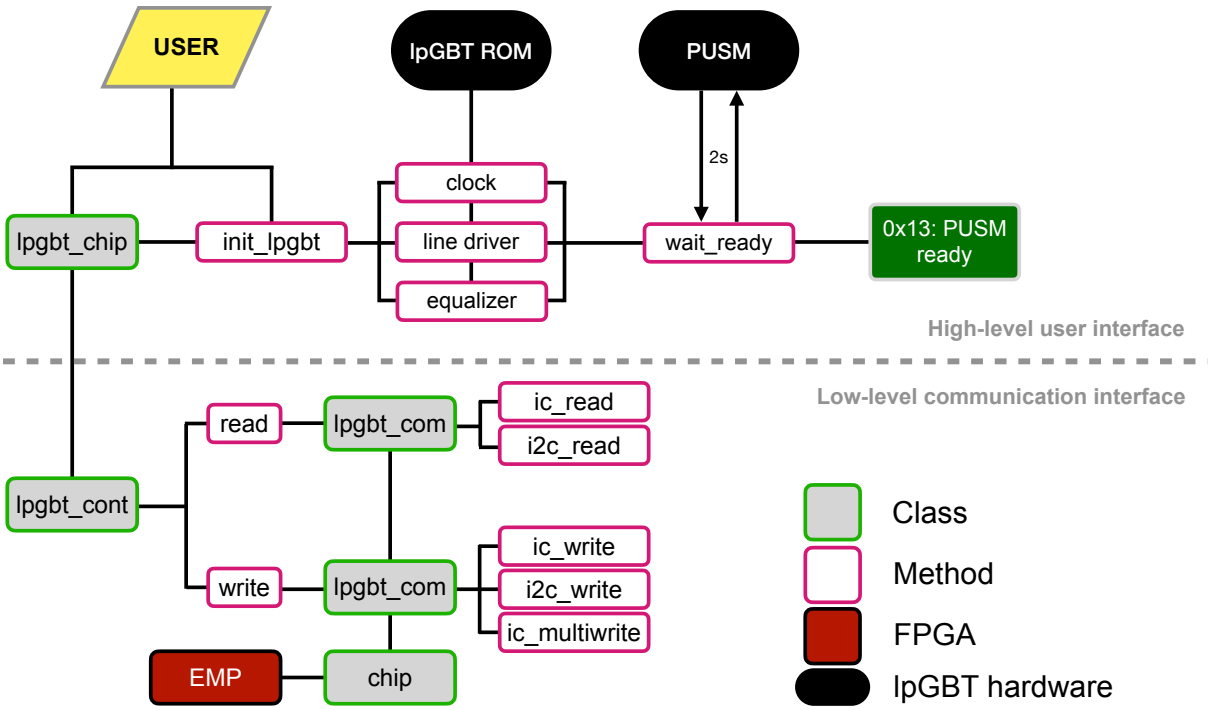

Figure 6.17: The lpGBT software architecture and the initialization procedure

a minimal lpGBT configuration for the connection to the counting room, the reference clock, the locking of the Phase-Locked-Loop (PLL) and the Delay-Locked-Loop (DLL) and finally the settings of the Clock and Data Recovery circuit (CDR) from a Read Only Memory (ROM). Furthermore, additional configurations must be applied to the downlink high-speed equalizer, high-speed line drivers (the transmission lines that connect the lpGBT with the laser driver) and EC/IC channel settings. These settings should be handled with care and their values should be rarely changed as it may lead to the serial link rupture. After this minimal configuration, it is possible to power up the lpGBT by specifying if the PLL and DLL configurations have been written. When the lpGBT is powered up, the chip will run an automatic configuration sequence controlled by a Finite-State Machine (FSM) called Power-Up State Machine (PUSM). The latter issues reset to various blocks and monitor their state until the complete chip is ready for operation. The software will wait until the PUSM is in the ready state (hex. 0x13). The lpGBT initialization process, along with the lpGBT software structure, is sketched in Figure 6.17.

After the lpGBT is powered up and in the ready state, the configuration of the chip can proceed. Further specifications on the EC connections are needed primarily to set the phase of the delay line. While receiving data from ASICs through the EC channel, only a fixed phase and a continuous phase tracking mode of operation are available for ePorts. Regarding transmission from EC ePorts, the main configurations concern the data-driver strength, the pre-emphasis and signal polarity inversion.

6.4.2.3 lpGBT - eLinks

In order to successfully connect to other peripherals, the eLinks and associated eClocks should be configured according to the hardware prescriptions. The eClocks (28) are configured by setting the clock driver strength to 2.5 mA, disabling the pre-emphasis, disabling the clock signal inversion and providing a full power supply to the filter resistance driver. All clocks are configured to operate at 160 MHz except for the last one. The 28th eLink is the only eLink that

operates at one fixed data rate of 80 Mb/s and is the one connected to the GBT-SCA. For this reason, the 28th ePort clock is set to 40 MHz.

The eLinks setup is split into two steps, one for the reception and one for the transmission. The former expects a DLL configuration for the uplink phase-aligner, shared among all ePort RX groups. It is configured with an 8 μA charge pump, the "late" information has to be reported by the phase-detector for 31 clock cycles, disabled clock and data gating of the DLL initialization state machine and disabled coarse detection of lock. The re-initialization in each ePortRx group, when the phase selection is detected out of range, is enabled. The ePortRX groups are then further configured. For both BTL and ETL all 7 ePortRX groups, each made of four eLinks (28 eLinks in total), are activated with a continuous phase tracking at a data rate of 320 Mb/s. For each eLink, the signal polarity is not inverted, the 100 Ω termination, as well as the AC biasing, are enabled and the fixed phase is given a null value as continuous phase tracking will be used that allows to dynamically tune the phase to an optimum value. The only group that is configured differently is the ePort RX group 3 (2) for the first (second) lpGBT on the BTL CC according to the laster version (v2.3). This group hosts the GBT-SCA eLink connection therefore only the 0-th (3rd) channel of group 3 (2) will be activated for the first (second) lpGBT on the CC.

The 4 transmission ePort TX groups, each made of 4 eLinks, do not implement DLL. Group 3 is the one hardwired to the GBT-SCA so it needs special treatment. All ePort Tx groups share the same configuration. All channels are enabled with a data rate of 80 Mb/s, disabled mirroring, 2.0 mA driver strength and disabled pre-emphasis. Only a few transmission eLinks are used in order to send data through the downlink. Specific channels for each group are activated in order to send trigger, RESYNC signals as well as data from the GBT-SCA.

The lpGBT configuration for eLink ePort groups RX/TX for both the ASICs implemented in the latest version of the CC is summarised in Table 6.3.

6.4.2.4 lpGBT - ADC and DAC

The lpGBT features a 10-bit ADC with 8 multiplexed external inputs, an internal temperature sensor, and the internal supply power as well as a 12-bit voltage DAC and a programmable current DAC that can be attached to any of the ADC inputs. Each of the ASIC pins associated with the ADC contains a current generator that allows them to work as current generators. The lpGBT offers a built-in reference voltage generator of 1.0 V. A PT1000 device can be connected to one of the ADC input pins providing an on-chip temperature measurement. Additionally, the analog input ports provide a measurement of the lpGBT internal or external reference voltages. Even if the MTD lpGBT won't be used for such slow controls, it is useful to be able to read temperature measurements to assess the reliability of the system and its hardware connections.

The accuracy of the reference voltage, ADC, current and voltage DAC as well as internal temperature sensors and VDD monitors is improved with a calibration routine performed at two temperatures during production testing. Chip calibrations are especially critical after irradiation as the absolute voltage and current measurements become inaccurate. It is important to estimate systematic uncertainties along the analog chain. Calibration data can only compensate for two sources of variations: chip-to-chip initial tolerances and temperature-dependent effects. Among other factors contributing to the precision and error of the analog circuits, the ADC, voltage and current DACs may additionally contribute with a slope and an offset error that should be measured. A critical component for all calibration procedures is the measurement of the lpGBT junction temperature. From laboratory measurements, the temperature difference between the PCBs and the junction is around 20 K with a spread of 10 K. The junction

	Receiving ePorts (RX)				Transmission ePorts (TX)			
	lpGBT0		lpGBT1		lpGBT0		lpGBT1	
Group.Channel	Function	[Mb/s]	Function	[Mb/s]	Function	[Mb/s]	Function	[Mb/s]
0.0	FE10.1	320	FE9.1	320	Trig	80	-	-
0.1	FE10.0	320	FE8.1	320	-	-	-	-
0.2	FE8.1	320	FE10.0	320	Rx	80	Trigger	80
0.3	FE8.0	320	FE10.1	320	-	-	-	-
1.0	FE7.1	320	FE8.0	320	RESYNC	80	Rx	80
1.1	FE7.0	320	FE9.0	320	-	-	-	-
1.2	FE1.0	320	FE7.1	320	Trigger Alt.	-	RESYNC	80
1.3	FE1.1	320	FE7.0	320	-	-	-	-
2.0	FE2.1	320	-	-	Rx Alt.	80	-	-
2.1	FE2.0	320	-	-	-	-	-	-
2.2	FE4.0	320	-	-	RESYNC Alt.	80	-	-
2.3	FE4.1	320	GBTB-IN	320	-	-	-	-
3.0	GBTA-IN	320	FE2.0	320	GBTA Out	80	GBTB Out	80
3.1	-	-	FE2.1	320	-	-	-	-
3.2	-	-	FE1.0	320	-	-	-	-
3.3	-	-	FE1.1	320	-	-	-	-
4.0	FE3.1	320	FE4.1	320				
4.1	FE3.0	320	FE4.0	320				
4.2	FE5.0	320	FE3.0	320				
4.3	FE6.1	320	FE3.1	320				
5.0	FE6.0	320	FE6.1	320				
5.1	FE5.1	320	FE6.0	320				
5.2	FE11.0	320	FE5.0	320				
5.3	FE11.1	320	FE5.1	320				
6.0	FE12.1	320	FE11.0	320				
6.1	FE12.0	320	FE11.1	320				
6.2	FE9.1	320	FE12.0	320				
6.3	FE9.0	320	FE12.1	320				

Table 6.3: Active lpGBT ePort connections from CC v2.3. board featuring two lpGBT ASICs (0 and 1)

temperature can also be estimated using the lpGBT uncalibrated ADC but typically this procedure yields a larger error. To calibrate the reference voltage optimal tune, so that its output is as close as possible to 1.0 V, a two-point linear calibration is used. The optimal tune, T_{VREF}, is defined as $T_{\mathrm{VREF}} = t_{\mathrm{J}} * \mathrm{S}_{\mathrm{VREF}} + \mathrm{O}_{\mathrm{VREF}}$ where t_{J} is the junction temperature, S and O are the slope and offset constants for the reference voltage, provided by the manufacturer for each device. The standard error on the reference voltage amounts to approximately 2.0 mV depending on the type of measurement for the t_{J} estimate. In the current BTL setup, the optimal tune was found to be 32.

Regarding slope and offset corrections across temperature to the ADC, one converter is shared among all analog inputs so no per-channel calibration is required. ADC readings may be converted to calibrated voltages $\mathrm{V}_{\mathrm{ADC}}$ using the following equation:

$$\mathrm{V}_{\mathrm{ADC}} = \mathrm{ADC}[9:0](\mathrm{O}^{\mathrm{ADC}}_{\mathrm{slope}}(G) + t_{\mathrm{J}}\mathrm{S}^{\mathrm{ADC}}_{\mathrm{slope}}(G)) + (\mathrm{O}_{\mathrm{off}^{\mathrm{ADC}}}(G) + t_{\mathrm{J}}\mathrm{S}^{\mathrm{ADC}}_{\mathrm{offset}}(G)) \tag{6.2}$$

where $\mathrm{ADC}[9:0]$ is the 10-bit conversion result returned by the ADC and all other calibration constants (S, O) are provided by the manufacturer for a specific gain G.

The voltage and current DAC slope and offset corrections have an identical analytical dependence on the junction temperature as the ADC ones. For the current DAC, its accuracy is limited by the knowledge of the temperature and voltage that may change the DAC slope. Additionally, the output resistance induces a dependency of the output on a per-channel basis. To obtain a calibrated output current C_{A} from one of the 8 channels n, neglecting the resistance effects, the following equation is used

$$\mathrm{CDAC}^n = (\mathrm{O}_{\mathrm{slope}}^{\mathrm{DAC}-n} + t_{\mathrm{J}}\mathrm{S}_{\mathrm{slope}}^{\mathrm{DAC}-n})\mathrm{C}_{\mathrm{A}} + \mathrm{O}_{\mathrm{off}}^{\mathrm{DAC}-n} + t_{\mathrm{J}}\mathrm{S}_{\mathrm{off}}^{\mathrm{DAC}-n} \tag{6.3}$$

Calibration coefficients O, S are provided by the manufacturer for each of the channels. Additionally, to obtain better estimates for the currents, the output resistance is also characterized and the correction has a linear dependence on t_{J} as $\mathrm{R}_{\mathrm{out}} = (\mathrm{O}_{\mathrm{R}}^{\mathrm{DAC}-n} + t_{\mathrm{J}}\mathrm{S}_{\mathrm{R}}^{\mathrm{DAC}-n})/\mathrm{CDAC}[n]$ The on-chip temperature measurements are calibrated using a linear slope and an offset correction.

In the BTL setup, with the latest CC (v2.3) comprising two lpGBTs, the available temperature and voltage measurements are limited by the hardware connections. If an ADC input port is not enabled it cannot be read. Table 6.4 summarises the available connections.

	lpGBT0			lpGBT1		
ADC Port	**Function**	**Enabled**	**Range**	**Function**	**Enabled**	**Range**
0	SiPM FE6 temp1	Yes	Pt1000	SiPM FE12 temp1	Yes	Pt1000
1	SiPM FE6 temp2	Yes	Pt1000	SiPM FE12 temp2	Yes	Pt1000
2	PCC A temp1	Yes	Pt1000	PCC B temp1	Yes	Pt1000
3	PCC A temp2	Yes	Pt1000	PCC B temp2	Yes	Pt1000
4	VDDA A voltage	No	0-2.5 V	VDDA C voltage	No	0-2.5 V
5	VDDA B voltage	No	0-2.5 V	VDDA D voltage	No	0-2.5 V
6	Vin voltage	No	0-15 V	CC temp2	Yes	Pt1000
7	CC temp1	Yes	Pt1000	CC temp3	Yes	Pt1000

Table 6.4: Active lpGBT analog connections from CC v2.3. board featuring two lpGBT ASICs (0 and 1)

Temperature of voltage readings are made by querying the ADC for a specific port and converting its value to volts. For voltage measurements, this value is sent back to the uplink to the counting room while for temperature reading the voltages are further converted to equivalent resistances. Calibrations to the ADC value are applied according to the calculated correction factors as

$$\mathrm{R}_{\mathrm{eq}} = 0.000962441 \cdot \mathrm{ADC}_{\mathrm{port}} - 0.0253751 \tag{6.4}$$

The temperature is then extracted from a linear interpolation of R_{eq} with an array of 200 tabulated resistance values with a 1°C temperature difference between two points covering a temperature range between -50 and 150°C.

6.4.2.5 lpGBT - GPIO

The lpGBT has 16 I/O pins logically divided into two ports: L(ow) and H(igh), each containing 8 pins. One port comprises eight pins. Each port pin can be configured as input or output with configurable driver and pull settings. All pin operations are synchronous with the internal system clock (40 MHz). GPIOs are connected to front-end ASICs for control and monitoring by providing simple logical functions. All functions are individually configurable per pin, but several pins can be configured in a single operation. Each pin is controlled by five registers, selecting the pin direction (output or input pins), low or high output pin drivers, state and direction of the pull-up/down pin resistor and the output driving capability which allows to limit output slew rate in order to reduce electromagnetic emission. While an input pin only has two states (0 and 1), an output pin can have 3 states two given by the output state (0 or 1) and one if the pin is driven low or high. All unused pins must be assigned a defined level. The simplest method to ensure a defined level of an unused pin is to enable the internal pull-up or pull-down resistor that prevents the floating that may happen if the pin is in the input state and not connected to anything and we try to read its state. Alternatively, unused pins should

be set as output pins. The function of the lpGBT GPIO pins, as implemented in the hardware design of the final version of the BTL CC (v2.3), is summarised in Table 6.5

	lpGBT0			lpGBT1		
Port	**Function**	**Dir.**	**Driv.**	**Function**	**Dir.**	**Driv.**
0	SCA_A Reset	Out	High	Not connected	-	-
1	Not connected	-	-	eLink Raphael pre-emphasis duration	In	-
2	CLK Raphael pre-emphasis configuration	Out	High	CLK Raphael pre-emphasis configuration	In	-
3	VDDA B Power Good	In	-	Calib Raphael pre-emphasis duration	In	-
4	1.2V Power Good	In	-	Not connected	-	-
5	VDDA A Power Good	In	-	CLK Raphael pre-emphasis duration	In	-
6	Calib Raphael pre-emphasis configuration	Out	High	VDDA B Power Good	In	-
7	Calib Raphael pre-emphasis duration	Out	High	Not connected	-	-
8	eLink Raphael pre-emphasis configuration	Out	High	eLink Raphael pre-emphasis configuration	In	-
9	eLink Raphael pre-emphasis duration	Out	High	Not connected	-	-
10	CLK Raphael pre-emphasis duration	Out	High	SCA_A Reset	Out	High
11	Not connected	-	-	Calib Raphael pre-emphasis configuration	In	-
12	Not connected	-	-	VDDA C Power Good	In	-
13	SCA_B Reset	Out	High	2.5V Power Good	In	-
14	Not connected	-	-	SCA_B Reset	Out	High
15	ALDO temp. shutdown disable	Out	High	ALDO temp. shutdown disable	Out	High

Table 6.5: GPIO functions as of v2.3 of the concentrator card for BTL featuring two lpGBT ASICs (0 and 1). Dir. stands for the GPIO pin direction (input or output pin) while Driv. indicates whether the pin is driven low or high.

6.4.2.6 GBT-SCA

The software abstraction of the GBT-SCA ASIC follows closely the developments for the lpGBT. The major concern when operating the SCA is to be able to read the slow controls from the front-end boards. This is achieved by configuring 32 general-purpose IO pins, 31 input analog ports multiplexed to a 12-bit ADC as well as 4 analog output ports controlled by four independent 8-bit DACs. As previously stated, the GBT-SCA ASIC is connected via a special ePort to the lpGBT and operated at 40 MHz with an effective data rate of 80 Mb/s. The chip disposes of two identical eLink ports. In the current CC v2.3 design each GBT-SCA is connected to both lpGBTs to allow a redundancy scheme, anticipating failures on the optical links. In this configuration, only one of the two GBT-SCA ports is active while the other is muted. The GBT-SCA provides 16 independent I2C master channels with individual programmable data rates from 100 kHz to 1 MHz generating 7- or 10-bit addresses. The I2C allows single- and multi-byte transactions in order to perform read, write and read/modify/write operations. In the CC v2.3, for the GBT-SCA "A", only one I2C master is available for communication through the VTRX+ on the lpGBT0. For the second GBT-SCA "B", two I2C masters are connected through the VTRX+ of lpGBT1 (master-0) and to the lpGBT slave I2C (master-15). The I2C communications have been thoroughly tested. Read and write operations to the GBT-SCA have been performed through the EC primary link. No tests have been conducted on the redundant e-link

Name	Channel	Description
CTRL	0x00	SCA configuration registers
SPI	0x01	Serial Peripheral master Interface
GPIO	0x02	GPIO interface
I2CN	0x03-0x12	I2C Serial interface – master N (0-15)
JTAG	0x13	JTAG serial master interface
ADC	0x14	Analog to digital converter
DAC	0x15	Digital to analog converter

Table 6.6: The GBT-SCA channel codes from the official documentation

connection. The GBT uses a fixed packet length of 120 bits. Payloads must be created according to the SCA and e-link transfer protocols both for read, write and reset operations. Queries for read and write actions only differ in the command field of the payload. When transmitting a payload, whether it specifies a read, write or reset command, the GBT-SCA will always send back a new payload with command 0x00 in case of control registers, or an error flag in other cases.

The payload is built in the software out of 4 components: the channel, which is specific for each command and summarised in Table 6.6, the length which is always 4 (1) for write (read) operations, the command itself which is a value from 0x00 to 0xFF (0-255 in binary) and the data that is composed of up to 32 bits. The commands are unique identifiers of actions (for example 0xFF will always do the same thing). The header of the payload is built from 3 out of the 4 fields, leaving out the data. The header is always made of 32 bits while data will be split in chunks of 8 bits. Padding of the payload fields to the required length is handled in the C++ software implementation and it is hidden from the user. The SOF/EOF instead are implemented in the firmware side for communication through EC. In order to read a register, a payload must be transmitted with an empty data field. The GBT-SCA will in turn send a payload with the requested data or with an error field. In write mode, the data payload should be filled at the specified locations and a payload will be received by the GBT-SCA and can be regarded as an acknowledgment message or as an error. If a 0x00 CMD/Err field is received no errors are encountered. Otherwise, each of the 8 bits describes the error if the bit is in the up state: bit-0 for generic errors, bit-1,2,3,4 for the invalid channel, command, transaction number and length of the returned payload, bit-5 for the channel not enabled, bit-6 for channel busy, bit-7 for command in treatment.

6.4.2.7 SCA - Internal registers

A logic block is dedicated to the internal and network channel supervision. It can be addressed by sending a message with the channel field equal to 0x0, 0x13 or 0x14. It comprises three 8-bit generic control registers, a 24-bit chip ID read-only register and a 32-bit single event upset counter. The control registers are summarised in Table 6.7, along with payload-specific values, and enable the GBT-SCA channel interfaces (I2C, JTAG, ADC, DAC, SPI). It is good practice to disable unused registers in order to save power consumption. One caveat is that to read the SCA ID one needs to enable the ADC first. The SCA ID is written on internal e-fuses during production and testing by the manufacturer and the e-fuses bank is part of the ADC block (0x14).

	Description				Payload							
	Mode	Bit	Name	Function		TYPE	CH	CMD	D[31:24]	D[23:16]	D[15:8]	D[7:0]
ID	r	23-0	Chip ID	SCA unique ID number	R	TX	0x14	0xD1	-	-	-	1
						RX	0x14	0x00	-	ID	ID	ID
CR-B	r/w	0	-	-	R	TX	0	0x03	-	-	-	-
	r/w	1	ENSPI	SPI enable flag								
	r/w	2	ENGPIO	GPIO enable flag		RX	0	0x00	VAL	-	-	-
	r/w	3	ENI2C0	I2C-0 enable flag								
	r/w	4	ENI2C1	I2C-1 enable flag	W	TX	0	0x02	VAL	-	-	-
	r/w	5	ENI2C2	I2C-2 enable flag								
	r/w	6	ENI2C3	I2C-3 enable flag		RX	0	0x00	-	-	-	-
	r/w	7	ENI2C4	I2C-4 enable flag								
CR-C	r/w	0	ENI2C5	I2C-5 enable flag	R	TX	0	0x05	-	-	-	-
	r/w	1	ENI2C6	I2C-6 enable flag								
	r/w	2	ENI2C7	I2C-7 enable flag		RX	0	0x00	VAL	-	-	-
	r/w	3	ENI2C8	I2C-8 enable flag								
	r/w	4	ENI2C9	I2C-9 enable flag	W	TX	0	0x04	VAL	-	-	-
	r/w	5	ENI2CA	I2C-10 enable flag								
	r/w	6	ENI2CB	I2C-11 enable flag		RX	0	0x00	-	-	-	-
	r/w	7	ENI2CC	I2C-12 enable flag								
CR-D	r/w	0	ENI2CD	I2C-13 enable flag	R	TX	0	0x07	-	-	-	-
	r/w	1	ENI2CE	I2C-14 enable flag								
	r/w	2	ENI2CF	I2C-15 enable flag		RX	0	0x00	VAL	-	-	-
	r/w	3	ENJTAG	JTAG enable flag								
	r/w	4	ENADC	ADC enable flag	W	TX	0	0x06	VAL	-	-	-
	r/w	5	-	-								
	r/w	6	ENDAC	DAC enable flag		RX	0	0x00	-	-	-	-
	r/w	7	-	-								
SEU	r	31-0	SEU	SEU counter	R	TX	0x13	0xF1	-	-	-	-
						RX	0x13	0x00	-	-	-	VAL
					Rs	TX	0x13	0xF0	-	-	-	0
						RX	0x13	0x00	-	-	-	-

Table 6.7: GBT-SCA internal control registers. Rs in the SEU field stands for Reset of the SEU counter. Type refers to a transmitted (TX) or a received (RX) payload. Where data fields are empty they should be assumed to be all 0 in the sent payload.

6.4.2.8 GBT-SCA - ADC

The 12-bit ADC for the GBT-SCA features 31 analog ports with a reference voltage of 1.0 V. The ADC implements an auto-calibrating procedure for the offset cancellation and implements internal gain correction, with a value (given by the manufacturer) stored in an appropriate register and loaded at power-up. These analog ports are used to measure temperatures and currents on the board. A pt1000 resistor is connected which allows temperature measurements in the range -50, +100°C similarly to what is done for the lpGBT. While the ADC will be used for reading temperatures and SiPM bias voltages, the software was only built to retrieve the former as a comprehensive TOFHIR firmware is not yet available. The software implemented to read the GBT-SCA ADC starts by enabling the ADC with the control register D described in the previous section. Next the 100 μA current on the chosen pin for temperature reading is enabled through a n-bit mask. The ADC is then queried for the count by specifying the port we want to read through an active input line register (line 31 is for the internal temperature sensor). A write operation is executed to issue the start of the ADC conversion and values are retrieved from the payload of a read operation on the ADC data register. The values are then calibrated to obtain the ADC voltage with a linear relationship $V = ADC * a + b$ where for the GBT-SCA "A" $a = 0.00024027834$, $b = 0.00068819$ and for GBT-SCA "B" $a = 0.00024428347$ and $b = 0.0008162533$. The voltage is then divided by a tabulated current value to obtain the resistance. The current values are 0.0001005337 for GBT-SCA "A" and 0.0001064 for GBT-SCA "B". Temperatures are retrieved from pt1000 tables by linear interpolation as was done in the lpGBT. The software also

Command	Function	TYPE	CH	CMD/ERR	D[31:24]	D[23:16]	D[15:8]	D[7:0]
ENADC	Enable ADC	TX	0	0x06	0x4	-	-	-
		RX	0	0x0	-	-	-	-
ADC_W_CURR	100 μA current	TX	0x14	0x60	D[31:24]	D[32:16]	D[15:8]	D[7:0]
		RX	0x14	Flag	-	-	-	-
ADC_W_MUX	Select active line	TX	0x14	0x50	-	-	-	D[4:0]
		RX	0x14	Flag	-	-	-	-
ADC_R_DATA	Read corrected ADC conversion	TX	0x14	0x21	-	-	-	1
		RX	0x14	Flag	-	-	D[11:8]	D[7:0]

Table 6.8: Sequence of commands issued to set up the GBT-SCA ADC and to read the latest gain and offset corrected conversion.

allows the calibration of the ADC voltage of slope and offset correction but has not been tested so far. Table 6.8 summarises the GBT-SCA payload in transmission and reception that are used for temperature and voltage readings while Table 6.9 summarises the CC v2.3 connections of the GBT-SCA analog input ports to the front-ends.

6.4.2.9 SCA - GPIO

The GBT-SCA comes with 32 digital I/O lines that, similarly to the lpGBT, can be configured individually as input or output (tri-state mode). Pins must be configured with a direction: 1 for output pins, and 0 for input pins. The GPIO interface of the GBT-SCA has been tested in a simple scenario for read-only operations. On the CC v2.3, the GPIOs serve the purpose of enabling the ALDO chips to provide the bias voltage to the TOFHIR and to configure the clock of the RAFAEL chip. Additionally, they enable the drain-to-drain voltage from the PCC components. As communication with TOFHIR is still an ongoing effort, the GPIO section of the GBT-SCA needs to be further improved following closely the developments on the firmware side. In this simplified example all pins are treated as input pins and only the communication has been tested, by reading each pin's status.

The software interacts with the GPIO by first enabling the corresponding bit in the control register, by setting the direction of the pin according to the CC v2.3 hardware specifications, and then by either writing to output pins or reading from input/output pins. Table 6.10 summarises the software actions needed for the GBT-SCA GPIO configuration while Table 6.11 enumerates the CC v2.3 hardware connections and their specific function.

6.4.2.10 VTRX+

The VTRX+ [257] are radiation-tolerant multi-gigabit optical transceivers that receive data from the eLinks of an lpGBT and transmit them to the back-end electronics. A VTRX+ module contains four transmitters (Tx) and one receiver (Rx), and it embeds a VCSEL laser diode driver (LDD) array or single die (for Tx), a radiation tolerant laser driver ASIC in quad-channel format (for Tx), a PIN diode single die and a radiation tolerant trans-impedance amplifier (TIA) in single-channel format (for Rx). At power-up, only the Tx channel 1 is active, while the others need to be enabled via I2C communication, established through the GBT-SCA. The GBT-SCA I2C channel address is 0 while for VTRX+ communication a 7-bit slave address composed of two fields is used. The most significant five bits (A6..A2) are hard-wired to "10100", while the least significant two bits (A1 and A0) can be set by the user through addresses ranging from 0x50 to 0x53.

The VTRX+ settings are sent through a multi-write operation, configuring the whole chip with a single I2C transaction. During the write operation, the master issues the START condition transmitting the quad LLD slave address and the R/W bit set to low. After acknowledgment

	GBT-SCA A			GBT-SCA B		
ADC Port	Function	Range (gain)	Enabled 100 μA	Function	Range	Enabled 100 μA
0	FE2 Bias Curr 3	0-2.247 mA (1/40) 0-44.94 mA (1/800)	No	FE9 Bias Curr 1	0-2.247 mA (1/40) 0-44.94 mA (1/800)	No
1	FE2 Bias Curr 4	0-2.247 mA (1/40) 0-44.94 mA (1/800)	No	FE9 Bias Curr 3	0-2.247 mA (1/40) 0-44.94 mA (1/800)	No
2	FE6 Bias Curr 4	0-2.247 mA (1/40) 0-44.94 mA (1/800)	No	FE9 Bias Curr 2	0-2.247 mA (1/40) 0-44.94 mA (1/800)	No
3	FE3 Bias Curr 4	0-2.247 mA (1/40) 0-44.94 mA (1/800)	No	FE9 Bias Curr 4	0-2.247 mA (1/40) 0-44.94 mA (1/800)	No
4	FE2 Bias Curr 2	0-2.247 mA (1/40) 0-44.94 mA (1/800)	No	FE8 Bias Curr 4	0-2.247 mA (1/40) 0-44.94 mA (1/800)	No
5	FE6 Bias Curr 3	0-2.247 mA (1/40) 0-44.94 mA (1/800)	No	FE8 Bias Curr 3	0-2.247 mA (1/40) 0-44.94 mA (1/800)	No
6	FE3 Bias Curr 3	0-2.247 mA (1/40) 0-44.94 mA (1/800)	No	FE12 Bias Curr 3	0-2.247 mA (1/40) 0-44.94 mA (1/800)	No
7	FE2 Bias Curr 1	0-2.247 mA (1/40) 0-44.94 mA (1/800)	No	FE8 Bias Curr 2	0-2.247 mA (1/40) 0-44.94 mA (1/800)	No
8	FE6 Bias Curr 1	0-2.247 mA (1/40) 0-44.94 mA (1/800)	No	FE10 Bias Curr 4	0-2.247 mA (1/40) 0-44.94 mA (1/800)	No
9	FE3 Bias Curr 1	0-2.247 mA (1/40) 0-44.94 mA (1/800)	No	FE12 Bias Curr 4	0-2.247 mA (1/40) 0-44.94 mA (1/800)	No
10	FE4 Bias Curr 4	0-2.247 mA (1/40) 0-44.94 mA (1/800)	No	FE8 Bias Curr 1	0-2.247 mA (1/40) 0-44.94 mA (1/800)	No
11	FE6 Bias Curr 2	0-2.247 mA (1/40) 0-44.94 mA (1/800)	No	FE10 Bias Curr 3	0-2.247 mA (1/40) 0-44.94 mA (1/800)	No
12	FE5 Bias Curr 4	0-2.247 mA (1/40) 0-44.94 mA (1/800)	No	FE12 Bias Curr 1	0-2.247 mA (1/40) 0-44.94 mA (1/800)	No
13	FE1 Bias Curr 4	0-2.247 mA (1/40) 0-44.94 mA (1/800)	No	FE7 Bias Curr 4	0-2.247 mA (1/40) 0-44.94 mA (1/800)	No
14	FE1 Temp 2	-50,100 °C	Yes	FE10 Bias Curr 2	0-2.247 mA (1/40) 0-44.94 mA (1/800)	No
15	FE1 Temp 1	-50,100 °C	Yes	FE12 Bias Curr 2	0-2.247 mA (1/40) 0-44.94 mA (1/800)	No
16	FE4 Bias Curr 3	0-2.247 mA (1/40) 0-44.94 mA (1/800)	No	FE7 Bias Curr 3	0-2.247 mA (1/40) 0-44.94 mA (1/800)	No
17	FE1 Bias Curr 3	0-2.247 mA (1/40) 0-44.94 mA (1/800)	No	FE7 Bias Curr 2	0-2.247 mA (1/40) 0-44.94 mA (1/800)	No
18	FE3 Bias Curr 1	0-2.247 mA (1/40) 0-44.94 mA (1/800)	No	FE10 Bias Curr 1	0-2.247 mA (1/40) 0-44.94 mA (1/800)	No
19	FE1 Bias Curr 2	0-2.247 mA (1/40) 0-44.94 mA (1/800)	No	FE7 Temp 1	-50,100 °C	No
20	FE5 Bias Curr 2	0-2.247 mA (1/40) 0-44.94 mA (1/800)	No	FE11 Bias Curr 4	0-2.247 mA (1/40) 0-44.94 mA (1/800)	No
21	FE4 Bias Curr 1	0-2.247 mA (1/40) 0-44.94 mA (1/800)	No	V Bias B	0-61 V	No
22	FE1 Bias Curr 1	0-2.247 mA (1/40) 0-44.94 mA (1/800)	No	FE7 Temp 2	-50,100 °C	No
23	FE4 Bias Curr 2	0-2.247 mA (1/40) 0-44.94 mA (1/800)	No	FE11 Bias Curr 3	0-2.247 mA (1/40) 0-44.94 mA (1/800)	No
24	FE5 Temp 2	-50,100 °C	Yes	FE11 Bias Curr 2	0-2.247 mA (1/40) 0-44.94 mA (1/800)	No
25	FE2 Temp 2	-50,100 °C	Yes	FE7 Bias Curr 1	0-2.247 mA (1/40) 0-44.94 mA (1/800)	No
26	FE5 Temp 1	-50,100 °C	Yes	FE11 Bias Curr 1	0-2.247 mA (1/40) 0-44.94 mA (1/800)	No
27	FE5 Bias Curr 3	0-2.247 mA (1/40) 0-44.94 mA (1/800)	No	FE11 Temp 2	-50,100 °C	Yes
28	FE2 Temp 1	-50,100 °C	Yes	FE8 Temp 2	-50,100 °C	Yes
29	FE5 Bias Curr 1	0-1.02 mA (1/40) 0-20.04 mA (1/800)	No	FE8 Temp 1	-50,100 °C	Yes
30	V Bias A	0-61 V	No	FE11 Temp 1	-50,100 °C	Yes

Table 6.9: Active GBT-SCA analog connections from CC v2.3 board featuring two SCA ASICs (A and B)

by the slave, the master further sends the write address in order to configure the internal address pointer. The master will then send one or more bytes of data and the slave will return an acknowledge response. The process is terminated by the master sending a STOP condition. The read operation is performed similarly as the master queries for slave data by giving an address and the R/W bit set to 1. Data is then transferred and the master returns an acknowledge response. The STOP command is issued by the master upon completion. The multi-read operation is available to retrieve all data of interest from multiple addresses in a single I2C transaction. An example of a write operation through I2C protocol is given in Figure 6.18

The VTRX+ software abstraction is composed of two classes. A high-level one for the user interface and a low-level one providing I2C read and write operations through a GBT-SCA object. The available VTRX+ 8-bit registers have been enumerated and can be configured for optimal operation. It is important to note that at power-up the quad LDD of the VTRX+ is configured with default driver settings which allow the device to be fully operational. The

Command	Function	TYPE	CH	CMD/ERR	D[31:24]	D[23:16]	D[15:8]	D[7:0]
ENGPIO	Enable GPIOs	TX	0	0x02	0x2	-	-	-
		RX	0	0x0	-	-	-	-
GPIO_W_CLKSEL	Enable 40 MHz clock	TX	0x02	0x80	0[31:24]	0[23:16]	0[15:8]	0[7:0]
		RX	0	0x0	-	-	-	-
GPIO_W_DIRECTION	Set the GPIO direction	TX	0x02	0x20	D[31:24]	D[32:16]	D[15:8]	D[7:0]
		RX	0x14	Flag	-	-	-	-
GPIO_R_DATAOUT	Read output pins	TX	0x02	0x11	-	-	-	-
		RX	0x02	Flag	D[31:24]	D[32:16]	D[15:8]	D[7:0]
GPIO_R_DATAIN	Read input pins	TX	0x02	0x01	-	-	-	-
		RX	0x02	Flag	D[31:24]	D[32:16]	D[15:8]	D[7:0]

Table 6.10: Sequence of commands issued to set up the GBT-SCA GPIOs and to read the input and output pins.

	GBT-SCA A		GBT-SCA B	
Port	Function	Dir.	Function	Dir.
0	FE2 ALDO ENABLE 2	In	FE9 ALDO Enable 2	-
1	FE5 ALDO Enable 2	-	FE9 ALDO Enable 1	In
2	FE8 ALDO Enable 2	In	PCC B VDDA C Enable	In
3	FE8 ALDO Enable 1	In	PCC B VDDA D Enable	In
4	FE11 ALDO Enable 2	In	Select clock RAFAEL 0	-
5	FE1 ALDO Enable 2	In	FE10 ALDO Enable 1	In
6	FE1 ALDO Enable 1	In	FE10 ALDO Enable 2	In
7	FE11 ALDO Enable 1	In	Not connected	-
8	FE2 ALDO Enable 1	In	FE7 ALDO Enable 1	In
9	FE4 ALDO Enable 1	In	FE7 ALDO Enable 2	-
10	FE12 ALDO Enable 1	In	RAFAEL MUX Calib	In
11	PCC A VDDA B ENABLE	-	FE3 ALDO Enable 1	In
12	PCC A VDDA A ENABLE	-	FE5 ALDO Enable 1	In
13	FE12 ALDO Enable 2	In	Enable clock RAFAEL 1	In
14	FE3 ALDO Enable 2	-	FE6 ALDO Enable 1	In
15	FE4 ALDO Enable 2	In	FE6 ALDO Enable 2	In
16	Not connected 2	In	FE12 ALDO Enable 2	-
17	FE6 ALDO Enable 1	-	FE3 ALDO Enable 2	In
18	FE6 ALDO Enable 2	In	FE4 ALDO Enable 2	In
19	RAFAEL MUX Calib	In	FE12 ALDO Enable 1	In
20	FE3 ALDO Enable 1	In	PCC A VDDA B ENABLE	-
21	FE5 ALDO Enable 1	In	PCC A VDDA A ENABLE	In
22	Enable clock RAFAEL 1	In	FE11 ALDO Enable 1	In
23	FE7 ALDO Enable 1	In	FE2 ALDO Enable 1	-
24	FE7 ALDO Enable 2	In	FE4 ALDO Enable 1	In
25	Select clock RAFAEL	In	FE11 ALDO Enable 2	-
26	FE9 ALDO Enable 2	In	FE2 ALDO Enable 2	In
27	FE9 ALDO Enable 1	-	FE1 ALDO Enable 1	In
28	PCC B VDDA D Enable	-	FE5 ALDO Enable 2	In
29	FE10 ALDO Enable 1	In	FE1 ALDO Enable 2	In
30	FE10 ALDO Enable 2	-	FE8 ALDO Enable 1	In
31	PCC B VDDA C Enable	In	FE8 ALDO Enable 2	In

Table 6.11: GPIO functions as of v2.3 of the concentrator card for BTL featuring two GBT-SCA ASICs (A and B). All pins are configured as input pins for simplicity as no front-end board is available. This will change in future developments of the BTL software.

implemented registers are summarised in Figure 6.19. Read and write operations to the VTRX+ through I2C, after the initialization of the GBT-SCA, have been tested successfully.

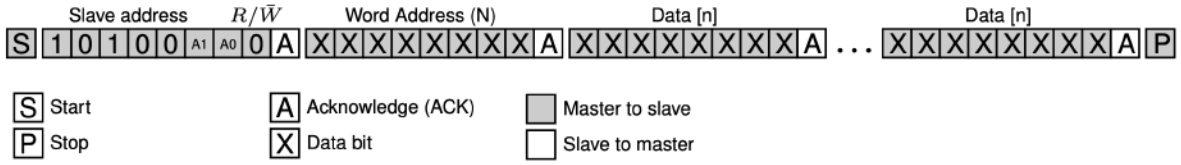

Figure 6.18: Example of an I2C write operation to the VTRX+ from a master through the I2C protocol

6.4.2.11 ReadoutUnit and the Configuration Parser

The building block of the BTL DAQ is the Readout unit (RU) as previously described. A RU connects the front-end electronics to the DAQ backend through the lpGBTs and has access to the slow controls thanks to the two GBT-SCA. The RU from a hardware perspective is just an ensemble of electronic components that coherently work together for the acquisition of all kinds of data. The list of ASICs contained in a single BTL RU is summarised in the following Table 6.12.

Component	TOFHIR	ALDO	GBT-SCA	lpGBT	VTRX+	PCC	RAFAEL
Number	24	24	2	2	2	2	6

Table 6.12: Number of ASICs for a single RU of BTL. The full detector will employ 432 of such RU.

This hardware configuration is abstracted in the software through the usage of a container RU class. The latter is thought to be an ensemble of sub-classes each representing one ASIC chip on the CC. The only task for the RU class is to initialize all the chips on the physical CC. The RU class is therefore the first handle to the detector from a user perspective. The input to the class are configuration files that describe the hardware components. Through a complex configuration parser it can decode the configuration files and parse the information to the single chip classes for a successful initialization and communication. An additional configuration file is reserved for the Serenity parameters such as its connection XML file and the mapping between the optical links and the lpGBTs and GBT-SCAs. Registers can be initialized in blocks. When redundancy can appear as in the case of eLinks, or when multiple registers can be accessed at the same time, the configuration uses keywords to expand the user need. As an example, the configuration of all the eLinks clocks with a frequency of 160 MHz is translated into a single line in the configuration file by appending the suffix "_all" to the desired field. The configuration can then be more granular with the suffixes "_group" and "_channel" with which the user can specify some common configurations for a group of eLinks or single channels. For very fine tunings the parsing of the configuration file also allows the user to address specific single registers and this feature is only useful for debugging purposes.

To be able to retain the modularity of the whole software framework, each ASIC is associated with a configuration file, for initialization and bookkeeping of operating conditions, and with a custom parser that can read the configuration and convert it from the user domain to the software domain. The RU has its configuration that simply enumerates the connected ASIC and assigns to each of them their desired configuration file. Additionally, the RU contains the table of Serenity connections that will be RU-specific. In this way, the system can be initialized as a whole, using the RU object, or the ASICs can be handled separately which is particularly useful for debugging purposes as summarised in Figure 6.20. For a single ASIC, such as lpGBT or GBT-SCA, the full initialization procedure from a configuration file takes approximately 15 ms.

NAME	ADDR	MODE	DEF.	7	6	5	4	3	2	1	0
GCR	0x00	R/W	0x01					CH4EN	CH3EN	CH2EN	CH1EN
reserved	0x01	R/W	0x00								
SDACNT	0x02	R/W	0x01							DRVSDA	SDADS
CH1BIAS	0x03	R/W	0x30		CH1BIAS[6:0]						
CH1MOD	0x04	R/W	0xA0	CH1MODEN	CH1MOD[6:0]						
CH1EMP	0x05	R/W	0x00				CH1EMPF	CH1EMPR	CH1EMPA[2:0]		
CH2BIAS	0x06	R/W	0x30		CH2BIAS[6:0]						
CH2MOD	0x07	R/W	0xA0	CH2MODEN	CH2MOD[6:0]						
CH2EMP	0x08	R/W	0x00				CH2EMPF	CH2EMPR	CH2EMPA[2:0]		
CH3BIAS	0x09	R/W	0x30		CH3BIAS[6:0]						
CH3MOD	0x0A	R/W	0xA0	CH3MODEN	CH3MOD[6:0]						
CH3EMP	0x0B	R/W	0x00				CH3EMPF	CH3EMPR	CH3EMPA[2:0]		
CH4BIAS	0x0C	R/W	0x30		CH4BIAS[6:0]						
CH4MOD	0x0D	R/W	0xA0	CH4MODEN	CH4MOD[6:0]						
CH4EMP	0x0E	R/W	0x00				CH4EMPF	CH4EMPR	CH4EMPA[2:0]		
reserved	0x0F	R/W	0x00								
reserved	0x10	R/W	0x00								
reserved	0x11	R/W	0x07								
reserved	0x12	R/W	0x00								
reserved	0x13	R/W	0x00								
STATUS	0x14	R	–					DIS	PORC	PORB	PORA
ID	0x15	R	–	CHIPID[3:0] = 0x1				REVID[3:0] = 0x5			
UID0	0x16	R	–	UID[7:0]							
UID1	0x17	R	–	UID[15:8]							
UID2	0x18	R	–	UID[23:16]							
UID3	0x19	R	–	UID[31:24]							
SEU0	0x1A	R/CLR	–	SEUCNT[7:0]							
SEU1	0x1B	R/CLR	–	SEUCNT[15:8]							
SEU2	0x1C	R/CLR	–	SEUCNT[23:16]							
SEU3	0x1D	R/CLR	–	SEUCNT[31:24]							

Figure 6.19: Register map for the Quad Laser Driver of the VTRX+ as implemented in the high-level MTD DAQ software.

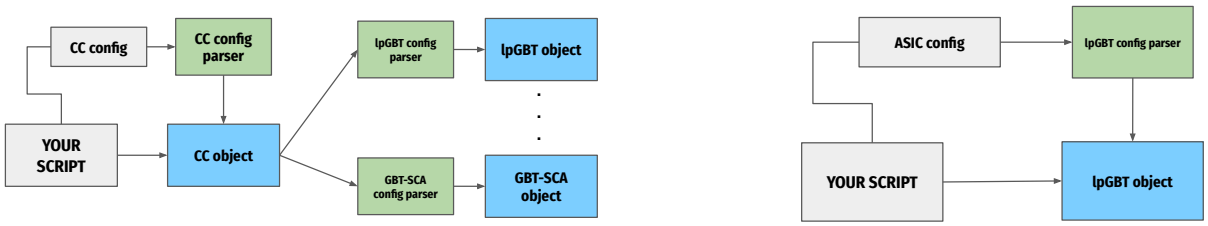

Figure 6.20: Left: the workflow for the initialization of the full RU starting from configuration files. Right: the modularity of the configurations software framework allows for the initialization of single ASICs for debugging purposes.

6.4.3 Graphic user interface for the MTD DAQ

At the time of writing the MTD project is starting its mechanical integration starting from single modules, then RU and trays to finally meet the full-size detector. At each of these steps, it is essential to have tools to monitor the performances of the assembled pieces and assess whether they meet the MTD standards for resolution. While Quality Assurance and Control (QA/QC) procedures are already in place for front-end modules, monitoring SiPMs and LYSO:Ce crystals, there is a need to perform tests at a larger scale for more complex systems such as RU or trays. For this purpose, it is necessary to connect the detector to the DAQ infrastructure, capable of handling a high rate of data, and control the full acquisition chain through the newly developed DAQ software and firmware. The MTD assembly centers, where the detector will be physically built, will need a set of high-level instruments in order to promptly collect data and monitor the performance of the detector. While the DAQ software is flexible and presents very high-level features, it still presents a high level of complexity and multiple subtleties that can slow the whole validation process in case the person-power is not familiar with the framework. Therefore there is a need to provide a yet higher level of abstraction to hide the complexity of the DAQ to the user, allowing for quick access to basic quality information (from single module up to a full tray) and a prompt displaying of of acquisition configurations and plots. These requirements can be achieved through the usage of a Graphic User Interface (GUI) built on top of the DAQ software. The design of such a GUI should follow some principles tailored to the needs of BTL assembly centers. It should be easy to use and understand therefore few functionalities, a light graphic and well-written documentation are preferred. The GUI should allow the user to select configurations from some predefined ones written by experts and stored in a database or, eventually, should allow the user to create new ones on the fly. For each acquisition, the GUI should be able to store metadata and configurations in a logbook. The reconstruction of the events should be automatic with the possibility to dispatch the steps to various workers to be more time-efficient. The GUI should be able to display the plots resulting from the analysis of the acquired data in quasi-realtime from a user-friendly interface with possibly redundant references to each run metadata.

A lightweight web-based GUI was designed for the upcoming needs of MTD and is sketched in Figure 6.21.

The web GUI is an Application Programming Interface (API) compliant with the REST architectural style. It comprises a front-end single-page application written in Vue.js and javascript and a backend, running on the Serenity CPU, fully Python-based made with Flask with the usage of web sockets (from Socket.IO) for the handling of continuous data streams from the backend to the client such as temperature or humidity readings. The client typically communicates with the serenity by sending HTTP requests to a Python controller that dispatches the action request. The controller has a built-in Finite State Machine (FSM) that follows the typical

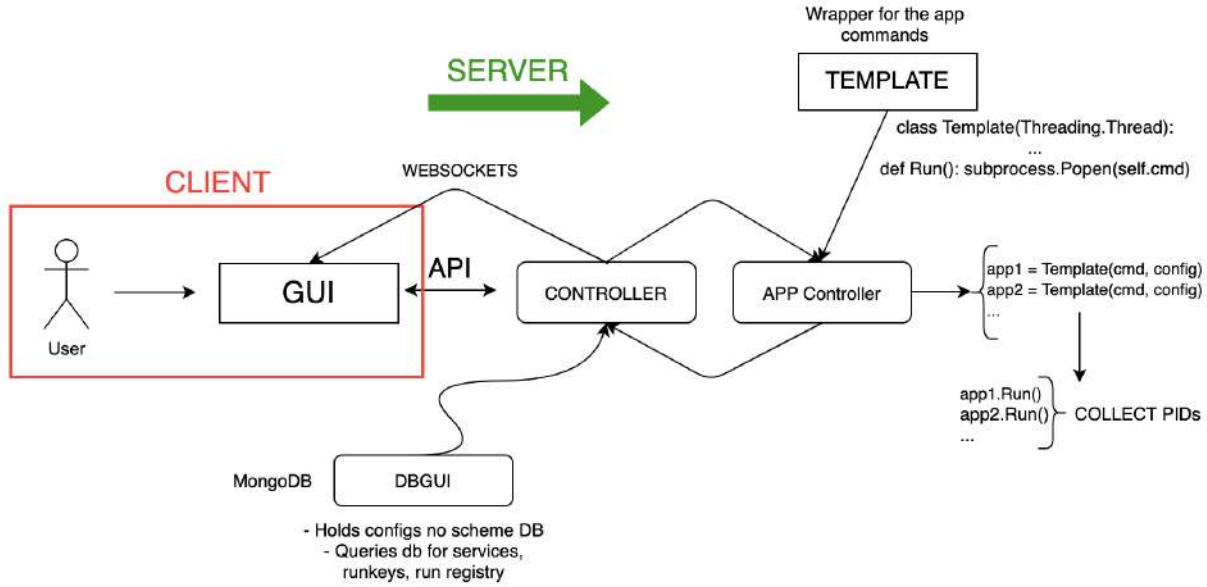

Figure 6.21: A schematic representation of the MTD GUI

data acquisition steps: an initialization state where all necessary services (such as the ASICs) are initialized, a configuration phase where the payloads are sent to the front-end boards (such as configurations of the lpGBT eLinks), a readout stage where the real data acquisition happens and a reconstruction step that takes the raw data and process them to obtain plots and figures of merit for that run. A configuration file should define all these steps. Typically there is no need to initialize the system after each run, or there is no need to run the reconstruction promptly, there is the possibility to leave fields empty. If an inexperienced user attempts to bypass these predefined stages, the FSM will halt and an error message will be displayed to the client web page. A display will tell the user the live status of the FSM and the applications in the queue specified by the configuration chosen. The display will differentiate steps and applications already executed, in execution and waiting for execution with different colours. An example of the main web page for data acquisition is displayed in Figure 6.22

The Controller is interfaced with a NoSQL database built in MongoDB and with an application that manages the commands called APP-Controller. The MongoDB will store all configurations and run metadata. The App controller handles the action request for example the acquisition of data. It was developed to be highly flexible and not tailored to a specific version of the MTD DAQ software. Actions should be pre-defined by experts as calls to low-level DAQ software scripts with the desired command line arguments specified in each configuration file. The App controller will instantiate a threading child process with the desired commands, will execute it and monitor them with the usage of application PIDs. Such a modular architecture allows for sequential or multi-threaded execution of the commands, a functionality that can be particularly useful in the reconstruction step.

Upon the completion of the action specified in the configuration file, or if an error is encountered, the run metadata is saved in the database run-registry. The database can be queried by the client at any time and it will be displayed on the web page as a table containing the run number, the date and time of acquisition, the status of the data taking, the steps required by the user, the configuration file and a link to the produced plots, as shown in Figure 6.23

Finally, a dedicated page is reserved for the configurations. The page will query the configurations database and will display all its content in the form of a table to the client similar to

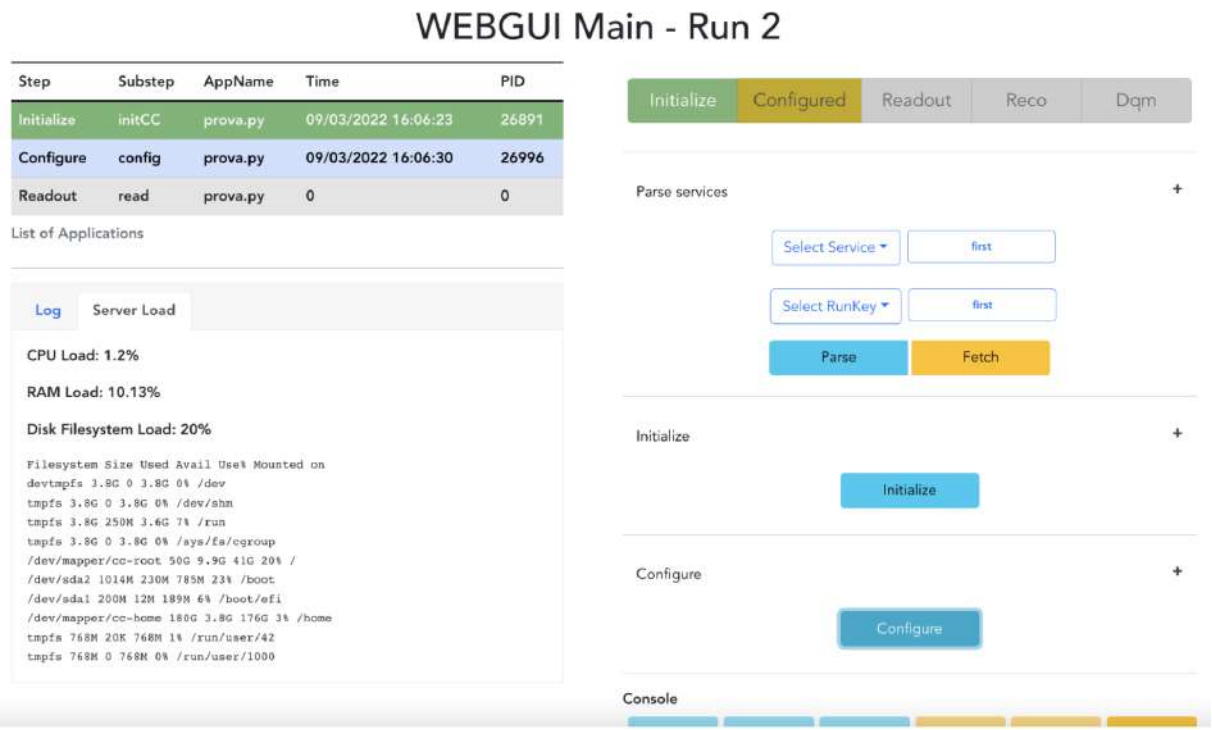

Figure 6.22: The main MTD web-GUI page for data acquisition. At the top of the left column, the GUI displays the executed commands (green), the running command (cyan) and the upcoming commands (grey). In the bottom left, the GUI displays live information from the Serenity backend about CPU, RAM and disk loads. At the top of the right column, the GUI displays the status of the backend FSM and the panels for the selection of the configuration files and for triggering the actions.

the run-registry. Users can modify the keys, to delete or add new keys on the fly by typing in the web browser application. Such configurations will be sent through an HTTP request to the backend and will be stored in the database. The ability to modify or delete the configurations can be deactivated, as during normal operation the GUI will be exploited by not-experienced users therefore error-prevention mechanisms should be put in place as much as possible.

The installation of the whole package on the Serenity CPU led to an increase in disk usage of 2.3 GB raising the occupancy from 1% to 2%. The heaviest dependencies are the essential ones to run the application such as NODEJS, VUEJS and the MONGODB client. When running the web GUI the CPU and RAM load are stable at a value of 0.8% and $\sim$ 10% respectively as shown in Figure 6.24

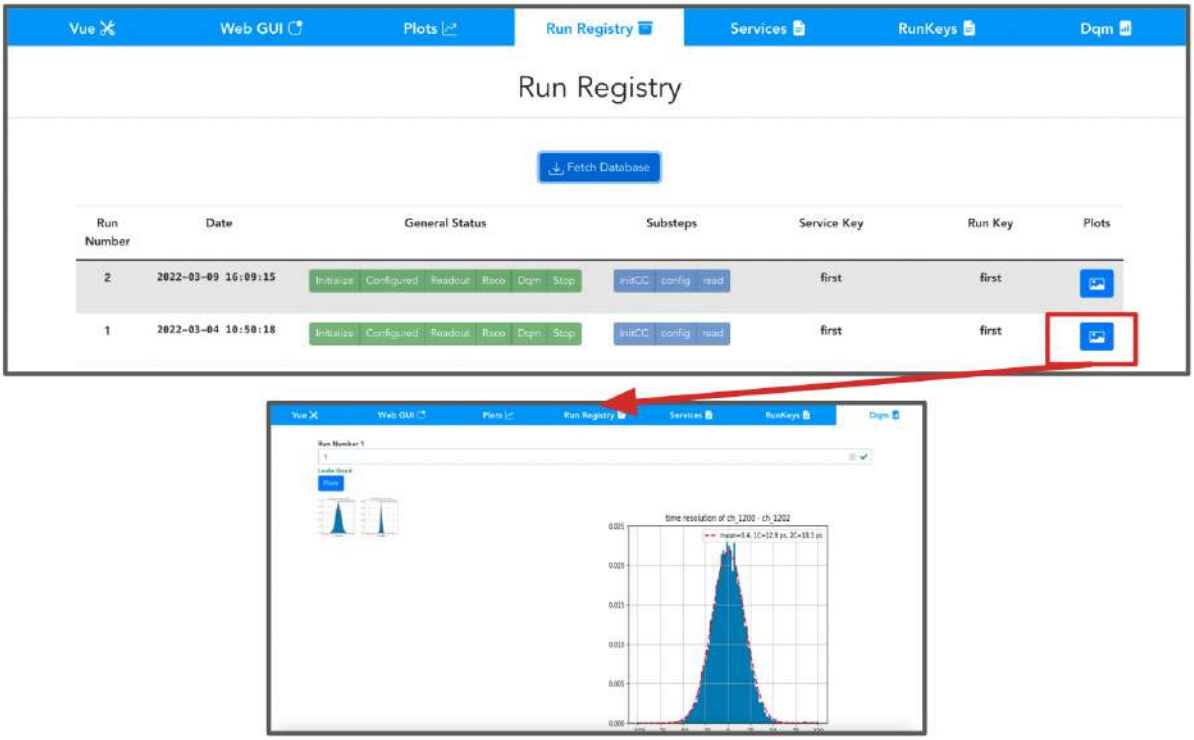

Figure 6.23: The main MTD run-registry page. The page displays the content of the run registry database that stores metadata for a particular run such as its number, date and time, general status (whether the acquisition was successful or not), the steps required by the user and the configuration with which that run was taken. Additionally, it provides a link to the plots that are stored on the backend

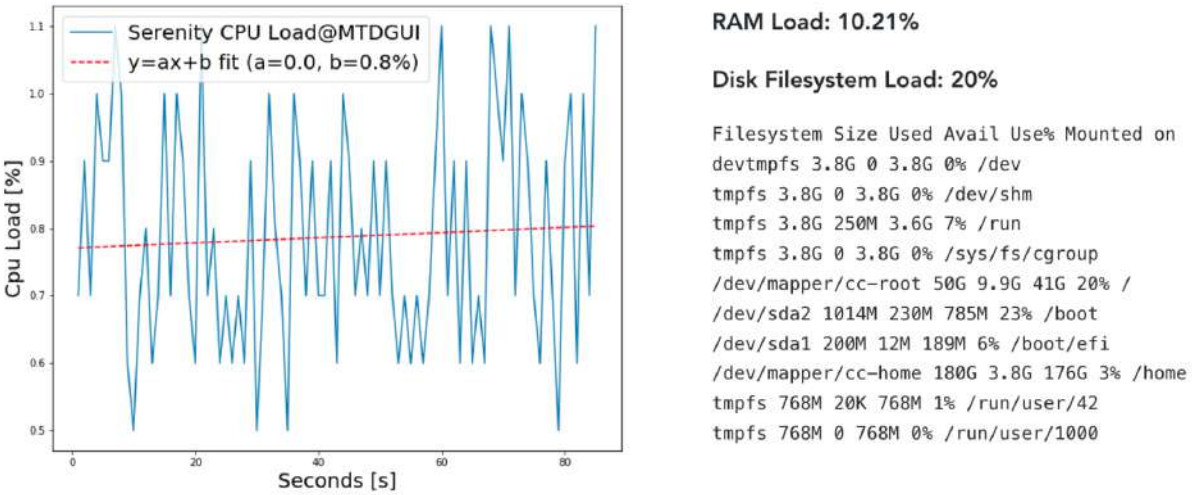

Figure 6.24: CPU load of the MTD GUI when running on the Serenity CPU

Chapter 7

Conclusions

This work reported three contributions concerning Large Hadron Collider (LHC) physics: the study of dimension-six Effective Field Theory (EFT) effects in Vector Boson Scattering (VBS) processes, firstly in a simplified parton-level combination exercise involving five VBS channels and a diboson one, secondly in a real-world scenario for the VBS process with a semileptonic final state $WVjj \to lvjjjj$. Additionally, the ongoing effort for the first full Run 2 VBS Standard Model (SM) combination was described. On the instrumental side, the development of the novel data acquisition system (DAQ) for the MIP Timing Detector (MTD) was described that will be used by the Compact Muon Solenoid (CMS) experiment during the high-luminosity (HL) phase of the LHC.

At the time of writing, state-of-the-art EFT analyses constrain less than 30 Wilson coefficients that gauge the strength of dimension-six operators. Such analyses are done through a statistical combination of Higgs boson, diboson and top quark measurements. While the theoretical and experimental precision will improve in the next decade, the increase in the integrated luminosity collected by LHC experiments will allow us to observe or get evidence of rare SM processes never seen before. VBS processes are among the rarest ones observed at the LHC, and provide an interesting signature in the EFT perspective, featuring tree-level sensitivity to operators modifying triple (TGC) and quartic (QGC) gauge couplings as well as Higgs boson couplings to electroweak (EW) vector bosons away from its mass-shell. While the VBS sensitivity to EFT dimension-six operators is expected to be sub-leading compared to dedicated top, Higgs boson and EW analyses featuring a higher cross-section, it could act as a link between the various measurements, allowing to resolve degenerate directions in a global combined fit of the full Warsaw basis. This assumption has been tested in this work by means of a comprehensive combination exercise at parton-level, involving five VBS channels and a diboson WW one to constrain 14 dimension-six operators [116]. The findings presented in this work show that VBS is particularly sensitive to four-fermion operators, operators affecting TGCs and QGCs and operators that modify fermion-gauge interactions. On the other hand, the analysis selections targeting the VBS signature suppress Higgs boson contributions, resulting in poorer constraints on operators affecting Higgs-gauge interactions. The complementarity between different VBS processes, as well as between VBS and diboson, was observed showing that a statistical combination of the channels significantly increases the sensitivity to physics Beyond the SM (BSM).

The sensitivity of VBS to dimension-six operators was then studied in a more realistic context for the scattering of a W boson decaying leptonically and another gauge boson (either $W^{\pm}$ or Z) decaying hadronically. The CMS collaboration recently gained strong evidence for this channel with an excess of $4.4\,\sigma$ above the background [105]. Eight dimension-six operators have been studied, treating VBS as a $2 \to 6$ process including non-resonant diagrams and EFT contributions both in the production and decay of the EW vector bosons. A statistical model

for EFT interpretations has been crafted for this measurement and its use is now widespread in the CMS collaboration, an important step towards a future global combination. The SM analysis was reproduced using the newly generated sample and individual limits for the eight operators (fixing all the other ones to their SM value) have been computed assuming an EFT parametrization that includes or neglects quadratic terms in the EFT Lagrangian expansion. While the comparison of the two latter results can prove the validity of the EFT expansion at the energy regime probed by the analysis, more realistic limits have been computed in the less optimistic scenario featuring all BSM terms freely floating in the maximum-likelihood fit. The expected results show that the VBS $WVjj \rightarrow lvjjjj$ process is particularly sensitive to the operator Q_W, inducing modifications in the TGCs involving three EW vector bosons, and to Q_{HW} that only modifies the coupling of the Higgs boson to EW vector bosons. The constraints on four remaining operators, namely $Q_{Hl}^{(1)}$, $Q_{H\Box}$, Q_{HWB} and Q_{HB}, that modify Higgs-gauge interactions, are found to be sub-dominant with respect to measurements targeting directly the Higgs boson signature. For two operators studied in this work, $Q_{Hj}^{(1)}$ and $Q_{HQ}^{(1)}$, no result has been found in literature. The expected results are in agreement with the findings from the simplified parton-level exercise.

This work also describes the development of the DAQ for the MTD sub-detector that will be employed at CMS during the high luminosity phase of the LHC. The excellent time resolution of MTD introduces a new handle to disentangle proton-proton collisions during the same bunch crossing. The beam-spot is sliced in consecutive time windows of less than 40 ps, effectively reducing the expected 140-200 pile-up collisions in consecutive frames containing less than 60 interactions each. The frames can be analyzed independently thus recovering the CMS performances of pileup reduction algorithms recorded so far. The finalization of the MTD back-end component necessitated a comprehensive revision of the DAQ firmware and software. The latter has been developed from scratch and tailored to the needs of the MTD barrel component (BTL) while simultaneously allowing for a smooth integration of the endcap (ETL) counterpart. It combines the strengths of C++ for optimization and Python for user-friendliness, resulting in a flexible, scalable, and efficient system that meets the specific requirements of the MTD. The software has been tested in a real-life scenario, where it was connected to a back-end board interfacing with a BTL readout unit. The latter comprises multiple ASICs such as the lpGBT, connecting the front-end electronics to the off-detector ones, the GBT-SCA for slow control and monitoring as well as the TOFHIR chip dedicated to the digitization of the SiPMs signals that are in turn connected to the scintillating LYSO:Ce tiles, which are the BTL active medium. Most of the features of each ASIC have been tested with the new software, proving that it is scalable, reliable and can accommodate efficiently the full MTD granularity. While the developed software offers a high level of abstraction, it may still pose challenges for inexperienced users. This will particularly be the case at upcoming MTD assembly centers, where the DAQ software plays a pivotal role in assessing detector quality at various complexity levels. In light of time constraints, users with varying levels of experience will need to interact with the DAQ software to quickly obtain fundamental quality information for the assembled detector. To address this need, a web-based graphical user interface (GUI) has been specifically designed to simplify the complexities of the MTD DAQ software. This GUI incorporates predefined routines for system initialization and data acquisition, leveraging a finite-state machine to prevent errors in the acquisition process. Furthermore, the GUI provides support for record-keeping tasks and real-time monitoring of detector parameters, such as temperature and humidity.

References

[1] J. Schwichtenberg, "Physics from Symmetry". Undergraduate Lecture Notes in Physics. Springer International Publishing, Cham, 2018. doi:10.1007/978-3-319-66631-0, ISBN 978-3-319-66630-3, 978-3-319-66631-0.

[2] W. Fulton and J. Harris, "Lie Algebras and Lie Groups", pp. 104–120. Springer New York, New York, NY, 2004. doi:10.1007/978-1-4612-0979-9_8.

[3] M. E. Peskin and D. V. Schroeder, "An Introduction to quantum field theory". Addison-Wesley, Reading, USA, 1995. ISBN 978-0-201-50397-5.

[4] A. Borel, "Essays in the history of lie groups and algebraic groups", AMS and London Mathematical Society, 2001.

[5] A. Einstein, "On the electrodynamics of moving bodies", *Annalen der Physik* (1905) 891–921.

[6] B. D. Popp, "On the Dynamics of the Electron", pp. 45–102. Springer International Publishing, Cham, 2020. doi:10.1007/978-3-030-48039-4_5.

[7] H. Stein, "On einstein–minkowski space–time", *The Journal of Philosophy* **65** (1968), no. 1, 5–23.

[8] L. D. Landau and E. M. Lifschits, "The Classical Theory of Fields", volume Volume 2 of *Course of Theoretical Physics*. Pergamon Press, Oxford, 1975. ISBN 978-0-08-018176-9.

[9] S. Weinberg, "The Quantum Theory of Fields", volume 1. Cambridge University Press, 1995. doi:10.1017/CBO9781139644167.

[10] H. B. G. Casimir, "Rotation of a rigid body in quantum-mechanics", *Nature* **129** (1932) 780–780.

[11] T. Choi and S. Y. Cho, "Spin operators and representations of the poincaré group", 2020.

[12] S. I. Kryuchkov, N. A. Lanfear, and S. K. Suslov, "The role of the pauli–lubań ski vector for the dirac, weyl, proca, maxwell and fierz–pauli equations", *Physica Scripta* **91** (feb, 2016) 035301, doi:10.1088/0031-8949/91/3/035301.

[13] P. A. M. Dirac, "The Lagrangian in quantum mechanics", *Phys. Z. Sowjetunion* **3** (1933) 64–72.

[14] R. P. Feynman and A. R. Hibbs, "Quantum mechanics and path integrals". International series in pure and applied physics. McGraw-Hill, New York, NY, 1965.

[15] J. S. Schwinger, "Quantum kinematics and dynamics", W.A. Benjamin Inc. Publisher, 1970.

[16] R. P. Feynman, "The Principle of Least Action in Quantum Mechanics.". PhD thesis, Princeton University, New Jersey, May, 1942.

[17] E. Noether, "Invariante variationsprobleme", *Nachrichten von der Gesellschaft der Wissenschaften zu Göttingen, Mathematisch-Physikalische Klasse* **1918** (1918) 235–257.

[18] K. G. Wilson, "Confinement of quarks", *Phys. Rev. D* **10** (Oct, 1974) 2445–2459, doi:10.1103/PhysRevD.10.2445.

[19] C. Ehresmann, "Les connexions infinitésimales dans un espace fibré différentiable", in *Séminaire Bourbaki : années 1948/49 - 1949/50 - 1950/51, exposés 1-49*, number 1 in Séminaire Bourbaki. Société mathématique de France, 1952. talk:24.

[20] P. A. M. Dirac, "The quantum theory of the electron", *Proc. Roy. Soc. Lond. A* **117** (1928) 610–624, doi:10.1098/rspa.1928.0023.

[21] P. A. M. Dirac, "A Theory of Electrons and Protons", *Proc. Roy. Soc. Lond. A* **126** (1930), no. 801, 360–365, doi:10.1098/rspa.1930.0013.

[22] A. Proca, "Particules libres photons et particules " charge pure "", *J. Phys. Radium* **8** (1937), no. 1, 23–28, doi:10.1051/jphysrad:019370080102300.

[23] A. Proca, "Sur la théorie ondulatoire des électrons positifs et négatifs", *J. Phys. Radium* **7** (1936), no. 8, 347–353, doi:10.1051/jphysrad:0193600708034700.

[24] C. N. Yang and R. L. Mills, "Conservation of isotopic spin and isotopic gauge invariance", *Phys. Rev.* **96** (Oct, 1954) 191–195, doi:10.1103/PhysRev.96.191.

[25] G. 't Hooft and M. J. G. Veltman, "Regularization and Renormalization of Gauge Fields", *Nucl. Phys. B* **44** (1972) 189–213, doi:10.1016/0550-3213(72)90279-9.

[26] G. 't Hooft, "Renormalization of Massless Yang-Mills Fields", *Nucl. Phys. B* **33** (1971) 173–199, doi:10.1016/0550-3213(71)90395-6.

[27] M. Gell-Mann, "Symmetries of baryons and mesons", *Phys. Rev.* **125** (1962) 1067–1084, doi:10.1103/PhysRev.125.1067.

[28] M. Gell-Mann, "A Schematic Model of Baryons and Mesons", *Phys. Lett.* **8** (1964) 214–215, doi:10.1016/S0031-9163(64)92001-3.

[29] Y. Nambu and G. Jona-Lasinio, "Dynamical model of elementary particles based on an analogy with superconductivity. II.", *Phys. Rev.* **124** (1961) 246–254, doi:10.1103/PhysRev.124.246.

[30] E. Fermi, "Tentativo di una teoria dell'emissione dei raggi beta", *Ric. Sci.* **4** (1933) 491–495.

[31] C. S. Wu et al., "Experimental test of parity conservation in beta decay", *Phys. Rev.* **105** (Feb, 1957) 1413–1415, doi:10.1103/PhysRev.105.1413.

[32] J. H. Christenson, J. W. Cronin, V. L. Fitch, and R. Turlay, "Evidence for the 2π decay of the k_2^0 meson", *Phys. Rev. Lett.* **13** (Jul, 1964) 138–140, doi:10.1103/PhysRevLett.13.138.

[33] S. L. Glashow, "The renormalizability of vector meson interactions", *Nuclear Physics* **10** (1959) 107–117.

[34] A. Salam, "Weak and Electromagnetic Interactions", *Conf. Proc. C* **680519** (1968) 367–377, doi:10.1142/9789812795915_0034.

[35] S. Weinberg, "A model of leptons", *Phys. Rev. Lett.* **19** (Nov, 1967) 1264–1266, doi:10.1103/PhysRevLett.19.1264.

[36] P. W. Higgs, "Broken symmetries and the masses of gauge bosons", *Phys. Rev. Lett.* **13** (Oct, 1964) 508–509, doi:10.1103/PhysRevLett.13.508.

[37] F. Englert and R. Brout, "Broken symmetry and the mass of gauge vector mesons", *Phys. Rev. Lett.* **13** (Aug, 1964) 321–323, doi:10.1103/PhysRevLett.13.321.

[38] G. S. Guralnik, C. R. Hagen, and T. W. B. Kibble, "Global conservation laws and massless particles", *Phys. Rev. Lett.* **13** (Nov, 1964) 585–587, doi:10.1103/PhysRevLett.13.585.

[39] S. L. Glashow, "Partial-symmetries of weak interactions", *Nuclear Physics* **22** (1961), no. 4, 579–588, doi:https://doi.org/10.1016/0029-5582(61)90469-2.

[40] G. Altarelli, "The standard electroweak theory and beyond", 2000.

[41] S. Coleman and E. Weinberg, "Radiative corrections as the origin of spontaneous symmetry breaking", *Phys. Rev. D* **7** (Mar, 1973) 1888–1910, doi:10.1103/PhysRevD.7.1888.

[42] J. Goldstone, "Field Theories with Superconductor Solutions", *Nuovo Cim.* **19** (1961) 154–164, doi:10.1007/BF02812722.

[43] ALEPH Collaboration, "Determination of the Number of Light Neutrino Species", *Phys. Lett. B* **231** (1989) 519–529, doi:10.1016/0370-2693(89)90704-1.

[44] Particle Data Group Collaboration, "Review of Particle Physics", *PTEP* **2022** (2022) 083C01, doi:10.1093/ptep/ptac097.

[45] T. Appelquist and J. Carazzone, "Infrared singularities and massive fields", *Phys. Rev. D* **11** (May, 1975) 2856–2861, doi:10.1103/PhysRevD.11.2856.

[46] J. Aebischer, J. Kumar, and D. M. Straub, "Wilson: a Python package for the running and matching of Wilson coefficients above and below the electroweak scale", *Eur. Phys. J. C* **78** (2018), no. 12, 1026, doi:10.1140/epjc/s10052-018-6492-7, arXiv:1804.05033.

[47] W. Buchmuller and D. Wyler, "Effective Lagrangian Analysis of New Interactions and Flavor Conservation", *Nucl. Phys. B* **268** (1986) 621–653, doi:10.1016/0550-3213(86)90262-2.

[48] I. Brivio and M. Trott, "The standard model as an effective field theory", *Physics Reports* **793** (feb, 2019) 1–98, doi:10.1016/j.physrep.2018.11.002.

[49] S. Weinberg, "Baryon- and lepton-nonconserving processes", *Phys. Rev. Lett.* **43** (Nov, 1979) 1566–1570, doi:10.1103/PhysRevLett.43.1566.

[50] E. E. Jenkins, A. V. Manohar, and P. Stoffer, "Low-energy effective field theory below the electroweak scale: operators and matching", *Journal of High Energy Physics* **2018** (mar, 2018) doi:10.1007/jhep03(2018)016.

[51] B. Grzadkowski, M. Iskrzyński, M. Misiak, and J. Rosiek, "Dimension-six terms in the standard model lagrangian", *Journal of High Energy Physics* **2010** (oct, 2010) doi:10.1007/jhep10(2010)085.

[52] G. Elgaard-Clausen and M. Trott, "On expansions in neutrino effective field theory", *Journal of High Energy Physics* **2017** (nov, 2017) doi:10.1007/jhep11(2017)088.

[53] L. F. Abbott and M. B. Wise, "Effective hamiltonian for nucleon decay", *Phys. Rev. D* **22** (Nov, 1980) 2208–2212, doi:10.1103/PhysRevD.22.2208.

[54] L. Lehman, "Extending the standard model effective field theory with the complete set of dimension-7 operators", *Physical Review D* **90** (dec, 2014) doi:10.1103/physrevd.90.125023.

[55] L. Lehman and A. Martin, "Low-derivative operators of the standard model effective field theory via hilbert series methods", *Journal of High Energy Physics* **2016** (feb, 2016) doi:10.1007/jhep02(2016)081.

[56] B. Henning, X. Lu, T. Melia, and H. Murayama, "2, 84, 30, 993, 560, 15456, 11962, 261485, ...: Higher dimension operators in the sm eft", 2019.

[57] M. Fierz, "Zur Fermischen Theorie des β-Zerfalls", *Z. Phys.* **104** (1937), no. 7-8, 553–565, doi:10.1007/bf01330070.

[58] K. Hagiwara, S. Ishihara, R. Szalapski, and D. Zeppenfeld, "Low energy effects of new interactions in the electroweak boson sector", *Phys. Rev. D* **48** (Sep, 1993) 2182–2203, doi:10.1103/PhysRevD.48.2182.

[59] G. F. Giudice, C. Grojean, A. Pomarol, and R. Rattazzi, "The strongly-interacting light higgs", *Journal of High Energy Physics* **2007** (jun, 2007) 045–045, doi:10.1088/1126-6708/2007/06/045.

[60] J. Elias-Miró, C. Grojean, R. S. Gupta, and D. Marzocca, "Scaling and tuning of EW and higgs observables", *Journal of High Energy Physics* **2014** (may, 2014) doi:10.1007/jhep05(2014)019.

[61] N. Cabibbo, "Unitary symmetry and leptonic decays", *Phys. Rev. Lett.* **10** (Jun, 1963) 531–533, doi:10.1103/PhysRevLett.10.531.

[62] M. Kobayashi and T. Maskawa, "CP Violation in the Renormalizable Theory of Weak Interaction", *Prog. Theor. Phys.* **49** (1973) 652–657, doi:10.1143/PTP.49.652.

[63] Z. Maki, M. Nakagawa, and S. Sakata, "Remarks on the unified model of elementary particles", *Prog. Theor. Phys.* **28** (1962) 870–880, doi:10.1143/PTP.28.870.

[64] B. Pontecorvo, "Inverse beta processes and nonconservation of lepton charge", *Zh. Eksp. Teor. Fiz.* **34** (1957) 247.

[65] I. Brivio, "SMEFTsim 3.0 — a practical guide", *Journal of High Energy Physics* **2021** (apr, 2021) doi:10.1007/jhep04(2021)073.

[66] I. Brivio and M. Trott, "Scheming in the SMEFT. . . and a reparameterization invariance!", *Journal of High Energy Physics* **2017** (jul, 2017) doi:10.1007/jhep07(2017)148.

[67] A. Denner and S. Dittmaier, "Electroweak radiative corrections for collider physics", *Physics Reports* **864** (jun, 2020) 1–163, doi:10.1016/j.physrep.2020.04.001.

[68] I. Brivio et al., "Electroweak input parameters", arXiv:2111.12515.

[69] R. Alonso, E. E. Jenkins, A. V. Manohar, and M. Trott, "Renormalization Group Evolution of the Standard Model Dimension Six Operators III: Gauge Coupling Dependence and Phenomenology", *JHEP* **04** (2014) 159, doi:10.1007/JHEP04(2014)159, arXiv:1312.2014.

[70] D. A. Faroughy, G. Isidori, F. Wilsch, and K. Yamamoto, "Flavour symmetries in the SMEFT", *JHEP* **08** (2020) 166, doi:10.1007/JHEP08(2020)166, arXiv:2005.05366.

[71] J. M. Gerard, "FERMION MASS SPECTRUM IN SU(2)-L x U(1)", *Z. Phys. C* **18** (1983) 145, doi:10.1007/BF01572477.

[72] A. L. Kagan, G. Perez, T. Volansky, and J. Zupan, "General Minimal Flavor Violation", *Phys. Rev. D* **80** (2009) 076002, doi:10.1103/PhysRevD.80.076002, arXiv:0903.1794.

[73] G. D'Ambrosio, G. Giudice, G. Isidori, and A. Strumia, "Minimal flavour violation: an effective field theory approach", *Nuclear Physics B* **645** (nov, 2002) 155–187, doi:10.1016/s0550-3213(02)00836-2.

[74] G. Blankenburg, G. Isidori, and J. Jones-Pérez, "Neutrino masses and LFV from minimal breaking of u(3)5 and u(2)5 flavor symmetries", *The European Physical Journal C* **72** (aug, 2012) doi:10.1140/epjc/s10052-012-2126-7.

[75] R. Barbieri, D. Buttazzo, F. Sala, and D. M. Straub, "Flavour physics from an approximate u(2)3 symmetry", *Journal of High Energy Physics* **2012** (jul, 2012) doi:10.1007/jhep07(2012)181.

[76] D. Barducci et al., "Interpreting top-quark LHC measurements in the standard-model effective field theory", arXiv:1802.07237.

[77] ATLAS Collaboration, "Observation of a new particle in the search for the Standard Model Higgs boson with the ATLAS detector at the LHC", *Phys. Lett. B* **716** (2012) 1–29, doi:10.1016/j.physletb.2012.08.020, arXiv:1207.7214.

[78] CMS Collaboration, "Observation of a New Boson at a Mass of 125 GeV with the CMS Experiment at the LHC", *Phys. Lett. B* **716** (2012) 30–61, doi:10.1016/j.physletb.2012.08.021, arXiv:1207.7235.

[79] CMS Collaboration, "A portrait of the Higgs boson by the CMS experiment ten years after the discovery", *Nature* **607** (2022), no. 7917, 60–68, doi:10.1038/s41586-022-04892-x, arXiv:2207.00043.

[80] ATLAS Collaboration, "A detailed map of Higgs boson interactions by the ATLAS experiment ten years after the discovery", *Nature* **607** (2022), no. 7917, 52–59, doi:10.1038/s41586-022-04893-w, arXiv:2207.00092. [Erratum: Nature 612, E24 (2022)].

[81] B. W. Lee, C. Quigg, and H. B. Thacker, "Weak interactions at very high energies: The role of the higgs-boson mass", *Phys. Rev. D* **16** (Sep, 1977) 1519–1531, doi:10.1103/PhysRevD.16.1519.

[82] B. W. Lee, C. Quigg, and H. B. Thacker, "Strength of weak interactions at very high energies and the higgs boson mass", *Phys. Rev. Lett.* **38** (Apr, 1977) 883–885, doi:10.1103/PhysRevLett.38.883.

[83] A. Denner and T. Hahn, "Radiative corrections to w+w- $\to$ w+w- in the electroweak standard model", *Nuclear Physics B* **525** (aug, 1998) 27–50, doi:10.1016/s0550-3213(98)00287-9.

[84] K. Cheung, C.-W. Chiang, and T.-C. Yuan, "Partially strong *ww* scattering", *Phys. Rev. D* **78** (Sep, 2008) 051701, doi:10.1103/PhysRevD.78.051701.

[85] E. da Silva Almeida et al., "Electroweak Sector Under Scrutiny: A Combined Analysis of LHC and Electroweak Precision Data", *Phys. Rev. D* **99** (2019), no. 3, 033001, doi:10.1103/PhysRevD.99.033001, arXiv:1812.01009.

[86] A. Biekoetter, T. Corbett, and T. Plehn, "The Gauge-Higgs Legacy of the LHC Run II", *SciPost Phys.* **6** (2019), no. 6, 064, doi:10.21468/SciPostPhys.6.6.064, arXiv:1812.07587.

[87] I. Brivio et al., "O new physics, where art thou? A global search in the top sector", *JHEP* **02** (2020) 131, doi:10.1007/JHEP02(2020)131, arXiv:1910.03606.

[88] S. Dawson, S. Homiller, and S. D. Lane, "Putting standard model EFT fits to work", *Phys. Rev. D* **102** (2020), no. 5, 055012, doi:10.1103/PhysRevD.102.055012, arXiv:2007.01296.

[89] J. Ellis et al., "Top, Higgs, Diboson and Electroweak Fit to the Standard Model Effective Field Theory", *JHEP* **04** (2021) 279, doi:10.1007/JHEP04(2021)279, arXiv:2012.02779.

[90] J. J. Ethier, R. Gomez-Ambrosio, G. Magni, and J. Rojo, "SMEFT analysis of vector boson scattering and diboson data from the LHC Run II", *Eur. Phys. J. C* **81** (2021), no. 6, 560, doi:10.1140/epjc/s10052-021-09347-7, arXiv:2101.03180.

[91] SMEFiT Collaboration, "Combined SMEFT interpretation of Higgs, diboson, and top quark data from the LHC", *JHEP* **11** (2021) 089, doi:10.1007/JHEP11(2021)089, arXiv:2105.00006.

[92] E. d. S. Almeida, A. Alves, O. J. P. Éboli, and M. C. Gonzalez-Garcia, "Electroweak legacy of the LHC run II", *Phys. Rev. D* **105** (2022), no. 1, 013006, doi:10.1103/PhysRevD.105.013006, arXiv:2108.04828.

[93] A. Falkowski and D. Straub, "Flavourful SMEFT likelihood for Higgs and electroweak data", *JHEP* **04** (2020) 066, doi:10.1007/JHEP04(2020)066, arXiv:1911.07866.

[94] S. Bißmann et al., "Constraining top-quark couplings combining top-quark and $\boldsymbol{B}$ decay observables", *Eur. Phys. J. C* **80** (2020), no. 2, 136, doi:10.1140/epjc/s10052-020-7680-9, arXiv:1909.13632.

[95] S. Bißmann, C. Grunwald, G. Hiller, and K. Kröninger, "Top and Beauty synergies in SMEFT-fits at present and future colliders", *JHEP* **06** (2021) 010, doi:10.1007/JHEP06(2021)010, arXiv:2012.10456.

[96] S. Bruggisser, R. Schäfer, D. van Dyk, and S. Westhoff, "The Flavor of UV Physics", *JHEP* **05** (2021) 257, doi:10.1007/JHEP05(2021)257, arXiv:2101.07273.

[97] CMS Collaboration, "Observation of electroweak production of same-sign W boson pairs in the two jet and two same-sign lepton final state in proton-proton collisions at $\sqrt{s} = 13$ TeV", *Phys. Rev. Lett.* **120** (2018), no. 8, 081801, doi:10.1103/PhysRevLett.120.081801, arXiv:1709.05822.

[98] ATLAS Collaboration, "Observation of electroweak production of a same-sign W boson pair in association with two jets in pp collisions at $\sqrt{s} = 13$ TeV with the ATLAS detector", *Phys. Rev. Lett.* **123** (2019), no. 16, 161801, doi:10.1103/PhysRevLett.123.161801, arXiv:1906.03203.

[99] CMS Collaboration, "Observation of electroweak W+W− pair production in association with two jets in proton-proton collisions at s=13TeV", *Phys. Lett. B* **841** (2023) 137495, doi:10.1016/j.physletb.2022.137495, arXiv:2205.05711.

[100] ATLAS Collaboration, "Observation of electroweak production of W^+W^- in association with jets using the ATLAS Detector", technical report, CERN, Geneva, 2023. All figures including auxiliary figures are available at https://atlas.web.cern.ch/Atlas/GROUPS/PHYSICS/CONFNOTES/ATLAS-CONF-2023-039.

[101] ATLAS Collaboration, "Observation of electroweak $W^{\pm}Z$ boson pair production in association with two jets in pp collisions at $\sqrt{s} = 13$ TeV with the ATLAS detector", *Phys. Lett. B* **793** (2019) 469–492, doi:10.1016/j.physletb.2019.05.012, arXiv:1812.09740.

[102] CMS Collaboration, "Measurement of electroweak WZ boson production and search for new physics in WZ + two jets events in pp collisions at $\sqrt{s} = 13$TeV", *Phys. Lett. B* **795** (2019) 281–307, doi:10.1016/j.physletb.2019.05.042, arXiv:1901.04060.

[103] ATLAS Collaboration, "Observation of electroweak production of two jets and a Z-boson pair with the ATLAS detector at the LHC", arXiv:2004.10612.

[104] CMS Collaboration, "Evidence for electroweak production of four charged leptons and two jets in proton-proton collisions at $\sqrt{s}$ = 13 TeV", *Phys. Lett. B* **812** (2021) 135992, doi:10.1016/j.physletb.2020.135992, arXiv:2008.07013.

[105] CMS Collaboration, "Evidence for WW/WZ vector boson scattering in the decay channel $\ell\nu$qq produced in association with two jets in proton-proton collisions at s=13 TeV", *Phys. Lett. B* **834** (2022) 137438, doi:10.1016/j.physletb.2022.137438, arXiv:2112.05259.

[106] ATLAS Collaboration, "Measurement of electroweak $Z\,(\nu\bar{\nu})\,\gamma jj$ production and limits on anomalous quartic gauge couplings in pp collisions at $\sqrt{s}$ = 13 TeV with the ATLAS detector", *JHEP* **06** (2023) 082, doi:10.1007/JHEP06(2023)082, arXiv:2208.12741.

[107] ATLAS Collaboration, "Evidence for electroweak production of two jets in association with a $Z\gamma$ pair in pp collisions at $\sqrt{s} = 13$ TeV with the ATLAS detector", *Phys. Lett. B* **803** (2020) 135341, doi:10.1016/j.physletb.2020.135341, arXiv:1910.09503.

[108] CMS Collaboration, "Measurement of the cross section for electroweak production of a Z boson, a photon and two jets in proton-proton collisions at $\sqrt{s} = 13$ TeV and constraints on anomalous quartic couplings", *JHEP* **06** (2020) 076, doi:10.1007/JHEP06(2020)076, arXiv:2002.09902.

[109] CMS Collaboration, "Observation of electroweak production of Wγ with two jets in proton-proton collisions at $\sqrt{s}$ = 13 TeV", *Phys. Lett. B* **811** (2020) 135988, doi:10.1016/j.physletb.2020.135988, arXiv:2008.10521.

[110] R. Covarelli, M. Pellen, and M. Zaro, "Vector-Boson scattering at the LHC: Unraveling the electroweak sector", *Int. J. Mod. Phys. A* **36** (2021), no. 16, 2130009, doi:10.1142/S0217751X2130009X, arXiv:2102.10991.

[111] O. J. P. Eboli, M. C. Gonzalez-Garcia, and J. K. Mizukoshi, "$pp \to jje^{\pm}\mu^{\mp}\nu\nu$ and $jje^{\pm}\mu^{\mp}\nu\nu$ at $O(\alpha_{em}^6)$ and $O(\alpha_{em}^4\alpha_s^2)$ for the study of the quartic electroweak gauge boson vertex at CERN LHC", *Phys. Rev. D* **74** (2006) 073005, doi:10.1103/PhysRevD.74.073005, arXiv:hep-ph/0606118.

[112] B. Jäger, A. Karlberg, and G. Zanderighi, "Electroweak $ZZjj$ production in the Standard Model and beyond in the POWHEG-BOX V2", *JHEP* **03** (2014) 141, doi:10.1007/JHEP03(2014)141, arXiv:1312.3252.

[113] R. Gomez-Ambrosio, "Studies of Dimension-Six EFT effects in Vector Boson Scattering", *Eur. Phys. J. C* **79** (2019), no. 5, 389, doi:10.1140/epjc/s10052-019-6893-2, arXiv:1809.04189.

[114] A. Dedes, P. Kozów, and M. Szleper, "Standard model EFT effects in vector-boson scattering at the LHC", *Phys. Rev. D* **104** (2021), no. 1, 013003, doi:10.1103/PhysRevD.104.013003, arXiv:2011.07367.

[115] J. J. Ethier, R. Gomez-Ambrosio, G. Magni, and J. Rojo, "SMEFT analysis of vector boson scattering and diboson data from the LHC run II", *The European Physical Journal C* **81** (jun, 2021) doi:10.1140/epjc/s10052-021-09347-7.

[116] R. Bellan et al., "A sensitivity study of VBS and diboson WW to dimension-6 EFT operators at the LHC", *JHEP* **05** (2022) 039, doi:10.1007/JHEP05(2022)039, arXiv:2108.03199.

[117] R. Bellan et al., "A sensitivity study of triboson production processes to dimension-6 eft operators at the lhc", *Journal of High Energy Physics* **2023** (2023), no. 8, 158, doi:10.1007/JHEP08(2023)158.

[118] S. Dawson and P. P. Giardino, "Electroweak corrections to Higgs boson decays to $\gamma\gamma$ and W^+W^- in standard model EFT", *Phys. Rev. D* **98** (2018), no. 9, 095005, doi:10.1103/PhysRevD.98.095005, arXiv:1807.11504.

[119] S. Dawson and P. P. Giardino, "Higgs decays to ZZ and $Z\gamma$ in the standard model effective field theory: An NLO analysis", *Phys. Rev. D* **97** (2018), no. 9, 093003, doi:10.1103/PhysRevD.97.093003, arXiv:1801.01136.

[120] I. Brivio, T. Corbett, and M. Trott, "The Higgs width in the SMEFT", *JHEP* **10** (2019) 056, doi:10.1007/JHEP10(2019)056, arXiv:1906.06949.

[121] C. Degrande et al., "Automated one-loop computations in the standard model effective field theory", *Phys. Rev. D* **103** (2021), no. 9, 096024, doi:10.1103/PhysRevD.103.096024, arXiv:2008.11743.

[122] I. Brivio, Y. Jiang, and M. Trott, "The SMEFTsim package, theory and tools", *JHEP* **12** (2017) 070, doi:10.1007/JHEP12(2017)070, arXiv:1709.06492.

[123] J. Alwall et al., "The automated computation of tree-level and next-to-leading order differential cross sections, and their matching to parton shower simulations", *JHEP* **07** (2014) 079, doi:10.1007/JHEP07(2014)079, arXiv:1405.0301.

[124] NNPDF Collaboration, "Parton distributions from high-precision collider data", *Eur. Phys. J.* **C77** (2017), no. 10, 663, doi:10.1140/epjc/s10052-017-5199-5, arXiv:1706.00428.

[125] O. Mattelaer, "On the maximal use of Monte Carlo samples: re-weighting events at NLO accuracy", *Eur. Phys. J. C* **76** (2016), no. 12, 674, doi:10.1140/epjc/s10052-016-4533-7, arXiv:1607.00763.

[126] CMS Collaboration, "W^+W^- boson pair production in proton-proton collisions at $\sqrt{s} =$ 13 TeV", *Phys. Rev. D* **102** (2020), no. 9, 092001, doi:10.1103/PhysRevD.102.092001, arXiv:2009.00119.

[127] ATLAS Collaboration, "Measurement of fiducial and differential W^+W^- production cross-sections at $\sqrt{s} = 13$ TeV with the ATLAS detector", *Eur. Phys. J. C* **79** (2019), no. 10, 884, doi:10.1140/epjc/s10052-019-7371-6, arXiv:1905.04242.

[128] ATLAS Collaboration, "Measurement and interpretation of same-sign W boson pair production in association with two jets in pp collisions at $\sqrt{s} = 13$ TeV with the ATLAS detector",.

[129] CMS Collaboration, "Measurements of production cross sections of WZ and same-sign WW boson pairs in association with two jets in proton-proton collisions at $\sqrt{s} = 13$ TeV", *Phys. Lett. B* **809** (2020) 135710, doi:10.1016/j.physletb.2020.135710, arXiv:2005.01173.

[130] CMS Collaboration, "Measurement of $W^{\pm}W^{\pm}$ scattering in proton-proton collisions at $\sqrt{s} = 13$ TeV in final states with one tau lepton", technical report, CERN, Geneva, 2023.

[131] M. Grossi, J. Novak, B. Kersevan, and D. Rebuzzi, "Comparing traditional and deep-learning techniques of kinematic reconstruction for polarization discrimination in vector boson scattering", *Eur. Phys. J. C* **80** (2020), no. 12, 1144, doi:10.1140/epjc/s10052-020-08713-1, arXiv:2008.05316.

[132] ATLAS Collaboration, "Evidence of pair production of longitudinally polarised vector bosons and study of CP properties in $ZZ \to 4\ell$ events with the ATLAS detector at $\sqrt{s} = 13$ TeV", arXiv:2310.04350.

[133] CMS Collaboration, "Measurement of vector boson scattering and constraints on anomalous quartic couplings from events with four leptons and two jets in proton–proton collisions at $\sqrt{s} = 13$ TeV", *Phys. Lett. B* **774** (2017) 682–705, doi:10.1016/j.physletb.2017.10.020, arXiv:1708.02812.

[134] "Jet identification in semi-leptonic WV vector boson scattering at the LHC". http://govoni.web.cern.ch/govoni/tesi/docs/Giacomo_Boldrini_Tesi.pdf. Bachelor thesis G. Boldrini.

[135] C. F. Anders et al., "Vector boson scattering: Recent experimental and theory developments", *Rev. Phys.* **3** (2018) 44–63, doi:10.1016/j.revip.2018.11.001, arXiv:1801.04203.

[136] CMS Collaboration, "Search for anomalous electroweak production of vector boson pairs in association with two jets in proton-proton collisions at 13 TeV", *Phys. Lett. B* **798** (2019) 134985, doi:10.1016/j.physletb.2019.134985, arXiv:1905.07445.

[137] A. Falkowski et al., "Anomalous Triple Gauge Couplings in the Effective Field Theory Approach at the LHC", *JHEP* **02** (2017) 115, doi:10.1007/JHEP02(2017)115, arXiv:1609.06312.

[138] J. de Blas, J. C. Criado, M. Perez-Victoria, and J. Santiago, "Effective description of general extensions of the Standard Model: the complete tree-level dictionary", *JHEP* **03** (2018) 109, doi:10.1007/JHEP03(2018)109, arXiv:1711.10391.

[139] Y. Jiang and M. Trott, "On the non-minimal character of the SMEFT", *Phys. Lett. B* **770** (2017) 108–116, doi:10.1016/j.physletb.2017.04.053, arXiv:1612.02040.

[140] A. Helset and M. Trott, "On interference and non-interference in the SMEFT", *JHEP* **04** (2018) 038, doi:10.1007/JHEP04(2018)038, arXiv:1711.07954.

[141] G. C. Fox and S. Wolfram, "Event shapes in e^+e^- annihilation", *Nuclear Physics B* **149** (1979), no. 3, 413–496, doi:10.1016/0550-3213(79)90003-8.

[142] C. Bernaciak et al., "Fox-Wolfram moments in Higgs physics", *Physical Review D* **87** (2013), no. 7, 073014, doi:10.1103/PhysRevD.87.073014.

[143] "LHC Machine", *JINST* **3** (2008) S08001, doi:10.1088/1748-0221/3/08/S08001.

[144] CMS Collaboration, "The CMS Experiment at the CERN LHC", *JINST* **3** (2008) S08004, doi:10.1088/1748-0221/3/08/S08004.

[145] CMS Tracker Group Collaboration, "The CMS Phase-1 Pixel Detector Upgrade", *JINST* **16** (2021), no. 02, P02027, doi:10.1088/1748-0221/16/02/P02027, arXiv:2012.14304.

[146] CMS Collaboration, "CMS Technical Design Report for the Pixel Detector Upgrade", doi:10.2172/1151650.

[147] CMS Collaboration, "The CMS electromagnetic calorimeter project: Technical Design Report",.

[148] P. Adzic et al., "Energy resolution of the barrel of the CMS electromagnetic calorimeter", *JINST* **2** (2007) P04004, doi:10.1088/1748-0221/2/04/P04004.

[149] CMS Collaboration, "Energy Calibration and Resolution of the CMS Electromagnetic Calorimeter in pp Collisions at $\sqrt{s} = 7$ TeV", *JINST* **8** (2013) P09009, doi:10.1088/1748-0221/8/09/P09009, arXiv:1306.2016.

[150] USCMS, ECAL/HCAL Collaboration, "The CMS barrel calorimeter response to particle beams from 2-GeV/c to 350-GeV/c", *Eur. Phys. J. C* **60** (2009) 359–373, doi:10.1140/epjc/s10052-009-0959-5. [Erratum: Eur.Phys.J.C 61, 353–356 (2009)].

[151] CMS Collaboration, "The CMS muon project: Technical Design Report",.

[152] CMS Collaboration, "CMS Physics: Technical Design Report Volume 1: Detector Performance and Software",.

[153] CMS Collaboration, "The Performance of the CMS Muon Detector in Proton-Proton Collisions at $\sqrt{s}$ = 7 TeV at the LHC", *JINST* **8** (2013) P11002, doi:10.1088/1748-0221/8/11/P11002, arXiv:1306.6905.

[154] G. Charpak, G. Melchart, G. Petersen, and F. Sauli, "High Accuracy Localization of Minimum Ionizing Particles Using the Cathode Induced Charge Center of Gravity Readout", *Nucl. Instrum. Meth.* **167** (1979) 455, doi:10.1016/0029-554X(79)90227-1.

[155] CMS Collaboration, "CMS Technical Design Report for the Level-1 Trigger Upgrade",.

[156] CMS Collaboration, "The Phase-2 Upgrade of the CMS Level-1 Trigger",.

[157] A. Zabi et al., "The CMS Level-1 Calorimeter Trigger for the LHC Run II", *JINST* **12** (2017), no. 01, C01065, doi:10.1088/1748-0221/12/01/C01065.

[158] A. Svetek et al., "The calorimeter trigger processor card: the next generation of high speed algorithmic data processing at cms", *Journal of Instrumentation* **11** (feb, 2016) C02011, doi:10.1088/1748-0221/11/02/C02011.

[159] D. Acosta et al., "The CMS Modular Track Finder boards, MTF6 and MTF7", *JINST* **8** (2013) C12034, doi:10.1088/1748-0221/8/12/C12034.

[160] CMS Collaboration, "The CMS trigger system", *JINST* **12** (2017), no. 01, P01020, doi:10.1088/1748-0221/12/01/P01020, arXiv:1609.02366.

[161] CMS Collaboration, "Particle-Flow Event Reconstruction in CMS and Performance for Jets, Taus, and MET",.

[162] ATLAS Collaboration, "Search for the electroweak diboson production in association with a high-mass dijet system in semileptonic final states in pp collisions at $\sqrt{s} = 13$ TeV with the ATLAS detector", *Phys. Rev. D* **100** (2019), no. 3, 032007, doi:10.1103/PhysRevD.100.032007, arXiv:1905.07714.

[163] P. Artoisenet, R. Frederix, O. Mattelaer, and R. Rietkerk, "Automatic spin-entangled decays of heavy resonances in Monte Carlo simulations", *JHEP* **03** (2013) 015, doi:10.1007/JHEP03(2013)015, arXiv:1212.3460.

[164] T. Sjöstrand et al., "An introduction to PYTHIA 8.2", *Comput. Phys. Commun.* **191** (2015) 159–177, doi:10.1016/j.cpc.2015.01.024, arXiv:1410.3012.

[165] B. Jäger et al., "Parton-shower effects in Higgs production via Vector-Boson Fusion", *Eur. Phys. J. C* **80** (2020), no. 8, 756, doi:10.1140/epjc/s10052-020-8326-7, arXiv:2003.12435.

[166] P. Nason, "A New method for combining NLO QCD with shower Monte Carlo algorithms", *JHEP* **11** (2004) 040, doi:10.1088/1126-6708/2004/11/040, arXiv:hep-ph/0409146.

[167] S. Frixione, P. Nason, and C. Oleari, "Matching NLO QCD computations with Parton Shower simulations: the POWHEG method", *JHEP* **11** (2007) 070, doi:10.1088/1126-6708/2007/11/070, arXiv:0709.2092.

[168] S. Alioli, P. Nason, C. Oleari, and E. Re, "A general framework for implementing NLO calculations in shower Monte Carlo programs: the POWHEG BOX", *JHEP* **06** (2010) 043, doi:10.1007/JHEP06(2010)043, arXiv:1002.2581.

[169] J. M. Campbell and R. K. Ellis, "An Update on vector boson pair production at hadron colliders", *Phys. Rev. D* **60** (1999) 113006, doi:10.1103/PhysRevD.60.113006, arXiv:hep-ph/9905386.

[170] J. M. Campbell, R. K. Ellis, and C. Williams, "Vector boson pair production at the LHC", *JHEP* **07** (2011) 018, doi:10.1007/JHEP07(2011)018, arXiv:1105.0020.

[171] GEANT4 Collaboration, "GEANT4–a simulation toolkit", *Nucl. Instrum. Meth. A* **506** (2003) 250–303, doi:10.1016/S0168-9002(03)01368-8.

[172] J. Thaler and K. Van Tilburg, "Identifying Boosted Objects with N-subjettiness", *JHEP* **03** (2011) 015, doi:10.1007/JHEP03(2011)015, arXiv:1011.2268.

[173] CMS Collaboration, "Measurements of differential Z boson production cross sections in proton-proton collisions at $\sqrt{s}$ = 13 TeV", *JHEP* **12** (2019) 061, doi:10.1007/JHEP12(2019)061, arXiv:1909.04133.

[174] CMS Collaboration, "Measurement of differential cross sections for top quark pair production using the lepton+jets final state in proton-proton collisions at 13 TeV", *Phys. Rev. D* **95** (2017), no. 9, 092001, doi:10.1103/PhysRevD.95.092001, arXiv:1610.04191.

[175] M. Czakon et al., "Top-pair production at the LHC through NNLO QCD and NLO EW", *JHEP* **10** (2017) 186, doi:10.1007/JHEP10(2017)186, arXiv:1705.04105.

[176] D. Bertolini, P. Harris, M. Low, and N. Tran, "Pileup Per Particle Identification", *JHEP* **10** (2014) 059, doi:10.1007/JHEP10(2014)059, arXiv:1407.6013.

[177] CMS Collaboration, "Pileup mitigation at CMS in 13 TeV data", *JINST* **15** (2020), no. 09, P09018, doi:10.1088/1748-0221/15/09/P09018, arXiv:2003.00503.

[178] M. Dasgupta, A. Fregoso, S. Marzani, and G. P. Salam, "Towards an understanding of jet substructure", *JHEP* **09** (2013) 029, doi:10.1007/JHEP09(2013)029, arXiv:1307.0007.

[179] J. M. Butterworth, A. R. Davison, M. Rubin, and G. P. Salam, "Jet substructure as a new Higgs search channel at the LHC", *Phys. Rev. Lett.* **100** (2008) 242001, doi:10.1103/PhysRevLett.100.242001, arXiv:0802.2470.

[180] A. J. Larkoski, S. Marzani, G. Soyez, and J. Thaler, "Soft Drop", *JHEP* **05** (2014) 146, doi:10.1007/JHEP05(2014)146, arXiv:1402.2657.

[181] CMS Collaboration, "Identification of heavy-flavour jets with the CMS detector in pp collisions at 13 TeV", *JINST* **13** (2018), no. 05, P05011, doi:10.1088/1748-0221/13/05/P05011, arXiv:1712.07158.

[182] D. L. Rainwater, R. Szalapski, and D. Zeppenfeld, "Probing color singlet exchange in Z + two jet events at the CERN LHC", *Phys. Rev. D* **54** (1996) 6680–6689, doi:10.1103/PhysRevD.54.6680, arXiv:hep-ph/9605444.

[183] D. P. Kingma and J. Ba, "Adam: A method for stochastic optimization", 2017.

[184] S. Lundberg and S.-I. Lee, "A unified approach to interpreting model predictions", 2017.

[185] J. S. Conway, "Incorporating Nuisance Parameters in Likelihoods for Multisource Spectra", in *PHYSTAT 2011*, pp. 115–120. 2011. arXiv:1103.0354. doi:10.5170/CERN-2011-006.115.

[186] ATLAS, CMS, LHC Higgs Combination Group Collaboration, "Procedure for the LHC Higgs boson search combination in Summer 2011",.

[187] G. Cowan, K. Cranmer, E. Gross, and O. Vitells, "Asymptotic formulae for likelihood-based tests of new physics", *Eur. Phys. J. C* **71** (2011) 1554, doi:10.1140/epjc/s10052-011-1554-0, arXiv:1007.1727. [Erratum: Eur.Phys.J.C 73, 2501 (2013)].

[188] S. S. Wilks, "The Large-Sample Distribution of the Likelihood Ratio for Testing Composite Hypotheses", *Annals Math. Statist.* **9** (1938), no. 1, 60–62, doi:10.1214/aoms/1177732360.

[189] W. Verkerke and D. P. Kirkby, "The RooFit toolkit for data modeling", *eConf* **C0303241** (2003) MOLT007, arXiv:physics/0306116.

[190] L. Moneta et al., "The RooStats Project", *PoS* **ACAT2010** (2010) 057, doi:10.22323/1.093.0057, arXiv:1009.1003.

[191] CMS Collaboration, "Extraction and validation of a new set of CMS PYTHIA8 tunes from underlying-event measurements",.

[192] G. Altarelli and G. Parisi, "Asymptotic Freedom in Parton Language", *Nucl. Phys. B* **126** (1977) 298–318, doi:10.1016/0550-3213(77)90384-4.

[193] F. Maltoni, T. McElmurry, R. Putman, and S. Willenbrock, "Choosing the Factorization Scale in Perturbative QCD", arXiv:hep-ph/0703156.

[194] J. C. Collins, "Choosing the factorization / renormalization scale in perturbative qcd calculations", in *25th Rencontres de Moriond: High-energy Hadronic Interactions*, pp. 123–128. 1990.

[195] V. Hirschi and O. Mattelaer, "Automated event generation for loop-induced processes", *JHEP* **10** (2015) 146, doi:10.1007/JHEP10(2015)146, arXiv:1507.00020.

[196] J. Brehmer, K. Cranmer, G. Louppe, and J. Pavez, "A Guide to Constraining Effective Field Theories with Machine Learning", *Phys. Rev. D* **98** (2018), no. 5, 052004, doi:10.1103/PhysRevD.98.052004, arXiv:1805.00020.

[197] S. Chen, A. Glioti, G. Panico, and A. Wulzer, "Parametrized classifiers for optimal EFT sensitivity", *JHEP* **05** (2021) 247, doi:10.1007/JHEP05(2021)247, arXiv:2007.10356.

[198] CMS Collaboration, "Search for physics beyond the standard model in top quark production with additional leptons in the context of effective field theory", arXiv:2307.15761.

[199] M. Neukum, "Constraints on anomalous couplings in the hadronic decay channel of vector boson scattering at $\sqrt{s}$=13 TeV with the CMS experiment". PhD thesis, KIT, Karlsruhe, 2023. doi:10.5445/IR/1000161725.

[200] CMS Collaboration, "Measurement of $W^{\pm}\gamma$ differential cross sections in proton-proton collisions at $\sqrt{s}$ = 13 TeV and effective field theory constraints", *Phys. Rev. D* **105** (2022), no. 5, 052003, doi:10.1103/PhysRevD.105.052003, arXiv:2111.13948.

[201] G. Panico, F. Riva, and A. Wulzer, "Diboson interference resurrection", *Phys. Lett. B* **776** (2018) 473–480, doi:10.1016/j.physletb.2017.11.068, arXiv:1708.07823.

[202] I. Brivio et al., "From models to SMEFT and back?", *SciPost Phys.* **12** (2022), no. 1, 036, doi:10.21468/SciPostPhys.12.1.036, arXiv:2108.01094.

[203] CMS Collaboration, "Measurement of the inclusive and differential WZ production cross sections, polarization angles, and triple gauge couplings in pp collisions at $\sqrt{s}$ = 13 TeV", *JHEP* **07** (2022) 032, doi:10.1007/JHEP07(2022)032, arXiv:2110.11231.

[204] CMS Collaboration, "Search for anomalous triple gauge couplings in WW and WZ production in lepton + jet events in proton-proton collisions at $\sqrt{s} = 13$ TeV", *JHEP* **12** (2019) 062, doi:10.1007/JHEP12(2019)062, arXiv:1907.08354.

[205] ATLAS Collaboration, "Combined effective field theory interpretation of differential cross-sections measurements of WW, WZ, 4l, and Z-plus-two-jets production using ATLAS data", technical report, CERN, Geneva, 2021. All figures including auxiliary figures are available at https://atlas.web.cern.ch/Atlas/GROUPS/PHYSICS/PUBNOTES/ATL-PHYS-PUB-2021-022.

[206] CMS Collaboration, "Electroweak production of two jets in association with a Z boson in proton–proton collisions at $\sqrt{s} = 13$ TeV", *Eur. Phys. J. C* **78** (2018), no. 7, 589, doi:10.1140/epjc/s10052-018-6049-9, arXiv:1712.09814.

[207] CMS Collaboration, "Measurement of electroweak production of a W boson in association with two jets in proton–proton collisions at $\sqrt{s} = 13$ TeV", *Eur. Phys. J. C* **80** (2020), no. 1, 43, doi:10.1140/epjc/s10052-019-7585-7, arXiv:1903.04040.

[208] ATLAS Collaboration, "Differential cross-section measurements for the electroweak production of dijets in association with a Z boson in proton–proton collisions at ATLAS", *Eur. Phys. J. C* **81** (2021), no. 2, 163, doi:10.1140/epjc/s10052-020-08734-w, arXiv:2006.15458.

[209] CMS Collaboration, "Constraints on anomalous Higgs boson couplings to vector bosons and fermions in its production and decay using the four-lepton final state", *Phys. Rev. D* **104** (2021), no. 5, 052004, doi:10.1103/PhysRevD.104.052004, arXiv:2104.12152.

[210] ATLAS Collaboration, "Fiducial and differential cross-section measurements for the vector-boson-fusion production of the Higgs boson in the $H \to WW^* \to e\nu\mu\nu$ decay channel at 13 TeV with the ATLAS detector", *Phys. Rev. D* **108** (2023), no. 7, 072003, doi:10.1103/PhysRevD.108.072003, arXiv:2304.03053.

[211] ATLAS Collaboration, "Measurements of differential cross-sections in four-lepton events in 13 TeV proton-proton collisions with the ATLAS detector", *JHEP* **07** (2021) 005, doi:10.1007/JHEP07(2021)005, arXiv:2103.01918.

[212] CMS Collaboration, "Study of vector boson scattering and search for new physics in events with two same-sign leptons and two jets", *Phys. Rev. Lett.* **114** (2015), no. 5, 051801, doi:10.1103/PhysRevLett.114.051801, arXiv:1410.6315.

[213] ATLAS Collaboration, "Evidence for Electroweak Production of $W^{\pm}W^{\pm}jj$ in pp Collisions at $\sqrt{s} = 8$ TeV with the ATLAS Detector", *Phys. Rev. Lett.* **113** (2014), no. 14, 141803, doi:10.1103/PhysRevLett.113.141803, arXiv:1405.6241.

[214] CMS Collaboration, "Measurement of the cross section for electroweak production of $Z\gamma$ in association with two jets and constraints on anomalous quartic gauge couplings in proton–proton collisions at $\sqrt{s} = 8$ TeV", *Phys. Lett. B* **770** (2017) 380–402, doi:10.1016/j.physletb.2017.04.071, arXiv:1702.03025.

[215] CMS Collaboration, "Measurement of electroweak-induced production of Wγ with two jets in pp collisions at $\sqrt{s} = 8$ TeV and constraints on anomalous quartic gauge couplings", *JHEP* **06** (2017) 106, doi:10.1007/JHEP06(2017)106, arXiv:1612.09256.

[216] D. Rainwater, R. Szalapski, and D. Zeppenfeld, "Probing color-singlet exchange in $z + 2$-jet events at the cern lhc", *Phys. Rev. D* **54** (Dec, 1996) 6680–6689, doi:10.1103/PhysRevD.54.6680.

[217] A. Hoecker et al., "Tmva - toolkit for multivariate data analysis", 2009.

[218] F. Caola, K. Melnikov, R. Röntsch, and L. Tancredi, "QCD corrections to ZZ production in gluon fusion at the LHC", *Phys. Rev. D* **92** (2015), no. 9, 094028, doi:10.1103/PhysRevD.92.094028, arXiv:1509.06734.

[219] CMS Collaboration, "Jet energy scale and resolution performance with 13 TeV data collected by CMS in 2016-2018",.

[220] R. J. Barlow and C. Beeston, "Fitting using finite Monte Carlo samples", *Comput. Phys. Commun.* **77** (1993) 219–228, doi:10.1016/0010-4655(93)90005-W.

[221] CMS Collaboration, "Measurement of $W^{\pm}W^{\pm}$ scattering in proton-proton collisions at $\sqrt{s} = 13$ TeV in final states with one tau lepton",.

[222] I. Zurbano Fernandez et al., "High-Luminosity Large Hadron Collider (HL-LHC): Technical design report", doi:10.23731/CYRM-2020-0010.

[223] A. Dainese et al., eds., "Report on the Physics at the HL-LHC,and Perspectives for the HE-LHC", volume 7/2019 of *CERN Yellow Reports: Monographs*. CERN, Geneva, Switzerland, 2019. doi:10.23731/CYRM-2019-007, ISBN 978-92-9083-549-3.

[224] M. Cepeda et al., "Report from Working Group 2: Higgs Physics at the HL-LHC and HE-LHC", *CERN Yellow Rep. Monogr.* **7** (2019) 221–584, doi:10.23731/CYRM-2019-007.221, arXiv:1902.00134.

[225] P. Azzi et al., "Report from Working Group 1: Standard Model Physics at the HL-LHC and HE-LHC", *CERN Yellow Rep. Monogr.* **7** (2019) 1–220, doi:10.23731/CYRM-2019-007.1, arXiv:1902.04070.

[226] X. Cid Vidal et al., "Report from Working Group 3: Beyond the Standard Model physics at the HL-LHC and HE-LHC", *CERN Yellow Rep. Monogr.* **7** (2019) 585–865, doi:10.23731/CYRM-2019-007.585, arXiv:1812.07831.

[227] HEP Software Foundation Collaboration, "A Roadmap for HEP Software and Computing R&D for the 2020s", *Comput. Softw. Big Sci.* **3** (2019), no. 1, 7, doi:10.1007/s41781-018-0018-8, arXiv:1712.06982.

[228] "Technical Proposal for the Phase-II Upgrade of the CMS Detector", doi:10.17181/CERN.VU8I.D59J.

[229] CMS Collaboration, "Particle-flow reconstruction and global event description with the CMS detector", *JINST* **12** (2017), no. 10, P10003, doi:10.1088/1748-0221/12/10/P10003, arXiv:1706.04965.

[230] CMS Collaboration, "Pileup Removal Algorithms",.

[231] CMS Collaboration, "A MIP Timing Detector for the CMS Phase-2 Upgrade",.

[232] CMS Collaboration, "The Phase-2 Upgrade of the CMS Tracker", doi:10.17181/CERN.QZ28.FLHW.

[233] S. Bonacini et al., "Characterization of a commercial 65 nm CMOS technology for SLHC applications", *JINST* **7** (2012) P01015, doi:10.1088/1748-0221/7/01/P01015.

[234] CMS Collaboration, "The Phase-2 Upgrade of the CMS Muon Detectors",.

[235] CMS Collaboration, "The Phase-2 Upgrade of the CMS Barrel Calorimeters", technical report, CERN, Geneva, 2017. This is the final version, approved by the LHCC.

[236] CMS Collaboration, "The Phase-2 Upgrade of the CMS Endcap Calorimeter",.

[237] F. Addesa et al., "Comparative characterization study of LYSO:Ce crystals for timing applications", *JINST* **17** (2022), no. 08, P08028, doi:10.1088/1748-0221/17/08/P08028, arXiv:2205.14890. 38 pages, 22 figures.

[238] F. M. Addesa, B. D'Orsi, R. Paramatti, and F. Santanastasio, "Optical spectroscopic characterization of lyso crystals at the calliope facility (enea casaccia r.c.)", 2020.

[239] CMS MTD Collaboration, "Test beam characterization of sensor prototypes for the CMS Barrel MIP Timing Detector", *JINST* **16** (2021), no. 07, P07023, doi:10.1088/1748-0221/16/07/P07023, arXiv:2104.07786.

[240] S. Palluotto, "Characterization of sensor modules for the CMS Barrel Timing Layer at HL-LHC", *Nuovo Cim. C* **46** (2023), no. 3, 58, doi:10.1393/ncc/i2023-23058-1.

[241] A. Heering et al., "Effects of very high radiation on SiPMs", *Nucl. Instrum. Meth. A* **824** (2016) 111–114, doi:10.1016/j.nima.2015.11.037.

[242] E. Garutti and Y. Musienko, "Radiation damage of SiPMs", *Nucl. Instrum. Meth. A* **926** (2019) 69–84, doi:10.1016/j.nima.2018.10.191, arXiv:1809.06361.

[243] A. Bornheim et al., "Integration of thermo-electric coolers into the CMS MTD SiPM arrays for operation under high neutron fluence", *JINST* **18** (2023), no. 08, P08020, doi:10.1088/1748-0221/18/08/P08020, arXiv:2306.00818.

[244] A. K. Jha, H. T. van Dam, M. A. Kupinski, and E. Clarkson, "Simulating silicon photomultiplier response to scintillation light", *IEEE Transactions on Nuclear Science* **60** (2013), no. 1, 336–351, doi:10.1109/TNS.2012.2234135.

[245] E. Albuquerque et al., "TOFHIR2: The readout ASIC of the CMS Barrel MIP Timing Detector", in *2020 IEEE Nuclear Science Symposium (NSS) and Medical Imaging Conference (MIC)*. 10, 2020. doi:10.1109/NSS/MIC42677.2020.9507749.

[246] CMS Collaboration, "The Phase-2 Upgrade of the CMS Data Acquisition", *EPJ Web Conf.* **251** (2021) 04023, doi:10.1051/epjconf/202125104023.

[247] CMS Collaboration, "The DAQ and clock distribution system of CMS MIP Timing Detector", technical report, CERN, Geneva, 2023. doi:10.1016/j.nima.2022.167802.

[248] M. Firlej et al., "A fast, ultra-low and frequency-scalable power consumption, 10-bit SAR ADC for particle physics detectors", *JINST* **10** (2015), no. 11, P11012, doi:10.1088/1748-0221/10/11/P11012.

[249] S. Bonacini, K. Kloukinas, and P. Moreira, "E-link: A Radiation-Hard Low-Power Electrical Link for Chip-to-Chip Communication", doi:10.5170/CERN-2009-006.422.

[250] P. Carniti, C. Gotti, and G. Pessina, "ALDO2, a multi-function rad-hard linear regulator for SiPM-based HEP detectors", *Nucl. Instrum. Meth. A* **1039** (2022) 167028, doi:10.1016/j.nima.2022.167028, arXiv:2203.16098.

[251] P. Moreira et al., "lpGBT documentation: release". 2022.

[252] A. Caratelli et al., "The GBT-SCA, a radiation tolerant ASIC for detector control and monitoring applications in HEP experiments", *JINST* **10** (2015), no. 03, C03034, doi:10.1088/1748-0221/10/03/C03034.

[253] CMS Collaboration, "DC-DC converters for the CMS MTD BTL and ECAL for HL-LHC", *JINST* **18** (2023), no. 02, C02038, doi:10.1088/1748-0221/18/02/C02038.

[254] J.-M. André et al., "The CMS Data Acquisition System for the Phase-2 Upgrade", arXiv:1806.08975.

[255] CMS Collaboration, "Serenity - An ATCA prototyping platform for CMS Phase-2", technical report, CERN, Geneva, 2019. doi:10.22323/1.343.0115.

[256] CMS Collaboration, "IPbus A flexible Ethernet-based control system for xTCA hardware", technical report, CERN, Geneva, 2014.

[257] C. Soós et al., "Versatile Link$^+$ transceiver production", *JINST* **18** (2023), no. 03, C03003, doi:10.1088/1748-0221/18/03/C03003.

Appendix A

Optimal observables SMEFT sensitivity study

	$c_{qq}^{(3,1)}$	$c_{qq}^{(1,1)}$	$c_{qq}^{(1)}$	c_W	$c_{Hl}^{(3)}$	$c_{Hq}^{(3)}$	$c_{ll}^{(1)}$	$c_{Hl}^{(1)}$	c_{HW}	$c_{Hq}^{(1)}$	c_{HD}	c_{HWB}	$c_{H\Box}$
$c_{qq}^{(3)}$	p_{T,j^2}	p_{T,j^1}	p_{T,j^1}	$\Delta\phi_{jj}$	p_{T,j^2}	p_{T,j^2}	p_{T,j^2}	p_{T,j^2}	$\Delta\phi_{jj}$	p_{T,j^1}	p_{T,j^2}	p_{T,j^1}	p_{T,j^2}
$c_{qq}^{(3,1)}$	-	p_{T,j^2}	p_{T,j^1}	$\Delta\phi_{jj}$	$\Delta\phi_{jj}$	p_{T,j^1}	$\Delta\phi_{jj}$	$\Delta\phi_{jj}$	$\Delta\phi_{jj}$	p_{T,j^1}	p_{T,j^1}	p_{T,j^1}	$\Delta\phi_{jj}$
$c_{qq}^{(1,1)}$	-	-	p_{T,j^1}	p_{T,j^1}	p_{T,j^1}	p_{T,j^1}	p_{T,j^1}	MET	p_{T,l^1}	p_{T,j^1}	p_{T,j^1}	p_{T,j^1}	p_{T,j^1}
$c_{qq}^{(1)}$	-	-	-	p_{T,j^1}	p_{T,j^1}	p_{T,j^1}	p_{T,j^1}	MET	p_{T,l^1}	p_{T,j^1}	p_{T,j^1}	p_{T,j^1}	p_{T,j^1}
c_W	-	-	-	-	p_{T,l^1}	p_{T,l^1}	p_{T,l^1}	p_{T,l^1}	m_{ll}	p_{T,l^1}	p_{T,l^1}	p_{T,j^1}	m_{ll}
$c_{Hl}^{(3)}$	-	-	-	-	-	p_{T,j^1}	η_{l^2}	m_{ll}	m_{ll}	p_{T,j^1}	m_{ll}	p_{T,j^1}	m_{ll}
$c_{Hq}^{(3)}$	-	-	-	-	-	-	p_{T,j^1}	p_{T,l^1}	m_{ll}	p_{T,j^1}	p_{T,l^1}	p_{T,j^1}	m_{ll}
$c_{ll}^{(1)}$	-	-	-	-	-	-	-	m_{ll}	m_{ll}	p_{T,j^1}	m_{ll}	p_{T,j^1}	m_{ll}
$c_{Hl}^{(1)}$	-	-	-	-	-	-	-	-	m_{ll}	p_{T,l^1}	m_{ll}	p_{T,l^1}	m_{ll}
c_{HW}	-	-	-	-	-	-	-	-	-	p_{T,l^1}	m_{ll}	m_{ll}	m_{ll}
$c_{Hq}^{(1)}$	-	-	-	-	-	-	-	-	-	-	p_{T,l^1}	p_{T,j^1}	p_{T,l^1}
c_{HD}	-	-	-	-	-	-	-	-	-	-	-	m_{ll}	m_{ll}
c_{HWB}	-	-	-	-	-	-	-	-	-	-	-	-	m_{ll}

Table A.1: Most sensitive observable for each pair of SMEFT Wilson coefficients for 2D fits to SSWW+2j-EW and including both linear and quadratic terms in the Wilson coefficients.

	$c_{qq}^{(3,1)}$	$c_{qq}^{(1,1)}$	$c_{qq}^{(1)}$	c_W	$c_{Hl}^{(3)}$	$c_{Hq}^{(3)}$	$c_{ll}^{(1)}$	$c_{Hl}^{(1)}$	c_{HW}	$c_{Hq}^{(1)}$	c_{HD}	c_{HWB}	$c_{H\Box}$
$c_{qq}^{(3)}$	p_{T,j^2}	p_{T,j^2}	p_{T,j^2}	p_{T,j^1}	p_{T,j^2}	p_{T,j^1}	p_{T,j^2}	MET	p_{T,j^1}	p_{T,j^1}	$\Delta\eta_{jj}$	p_{T,j^1}	m_{ll}
$c_{qq}^{(3,1)}$	-	p_{T,j^2}	p_{T,j^2}	p_{T,j^1}	p_{T,j^2}	p_{T,j^1}	p_{T,j^2}	MET	p_{T,j^1}	p_{T,j^1}	$\Delta\eta_{jj}$	p_{T,j^1}	m_{ll}
$c_{qq}^{(1,1)}$	-	-	p_{T,j^2}	p_{T,j^1}	p_{T,j^2}	p_{T,j^1}	p_{T,j^2}	MET	p_{T,j^1}	p_{T,j^1}	$\Delta\eta_{jj}$	p_{T,j^1}	m_{ll}
$c_{qq}^{(1)}$	-	-	-	p_{T,j^1}	p_{T,j^2}	p_{T,j^1}	p_{T,j^2}	MET	p_{T,j^1}	p_{T,j^1}	$\Delta\eta_{jj}$	p_{T,j^1}	m_{ll}
c_W	-	-	-	-	m_{ll}	m_{ll}	m_{ll}	m_{ll}	m_{ll}	m_{ll}	$\Delta\eta_{jj}$	m_{ll}	m_{ll}
$c_{Hl}^{(3)}$	-	-	-	-	-	m_{ll}	m_{jj}	MET	m_{ll}	m_{ll}	$\Delta\eta_{jj}$	m_{ll}	m_{ll}
$c_{Hq}^{(3)}$	-	-	-	-	-	-	m_{ll}	m_{ll}	m_{ll}	m_{ll}	$\Delta\eta_{jj}$	m_{ll}	m_{ll}
$c_{ll}^{(1)}$	-	-	-	-	-	-	-	MET	m_{ll}	m_{ll}	$\Delta\eta_{jj}$	m_{ll}	m_{ll}
$c_{Hl}^{(1)}$	-	-	-	-	-	-	-	-	m_{ll}	m_{ll}	$\Delta\eta_{jj}$	m_{ll}	m_{ll}
c_{HW}	-	-	-	-	-	-	-	-	-	p_{T,j^1}	$\Delta\eta_{jj}$	m_{ll}	m_{ll}
$c_{Hq}^{(1)}$	-	-	-	-	-	-	-	-	-	-	$\Delta\eta_{jj}$	m_{ll}	m_{ll}
c_{HD}	-	-	-	-	-	-	-	-	-	-	-	$\Delta\eta_{jj}$	m_{ll}
c_{HWB}	-	-	-	-	-	-	-	-	-	-	-	-	m_{ll}

Table A.2: Most sensitive observable for each pair of SMEFT Wilson coefficients for 2D fits to OSWW+2j (EW and QCD) and including both linear and quadratic terms in the Wilson coefficients.

	$c_{qq}^{(3,1)}$	$c_{qq}^{(1,1)}$	$c_{qq}^{(1)}$	c_W	$c_{Hl}^{(3)}$	$c_{Hq}^{(3)}$	$c_{ll}^{(1)}$	$c_{Hl}^{(1)}$	c_{HW}	$c_{Hq}^{(1)}$	c_{HD}	c_{HWB}	$c_{H\Box}$
$c_{qq}^{(3)}$	p_{T,j^2}	p_{T,j^2}	p_{T,j^1}	p_{T,j^1}	p_{T,j^2}	p_{T,j^1}	p_{T,j^2}	p_{T,j^2}	m_{WZ}	p_{T,j^1}	p_{T,j^2}	m_{WZ}	m_{WZ}
$c_{qq}^{(3,1)}$	-	p_{T,j^2}	p_{T,j^2}	p_{T,j^1}	p_{T,j^2}	p_{T,j^1}	p_{T,j^2}	p_{T,j^2}	m_{WZ}	p_{T,j^1}	p_{T,j^2}	m_{WZ}	m_{WZ}
$c_{qq}^{(1,1)}$	-	-	p_{T,j^2}	p_{T,j^1}	p_{T,j^2}	p_{T,j^1}	p_{T,j^2}	p_{T,j^2}	m_{WZ}	p_{T,j^1}	p_{T,j^2}	m_{WZ}	m_{WZ}
$c_{qq}^{(1)}$	-	-	-	p_{T,j^1}	p_{T,j^2}	p_{T,j^1}	p_{T,j^2}	p_{T,j^2}	m_{WZ}	p_{T,j^1}	p_{T,j^2}	p_{T,j^1}	m_{WZ}
c_W	-	-	-	-	m_{WZ}	m_{WZ}	m_{WZ}	m_{WZ}	m_{WZ}	m_{WZ}	m_{WZ}	m_{WZ}	m_{WZ}
$c_{Hl}^{(3)}$	-	-	-	-	-	m_{WZ}	m_{jj}	m_{WZ}	m_{WZ}	m_{WZ}	m_{ee}	m_{WZ}	m_{WZ}
$c_{Hq}^{(3)}$	-	-	-	-	-	-	m_{WZ}	m_{WZ}	m_{WZ}	p_{T,j^1}	p_{T,l^2}	m_{WZ}	m_{WZ}
$c_{ll}^{(1)}$	-	-	-	-	-	-	-	m_{WZ}	m_{WZ}	m_{WZ}	m_{ee}	m_{WZ}	m_{WZ}
$c_{Hl}^{(1)}$	-	-	-	-	-	-	-	-	m_{WZ}	m_{WZ}	m_{ee}	m_{WZ}	m_{WZ}
c_{HW}	-	-	-	-	-	-	-	-	-	m_{WZ}	m_{WZ}	m_{WZ}	m_{WZ}
$c_{Hq}^{(1)}$	-	-	-	-	-	-	-	-	-	-	p_{T,j^1}	m_{WZ}	m_{WZ}
c_{HD}	-	-	-	-	-	-	-	-	-	-	-	m_{WZ}	m_{WZ}
c_{HWB}	-	-	-	-	-	-	-	-	-	-	-	-	m_{WZ}

Table A.3: Most sensitive observable for each pair of SMEFT Wilson coefficients for 2D fits to WZ+2j (EW and QCD) and including both linear and quadratic terms in the Wilson coefficients.

	$c_{qq}^{(3,1)}$	$c_{qq}^{(1,1)}$	$c_{qq}^{(1)}$	c_W	$c_{Hl}^{(3)}$	$c_{Hq}^{(3)}$	$c_{ll}^{(1)}$	$c_{Hl}^{(1)}$	c_{HW}	$c_{Hq}^{(1)}$	c_{HD}	c_{HWB}	$c_{H\Box}$
$c_{qq}^{(3)}$	p_{T,j^1}	p_{T,j^1}	p_{T,j^2}	p_{T,l^1}	p_{T,j^2}	p_{T,j^1}	p_{T,j^2}	p_{T,j^2}	p_{T,l^1}	p_{T,j^1}	p_{T,j^1}	p_{T,j^1}	p_{T,j^1}
$c_{qq}^{(3,1)}$	-	p_{T,j^1}	p_{T,j^2}	p_{T,l^1}	p_{T,j^2}	p_{T,j^1}	p_{T,j^2}	p_{T,j^2}	p_{T,l^1}	p_{T,j^1}	p_{T,j^2}	p_{T,j^1}	p_{T,j^1}
$c_{qq}^{(1,1)}$	-	-	p_{T,j^2}	p_{T,l^1}	p_{T,j^2}	p_{T,j^1}	p_{T,j^2}	p_{T,j^2}	p_{T,l^1}	p_{T,j^1}	p_{T,j^2}	p_{T,j^1}	p_{T,j^1}
$c_{qq}^{(1)}$	-	-	-	p_{T,l^1}	p_{T,j^2}	p_{T,j^1}	p_{T,j^2}	p_{T,j^2}	p_{T,l^1}	p_{T,j^1}	p_{T,j^2}	p_{T,j^1}	p_{T,j^1}
c_W	-	-	-	-	p_{T,l^1}	p_{T,l^1}	p_{T,l^1}	p_{T,l^1}	p_{T,l^1}	p_{T,l^1}	p_{T,l^1}	p_{T,l^1}	m_{4l}
$c_{Hl}^{(3)}$	-	-	-	-	-	p_{T,j^1}	m_{jj}	m_{jj}	$p_{T,ee}$	p_{T,j^1}	m_{jj}	m_{jj}	m_{4l}
$c_{Hq}^{(3)}$	-	-	-	-	-	-	p_{T,j^1}	p_{T,j^1}	p_{T,l^1}	p_{T,j^1}	p_{T,l^1}	p_{T,l^1}	p_{T,l^2}
$c_{ll}^{(1)}$	-	-	-	-	-	-	-	m_{jj}	$p_{T,Z}$	p_{T,j^1}	$p_{T,e^-\mu^-}$	$p_{T,Z}$	p_{T,j^2}
$c_{Hl}^{(1)}$	-	-	-	-	-	-	-	-	m_{4l}	p_{T,j^1}	$p_{T,e^+\mu^+}$	$p_{T,ee}$	$\Delta\eta_{jj}$
c_{HW}	-	-	-	-	-	-	-	-	-	p_{T,l^1}	m_{4l}	$p_{T,Z}$	m_{4l}
$c_{Hq}^{(1)}$	-	-	-	-	-	-	-	-	-	-	$p_{T,e^-\mu^-}$	$p_{T,e^-\mu^-}$	p_{T,l^2}
c_{HD}	-	-	-	-	-	-	-	-	-	-	-	m_{4l}	$\Delta\eta_{jj}$
c_{HWB}	-	-	-	-	-	-	-	-	-	-	-	-	m_{4l}

Table A.4: Most sensitive observable for each pair of SMEFT Wilson coefficients for 2D fits to ZZ+2j (EW and QCD) and including both linear and quadratic terms in the Wilson coefficients. The variable $p_{T,Z}$ is defined as the transverse momentum of the same-flavour dilepton system with invariant mass closest to m_Z

	$c_{Hl}^{(3)}$	$c_{Hq}^{(3)}$	$c_{ll}^{(1)}$	$c_{Hl}^{(1)}$	$c_{Hq}^{(1)}$	c_{HD}	c_{HWB}
c_W	MET	MET	MET	MET	MET	MET	MET
$c_{Hl}^{(3)}$	-	MET	η_{l^2}	MET	MET	p_{T,l^1}	MET
$c_{Hq}^{(3)}$	-	-	p_{T,l^1}	MET	MET	p_{T,l^1}	MET
$c_{ll}^{(1)}$	-	-	-	MET	MET	p_{T,l^1}	MET
$c_{Hl}^{(1)}$	-	-	-	-	MET	MET	MET
$c_{Hq}^{(1)}$	-	-	-	-	-	MET	MET
c_{HD}	-	-	-	-	-	-	p_{T,l^1}

Table A.5: Most sensitive observable for each pair of SMEFT Wilson coefficients for 2D fits to diboson WW and including both linear and quadratic terms in the Wilson coefficients.

Appendix B

EFT statistical model derivation

The additional EFT contributions are translated to the amplitude of the scattering matrix as

$$\mathcal{A} = \mathcal{A}_{SM} + k_i \mathcal{A}_{Q_i} \tag{B.1}$$

Namely, the effect of the new operator (Q_i) scaled by a coupling (k_i). This amplitude reflects in expected number of events, in each phase space, as:

$$\mathrm{N} = \mathrm{SM} + k \cdot \mathrm{Lin}_i + k^2 \cdot \mathrm{Quad}_i \tag{B.2}$$

where SM is the Standard Model contribution, Lin is the linear term (namely the interference between the SM and the new operator effect $2\Re(\mathcal{A}_{\mathrm{SM}}\mathcal{A}^{\dagger}_{Q_i})$) and Quad is the quadratic term (namely the pure BSM contribution $|\mathcal{A}_{Q_i}|^2$).

In case of handling more operators at the same time, the previous formulation presents additional terms namely the interference between two EFT amplitudes due to different operators $\mathrm{Mix}_{ij} = \mathcal{A}_{Q_i}\mathcal{A}^{\dagger}_{Q_j}$:

$$N = \mathrm{SM} + \sum_i \left(k_i \cdot \mathrm{Lin}_i + k_i^2 \cdot \mathrm{Quad}_i\right) + \sum_{i \neq j} k_i \cdot k_j \cdot \mathrm{Mix}_{ij} \tag{B.3}$$

The derivation of the algebra follows simple principles, reminding the nomenclature:

$$\sum_{i \neq j} k_i \cdot k_j \cdot \mathrm{Mix}_{ij} = \sum_{i, i \neq j} \sum_j k_i \cdot k_j \cdot \mathrm{Mix}_{ij} \tag{B.4}$$

Starting from equation B.3 and abbreviating $\mathrm{SM} = \mathrm{S}$, $\mathrm{Lin}_i = \mathrm{L}_i$, $\mathrm{Quad}_i = \mathrm{Q}_i$ and $\mathrm{Mix}_{ij} = \mathrm{M}_{ij}$ the derivation reads as

$$\begin{aligned}
N &= \mathrm{S} + \sum_i \left(k_i \cdot \mathrm{L}_i + k_i^2 \cdot \mathrm{Q}_i\right) + \sum_{i \neq j} k_i \cdot k_j \cdot \mathrm{M}_{ij} \\
&= \mathrm{S} + \sum_i k_i \cdot \mathrm{L}_i + \sum_i k_i^2 \cdot \mathrm{Q}_i + \sum_{i \neq j} k_i \cdot k_j \cdot \mathrm{M}_{ij} \\
&= \mathrm{S} + \sum_i k_i \cdot (\mathrm{L}_i + \mathrm{S} + \mathrm{Q}_i) - \sum_i k_i \cdot \mathrm{S} - \sum_i k_i \cdot \mathrm{Q}_i + \sum_i k_i^2 \cdot \mathrm{Q}_i + \sum_{i \neq j} k_i \cdot k_j \cdot \mathrm{M}_{ij} \\
&= \mathrm{S} \cdot (1 - \sum_i k_i) + \sum_i k_i \cdot (\mathrm{L}_i + \mathrm{S} + \mathrm{Q}_i) + \sum_i \left(k_i^2 - k_i\right) \cdot \mathrm{Q}_i + \sum_{i \neq j} k_i \cdot k_j \cdot \mathrm{M}_{ij}
\end{aligned} \tag{B.5}$$

Now, considering Eq. B.4, the last part can be rewritten as:

$$\begin{aligned}
&\sum_{i\neq j} k_i \cdot k_j \cdot \mathrm{M}_{ij} \\
&\sum_{i,i\neq j} \sum_{j} k_i \cdot k_j \cdot \mathrm{M}_{ij} \\
&\sum_{i,i<j} \sum_{j} k_i \cdot k_j \cdot 2 \cdot \mathrm{M}_{ij} \\
&\sum_{i,i<j} \sum_{j} k_i \cdot k_j \cdot \Big[2 \cdot \mathrm{M}_{ij} + \mathrm{S} + \mathrm{L}_i + \mathrm{L}_j + \mathrm{Q}_i + \mathrm{Q}_j\Big] - \sum_{i,i<j} \sum_{j} k_i \cdot k_j \cdot \Big[\mathrm{S} + \mathrm{L}_i + \mathrm{L}_j + \mathrm{Q}_i + \mathrm{Q}_j\Big]
\end{aligned} \tag{B.6}$$

Now concentrating on the last component:

$$\begin{aligned}
&\sum_{i,i<j} \sum_{j} k_i \cdot k_j \Big(\mathrm{S} + \mathrm{L}_i + \mathrm{L}_j + \mathrm{Q}_i + \mathrm{Q}_j\Big) \\
&\sum_{i,i<j} \sum_{j} k_i \cdot k_j \Big(\mathrm{S} + \mathrm{L}_i + \mathrm{Q}_i + \mathrm{S} + \mathrm{L}_j + \mathrm{Q}_j - \mathrm{S}\Big) \\
&\sum_{i,i<j} \sum_{j} k_i \cdot k_j \Big(\mathrm{S} + \mathrm{L}_i + \mathrm{Q}_i + \mathrm{S} + \mathrm{L}_j + \mathrm{Q}_j\Big) - \mathrm{S} \sum_{i,i<j} \sum_{j} k_i \cdot k_j
\end{aligned} \tag{B.7}$$

Now renaming

$$\mathrm{S} + \mathrm{L}_i + \mathrm{Q}_i = \mathrm{T}_i$$

T_i standing for "Total$_i$", one gets

$$\begin{aligned}
&\sum_{i,i<j} \sum_{j} k_i \cdot k_j \Big(\mathrm{S} + \mathrm{L}_i + \mathrm{Q}_i + \mathrm{S} + \mathrm{L}_j + \mathrm{Q}_j\Big) \\
&\sum_{i,i<j} \sum_{j} k_i \cdot k_j \Big(\mathrm{T}_i + \mathrm{T}_j\Big) \\
&\sum_{i,i<j} \sum_{j} k_i \cdot k_j \cdot \mathrm{T}_i + \sum_{i,i<j} \sum_{j} k_i \cdot k_j \cdot \mathrm{T}_j \\
&2 \sum_{i,i<j} \sum_{j} k_i \cdot k_j \cdot \mathrm{T}_i \\
&\sum_{i\neq j} k_i \cdot k_j \cdot \mathrm{T}_i
\end{aligned} \tag{B.8}$$

Thus putting all together:

$$
\begin{aligned}
N &= \mathrm{S} + \sum_i \left(k_i \cdot \mathrm{L}_i + k_i^2 \cdot \mathrm{Q}_i\right) + \sum_{i \neq j} k_i \cdot k_j \cdot \mathrm{M}_{ij} \\
&= \mathrm{S} \cdot (1 - \sum_i k_i) + \sum_i k_i \cdot (\mathrm{L}_i + \mathrm{S} + \mathrm{Q}_i) + \sum_i \left(k_i^2 - k_i\right) \cdot \mathrm{Q}_i + \sum_{i \neq j} k_i \cdot k_j \cdot \mathrm{M}_{ij} \\
&= \mathrm{S} \cdot (1 - \sum_i k_i) \\
&+ \sum_i k_i \cdot (\mathrm{L}_i + \mathrm{S} + \mathrm{Q}_i) \\
&+ \sum_i \left(k_i^2 - k_i\right) \cdot \mathrm{Q}_i \\
&+ \sum_{i, i<j} \sum_j k_i \cdot k_j \cdot \left[2 \cdot \mathrm{M}_{ij} + \mathrm{S} + \mathrm{L}_i + \mathrm{L}_j + \mathrm{Q}_i + \mathrm{Q}_j\right] \\
&- \sum_{i \neq j} k_i \cdot k_j \cdot (\mathrm{S} + \mathrm{L}_i + \mathrm{Q}_i) \\
&+ \mathrm{S} \sum_{i, i<j} \sum_j k_i \cdot k_j \\
&= \mathrm{S} \cdot (1 - \sum_i k_i + \sum_{i, i<j} \sum_j k_i \cdot k_j) \\
&+ \left[\sum_i k_i - \sum_{i \neq j} k_i \cdot k_j\right] \cdot (\mathrm{L}_i + \mathrm{S} + \mathrm{Q}_i) \\
&+ \sum_i \left(k_i^2 - k_i\right) \cdot \mathrm{Q}_i \\
&+ \sum_{i, i<j} \sum_j k_i \cdot k_j \cdot \left[2 \cdot \mathrm{M}_{ij} + \mathrm{S} + \mathrm{L}_i + \mathrm{L}_j + \mathrm{Q}_i + \mathrm{Q}_j\right]
\end{aligned}
\tag{B.9}
$$

As previously stated, in Eq. 4.9 all the components are non-negative defined. The formula in Eq. B.3 can be expressed in other non-negative terms, such as S, $\mathrm{S} + \mathrm{L}_i + \mathrm{Q}_i$, Q_i and $\mathrm{Q}_i + \mathrm{Q}_j + \mathrm{M}_{ij} + \mathrm{M}_{ji}$. In those terms, the formula in Eq. B.3 becomes Eq. 4.10. Derivation in the following, starting from Eq. B.5, as done in Eq. B.7:

$$
\begin{aligned}
&\sum_{i \neq j} k_i \cdot k_j \cdot \mathrm{M}_{ij} \\
&\sum_{i, i \neq j} \sum_j k_i \cdot k_j \cdot \mathrm{M}_{ij} \\
&\sum_{i, i<j} \sum_j k_i \cdot k_j \cdot 2 \cdot \mathrm{M}_{ij} \\
&\sum_{i, i<j} \sum_j k_i \cdot k_j \cdot \left[2 \cdot \mathrm{M}_{ij} + \mathrm{Q}_i + \mathrm{Q}_j\right] - \sum_{i, i<j} \sum_j k_i \cdot k_j \cdot \left[\mathrm{Q}_i + \mathrm{Q}_j\right] \\
&\sum_{i, i<j} \sum_j k_i \cdot k_j \cdot \left[2 \cdot \mathrm{M}_{ij} + \mathrm{Q}_i + \mathrm{Q}_j\right] - \sum_{i, i<j} \sum_j k_i \cdot k_j \cdot \mathrm{Q}_i - \sum_{i, i<j} \sum_j k_i \cdot k_j \cdot \mathrm{Q}_j \\
&\sum_{i, i<j} \sum_j k_i \cdot k_j \cdot \left[2 \cdot \mathrm{M}_{ij} + \mathrm{Q}_i + \mathrm{Q}_j\right] - \sum_{i \neq j} k_i \cdot k_j \cdot \mathrm{Q}_i
\end{aligned}
\tag{B.10}
$$

Thus, adding all together:

$$
\begin{aligned}
N &= \mathrm{S} + \sum_i \left(k_i \cdot L_i + k_i^2 \cdot \mathrm{Q}_i\right) + \sum_{i \neq j} k_i \cdot k_j \cdot \mathrm{M}_{ij} \\
&= \mathrm{S} \cdot (1 - \sum_i k_i) + \sum_i k_i \cdot (\mathrm{L}_i + \mathrm{S} + \mathrm{Q}_i) + \sum_i \left(k_i^2 - k_i\right) \cdot \mathrm{Q}_i + \sum_{i \neq j} k_i \cdot k_j \cdot \mathrm{M}_{ij} \\
&= \mathrm{S} \cdot (1 - \sum_i k_i) \\
&+ \sum_i k_i \cdot (\mathrm{L}_i + \mathrm{S} + \mathrm{Q}_i) \\
&+ \sum_i \left(k_i^2 - k_i\right) \cdot \mathrm{Q}_i \\
&+ \sum_{i, i<j} \sum_j k_i \cdot k_j \cdot \left[2 \cdot \mathrm{M}_{ij} + \mathrm{Q}_i + \mathrm{Q}_j\right] \\
&- \sum_{i \neq j} k_i \cdot k_j \cdot \mathrm{Q}_i \\
&= \mathrm{S} \cdot (1 - \sum_i k_i) \\
&+ \sum_i k_i \cdot (\mathrm{S} + \mathrm{L}_i + \mathrm{Q}_i) \\
&+ \sum_i \left(k_i^2 - k_i - \sum_{i \neq j} k_i \cdot k_j\right) \cdot \mathrm{Q}_i \\
&+ \sum_{i, i<j} \sum_j k_i \cdot k_j \cdot \left[2 \cdot \mathrm{M}_{ij} + \mathrm{Q}_i + \mathrm{Q}_j\right]
\end{aligned}
\tag{B.11}
$$

Appendix C

VBS WV EFT analysis supplement materials

VBS WV SM and EFT yields tables

	ee+ssyst+2016	ee+ss+DNN+bdy+2016	ee+sig+ss+DNN+bdy+2016	boost+ss+2016	boost+sig+ss+DNN+bdy+2016	boost+sig+ss+DNN+bdy+2016	boost+ss+2016	ee+sig+ss+DNN+2016	boost+sig+ss+DNN+2016	mu+ssyst+2016	mu+ss+DNN+bdy+2016	boost+sig+ss+DNN+bdy+2016	mu+sig+ss+DNN+2016	boost+sig+ss+DNN+2016	boost+ss+2016
sm-lin-quad-mixed-cW+cHQ	107.52 +/- 6.76 (7 %)	311.01 +/- 26.07 (10 %)	307.23 +/- 25.94 (10 %)	42.95 +/- 2.94 (7 %)	99.84 +/- 13.64 (9 %)	99.84 +/- 13.64 (9 %)	87.13 +/- 4.88 (6 %)	110.23 +/- 6.87 (7 %)	253.98 +/- 3.89 (15 %)	56.99 +/- 6.42 (7 %)	132.49 +/- 18.08 (9 %)	132.49 +/- 18.08 (9 %)	107.85 +/- 5.53 (6 %)	134.115 +/- 10.08 (7 %)	42.57 +/- 2.24 (5 %)	106.97 +/- 18.18 (10 %)	106.97 +/- 18.18 (10 %)	87.37 +/- 18.21 (10 %)	107.37 +/- 18.21 (10 %)	42.57 +/- 2.24 (5 %)	106.97 +/- 18.18 (10 %)	106.97 +/- 18.18 (10 %)	87.37 +/- 18.21 (10 %)	107.37 +/- 18.21 (10 %)	42.57 +/- 2.24 (5 %)
sm-lin-quad-mixed-cW-cHB	104.25 +/- 6.84 (7 %)	312.18 +/- 27.71 (10 %)	307.23 +/- 25.94 (10 %)	43.33 +/- 2.95 (7 %)	89.70 +/- 5.10 (6 %)	89.70 +/- 5.10 (6 %)	121.16 +/- 8.83 (7 %)	26.63 +/- 3.98 (15 %)	38.69 +/- 5.70 (15 %)	58.93 +/- 6.80 (7 %)	116.69 +/- 11.06 (7 %)	116.69 +/- 11.06 (7 %)	89.70 +/- 5.10 (6 %)	116.69 +/- 11.06 (7 %)	43.65 +/- 2.29 (5 %)	132.42 +/- 11.04 (7 %)	132.42 +/- 11.04 (7 %)	107.76 +/- 18.21 (10 %)	132.42 +/- 11.04 (7 %)	43.65 +/- 2.29 (5 %)	132.42 +/- 11.04 (7 %)	132.42 +/- 11.04 (7 %)	107.76 +/- 18.21 (10 %)	132.42 +/- 11.04 (7 %)	43.65 +/- 2.29 (5 %)
sm-lin-quad-mixed-cHDD+cHB	82.15 +/- 5.97 (7 %)	293.52 +/- 28.79 (10 %)	293.52 +/- 28.79 (10 %)	42.29 +/- 3.06 (7 %)	68.69 +/- 5.41 (8 %)	68.69 +/- 5.41 (8 %)	27.47 +/- 1.65 (6 %)	9.09 +/- 1.46 (16 %)	9.09 +/- 1.46 (16 %)	78.29 +/- 5.82 (7 %)	13.35 +/- 1.92 (14 %)	13.35 +/- 1.92 (14 %)	68.69 +/- 5.41 (8 %)	13.35 +/- 1.92 (14 %)	13.54 +/- 0.75 (5 %)	124.46 +/- 9.61 (7 %)	124.46 +/- 9.61 (7 %)	104.81 +/- 17.51 (10 %)	124.46 +/- 9.61 (7 %)	13.54 +/- 0.75 (5 %)	124.46 +/- 9.61 (7 %)	124.46 +/- 9.61 (7 %)	104.81 +/- 17.51 (10 %)	124.46 +/- 9.61 (7 %)	13.54 +/- 0.75 (5 %)
sm-lin-quad-mixed-cHWB+cHQ	79.80 +/- 5.74 (7 %)	295.48 +/- 28.58 (10 %)	295.48 +/- 28.58 (10 %)	41.41 +/- 3.00 (7 %)	59.58 +/- 4.26 (7 %)	59.58 +/- 4.26 (7 %)	27.11 +/- 1.64 (6 %)	9.13 +/- 1.46 (16 %)	9.13 +/- 1.46 (16 %)	76.84 +/- 5.20 (7 %)	13.43 +/- 1.94 (15 %)	13.43 +/- 1.94 (15 %)	59.58 +/- 4.26 (7 %)	13.43 +/- 1.94 (15 %)	13.29 +/- 0.75 (5 %)	119.79 +/- 17.30 (10 %)	119.79 +/- 17.30 (10 %)	104.81 +/- 17.51 (10 %)	119.79 +/- 17.30 (10 %)	13.29 +/- 0.75 (5 %)	119.79 +/- 17.30 (10 %)	119.79 +/- 17.30 (10 %)	104.81 +/- 17.51 (10 %)	119.79 +/- 17.30 (10 %)	13.29 +/- 0.75 (5 %)
sm-lin-quad-mixed-cHDD+cHQ	83.00 +/- 5.97 (7 %)	297.07 +/- 29.02 (10 %)	61.47 +/- 4.54 (7 %)	23.61 +/- 1.73 (7 %)	20.80 +/- 1.53 (6 %)	20.80 +/- 1.53 (6 %)	30.59 +/- 1.78 (6 %)	10.33 +/- 7.97 (7 %)	9.72 +/- 1.55 (16 %)	79.05 +/- 5.56 (7 %)	14.12 +/- 2.04 (15 %)	14.12 +/- 2.04 (15 %)	20.80 +/- 1.53 (6 %)	14.12 +/- 2.04 (15 %)	16.73 +/- 0.88 (5 %)	126.70 +/- 17.64 (10 %)	126.70 +/- 17.64 (10 %)	107.85 +/- 18.03 (10 %)	126.70 +/- 17.64 (10 %)	16.73 +/- 0.88 (5 %)	126.70 +/- 17.64 (10 %)	126.70 +/- 17.64 (10 %)	107.85 +/- 18.03 (10 %)	126.70 +/- 17.64 (10 %)	16.73 +/- 0.88 (5 %)
quad-cHB	0.00 +/- 0.00 (0 %)	0.00 +/- 0.00 (0 %)	0.00 +/- 0.00 (28 %)	0.00 +/- 0.00 (28 %)	0.00 +/- 0.00 (14 %)	0.00 +/- 0.00 (14 %)	0.00 +/- 0.00 (28 %)	0.00 +/- 0.00 (66 %)	0.00 +/- 0.00 (66 %)	0.00 +/- 0.00 (66 %)	0.00 +/- 0.00 (66 %)	0.00 +/- 0.00 (66 %)	0.00 +/- 0.00 (14 %)	0.00 +/- 0.00 (66 %)	0.00 +/- 0.00 (16 %)	0.00 +/- 0.00 (29 %)	0.00 +/- 0.00 (29 %)	0.00 +/- 0.00 (29 %)	0.00 +/- 0.00 (29 %)	0.00 +/- 0.00 (16 %)	0.00 +/- 0.00 (29 %)	0.00 +/- 0.00 (29 %)	0.00 +/- 0.00 (29 %)	0.00 +/- 0.00 (29 %)	0.00 +/- 0.00 (16 %)
sm-lin-quad-mixed-cHDD-cHB	104.02 +/- 6.82 (7 %)	313.21 +/- 23.07 (9 %)	72.36 +/- 5.24 (7 %)	47.57 +/- 3.24 (7 %)	90.76 +/- 7.64 (6 %)	90.76 +/- 7.64 (6 %)	88.21 +/- 4.91 (6 %)	121.09 +/- 8.88 (7 %)	121.09 +/- 8.88 (7 %)	90.75 +/- 5.56 (7 %)	29.03 +/- 4.01 (15 %)	29.74 +/- 4.01 (15 %)	90.76 +/- 7.64 (6 %)	29.74 +/- 4.01 (15 %)	49.22 +/- 2.48 (5 %)	99.92 +/- 13.69 (7 %)	99.92 +/- 13.69 (7 %)	79.97 +/- 17.14 (10 %)	99.92 +/- 13.69 (7 %)	49.22 +/- 2.48 (5 %)	99.92 +/- 13.69 (7 %)	99.92 +/- 13.69 (7 %)	79.97 +/- 17.14 (10 %)	99.92 +/- 13.69 (7 %)	49.22 +/- 2.48 (5 %)
sm-lin-quad-mixed-cHDD-cHW	104.94 +/- 6.87 (7 %)	314.79 +/- 26.27 (10 %)	314.79 +/- 26.27 (10 %)	42.88 +/- 3.02 (7 %)	94.83 +/- 6.98 (7 %)	94.83 +/- 6.98 (7 %)	89.14 +/- 4.96 (6 %)	122.71 +/- 8.99 (7 %)	122.71 +/- 8.99 (7 %)	91.94 +/- 5.63 (7 %)	29.41 +/- 4.06 (15 %)	30.14 +/- 4.06 (15 %)	94.83 +/- 6.98 (7 %)	30.14 +/- 4.06 (15 %)	49.86 +/- 2.51 (5 %)	101.24 +/- 13.87 (7 %)	101.24 +/- 13.87 (7 %)	81.02 +/- 17.36 (10 %)	101.24 +/- 13.87 (7 %)	49.86 +/- 2.51 (5 %)	101.24 +/- 13.87 (7 %)	101.24 +/- 13.87 (7 %)	81.02 +/- 17.36 (10 %)	101.24 +/- 13.87 (7 %)	49.86 +/- 2.51 (5 %)
quad-cHW	1.12 +/- 0.03 (4 %)	1.12 +/- 0.03 (4 %)	0.78 +/- 0.04 (6 %)	0.34 +/- 0.02 (5 %)	3.20 +/- 0.14 (4 %)	3.20 +/- 0.14 (4 %)	0.37 +/- 0.03 (7 %)	0.51 +/- 0.09 (17 %)	0.51 +/- 0.09 (17 %)	1.46 +/- 0.09 (6 %)	0.73 +/- 0.12 (16 %)	0.73 +/- 0.12 (16 %)	3.20 +/- 0.14 (4 %)	0.73 +/- 0.12 (16 %)	1.47 +/- 0.07 (5 %)	1.12 +/- 0.07 (7 %)	1.12 +/- 0.07 (7 %)	1.13 +/- 0.07 (7 %)	1.12 +/- 0.07 (7 %)	1.47 +/- 0.07 (5 %)	1.12 +/- 0.07 (7 %)	1.12 +/- 0.07 (7 %)	1.13 +/- 0.07 (7 %)	1.12 +/- 0.07 (7 %)	1.47 +/- 0.07 (5 %)
sm-lin-quad-cHJ1	81.80 +/- 5.87 (7 %)	293.40 +/- 28.77 (10 %)	60.16 +/- 4.46 (7 %)	23.24 +/- 1.62 (7 %)	18.38 +/- 1.39 (8 %)	18.38 +/- 1.39 (8 %)	27.04 +/- 1.62 (6 %)	10.24 +/- 7.79 (8 %)	9.00 +/- 1.41 (16 %)	77.37 +/- 5.44 (7 %)	13.24 +/- 1.91 (14 %)	13.24 +/- 1.91 (14 %)	18.38 +/- 1.39 (8 %)	13.24 +/- 1.91 (14 %)	15.34 +/- 0.72 (5 %)	121.42 +/- 8.59 (7 %)	121.42 +/- 8.59 (7 %)	101.76 +/- 17.61 (10 %)	121.42 +/- 8.59 (7 %)	15.34 +/- 0.72 (5 %)	121.42 +/- 8.59 (7 %)	121.42 +/- 8.59 (7 %)	101.76 +/- 17.61 (10 %)	121.42 +/- 8.59 (7 %)	15.34 +/- 0.72 (5 %)
sm-lin-quad-mixed-cHQ1-cHJ1	102.35 +/- 6.75 (7 %)	311.61 +/- 29.67 (10 %)	296.98 +/- 25.67 (10 %)	42.89 +/- 2.94 (7 %)	59.58 +/- 3.52 (6 %)	59.58 +/- 3.52 (6 %)	86.78 +/- 4.86 (6 %)	119.03 +/- 8.75 (7 %)	253.93 +/- 3.89 (15 %)	96.67 +/- 6.41 (7 %)	29.59 +/- 3.89 (15 %)	29.59 +/- 3.89 (15 %)	59.58 +/- 3.52 (6 %)	29.59 +/- 3.89 (15 %)	42.43 +/- 2.23 (5 %)	146.92 +/- 9.86 (7 %)	146.92 +/- 9.86 (7 %)	126.06 +/- 18.11 (10 %)	146.92 +/- 9.86 (7 %)	42.43 +/- 2.23 (5 %)	146.92 +/- 9.86 (7 %)	146.92 +/- 9.86 (7 %)	126.06 +/- 18.11 (10 %)	146.92 +/- 9.86 (7 %)	42.43 +/- 2.23 (5 %)
sm-lin-quad-mixed-cHJ1-cHB	82.89 +/- 5.98 (7 %)	299.96 +/- 25.15 (10 %)	61.66 +/- 4.55 (7 %)	23.93 +/- 1.75 (6 %)	19.57 +/- 1.53 (8 %)	19.57 +/- 1.53 (8 %)	28.79 +/- 1.75 (6 %)	10.46 +/- 7.96 (7 %)	9.93 +/- 1.60 (16 %)	78.56 +/- 5.47 (7 %)	14.61 +/- 2.14 (15 %)	14.61 +/- 2.14 (15 %)	19.57 +/- 1.53 (8 %)	14.61 +/- 2.14 (15 %)	15.78 +/- 0.94 (5 %)	129.12 +/- 17.74 (10 %)	129.12 +/- 17.74 (10 %)	107.85 +/- 18.03 (10 %)	129.12 +/- 17.74 (10 %)	15.78 +/- 0.94 (5 %)	129.12 +/- 17.74 (10 %)	129.12 +/- 17.74 (10 %)	107.85 +/- 18.03 (10 %)	129.12 +/- 17.74 (10 %)	15.78 +/- 0.94 (5 %)
sm-lin-quad-mixed-cHQ1-cHB	102.35 +/- 6.75 (7 %)	311.61 +/- 29.67 (10 %)	296.98 +/- 25.67 (10 %)	42.89 +/- 2.94 (7 %)	59.58 +/- 3.52 (6 %)	59.58 +/- 3.52 (6 %)	86.78 +/- 4.86 (6 %)	119.03 +/- 8.75 (7 %)	253.93 +/- 3.89 (15 %)	96.67 +/- 6.41 (7 %)	29.59 +/- 3.89 (15 %)	29.59 +/- 3.89 (15 %)	59.58 +/- 3.52 (6 %)	29.59 +/- 3.89 (15 %)	42.43 +/- 2.23 (5 %)	146.92 +/- 9.86 (7 %)	146.92 +/- 9.86 (7 %)	126.06 +/- 18.11 (10 %)	146.92 +/- 9.86 (7 %)	42.43 +/- 2.23 (5 %)	146.92 +/- 9.86 (7 %)	146.92 +/- 9.86 (7 %)	126.06 +/- 18.11 (10 %)	146.92 +/- 9.86 (7 %)	42.43 +/- 2.23 (5 %)
sm-lin-quad-mixed-cHWB+cHB	79.79 +/- 5.72 (7 %)	292.22 +/- 28.41 (10 %)	292.22 +/- 28.41 (10 %)	41.61 +/- 3.01 (7 %)	58.60 +/- 4.24 (7 %)	58.60 +/- 4.24 (7 %)	27.67 +/- 1.67 (6 %)	9.19 +/- 1.47 (16 %)	9.19 +/- 1.47 (16 %)	76.60 +/- 5.70 (7 %)	13.52 +/- 1.97 (15 %)	13.52 +/- 1.97 (15 %)	58.60 +/- 4.24 (7 %)	13.52 +/- 1.97 (15 %)	13.30 +/- 0.74 (5 %)	119.94 +/- 18.23 (10 %)	119.94 +/- 18.23 (10 %)	104.81 +/- 17.51 (10 %)	119.94 +/- 18.23 (10 %)	13.30 +/- 0.74 (5 %)	119.94 +/- 18.23 (10 %)	119.94 +/- 18.23 (10 %)	104.81 +/- 17.51 (10 %)	119.94 +/- 18.23 (10 %)	13.30 +/- 0.74 (5 %)
sm-lin-quad-mixed-cHWB-cHB	83.07 +/- 5.96 (7 %)	303.87 +/- 26.83 (10 %)	303.87 +/- 26.83 (10 %)	41.78 +/- 3.02 (7 %)	61.41 +/- 4.55 (7 %)	61.41 +/- 4.55 (7 %)	28.79 +/- 1.74 (6 %)	9.62 +/- 1.53 (16 %)	9.62 +/- 1.53 (16 %)	78.83 +/- 5.86 (7 %)	13.98 +/- 2.07 (15 %)	13.98 +/- 2.07 (15 %)	61.41 +/- 4.55 (7 %)	13.98 +/- 2.07 (15 %)	16.69 +/- 0.82 (5 %)	126.20 +/- 18.67 (10 %)	126.20 +/- 18.67 (10 %)	107.85 +/- 18.03 (10 %)	126.20 +/- 18.67 (10 %)	16.69 +/- 0.82 (5 %)	126.20 +/- 18.67 (10 %)	126.20 +/- 18.67 (10 %)	107.85 +/- 18.03 (10 %)	126.20 +/- 18.67 (10 %)	16.69 +/- 0.82 (5 %)
sm-lin-quad-mixed-cHWB-cHW	84.12 +/- 6.04 (7 %)	306.38 +/- 27.07 (10 %)	306.38 +/- 27.07 (10 %)	41.42 +/- 3.00 (7 %)	61.42 +/- 4.54 (7 %)	61.42 +/- 4.54 (7 %)	28.79 +/- 1.73 (6 %)	9.71 +/- 1.55 (16 %)	9.71 +/- 1.55 (16 %)	78.99 +/- 5.83 (7 %)	14.11 +/- 2.09 (15 %)	14.11 +/- 2.09 (15 %)	61.42 +/- 4.54 (7 %)	14.11 +/- 2.09 (15 %)	16.73 +/- 0.84 (5 %)	126.70 +/- 18.75 (10 %)	126.70 +/- 18.75 (10 %)	107.85 +/- 18.03 (10 %)	126.70 +/- 18.75 (10 %)	16.73 +/- 0.84 (5 %)	126.70 +/- 18.75 (10 %)	126.70 +/- 18.75 (10 %)	107.85 +/- 18.03 (10 %)	126.70 +/- 18.75 (10 %)	16.73 +/- 0.84 (5 %)
sm-lin-quad-mixed-cHWB-cHJ1	83.18 +/- 5.98 (7 %)	307.23 +/- 26.88 (10 %)	307.23 +/- 26.88 (10 %)	41.54 +/- 3.01 (7 %)	61.54 +/- 4.55 (7 %)	61.54 +/- 4.55 (7 %)	28.77 +/- 1.74 (6 %)	9.92 +/- 1.60 (16 %)	9.92 +/- 1.60 (16 %)	79.14 +/- 5.86 (7 %)	14.29 +/- 2.14 (15 %)	14.29 +/- 2.14 (15 %)	61.54 +/- 4.55 (7 %)	14.29 +/- 2.14 (15 %)	16.78 +/- 0.82 (5 %)	127.15 +/- 18.41 (10 %)	127.15 +/- 18.41 (10 %)	107.85 +/- 18.03 (10 %)	127.15 +/- 18.41 (10 %)	16.78 +/- 0.82 (5 %)	127.15 +/- 18.41 (10 %)	127.15 +/- 18.41 (10 %)	107.85 +/- 18.03 (10 %)	127.15 +/- 18.41 (10 %)	16.78 +/- 0.82 (5 %)
sm-lin-quad-mixed-cHJ1-cHW	82.85 +/- 5.96 (7 %)	298.84 +/- 28.96 (10 %)	61.61 +/- 4.57 (7 %)	23.77 +/- 1.74 (6 %)	18.83 +/- 1.41 (8 %)	18.83 +/- 1.41 (8 %)	28.37 +/- 1.74 (6 %)	9.92 +/- 1.60 (16 %)	9.92 +/- 1.60 (16 %)	78.31 +/- 5.84 (7 %)	14.00 +/- 2.13 (15 %)	14.00 +/- 2.13 (15 %)	18.83 +/- 1.41 (8 %)	14.00 +/- 2.13 (15 %)	15.53 +/- 0.81 (5 %)	122.26 +/- 18.04 (10 %)	122.26 +/- 18.04 (10 %)	101.76 +/- 17.61 (10 %)	122.26 +/- 18.04 (10 %)	15.53 +/- 0.81 (5 %)	122.26 +/- 18.04 (10 %)	122.26 +/- 18.04 (10 %)	101.76 +/- 17.61 (10 %)	122.26 +/- 18.04 (10 %)	15.53 +/- 0.81 (5 %)
sm-lin-quad-mixed-cHQ3	102.49 +/- 6.76 (7 %)	314.76 +/- 25.96 (9 %)	71.17 +/- 5.13 (7 %)	43.35 +/- 2.97 (7 %)	99.60 +/- 7.53 (6 %)	99.60 +/- 7.53 (6 %)	86.80 +/- 4.86 (6 %)	27.07 +/- 1.65 (6 %)	23.94 +/- 3.89 (15 %)	96.92 +/- 6.41 (7 %)	27.79 +/- 5.57 (15 %)	27.79 +/- 5.57 (15 %)	99.60 +/- 7.53 (6 %)	27.79 +/- 5.57 (15 %)	42.45 +/- 2.24 (5 %)	188.84 +/- 19.29 (10 %)	188.84 +/- 19.29 (10 %)	168.08 +/- 25.57 (15 %)	188.84 +/- 19.29 (10 %)	42.45 +/- 2.24 (5 %)	188.84 +/- 19.29 (10 %)	188.84 +/- 19.29 (10 %)	168.08 +/- 25.57 (15 %)	188.84 +/- 19.29 (10 %)	42.45 +/- 2.24 (5 %)
sm-lin-quad-mixed-cHQ3-cHB	79.79 +/- 5.72 (7 %)	292.22 +/- 28.41 (10 %)	292.22 +/- 28.41 (10 %)	41.61 +/- 3.01 (7 %)	58.60 +/- 4.24 (7 %)	58.60 +/- 4.24 (7 %)	27.67 +/- 1.67 (6 %)	9.19 +/- 1.47 (16 %)	9.19 +/- 1.47 (16 %)	76.60 +/- 5.70 (7 %)	13.52 +/- 1.97 (15 %)	13.52 +/- 1.97 (15 %)	58.60 +/- 4.24 (7 %)	13.52 +/- 1.97 (15 %)	15.30 +/- 0.74 (5 %)	119.94 +/- 18.23 (10 %)	119.94 +/- 18.23 (10 %)	104.81 +/- 17.51 (10 %)	119.94 +/- 18.23 (10 %)	15.30 +/- 0.74 (5 %)	119.94 +/- 18.23 (10 %)	119.94 +/- 18.23 (10 %)	104.81 +/- 17.51 (10 %)	119.94 +/- 18.23 (10 %)	15.30 +/- 0.74 (5 %)
sm-lin-quad-mixed-cHQ3-cHW	84.12 +/- 6.04 (7 %)	306.38 +/- 27.07 (10 %)	306.38 +/- 27.07 (10 %)	41.42 +/- 3.00 (7 %)	61.42 +/- 4.54 (7 %)	61.42 +/- 4.54 (7 %)	28.79 +/- 1.73 (6 %)	9.71 +/- 1.55 (16 %)	9.71 +/- 1.55 (16 %)	78.99 +/- 5.83 (7 %)	14.11 +/- 2.09 (15 %)	14.11 +/- 2.09 (15 %)	61.42 +/- 4.54 (7 %)	14.11 +/- 2.09 (15 %)	16.73 +/- 0.84 (5 %)	126.70 +/- 18.75 (10 %)	126.70 +/- 18.75 (10 %)	107.85 +/- 18.03 (10 %)	126.70 +/- 18.75 (10 %)	16.73 +/- 0.84 (5 %)	126.70 +/- 18.75 (10 %)	126.70 +/- 18.75 (10 %)	107.85 +/- 18.03 (10 %)	126.70 +/- 18.75 (10 %)	16.73 +/- 0.84 (5 %)
sm-lin-quad-mixed-cHQ3-cHJ1	83.18 +/- 5.98 (7 %)	307.23 +/- 26.88 (10 %)	307.23 +/- 26.88 (10 %)	41.54 +/- 3.01 (7 %)	61.54 +/- 4.55 (7 %)	61.54 +/- 4.55 (7 %)	28.77 +/- 1.74 (6 %)	9.92 +/- 1.60 (16 %)	9.92 +/- 1.60 (16 %)	79.14 +/- 5.86 (7 %)	14.29 +/- 2.14 (15 %)	14.29 +/- 2.14 (15 %)	61.54 +/- 4.55 (7 %)	14.29 +/- 2.14 (15 %)	16.78 +/- 0.82 (5 %)	127.15 +/- 18.41 (10 %)	127.15 +/- 18.41 (10 %)	107.85 +/- 18.03 (10 %)	127.15 +/- 18.41 (10 %)	16.78 +/- 0.82 (5 %)	127.15 +/- 18.41 (10 %)	127.15 +/- 18.41 (10 %)	107.85 +/- 18.03 (10 %)	127.15 +/- 18.41 (10 %)	16.78 +/- 0.82 (5 %)
sm-lin-quad-mixed-cHQ3-cHW	84.12 +/- 6.04 (7 %)	306.38 +/- 27.07 (10 %)	306.38 +/- 27.07 (10 %)	41.42 +/- 3.00 (7 %)	61.42 +/- 4.54 (7 %)	61.42 +/- 4.54 (7 %)	28.79 +/- 1.73 (6 %)	9.71 +/- 1.55 (16 %)	9.71 +/- 1.55 (16 %)	78.99 +/- 5.83 (7 %)	14.11 +/- 2.09 (15 %)	14.11 +/- 2.09 (15 %)	61.42 +/- 4.54 (7 %)	14.11 +/- 2.09 (15 %)	16.73 +/- 0.84 (5 %)	126.70 +/- 18.75 (10 %)	126.70 +/- 18.75 (10 %)	107.85 +/- 18.03 (10 %)	126.70 +/- 18.75 (10 %)	16.73 +/- 0.84 (5 %)	126.70 +/- 18.75 (10 %)	126.70 +/- 18.75 (10 %)	107.85 +/- 18.03 (10 %)	126.70 +/- 18.75 (10 %)	16.73 +/- 0.84 (5 %)
sm-lin-quad-mixed-cHJ1-cHB	81.31 +/- 5.85 (7 %)	293.40 +/- 28.78 (10 %)	60.16 +/- 4.46 (7 %)	23.22 +/- 1.68 (7 %)	18.61 +/- 1.41 (8 %)	18.61 +/- 1.41 (8 %)	27.39 +/- 1.64 (6 %)	10.54 +/- 7.81 (8 %)	9.07 +/- 1.45 (16 %)	77.75 +/- 5.46 (7 %)	13.32 +/- 1.93 (14 %)	13.32 +/- 1.93 (14 %)	18.61 +/- 1.41 (8 %)	13.32 +/- 1.93 (14 %)	15.50 +/- 0.74 (5 %)	121.72 +/- 8.52 (7 %)	121.72 +/- 8.52 (7 %)	101.76 +/- 17.61 (10 %)	121.72 +/- 8.52 (7 %)	15.50 +/- 0.74 (5 %)	121.72 +/- 8.52 (7 %)	121.72 +/- 8.52 (7 %)	101.76 +/- 17.61 (10 %)	121.72 +/- 8.52 (7 %)	15.50 +/- 0.74 (5 %)
sm-lin-quad-mixed-cHJ1-cHW	83.39 +/- 6.00 (7 %)	298.03 +/- 28.84 (10 %)	62.08 +/- 4.62 (7 %)	23.18 +/- 1.73 (7 %)	18.86 +/- 1.43 (8 %)	18.86 +/- 1.43 (8 %)	27.39 +/- 1.64 (6 %)	10.57 +/- 7.92 (8 %)	9.75 +/- 1.57 (16 %)	79.39 +/- 5.60 (7 %)	14.14 +/- 2.06 (15 %)	14.14 +/- 2.06 (15 %)	18.86 +/- 1.43 (8 %)	14.14 +/- 2.06 (15 %)	15.48 +/- 0.74 (5 %)	121.72 +/- 8.52 (7 %)	121.72 +/- 8.52 (7 %)	101.76 +/- 17.61 (10 %)	121.72 +/- 8.52 (7 %)	15.48 +/- 0.74 (5 %)	121.72 +/- 8.52 (7 %)	121.72 +/- 8.52 (7 %)	101.76 +/- 17.61 (10 %)	121.72 +/- 8.52 (7 %)	15.48 +/- 0.74 (5 %)
sm-lin-quad-mixed-cHJ3	102.49 +/- 6.76 (7 %)	314.76 +/- 25.96 (9 %)	71.17 +/- 5.13 (7 %)	43.35 +/- 2.97 (7 %)	99.60 +/- 7.53 (6 %)	99.60 +/- 7.53 (6 %)	86.80 +/- 4.86 (6 %)	27.07 +/- 1.65 (6 %)	23.94 +/- 3.89 (15 %)	96.92 +/- 6.41 (7 %)	27.79 +/- 5.57 (15 %)	27.79 +/- 5.57 (15 %)	99.60 +/- 7.53 (6 %)	27.79 +/- 5.57 (15 %)	42.45 +/- 2.24 (5 %)	188.84 +/- 19.29 (10 %)	188.84 +/- 19.29 (10 %)	168.08 +/- 25.57 (15 %)	188.84 +/- 19.29 (10 %)	42.45 +/- 2.24 (5 %)	188.84 +/- 19.29 (10 %)	188.84 +/- 19.29 (10 %)	168.08 +/- 25.57 (15 %)	188.84 +/- 19.29 (10 %)	42.45 +/- 2.24 (5 %)
sm-lin-quad-mixed-cHJ3-cHB	79.79 +/- 5.72 (7 %)	292.22 +/- 28.41 (10 %)	292.22 +/- 28.41 (10 %)	41.61 +/- 3.01 (7 %)	58.60 +/- 4.24 (7 %)	58.60 +/- 4.24 (7 %)	27.67 +/- 1.67 (6 %)	9.19 +/- 1.47 (16 %)	9.19 +/- 1.47 (16 %)	76.60 +/- 5.70 (7 %)	13.52 +/- 1.97 (15 %)	13.52 +/- 1.97 (15 %)	58.60 +/- 4.24 (7 %)	13.52 +/- 1.97 (15 %)	15.30 +/- 0.74 (5 %)	119.94 +/- 18.23 (10 %)	119.94 +/- 18.23 (10 %)	104.81 +/- 17.51 (10 %)	119.94 +/- 18.23 (10 %)	15.30 +/- 0.74 (5 %)	119.94 +/- 18.23 (10 %)	119.94 +/- 18.23 (10 %)	104.81 +/- 17.51 (10 %)	119.94 +/- 18.23 (10 %)	15.30 +/- 0.74 (5 %)
sm-lin-quad-mixed-cHJ3-cHW	84.12 +/- 6.04 (7 %)	306.38 +/- 27.07 (10 %)	306.38 +/- 27.07 (10 %)	41.42 +/- 3.00 (7 %)	61.42 +/- 4.54 (7 %)	61.42 +/- 4.54 (7 %)	28.79 +/- 1.73 (6 %)	9.71 +/- 1.55 (16 %)	9.71 +/- 1.55 (16 %)	78.99 +/- 5.83 (7 %)	14.11 +/- 2.09 (15 %)	14.11 +/- 2.09 (15 %)	61.42 +/- 4.54 (7 %)	14.11 +/- 2.09 (15 %)	16.73 +/- 0.84 (5 %)	126.70 +/- 18.75 (10 %)	126.70 +/- 18.75 (10 %)	107.85 +/- 18.03 (10 %)	126.70 +/- 18.75 (10 %)	16.73 +/- 0.84 (5 %)	126.70 +/- 18.75 (10 %)	126.70 +/- 18.75 (10 %)	107.85 +/- 18.03 (10 %)	126.70 +/- 18.75 (10 %)	16.73 +/- 0.84 (5 %)
sm-lin-quad-mixed-cHJ3-cHJ1	83.18 +/- 5.98 (7 %)	307.23 +/- 26.88 (10 %)	307.23 +/- 26.88 (10 %)	41.54 +/- 3.01 (7 %)	61.54 +/- 4.55 (7 %)	61.54 +/- 4.55 (7 %)	28.77 +/- 1.74 (6 %)	9.92 +/- 1.60 (16 %)	9.92 +/- 1.60 (16 %)	79.14 +/- 5.86 (7 %)	14.29 +/- 2.14 (15 %)	14.29 +/- 2.14 (15 %)	61.54 +/- 4.55 (7 %)	14.29 +/- 2.14 (15 %)	16.78 +/- 0.82 (5 %)	127.15 +/- 18.41 (10 %)	127.15 +/- 18.41 (10 %)	107.85 +/- 18.03 (10 %)	127.15 +/- 18.41 (10 %)	16.78 +/- 0.82 (5 %)	127.15 +/- 18.41 (10 %)	127.15 +/- 18.41 (10 %)	107.85 +/- 18.03 (10 %)	127.15 +/- 18.41 (10 %)	16.78 +/- 0.82 (5 %)
sm-lin-quad-mixed-cHJ3-cHW	84.12 +/- 6.04 (7 %)	306.38 +/- 27.07 (10 %)	306.38 +/- 27.07 (10 %)	41.42 +/- 3.00 (7 %)	61.42 +/- 4.54 (7 %)	61.42 +/- 4.54 (7 %)	28.79 +/- 1.73 (6 %)	9.71 +/- 1.55 (16 %)	9.71 +/- 1.55 (16 %)	78.99 +/- 5.83 (7 %)	14.11 +/- 2.09 (15 %)	14.11 +/- 2.09 (15 %)	61.42 +/- 4.54 (7 %)	14.11 +/- 2.09 (15 %)	16.73 +/- 0.84 (5 %)	126.70 +/- 18.75 (10 %)	126.70 +/- 18.75 (10 %)	107.85 +/- 18.03 (10 %)	126.70 +/- 18.75 (10 %)	16.73 +/- 0.84 (5 %)	126.70 +/- 18.75 (10 %)	126.70 +/- 18.75 (10 %)	107.85 +/- 18.03 (10 %)	126.70 +/- 18.75 (10 %)	16.73 +/- 0.84 (5 %)
signal	2210.64 +/- 37.32 (1 %)	1107.37 +/- 25.76 (2 %)	1076.69 +/- 12.25 (1 %)	1076.69 +/- 12.25 (1 %)	1886.95 +/- 12.82 (1 %)	1886.95 +/- 12.82 (1 %)	1391.20 +/- 13.99 (1 %)	3980.48 +/- 48.69 (1 %)	3980.48 +/- 48.69 (1 %)	3160.62 +/- 34.58 (1 %)	3160.62 +/- 34.58 (1 %)	3160.62 +/- 34.58 (1 %)	1391.20 +/- 13.99 (1 %)	3160.62 +/- 34.58 (1 %)	2172.79 +/- 17.60 (1 %)	3383.69 +/- 60.97 (1 %)	3383.69 +/- 60.97 (1 %)	3383.69 +/- 60.97 (1 %)	3383.69 +/- 60.97 (1 %)	2172.79 +/- 17.60 (1 %)	3383.69 +/- 60.97 (1 %)	3383.69 +/- 60.97 (1 %)	3383.69 +/- 60.97 (1 %)	3383.69 +/- 60.97 (1 %)	2172.79 +/- 17.60 (1 %)
Wpbe-cat-4	211.55 +/- 9.81 (5 %)	40.13 +/- 2.45 (6 %)	85.73 +/- 7.59 (9 %)	-	-	-	157.09 +/- 13.26 (8 %)	-	-	33.08 +/- 2.24 (7 %)	-	-	29.62 +/- 14.34 (5 %)	-	-	21.88 +/- 1.08 (5 %)	-	-	95.63 +/- 2.58 (3 %)	-	-	-	-
Wpbe-cat-5	819.97

Table C.2: Yields of the VBS WV backgrounds and of the 45 EFT templates according to the statistical model defined in Section 4.2.4 for the 2017 year. All signal and control regions are provided and split for lepton flavour (e, μ).

	res-sig-mu-DNN-leq-0p5-2018	boost-sig-ele-DNN-leq-0p5-2018	boost-topcr-ele-2018	boost-sig-mu-DNN-leq-0p5-2018	boost-wjetcr-ele-2018	boost-sig-mu-DNN-geq-0p5-2018	res-sig-ele-DNN-leq-0p5-2018	res-wjetcr-ele-2018	res-topcr-mu-2018	res-wjetcr-mu-2018	boost-topcr-mu-2018	boost-wjetcr-mu-2018	res-topcr-ele-2018	boost-sig-ele-DNN-geq-0p5-2018	res-sig-mu-DNN-geq-0p5-2018	res-sig-ele-DNN-geq-0p5-2018
sm-lin-quad-mixed-cHW-cHj1	159.57 +/- 14.70 (9 %)	31.65 +/- 1.74 (5 %)	46.02 +/- 3.57 (8 %)	44.05 +/- 2.09 (5 %)	18.91 +/- 1.32 (7 %)	44.16 +/- 2.07 (5 %)	101.09 +/- 9.11 (9 %)	138.02 +/- 12.33 (9 %)	482.48 +/- 64.82 (13 %)	211.33 +/- 20.02 (9 %)	67.40 +/- 5.22 (8 %)	27.18 +/- 1.94 (7 %)	305.13 +/- 41.72 (14 %)	31.36 +/- 1.48 (5 %)	170.75 +/- 13.41 (8 %)	112.42 +/- 8.94 (8 %)
sm-lin-quad-mixed-cW-cHB	180.94 +/- 16.19 (9 %)	75.92 +/- 4.27 (6 %)	66.07 +/- 4.57 (7 %)	104.65 +/- 5.19 (5 %)	53.50 +/- 3.35 (6 %)	128.76 +/- 5.57 (4 %)	118.45 +/- 10.53 (9 %)	172.77 +/- 14.13 (8 %)	506.67 +/- 66.59 (13 %)	257.25 +/- 22.79 (9 %)	94.58 +/- 6.86 (7 %)	71.42 +/- 4.48 (6 %)	321.76 +/- 42.79 (13 %)	96.06 +/- 4.14 (4 %)	209.38 +/- 15.68 (7 %)	141.44 +/- 10.65 (8 %)
sm-lin-quad-mixed-cW-cHW	183.97 +/- 16.40 (9 %)	78.35 +/- 4.37 (6 %)	66.71 +/- 4.62 (7 %)	107.28 +/- 5.27 (5 %)	54.71 +/- 3.43 (6 %)	133.21 +/- 5.76 (4 %)	120.42 +/- 10.68 (9 %)	175.88 +/- 14.37 (8 %)	507.56 +/- 66.69 (13 %)	261.00 +/- 22.95 (9 %)	95.43 +/- 6.89 (7 %)	72.88 +/- 4.59 (6 %)	322.43 +/- 42.84 (13 %)	99.33 +/- 4.28 (4 %)	213.12 +/- 15.93 (7 %)	144.13 +/- 10.83 (8 %)
sm-lin-quad-mixed-cHbox-cHB	154.48 +/- 14.47 (9 %)	23.72 +/- 1.07 (5 %)	37.82 +/- 2.86 (8 %)	33.50 +/- 1.42 (4 %)	15.81 +/- 1.09 (7 %)	37.09 +/- 1.74 (5 %)	97.88 +/- 8.94 (9 %)	132.98 +/- 12.01 (9 %)	475.04 +/- 64.19 (14 %)	205.55 +/- 19.88 (10 %)	55.58 +/- 4.30 (8 %)	23.07 +/- 1.69 (7 %)	299.11 +/- 41.17 (14 %)	25.87 +/- 1.21 (5 %)	166.45 +/- 13.30 (8 %)	108.95 +/- 8.74 (8 %)
sm-lin-quad-mixed-cHWB-cHQ1	148.50 +/- 13.52 (9 %)	23.32 +/- 1.04 (4 %)	38.76 +/- 2.87 (7 %)	32.94 +/- 1.40 (4 %)	15.89 +/- 1.08 (7 %)	36.68 +/- 1.70 (5 %)	94.14 +/- 8.35 (9 %)	129.43 +/- 11.41 (9 %)	478.39 +/- 63.51 (13 %)	199.45 +/- 18.88 (9 %)	57.09 +/- 4.37 (8 %)	23.21 +/- 1.68 (7 %)	300.90 +/- 40.64 (14 %)	25.58 +/- 1.19 (5 %)	162.89 +/- 12.65 (8 %)	106.67 +/- 8.32 (8 %)
sm-lin-quad-mixed-cHW-cHQ1	156.16 +/- 14.43 (9 %)	25.99 +/- 1.16 (4 %)	39.10 +/- 2.94 (8 %)	36.53 +/- 1.54 (4 %)	16.93 +/- 1.17 (7 %)	41.71 +/- 1.94 (5 %)	98.83 +/- 8.98 (9 %)	134.96 +/- 12.05 (9 %)	480.78 +/- 64.56 (13 %)	207.21 +/- 19.68 (9 %)	57.54 +/- 4.42 (8 %)	24.46 +/- 1.78 (7 %)	302.85 +/- 41.40 (14 %)	29.24 +/- 1.34 (5 %)	169.08 +/- 13.41 (8 %)	111.05 +/- 8.85 (8 %)
sm-lin-quad-cHl1	152.26 +/- 14.15 (9 %)	23.39 +/- 1.05 (4 %)	37.77 +/- 2.86 (8 %)	33.08 +/- 1.40 (4 %)	15.66 +/- 1.07 (7 %)	36.50 +/- 1.71 (5 %)	96.72 +/- 8.79 (9 %)	131.37 +/- 11.78 (9 %)	474.80 +/- 64.16 (14 %)	202.56 +/- 19.42 (10 %)	55.50 +/- 4.30 (8 %)	22.85 +/- 1.68 (7 %)	298.95 +/- 41.15 (14 %)	25.36 +/- 1.19 (5 %)	165.07 +/- 13.13 (8 %)	108.17 +/- 8.63 (8 %)
quad-cHl1	0.00 +/- 0.00 (53 %)	0.00 +/- 0.00 (6 %)	0.00 +/- 0.00 (4 %)	0.00 +/- 0.00 (12 %)	0.00 +/- 0.00 (13 %)	0.00 +/- 0.00 (6 %)	0.00 +/- 0.00 (8 %)	0.00 +/- 0.00 (8 %)	0.00 +/- 0.00 (7 %)	0.00 +/- 0.00 (14 %)	0.00 +/- 0.00 (11 %)	0.00 +/- 0.00 (4 %)	0.00 +/- 0.00 (7 %)	0.00 +/- 0.00 (26 %)	0.00 +/- 0.00 (10 %)	0.00 +/- 0.00 (13 %)
sm-lin-quad-mixed-cW-cHj1	183.85 +/- 16.46 (9 %)	80.81 +/- 4.64 (6 %)	74.22 +/- 5.34 (7 %)	111.53 +/- 5.70 (5 %)	55.19 +/- 3.46 (6 %)	130.57 +/- 5.68 (4 %)	120.75 +/- 10.73 (9 %)	175.76 +/- 14.29 (8 %)	513.67 +/- 67.23 (13 %)	261.41 +/- 23.00 (9 %)	105.72 +/- 7.72 (7 %)	73.68 +/- 4.67 (6 %)	327.13 +/- 43.28 (13 %)	97.58 +/- 4.18 (4 %)	211.29 +/- 15.73 (7 %)	142.93 +/- 10.74 (8 %)
sm-lin-quad-mixed-cHl1-cHQ1	152.37 +/- 14.15 (9 %)	23.39 +/- 1.05 (4 %)	38.52 +/- 2.90 (8 %)	33.10 +/- 1.40 (4 %)	15.67 +/- 1.07 (7 %)	36.53 +/- 1.71 (5 %)	96.77 +/- 8.80 (9 %)	131.54 +/- 11.79 (9 %)	479.81 +/- 64.49 (13 %)	202.89 +/- 19.45 (10 %)	56.65 +/- 4.37 (8 %)	22.88 +/- 1.68 (7 %)	302.11 +/- 41.35 (14 %)	25.38 +/- 1.19 (5 %)	165.17 +/- 13.14 (8 %)	108.23 +/- 8.64 (8 %)
quad-cHj1	4.46 +/- 0.46 (10 %)	5.94 +/- 0.68 (11 %)	8.81 +/- 0.80 (9 %)	7.90 +/- 0.63 (8 %)	2.20 +/- 0.19 (9 %)	3.30 +/- 0.20 (6 %)	3.09 +/- 0.20 (7 %)	4.47 +/- 0.41 (9 %)	11.75 +/- 0.99 (8 %)	6.23 +/- 0.45 (7 %)	12.41 +/- 0.98 (8 %)	3.07 +/- 0.25 (8 %)	8.88 +/- 0.88 (10 %)	2.53 +/- 0.16 (6 %)	3.60 +/- 0.23 (6 %)	2.57 +/- 0.17 (7 %)
quad-cHWB	1.02 +/- 0.13 (13 %)	0.45 +/- 0.03 (7 %)	0.53 +/- 0.03 (6 %)	0.59 +/- 0.03 (6 %)	0.29 +/- 0.02 (8 %)	0.90 +/- 0.06 (6 %)	0.68 +/- 0.06 (9 %)	0.86 +/- 0.10 (12 %)	2.28 +/- 0.28 (12 %)	1.33 +/- 0.16 (12 %)	0.73 +/- 0.05 (8 %)	0.38 +/- 0.04 (11 %)	1.53 +/- 0.21 (14 %)	0.65 +/- 0.03 (5 %)	0.85 +/- 0.08 (10 %)	0.59 +/- 0.06 (10 %)
sm-lin-quad-mixed-cHB-cHj1	156.15 +/- 14.52 (9 %)	29.39 +/- 1.65 (6 %)	45.49 +/- 3.53 (8 %)	40.87 +/- 1.96 (5 %)	17.77 +/- 1.23 (7 %)	39.41 +/- 1.87 (5 %)	99.20 +/- 8.98 (9 %)	134.94 +/- 12.07 (9 %)	481.62 +/- 64.78 (13 %)	207.56 +/- 19.81 (10 %)	66.62 +/- 5.18 (8 %)	25.77 +/- 1.87 (7 %)	304.47 +/- 41.68 (14 %)	27.86 +/- 1.34 (5 %)	167.39 +/- 13.17 (8 %)	109.79 +/- 8.76 (8 %)
sm-lin-quad-cHW	156.05 +/- 14.41 (9 %)	25.99 +/- 1.16 (4 %)	38.34 +/- 2.90 (8 %)	36.51 +/- 1.54 (4 %)	16.91 +/- 1.17 (7 %)	41.69 +/- 1.93 (5 %)	98.77 +/- 8.97 (9 %)	134.79 +/- 12.04 (9 %)	475.72 +/- 64.21 (13 %)	206.88 +/- 19.64 (9 %)	56.39 +/- 4.34 (8 %)	24.44 +/- 1.78 (7 %)	299.67 +/- 41.20 (14 %)	29.21 +/- 1.34 (5 %)	168.97 +/- 13.39 (8 %)	110.98 +/- 8.84 (8 %)
sm-lin-quad-cW	180.62 +/- 16.15 (9 %)	75.68 +/- 4.25 (6 %)	66.04 +/- 4.57 (7 %)	104.32 +/- 5.17 (5 %)	53.39 +/- 3.34 (6 %)	128.28 +/- 5.54 (4 %)	118.26 +/- 10.51 (9 %)	172.47 +/- 14.08 (8 %)	506.63 +/- 66.59 (13 %)	256.82 +/- 22.75 (9 %)	94.52 +/- 6.85 (7 %)	71.27 +/- 4.47 (6 %)	321.72 +/- 42.78 (13 %)	95.65 +/- 4.11 (4 %)	209.12 +/- 15.66 (7 %)	141.26 +/- 10.63 (8 %)
sm-lin-quad-cHWB	148.38 +/- 13.51 (9 %)	23.32 +/- 1.03 (4 %)	37.98 +/- 2.83 (7 %)	32.92 +/- 1.39 (4 %)	15.88 +/- 1.08 (7 %)	36.66 +/- 1.70 (5 %)	94.08 +/- 8.35 (9 %)	129.25 +/- 11.41 (9 %)	473.06 +/- 63.14 (13 %)	199.11 +/- 18.85 (9 %)	55.90 +/- 4.30 (8 %)	23.18 +/- 1.68 (7 %)	297.55 +/- 40.42 (14 %)	25.56 +/- 1.19 (5 %)	162.79 +/- 12.63 (8 %)	106.60 +/- 8.32 (8 %)
sm-lin-quad-mixed-cW-cHWB	176.55 +/- 15.52 (9 %)	75.48 +/- 4.21 (6 %)	65.90 +/- 4.52 (7 %)	104.02 +/- 5.16 (5 %)	53.55 +/- 3.34 (6 %)	128.18 +/- 5.50 (4 %)	115.57 +/- 10.06 (9 %)	170.29 +/- 13.71 (8 %)	504.69 +/- 65.55 (13 %)	253.31 +/- 22.16 (9 %)	94.43 +/- 6.81 (7 %)	71.48 +/- 4.46 (6 %)	320.15 +/- 42.03 (13 %)	95.64 +/- 4.11 (4 %)	206.77 +/- 15.14 (7 %)	139.68 +/- 10.31 (7 %)
sm-lin-quad-mixed-cW-cHbox	182.49 +/- 16.43 (9 %)	75.79 +/- 4.25 (6 %)	66.03 +/- 4.57 (7 %)	104.44 +/- 5.17 (5 %)	53.42 +/- 3.34 (6 %)	128.49 +/- 5.55 (4 %)	119.24 +/- 10.63 (9 %)	173.77 +/- 14.27 (8 %)	506.81 +/- 66.60 (13 %)	259.39 +/- 23.16 (9 %)	94.56 +/- 6.85 (7 %)	71.34 +/- 4.47 (6 %)	321.83 +/- 42.79 (13 %)	95.80 +/- 4.12 (4 %)	210.24 +/- 15.80 (8 %)	141.88 +/- 10.73 (8 %)
quad-cHB	0.22 +/- 0.03 (13 %)	0.25 +/- 0.02 (8 %)	0.04 +/- 0.00 (5 %)	0.32 +/- 0.02 (5 %)	0.11 +/- 0.01 (9 %)	0.53 +/- 0.04 (7 %)	0.13 +/- 0.01 (5 %)	0.24 +/- 0.03 (11 %)	0.04 +/- 0.00 (10 %)	0.38 +/- 0.04 (11 %)	0.06 +/- 0.01 (8 %)	0.15 +/- 0.01 (9 %)	0.03 +/- 0.00 (14 %)	0.40 +/- 0.02 (5 %)	0.22 +/- 0.02 (10 %)	0.14 +/- 0.02 (11 %)
quad-cHW	1.62 +/- 0.22 (14 %)	2.11 +/- 0.10 (5 %)	0.49 +/- 0.03 (6 %)	2.89 +/- 0.12 (4 %)	1.07 +/- 0.08 (8 %)	4.57 +/- 0.20 (4 %)	1.01 +/- 0.08 (8 %)	1.75 +/- 0.11 (6 %)	0.41 +/- 0.03 (9 %)	3.32 +/- 0.27 (8 %)	0.66 +/- 0.04 (6 %)	1.38 +/- 0.10 (8 %)	0.24 +/- 0.02 (8 %)	3.73 +/- 0.16 (4 %)	1.85 +/- 0.12 (6 %)	1.16 +/- 0.09 (8 %)
sm-lin-quad-mixed-cW-cHl1	180.61 +/- 16.15 (9 %)	75.68 +/- 4.25 (6 %)	66.04 +/- 4.57 (7 %)	104.32 +/- 5.17 (5 %)	53.39 +/- 3.34 (6 %)	128.29 +/- 5.54 (4 %)	118.27 +/- 10.51 (9 %)	172.47 +/- 14.08 (8 %)	506.62 +/- 66.59 (13 %)	256.82 +/- 22.75 (9 %)	94.52 +/- 6.85 (7 %)	71.27 +/- 4.47 (6 %)	321.71 +/- 42.78 (13 %)	95.64 +/- 4.11 (4 %)	209.13 +/- 15.66 (7 %)	141.27 +/- 10.63 (8 %)
sm-lin-quad-mixed-cHbox-cHQ1	154.24 +/- 14.42 (9 %)	23.47 +/- 1.05 (4 %)	38.52 +/- 2.90 (8 %)	33.20 +/- 1.41 (4 %)	15.72 +/- 1.08 (7 %)	36.61 +/- 1.71 (5 %)	97.73 +/- 8.92 (9 %)	132.84 +/- 11.97 (9 %)	479.98 +/- 64.51 (13 %)	205.43 +/- 19.86 (10 %)	56.67 +/- 4.38 (8 %)	22.95 +/- 1.68 (7 %)	302.21 +/- 41.37 (14 %)	25.48 +/- 1.19 (5 %)	166.27 +/- 13.27 (8 %)	108.83 +/- 8.72 (8 %)
sm-lin-quad-mixed-cHl1-cHj1	155.79 +/- 14.47 (9 %)	29.12 +/- 1.63 (6 %)	45.44 +/- 3.52 (8 %)	40.52 +/- 1.95 (5 %)	17.66 +/- 1.22 (7 %)	38.88 +/- 1.84 (5 %)	99.00 +/- 8.95 (9 %)	134.63 +/- 12.03 (9 %)	481.55 +/- 64.78 (13 %)	207.11 +/- 19.77 (10 %)	66.55 +/- 5.17 (8 %)	25.61 +/- 1.85 (7 %)	304.42 +/- 41.66 (14 %)	27.44 +/- 1.32 (5 %)	167.10 +/- 13.14 (8 %)	109.61 +/- 8.74 (8 %)
sm-lin-quad-mixed-cW-cHQ1	180.72 +/- 16.16 (9 %)	75.69 +/- 4.25 (6 %)	66.82 +/- 4.62 (7 %)	104.35 +/- 5.17 (5 %)	53.40 +/- 3.34 (6 %)	128.30 +/- 5.54 (4 %)	118.32 +/- 10.52 (9 %)	172.65 +/- 14.10 (8 %)	511.80 +/- 66.93 (13 %)	257.14 +/- 22.78 (9 %)	95.62 +/- 6.91 (7 %)	71.30 +/- 4.47 (6 %)	324.98 +/- 42.99 (13 %)	95.67 +/- 4.11 (4 %)	209.23 +/- 15.67 (7 %)	141.33 +/- 10.63 (8 %)
sm-lin-quad-mixed-cHWB-cHB	148.62 +/- 13.54 (9 %)	23.71 +/- 1.06 (4 %)	38.04 +/- 2.83 (7 %)	33.40 +/- 1.42 (4 %)	16.03 +/- 1.09 (7 %)	37.48 +/- 1.74 (5 %)	94.25 +/- 8.36 (9 %)	129.51 +/- 11.45 (9 %)	473.11 +/- 63.15 (13 %)	199.43 +/- 18.88 (9 %)	55.98 +/- 4.30 (8 %)	23.39 +/- 1.70 (7 %)	297.59 +/- 40.43 (14 %)	26.22 +/- 1.22 (5 %)	163.04 +/- 12.66 (8 %)	106.78 +/- 8.34 (8 %)
sm-lin-quad-mixed-cHW-cHB	156.47 +/- 14.47 (9 %)	26.32 +/- 1.19 (5 %)	38.39 +/- 2.90 (8 %)	36.90 +/- 1.56 (4 %)	17.04 +/- 1.18 (7 %)	42.33 +/- 1.97 (5 %)	99.02 +/- 9.01 (9 %)	135.16 +/- 12.07 (9 %)	475.77 +/- 64.22 (13 %)	207.44 +/- 19.71 (10 %)	56.45 +/- 4.34 (8 %)	24.61 +/- 1.80 (7 %)	299.71 +/- 41.21 (14 %)	29.74 +/- 1.37 (5 %)	169.32 +/- 13.44 (8 %)	111.21 +/- 8.86 (8 %)
sm-lin-quad-mixed-cHWB-cHW	152.06 +/- 13.76 (9 %)	26.20 +/- 1.17 (4 %)	38.58 +/- 2.87 (7 %)	36.70 +/- 1.55 (4 %)	17.22 +/- 1.19 (7 %)	42.44 +/- 1.96 (5 %)	96.10 +/- 8.54 (9 %)	132.54 +/- 11.63 (9 %)	473.96 +/- 63.21 (13 %)	203.23 +/- 19.05 (9 %)	56.83 +/- 4.34 (8 %)	24.88 +/- 1.80 (7 %)	298.26 +/- 40.48 (14 %)	29.87 +/- 1.37 (5 %)	166.61 +/- 12.90 (8 %)	109.38 +/- 8.53 (8 %)
sm-lin-quad-cHj1	155.80 +/- 14.47 (9 %)	29.11 +/- 1.63 (6 %)	45.44 +/- 3.52 (8 %)	40.52 +/- 1.95 (5 %)	17.66 +/- 1.22 (7 %)	38.88 +/- 1.84 (5 %)	98.99 +/- 8.95 (9 %)	134.63 +/- 12.03 (9 %)	481.55 +/- 64.78 (13 %)	207.11 +/- 19.77 (10 %)	66.55 +/- 5.17 (8 %)	25.61 +/- 1.85 (7 %)	304.43 +/- 41.66 (14 %)	27.44 +/- 1.32 (5 %)	167.10 +/- 13.14 (8 %)	109.61 +/- 8.74 (8 %)
sm-lin-quad-cHQ1	152.38 +/- 14.15 (9 %)	23.39 +/- 1.05 (4 %)	38.52 +/- 2.90 (8 %)	33.09 +/- 1.40 (4 %)	15.67 +/- 1.07 (7 %)	36.53 +/- 1.71 (5 %)	96.76 +/- 8.80 (9 %)	131.54 +/- 11.79 (9 %)	479.81 +/- 64.49 (13 %)	202.88 +/- 19.45 (10 %)	56.65 +/- 4.37 (8 %)	22.88 +/- 1.68 (7 %)	302.12 +/- 41.35 (14 %)	25.38 +/- 1.19 (5 %)	165.17 +/- 13.14 (8 %)	108.23 +/- 8.64 (8 %)
quad-cHQ1	0.03 +/- 0.01 (22 %)	0.01 +/- 0.00 (15 %)	0.18 +/- 0.03 (16 %)	0.01 +/- 0.00 (20 %)	0.00 +/- 0.00 (15 %)	0.00 +/- 0.00 (6 %)	0.02 +/- 0.00 (12 %)	0.03 +/- 0.00 (6 %)	0.68 +/- 0.07 (11 %)	0.04 +/- 0.00 (8 %)	0.33 +/- 0.04 (12 %)	0.01 +/- 0.00 (38 %)	0.49 +/- 0.05 (11 %)	0.00 +/- 0.00 (27 %)	0.01 +/- 0.00 (12 %)	0.01 +/- 0.00 (11 %)
sm-lin-quad-mixed-cHWB-cHj1	152.32 +/- 13.88 (9 %)	29.24 +/- 1.62 (6 %)	45.90 +/- 3.52 (8 %)	40.62 +/- 1.95 (5 %)	17.97 +/- 1.24 (7 %)	39.23 +/- 1.84 (5 %)	96.66 +/- 8.53 (9 %)	132.91 +/- 11.67 (9 %)	480.68 +/- 63.85 (13 %)	204.21 +/- 19.27 (9 %)	67.30 +/- 5.19 (8 %)	26.06 +/- 1.87 (7 %)	303.63 +/- 40.99 (14 %)	27.77 +/- 1.33 (5 %)	165.22 +/- 12.69 (8 %)	108.34 +/- 8.45 (8 %)
quad-cW	27.09 +/- 2.01 (7 %)	53.08 +/- 3.15 (6 %)	29.31 +/- 1.71 (6 %)	71.02 +/- 3.78 (5 %)	36.60 +/- 2.27 (6 %)	94.48 +/- 4.12 (4 %)	19.87 +/- 1.61 (8 %)	39.47 +/- 1.96 (5 %)	26.61 +/- 2.15 (8 %)	51.57 +/- 3.34 (6 %)	41.01 +/- 2.70 (7 %)	48.45 +/- 2.85 (6 %)	19.88 +/- 1.49 (8 %)	71.13 +/- 3.19 (4 %)	36.73 +/- 2.15 (6 %)	27.92 +/- 1.77 (6 %)
sm-lin-quad-mixed-cHbox-cHj1	157.68 +/- 14.75 (9 %)	29.18 +/- 1.63 (6 %)	45.44 +/- 3.52 (8 %)	40.62 +/- 1.95 (5 %)	17.70 +/- 1.23 (7 %)	38.94 +/- 1.85 (5 %)	99.96 +/- 9.07 (9 %)	135.96 +/- 12.20 (9 %)	481.74 +/- 64.81 (13 %)	209.68 +/- 20.18 (10 %)	66.57 +/- 5.18 (8 %)	25.68 +/- 1.85 (7 %)	304.54 +/- 41.69 (14 %)	27.51 +/- 1.33 (5 %)	168.23 +/- 13.28 (8 %)	110.22 +/- 8.83 (8 %)
sm-lin-quad-mixed-cHQ1-cHj1	155.91 +/- 14.48 (9 %)	29.12 +/- 1.63 (6 %)	46.23 +/- 3.57 (8 %)	40.54 +/- 1.95 (5 %)	17.67 +/- 1.22 (7 %)	38.90 +/- 1.84 (5 %)	99.05 +/- 8.96 (9 %)	134.81 +/- 12.04 (9 %)	486.63 +/- 65.11 (13 %)	207.44 +/- 19.80 (10 %)	67.75 +/- 5.25 (8 %)	25.64 +/- 1.85 (7 %)	307.65 +/- 41.87 (14 %)	27.46 +/- 1.32 (5 %)	167.20 +/- 13.15 (8 %)	109.67 +/- 8.75 (8 %)
sm-lin-quad-cHbox	154.14 +/- 14.42 (9 %)	23.46 +/- 1.05 (4 %)	37.77 +/- 2.86 (8 %)	33.18 +/- 1.41 (4 %)	15.70 +/- 1.08 (7 %)	36.58 +/- 1.71 (5 %)	97.67 +/- 8.91 (9 %)	132.67 +/- 11.96 (9 %)	474.99 +/- 64.18 (14 %)	205.10 +/- 19.83 (10 %)	55.52 +/- 4.30 (8 %)	22.92 +/- 1.67 (7 %)	299.06 +/- 41.16 (14 %)	25.46 +/- 1.19 (5 %)	166.17 +/- 13.26 (8 %)	108.77 +/- 8.72 (8 %)
sm-lin-quad-cHB	152.61 +/- 14.19 (9 %)	23.64 +/- 1.07 (5 %)	37.81 +/- 2.86 (8 %)	33.40 +/- 1.42 (4 %)	15.76 +/- 1.08 (7 %)	37.01 +/- 1.73 (5 %)	96.91 +/- 8.81 (9 %)	131.68 +/- 11.82 (9 %)	474.86 +/- 64.16 (14 %)	203.00 +/- 19.47 (10 %)	55.56 +/- 4.30 (8 %)	23.00 +/- 1.69 (7 %)	299.00 +/- 41.15 (14 %)	25.77 +/- 1.21 (5 %)	165.35 +/- 13.15 (8 %)	108.35 +/- 8.65 (8 %)
sm-lin-quad-mixed-cHB-cHQ1	152.72 +/- 14.19 (9 %)	23.64 +/- 1.07 (5 %)	38.56 +/- 2.90 (8 %)	33.42 +/- 1.42 (4 %)	15.78 +/- 1.08 (7 %)	37.04 +/- 1.73 (5 %)	96.96 +/- 8.83 (9 %)	131.86 +/- 11.83 (9 %)	479.87 +/- 64.50 (13 %)	203.33 +/- 19.50 (10 %)	56.71 +/- 4.38 (8 %)	23.03 +/- 1.69 (7 %)	302.16 +/- 41.36 (14 %)	25.79 +/- 1.21 (5 %)	165.45 +/- 13.17 (8 %)	108.41 +/- 8.65 (8 %)
sm-lin-quad-mixed-cHl1-cHB	152.60 +/- 14.19 (9 %)	23.65 +/- 1.07 (5 %)	37.81 +/- 2.86 (8 %)	33.40 +/- 1.42 (4 %)	15.76 +/- 1.08 (7 %)	37.01 +/- 1.74 (5 %)	96.92 +/- 8.82 (9 %)	131.68 +/- 11.82 (9 %)	474.86 +/- 64.16 (14 %)	203.01 +/- 19.47 (10 %)	55.56 +/- 4.30 (8 %)	23.01 +/- 1.69 (7 %)	298.99 +/- 41.15 (14 %)	25.77 +/- 1.21 (5 %)	165.35 +/- 13.16 (8 %)	108.35 +/- 8.65 (8 %)
sm-lin-quad-mixed-cHbox-cHW	157.87 +/- 14.68 (9 %)	26.06 +/- 1.17 (4 %)	38.35 +/- 2.90 (8 %)	36.61 +/- 1.55 (4 %)	16.95 +/- 1.18 (7 %)	41.73 +/- 1.93 (5 %)	99.71 +/- 9.09 (9 %)	136.04 +/- 12.20 (9 %)	475.88 +/- 64.24 (13 %)	209.13 +/- 20.02 (10 %)	56.41 +/- 4.34 (8 %)	24.50 +/- 1.78 (7 %)	299.78 +/- 41.23 (14 %)	29.29 +/- 1.35 (5 %)	169.90 +/- 13.52 (8 %)	111.50 +/- 8.93 (8 %)
quad-cHbox	0.19 +/- 0.02 (11 %)	0.06 +/- 0.00 (5 %)	0.02 +/- 0.00 (5 %)	0.08 +/- 0.00 (5 %)	0.03 +/- 0.00 (10 %)	0.17 +/- 0.01 (7 %)	0.11 +/- 0.01 (11 %)	0.13 +/- 0.02 (13 %)	0.03 +/- 0.00 (11 %)	0.24 +/- 0.03 (13 %)	0.02 +/- 0.00 (7 %)	0.05 +/- 0.01 (11 %)	0.02 +/- 0.00 (12 %)	0.14 +/- 0.01 (8 %)	0.17 +/- 0.02 (12 %)	0.10 +/- 0.01 (11 %)
sm-lin-quad-mixed-cHW-cHl1	156.04 +/- 14.42 (9 %)	25.99 +/- 1.16 (4 %)	38.34 +/- 2.90 (8 %)	36.51 +/- 1.54 (4 %)	16.91 +/- 1.17 (7 %)	41.68 +/- 1.93 (5 %)	98.78 +/- 8.97 (9 %)	134.79 +/- 12.04 (9 %)	475.71 +/- 64.21 (13 %)	206.88 +/- 19.64 (9 %)	56.39 +/- 4.34 (8 %)	24.44 +/- 1.78 (7 %)	299.66 +/- 41.20 (14 %)	29.21 +/- 1.34 (5 %)	168.98 +/- 13.39 (8 %)	110.98 +/- 8.84 (8 %)
sm-lin-quad-mixed-cHWB-cHl1	148.37 +/- 13.51 (9 %)	23.32 +/- 1.03 (4 %)	37.98 +/- 2.83 (7 %)	32.93 +/- 1.40 (4 %)	15.88 +/- 1.08 (7 %)	36.66 +/- 1.70 (5 %)	94.09 +/- 8.35 (9 %)	129.25 +/- 11.41 (9 %)	473.05 +/- 63.15 (13 %)	199.11 +/- 18.85 (9 %)	55.90 +/- 4.30 (8 %)	23.18 +/- 1.68 (7 %)	297.54 +/- 40.42 (14 %)	25.56 +/- 1.19 (5 %)	162.79 +/- 12.63 (8 %)	106.60 +/- 8.32 (8 %)
sm-lin-quad-mixed-cHbox-cHl1	154.13 +/- 14.42 (9 %)	23.47 +/- 1.05 (4 %)	37.77 +/- 2.86 (8 %)	33.18 +/- 1.41 (4 %)	15.70 +/- 1.08 (7 %)	36.58 +/- 1.71 (5 %)	97.68 +/- 8.92 (9 %)	132.67 +/- 11.96 (9 %)	474.98 +/- 64.18 (14 %)	205.11 +/- 19.83 (10 %)	55.52 +/- 4.30 (8 %)	22.92 +/- 1.68 (7 %)	299.06 +/- 41.16 (14 %)	25.45 +/- 1.19 (5 %)	166.17 +/- 13.27 (8 %)	108.77 +/- 8.72 (8 %)
sm	152.27 +/- 14.15 (9 %)	23.39 +/- 1.27 (5 %)	37.78 +/- 3.17 (8 %)	33.07 +/- 1.33 (4 %)	15.66 +/- 1.04 (7 %)	36.50 +/- 1.71 (5 %)	96.76 +/- 8.99 (9 %)	131.44 +/- 12.11 (9 %)	474.81 +/- 64.16 (14 %)	202.56 +/- 19.34 (10 %)	55.50 +/- 4.35 (8 %)	22.85 +/- 1.81 (8 %)	299.09 +/- 41.66 (14 %)	25.37 +/- 1.37 (5 %)	165.06 +/- 13.27 (8 %)	108.21 +/- 8.62 (8 %)
sm-lin-quad-mixed-cHWB-cHbox	150.29 +/- 13.79 (9 %)	23.41 +/- 1.04 (4 %)	37.99 +/- 2.83 (7 %)	33.04 +/- 1.40 (4 %)	15.92 +/- 1.09 (7 %)	36.76 +/- 1.70 (5 %)	95.07 +/- 8.46 (9 %)	130.57 +/- 11.59 (9 %)	473.24 +/- 63.16 (13 %)	201.70 +/- 19.27 (10 %)	55.93 +/- 4.30 (8 %)	23.26 +/- 1.68 (7 %)	297.66 +/- 40.44 (14 %)	25.68 +/- 1.19 (5 %)	163.93 +/- 12.78 (8 %)	107.23 +/- 8.41 (8 %)
signal	5940.62 +/- 89.24 (2 %)	1414.34 +/- 14.31 (1 %)	1737.69 +/- 21.21 (1 %)	1966.08 +/- 17.56 (1 %)	950.64 +/- 11.56 (1 %)	2256.23 +/- 19.01 (1 %)	3799.72 +/- 56.05 (1 %)	5287.46 +/- 75.47 (1 %)	17954.94 +/- 393.58 (2 %)	8061.71 +/- 123.46 (2 %)	2529.59 +/- 31.61 (1 %)	1325.58 +/- 16.13 (1 %)	11340.09 +/- 252.68 (2 %)	1633.04 +/- 13.96 (1 %)	6544.67 +/- 83.46 (1 %)	4328.32 +/- 55.54 (1 %)
Wjets-res-6	335.52 +/- 36.59 (11 %)	-	-	-	-	-	223.61 +/- 25.60 (11 %)	520.89 +/- 44.59 (9 %)	72.18 +/- 6.86 (10 %)	811.45 +/- 76.40 (9 %)	-	-	56.19 +/- 4.70 (8 %)	-	125.93 +/- 14.21 (11 %)	72.67 +/- 4.45 (6 %)
Wjets-res-4	1156.27 +/- 147.86 (13 %)	-	-	-	-	-	723.32 +/- 52.34 (7 %)	1550.33 +/- 174.38 (11 %)	200.02 +/- 12.11 (6 %)	2456.25 +/- 133.87 (5 %)	-	-	140.69 +/- 12.71 (9 %)	-	276.58 +/- 52.37 (19 %)	148.23 +/- 17.64 (12 %)
Wjets-res-5	450.12 +/- 41.46 (9 %)	-	-	-	-	-	273.91 +/- 22.88 (8 %)	573.44 +/- 66.58 (12 %)	72.62 +/- 10.50 (14 %)	938.04 +/- 70.54 (8 %)	-	-	47.38 +/- 3.73 (8 %)	-	93.24 +/- 6.13 (7 %)	58.22 +/- 8.48 (15 %)
Wjets-res-2	3740.80 +/- 413.10 (11 %)	-	-	-	-	-	2119.67 +/- 273.16 (13 %)	4693.37 +/- 618.31 (13 %)	446.07 +/- 44.38 (10 %)	7924.09 +/- 911.72 (12 %)	-	-	317.46 +/- 31.56 (10 %)	-	296.16 +/- 46.26 (16 %)	184.25 +/- 13.60 (7 %)
Wjets-res-3	2071.38 +/- 212.72 (10 %)	-	-	-	-	-	1228.14 +/- 141.74 (12 %)	2565.22 +/- 262.16 (10 %)	293.40 +/- 24.33 (8 %)	4399.09 +/- 449.27 (10 %)	-	-	154.10 +/- 22.13 (14 %)	-	278.51 +/- 73.05 (26 %)	171.84 +/- 27.30 (16 %)
Wjets-res-8	2642.87 +/- 415.16 (16 %)	-	-	-	-	-	1866.07 +/- 297.04 (16 %)	3912.15 +/- 548.71 (14 %)	312.62 +/- 35.05 (11 %)	5577.26 +/- 785.35 (14 %)	-	-	203.56 +/- 54.62 (27 %)	-	265.58 +/- 38.06 (14 %)	199.61 +/- 37.30 (19 %)
Wjets-res-9	1587.58 +/- 187.94 (12 %)	-	-	-	-	-	1133.98 +/- 142.94 (13 %)	2443.68 +/- 313.03 (13 %)	275.94 +/- 25.18 (9 %)	3505.42 +/- 452.52 (13 %)	-	-	183.47 +/- 20.95 (11 %)	-	261.73 +/- 63.33 (24 %)	181.89 +/- 24.48 (13 %)
Wjets-res-21	189.24 +/- 27.95 (15 %)	-	-	-	-	-	142.95 +/- 23.00 (16 %)	278.54 +/- 38.11 (14 %)	35.28 +/- 4.57 (13 %)	375.38 +/- 57.72 (15 %)	-	-	24.38 +/- 3.18 (13 %)	-	42.95 +/- 6.88 (16 %)	33.07 +/- 3.97 (12 %)
Wjets-res-20	79.81 +/- 8.73 (11 %)	-	-	-	-	-	66.74 +/- 11.31 (17 %)	135.44 +/- 19.48 (14 %)	18.44 +/- 1.89 (10 %)	186.51 +/- 21.26 (11 %)	-	-	15.32 +/- 1.22 (8 %)	-	25.40 +/- 3.99 (16 %)	19.77 +/- 6.09 (31 %)
VV-WZjj	475.90 +/- 52.31 (11 %)	51.54 +/- 4.36 (8 %)	40.35 +/- 3.66 (9 %)	72.56 +/- 5.40 (7 %)	44.85 +/- 3.46 (8 %)	8.73 +/- 0.56 (6 %)	329.56 +/- 34.50 (10 %)	407.23 +/- 37.52 (9 %)	301.82 +/- 34.61 (11 %)	593.26 +/- 55.75 (9 %)	57.01 +/- 5.21 (9 %)	60.89 +/- 4.40 (7 %)	209.80 +/- 25.17 (12 %)	6.69 +/- 0.46 (7 %)	87.26 +/- 7.93 (9 %)	59.65 +/- 5.48 (9 %)
VBF-V-dipole	193.99 +/- 41.14 (21 %)	22.77 +/- 4.06 (18 %)	20.08 +/- 5.70 (28 %)	69.49 +/- 7.54 (11 %)	79.95 +/- 11.40 (14 %)	28.63 +/- 8.94 (31 %)	130.25 +/- 21.74 (17 %)	624.58 +/- 138.71 (22 %)	57.11 +/- 14.73 (26 %)	968.84 +/- 203.90 (21 %)	44.69 +/- 4.12 (9 %)	96.29 +/- 16.37 (17 %)	44.90 +/- 11.49 (26 %)	18.06 +/- 2.05 (11 %)	66.22 +/- 13.51 (20 %)	43.98 +/- 16.87 (38 %)
VV-osWW	1499.62 +/- 188.24 (13 %)	177.20 +/- 13.63 (8 %)	65.70 +/- 6.03 (9 %)	242.55 +/- 19.22 (8 %)	101.99 +/- 6.96 (7 %)	30.84 +/- 1.79 (6 %)	1050.07 +/- 130.52 (12 %)	1369.90 +/- 131.27 (10 %)	428.57 +/- 54.00 (13 %)	1976.37 +/- 197.10 (10 %)	92.97 +/- 7.97 (9 %)	138.53 +/- 9.51 (7 %)	299.64 +/- 37.85 (13 %)	20.80 +/- 1.73 (8 %)	243.97 +/- 26.33 (11 %)	167.08 +/- 19.42 (12 %)
ggWW	75.40 +/- 2.23 (3 %)	9.11 +/- 0.28 (3 %)	0.74 +/- 0.07 (9 %)	11.96 +/- 0.36 (3 %)	3.15 +/- 0.09 (3 %)	4.48 +/- 0.16 (3 %)	51.89 +/- 1.64 (3 %)	59.70 +/- 1.81 (3 %)	6.88 +/- 0.20 (3 %)	85.90 +/- 2.53 (3 %)	3.25 +/- 0.15 (5 %)	3.94 +/- 0.15 (4 %)	6.83 +/- 0.53 (8 %)	3.91 +/- 0.16 (4 %)	20.01 +/- 0.59 (3 %)	11.42 +/- 0.33 (3 %)
VgS	25.59 +/- 0.84 (3 %)	1.37 +/- 0.07 (5 %)	0.21 +/- 0.01 (4 %)	1.15 +/- 0.04 (3 %)	1.59 +/- 0.06 (4 %)	3.09 +/- 0.20 (6 %)	22.99 +/- 0.73 (3 %)	48.67 +/- 2.06 (4 %)	2.21 +/- 0.14 (6 %)	54.52 +/- 1.80 (3 %)	0.14 +/- 0.02 (13 %)	2.03 +/- 0.12 (6 %)	1.94 +/- 0.06 (3 %)	0.13 +/- 0.01 (5 %)	2.78 +/- 0.10 (4 %)	2.78 +/- 0.12 (4 %)
Wjets-res-7	8433.06 +/- 2163.45 (26 %)	-	-	-	-	-	5786.66 +/- 1384.82 (24 %)	12458.46 +/- 2933.52 (24 %)	762.89 +/- 177.69 (23 %)	18044.38 +/- 4400.95 (24 %)	-	-	580.01 +/- 118.65 (20 %)	-	284.84 +/- 61.76 (22 %)	202.65 +/- 50.86 (25 %)
VV-WZll	77.72 +/- 9.79 (13 %)	15.23 +/- 0.95 (6 %)	3.91 +/- 0.36 (9 %)	12.38 +/- 1.32 (11 %)	10.02 +/- 0.70 (7 %)	1.32 +/- 0.11 (8 %)	99.07 +/- 11.89 (12 %)	101.85 +/- 8.65 (8 %)	13.90 +/- 1.55 (11 %)	88.89 +/- 8.15 (9 %)	2.90 +/- 0.28 (10 %)	8.57 +/- 0.71 (8 %)	16.70 +/- 1.90 (11 %)	1.83 +/- 0.19 (10 %)	11.16 +/- 1.06 (9 %)	15.17 +/- 1.75 (12 %)
Wjets-res-1	13879.82 +/- 3512.61 (25 %)	-	-	-	-	-	7961.37 +/- 1800.32 (23 %)	17124.52 +/- 3747.43 (22 %)	1067.68 +/- 201.41 (19 %)	29419.41 +/- 7335.69 (25 %)	-	-	703.17 +/- 122.47 (17 %)	-	267.22 +/- 62.93 (24 %)	186.67 +/- 57.79 (31 %)
VVV	17.02 +/- 1.76 (10 %)	3.60 +/- 0.33 (9 %)	1.76 +/- 0.10 (6 %)	5.05 +/- 0.50 (10 %)	1.55 +/- 0.14 (9 %)	0.44 +/- 0.07 (16 %)	12.82 +/- 1.43 (11 %)	11.63 +/- 1.54 (13 %)	6.01 +/- 0.51 (8 %)	17.37 +/- 1.61 (9 %)	1.84 +/- 0.29 (16 %)	2.26 +/- 0.14 (6 %)	4.93 +/- 0.82 (17 %)	0.41 +/- 0.12 (30 %)	3.00 +/- 0.33 (11 %)	3.48 +/- 0.63 (18 %)
Wjets-boost-3	-	366.73 +/- 25.24 (7 %)	55.44 +/- 4.92 (9 %)	510.20 +/- 37.39 (7 %)	396.36 +/- 32.04 (8 %)	44.29 +/- 4.47 (10 %)	-	-	-	-	84.06 +/- 6.89 (8 %)	565.35 +/- 43.58 (8 %)	-	24.54 +/- 2.06 (8 %)	-	-
Wjets-boost-2	-	278.05 +/- 25.23 (9 %)	52.43 +/- 3.85 (7 %)	442.86 +/- 31.18 (7 %)	333.13 +/- 28.02 (8 %)	42.05 +/- 3.44 (8 %)	-	-	-	-	92.32 +/- 8.73 (9 %)	518.64 +/- 40.94 (8 %)	-	21.41 +/- 1.39 (6 %)	-	-
Wjets-boost-1	-	141.91 +/- 11.43 (8 %)	22.44 +/- 1.64 (7 %)	244.69 +/- 17.14 (7 %)	135.23 +/- 8.57 (6 %)	13.50 +/- 1.86 (14 %)	-	-	-	-	39.94 +/- 2.45 (6 %)	235.57 +/- 16.29 (7 %)	-	9.81 +/- 0.76 (8 %)	-	-
Wjets-boost-7	-	72.14 +/- 9.48 (13 %)	14.14 +/- 2.33 (16 %)	99.68 +/- 15.35 (15 %)	168.89 +/- 17.25 (10 %)	20.81 +/- 1.35 (6 %)	-	-	-	-	20.27 +/- 3.15 (16 %)	213.27 +/- 24.69 (12 %)	-	18.02 +/- 1.60 (9 %)	-	-
Wjets-boost-6	-	128.88 +/- 15.53 (12 %)	20.18 +/- 3.32 (16 %)	171.75 +/- 17.55 (10 %)	173.33 +/- 16.99 (10 %)	19.30 +/- 2.51 (13 %)	-	-	-	-	21.04 +/- 4.30 (20 %)	259.71 +/- 27.44 (11 %)	-	18.99 +/- 3.23 (17 %)	-	-
Wjets-boost-5	-	319.94 +/- 33.55 (10 %)	51.57 +/- 3.47 (7 %)	401.82 +/- 45.72 (11 %)	392.88 +/- 36.99 (9 %)	44.71 +/- 4.31 (10 %)	-	-	-	-	72.28 +/- 5.24 (7 %)	533.74 +/- 48.86 (9 %)	-	33.49 +/- 2.50 (7 %)	-	-
Wjets-boost-4	-	276.07 +/- 31.06 (11 %)	52.95 +/- 5.12 (10 %)	368.03 +/- 48.20 (13 %)	312.32 +/- 30.02 (10 %)	30.09 +/- 2.71 (9 %)	-	-	-	-	59.75 +/- 9.49 (16 %)	415.92 +/- 46.65 (11 %)	-	28.87 +/- 3.98 (14 %)	-	-
top	6635.07 +/- 755.09 (11 %)	406.89 +/- 32.06 (8 %)	10503.14 +/- 902.19 (9 %)	581.46 +/- 39.36 (7 %)	221.65 +/- 11.47 (5 %)	52.19 +/- 4.37 (8 %)	4461.21 +/- 517.72 (12 %)	4080.80 +/- 392.78 (10 %)	153428.42 +/- 19133.16 (12 %)	6160.47 +/- 589.03 (10 %)	15008.53 +/- 1276.20 (9 %)	285.91 +/- 16.73 (6 %)	101275.03 +/- 12384.62 (12 %)	51.21 +/- 2.79 (5 %)	902.64 +/- 101.19 (11 %)	613.98 +/- 56.95 (9 %)
VV-ZZ	21.13 +/- 3.06 (15 %)	3.72 +/- 0.42 (11 %)	1.98 +/- 0.27 (13 %)	1.71 +/- 0.37 (22 %)	2.21 +/- 0.32 (15 %)	0.09 +/- 0.01 (9 %)	29.39 +/- 5.53 (19 %)	31.89 +/- 3.13 (10 %)	14.91 +/- 1.47 (10 %)	28.98 +/- 4.62 (16 %)	2.42 +/- 0.54 (22 %)	2.65 +/- 0.42 (16 %)	16.93 +/- 1.40 (8 %)	0.14 +/- 0.02 (16 %)	1.14 +/- 0.51 (44 %)	2.49 +/- 0.42 (17 %)
VV-ssWW	17.77 +/- 2.19 (12 %)	2.60 +/- 0.17 (7 %)	0.27 +/- 0.06 (21 %)	3.19 +/- 0.25 (8 %)	2.38 +/- 0.15 (6 %)	0.37 +/- 0.03 (8 %)	12.10 +/- 1.52 (13 %)	17.33 +/- 1.36 (8 %)	2.21 +/- 0.36 (16 %)	26.00 +/- 1.79 (7 %)	0.48 +/- 0.08 (18 %)	3.09 +/- 0.23 (7 %)	1.35 +/- 0.17 (13 %)	0.36 +/- 0.04 (10 %)	3.57 +/- 0.29 (8 %)	2.70 +/- 0.24 (9 %)
Fake	16127.36 +/- 4838.21 (30 %)	545.88 +/- 163.76 (30 %)	565.05 +/- 169.51 (30 %)	436.67 +/- 131.00 (30 %)	514.86 +/- 154.46 (30 %)	48.32 +/- 14.50 (30 %)	16197.38 +/- 4859.21 (30 %)	30313.29 +/- 9093.99 (30 %)	21244.50 +/- 6373.35 (30 %)	30406.53 +/- 9121.96 (30 %)	1590.72 +/- 477.22 (30 %)	432.83 +/- 129.85 (30 %)	6515.99 +/- 1954.80 (30 %)	42.45 +/- 12.74 (30 %)	1277.61 +/- 383.28 (30 %)	758.85 +/- 227.66 (30 %)
DY	3834.34 +/- 867.36 (23 %)	245.35 +/- 27.41 (11 %)	58.94 +/- 6.05 (10 %)	195.56 +/- 20.63 (11 %)	296.66 +/- 30.57 (10 %)	15.50 +/- 1.65 (11 %)	5935.73 +/- 1420.89 (24 %)	12404.98 +/- 2618.52 (21 %)	673.15 +/- 130.15 (19 %)	7890.56 +/- 1661.30 (21 %)	54.57 +/- 6.21 (11 %)	254.69 +/- 24.32 (10 %)	939.56 +/- 189.33 (20 %)	21.37 +/- 2.29 (11 %)	295.01 +/- 48.20 (16 %)	457.36 +/- 96.05 (21 %)
Wjets-res-18	227.65 +/- 32.81 (14 %)	-	-	-	-	-	164.05 +/- 30.50 (19 %)	393.37 +/- 46.35 (12 %)	52.87 +/- 5.77 (11 %)	495.97 +/- 57.54 (12 %)	-	-	37.70 +/- 5.37 (14 %)	-	72.81 +/- 7.90 (11 %)	60.36 +/- 8.51 (14 %)
Wjets-res-19	215.28 +/- 45.36 (21 %)	-	-	-	-	-	145.82 +/- 32.39 (22 %)	305.72 +/- 47.37 (15 %)	31.21 +/- 9.65 (31 %)	408.54 +/- 64.66 (16 %)	-	-	21.63 +/- 6.02 (28 %)	-	26.15 +/- 4.63 (18 %)	15.90 +/- 2.23 (14 %)
Wjets-res-10	1080.71 +/- 118.85 (11 %)	-	-	-	-	-	725.30 +/- 81.32 (11 %)	1532.77 +/- 168.62 (11 %)	169.53 +/- 21.49 (13 %)	2388.94 +/- 307.28 (13 %)	-	-	116.08 +/- 12.98 (11 %)	-	216.92 +/- 30.72 (14 %)	140.45 +/- 19.95 (14 %)
Wjets-res-11	389.93 +/- 36.81 (9 %)	-	-	-	-	-	266.95 +/- 32.54 (12 %)	587.38 +/- 57.80 (10 %)	66.94 +/- 10.69 (16 %)	905.77 +/- 115.63 (13 %)	-	-	51.58 +/- 7.25 (14 %)	-	97.15 +/- 13.72 (14 %)	69.21 +/- 6.56 (9 %)
Wjets-res-12	326.17 +/- 38.00 (12 %)	-	-	-	-	-	239.62 +/- 28.25 (12 %)	572.23 +/- 58.62 (10 %)	78.26 +/- 9.89 (13 %)	845.37 +/- 85.06 (10 %)	-	-	51.82 +/- 6.06 (12 %)	-	147.30 +/- 16.54 (11 %)	92.44 +/- 19.05 (21 %)
Wjets-res-13	2779.28 +/- 562.29 (20 %)	-	-	-	-	-	2088.37 +/- 459.46 (22 %)	4342.07 +/- 803.90 (19 %)	325.32 +/- 57.49 (18 %)	5652.59 +/- 1057.16 (19 %)	-	-	249.13 +/- 51.14 (21 %)	-	228.50 +/- 69.45 (30 %)	159.30 +/- 41.62 (26 %)
Wjets-res-14	425.55 +/- 53.26 (13 %)	-	-	-	-	-	316.59 +/- 51.32 (16 %)	686.14 +/- 112.36 (16 %)	71.09 +/- 6.61 (9 %)	902.20 +/- 123.24 (14 %)	-	-	49.65 +/- 6.63 (13 %)	-	94.02 +/- 13.63 (14 %)	60.53 +/- 7.00 (12 %)
Wjets-res-15	181.52 +/- 27.51 (15 %)	-	-	-	-	-	131.51 +/- 12.20 (9 %)	274.23 +/- 30.72 (11 %)	35.79 +/- 6.77 (19 %)	376.01 +/- 43.56 (12 %)	-	-	32.11 +/- 5.46 (17 %)	-	46.41 +/- 8.67 (19 %)	30.67 +/- 4.60 (15 %)
Wjets-res-16	145.96 +/- 19.75 (14 %)	-	-	-	-	-	109.09 +/- 9.86 (9 %)	281.89 +/- 36.45 (13 %)	38.18 +/- 3.10 (8 %)	367.16 +/- 38.63 (11 %)	-	-	25.39 +/- 3.09 (12 %)	-	63.88 +/- 6.32 (10 %)	51.07 +/- 5.06 (10 %)
Wjets-res-17	760.17 +/- 151.94 (20 %)	-	-	-	-	-	549.85 +/- 111.08 (20 %)	1063.28 +/- 172.15 (16 %)	82.79 +/- 14.95 (18 %)	1356.66 +/- 214.00 (16 %)	-	-	71.02 +/- 16.27 (23 %)	-	71.89 +/- 15.31 (21 %)	47.20 +/- 7.36 (16 %)
Vg	468.52 +/- 26.96 (6 %)	35.94 +/- 1.92 (5 %)	0.72 +/- 0.04 (6 %)	27.41 +/- 1.70 (6 %)	52.11 +/- 2.70 (5 %)	3.72 +/- 0.27 (7 %)	389.13 +/- 18.87 (5 %)	833.22 +/- 41.12 (5 %)	79.09 +/- 5.32 (7 %)	1068.20 +/- 53.90 (5 %)	8.10 +/- 0.56 (7 %)	36.92 +/- 2.07 (6 %)	13.01 +/- 0.81 (6 %)	3.97 +/- 0.41 (10 %)	47.60 +/- 2.89 (6 %)	48.93 +/- 2.41 (5 %)
background	70568.14 +/- 6527.10 (9%)	3104.92 +/- 180.69 (6%)	11531.99 +/- 918.10 (8%)	3900.15 +/- 164.98 (4%)	3245.11 +/- 172.81 (5%)	412.48 +/- 19.61 (5%)	54985.18 +/- 5614.42 (10%)	106600.21 +/- 10677.97 (10%)	180767.90 +/- 20169.29 (11%)	136702.41 +/- 12758.37 (9%)	17257.27 +/- 1362.66 (8%)	4070.82 +/- 166.98 (4%)	112478.47 +/- 12540.96 (11%)	326.45 +/- 14.99 (5%)	6245.17 +/- 437.06 (7%)	4373.86 +/- 277.60 (6%)

Table C.3: Yields of the VBS WV backgrounds and of the 45 EFT templates according to the statistical model defined in Section 4.2.4 for the 2018 year. All signal and control regions are provided and split for lepton flavour (e, μ).

One dimensional EFT constraints

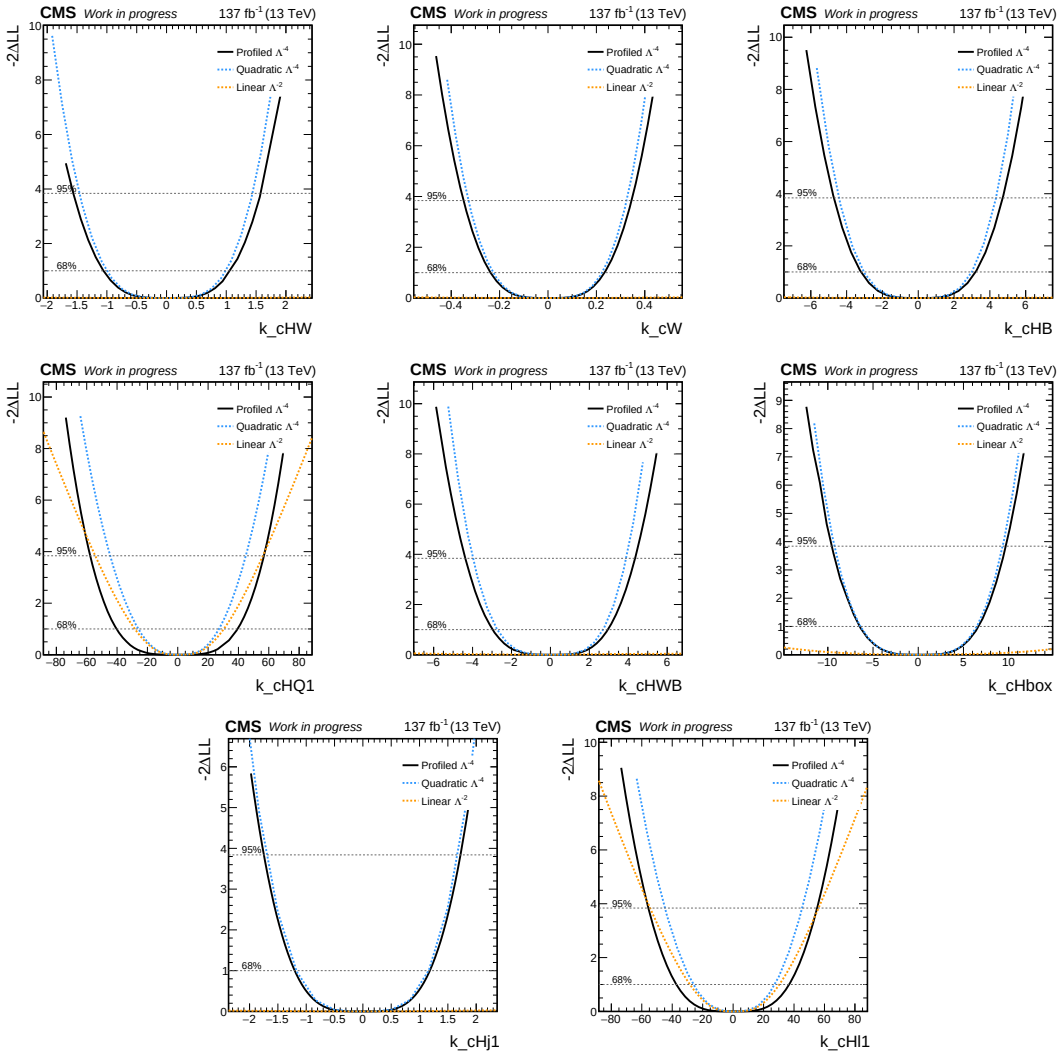

Figure C.1: One dimensional likelihood profiles for all the eight studied in the VBS WV analysis. In the maximum likelihood fits all Wilson coefficients are left free to float including linear and quadratic contributions (Black), freezed to their SM expectation including linear and quadratic contributions (blue) and freezed to their SM expectation including linear-only contributions (orange). Data in the CR are used to constrain nuisances and to allow the W+jets differential data-driven correction.

Bi-dimensional EFT constraints

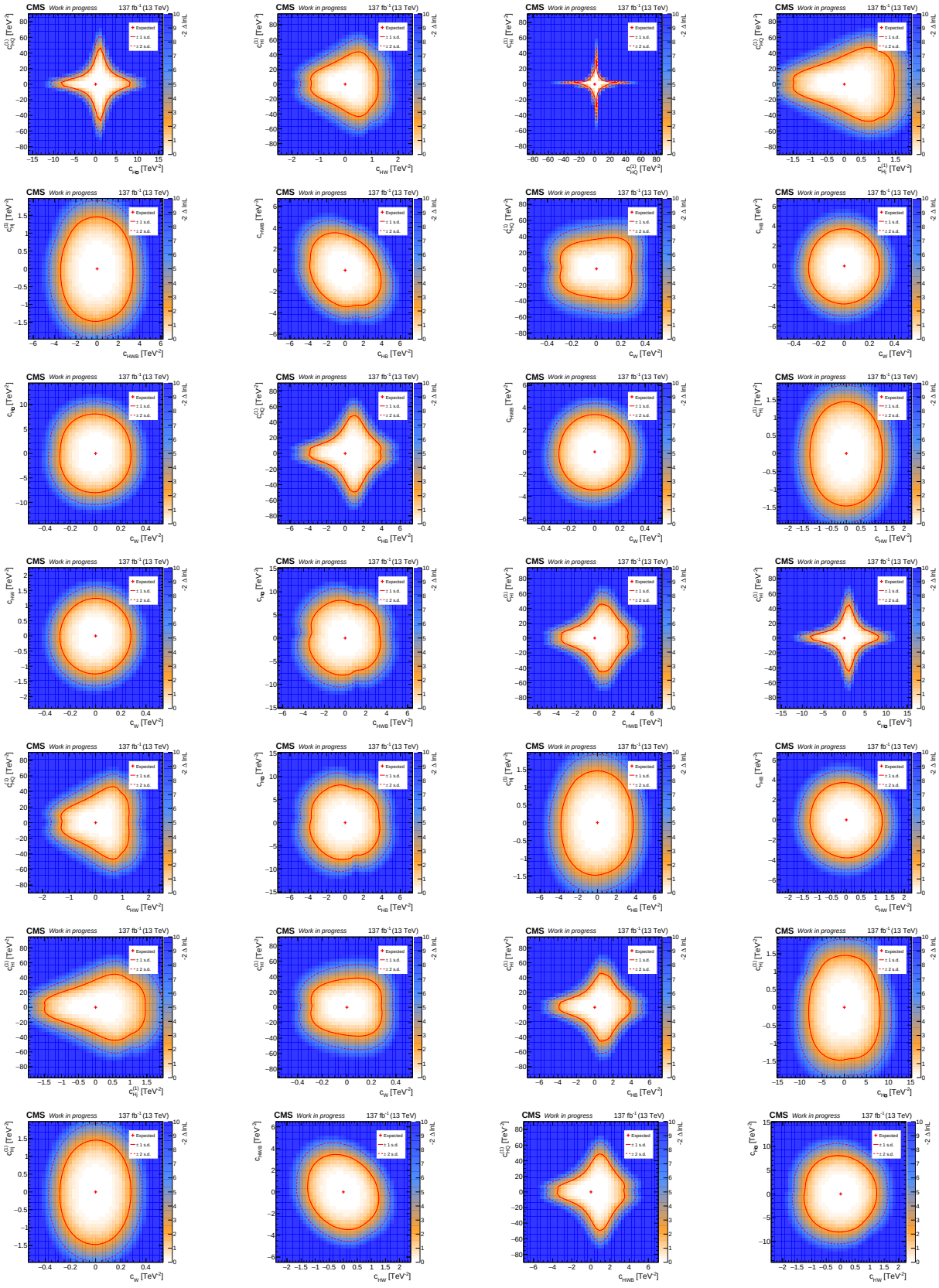

Figure C.2: Bi-dimensional likelihood profiles for all possible pairs of Wilson coefficients from the eight studied in the VBS WV analysis. In the maximum likelihood fits only two Wilson coefficients are free to float while the other ones are freezed to their SM value. All nuisances, the differential W+jets correction and top sample normalization are included in the fit. Data in the CR are used to constrain nuisances and to allow the W+jets differential data-driven correction.

Appendix D

VBS combination post-fit distributions

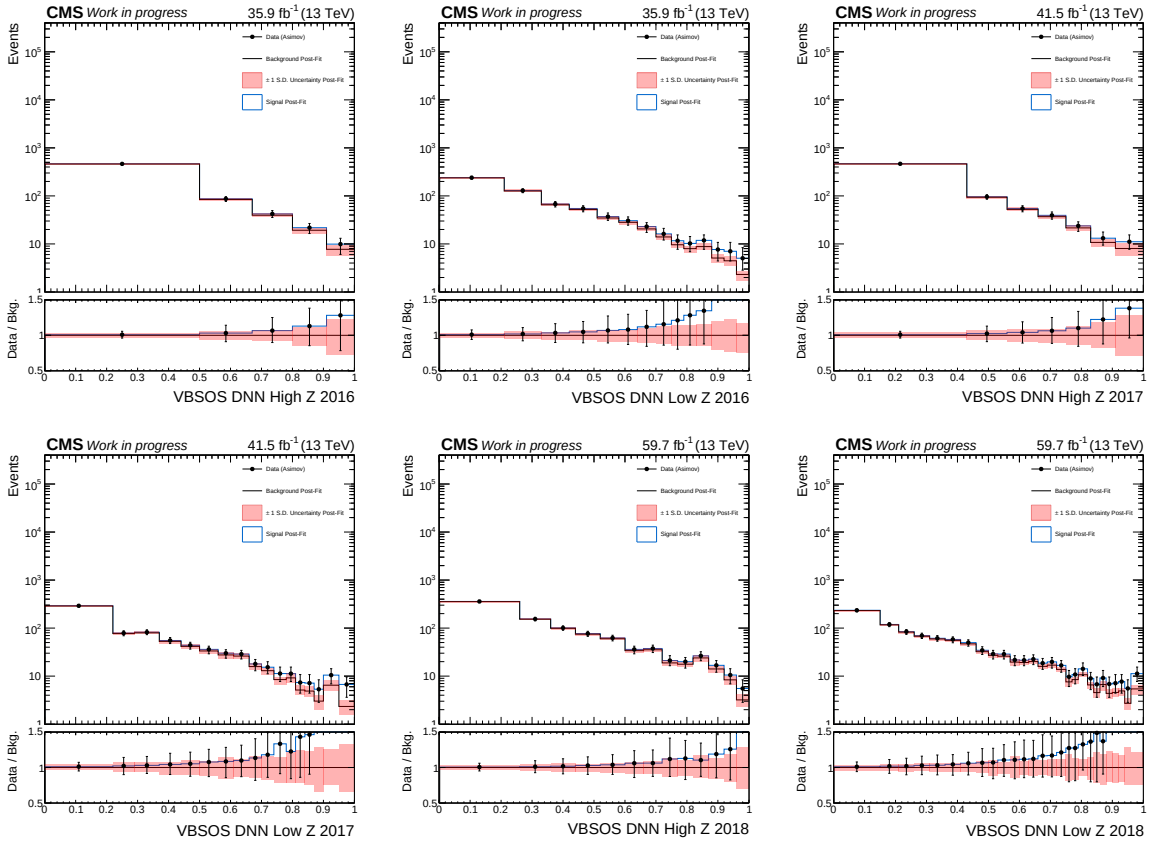

Figure D.1: Post-fit distributions of the DNN scores of the OSWW analysis in the signal $e\mu$ region. The signal region is split in two sub-regions with low and high values of the Zeppenfeld variable (Z_{ll}). From left to right, top to bottom: 2016 high Z_{ll}, 2016 low Z_{ll}, 2017 high Z_{ll}, 2017 low Z_{ll}, 2018 high Z_{ll}, 2018 low Z_{ll}

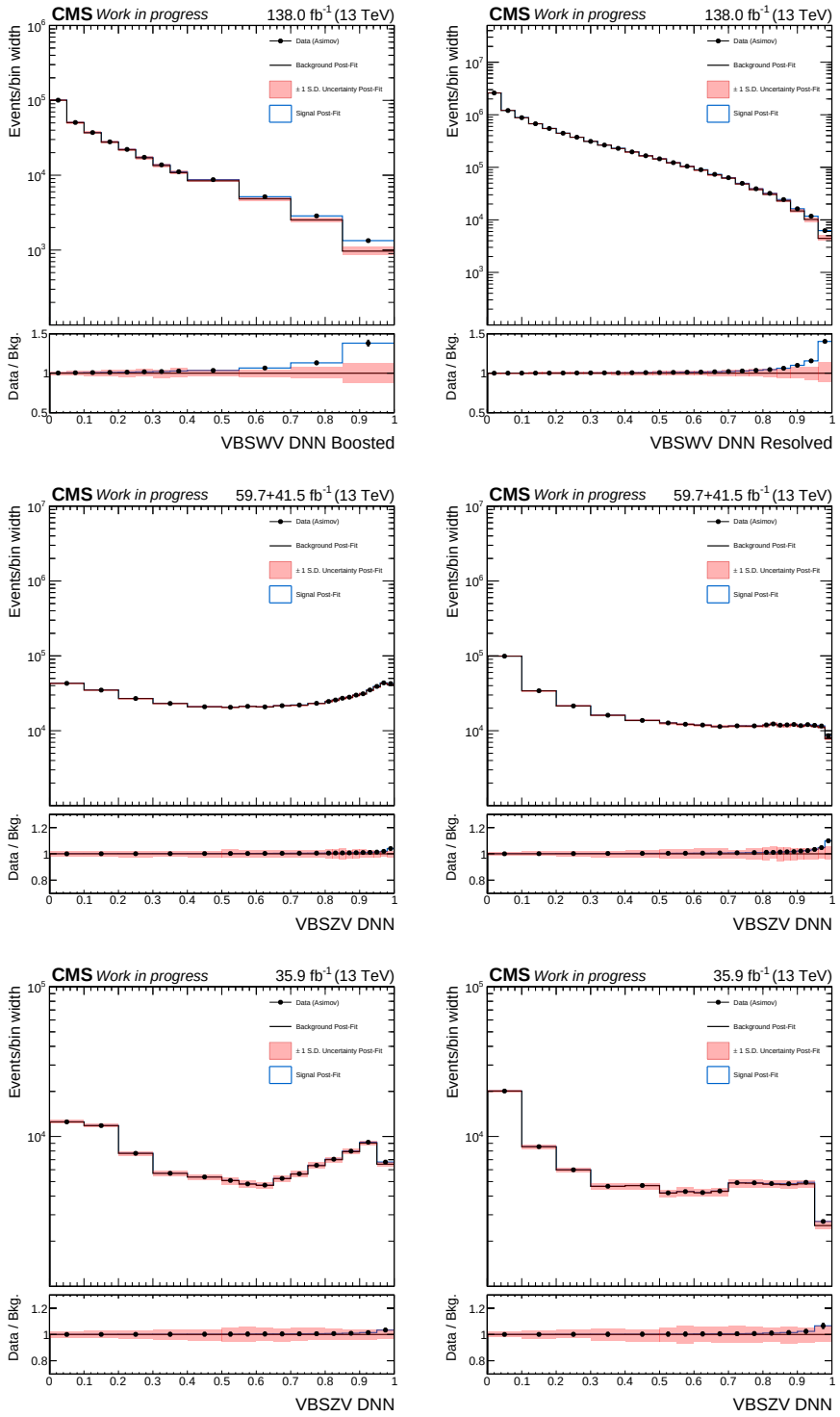

Figure D.2: Post-fit distributions for the signal regions of the semileptonic VBS analyses. The top row shows the DNN spectra of the WV analysis merged for the electron and muon cateogries in the boosted signal region (left) and in the resolved signal region (right). The middle and bottom rows show the DNN spectra of the ZV analysis from left to right, top to bottom: 2017+2018 *b*-tag region, 2017+2018 *b*-veto region, 2016 *b*-tag region, 2016 *b*-veto region

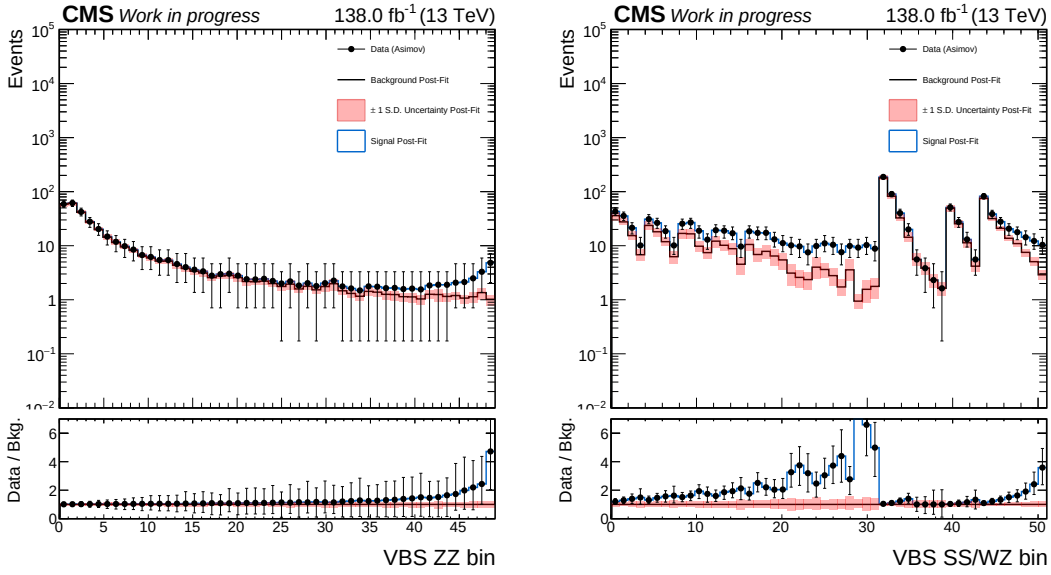

Figure D.3: Post-fit distributions for the VBS-ZZ(4l) signal region (left) showing the K_D discriminant used to separate the VBS EW ZZ production from the QCD-induced one. The right plot shows the distribution of the SSWW and WZ analyses in all signal and control regions entering in the combined fit.